OCTOBER 2019

AJNR

VOLUME 40 • PP 1609–1790

AJNR
AMERICAN JOURNAL OF NEURORADIOLOGY

OCTOBER 2019
VOLUME 40
NUMBER 10
WWW.AJNR.ORG

THE JOURNAL OF DIAGNOSTIC AND INTERVENTIONAL NEURORADIOLOGY

Board certification characteristics of practicing neuroradiologists

Intracranial hemorrhage in Moyamoya

Vessel wall MRI in patients with ischemic stroke

Official Journal ASNR • ASFNR • ASHNR • ASPNR • ASSR

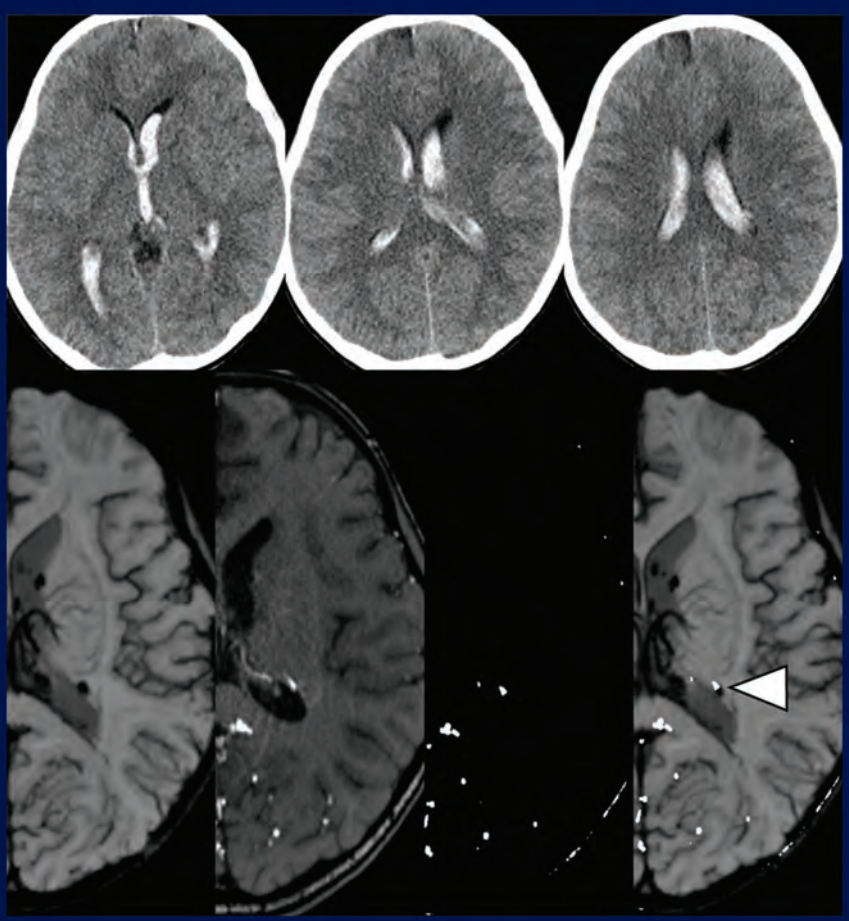

MicroVention®
TERUMO

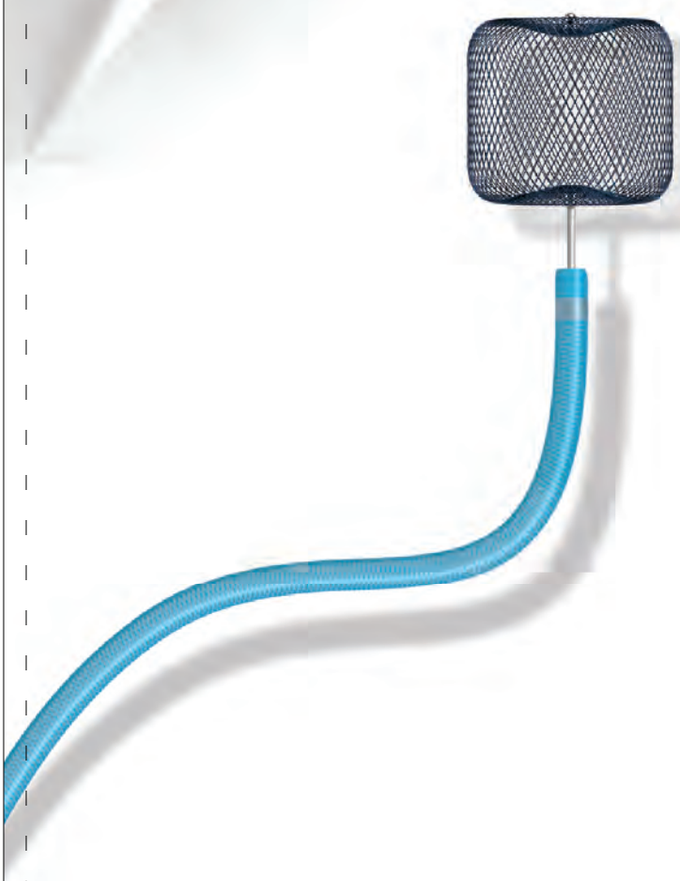

NE AND DONE

INDICATIONS FOR USE:

The WEB Aneurysm Embolization System is indicated for use at the middle cerebral artery (MCA) bifurcation, internal carotid artery (ICA) terminus, anterior communicating artery (AComm) complex, or basilar artery apex for the endovascular treatment of adult patients with saccular, wide neck bifurcation intracranial aneurysms with dome diameter from 3 mm to 10 mm and either neck size 4 mm or greater or the dome-to-neck ratio is greater than 1 and less than 2.

The WEB Aneurysm Embolization System is contraindicated for patients with known bacterial infection that may interfere with or negatively affect the implantation procedure and patients with known hypersensitivity to nickel. For complete indications, contraindications, potential complications, warnings, precautions, and instructions, see instructions for use (IFU provided with the device).

The VIA® Catheter is intended for the introduction of non-liquid interventional devices (such as stents/_ ow diverters) and infusion of diagnostic (such as contrast media) or non-liquid therapeutic agents into the neuro, peripheral, and coronary vasculature. The VIA Catheter is contraindicated for use with liquid embolic materials, such as n-butyl 2-cyanoacrylate or ethylene vinyl alcohol & DMSO (dimethyl sulfoxide). The VIA Catheter is contraindicated for use in the pediatric population (<22 yrs of age).

Caution: Federal law restricts these devices to sale by or on the order of a physician.

CE 0297

WEB®

Aneurysm Embolization System

MicroVention® delivers the first intrasaccular solution for wide neck bifurcation aneurysms.

The **world leader** and **first PMA-approved device** in an important new category of intrasaccular flow disruptors.

The WEB® System is a safe and effective single-device solution for treating wide neck bifurcation aneurysms.

SL Device

SLS Device

Contact a MicroVention sales associate to learn more about integrating the WEB® device into your practice.

MicroVention® TERUMO

MicroVention Worldwide Innovation Center PH +1.714.247.8000
35 Enterprise
Aliso Viejo, CA 92656 USA
MicroVention UK Limited PH +44 (0) 191 258 6777
MicroVention Europe, S.A.R.L. PH +33 (1) 39 21 77 46
MicroVention Deutschland GmbH PH +49 211 210 798-0
microvention.com

stryker

Become elite

Upgrade to the iVAS Elite system and gain total control over your procedural approach

When we added the iVAS Elite system to our industry-leading portfolio, your single source became your elite source for vertebral augmentation.

strykerivs.com/ivas-elite

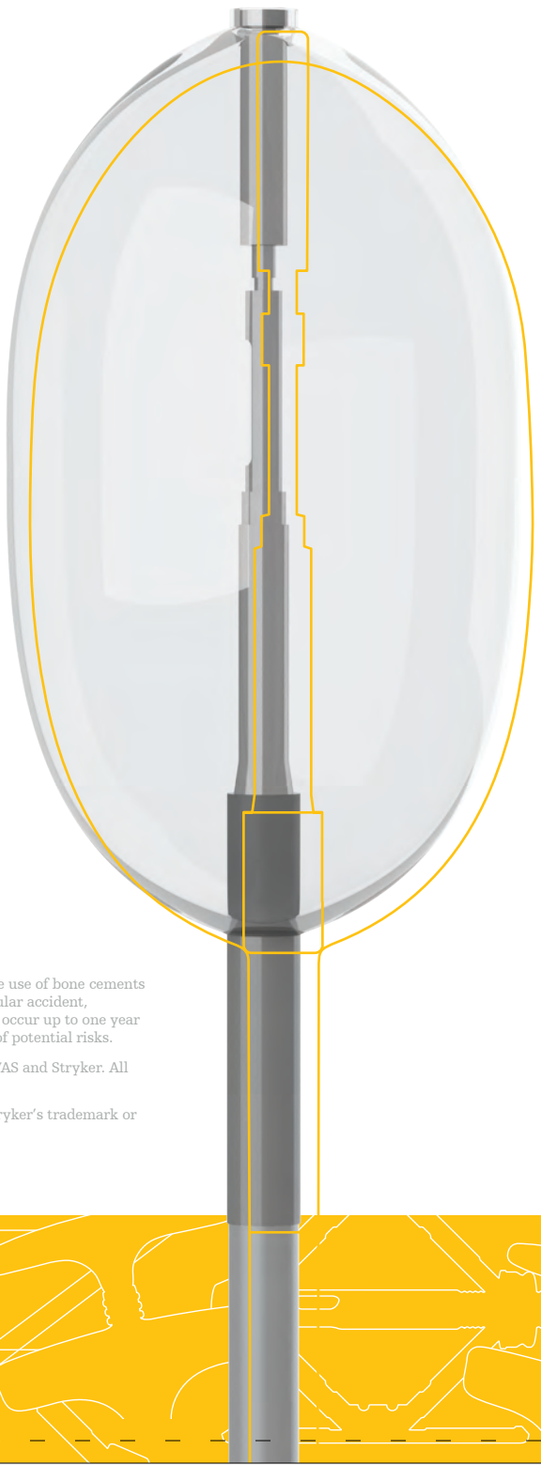

Bone cement: Complications are rare. Serious adverse events, some with fatal outcome, associated with the use of bone cements for vertebroplasty, kyphoplasty and sacroplasty include myocardial infarction, cardiac arrest, cerebrovascular accident, pulmonary embolism, and cardiac embolism. Although it is rare, some adverse events have been known to occur up to one year post-operatively. Additional risks exist with the use of bone cement. Please see the IFU for a complete list of potential risks.

D0000018656 | Copyright © 2019 Stryker

stryker

The results say it all

Now **PMA** approved

Clinically proven

84.7%
Primary efficacy endpoint

Safe

4.4%
Primary safety endpoint

Durable

3.8%
Retreatment rate

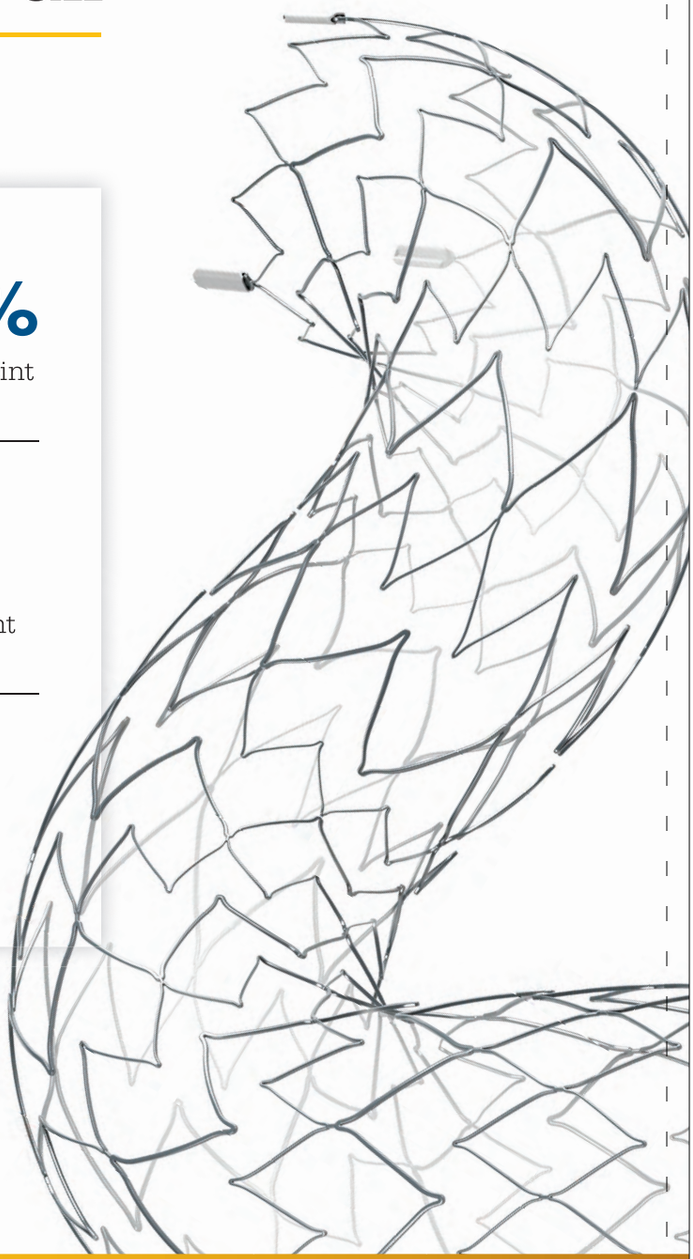

The ATLAS IDE Study is the largest of its class with **182 patients treated.**

Neuroform Atlas®
Stent System

ASNR 58th Annual Meeting & The Foundation of the ASNR Symposium 2020

CALL FOR ABSTRACTS

Join us May 30-June 4, 2020 at Caesars Palace in Las Vegas to present the best scientific research in Neuroradiology.

Submission Deadline: Friday, November 1, 2019 (8:00PM EST)

Submit online at ASNR.org/AnnualMeeting

Acceptance notifications will be sent on or before January 15, 2020 upon conclusion of peer review.

Submit an abstract for the ASNR 58th Annual Meeting (May 30 - June 4, 2020, Las Vegas, NV) in one of the following presentation categories:

- Scientific Paper . . . . . Oral
- Excerpta . . . . . Oral
- Scientific Poster . . . . . Print
- Electronic Scientific Poster . . . . Electronic
- Electronic Educational Exhibit . . Electronic
- Educational Exhibit Poster . . . . . Print

Abstract Submissions Information and Criteria

1. Abstracts should describe the learning objectives of the presentation.
2. The *American Journal of Neuroradiology (AJNR)* encourages presenters to submit manuscripts based on their work to *AJNR* before considering other journals.
3. Presenters of accepted abstracts **must register** for the ASNR 58th Annual Meeting and/or the Foundation of the ASNR Symposium 2020.
4. Published or previously presented works should NOT be submitted.
5. Submission topic areas include: **Adult Brain, Spine, Head and Neck, Pediatrics, Functional/Advanced Imaging, Interventional, Health Policy, AI/ Informatics, and Professional Development**.
6. Submit each abstract in **one** category only.
7. Format abstract text using headings required for submission category.
8. Maximum length: **2,500 characters**, not including title, authors, images, figures.
9. Submission site allows uploading of files into the system.
10. Changes can be made to the abstract until the deadline.

Questions?

Contact the ASNR Education Department at ekruse@asnr.org.

ASNR
American Society of Neuroradiology

AJNR go green

AJNR urges American Society of Neuroradiology members to reduce their environmental footprint by voluntarily suspending their print subscription.

The savings in paper, printing, transportation, and postage directly fund new electronic enhancements and expanded content.

The digital edition of *AJNR* presents the print version in its entirety, along with extra features including:

- **Publication Preview**
- **Case Collection**
- **Podcasts**
- **The *AJNR* News Digest**
- **The *AJNR* Blog**

It also reaches subscribers much faster than print. An electronic table of contents will be sent directly to your mailbox to notify you as soon as it publishes.

Readers can search, reference, and bookmark current and archived content 24 hours a day on www.ajnr.org.

ASNR members who wish to opt out of print can do so by using the AJNR Go Green link on the *AJNR* Website (http://www.ajnr.org/content/subscriber-help-and-services). Just type your name in the email form to stop print and spare our ecosystem.

Simplify
the MOC Process

Manage
your CME Credits Online

CMEgateway.org

It's Easy and Free!

Log on to CME Gateway to:

- View or print reports of your CME credits from multiple societies from a single access point.
- Print an aggregated report or certificate from each participating organization.
- Link to SAMs and other tools to help with maintenance of certification.

American Board of Radiology (ABR) participation!

By activating ABR in your organizational profile, your MOC–fulfilling CME and SAM credits can be transferred to your own personalized database on the ABR Web site.

Sign Up Today!

go to CMEgateway.org

Available to Members of Participating Societies

- American Board of Radiology (ABR)
- American College of Radiology (ACR)
- American Roentgen Ray Society (ARRS)
- American Society of Neuroradiology (ASNR)
- Commnission on Accreditation of Medical Physics Educational Programs, Inc. (CAMPEP)
- Radiological Society of North America (RSNA)
- Society of Interventional Radiology (SIR)
- SNM
- The Society for Pediatric Radiology (SPR)

Neuroform Atlas® Stent System

RX ONLY

See package insert for complete indications, contraindications, warnings and instructions for use.

Indications for use

The Neuroform Atlas Stent System is indicated for use with neurovascular embolization coils in the anterior circulation of the neurovasculature for the endovascular treatment of patients ≥ 18 years of age with saccular wide-necked (neck width ≥ 4 mm or a dome-to-neck ratio of < 2) intracranial aneurysms arising from a parent vessel with a diameter of ≥ 2.0 mm and ≤ 4.5 mm.

Contraindications

- Patients in whom the parent vessel size does not fall within the indicated range.
- Patients in whom antiplatelet and/or anticoagulation therapy (e.g., aspirin and clopidogrel) is contraindicated.
- Patients who have not received anti-platelet agents prior to stent implantation.
- Patients with an active bacterial infection.
- Patients in whom angiography demonstrates the anatomy is not appropriate for endovascular treatment due to conditions such as:
- Severe intracranial vessel tortuosity or stenosis;
- Intracranial vasospasm not responsive to medical therapy.
- Patients in whom a pre-existing stent is in place in the parent artery at the target intracranial aneurysm location.

Potential adverse events

The potential adverse events listed below, as well as others, may be associated with the use of the Neuroform Atlas Stent System or with the procedure:

- Aphasia
- Allergic reaction to Nitinol metal and medications
- Aneurysm perforation/rupture, leak or contrast extravasation
- Blindness
- Cardiac arrhythmia
- Coil herniation through stent into parent vessel
- Cranial neuropathy
- Death
- Embolus
- Headache
- Hemiplegia
- Hemorrhage (i.e., intracerebral, subarachnoid, retroperitoneal, or in other locations)
- Hydrocephalus
- In-stent stenosis
- Infection
- Ischemia
- Mass effect
- Myocardial infarction
- Neurological deficit/intracranial sequelae
- Pseudoaneurysm
- Reaction to radiation exposure (i.e., alopecia, burns ranging in severity from skin reddening to ulcers, cataracts, or delayed neoplasia)
- Reactions to anti-platelet/anti-coagulant agents
- Renal failure
- Seizure
- Stent fracture, migration/embolization, or misplacement
- Stent thrombosis
- Stroke
- Transient ischemic attack
- Vasospasm
- Vessel occlusion or closure including parent vessel or non-target side-branches
- Vessel perforation/rupture, dissection, trauma or damage
- Vessel thrombosis
- Visual impairment
- Other procedural complications including but not limited to anesthetic and contrast media risks, hypotension, hypertension, access site complications (including pain, hematoma, local bleeding, local infection, and injury to the artery (i.e. dissection), vein, or adjacent nerves)
- Unplanned intervention

Warnings

Contents supplied STERILE using an ethylene oxide (EO) process. Do not use if sterile barrier is damaged. If damage is found, call your Stryker Neurovascular representative.

For single use only. Do not reuse, reprocess or resterilize. Reuse, reprocessing or resterilization may compromise the structural integrity of the device and/or lead to device failure which, in turn, may result in patient injury, illness or death. Reuse, reprocessing or resterilization may also create a risk of contamination of the device and/or cause patient infection or cross-infection, including, but not limited to, the transmission of infectious disease(s) from one patient to another. Contamination of the device may lead to injury, illness or death of the patient.

After use, dispose of product and packaging in accordance with hospital, administrative and/or local government policy.

- This device should only be used by physicians who have received appropriate training in interventional neuroradiology or interventional radiology and preclinical training on the use of this device as established by Stryker Neurovascular.
- Persons allergic to nickel titanium (Nitinol) may suffer an allergic response to this stent implant.
- Higher adverse event rates may be experienced for distal aneurysms located in the anterior and middle cerebral arteries.
- Do not use device to treat patients with ruptured intracranial aneurysms within a minimum of 30 days from the aneurysm rupture.

Cautions / precautions

- Take all necessary precautions to limit X-ray radiation doses to clinical operators by using sufficient shielding, reducing fluoroscopy times, and modifying X-ray technical factors whenever possible.
- The Neuroform Atlas stent may create local field inhomogeneity and susceptibility artifacts during magnetic resonance angiography (MRA), which may degrade the diagnostic quality to assess effective intracranial aneurysm occlusion.
- Safety and effectiveness of the Neuroform Atlas Stent System in patients below the age of 18 has not been established.
- The benefits may not outweigh the risks of device use in patients with small and medium asymptomatic extradural intracranial aneurysms, including those located in the cavernous internal carotid artery.
- Carefully weigh the benefits vs. risks of device treatment for each individual patient based on their medical health status and risk factors for intracranial aneurysm rupture during their expected life time such as age, comorbidities, history of smoking, intracranial aneurysm size, location, and morphology, family history, history of prior asymptomatic subarachnoid hemorrhage (aSAH), documented growth of intracranial aneurysm on serial imaging, presence of multiple intracranial aneurysms, and presence of concurrent pathology. The benefits may not outweigh the risks associated with device use in certain patients; therefore, judicious patient selection is recommended based on clinical practice guidelines or tools to assess the life time risk of intracranial aneurysm rupture.

Safety Information Magnetic Resonance Conditional

Non-clinical testing and analysis have demonstrated that the Neuroform Atlas Stent is MR Conditional alone, or when overlapped with a second stent, and adjacent to a Stryker Neurovascular coil mass. A patient with the Neuroform Atlas Stent can be safely scanned immediately after placement of this implant, under the following conditions:

- Static magnetic field of 1.5 and 3.0 Tesla
- Maximum spatial gradient field up to 2500 Gauss/cm (25 Tesla/m)
- Maximum MR system reported whole body averaged specific absorption rate of 2 W/kg (Normal Operating Mode) and head averaged specific absorption rate of 3.2 W/kg.

Under the scan conditions defined above, the Neuroform Atlas Stent is expected to produce a maximum temperature rise of 4 °C after 15 minutes of continuous scanning. The Neuroform Atlas Stent should not migrate in this MRI environment.

In non-clinical testing, the image artifact caused by the device extends approximately 2 mm from the Neuroform Atlas Stent when imaged with a spin echo pulse sequence and 3 Tesla MRI System. The artifact may obscure the device lumen. It may be necessary to optimize MR imaging parameters for the presence of this implant. See additional precaution related to the image artifact from the implant in the "Precautions" section of this labeling.

Stryker Neurovascular
47900 Bayside Parkway
Fremont, CA 94538

strykerneurovascular.com

Date of Release: MAY/2019

EX_EN_US

AXS Catalyst® Distal Access Catheter

RX ONLY

See package insert for complete indications, complications, warnings, and instructions for use.

Indication for use as a conduit

The AXS Catalyst Distal Access Catheter is indicated for use in facilitating the insertion and guidance of appropriately sized interventional devices into a selected blood vessel in the peripheral and neurovascular systems. The AXS Catalyst Distal Access Catheter is also indicated for use as a conduit for retrieval devices.

Indication for use as a revascularization device

The AXS Catalyst Distal Access Catheter is indicated for use in the revascularization of patients with acute ischemic stroke secondary to intracranial large vessel occlusive disease (in the internal carotid, middle cerebral - M1 and M2 segments, basilar, and vertebral arteries) within 8 hours of symptom onset. Patients who are ineligible for intravenous tissue plasminogen activator (IV t-PA) or who failed IV t-PA are candidates for treatment.

Device description when use as a revascularization device

The AXS Universal Aspiration System is composed of the following components:

- AXS Catalyst Distal Access Catheter
- AXS Universal Aspiration Tubing
- Medela Dominant Flex Pump
- AXS Universal Liner Set

The AXS Universal Aspiration System is designed to remove thrombus from the neurovasculature using continuous aspiration.

The AXS Catalyst Distal Access Catheter delivers aspiration from the Medela Dominant Flex Pump directly to the site of the occlusion to remove the clot. The AXS Catalyst Distal Access Catheter is a sterile, single lumen, variable stiffness catheter. The catheter shaft has a hydrophilic coating to reduce friction during use, includes a radiopaque marker on the distal end for angiographic visualization, and includes a luer hub on the proximal end allowing attachments for flushing and aspiration. It is packaged with a Rotating Hemostasis Valve (RHV), Tuohy Borst Valve with Sideport, and Peel Away Introducer. The Rotating Hemostasis Valve and Tuohy Borst valve with sideport are used for flushing, insertion of catheters, and aspiration. The peel away introducer sheaths are designed to protect the distal tip of the catheter during insertion into the RHV or Tuohy Borst. The AXS Catalyst Distal Access Catheter is the only component of the AXS Universal Aspiration System that is used intravascularly.

AXS Universal Aspiration System
The AXS Universal Aspiration Tubing serves as a conduit to supply vacuum from the Medela Dominant Flex Pump to the distal tip of the AXS Catalyst Distal Access Catheter. The AXS Universal Aspiration Tubing provides a connection between the sterile and non-sterile environments. The proximal end of the AXS Universal Aspiration Tubing is connected to the AXS Universal Liner Set (outside of the sterile environment) while the distal end of the AXS Universal Aspiration Tubing is connected to the AXS Catalyst Distal Access Catheter (inside the sterile environment). The AXS Universal Liner Set is connected to the Medela Dominant Flex Pump (also outside of the sterile environment).

The Medela Dominant Flex Pump is designed to generate vacuum for the AXS Universal Aspiration System. When used as part of the AXS Universal Aspiration System, the AXS Catalyst Distal Access Catheter requires a minimum vacuum pressure of -68 kPa [-20.08 in Hg] from the Medela Dominant Flex Pump. The Medela Dominant Flex Pump is reusable, non-sterile, and intended to be utilized outside of the sterile environment.

The AXS Universal Liner Set is provided non-sterile and consists of an individually packaged canister liner and a ClotFinder specimen cup. The AXS Universal Liner Set is offered with and without a desiccant. The AXS Universal Liner Set is single-use and the repository for aspirated material.

Contraindications

None known.

Adverse events

Potential adverse events associated with the use of catheters or with the endovascular procedures include, but are not limited to:

- Access site complications
- Allergic reaction
- Aneurysm perforation
- Aneurysm rupture
- Death
- Embolism (air, foreign body, plaque, thrombus)
- Hematoma
- Hemorrhage
- Infection
- Ischemia
- Neurological deficits
- Pseudoaneurysm
- Stroke
- Transient Ischemic Attack
- Vasospasm
- Vessel dissection
- Vessel occlusion
- Vessel perforation
- Vessel rupture
- Vessel thrombosis

Use of device requires fluoroscopy which presents potential risks to physicians and patients associated with x-ray exposure. Possible risks include, but are not limited to, the following:

- Alopecia
- Burns ranging in severity from skin reddening to ulcers
- Cataracts
- Delayed neoplasia

Warnings for both indications

Contents supplied STERILE using an ethylene oxide (EO) process. Do not use if sterile barrier is damaged. If damage is found, call your Stryker Neurovascular representative.

For single use only. Do not reuse, reprocess or resterilize. Reuse, reprocessing or resterilization may compromise the structural integrity of the device and/or lead to device failure which, in turn, may result in patient injury, illness or death. Reuse, reprocessing or resterilization may also create a risk of contamination of the device and/or cause patient infection or cross-infection, including, but not limited to, the transmission of infectious disease(s) from one patient to another. Contamination of the device may lead to injury, illness or death of the patient.

After use, dispose of product and packaging in accordance with hospital, administrative and/or local government policy.

- Limited testing has been performed with solutions such as contrast media, and saline. The use of these catheters for delivery of solutions other than the types that have been tested for compatibility is not recommended.
- Not intended for use with power injectors.
- If flow through catheter becomes restricted, do not attempt to clear catheter lumen by infusion. Doing so may cause catheter damage or patient injury. Remove and replace catheter.
- Never advance or withdraw an intravascular device against resistance until the cause of the resistance is determined by fluoroscopy. Movement of the device against resistance could dislodge a clot, perforate a vessel wall, or damage the device.

Additional warning for revascularization indication only

- Excessive aspiration may cause patient complications.

Precautions

- Carefully inspect all devices prior to use. Verify size, length, and condition are suitable for the specific procedure. Ensure the catheter's labeled outer diameter is smaller than the treatment vessel diameter. Do not use a device that has been damaged in any way. Damaged device may cause complications.
- To control the proper introduction, movement, positioning and removal of the catheter within the vascular system, users should employ standard clinical angiographic and fluoroscopic practices and techniques throughout the interventional procedure.
- Use the product prior to the "Use By" date printed on the label.
- To prevent thrombus formation and contrast media crystal formation, maintain a constant infusion of appropriate flush solution through catheter lumen.
- Torquing the catheter may cause damage which could result in kinking or separation of the catheter shaft.

Stryker Neurovascular
47900 Bayside Parkway
Fremont, CA 94538

strykerneurovascular.com

Date of Release: MAY/2019

EX_EN_US

stryker

Trap more.

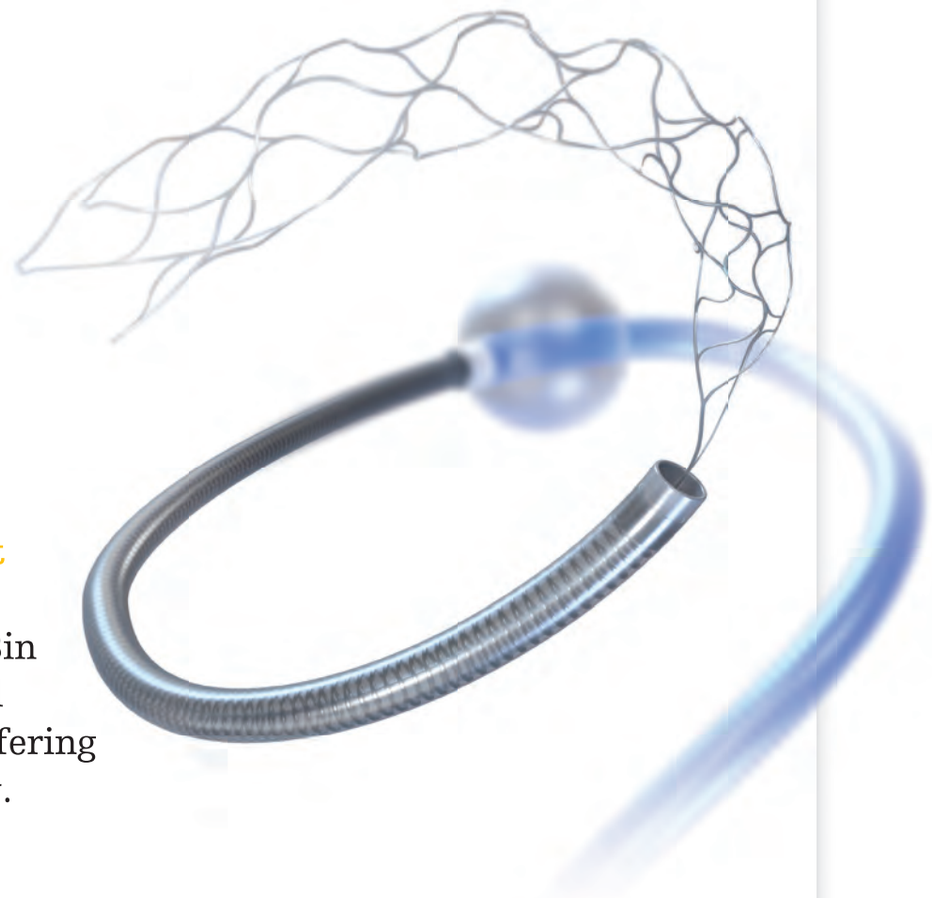

Empowering first pass retrieval with the new 0.068in lumen CAT 7 Distal Access Catheter, offering ultimate versatility.

AXS Catalyst® 7
Distal Access Catheter

CAT 7 lumen is bigger than CAT 6 lumen.

AJNR

AMERICAN JOURNAL OF NEURORADIOLOGY

OCTOBER 2019
VOLUME 40
NUMBER 10
WWW.AJNR.ORG

Publication Preview at www.ajnr.org features articles released in advance of print. Visit www.ajnrblog.org to comment on AJNR content and chat with colleagues and AJNR's News Digest at http://ajnrdigest.org to read the stories behind the latest research in neuroimaging.

AJNR (Am J Neuroradiol ISSN 0195–6108) is a journal published monthly, owned and published by the American Society of Neuroradiology (ASNR), 800 Enterprise Drive, Suite 205, Oak Brook, IL 60523. Annual dues for the ASNR include $170.00 for journal subscription. The journal is printed by Cadmus Journal Services, 5457 Twin Knolls Road, Suite 200, Columbia, MD 21045; Periodicals postage paid at Oak Brook, IL and additional mailing offices. Printed in the U.S.A. POSTMASTER: Please send address changes to American Journal of Neuroradiology, P.O. Box 3000, Denville, NJ 07834, U.S.A. Subscription rates: nonmember $410 ($480 foreign) print and online, $320 online only; institutions $470 ($540 foreign) print and basic online, $935 ($1000 foreign) print and extended online, $380 online only (basic), extended online $825; single copies are $35 each ($40 foreign). Indexed by PubMed/Medline, BIOSIS Previews, Current Contents (Clinical Medicine and Life Sciences), EMBASE, Google Scholar, HighWire Press, Q-Sensei, RefSeek, Science Citation Index, SCI Expanded, Meta/CZI and ReadCube.

ONLINE FEATURES

LETTERS

BOOK REVIEWS *R.M. Quencer, Section Editor*

Please visit www.ajnrblog.org to read and comment on Book Reviews.

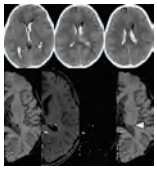

CT and MR images from 7-year-old boy with acute intraventricular hemorrhage. The arrowhead shows the bleeding point at which the signal from the abnormally extended artery on TOF-MRA overlaps the hypointense spot on SWI.

Indicates Editor's Choices selection

Indicates Fellows' Journal Club selection

Indicates open access to non-subscribers at www.ajnr.org

Indicates article with supplemental on-line table

Indicates article with supplemental on-line photo

Indicates article with supplemental on-line video

Evidence-Based Medicine Level 1

Evidence-Based Medicine Level 2

AJNR

AMERICAN JOURNAL OF NEURORADIOLOGY

Publication Preview at www.ajnr.org features articles released in advance of print. Visit www.ajnrblog.org to comment on AJNR content and chat with colleagues and AJNR's News Digest at http://ajnrdigest.org to read the stories behind the latest research in neuroimaging.

OCTOBER 2019 • VOLUME 40 • NUMBER 10 • WWW.AJNR.ORG

Title: Eclipse. This photo was taken at the totality of the 2017 summer eclipse in Salem, Oregon.

Stephen L.G. Rothman, MD, Los Angeles, California

Board Certification Characteristics of Practicing Neuroradiologists

A.B. Rosenkrantz, G.N. Nicola, J.A. Hirsch, and R. Duszak Jr.

ABSTRACT

BACKGROUND AND PURPOSE: Insight into the status of neuroradiology subspecialty certification across the United States could help to understand neuroradiologists' perceived value of subspecialty certification as well as guide efforts to optimize pathways for broader voluntary certification participation. Our aim was to assess board certification characteristics of practicing US neuroradiologists.

MATERIALS AND METHODS: The American Board of Radiology public search engine was used to link Medicare-participating radiologists with American Board of Radiology diplomates. Among linked diplomates, 4670 neuroradiologists were identified on the basis of 3 criteria: current or prior neuroradiology subspecialty certification or currently >50% clinical work effort in neuroradiology based on work relative value unit–weighted national Medicare claims ("majority-practice neuroradiologists"). Subspecialty certification status was studied in each group, using Centers for Medicare & Medicaid Services data to identify additional physician characteristics.

RESULTS: Of 3769 included radiologists ever subspecialty certified, 84.1% are currently subspecialty certified. Of 1777/3769 radiologists ever subspecialty-certified and with lifetime primary certificates (ie, nonmandated Maintenance of Certification), only 66.6% are currently subspecialty certified. Of 3341 included majority-practice neuroradiologists, 73.0% were ever subspecialty certified; of these, 89.1% are currently subspecialty certified. Of 3341 majority-practice neuroradiologists, the fraction currently subspecialty certified was higher for those in academic (81.3%) versus nonacademic (58.2%) practices, larger versus smaller practices (72.1% for those in ≥100 versus 36.1% for <10-member practices), US regions other than the West (64.1%–70.6% versus 56.5%), fewer years in practice (77.5% for 11–20 years versus 31.3% for >50 years), and time-limited (73.5%) versus lifetime (54.9%) primary certificates.

CONCLUSIONS: More than one-quarter of majority-practice neuroradiologists never obtained neuroradiology subspecialty certification. Even when initially obtained, that certification is commonly not maintained, particularly by lifetime primary certificate diplomates and those in nonacademic and smaller practices. Further investigation is warranted to better understand neuroradiologists' decisions regarding attaining and maintaining subspecialty certification.

ABBREVIATIONS: ABR = American Board of Radiology; CMS = Centers for Medicare & Medicaid Services; DR = diagnostic radiology; MOC = Maintenance of Certification; IR = interventional radiology

Neuroradiology is one of the few diagnostic radiology subspecialties for which the American Board of Radiology (ABR) offers subspecialty certification. Beginning in 1995, the ABR offered neuroradiologists the opportunity to undergo additional advanced testing to receive this certification beyond their primary radiology certificates.[1,2] The additional certification is intended to demonstrate to the public that such diplomates have attained the knowledge, problem-solving ability, and skills to be capable of working safely and effectively in various sectors of the subspecialty.[3] Furthermore, subspecialty diplomates are required to engage in periodic cognitive assessment to demonstrate life-long learning and practice improvement.[2,4,5] The processes for receiving and maintaining neuroradiology subspecialty certification have been described as elevating the nationwide level of neuroradiology practice.[2]

Neuroradiology subspecialty certification (initially designated as a Certificate of Added Qualification) has evolved as part of a broader shift in board certification throughout medicine.

Received July 15, 2019; accepted after revision August 7.

From the Department of Radiology (A.B.R.), NYU Langone Medical Center, New York, New York; Hackensack Radiology Group, P.A. (G.N.N.), River Edge, New Jersey; Department of Radiology (J.A.H.), Massachusetts General Hospital, Harvard Medical School, Boston, Massachusetts; and Department of Radiology and Imaging Sciences (R.D.), Emory University School of Medicine, Atlanta, Georgia.

Drs. Rosenkrantz, Hirsch, and Duszak are supported by research grants from the Harvey L. Neiman Health Policy Institute.

Please address correspondence to Andrew B. Rosenkrantz, MD, Department of Radiology, NYU Langone Health, 660 First Ave, New York, NY 10016; e-mail: Andrew.Rosenkrantz@nyumc.org; @arosenkrantzmd

http://dx.doi.org/10.3174/ajnr.A6225

Table 1: Descriptions of the terms used in identifying the study sample

Term	Description
Currently subspecialty certified	Attained ABR neuroradiology subspecialty certification, with this subspecialty certificate currently in MOC
Previously subspecialty certified	Attained ABR neuroradiology subspecialty certification, with this subspecialty certificate not currently in MOC
Never subspecialty certified	Never attained ABR neuroradiology subspecialty certification
Majority-neuroradiology practice	Has highest relative work effort in neuroradiology, with this neuroradiology work effort exceeding 50% on a work relative value unit basis

Historically, it was achieved after passing an oral examination separate from the oral examination undertaken to obtain primary certification.[6] Currently, in order to be eligible, radiologists must first obtain primary certification in diagnostic radiology (DR), interventional radiology/diagnostic radiology (IR/DR), or general radiology (a historical primary certificate no longer offered by the ABR).[3] For eligible diplomates, neuroradiology subspecialty certification entails completing a 1-year accredited neuroradiology fellowship, 1 year of clinical practice (or additional approved training, at least a third of which must be in neuroradiology), and a dedicated computer-based image-rich neuroradiology subspecialty certification examination.[7] The latter is distinct from the DR or other primary certifying examinations, comprising exclusively modules of advanced-level questions in brain, head and neck, and spine imaging, as well as an additional certification fee.[7,8] When primary certificates were used to provide lifetime certification, the periodic testing for neuroradiology subspecialty Maintenance of Certification (MOC) represented additional testing that DR and other primary certificate diplomates otherwise were not required to undergo as a condition of the primary certificate.[2] However, in the current era of time-limited primary certificates and subsequent mandated primary certificate MOC, the MOC processes for the primary DR and neuroradiology subspecialty certificates are integrated into a single MOC program—that is, DR diplomates are able to fulfill the MOC requirements for both certificates by completing the same number of MOC questions as for an individual certificate and paying only a single MOC fee to the ABR.[9]

There are currently few available data regarding the status of neuroradiology subspecialty certification across the United States, including, for example, its overall presence among neuroradiologists as well as the clinical contexts and practice patterns in which it is most common. Such information could be useful for understanding neuroradiologists' perceived value of subspecialty certification as well as guiding effort to optimize pathways for broader voluntary certification participation. We therefore conducted this study to assess board certification characteristics of practicing US neuroradiologists.

MATERIALS AND METHODS

This retrospective study of publicly available data did not represent human subjects' research and therefore did not require oversight by our institutional review boards.

The 2016 Centers for Medicare & Medicaid Services (CMS) Physician and Other Supplier: Provider Utilization Public Use File was used to identify US radiologists participating in the Medicare program. These radiologists were then linked to diplomates certified by the ABR on the basis of data provided by the ABR in its public search engine, consistent with the methodology in an earlier work.[10] This linkage process was based on identification of the optimal match between radiologists in the separate CMS and ABR datasets, wherein radiologists were excluded when no single unambiguous linkage was identified. For linked radiologists, we extracted information from the ABR search engine to determine awarded ABR certificates, whether such certificates were maintained in the MOC program of the ABR, and whether primary certificates had lifetime or time-limited status. A claims-based system incorporating work relative value unit–weighting that maps imaging families to radiology subspecialties was used to compute each radiologist's percentage of billed work effort in neuroradiology.[11-13]

Radiologists who could be linked between CMS and ABR data sources were then selected for inclusion within this investigation if they met any 3 of the following nonoverlapping criteria: 1) having attained neuroradiology subspecialty certification with this subspecialty certificate currently in MOC (currently subspecialty certified), 2) having attained neuroradiology subspecialty certification with this subspecialty certificate not currently in MOC (previously subspecialty certified), or 3) having never attained neuroradiology subspecialty certification (never subspecialty certified) though having their highest relative work effort in neuroradiology and this neuroradiology work effort exceeding 50% on a work relative value unit basis (majority-neuroradiology practice). Table 1 summarizes the designations used in these criteria. Additional information for included radiologists was then extracted from both the 2016 Provider Utilization Public Use File and the separate CMS Physician Compare national downloadable file[14] datasets, including group practice size, medical school graduation year (which was used to estimate years in practice), academic status using practice affiliations provided by CMS, and an academic status classification system.[15]

All included radiologists were summarized in a descriptive fashion, stratified by various combinations of radiologist, certification, and radiology practice characteristics. Multivariable logistic regression was performed to identify factors independently associated with neuroradiology subspecialty certification in MOC among majority-practice neuroradiologists. These rates were also determined at the state level and depicted graphically (USA Heat Map Generator; Someka, Excel Solutions; https://www.someka.net/). The analysis was performed using Excel for Windows (Microsoft; Redmond, Washington) and MedCalc for Windows (MedCalc Software, Mariakerke, Belgium).

Table 2: Distribution of physician and practice characteristics, stratified by the 3 study inclusion criteria[a]

	Currently Subspecialty Certified	Previously Subspecialty Certified	Never Subspecialty Certified, Majority-Neuroradiology Practice
No.	3168	601	901
Mean neuroradiology work effort	69.0%	52.2%	72.4%
Academic	30.0%	14.1%	15.0%
Group practice size			
<10	9.6%	27.5%	19.6%
10–49	31.9%	37.1%	29.9%
50–99	14.4%	9.8%	13.8%
≥100	44.0%	25.6%	36.7%
Region			
Midwest	22.6%	17.6%	18.5%
Northeast	24.1%	21.6%	19.8%
South	31.2%	37.8%	31.0%
West	22.1%	23.0%	30.7%
Years in practice			
≤10	7.4%	0.0%	10.4%
11–20	42.5%	1.3%	32.8%
21–30	26.6%	24.3%	29.5%
31–40	19.7%	53.2%	19.8%
41–50	3.4%	17.5%	6.1%
≥51	0.4%	3.6%	1.3%
Primary certificate			
Lifetime	37.4%	98.7%	46.4%
Time-limited	62.6%	1.3%	53.6%

[a] Cells in columns for given characteristics add up to 100%.

RESULTS

The final cohort consisted of 4670 radiologists linked between CMS and ABR datasets and who met further inclusion criteria. This cohort included 3168 currently subspecialty-certified neuroradiologists, 601 previously subspecialty-certified neuroradiologists, and 901 never subspecialty-certified radiologists with majority-neuroradiology practices. Included radiologists' primary certificates were DR in 4510, IR/DR in 125, and general radiology in 35.

A total of 84.1% (3168/3769) of radiologists with neuroradiology subspecialty certification were currently subspecialty certified. Among the 3769 included radiologists having ever attained neuroradiology subspecialty certification, 1777 had a lifetime primary certificate. Among these, 1184 (66.6%) were currently subspecialty certified. Among the 3769 who ever attained neuroradiology subspecialty certification, 1992 had a time-limited primary certificate. Among these, 1984 (99.6%) were currently subspecialty certified. Among 3341 included radiologists with majority-neuroradiology practices, 2440 (73.0%) had ever obtained neuroradiology subspecialty certification; and of these, 2175 (89.1%) were currently subspecialty certified.

Table 2 summarizes the distribution of physician and practice characteristics based on the 3 separate inclusion criteria of the study. The mean neuroradiology work effort was 69.0% for those currently

Table 3: Distribution of physician and practice characteristics, stratified by combinations of primary certificate status and neuroradiology subspecialty certification status[a]

	Lifetime Primary; Currently Subspecialty Certified	Lifetime Primary; Previously Subspecialty Certified	Lifetime Primary; Never Subspecialty Certified	Time-Limited Primary; Currently Subspecialty Certified	Time-Limited Primary; Never Subspecialty Certified
No.	1184	593	418	1984	483
Mean neuroradiology work effort	70.5%	52.4%	73.2%	68.1%	71.8%
Academic practice status					
Academic	29.2%	14.0%	10.0%	30.5%	19.3%
Nonacademic	70.8%	86.0%	90.0%	69.5%	80.7%
Group practice size					
<10	14.0%	27.7%	25.8%	7.0%	14.3%
10–49	31.9%	36.8%	33.3%	32.0%	26.9%
50–99	13.5%	9.9%	14.4%	15.0%	13.3%
≥100	40.5%	25.6%	26.6%	46.1%	45.5%
Region					
Midwest	22.3%	17.7%	17.0%	22.8%	19.9%
Northeast	25.3%	21.6%	21.8%	23.3%	18.0%
South	34.1%	37.9%	31.6%	29.5%	30.4%
West	18.3%	22.8%	29.7%	24.4%	31.7%
Years in practice					
≤10	0.0%	0.0%	0.0%	11.7%	18.7%
11–20	0.1%	0.8%	0.0%	67.3%	58.8%
21–30	43.3%	24.1%	41.8%	16.8%	19.8%
31–40	46.5%	53.9%	41.8%	4.1%	2.4%
41–50	9.1%	17.6%	13.5%	0.2%	0.2%
≥51	1.1%	3.7%	3.0%	0.0%	0.0%

[a] Cells in columns for given characteristic add up to 100%. Columns 1 and 4 in this table together reflect column 1 in Table 2; columns 3 and 5 in this table together reflect column 3 in Table 2. Column 2 in this table is a subset of column 2 in Table 2.

Table 4: Distribution of neuroradiology subspecialty certification statuses among majority-practice neuroradiologists with varying characteristics[a]

	No.	Currently Subspecialty Certified	Previously Subspecialty Certified	Never Subspecialty Certified
Academic status				
Nonacademic	1364	58.2%	9.1%	32.7%
Academic	811	81.3%	5.1%	13.5%
Group practice size				
<10	132	36.1%	15.6%	48.4%
10–49	623	63.2%	9.5%	27.3%
50–99	356	69.4%	6.4%	24.2%
≥100	1064	72.1%	5.5%	22.4%
Geographic region				
Midwest	505	70.6%	6.0%	23.4%
Northeast	563	69.8%	8.2%	22.1%
South	674	64.1%	9.4%	26.5%
West	433	56.5%	7.4%	36.1%
Years in practice				
≤10	149	63.4%	0.0%	36.6%
11–20	936	77.5%	0.1%	22.4%
21–30	544	65.0%	6.0%	29.0%
31–40	414	59.1%	17.6%	23.3%
41–50	73	43.7%	26.3%	29.9%
≥51	10	31.3%	34.4%	34.4%
Primary certificate				
Lifetime	828	54.9%	17.4%	27.7%
Time-limited	1347	73.5%	0.1%	26.4%

[a] Cells in rows add up to 100%. Columns 1 and 2 in this table reflect subsets of columns 1 and 2 in Table 2; column 3 in this table reflects the same neuroradiologists as in column 3 of Table 2.

Table 5: Results of multivariable regression analysis for identifying factors associated with current subspecialty certification among radiologists with a majority-neuroradiology practice

Reference	Criterion	Odds Ratio	95% CI	*P*
Nonacademic	Academic	2.82	2.27–3.50	<.001
<10 Members	10–49 members	2.03	1.48–2.80	<.001
<10 Members	50–99 members	2.51	1.77–3.55	<.001
<10 Members	100+ members	1.94	1.40–2.70	<.001
West	Midwest	1.65	1.30–2.09	<.001
West	Northeast	1.63	1.29–2.06	.022
West	South	1.45	1.18–1.80	<.001
≥51 yr	≤10 yr	2.81	1.16–6.81	<.001
≥51 yr	11–20 yr	6.12	2.61–14.38	<.001
≥51 yr	21–30 yr	4.08	1.81–9.20	<.001
≥51 yr	31–40 yr	3.44	1.53–7.72	.003
≥51 yr	41–50 yr	1.72	0.73–4.02	.214
Lifetime primary	Time-limited primary	1.41	1.06–1.88	.017

subspecialty certified, 52.2% for those previously subspecialty certified, and 72.4% for those never subspecialty certified with majority-neuroradiology practices. The fraction in academic practice was 30.0% for those currently subspecialty certified, 14.1% for those previously subspecialty certified, and 15.0% for those never subspecialty certified with majority-neuroradiology practices. The fraction with lifetime primary certificates was 37.4% among those currently subspecialty certified, 98.7% among those previously subspecialty certified, and 46.4% among those never subspecialty certified with majority-neuroradiology practices.

Table 3 summarizes these same characteristics based on 5 different nonoverlapping combinations of primary certificate status and neuroradiology subspecialty certification status. Mean neuroradiology work effort varied from 52.4% to 73.2% across these groups. For lifetime primary certificate holders, the fractions in an academic practice were the following: 29.2% for those currently subspecialty certified, 14.0% for those previously subspecialty certified, and 10.0% for those never subspecialty certified. For time-limited primary certificate holders, the fractions in an academic practice were 30.5% for those currently subspecialty certified and 19.3% for those previously subspecialty certified.

Among 3341 radiologists with majority-neuroradiology practices (Table 4), the fraction currently subspecialty certified was higher for those in academic (81.3%) versus nonacademic (58.2%) practices, larger-versus-smaller practices (72.1% for those in ≥100 versus 36.1% for <10-member practices), US regions other than the West (64.1%–70.6% versus 56.5%), with fewer years in practice (77.5% for 11–20 years versus 31.3% for >50 years), and time-limited (73.5%) versus lifetime (54.9%) primary certificates.

At multivariable regression among radiologists with a majority-neuroradiology practice (Table 5), all of the included physician and practice characteristics were significant independent predictors of being currently subspecialty certified. The strongest such predictors were earlier career stage (odds ratio = 6.12 for 11–20 years in practice relative to ≥51 years in practice) and academic practice status (odds ratio = 2.82 relative to nonacademic practice status). The Figure demonstrates the state-level percentage of majority-practice neuroradiologists currently subspecialty certified. The fraction was highest (≥80%) in South Dakota, Vermont, and Idaho and lowest (≤20%) in North Dakota, Wyoming, and Alaska.

DISCUSSION

Identifying radiologists by linking ABR search engine data to 2 different CMS datasets, we characterized subspecialty-certification characteristics of neuroradiologists and observed that more than one-quarter of radiologists with a majority-neuroradiology practice had never obtained subspecialty certification. Numerous physician and practice characteristics were associated with the likelihood of doing so. Across numerous analyses, attaining neuroradiology subspecialty certification was substantially more common among academic radiologists. The reasons for the lack of such certification among neuroradiologists in nonacademic practices are unknown, but on the basis of our data, warrant further investigation.

Among the requirements for seeking subspecialty certification, completing a neuroradiology fellowship and having additional practice experience in the subspecialty would not seem to pose a challenge from a practical standpoint. However, a barrier or disincentive to some majority-neuroradiology practice radiologists may be the additional certification examination. This examination entails additional test preparation, additional time away from work to travel to the examination center (currently

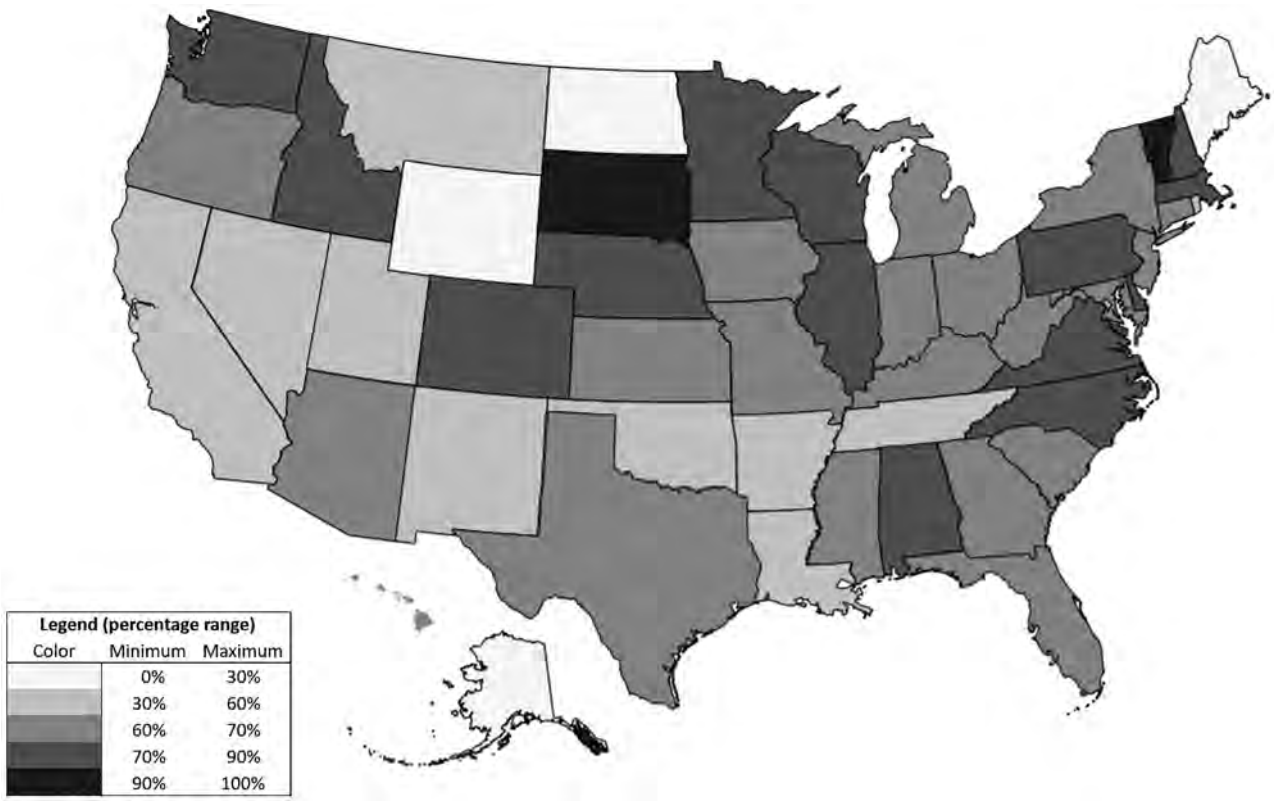

FIGURE. State-level variation among radiologists with a majority-neuroradiology practice in terms of being currently subspecialty certified. The intermediate shade corresponds with a percentage within a 60%–70% range, approaching the overall national rate of 65%. Lighter shades correspond with a rate under 60%, and darker shades correspond with a rate of at least 70%.

offered on only 2 dates in the year and in only 2 different US cities),[8] an additional examination fee, as well as the stress of the examination itself. A neuroradiologist might be motivated to undertake this process if perceiving some tangible benefit from achieving that additional certificate. However, subspecialty certification is generally not needed from a credentialing standpoint or for other reasons to practice within the discipline. It is possible that individual diplomates are internally motivated to seek additional certification due to a sense of fulfillment or accomplishment through the formal recognition by the ABR. Individuals may also be motivated by external factors such as a desire to be more competitive when seeking employment; to fulfill an expectation if attaining employment in a group in which the certification is the norm among the group's neuroradiologists; or, even if working in a group where it is not the norm, to, nonetheless, attain prestige, respect, or standing within one's group. Individuals may also pursue certification to enhance their public reputation, given that the public can readily identify whether a neuroradiologist has subspecialty certification through the certificate verification public search engine of the ABR.[16] Some of these factors, such as prestige or fitting the norm or group expectation, may be more relevant for academic practices.

Some of the other factors we identified associated with subspecialty certification are expected. Subspecialty certification was more common for radiologists in larger practices, which themselves may be more academic and more subspecialized. In addition, subspecialty certification was more common for earlier career radiologists. This is also not unexpected because neuroradiology subspecialty certification was only first offered in 1995 so that it was not available at the time that more senior radiologists were completing training and beginning their careers (ie, the stage when radiologists are more likely to undergo testing and pursue certification). According to 1 report, the number of registrants for the neuroradiology subspecialty certification examination increased from approximately 80 from 2003–2005 to 134 in 2006, and 160 in 2007, supporting a gradual rise in the subspecialty certification since first being introduced.[1] Most interesting, certification rates were least common in the Western United States and were not consistently high or low in either large or small states or in neighboring states, indicating possible regional cultural influences on seeking certification. Targeted survey-based studies could complement our present analysis to better understand neuroradiologists' motivations for seeking (or not seeking) subspecialty certification but would operationally require e-mail contact information not made publicly available by the ABR or CMS.

Overall, staying currently subspecialty-certified was very common for those with time-limited primary certificates (ie, MOC already required for the primary certificate), which would be expected given that the ABR has integrated its MOC programs for primary and secondary certificates—that is, diplomates fulfill the MOC requirements of both certificates

without having to answer any additional test questions or pay any additional fees beyond that for their primary certificates. In this regard, there are currently larger barriers to initially attaining, rather than to subsequently maintaining, subspecialty certification.

In comparison, approximately a third of neuroradiologists with lifetime primary certificates (ie, MOC not required for their primary certificates) and who had, at some point, obtained subspecialty certification were no longer currently subspecialty certified. These rates were particularly low for lifetime certificate holders in nonacademic and smaller practices. The underlying factors behind the lack of MOC participation in these groups may be similar to those influencing these radiologists' lower rates of attaining subspecialty certification in the first place. A national survey in 2008 observed high rates of misunderstanding regarding the MOC by neuroradiologists, as well as unfavorable views of the MOC relating to inconvenience and cost, contributing to resistance and noncompliance.[17] While the ABR has taken steps to simplify its MOC process through the introduction of its Online Longitudinal Assessment initiative,[18] lingering misconceptions and negative perspectives could continue to influence decisions regarding voluntary MOC. In this regard, our present study provides a baseline assessment; further longitudinal investigations would be necessary to determine how and if the Online Longitudinal Assessment initiative might be more widely accepted.

ABR leadership has indicated that the advent of neuroradiology subspecialty certification has elevated the level of neuroradiology practice nationally.[1,2] If this is indeed the case, professional thought leaders need a better understanding of neuroradiologists' motivations to attain certification. This, in turn, may be facilitated by insight into which neuroradiologists are-versus-are not participating, for which our analysis provides concrete data. It has also been proposed that national specialty societies such as the American Society of Neuroradiology should play a leading role in educating neuroradiologists and providing resources to encourage subspecialty certification participation.[17] Ultimately, to be successful in incentivizing greater participation, proponents of certification will need to make a compelling case for the value added to their intended audiences.

This study has several limitations. First, given the public availability from CMS of claims resources to identify actively practicing radiologists, we only included neuroradiologists participating in the Medicare program. Pediatric neuroradiologists may thus be underrepresented. In addition, the ABR has, in recent years, changed aspects of its program for primary certificate initial certification, primary certification maintenance, subspecialty certificate initial certification, and subspecialty certificate maintenance. Thus, board participation characteristics may remain a moving target that can be difficult to precisely quantify, given that available data reflect a conglomerate of physicians' behavior across different ABR certification policies. Also, it is possible that some radiologists with a majority-neuroradiology practice did not seek subspecialty certification due to never having completed a neuroradiology fellowship (thus making them ineligible for the certification through the standard pathway). However, we are unaware of any publicly available dataset listing radiologists' fellowships. Furthermore, while the ABR provides an alternate pathway to subspecialty certification for those who did not complete an accredited fellowship,[19] the ABR public search engine does not indicate whether subspecialty diplomates followed the standard or alternate pathway, precluding inclusion of this factor in our investigation. Finally, because this study was focused entirely on neuroradiology subspecialty certification, it is not clear whether the observed patterns apply, in a similar fashion, to other ABR radiology subspecialty certificates (eg, nuclear radiology and pediatric radiology).

CONCLUSIONS

More than one-quarter of radiologists with a majority-neuroradiology practice have never obtained neuroradiology subspecialty certification. Even when initially obtained, that certification is commonly not maintained, particularly among lifetime primary certificate diplomates. Neuroradiologists in nonacademic practices were less likely to both initially attain and subsequently maintain neuroradiology subspecialty certification. Further investigation is warranted to better understand such decisions by neuroradiologists regarding subspecialty certification participation.

Disclosures: Andrew B. Rosenkrantz—*RELATED*: *Grant*: Harvey L. Neiman Health Policy Institute.* Richard Duszak—*RELATED*: *Grant*: Harvey L. Neiman Health Policy Institute.* *Money paid to the institution.

REFERENCES

1. Forbes GS, Yock DH. **Maintaining subspecialty certification in neuroradiology**. *AJNR Am J Neuroradiol* 2008;29:228 CrossRef Medline
2. Lukin RR, Forbes GS. **Why I should take my CAQ recertification examination.** *AJNR Am J Neuroradiol* 2004;25:668–69
3. American Board of Radiology. **Neuroradiology**. https://www.theabr.org/diagnostic-radiology/subspecialties/neuroradiology. Accessed June 27, 2019
4. Hirsch JA, Becker GJ, Derdeyn CP, et al. **Maintenance of certification: Part 2, continuous certification**. *J Neurointerv Surg* 2014;6:156–60 CrossRef Medline
5. Hirsch JA, Meyers PM. **Maintenance of certification: historical context**. *J Neurointervent Surg* 2013;5:612–14 CrossRef Medline
6. Zimmerman R. **Changing Structure of the ABR Exams and the Effect on Neuroradiology. AJNR Blog**. http://www.ajnrblog.org/2009/10/27/changing-structure-of-the-abr-exams-and-the-effect-on-neuroradiology/. Published on October 27, 2009. Accessed June 27, 2019
7. American Board of Radiology. **Requirements and Registration**. https://www.theabr.org/diagnostic-radiology/subspecialties/neuroradiology/requirements-registration. Accessed June 27, 2019
8. American Board of Radiology. Dates, Locations, Fees. https://www.theabr.org/diagnostic-radiology/subspecialties/neuroradiology/dates-locations-fees. Accessed June 27, 2019
9. American Board of Radiology. **Maintenance of Certification for Diagnostic Radiology**. https://www.theabr.org/diagnostic-radiology/maintenance-of-certification. Accessed June 27, 2019
10. Rosenkrantz AB, Berland LL, Heitkamp DE, et al. **Diagnostic radiologists' participation in the American Board of Radiology's**

maintenance of certification program. *AJR Am J Roentgenol*. In press
11. Rosenkrantz AB, Wang W, Hughes DR, et al. **Academic radiologist subspecialty identification using a novel claims-based classification system**. *AJR Am J Roentgenol* 2017;208:1249–55 CrossRef Medline
12. >Rosenkrantz AB, Wang W, Bodapati S, et al. **Private practice radiologist subspecialty classification using medicare claims**. *J Am Coll Radiology* 2017;14:1419–25 CrossRef Medline
13. Rosenkrantz AB, Wang W, Hughes DR, et al. **Generalist versus subspecialist characteristics of the U.S. radiologist workforce**. *Radiology* 2018;286:929–37 CrossRef Medline
14. Centers for Medicare & Medicaid Services. **Physician Compare data sets; downloadable file**. https://data.medicare.gov/data/physician-compare. Accessed February 26, 2019
15. Harvey L. Neiman Health Policy Institute. **Identification of Academic Radiology Practices**. http://www.neimanhpi.org/academic-radiology-practices/. Accessed October 13, 2018
16. American Board of Radiology. **Verify Board Certification Status**. https://www.theabr.org/myabr/find-a-radiologist. Accessed January 8, 2019
17. Yousem DM. **Maintenance of certification: current attitudes of members of the American Society of Neuroradiology**. *AJNR Am J Neuroradiol* 2008;29:224–27 CrossRef Medline
18. American Board of Radiology. **Online Longitudinal Assessment (OLA)**. https://www.theabr.org/online-longitudinal-assessment-ola. Accessed March 19, 2019
19. American Board of Radiology. **Alternate Pathway to Subspecialty Certification**. https://www.theabr.org/diagnostic-radiology/subspecialties/neuroradiology/alternate-pathway. Accessed August 5, 2019

Virtual Monoenergetic Images from Spectral Detector CT Enable Radiation Dose Reduction in Unenhanced Cranial CT

R.P. Reimer, D. Flatten, T. Lichtenstein, D. Zopfs, V. Neuhaus, C. Kabbasch, D. Maintz, J. Borggrefe, and N. Große Hokamp

ABSTRACT

BACKGROUND AND PURPOSE: Our aim was to evaluate whether improved gray-white matter differentiation in cranial CT by means of 65-keV virtual monoenergetic images enables a radiation dose reduction compared to conventional images.

MATERIALS AND METHODS: One hundred forty consecutive patients undergoing 171 spectral detector CTs of the head between February and November 2017 (56 ± 19 years of age; male/female ratio, 56%/44%) were retrospectively included. The tube current–time product was reduced during the study period, resulting in 61, 55, and 55 patients being examined with 320, 290, and 260 mAs, respectively. All other scanning parameters were kept identical. The volume CT dose index was recorded. ROIs were placed in gray and white matter on conventional images and copied to identical positions in 65-keV virtual monoenergetic images. The contrast-to-noise ratio was calculated. Two radiologists blinded to the reconstruction technique evaluated image quality on a 5-point Likert-scale. Statistical assessment was performed using ANOVA and Wilcoxon test adjusted for multiple comparisons.

RESULTS: The mean volume CT dose index was 55, 49.8, and 44.7 mGy using 320, 290, and 260 mAs, respectively. Irrespective of the volume CT dose index, noise was significantly lower in 65-keV virtual monoenergetic images compared with conventional images (65-keV virtual monoenergetic images/conventional images: extraocular muscle with 49.8 mGy, 3.7 ± 1.3/5.6 ± 1.6 HU, $P < .001$). Noise slightly increased with a reduced radiation dose (eg, extraocular muscle in conventional images: 5.3 ± 1.4/5.6 ± 1.6/6.1 ± 2.1 HU). Overall, the contrast-to-noise ratio in 65-keV virtual monoenergetic images was superior to that in conventional images irrespective of the volume CT dose index ($P < .001$). Particularly, 65-keV virtual monoenergetic images with 44.7 mGy showed significantly lower noise and a higher contrast-to-noise ratio than conventional images with 55 mGy ($P < .001$). Subjective analysis confirmed better image quality in 65-keV virtual monoenergetic images, even using 44.7 mGy.

CONCLUSIONS: The 65-keV virtual monoenergetic images from spectral detector CT allow radiation dose reduction in cranial CT. While this proof of concept included a radiation dose reduction of 19%, our data suggest that even greater reduction appears achievable.

ABBREVIATIONS: CI = conventional images; CNR = contrast-to-noise ratio; $CTDI_{vol}$ = volume CT dose index; VMI = virtual monoenergetic images

Unenhanced cranial CT is the standard examination for patients with acute neurologic deficits to allow fast diagnosis of emergencies, for instance, intracranial hemorrhage or ischemia.[1-4] There are approximately 70 million cranial CT scans annually in the United States alone; out of these, several scans are performed in the same patient, so that they undergo repetitive scanning.[5] Despite rapid advances in the field of CT imaging such as dose modulation or iterative image reconstruction, few of these have been applied to cranial CT for 2 main reasons: First, there are only subtle differences in attenuation between gray and white matter. Yet, this is one of the most important aspects to evaluate, in particular in light of suspected ischemia. Second, the surrounding skull causes beam-hardening and therefore an increase in image noise due to beam-hardening.[6-9] Hence, possibilities for dose reduction are limited, despite radiosensitive tissues such as the eye lenses being exposed.[10-13]

A recent development in the field of CT is dual-energy CT, which has been evolving for the past decade. Dual-energy CT is known to improve soft-tissue contrast by means of virtual monoenergetic images (VMI).[14-16] These VMI further reduce artifacts

Received May 17, 2019; accepted after revision August 5.

From the Department of Diagnostic and Interventional Radiology, University of Cologne, Faculty of Medicine and University Hospital Cologne, Cologne, Germany.

R.P. Reimer and D. Flatten contributed equally to this work.

Please address correspondence to Nils Große Hokamp, MD, Department of Diagnostic and Interventional Radiology, University Hospital Cologne, Cologne, Germany, Kerpener Str 62, 50937 Köln, Germany; e-mail: nils.grosse-hokamp@uk-koeln.de

http://dx.doi.org/10.3174/ajnr.A6220

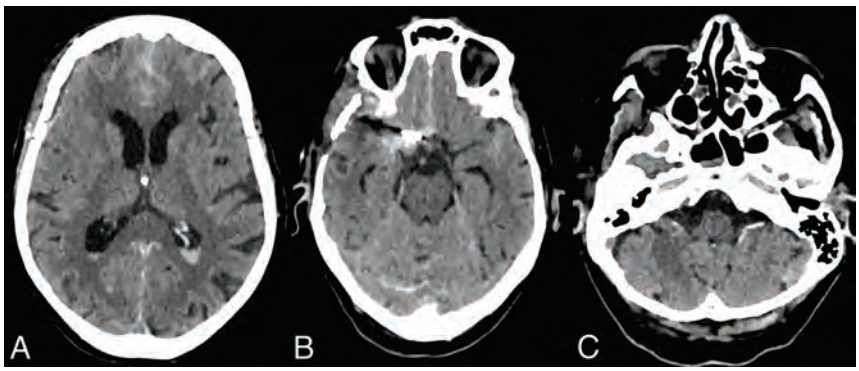

FIG 1. ROI placement in the cortical gray and juxtacortical white matter, in the thalamic parenchyma and posterior limb of the internal capsule, in the caudate nucleus (*orange ROIs*), in an extraocular muscle (*red ROI*), and in the medulla oblongata (*blue ROI*) on an axial plane showing the basal ganglia (*A*), the orbital cavity (*B*), and the posterior fossa (*C*).

occurring due to beam-hardening. In light of neuroimaging, dual-energy CT demonstrated improved image quality and lesion characterization, while it also allowed material separation for iodine.[15,17-22]

Dual-energy CT systems register low- and high-energy data attenuation profiles. By linear blending of these datasets, VMI can be reconstructed. VMI represent virtually approximated images, which would result from acquisition with a true monoenergetic x-ray beam. They are typically available in a range from 40 to 200 keV, depending on the dual-energy CT system used.[23,24]

Different emission-based dual-energy CT systems have been available for several years using emission spectra with lower and higher mean energy.[25,26] More recently, a detector-based approach was introduced, referred to as spectral detector CT. Here, low- and high-energy photons are registered separately using a dual-layer detector.[24,26] The upper layer is yttrium-based and registers lower energy photons, while the lower layer is gadolinium oxysulfide–based, registering higher energy photons.[8,24,26]

In a recent study, VMI from spectral detector CT showed superior image quality in examinations of the head compared with conventional images (CI). Corticomedullary differentiation was found to be best in 65-keV VMI (VMI_{65keV}), while in lower kiloelectron volt images, beam-hardening artifacts close to the calvaria distorted image quality.[6] Their data suggest a VMI-enabled radiation dose reduction.

Therefore, the aim of our study was to compare VMI_{65keV} with CI from unenhanced spectral detector CT datasets of the head acquired with different acquisition protocols to evaluate whether improved image quality in VMI_{65keV} allows a reduction of radiation dose.

MATERIALS AND METHODS

To meet national requirements for radiation dose, we modified protocols for cranial CT examinations, including a reduction in the radiation dose. The institutional review board later approved the scientific evaluation of these data and waived informed consent due to the retrospective study design. A structured search in the radiology information system was performed with the following inclusion criteria: 1) older than 18 years of age, 2) an unenhanced spectral detector CT of the head between the February 1, 2017, and November 30, 2017, and 3) a standardized imaging protocol as described below. Exclusion criteria were the following: 1) extensive intracranial hemorrhage or edema, 2) craniectomy or hemicraniectomy, and 3) artifacts due to patient movement or implants. Eventually, 140 patients with 171 CT scans were included in this study.

Acquisition Parameters

All CT scans were performed for clinical indications on the same spectral detector CT scanner (IQon Spectral CT; Philips Healthcare, Best, the Netherlands). Sixty-one of the identified CT scans were obtained with a tube current–time product of 320 mAs, 55 with 290 mAs, and 55 with 260 mAs. All other scan parameters were kept identical: tube voltage = 120 kV (peak), pitch = 0.36, rotation time = 0.33 seconds, and collimation = 64 × 0.625. CI were reconstructed using a hybrid iterative reconstruction algorithm (iDose4, Filter UB; Philips Healthcare). VMI_{65keV} were reconstructed using a dedicated spectral image-reconstruction algorithm (Spectral, Filter UB; Philips Healthcare). Denoising for both was set to a medium level (level 3 of 7). All images were reconstructed with a section thickness of 1 mm and a section increment of 1 mm.

Dose-length product and volume CT dose index ($CTDI_{vol}$) were recorded from the radiation dose report. We further compared the anterior-posterior and lateral dimensions of the head between groups to exclude this as a confounder.

Quantitative Analysis

Quantitative analysis was performed using ROI-based measurements of attenuation and SD in the following areas on a representative axial plane: 1) cortical gray and 2) adjacent juxtacortical white matter of the frontal and parietal lobes, 3) thalamic parenchyma, 4) adjacent posterior limb of the internal capsule, 5) caudate nucleus, 6) extraocular muscle, and 7) medulla oblongata (Fig 1).

ROIs were placed on CI and copied to identical positions in VMI_{65keV}. The size of the ROIs was kept constant at 25 mm^2, except for the ROI in the medulla oblongata (100 mm^2), and was only adjusted to avoid inclusion of unrepresentative tissue. One radiologist with 2 years of experience in cranial CT interpretation performed the quantitative analysis. In a randomly chosen subgroup of 30 cranial CT scans, a second reader repeated the ROI placement to assess interrater reliability.

Image noise was considered as an SD of extraocular muscle. The contrast-to-noise ratio (CNR) of the gray and white matter of the frontal and parietal lobes was calculated as the difference of the average Hounsfield unit, divided by the square root of the sum of the SD of the 2 adjacent ROIs.[6,15]

Qualitative Analysis

Qualitative analysis was performed independently by 2 fellowship-trained trained neuroradiologists. Readers were blinded to

the reconstruction technique. Rating was performed on 5-point Likert scales with regard to assessment of gray-white matter differentiation in the following areas: 1) the basal ganglia, 2) the supratentorial cortex, 3) the infratentorial cortex, and 4) the subcalvarial space (1 = not diagnostic; 2 = severely impaired assessment; 3 = moderate assessment; 4 = fair assessment; 5 = good assessment, fully diagnostic). Furthermore, visually perceived image noise and beam-hardening artifacts in the subcalvarial space were evaluated (1 = excessive; 2 = severe; 3 = moderate; 4 = some; 5 = no visually perceptible noise).

Statistical Analysis

All analyses were performed using JMP Software (Version 12; SAS Institute, Cary, North Carolina) unless specified below. To compare groups, we used ANOVA or Wilcoxon tests, adjusted for multiple comparisons if appropriate. A P value $<$ .05 was considered significant. Results are shown as mean ± SD. Interrater reliability was determined by means of intraclass correlation estimates using R Studio (Version 1.1.456; http://rstudio.org/download/desktop) based on a single rater, consistency, 2-way mixed-effects model for the quantitative analysis and based on a mean of 2 raters, consistency, 2-way mixed-effects model for the qualitative analysis.[27] Interrater agreement was evaluated as described earlier: excellent (intraclass correlation coefficient $>$ 0.8), good (intraclass correlation coefficient $>$ 0.6), moderate (intraclass correlation coefficient $>$ 0.4), and poor agreement (intraclass correlation coefficient $\leq$ 0.4).[28,29]

RESULTS

The mean age of patients was 55.8 ± 18.6 years; of these patients, 61 (43.6%) were women and 79 (56.4%) men.

Radiation Dose

$CTDI_{vol}$ was 55, 49.8, and 44.7 mGy in examinations with 320, 290, and 260 mAs, respectively. The dose-length product was 1014.9 ± 56.9, 937.7 ± 40.2, and 837.7 ± 45.6 mGy × cm ($P < .001$) (Table 1). Regarding the $CTDI_{vol}$, the radiation dose was reduced by 9.5% and 18.7%. No significant differences in head size between groups were found ($P \geq .05$).

Quantitative Analysis

The intraclass correlation between the 2 independent readers was 0.984 with a 95% confidence interval of 0.982–0.985, indicating an excellent interreader reliability.

Attenuation

For the same $CTDI_{vol}$, attenuation in gray matter was significantly higher in VMI_{65keV} compared with CI ($P \leq .01$ (Table 2). On the other hand, attenuation in white matter was slightly higher in CI compared with VMI_{65keV} for 55- and 49.8-mGy protocols without reaching a significant difference ($P > .05$), while for 44.7 mGy, it was slightly higher in VMI_{65keV} compared with CI ($P > .05$).

Noise

Image noise as indicated by an SD within the extraocular muscle was significantly lower in VMI_{65keV} compared with CI, irrespective of the $CTDI_{vol}$ ($P < .001$ (Table 2 and Fig 2; eg, in 44.7-mGy protocol: 4.2 ± 1.6 versus 6.1 ± 2.1). Image noise slightly increased from 55 to 49.8 and 44.7 mGy, reaching a significant difference between 55- and 44.7-mGy protocols for the same reconstruction technique (eg, in CI: 5.3 ± 1.4 mGy versus 6.1 ± 2.1

Table 1: Radiation dose

Tube Current–Time Product (mAs)	320	290	260
DLP (mGy × cm)[a]	1014.9 ± 56.9	937.7 ± 40.2	837.7 ± 45.6
Radiation dose reduction		−7.6%	−17.5%
$CTDI_{vol}$ (mGy)	55	49.8	44.7
Radiation dose reduction		−9.5%	−18.7%

Note:—DLP indicates dose-length product.
[a] Results are means ± SDs.

Table 2: Quantitative results of attenuation, noise, and CNR[a]

	CI			VMI_{65keV}		
$CTDI_{vol}$ (mGy)	55	49.8	44.7	55	49.8	44.7
Attenuation						
GM	34.0 ± 1.4	33.4 ± 1.5	34.1 ± 1.7	34.6 ± 1.3	34.2 ± 1.2	35.1 ± 1.5
WM	26.5 ± 1.2	26.1 ± 1.5	27.0 ± 1.6	26.4 ± 1.1	26.0 ± 1.3	27.1 ± 1.4
Thalamus	33.6 ± 1.5	33.2 ± 1.6	34.4 ± 1.9	34.4 ± 1.4	33.9 ± 1.4	35.5 ± 1.8
Posterior limb	26.5 ± 2.2	26.3 ± 2.0	26.6 ± 2.2	26.1 ± 1.4	26.0 ± 1.7	26.6 ± 2.0
Caudate nucleus	34.5 ± 4.4	35.2 ± 2.1	35.4 ± 2.3	35.7 ± 1.5	35.8 ± 1.8	36.3 ± 2.1
Extraocular muscle	32.8 ± 5.6	31.1 ± 6.4	33.2 ± 8.1	31.9 ± 5.6	30.8 ± 6.2	35.4 ± 9.9
Medulla oblongata	31.5 ± 4.3	32.0 ± 4.5	34.6 ± 4.9	31.1 ± 3.3	31.0 ± 3.0	33.9 ± 3.7
Noise						
GM	4.5 ± 0.8	4.6 ± 0.7	4.8 ± 0.8	3.1 ± 0.6	3.1 ± 0.5	3.2 ± 0.5
WM	4.5 ± 0.7	4.8 ± 0.8	4.9 ± 0.7	3.0 ± 0.5	3.2 ± 0.5	3.3 ± 0.6
Thalamus	5.8 ± 0.8	6.0 ± 1.0	6.1 ± 1.1	4.0 ± 0.7	4.2 ± 0.8	4.3 ± 0.9
Posterior limb	5.2 ± 1.0	5.5 ± 1.1	5.6 ± 1.3	3.6 ± 0.8	3.7 ± 0.9	3.9 ± 1.0
Caudate nucleus	5.4 ± 1.1	5.6 ± 1.2	5.6 ± 0.8	3.7 ± 0.9	3.8 ± 0.8	3.8 ± 0.6
Extraocular muscle	5.3 ± 1.4	5.6 ± 1.6	6.1 ± 2.1	3.6 ± 1.1	3.7 ± 1.3	4.2 ± 1.6
Medulla oblongata	6.1 ± 1.2	6.4 ± 1.2	6.7 ± 1.4	4.4 ± 1.0	4.6 ± 0.9	4.7 ± 0.9
GM-WM CNR	2.5 ± 0.5	2.4 ± 0.5	2.3 ± 0.5	3.4 ± 0.5	3.3 ± 0.5	3.2 ± 0.5

[a] Results are means ± SDs.

mGy, $P = .004$). Yet, image noise in VMI_{65keV} with the 44.7-mGy protocol was significantly lower compared with CI and 55 mGy (4.2 ± 1.6 versus 5.3 ± 1.4 mGy, $P < .001$).

CNR

Overall, the CNR for gray-white matter differentiation was significantly higher in VMI_{65keV} compared with CI, irrespective of $CTDI_{vol}$ ($P < .001$) (Table 2 and Fig 3). In line with noise, the CNR slightly decreased from 55 to 49.8 and 44.7 mGy, reaching a significant difference between 55- and 44.7-mGy protocols regarding the same reconstruction technique (eg, in VMI_{65keV}: 3.4 ± 0.5 versus 3.2 ± 0.5 mGy, $P = .04$). Yet, the CNR in VMI_{65keV} with 44.7 mGy was higher compared with CI with 55 mGy (3.2 ± 0.5 versus 2.5 ± 0.5 mGy, $P < .001$).

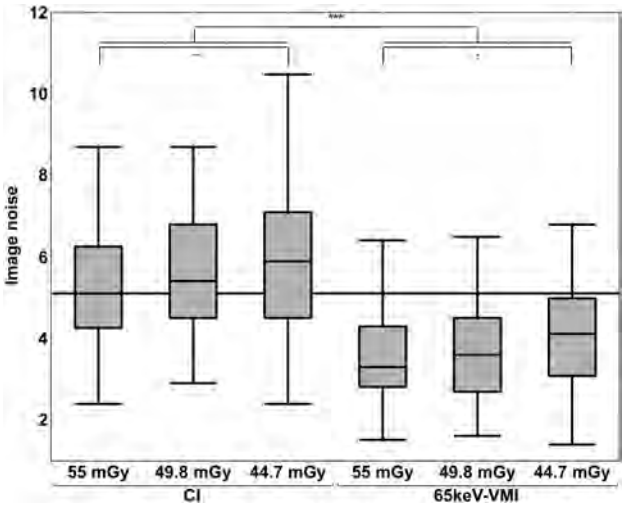

FIG 2. Image noise in extraocular muscle in CI compared with 65-keV virtual monoenergetic images regarding different radiation dose protocols. Significant differences are indicated. The *asterisk* indicates $P = .02$; *double asterisks*, $P = .004$; *triple asterisks*, $P < .001$).

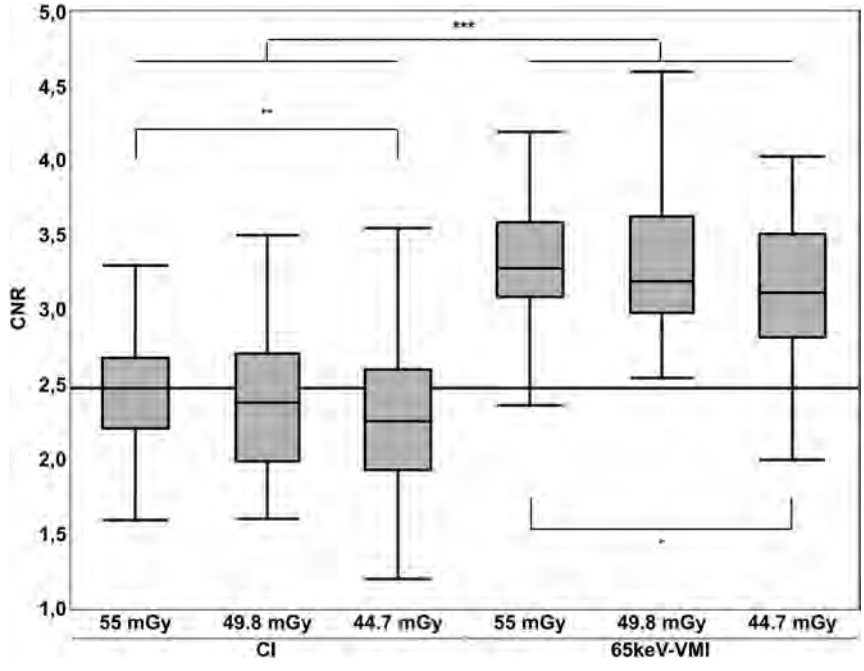

FIG 3. The CNR of gray-white matter differentiation in CI compared with 65-keV virtual monoenergetic images regarding different radiation dose protocols. Significant differences are indicated (*asterisk*, $P = .04$; *double asterisks*, $P = .02$; *triple asterisks*, $P < .001$).

Qualitative Analysis

The intraclass correlation between the 2 independent readers was 0.887, indicating an excellent interreader reliability.

VMI_{65keV} were rated better compared with CI for all criteria (Fig 4). Irrespective of the $CTDI_{vol}$, gray-white matter differentiation of the basal ganglia, supra- and infratentorial corticomedullar differentiation, subjective image noise, and beam-hardening artifacts caused by the skull received superior Likert scores in VMI_{65keV} compared with CI ($P < .001$, Table 3). In the assessment of the subcalvarial space, all VMI_{65keV} were rated as significantly better than CI ($P < .001$), except for VMI_{65keV} with 49.8 mGy compared with CI with 55 and 44.7 mGy ($P < .05$).

DISCUSSION

This study compared the image quality of 65-keV virtual monoenergetic images with conventional images from unenhanced spectral detector CT datasets of the head acquired with different radiation doses. We were able to show that improved image quality in VMI_{65keV} allows dose reduction in cranial CT.

Our study included a radiation dose reduction of 9.5% and 18.7% in terms of $CTDI_{vol}$. In VMI_{65keV}, we observed significantly higher attenuation in gray matter concerning the same radiation dose and no significant differences in white matter. Image noise, on the other hand, was significantly lower compared with CI, irrespective of the radiation dose. This reduction resulted in a significantly higher CNR for gray-white matter differentiation in VMI_{65keV}. Hence, objective image-quality parameters were significantly better in VMI_{65keV} compared with CI, irrespective of $CTDI_{vol}$. Accordingly, subjective image analysis indicated superiority of VMI_{65keV} over CI with regard to the diagnostic assessment, except for the assessment of the subcalvarial space, which was not significantly superior in all different radiation doses.

Because unenhanced cranial CT is the imaging method of choice for patients with neurologic deficits and to diagnose neurocranial traumatic lesions, there is a need for excellent image quality.[3,30] At the same time, the radiation dose has to be as low as reasonably achievable because sensitive tissues are exposed.[10,11,13] The observed image-quality parameters are in accordance with a recent study in which the same scanner and comparable image-acquisition parameters were used.[6] Compared with a study by Pomerantz et al[15] using a

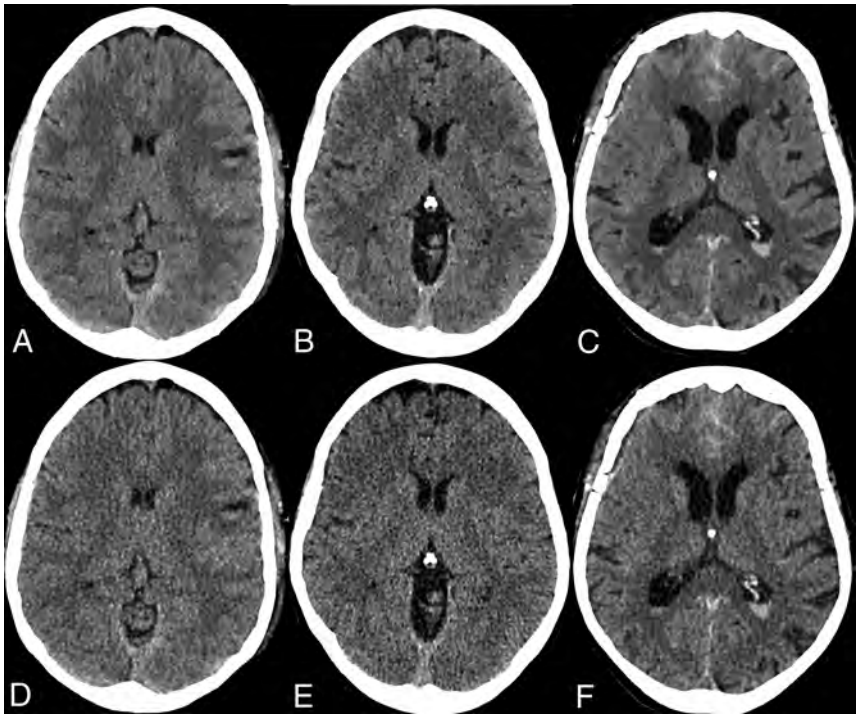

FIG 4. Examples of improved image quality in 65-keV virtual monoenergetic images acquired with a $CTDI_{vol}$ with 55 mGy (*A*), 49.8 mGy (*B*), and 44.7 mGy (*C*) compared with CI, respectively (*D–F*).

Table 3: Qualitative results of subjective image parameters[a]

	CI			VMI_{65keV}		
$CTDI_{vol}$ (mGy)	55	49.8	44.7	55	49.8	44.7
GWMA	3 (3–3)	3 (3–3)	3 (3–3)	5 (5–5)	5 (5–5)	5 (4–5)
CMAS	3 (3–3)	3 (3–3)	3 (3–4)	5 (5–5)	5 (5–5)	5 (5–5)
CMAI	3 (3–3)	3 (3–3)	3 (2–3)	5 (5–5)	5 (5–5)	4 (4–5)
SSA	4 (4–5)	4 (4–4)	4 (4–5)	4 (4–5)	4 (4–5)	4 (4–5)
Noise	3 (3–3)	2 (2–3)	3 (3–3)	4 (4–4)	4 (4–4)	4 (4–4)
Artifacts	3 (3–4)	3 (2–3)	3 (2–3)	4 (4–5)	4 (4–5)	4 (4–4)

Note:—GWMA indicates assessment of gray-white matter differentiation of the basal ganglia; CMAS, assessment of corticomedullary differentiation supratentorially; CMAI, assessment of corticomedullary differentiation infratentorially; SSA, assessment of subcalvarial space.

[a] Results are medians (quartiles).

kilovolt-switching dual-energy CT system with a $CTDI_{vol}$ of 72.65 mGy, our CNR values are about 1.5 times higher and image noise is slightly lower. This result is likely due to advantages regarding image noise enabled by the detector-based approach.[24,31] While we compared VMI_{65keV} with a state-of-the-art hybrid iterative reconstruction algorithm, whether most recent model-based image reconstructions can outperform noise reduction enabled by means of VMI remains elusive.[32]

So far, only a few studies have investigated dose reduction in head imaging by means of VMI compared with polychromatic CT using a kilovolt-switching dual-energy CT system. Kamiya et al[33] included a radiation dose reduction of 11% in VMI_{65keV} compared with CI ($CTDI_{vol}$: 70.2 ± 0.3 mGy versus 78.9 ± 2.1 mGy), while maintaining comparable image quality. However, they reported significantly higher subjective image noise in VMI_{65keV}. On the contrary, besides an overall lower radiation dose in our study of 18.7%, we yielded superior image quality quantitatively and qualitatively in VMI_{65keV}. In line with the study by Pomerantz et al,[15] Kamiya et al[33] reported a lower CNR and higher noise as opposed to the results reported in this study. While the aforementioned results were reported for the supratentorial parenchyma only, we included a detailed analysis of the posterior fossa to address the most challenging region in cranial CT. Here, we report superior image quality in VMI_{65keV} compared with CI, even with a reduced radiation dose.

A more recent study by Hwang et al[34] investigated a radiation dose reduction of up to 37% compared with CI ($CTDI_{vol}$ = 28.0 ± 0.9 mGy versus 44.1 ± 1.7 mGy) using VMI with different kiloelectron volt values in their analyses. Yet, they conducted only a subjective analysis of image quality, reporting no significant difference. In their study, subjective overall image noise was optimal in VMI from 60 to 70 keV, which is in accordance with a few prior studies investigating optimal kiloelectron volt values for VMI in cranial CT.[6,15]

There are several limitations to this study. First, this was a retrospective study performed at a single institution. We were only able to include a limited number of patients because the radiation dose reduction was conducted in the run of the clinical routine; therefore, no prior power analysis was conducted. Thus, no greater reduction of the radiation dose could be evaluated, though our data suggest that this is achievable. We compared the radiation dose based on the $CTDI_{vol}$ alone because there is no established method to normalize radiation dose to the size of the head (unlike the size-specific dose estimates for body CT).[35,36] Although our qualitative analysis was conducted in a blinded fashion, differences between CI and VMI_{65keV} are likely detectable by an experienced reader due to differences in image texture.[32,37] Last, we quantitatively and qualitatively assessed image-quality parameters; however, an evaluation of diagnostic certainty and accuracy in pathologies was beyond the scope of this study.

CONCLUSIONS

The 65-keV virtual monoenergetic images from spectral detector CT enable a radiation dose reduction of 19% in cranial CT, while maintaining superior image quality over conventional images

from full-dose acquisitions. Our data further suggest that an even greater dose reduction seems achievable.

Disclosures: Jan Borggrefe—*UNRELATED*: *Payment for Lectures Including Service on Speakers Bureaus*: Philips Healthcare, *Comments*: I was paid 2 times for scientific lectures in 2017 and 2018. Nils Große Hokamp—*UNRELATED*: *Grants/Grants Pending*: Philips Healthcare*; *Payment for Lectures Including Service on Speakers Bureaus*: Philips Healthcare; *Payment for Development of Educational Presentations*: Philips Healthcare. *Money paid to institution.

REFERENCES

1. Chalela JA, Kidwell CS, Nentwich LM, et al. **Magnetic resonance imaging and computed tomography in emergency assessment of patients with suspected acute stroke: a prospective comparison.** *Lancet* 2007;369:293–98 CrossRef Medline
2. Farzad A, Radin B, Oh JS, et al. **Emergency diagnosis of subarachnoid hemorrhage: an evidence-based debate.** *J Emerg Med* 2013; 44:1045–53 CrossRef Medline
3. Kim ES, Yoon DY, Lee HY, et al. **Comparison of emergency cranial CT interpretation between radiology residents and neuroradiologists: transverse versus three-dimensional images.** *Diagn Interv Radiology* 2014;20:277–84 CrossRef Medline
4. Hemphill JC, 3rd, Greenberg SM, Anderson CS, et al. **Guidelines for the Management of Spontaneous Intracerebral Hemorrhage: A Guideline for Healthcare Professionals from the American Heart Association/American Stroke Association.** *Stroke* 2015;46:2032–60 CrossRef Medline
5. Brenner DJ. **Slowing the increase in the population dose resulting from CT scans.** *Radiat Res* 2010;174:809–15 CrossRef Medline
6. Neuhaus V, Abdullayev N, Große Hokamp N, et al. **Improvement of image quality in unenhanced dual-layer CT of the head using virtual monoenergetic images compared with polyenergetic single-energy CT.** *Invest Radiol* 2017;52:470–76 CrossRef Medline
7. Liu X, Chen L, Qi W, et al. **Thin-slice brain CT with iterative model reconstruction algorithm for small lacunar lesions detection: image quality and diagnostic accuracy evaluation.** *Medicine (Baltimore)* 2017;96:e9412 CrossRef Medline
8. Lennartz S, Laukamp KR, Neuhaus V, et al. **Dual-layer detector CT of the head: Initial experience in visualization of intracranial hemorrhage and hypodense brain lesions using virtual monoenergetic images.** *Eur J Radiol* 2018;108:177–83 CrossRef Medline
9. Neverauskiene A, Maciusovic M, Burkanas M, et al. **Image based simulation of the low dose computed tomography images suggests 13 mAs 120kV suitability for non-syndromic craniosynostosis diagnosis without iterative reconstruction algorithms.** *Eur J Radiol* 2018;105:168–74 CrossRef Medline
10. Stewart FA, Akleyev AV, Akleyev AV, et al; Authors on Behalf of ICRP. **ICRP publication 118: ICRP statement on tissue reactions and early and late effects of radiation in normal tissues and organs–threshold doses for tissue reactions in a radiation protection context.** *Ann ICRP* 2012;41:1–322 CrossRef Medline
11. Sanchez RM, Vano E, Fernandez JM, et al. **Brain radiation doses to patients in an interventional neuroradiology laboratory.** *AJNR Am J Neuroradiol* 2014;35:1276–80 CrossRef Medline
12. Guzinski M, Waszczuk L, Sasiadek MJ. **Head CT: image quality improvement of posterior fossa and radiation dose reduction with ASiR—comparative studies of CT head examinations.** *Eur Radiol* 2016;26:3691–96 CrossRef Medline
13. Guberina N, Forsting M, Ringelstein A. **Efficacy of lens protection systems: dependency on different cranial CT scans in the acute stroke setting.** *Radiat Prot Dosimetry* 2017;175:279–83 CrossRef Medline
14. Silva AC, Morse BG, Hara AK, et al. **Dual-energy (spectral) CT: applications in abdominal imaging.** *Radiographics* 2011;31:1031–1046 discussion 1047–50 CrossRef Medline
15. Pomerantz SR, Kamalian S, Zhang D, et al. **Virtual monochromatic reconstruction of dual-energy unenhanced head CT at 65-75 keV maximizes image quality compared with conventional polychromatic CT.** *Radiology* 2013;266:318–25 CrossRef Medline
16. Schneider D, Apfaltrer P, Sudarski S, et al. **Optimization of kiloelectron volt settings in and cervical dual-energy CT angiography determined with virtual monoenergetic imaging.** *Acad Radiol* 2014;21:431–36 CrossRef Medline
17. Tawfik AM, Kerl JM, Razek AA, et al. **Image quality and radiation dose of dual-energy CT of the head and neck compared with a standard 120-kVp acquisition.** *AJNR Am J* 2011;32:1994–99 CrossRef Medline
18. Bodanapally UK, Dreizin D, Issa G, et al. **Dual-energy CT in enhancing subdural effusions that masquerade as subdural hematomas: diagnosis with virtual high-monochromatic (190-keV) images.** *AJNR Am J Neuroradiol* 2017;38:1946–52 CrossRef Medline
19. Van Hedent S, Große Hokamp N, Laukamp KR, et al. **Differentiation of hemorrhage from iodine using spectral detector CT: a phantom study.** *AJNR Am J Neuroradiol* 2018;39:2205–10 CrossRef Medline
20. Kaemmerer N, Brand M, Hammon M, et al. **Dual-energy computed tomography angiography of the head and neck with single-source computed tomography: a new technical (split filter) approach for bone removal.** *Invest Radiol* 2016;51:618–23 CrossRef Medline
21. Mannil M, Ramachandran J, Vittoria de Martini I, et al. **Modified dual-energy algorithm for calcified plaque removal: evaluation in carotid computed tomography angiography and comparison with digital subtraction angiography.** *Invest Radiol* 2017;52:680–85 CrossRef Medline
22. Borggrefe J, Kottlors J, Mirza M, et al. **Diffrentiation of clot composition using conventional and dual-energy computed tomography.** *Clin Neuroadiol* 2018;4:515–22 CrossRef Medline
23. Alvarez RE, Macovski A. **Energy-selective reconstructions in X-ray computerized.** *Phys Med Biol* 1976;21:733–44 CrossRef Medline
24. Große Hokamp N, Höink AJ, Doerner J, et al. **Assessment of arterially hyper-enhancing liver lesions using virtual monoenergetic images from spectral detector CT: phantom and patient experience.** *Abdom Radiol (NY)* 2018;43:2066–74 CrossRef Medline
25. Flohr TG, McCollough CH, Bruder H, et al. **First performance evaluation of a dual-source CT (DSCT) system.** *Eur Radiol* 2006;16:256–68 CrossRef Medline
26. McCollough CH, Leng S, Yu L, et al. **Dual- and multi-energy CT: principles, technical approaches, and clinical applications.** *Radiology* 2015;276:637–53 CrossRef Medline
27. Gamer M, Lemon J, Fellows I, et al. **Package irr: various coefficients of interrater reliability and agreement.** 2012. https://CRAN.R-project.org/package.org/package-irr. Accessed March 25, 2019
28. Cohen J. **A coefficient of agreement for nominal scales.** *Educational and Psychological Measurement* 1960;20:37–46 CrossRef
29. Fleiss JL, Cohen J. **The equivalence of weighted kappa and the intraclass correlation coefficient as measures of reliability.** *Educational and Psychological Measurement* 1973;33:613–19 CrossRef
30. Smits M, Dippel DW, de Haan GG, et al. **External validation of the Canadian CT Head Rule and the New Orleans Criteria for CT scanning in patients with minor head injury.** *JAMA* 2005;294:1519–25 CrossRef Medline
31. Große Hokamp N, Hellerbach A, Gierich A, et al. **Reduction of artifacts caused by deep brain stimulating electrodes in cranial computed tomography imaging by means of virtual monoenergetic images, metal artifact reduction algorithms, and their combination.** *Invest Radiol* 2018;53:424–31 CrossRef Medline
32. Große Hokamp N, Gilkeson R, Jordan MK, et al. **Virtual monoenergetic images from spectral detector CT as a surrogate for conventional CT images: unaltered attenuation characteristics with reduced image noise.** *Eur J Radiol* 2019;117:49–55 CrossRef Medline
33. Kamiya K, Kunimatsu A, Mori H, et al. **Preliminary report on virtual monochromatic spectral imaging with fast kVp switching dual energy head CT: comparable image quality to that of 120-kVp CT**

without increasing the radiation dose. *Jpn J Radiol* 2013;31:293–98 CrossRef Medline
34. Hwang WD, Mossa-Basha M, Andre JB, et al. **Qualitative comparison of noncontrast head dual-energy computed tomography using rapid voltage switching technique and conventional computed tomography.** *J Comput Assist Tomogr* 2016;40:320–25 CrossRef Medline
35. American Association of Physicists in Medicine (TaskGroup204). **Size-specific dose estimates (SSDE) in pediatric and adult body CT examinations.** 2011. https://www.aapm.org/pubs/reports/detail.asp?docid=143. Accessed April 12, 2019
36. McMillan K, Bostani M, Cagnon C, et al. **Size-specific, scanner-independent organ dose estimates in contiguous axial and helical head CT examinations.** *Med Phys* 2014;41:121909 CrossRef Medline
37. Kalisz K, Rassouli N, Dhanantwari A, et al. **Noise characteristics of virtual monoenergetic images from a novel detector-based spectral CT scanner.** *Eur J Radiol* 2018;98:118–25 CrossRef Medline

PACS Integration of Semiautomated Imaging Software Improves Day-to-Day MS Disease Activity Detection

A. Dahan, R. Pereira, C.B. Malpas, T. Kalincik, and F. Gaillard

ABSTRACT

BACKGROUND AND PURPOSE: The standard for evaluating interval radiologic activity in MS, side-by-side MR imaging comparison, is restricted by its time-consuming nature and limited sensitivity. VisTarsier, a semiautomated software for comparing volumetric FLAIR sequences, has shown better disease-activity detection than conventional comparison in retrospective studies. Our objective was to determine whether implementing this software in day-to-day practice would show similar efficacy.

MATERIALS AND METHODS: VisTarsier created an additional coregistered image series for reporting a color-coded disease-activity change map for every new MS MR imaging brain study that contained volumetric FLAIR sequences. All other MS studies, including those generated during software-maintenance periods, were interpreted with side-by-side comparison only. The number of new lesions reported with software assistance was compared with those observed with traditional assessment in a generalized linear mixed model. Questionnaires were sent to participating radiologists to evaluate the perceived day-to-day impact of the software.

RESULTS: Nine hundred six study pairs from 538 patients during 2 years were included. The semiautomated software was used in 841 study pairs, while the remaining 65 used conventional comparison only. Twenty percent of software-aided studies reported having new lesions versus 9% with standard comparison only. The use of this software was associated with an odds ratio of 4.15 for detection of new or enlarging lesions ($P = .040$), and 86.9% of respondents from the survey found that the software saved at least 2–5 minutes per scan report.

CONCLUSIONS: VisTarsier can be implemented in real-world clinical settings with good acceptance and preservation of accuracy demonstrated in a retrospective environment.

ABBREVIATIONS: AIC = akaike information criterion; CSSC = conventional side-by-side comparison; EDSS = Expanded Disability Status Scale; VT = VisTarsier

Multiple sclerosis is a common immune-mediated inflammatory disease of the central nervous system and the most frequent neurologic cause of disability in young adults.[1,2] With the ongoing development and approval of disease-modifying drugs, the armamentarium of therapies to reduce relapse frequency, radiological disease activity and progression continues to grow. With these therapies, no evidence of disease activity has become a new treatment target, making disease monitoring more important than ever.[3,4]

MR imaging is the most commonly used surrogate marker of MS activity.[5,6] Radiologists typically evaluate MR imaging studies for the development of new MS lesions by comparing the current study with a prior study in adjacent view ports on a monitor, usually in multiple planes, which we will refer to as conventional side-by-side comparison (CSSC). The sensitivity of such a comparison is degraded by multiple human and technologic factors, including the quality of MR imaging protocols and the expertise of radiologists evaluating the examinations.[7-9] Although it is routinely accepted in phase II and III trials, the demanding nature and relative inaccuracy of visual inspection of MRIs compared with novel methods including computer-assisted lesion detection pose an important limitation to utility in clinical practice.[10,11]

Indeed, computer-assisted lesion-detection software has shown promise by increasing the specificity and sensitivity

Received May 30, 2019; accepted after revision July 19.

From the Department of Radiology (A.D.), Austin Hospital, Heidelberg, Australia; Departments of Radiology (R.P., F.G.) and Neurology (T.K., C.M.), Royal Melbourne Hospital, Parkville, Victoria, Australia; Department of Radiology (R.P.), University of Queensland, Brisbane, Queensland, Australia; and Clinical Outcomes Research Unit (CORe) (C.M., T.K.), Departments of Medicine and Radiology (F.G.), University of Melbourne, Melbourne, Australia.

Please address correspondence to Ariel Dahan, MD, MSc, Radiology Department, Lance Townsend Bldg, Austin Hospital, 145 Studley Rd, Heidelberg 3084, Australia; e-mail: ariel.dahan@austin.org.au

Indicates article with supplemental on-line table.

Indicates article with supplemental on-line photo.

http://dx.doi.org/10.3174/ajnr.A6195

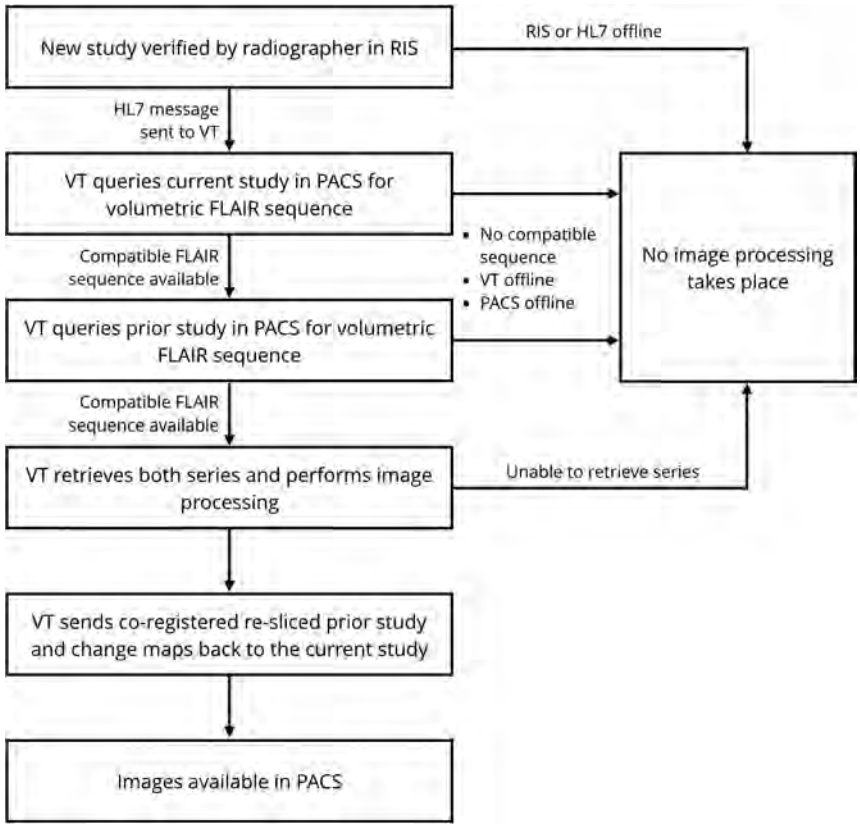

FIG 1. Software integration into PACS workflow. This flow diagram outlines how the new MR imaging studies for patients with MS are processed by the VisTarsier software in a virtual machine once they are signed off in the radiology information system (RIS) by the radiographer. Successful processing requires all systems to be operational and compatible sequences to be available.

of MS disease-activity monitoring.[8,12,13] One such software, VisTarsier (VT; open-source available at github.com/mh-cad/vistarsier) has been validated in a series of retrospective studies, allowing radiologists, regardless of training level, to detect up to 3 times as many new MS lesions on monitoring scans compared with CSSC.[8,9,14] These validation studies, however, were performed on a dedicated research workstation with axial, coronal, sagittal and semitransparent 3D "overview" images, rather than on a conventional PACS workstation during normal clinical practice.

In this prospective, observational cohort study, we sought to share our experiences implementing this assistive software in the Royal Melbourne Hospital PACS and to demonstrate that once implemented, it would augment radiologists' capacity to detect increases in MS disease-activity detection compared with CSSC.

MATERIALS AND METHODS

Software Integration into PACS

Every new MR imaging brain demyelination protocol study generated using 3T magnets (Tim Trio, 12-channel head coil; Siemens, Erlangen, Germany) for a patient with a previous study obtained with the same MR imaging protocol was automatically processed by the software. The automated process (Fig 1) is triggered as soon as a study is verified in our radiology information system (Karisma; Kestral, Perth, Australia) by the radiographer, with the radiology information system automatically sending a completion HL7 message (NextGen Connect; NextGen Health care, Irvine, California) to the software virtual machine (Xeon Processer E5645, 8 VCPU cores @ 2.40 GHz, 8 GB DDR3 RAM, 500 GB SATA3 7200 RPM hard disk drive, no 3D/GPU acceleration [Intel, Santa Clara, California, Windows 7 Professional 64-bit operating system [Microsoft, Redmond, Washington]). The software then queries the PACS and searches the study for a series that is deemed compatible on the basis of a list of possible series descriptors (eg, FLAIR sagittal 3D). If a compatible series exists in the new study, the software then queries the PACS for previous MR imaging studies of the same patient. Once a compatible series is found in the previous most recent MR imaging, the 2 series are retrieved and processed. Software processing includes brain-surface extraction and masking of volumetric FLAIR sequences, followed by intensity normalization, 6-*df* registration, automated change detection, and reslicing to generate 3 new coregistered series: 1) A resliced prior study sagittal FLAIR (~160 images, preserving original resolution, one 16-bit grayscale channel); 2) an increased signal intensity color map (~160 images, 256 × 256, three 8-bit RGB channels); and 3) a decreased signal intensity color map (~160 images, 256 × 256, three 8-bit RGB channels). Once processing is complete, the virtual machine sends the 3 series (typical total size ~150 megabytes) back to the new study as additional series. These series are then available as part of the normal clinical study for staff radiologists to report in real-time in the usual PACS environment (see the On-line Figure for an example of the output series generated by VisTarsier).

Most important, these change maps do not replace routine sequences and reformats but are in addition to routine imaging. They merely draw the attention of reporting radiologists to areas that may represent new or enlarging lesions (orange). These areas are then assessed normally on routine imaging, and a determination is made as to whether they represent disease activity.

Participants and Data Collection

In July 2015, the software underwent a soft launch within our tertiary hospital's PACS (ethics approval number QA2015161). Eligibility criteria included the following: consecutive studies in patients with a confirmed diagnosis of multiple sclerosis (as per 2017 revised McDonald criteria) and an MR imaging including a

Table 1: Demographic and clinical data across each group[a]

	Proportion	CSSC	Software-Assisted		*P* Value
Scans belonging to female patients	52/65 (80.00%)		599/841 (71.22%)		.23
Primary reporting doctors with fellowship certification	47/65 (72.31%)		586/841 (69.68%)		.36
Age at scan	Mean, 44 yr, 139 days	SD, 11 yr, 223 days	Mean, 43 yr, 15 days	SD,11 yr, 256 days	.72
Time since diagnosis	Mean, 10 yr, 47 days	SD, 6 yr, 230 days	Mean, 9 yr, 58 days	SD, 6 yr, 234 days	.61
EDSS	Median, 2.0	Quartiles, 25% = 1.9, 75% = 3.1	Median, 2.0	Quartiles, 25% = 1.0, 75% = 3.5	.45

[a] This table summarizes the demographic and clinical details for all eligible patients who underwent an MR imaging brain scan at the Royal Melbourne Hospital from July 1, 2015, until June 30, 2017. χ^2 and *t* test statistics were performed to confirm group similarities.[31]

volumetric FLAIR sequence (FOV = 250, 160 sections, section thickness = 0.98 mm, matrix = 258 × 258, in-plane resolution = 0.97 mm, TR = 5000 ms, TE = 350 ms, TI = 1800 ms, 72 degree selective inversion recovery magnetic preparation).[15]

For all studies not meeting the automated criteria for software assistance, only CSSC was used by staff radiologists to report MS disease progression. At our hospital, the software runs as a virtual machine on a server that hosts several other research and nonessential clinical services. Thus, upgrades, power outages, and hospital network reconfigurations lead to a small amount of downtime. In cases in which studies were performed during these times or due to other software-based failures illustrated in Fig 1, VT-assisted series were not automatically generated, and only CSSC was used by reporting radiologists. Unfortunately, a detailed breakdown of the various causes of nonprocessing could not be collated prospectively and cannot be established retrospectively.

We collected imaging reports for all studies performed with the above protocol prospectively from July 1, 2015, to June 30, 2017. All imaging reports for studies meeting the inclusion and exclusion criteria were assessed for written evidence of interval radiologic disease activity. Disease activity was defined as the presence of new or enlarging lesions as stated in the report body and/or conclusion available to the referring clinician. Demographic and clinical details for each patient were included in the study.

After study completion, a brief survey was sent to assess the real-world impact of the software on the day-to-day lives of reporting radiologists and trainees. The results of this survey will be summarized without statistical analysis.

Statistical Analysis

Assessed demographic and clerical variables included the following: the presence of VT-generated series, age at scanning, sex, and reporting radiologist's training level. Assessed clinical variables included disease-modifying drug use, Expanded Disability Status Scale (EDSS), time from diagnosis to the date of the scan, and annualized rate of MR imaging scans (ie, the number of MR imaging scans per year). Because available MS subtype data were incomplete, EDSS, time since diagnosis, and annualized scan rates were used as surrogate markers of disease activity and trajectory. The distributions of the variables were compared between the groups, using *t* tests and χ^2 tests. Generalized linear mixed models were computed to assess the difference in rates of disease progression with the software compared with CSSC. For the primary analysis, interval radiologic activity was entered as the dependent variable. All other assessed variables were entered as independent variables. Continuous variables were centered and scaled. A random intercept term for each participant was specified to allow multiple observations per person. Parameter estimation was performed using maximum likelihood. Because the dependent variable was binary, a binomial response family was used with a logit-link function. We also performed an additional sensitivity analysis with a stepwise forward variable selection for the multivariable generalized linear mixed model. An estimated odds ratio was computed for each variable. A 2-sided critical *P* value of .05 was used to assess statistical significance. Confidence intervals at the 95% level are presented when relevant. Data were analyzed with R statistical and computing software (http://www.r-project.org).[16]

RESULTS

During the 2-year study period, 906 study pairs for 538 patients met the inclusion criteria. VT was automatically activated in 841 study pairs. This activation occurred only on the occasions when both studies included a volumetric 3D-FLAIR sequence, the software was active at the time of image migration to PACS, and both studies had the same series labeling. Thus, all studies protocoled for MS follow-up should have been automatically processed by VT, and the instances in which this was not the case were random, resulting from technical reasons unrelated to patient factors (eg, server being restarted, Fig 1). These random cases occurred in the remaining 65 study pairs, which allowed CSSC only.

Processing times for the software-generated series varied depending on a few factors, including ease of brain-surface extraction and workload of the server due to additional services (average processing time = 5 minutes 11 seconds ± 22 seconds).

Clinical and demographic data are summarized in Table 1, with both groups showing a similar distribution of key variables. Age at scan, sex, and EDSS were comparable across the CSSC and software-assisted groups. As shown in Table 2, pharmacologic treatment was also comparable across groups.

In the first year following the introduction of the software, 20.49% (95% CI, 16.36%–24.63%) of studies using the software reported having new lesions versus 9.76% (95% CI, 0.67%–18.84%) with CSSC. Similarly, in the second year, 20.21% (95% CI, 16.6%–23.82%) of studies using the software reported new

Table 2: Treatment used at scanning for each study group[a]

Medication	CSSC (No.)	Software-Assisted (No.)
Fingolimod	35.85% (19)	37.30% (282)
Natalizumab	32.08% (17)	27.12% (205)
Dimethyl fumarate	3.77% (2)	7.80% (59)
Alemtuzumab	1.89% (1)	3.44% (26)
Glatiramer acetate	5.66% (3)	2.78% (21)
Interferon β	5.66% (3)	3.57% (27)
Other[b]	9.43% (5)	6.61% (50)
No active treatment	5.66% (3)	11.38% (86)
Total	100% (53)	100% (756)
Proportion on higher efficacy therapies (fingolimod/natalizumab/alemtuzumab)	69.87%	67.84%

[a] This table summarizes the number and proportion for each disease-modifying agent at scanning.
[b] Other treatments include teriflunomide, ocrelizumab, rituximab, stem cell transplantation.

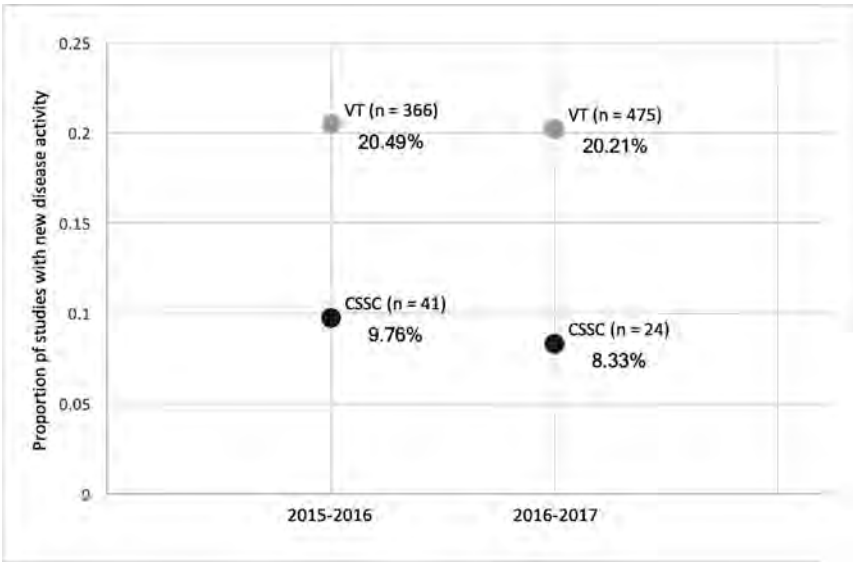

FIG 2. The proportion of scans showing MS progression within each year. This scatterplot highlights the number of scans and the proportion in which new and enlarging lesions were detected for each study group during each year. The position on the vertical axis corresponds to the proportion of scans showing progression. The position along the horizontal axis corresponds to the study year. The lighter shade corresponds to scans generated with the software.

lesions versus 8.33% (95% CI, −2.72%–19.39%) with CSSC. These findings are illustrated in Fig 2.

The fully adjusted multivariable generalized linear mixed model found a greater probability of identifying new/enlarging lesions compared with CSSC with an estimated odds ratio of 4.15 (95% CI, 1.07–16.14; $P = .04$). It was adjusted for age at scanning, sex, whether a scan was reported by a staff radiologist or a radiology resident, EDSS, time since diagnosis, and annualized rate of MR imaging scans. The On-line Table outlines the results of each partially adjusted model computed as part of our sensitivity analysis. These highlight the sustained effect of the software when adjusting for each additional variable independently. The Akaike information criterion (AIC) for the fully adjusted model was 586.8.

Of the 39 individuals reporting MR imaging to whom the impact assessment survey was sent, 23 responded, of whom eight (34.8%) were radiology residents and thirteen (56.5%) were staff radiologists, including eight (34.8%) fellowship-trained neuroradiologists and two (8.7%) radiology fellows. Twenty-one (91.3%) reported always using the software when available, and 22 (95.7%) felt comfortable using it as an additional series for reporting. Twenty-one (91.3%) believed it saved them at least 2–5 minutes of reporting time per scan. None of the respondents believed the software added to their reporting time, and 21 (91.3%) stated that they would like to see it implemented in other areas soon.

DISCUSSION

Semiautomated imaging software has shown great promise in the field of MS disease monitoring.[17-19] Earlier studies of VT concluded that it allowed higher lesion detection with improved interreader reliability and decreased reporting times when used by readers of all radiology training levels (ie, ranging from medical student to fellowship-trained neuroradiologist) compared with their performance using CSSC.[8,9,14] The main caveats of prior research in this area, however, included the retrospective design, artificial research conditions, and/or relatively small sample sizes.

In this translational study, we used a previously retrospectively validated open-source software for MS follow-up. We used prospectively acquired data, accounting for several potential demographic and clinical confounders. We sought to demonstrate the efficacy of semiautomated imaging when implemented in a real-world clinical setting and to share our experience integrating one such software in our daily practice. We used a permissive research design to mitigate any distortion created by a research setting. Department staff were given an in-service brief and informal overview of how the software worked and of prior validation; then radiologists were left to work as they would outside a trial environment. There was no pressure to use the software, to pay attention to or record their usage pattern, or to focus on time. We thought that any such intervention would potentially mislead what another department could expect if they were to implement this sort of assistive software.

More than 800 of 906 new hospital scans had VT-assisted series automatically generated and available to the reporting radiologist in real-time, with only a few minutes elapsing before the color-mapped image series became available on the PACS for

reporting. This feature yielded a >4-fold increase in new lesion detection compared with those scans reported using CSSC. While <10% of studies using CSSC showed disease progression, it was reported in >20% of those using software assistance. In a post-study survey, almost all radiologists and radiology trainees used VT and thought that it cut down on their reporting times for MS comparison studies.

The results observed in this prospective study of >800 scans demonstrate an effect equivalent to the ones seen in our earlier retrospective studies. Similar demographic data were seen across both study groups and were specifically included in our analysis model to limit the amount of confounding. The software was the sole variable associated with a difference in lesion detection compared with age, sex, disease state, and time course; reporting radiologist; and annualized rate of scanning.

MR imaging remains the most widely used and reliable surrogate marker to monitor disease activity in patients in the real-world clinical setting.[5,6,8] Physical and psychological disabilities seen in MS are associated with the number of demyelinating lesions, some of which can be visualized on neuroimaging with FLAIR and T2-weighted sequences.[20-22] Recently, the importance of accurate interval MR imaging activity has become even greater because postcontrast imaging is no longer recommended for routine follow-up, largely due to concerns about the presence of residual contrast in the brain after repeat exposure to gadolinium-based agents.[23,24]

Semiautomated imaging represents a growing field of MS and radiology research, with methods ranging from assisted lesion assessment to brain volumetric analysis.[6,19,25] Similar growth is seen with an extension of computer-assisted detection called "radiomics," which converts images to minable data for deep learning.[26] Image coregistration is a crucial component of traditional MR imaging comparison. Although image coregistration is routinely performed on a PACS, minor changes in alignment are inevitable without reslicing.[27-30] Thus, if not via the color-change maps, the automated reslicing and coregistration availed by the software rapidly and effectively provide an important and known means to optimal image comparison and assessment. After incorporating VT-assisted imaging in our hospital's daily MR imaging reporting activities, our findings are in line with other smaller prospective studies that have shown an absolute increase of 13% (22% relative increase) in new MS lesion detection using similar semiautomated software.[19]

Perhaps more important, implementation of this software in our department was largely seamless and did not appreciably increase transfer times to PACS or data memory burden. Similarly, a post hoc survey of staff in our department showed an overwhelmingly positive response to the integration of the software in our daily practice.

Limitations

The main limitation in this study is the relatively smaller number of scans in the CSSC group. Because our PACS is programmed to automatically process new images with the software whenever possible, the number of unaided scans was limited to the days when VT was unavailable, such as when servers were undergoing maintenance. These factors contributing to the group size discrepancy were random and were not associated with the probability of MR imaging activity. This discrepancy was also further addressed by the statistical design of our analysis.

For those wishing to implement a similar system in their practice, the mentioned downtime could be addressed by having a dedicated server for the software. Similarly, series description and naming in PACS was another potential source of exclusion from automated VisTarsier integration. Similarly, our protocols included 3D-FLAIR sequence series that were all named "FLAIR 3D Sag"; however, at times this could be changed manually, resulting in a matching study not being found. This could be addressed by raising awareness of the importance of standardized series naming. Unfortunately, the reason that a given scan from the CSSC cohort did not meet the automated criteria was not recorded prospectively, and it could not be reconstructed retrospectively.

Although a survey sent to all reporting doctors within the radiology department yielded highly positive results in terms of ease of use and time-saving capabilities of the software, we did not track reporting times as in previous retrospective studies. Unfortunately, these data were not retrospectively mineable on our department's PACS. The qualitative nature of these data thus makes them an adjunct, rather than a statistically rigorous end point.

Last, the inherent limitations of a pragmatic real-world prospective observational cohort study mean that we cannot explicitly control how the studies are read by radiologists, and we do not have the ability to generate inter- or intrareader descriptive statistics. These limitations have, however, previously been established in retrospective validation studies.[8] This is, in our opinion, offset by being able to describe the effect of implementing VisTarsier in a routine clinical environment, which is more likely to be of relevance to other institutions.

CONCLUSIONS

Semiautomated lesion-detection software improves the standard of reporting of new or enlarging T2/FLAIR hyperintense lesions in patients with multiple sclerosis. VisTarsier has improved reporting standards in cerebral MR imaging from patients with MS using standardized volumetric sequences and uniform scanning protocols. Most important, implementing this software in our practice's PACS was relatively seamless and very well received by staff. Future research should validate its capacity to improve reporting in a more heterogeneous sample of images. It should also seek to measure reporting times behind the scenes as a surrogate for workflow efficiency and to demonstrate a change in disease management as a marker of clinical relevance. Computer-aided detection systems promise to improve radiologists' ability to detect disease activity in patients with MS.

ACKNOWLEDGMENTS

We again acknowledge the National Information and Communications Technology of Australia Research Center of Excellence Victorian Research Laboratory for their contribution

in aiding the development of the semiautomated imaging software.

Disclosures: Tomas Kalincik—*UNRELATED*: *Board Membership*: Roche, Sanofi Genzyme, Novartis, Merck, Biogen; *Consultancy*: Novartis, Biogen, Merck, brain atrophy initiative by Sanofi Genzyme; *Grants/Grants Pending*: National Health and Medical Research Council, Medical Research Future Fund, Australian Research Council, MS Research Australia, Eugène Devic EDMUS Foundation/Association pour la Recherche contre la Sclérose en Plaques, Multiple Sclerosis International Federation, Biogen; *Payment for Lectures Including Service on Speakers Bureaus*: WebMD Global, Novartis, Biogen, Sanofi Genzyme, Teva Pharmaceutical Industries, BioCSL, Merck; *Payment for Development of Educational Presentations*: WebMD Global, Novartis, Biogen, Sanofi Genzyme, Teva Pharmaceutical Industries, BioCSL, Merck; *Travel/Accommodations/Meeting Expenses Unrelated to Activities Listed*: WebMD Global, Novartis, Biogen, Sanofi Genzyme, Teva Pharmaceutical Industries, BioCSL, Merck. Frank Gaillard—*UNRELATED*: *Grant*: Royal Melbourne Hospital Foundation, *Comments*: The grant was internal (Royal Melbourne Hospital raises funds to support local projects) and was awarded to continue development of VisTariser software, make it available under an open-source license, and perform this prospective validation. No external funding was received for this project*; *OTHER RELATIONSHIPS:* Founder CEO of Radiopedia.org. *Money paid to the institution.

REFERENCES

1. Ramagopalan SV, Sadovnick AD. **Epidemiology of multiple sclerosis.** *Neurol Clin* 2011;40:207–17 CrossRef Medline
2. Degenhardt A, Ramagopalan SV, Scalfari A, et al. **Clinical prognostic factors in multiple sclerosis: a natural history review.** *Nat Rev Neurol* 2009;5:672–82 CrossRef Medline
3. Weiner HL. **The challenge of multiple sclerosis: how do we cure a chronic heterogeneous disease?** *Ann Neurol* 2009;65:239–48 CrossRef Medline
4. Havrdova E, Galetta S, Stefoski D, et al. **Freedom from disease activity in multiple sclerosis.** *Neurology* 2010;74(Suppl 3):S3–7 CrossRef Medline
5. Fisniku LK, Brex PA, Altmann DR, et al. **Disability and T2 MRI lesions: a 20-year follow-up of patients with relapse onset of multiple sclerosis.** *Brain* 2008;131:808–17 CrossRef Medline
6. Bar-Zohar D, Agosta F, Goldstaub D, et al. **Magnetic resonance imaging metrics and their correlation with clinical outcomes in multiple sclerosis: a review of the literature and future perspectives.** *Mult Scler* 2008;14:719–27 CrossRef Medline
7. Abraham AG, Duncan DD, Gange SJ, et al. **Computer-aided assessment of diagnostic images for epidemiological research.** *BMC Med Res Methodol* 2009;9:74 CrossRef Medline
8. van Heerden J, Rawlinson D, Zhang A, et al. **Improving multiple sclerosis plaque detection using a semiautomated assistive approach.** *AJNR Am J Neuroradiol* 2015;36:1465–71 CrossRef Medline
9. Wang W, van Heerden J, Tacey MA, et al. **Neuroradiologists compared with non-neuroradiologists in the detection of new multiple sclerosis plaques.** *AJNR Am J Neuroradiol* 2017;38:1323–*27* CrossRef Medline
10. Filippi M, Grossman RI. **MRI techniques to monitor MS evolution: the present and the future.** *Neurology* 2002;58:1147–53 CrossRef Medline
11. Goodin DS. **Magnetic resonance imaging as a surrogate outcome measure of disability in multiple sclerosis: have we been overly harsh in our assessment?** *Ann Neurol* 2006;59:597–605 CrossRef Medline
12. Bilello M, Arkuszewski M, Nasrallah I, et al. **Multiple sclerosis lesions in the brain: computer-assisted assessment of lesion load dynamics on 3D FLAIR MR images.** *Neuroradiol J* 2012;25:17–21 CrossRef Medline
13. Moraal B, Meier DS, Poppe PA, et al. **Subtraction MR images in a multiple sclerosis multicenter clinical trial setting.** *Radiology* 2009;250:506–14 CrossRef Medline
14. Dahan A, Wang W, Gaillard F. **Computer-aided detection can bridge the skill gap in multiple sclerosis monitoring.** *J Am Coll Radiol* 2018;15(1 Pt A):93–96 CrossRef Medline
15. Polman CH, Reingold SC, Banwell B, et al. **Diagnostic criteria for multiple sclerosis: 2010 revisions to the McDonald criteria.** *Ann Neurol* 2011;69:29–302 CrossRef Medline
16. The R Core Team. *R: A Language and Environment for Statistical Computing*. Vienna, Austria: R Foundation for Statistical Computing; 2014
17. Jain S, Sima DM, Ribbens A, et al. **Automatic segmentation and volumetry of multiple sclerosis brain lesions from MR images.** *Neuroimage Clin* 2015;8:367–75 CrossRef Medline
18. Schmidt P, Gaser C, Arsic M, et al. **An automated tool for detection of FLAIR-hyperintense white-matter lesions in multiple sclerosis.** *Neuroimage* 2012;59:3774–83 CrossRef Medline
19. Galletto Pregliasco AG, Collin A, Guéguen A, et al. **Improved detection of new MS lesions during follow-up using an automated MR coregistration-fusion method.** *AJNR Am J Neuroradiol* 2018;39:1226–32 CrossRef Medline
20. Mortazavi D, Kouzani AZ, Soltanian-Zadeh H. **Segmentation of multiple sclerosis lesions in MR images: a review.** *Neuroradiology* 2012;54:299–320 CrossRef Medline
21. Caramanos Z, Francis S, Narayanan S, et al. **Large, nonplateauing relationship between clinical disability and cerebral white matter lesion load in patients with multiple sclerosis.** *Arch Neurol* 2012;69:89–95 CrossRef Medline
22. Sormani MP, Rovaris M, Comi G, et al. **A reassessment of the plateauing relationship between T2 lesion load and disability in MS.** *Neurology* 2009;73:1538–42 CrossRef Medline
23. Traboulsee A, Simon J, Stone L, et al. **Revised recommendations of the consortium of MS centers task force for a standardized MRI protocol and clinical guidelines for the diagnosis and follow-up of multiple sclerosis.** *AJNR Am J Neuroradiol* 2016;37:394–401 CrossRef Medline
24. Kanda T, Nakai Y, Hagiwara A, et al. **Distribution and chemical forms of gadolinium in the brain: a review.** *Br J Radiology* 2017;90:20170115. CrossRef Medline
25. Wang C, Beadnall HN, Hatton SN, et al. **Automated brain volumetrics in multiple sclerosis: a step closer to clinical application.** *J Neurol Neurosurg Psychiatry* 2016;87:754–57 CrossRef Medline
26. Giger ML. **Machine learning in medical imaging.** *J Am Coll Radiol* 2018;15:512–20 CrossRef Medline
27. Goodkin DE, Vanderburg-Medendorp S, Ross J. **The effect of repositioning error on serial magnetic resonance imaging scans.** *Arch Neurol* 1993;50:569–70 CrossRef Medline
28. Gawne-Cain ML, Webb S, Tofts P, et al. **Lesion volume measurement in multiple sclerosis: how important is accurate repositioning?** *J Magn Reson Imaging* 1996;6:705–13 Medline
29. Molyneux PD, Miller DH, Filippi M, et al. **Visual analysis of serial T2-weighted MRI in multiple sclerosis: intra- and interobserver reproducibility.** *Neuroradiology* 1999;41:882–88 Medline
30. Duan Y, Hildenbrand PG, Sampat MP, et al. **Segmentation of subtraction images for the measurement of lesion change in multiple sclerosis.** *AJNR Am J Neuroradiol* 2008;29:340–46 CrossRef
31. Kurtzke JF. **Rating neurologic impairment in multiple sclerosis: an Expanded Disability Status Scale (EDSS).** *Neurology* 1983;33:1444–52 CrossRef Medline

Cerebral Damage after Carbon Monoxide Poisoning: A Longitudinal Diffusional Kurtosis Imaging Study

Y. Zhang, T. Wang, J. Lei, S. Guo, S. Wang, Y. Gu, S. Wang, Y. Dou, and X. Zhuang

ABSTRACT

BACKGROUND AND PURPOSE: Previous DTI cross-sectional studies have showed the cerebral damage feature was different in the three clinical stages after carbon monoxide poisoning. Diffusional kurtosis imaging (DKI) is an advanced diffusion imaging model and considered to better provide microstructural contrast in comparison with DTI parameters. The primary aim of this study was to assess microstructural changes in gray and white matter with diffusional kurtosis imaging in the acute, delayed neuropsychiatric, and chronic phases after acute carbon monoxide (CO) poisoning. The secondary aim was to relate diffusional kurtosis imaging measures to neuropsychiatric outcomes of acute carbon monoxide poisoning.

MATERIALS AND METHODS: In all, 17 patients with acute carbon monoxide poisoning and 30 sex- and age-matched healthy volunteers were enrolled in the study. Patients were scanned within 1 week, 3–8 weeks, and 6 months after acute carbon monoxide poisoning. Diffusional kurtosis imaging metrics including mean kurtosis, mean diffusivity, fractional anisotropy, and kurtosis fractional anisotropy were measured in 11 ROIs and then further correlated with neuropsychiatric scores.

RESULTS: In WM, mean kurtosis tended to increase from the acute-to-delayed neuropsychiatric phases and then decrease in the chronic phase, while in GM mean kurtosis showed a constant decline. Contrary to mean kurtosis, mean diffusivity first decreased then tended to increase in WM, while in GM, from the acute to chronic phases, mean diffusivity showed a constant increase. In both WM and GM, the fractional anisotropy and kurtosis fractional anisotropy values progressively declined with time. Kurtosis fractional anisotropy showed the best diagnostic efficiency with an area under the curve of 0.812 ($P = .000$). Along with neuropsychiatric scores, kurtosis fractional anisotropy of the centrum semiovale and Digit Span Backward were most relevant ($r = 0.476$, $P = .000$).

CONCLUSIONS: Longitudinally, microstructural changes were inconsistent in WM and GM with time after acute carbon monoxide poisoning. Diffusional kurtosis imaging metrics provided important complementary information to quantify the damage to cognitive impairment.

ABBREVIATIONS: CS = centrum semiovale; DKI = diffusional kurtosis imaging; DNS = delayed neuropsychiatric; FA = fractional anisotropy; GP = globus pallidus; KFA = kurtosis fractional anisotropy; MD = mean diffusivity; MK = mean kurtosis; CC = corpus callosum

Carbon monoxide (CO) poisoning often results in serious cerebral damage. On the basis of clinical behavior, surviving patients usually present with 3 clinical phases: the acute, delayed neuropsychiatric (DNS), and chronic. In the acute phase, a patient with a definite history of acute CO poisoning presents with acute and transient clinical symptoms. The DNS phase represents recurrent neuropsychiatric symptoms after the apparent resolution of acute symptoms (a lucid interval from 2 to 40 days; mean duration, 22 days). Furthermore, patients in the chronic phase present symptoms from the acute to chronic phases (even after 1 year).[1]

Necrosis in the globus pallidus (GP) and demyelination in the white matter have been described as the principal pathologic findings of brain damage with CO poisoning in previous reports.[1,2] For the past few years, diffusion-weighted imaging and

Received April 25, 2019; accepted after revision July 25.

From the Department of Radiology (Y.Z., J.L., S.G., Shuaiwen Wang, Y.D., X.Z.), The First Hospital of Lan Zhou University, Intelligent Imaging Medical Engineering Research Center of Gansu Province, Accurate Image Collaborative Innovation International Science and Technology Cooperation Base of Gansu Province, Lanzhou, China; Department of Neurology (T.W., Y.G.), The First Hospital of Lan Zhou University, Lan Zhou, China; and MR Scientific Marketing (Shaoyu Wang), Siemens Healthineers, Xi'an, China.

Y. Zhang and T. Wang contributed equally to this work.

This study was supported by grants from the Research Project of Gansu Provincial Administration of Traditional Chinese Medicine (No.GZK-2018-47).

Please address correspondence to Yanli Zhang, MD, Department of Radiology, The First Hospital of Lan Zhou University, Lan Zhou, China, 730000; e-mail: 994931548@qq.com

Indicates open access to non-subscribers at www.ajnr.org
Indicates article with supplemental on-line table.

http://dx.doi.org/10.3174/ajnr.A6201

diffusion tensor imaging have been popular methods of assessing the above changes. The results indicated that the apparent diffusion coefficient and fractional anisotropy (FA) values were highly correlated with neuropsychiatric scores.[3-7]

Diffusional kurtosis imaging (DKI) is a straightforward extension of the DTI model and is considered to better provide microstructural contrast in comparison with DTI parameters.[8,9] DKI has been experimentally demonstrated to be suitable in both WM and gray matter.[10] The kurtosis reveals the degree of diffusion restriction and tissue microstructural complexity.[11] Evidence from previous research supports elevated kurtosis indicating increased cellular microstructural density, such as with cytotoxic edema or the growth of tumor cells. In contrast, decreasing kurtosis in normal aging and degenerative diseases often suggests myelin destruction or cell loss.[12] Previous research has already depicted brain damage by DKI, but this was a cross-sectional study and observed only WM damage.[13] Due to the longitudinal nature of this study, we were able to observe the dynamic characterization of damage. In addition, this study is comprehensive because we chose both the WM and GM as the ROIs.

Among the parameters we chose, mean kurtosis (MK) was the average of the diffusion kurtosis along all diffusion directions, and higher MK indicated increased microstructural complexity. Mean diffusivity (MD) was viewed as a measurement of isotropic diffusion in the context of free movement of water, and a lower MD value indicated cytotoxic edema, while a higher value represented angiogenic edema. FA reflected water diffusion anisotropy along the 3 principal directions; kurtosis fractional anisotropy (KFA) was mathematically analogous to FA but reflected the anisotropy of the kurtosis tensor.[14] Decline in FA and KFA indicated injured WM fiber integrity.

Our hypothesis was that the evolution of MD, MK, FA, and KFA in the ROIs might be dynamic in the 3 clinical periods; thus, the main purpose of this study was to determine whether DKI metrics could be sensitive enough to dynamically detect microstructural injuries of WM and GM after acute CO poisoning and whether this was useful in evaluating cognitive and executive outcomes.

MATERIALS AND METHODS

Patient Enrollment

The Department of Neurology of the First Hospital of Lanzhou University recruited patients with CO exposure from October 2015 to September 2018. Patients were selected using the following criteria: a clear history of recent CO exposure and DNS occurrence at follow-up. The exclusion criteria were as follows: age younger than 20 years or older than 70 years and a history of brain disorders, including traumatic brain injury, neuropsychiatric disorder, an operation, irradiation, stroke, infection, neoplasm, and demyelinating disease. After initial screening, 17 patients were enrolled in this study. The Ethics Committee of The First Hospital of Lanzhou University approved the study program (LDYYLL2018-114).

Baseline scans and cognitive evaluations were performed within 7 days after acute CO poisoning; follow-up scans were performed within 7 days after DNS occurrence and after 6 months of acute CO poisoning.

Thirty sex- and age-matched healthy subjects were enrolled as controls. All of them had normal MR imaging findings and basic blood test results.

Cognitive Testing

Neuropsychological tests were administered by Tianhong Wang (associate chief physician in neurology) before MR imaging on the same day. The Mini-Mental State Examination was used to assess general intellectual function.[15] Executive function assessments included Digit Forward Span and Digit Backward Span. To evaluate verbal fluency, we asked subjects to name as many items as possible from semantic categories (animals and vegetables). The Barthel Index was used to measure biologic and psychosocial functions.[16]

MR Imaging Protocols

All subjects were scanned on a 3T MR imaging system (Magneton Skyra; Siemens, Erlangen, Germany). The sequences and parameters were as follows:

T1-weighted imaging: TR = 1670 ms, TE = 11 ms, FOV = 240 × 240 mm, 320 × 224 matrix, and slice thickness = 2.5 mm.
DWI: single-shot echo-planar sequence—TR = 4500 ms, TE = 102 ms, FOV = 240 × 240 mm, matrix = 192 × 192, and slice thickness = 2.5 mm. A b-value of 1000 s/mm^2 was chosen.
DKI: spin-echo EPI diffusion sequence with a total of 30 different diffusion-encoding directions. On the basis of previous studies, the b-value in WM should be higher than that in GM, where 2500∼3000 s/mm^2 was found to be ideal in WM.[17,18] Therefore, the b-values of 0, 1000, and 3000 s/mm^2 were used in this scan.

Axial images were acquired using the following parameters: TR = 6000 ms, TE = 96 ms, FOV = 240 × 240 mm, matrix = 192 × 192, and section thickness = 2.5 mm.

The baseline and followed-up scans were performed by the same technician (Xin Zhuang), and the same positioning baseline and parameters. Images were corrected for motion and eddy currents using the eddy-correct tool of the FMRIB Software Library (FSL; https://fsl.fmrib.ox.ac.uk/fsl/fslwiki/). DKI postprocessing was performed using the free software Diffusion Kurtosis Estimator (http://www.nitrc.org/projects/dke), which generated parametric maps including FA, MD, MK, and KFA. ROI delineation and measurement were performed on the software MRIcron (https://www.nitrc.org/projects/mricron/).

MD, MK, FA, and KFA Data Analysis

As the vulnerable damage regions and important functional areas,[2,19,20] the GP, caudate nucleus, thalamus, centrum semiovale (CS), corpus callosum (CC), frontal lobe, occipital lobe, temporal lobe, and parietal lobe were chosen as our ROIs. Every ROI was represented by a sphere with a diameter of 3 mm to lessen partial volume effects, and they were manually placed on T1WI (Fig 1)[13-21] and transferred onto the corresponding parametric map. After ensuring the same scan section, we applied the initially defined ROIs to the follow-up maps. Except for the CC genu, body, and splenium, other ROIs were placed bilaterally, and the mean value was extracted.

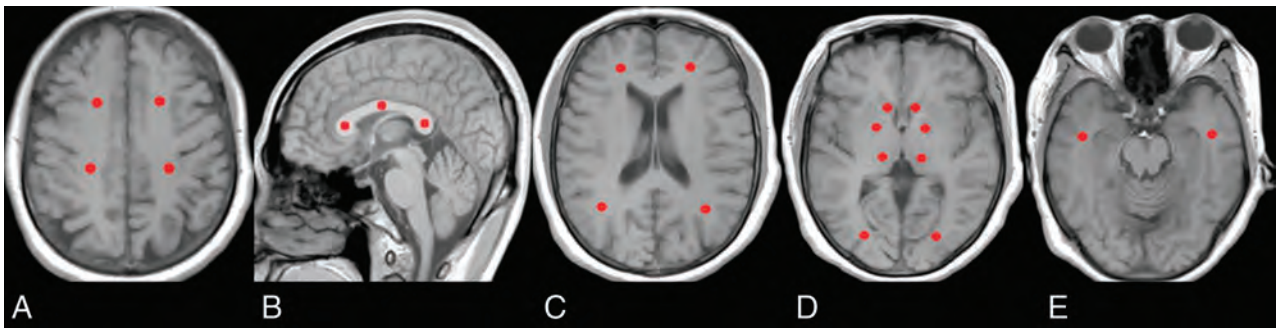

FIG 1. Location of the ROIs. *A*, Centrum semiovale. *B*, Genu, body, and splenium of the corpus callosum. *C*, Frontal and parietal lobes. *D*, Globus pallidus, caudate nucleus, thalamus, and occipital lobe. *E*, Temporal lobe.

Table 1: Clinical variables of patients in different stages of CO exposure[a]

	CO-Exposure Group (n = 17)			
	Acute Stage	DNS Stage	Chronic Stage	Controls (n = 30)
Average days to evaluation	5.53 ± 1.07	30.76 ± 5.90	196.41 ± 9.21	
Sex (male/female) (No.)	8:9	8:9	8:9	15:15
Age (yr)	47.41 ± 11.50	47.41 ± 11.50	47.41 ± 11.50	48.40 ± 9.84
Education (yr)	14.00 (9.50 ± 14.00)	14.00 (9.50 ± 14.00)	14.00 (9.50 ± 14.00)	14.00 (11.00 ± 14.00)
MMSE	26.00 ± 2.50[b,c]	18.59 ± 4.21[c,d]	24.59 ± 2.81[c]	29.00 (28.00–29.00)
Barthel Index	90.00 (80.00–100.00)[b,c]	25.00 (16.00–45.00)[c,d]	98.00 (92.50–100.00)[c]	100.00 (100.00-100.00)
Digit span test				
Forward	6.00 ± 1.46[b,c]	2.00 (1.50–3.00)[c,d]	5.06 ± 1.98[c]	7.00 (7.00–8.00)
Backward	3.76 ± 1.25[b,c]	1.00 (1.00–1.00)[c,d]	2.41 ± 0.94[c]	5.00 (4.00–5.00)
Verbal fluency test				
Animals	11.18 ± 3.36[b,c]	5.47 ± 2.90[c,d]	9.53 ± 3.15[c]	15.00 (14.75.00–16.00)
Vegetables	11.59 ± 2.29[b,c]	5.00 (3.50–6.00)[c,d]	11.00 (9.50–12.00)[c]	13.87 ± 1.50

Note:—MMSE indicates Mini-Mental State Examination.
[a] Data are expressed as mean ± SD and median (25th to 75th quartiles).
[b] $P < .05$ (acute versus DNS).
[c] $P < .05$ (versus controls).
[d] $P < .05$ (DNS versus chronic).

AQ: J

Statistical Analyses

The statistical analysis was performed using the Statistical Package for Social Sciences software package (Version 22 for Windows; IBM, Armonk, New York). The Friedman test and post hoc pair-wise comparisons were used to assess neuropsychiatric scores and DKI parameters of the 3 clinical periods. In post hoc pair-wise comparisons, P values adjusted by the Bonferroni correction (the original P values multiplied by 3) were compared, with the usual nominal threshold of .05. Two independent-samples t tests or Mann-Whitney U tests were used to compare the differences between patients and controls. The area under the curve of each DKI parameter in different regions was calculated by receiver operating characteristics. Spearman correlation analysis was used to explore the relationship between the cognitive score and the DKI-derived parameter. P values $< .05$ were considered significant for the tests.

RESULTS

Demographic and Neuropsychiatric Data

Table 1 summarizes the clinical data of the 2 groups. The CO-exposure group had significantly lower neuropsychiatric scores than the control group ($P < .05$). These scores decreased from the acute-to-DNS phases and then increased at the chronic phase ($P < .05$).

Comparisons of DKI-Derived Parameters

The change in DKI metrics is shown in the On-line Table and Fig 2. Compared with the control value, the FA and KFA values of all ROIs showed a decreasing trend in the CO-exposure group. In the CS, corpus callosum body, and corpus callosum splenium, a significant increase in MK and a decrease in MD emerged in the DNS phase. In the GP, however, the highest MK and lowest MD values appeared in the acute phase ($P < .05$).

Among the CO-exposure group, MK in WM showed a trend of increasing from the acute to DNS phases and then decreased at the chronic phase. Contrary to MK, MD first decreased from baseline to the DNS phase and then increased in the chronic phase.

In the GM, from the acute to chronic phase, MK progressively decreased, while MD continually increased. However, in both the WM and GM, the values of FA and KFA showed a trend toward progressive reduction with time.

Comparison of Positive Imaging Characteristics in the 3 Clinical Phases

Figures 3 and 4 represent evolving lesions in the GP and CS, respectively, depicted in the 5 imaging maps in patients 1 and 2 with acute CO poisoning, arranged in the acute, DNS, and chronic phases.

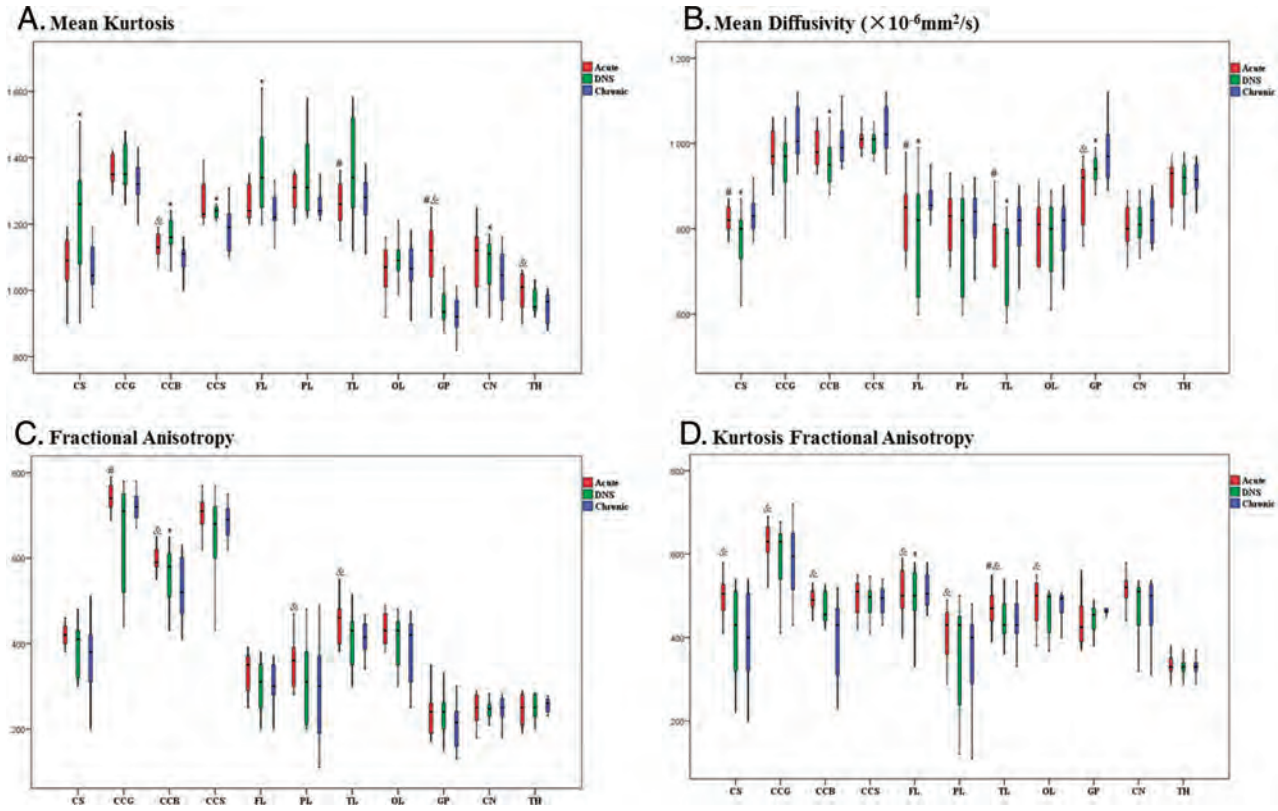

FIG 2. Boxplots of diffusional kurtosis imaging in ROIs in the acute phase (*red bar*), DNS phase (*green bar*), and chronic phase (*blue bar*) with CO intoxication. The *hashtag* indicates $P < .05$ (acute versus DNS); *ampersand*, $P < .05$ (acute versus chronic); and *asterisk*, $P < .05$ (DNS versus chronic).

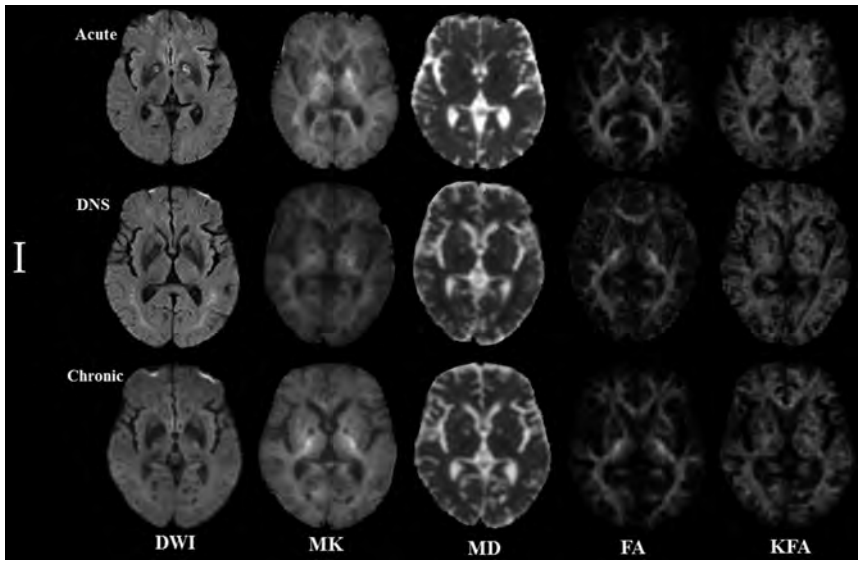

FIG 3. Patient 1: A 54-year-old man. The lesion evolution in the globus pallidus in the acute (5 days), delayed neuropsychiatric (39 days), and chronic (192 days) phases.

In patient 1, symmetric hyperintense lesions in the GP on DWI and MK maps in the acute phase were hypointense lesions on other maps. In the DNS phase, the lesions decreased to isointense lesions on DWI, while they were hypointense lesions on MK and hyperintense lesions on MD maps; in the chronic phase, the intensity of lesions was lower than in the DNS phase on MK maps but higher on MD maps. In both the DNS and chronic phases, the lesions on the FA and KFA maps had lower intensity than those in the acute phase. Notably, in the DNS phase, new hyperintensity lesions emerged in the WM.

In patient 2, slightly hyperintense lesions appeared in the CS in the acute phase on the DWI and MK maps but were isointense lesions on other maps. In the DNS phase, they were higher on the DWI and MK maps and were hypointense lesions on the MD, FA, and KFA maps. In the chronic phase, the intensity significantly decreased on the MK map but increased on the MD map, yet the lesions were still hypointense on the FA and KFA maps.

Diagnostic Performance of DKI-Derived Parameters

In the WM region, KFA had a higher area under the curve than the other measures, among which KFA in the CS had the best performance to differentiate patients in the DNS phase from controls with an area under the curve of 0.812 ($P = .000$) (Table 2). Unlike WM, in the GM region, MK had better differentiation performance than other measures.

KFA Value Predicted Cognitive Performance

The correlations between KFA in the selected ROIs and neuropsychiatric scores are shown in Table 3. The results show that reduction in KFA in the CS, corpus callosum genu, corpus callosum splenium, frontal lobe, parietal lobe, and GP was significantly associated with a decline in the Mini-Mental State Examination scores ($P < .05$). A decline in the Digit Span Backward score was associated with a KFA decrease in the CS, corpus callosum genu, corpus callosum body, corpus callosum splenium, frontal lobe, parietal lobe, and GP ($P < .05$). However, the Barthel Index, Digit Span Forward, and verbal fluency scores had a slight correlation with all regions.

DISCUSSION

Dynamic Changes in the MK and MD

Physiopathologic changes induced by hypoxic-ischemic damage with CO poisoning included mainly intracellular tortuosity and viscosity changes, which were subsequent to the breakdown of cytoskeletal structures and swelling of the mitochondria, and augmented the complexity or heterogeneity of the microenvironment, eventually leading to an increase in MK. Meanwhile, the cytotoxic edema reduced the extracellular volume and restriction in water motion, which gave rise to a decrease in MD. Our results showed that the change in MK was always contrary to that in MD, both in WM and GM. Accompanied by cell necrosis, liquefaction, apoptosis, and atrophy, the complexity of the tissue appeared to significantly decrease and the vasogenic edema increased. The former resulted in a decrease in MK,[22] and the latter resulted in the increase in MD.

Notably, our results show that increasing MK and decreasing MD appeared earlier in GM than in WM. This finding might be attributed to the increased vulnerability to hypoxia of GM because neurons in GM have high blood demand. In addition, it also indicates that obvious damage in WM occurred in the DNS phase. As we observed, all patients had typical bilateral hyperintensity of WM on DWI in the DNS phase, while in the acute phase, only 5 patients had multiple focal lesions in the WM. These findings were consistent with previous research showing that hyperintense areas in WM on T2-weighted imaging were more widespread after the appearance of the DNS phase than before it.[23,24]

In a previous report, the kurtosis values in the WM region were lower in patients than in controls.[13] However, our results showed that MK was higher in the acute and DNS stages in the CO-exposure group than in the control group; this finding indicates the increased microstructural complexity in the early stages of poisoning. In fact, an increase of MK also occurred in acute stroke research. Jensen et al[25] found

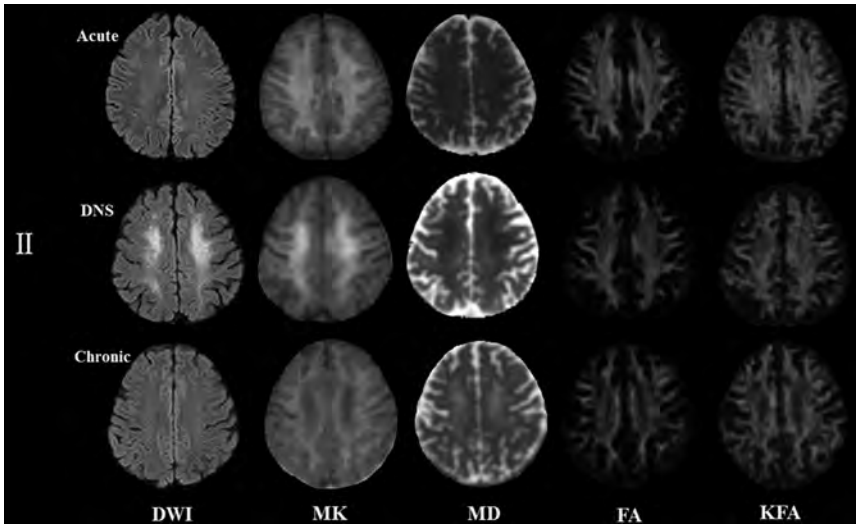

FIG 4. Patient 2: A 42-year-old woman. The lesion evolution in the centrum semiovale in the acute (4 days), delayed neuropsychiatric (25 days), and chronic (223 days) phases.

Table 2: Diagnostic performance of DKI parameters in differentiating patients with CO exposure from controls

	Area under the ROC Curve											
	Acute Stage				DNS Stage				Chronic Stage			
Brain Regions/ROIs	MK	MD	FA	KFA	MK	MD	FA	KFA	MK	MD	FA	KFA
White matter												
Centrum semiovale	0.588[a]	0.549	0.555	0.667	0.774[a]	0.770[a]	0.667	0.812[a]	0.516	0.521	0.732[a]	0.802[a]
Corpus callosum												
Genu	0.126	0.522	0.499	0.701[a]	0.599	0.642	0.700[a]	0.753[a]	0.574	0.663[a]	0.681[a]	0.766[a]
Body	0.618	0.601	0.570	0.602	0.759[a]	0.714[a]	0.699[a]	0.780[a]	0.649	0.586	0.789[a]	0.810
Splenium	0.578	0.719[a]	0.600	0.749[a]	0.674	0.768	0.707[a]	0.770[a]	0.720[a]	0.416	0.729[a]	0.811[a]
Frontal	0.651	0.564	0.602	0.671	0.726[a]	0.640	0.736[a]	0.741[a]	0.503	0.612	0.757[a]	0.771[a]
Parietal	0.532	0.583	0.557	0.646	0.637	0.639	0.656	0.697[a]	0.605	0.429	0.697[a]	0.762[a]
Temporal	0.567	0.622	0.575	0.731[a]	0.671	0.745[a]	0.749[a]	0.806[a]	0.604	0.509	0.699	0.775[a]
Occipital	0.645	0.515	0.671	0.693	0.701[a]	0.609	0.733[a]	0.775[a]	0.287[a]	0.503	0.761[a]	0.791[a]
Gray matter												
Globus pallidus	0.800[a]	0.76[a]	0.541	0.633	0.649	0.448	0.553	0.541	0.724[a]	0.640	0.660	0.602
Caudate nucleus	0.562	0.516	0.520	0.501	0.539	0.514	0.551	0.514	0.659[a]	0.535	0.603	0.613
Thalamus	0.590	0.585	0.556	0.477	0.550	0.379	0.509	0.520	0.700[a]	0.400	0.534	0.537

Note:—ROC indicates receiver operating characteristic.
[a] <.05 indicates significance.

Table 3: Correlation study between KFA and cognitive tests in patients with CO intoxication

Brain Regions/ROIs	MMSE	Barthel Index	Digit Span		Verbal Fluency	
			Forward	Backward	Animals	Vegetables
White matter						
Centrum semiovale	r = 0.399[a] P = .000	r = 0.125 P = .268	r = 0.212 P = .057	r = 0.476[a] P = .000	r = 0.164 P = .145	r = 0.221[a] P = .048
Corpus callosum						
Genu	r = 0.283[a] P = .010	r = 0.141 P = .209	r = 0.218 P = .051	r = 0.374[a] P = .001	r = 0.167 P = .136	r = 0.188 P = .092
Body	r = 0.206 P = .065	r = 0.211 P = .059	r = 0.232[a] P = .037	r = 0.364[a] P = .001	r = 0.219[a] P = .049	r = 0.176 P = .117
Splenium	r = 0.346[a] P = .002	r = 0.252[a] P = .023	r = 0.201 P = .073	r = 0.270[a] P = .015	r = 0.200 P = .073	r = 0.282[a] P = .011
Frontal	r = 0.324[a] P = .003	r = 0.155 P = .167	r = 0.173 P = .123	r = 0.391[a] P = .000	r = 0.203 P = .069	r = 0.170 P = .129
Parietal	r = 0.222[a] P = .047	r = 0.122 P = .279	r = 0.158 P = .159	r = 0.413[a] P = .000	r = 0.141 P = .211	r = 0.152 P = .174
Temporal	r = 0.174 P = .119	r = 0.171 P = .127	r = 0.246[a] P = .027	r = 0.172 P = .124	r = 0.091 P = .417	r = −0.007 P = .948
Occipital	r = 0.151 P = .178	r = 0.115 P = .305	r = 0.187 P = .095	r = 0.141 P = .210	r = 0.142 P = .208	r = 0.087 P = .442
Gray matter						
Globus pallidus	r = 0.282[a] P = .011	r = 0.206 P = .065	r = 0.280[a] P = .011	r = 0.264[a] P = .017	r = 0.217 P = .051	r = 0.175 P = .119
Caudate nucleus	r = −0.052 P = .645	r = −0.148 P = .188	r = −0.185 P = .099	r = 0.108 P = .338	r = −0.115 P = .308	r = −0.118 P = .294
Thalamus	r = 0.068 P = .544	r = 0.039 P = .726	r = −0.018 P = .871	r = 0.054 P = .630	r = 0.111 P = .323	r = 0.040 P = .720

Note:—MMSE indicates Mini-Mental State Examination.
[a] Significant indicated by<.05.

substantially increased diffusional kurtosis within the cerebral ischemic lesions of 3 subjects with stroke 13-26 hours following the onset of symptoms by application of the DKI MR imaging method. In CO poisoning, these similar results might be explained by secondary ischemic injury caused by hypoxia in the early stage.

By comparing the diagnostic efficiency, we found that MK had a higher sensitivity than MD for monitoring GM damage. This was consistent with previous findings with regard to stroke, Alzheimer disease, Parkinson disease, and neoplastic lesions.[26-31] Compared with other deep GM structures such as the caudate nucleus and thalamus, the GP showed the greatest sensitivity, therefore revealing selective damage to the GP.

Progressive Decrease in FA and KFA

Our results show that FA and KFA of WM progressively decreased with time, which was a finding reported in a previous study: Lo et al[6] reported that a significantly lower mean FA value was found in patients in the DNS phase compared with the control group both before and 3 months after hyperbaric oxygen therapy. Chang et al[32] reported on 17 patients with CO poisoning who underwent DTI assessment 4–6 months after hyperbaric oxygen therapy, and they found that the extensive WM areas with FA decreased. The breakdown of myelin and nerve fiber rarefaction may be an important component of the pathologic process.[14] In addition, we found that the decreases in FA and KFA were more obvious in the DNS and chronic phases than in the acute phase. The underlying mechanisms might be related to neuronal injury that was originally caused by global brain anoxia or ischemia in the acute phase and then resulted in secondary Wallerian degeneration of WM.[33]

In terms of diagnostic efficiency, KFA showed a better efficiency than FA in detecting WM damage. Indeed, previous reports have demonstrated that KFA supplements the contrast in other diffusion MR imaging metrics, particularly FA, which vanishes in near-orthogonal fiber arrangements such as in the superior corona radiata and centrum semiovale, whereas KFA does not.[13,34]

KFA Value Predicted Clinical Performance

Cognitive and executive capacity dysfunction was the common clinical issue for survivors of CO poisoning. Recently, a study based on a total of 9041 adults showed that the dementia incidence was 1.6-fold higher in the CO-exposed cohort than in the nonexposed cohort.[35] Neuropsychiatric deficits related to CO poisoning were also found in our patients. In our study, the positive correlation between the neuropsychiatric score and KFA in multiple WM regions supported the hypothesis that WM microstructural changes may contribute to the decline in cognitive and executive functions. In fact, there were 5 patients in our study who still had poor neuropsychiatric performance regarding incapacity of life, disturbance of intelligence, or hemiplegic paralysis at the chronic stage and had much lower KFA values (0.102∼0.303) in the CS than others.

Relative to other scores, Digit Span Backward was found to have better correlation with most regions in WM, such as the CS, corpus callosum genu, corpus callosum body, frontal lobe, and parietal lobe. This finding might be because the performance on Digit Span Backward is thought to reflect higher-order executive

abilities.[36] Anatomically, the CS is adjacent to the CC, which consists of large projection fibers such as the corticospinal, corticobulbar, and corticopontine tracts. These large projection fibers widely connect the cerebral cortex of the frontal lobe and parietal lobe regions, mediating mainly executive functions.[37]

In addition, due to the GP being related to the extrapyramidal tract, damage usually caused abnormalities in motor function, eventually leading to a decrease in executive capacity.[38] In our study, 6 patients emerged with Parkinson's symptoms which all occurred in the DNS stage.

Last, with respect to the correlation among levels of CO exposure, neuropsychiatric scores, and DKI metrics, previous studies have shown that there is no definite relationship among carboxyhemoglobin levels, the severity of MR imaging findings, and the length of exposure time.[39]

Limitations

First, DKI metrics were measured on the basis of ROIs manually placed in various regions, which might yield imperfect reference values and were thus biased. Second, only limited neuropsychological tests were performed, possibly underestimating the cognitive sequelae.

CONCLUSIONS

We confirmed our initial hypothesis that the evolution of brain damage with CO intoxication was dynamic across time. WM and GM responses to CO exposure might not be identical. KFA could be a surrogate biomarker for tissue damage and reflected the performance of cognitive and executive functions correlated with prognosis.

REFERENCES

1. Beppu T. **The role of MR imaging in assessment of brain damage from carbon monoxide poisoning: a review of the literature.** *AJNR Am J Neuroradiol* 2014;35:625–31 CrossRef Medline
2. Jeon SB, Sohn CH, Seo DW, et al. **Acute brain lesions on magnetic resonance imaging and delayed neurological sequelae in carbon monoxide poisoning.** *JAMA Neurol* 2018;75:436–43 CrossRef Medline
3. Chen NC, Huang CW, Lui CC, et al. **Diffusion-weighted imaging improves prediction in cognitive outcome and clinical phases in patients with carbon monoxide intoxication.** *Neuroradiology* 2013;55:107–15 CrossRef Medline
4. Fujiwara S, Beppu T, Nishimoto H, et al. **Detecting damaged regions of cerebral white matter in the subacute phase after carbon monoxide poisoning using voxel-based analysis with diffusion tensor imaging.** *Neuroradiology* 2012;54:681–89 CrossRef Medline
5. Lin WC, Lu CH, Lee YC, et al. **White matter damage in carbon monoxide intoxication assessed in vivo using diffusion tensor MR imaging.** *AJNR Am J Neuroradiol* 2009;30:1248–55 CrossRef Medline
6. Lo CP, Chen SY, Chou MC, et al. **Diffusion-tensor MR imaging for evaluation of the efficacy of hyperbaric oxygen therapy in patients with delayed neuropsychiatric syndrome caused by carbon monoxide inhalation.** *Eur J Neurol* 2007;14:777–82 CrossRef Medline
7. Terajima K, Igarashi H, Hirose M, et al. **Serial assessments of delayed encephalopathy after carbon monoxide poisoning using magnetic resonance spectroscopy and diffusion tensor imaging on 3.0T system.** *Eur Neurol* 2008;59:55–61 CrossRef Medline
8. Lu H, Jensen JH, Ramania, et al. **Three-dimensional characterization of non-Gaussian water diffusion in humans using diffusion kurtosis imaging.** *NMR Biomed* 2006;19:236–47 CrossRef Medline
9. Jensen JH, Helpern JA. **MRI quantification of non-Gaussian water diffusion by of non-Gaussian water diffusion by analysis.** *NMR Biomed* 2010;23:698–10 CrossRef Medline
10. Assaf Y, Cohen Y. **Non-mono-exponential attenuation of water and N-acetyl aspartate signals due to diffusion in brain tissue.** *J Magn Reson* 1998;131:69–85 CrossRef Medline
11. Lazar M, Jensen JH, Xuan L, et al. **Estimation of the orientation distribution function from diffusional kurtosis imaging.** *Magn Reson Med* 2008;60:774–81 CrossRef Medline
12. Marrale M, Collura G, Brai M, et al. **Physics-techniques and review of neuroradiological applications of diffusion kurtosis imaging (DKI).** *Clin Neuroradiol* 2016;26:391–03 CrossRef Medline
13. Lee JJ, Chang WN, Hsu JL, et al. **Diffusion kurtosis imaging as a neuroimaging biomarker in patients with carbon monoxide intoxication.** *Neurotoxicology* 2018;68:38–46 CrossRef Medline
14. Hansen B, Jespersen SN. **Kurtosis fractional anisotropy: its contrast and estimation by proxy.** *Sci Rep* 2016;6:23999 CrossRef Medline
15. Folstein MF, Folstein SE, McHugh PR. **Mini-mental state: a practical method for grading the cognitive state of patients for the clinician.** *J Psychiatr Res* 1975;12:189–98 CrossRef Medline
16. Sidney K, Amasa BF, Roland WM, et al. **Studies of illness in the aged. The index of ADL: a standardized measure of biological and psychosocial function.** *JAMA* 1963;185:914–19 CrossRef Medline
17. Chuhutin A, Hansen B, Jespersen SN. **Precision and accuracy of diffusion kurtosis estimation and the influence of b-value selection.** *NMR Biomed* 2017;30 CrossRef Medline
18. Hansen B, Jespersen SN. **Recent developments in fast kurtosis imaging.** *Front Phys* 2017;5:1–15 CrossRef
19. Barha CK, Nagamatsu LS, Liu-Ambrose T. **Basics of neuroanatomy and neurophysiology.** *Handb Clin Neurol* 2016;138:53–68 CrossRef Medline
20. Schmahmann JD, Smith EE, Eichler FS, et al. **Cerebral white matter: neuroanatomy- clinical neurology-and neurobehavioral correlates.** *Ann N Y Acad Sci* 2008;1142:266–09 CrossRef Medline
21. Kanda T, Ishii K, Kawaguchi H, et al. **High signal intensity in the dentate nucleus and globus pallidus on unenhanced T1-weighted MR images: relationship with increasing cumulative dose ofa gadolinium-based contrast material.** *Radiology* 2014;270:834–41 CrossRef Medline
22. Coutu JP, Chen JJ, Rosas HD, et al. **Non-Gaussian water diffusion in aging white matter.** *Neurobiol Aging* 2014;35:1412–21 CrossRef Medline
23. Inagaki T, Ishino H, Seno H, et al. **A long-term follow-up study of serial magnetic resonance images in patients with delayed encephalopathy after acute carbon monoxide poisoning.** *Psychiatry Clin Neurosci* 1997;51:421–23 CrossRef Medline
24. Vila JF, Meli FJ, Serqueira OE, et al. **Diffusion tensor magnetic resonance imaging: a promising technique to characterize and track delayed encephalopathy after acute carbon monoxide poisoning.** *Undersea Hyperb Med* 2005;32:151–56 Medline
25. Jensen JH, Falangola MF, Hu C, et al. **Preliminary observations of increased diffusional kurtosis in human brain following recent cerebral infarction.** *NMR Biomed* 2011;24:452–57 CrossRef Medline
26. Hui ES, Fieremans E, Jensen JH, et al. **Stroke assessment with diffusional kurtosis imaging.** *Stroke* 2012;43:2968–73 CrossRef Medline
27. Falangola MF, Jensen JH, Tabesha, et al. **Non-Gaussian diffusion MRI assessment of brain microstructure in mild cognitive impairment and Alzheimer's disease.** *Magn Reson Imaging* 2013;31:840–46 CrossRef Medline
28. Kamagata K, Tomiyama H, Motoi Y, et al. **Diffusional kurtosis imaging of cingulate fibers in Parkinson disease: comparison with conventional diffusion tensor imaging.** *Magn Reson Imaging* 2013;31:1501–06 CrossRef Medline

29. Wang JJ, Lin WY, Lu CS, et al. **Parkinson disease: diagnostic utility of diffusion kurtosis imaging.** *Radiology* 2011;261:210–17 CrossRef Medline
30. Van Cauter S, Veraart J, Sijbers J, et al. **Gliomas: diffusion kurtosis MR imaging in grading.** *Radiology* 2012;263:492–01 CrossRef Medline
31. Cheung JS, Wang E, Lo EH, et al. **Stratification of heterogeneous diffusion MRI ischemic lesion with kurtosis imaging: evaluation of mean diffusion and kurtosis MRI mismatch in an animal model of transient focal ischemia.** *Stroke* 2012;43:2252–54 CrossRef Medline
32. Chang CC, Lee YC, Chang WN, et al. **Damage of white matter tract correlated with neuropsychological deficits in carbon monoxide intoxication after hyperbaric oxygen.** *J Neurotrauma* 2009;26:1263–70 CrossRef Medline
33. Bartzokis G. **Age-related myelin break down: a developmental model of cognitive decline and Alzheimer's disease.** *Neurobiol Aging* 2004;25:5–18 CrossRef Medline
34. Pantoni L, Garcia JH, Gutierrez JA. **Cerebral white matter is highly vulnerable to ischemia.** *Stroke* 1996;27:1641–46 Medline
35. Lai CY, Huang YW, Tseng CH, et al. **Patients with carbon monoxide poisoning and subsequent dementia: a population-based cohort study.** *Medicine (Baltimore)* 2016;95:e2418. CrossRef Medline
36. O'Donnell JP, MacGregor LA, Dabrowski JJ, et al. **Construct validity of neuropsychological tests of conceptual and attentional abilities.** ***J*** *Clin Psychol* 1994;50:596–600 CrossRef Medline
37. Baddeley A, Della Sala S. **Working memory and executive control.** *Philos Trans R Soc Lond B Biol Sci* 1996;351:1397–03 CrossRef Medline
38. Saga Y, Hoshi E, Tremblay L. **Roles of multiple globus pallidus territories of monkey and humans in motivation, cognition and action: an anatomical, physiological and pathophysiological review.** *Front Neuroanat* 2017;10;11 CrossRef
39. Kim DM, Lee IH, Park JY, et al. **Acute carbon monoxide poisoning: MR imaging findings with clinical correlation.** *Diagn Interv Imaging* 2017;98:299–06 CrossRef Medline

An Introduction to Kurtosis Fractional Anisotropy

Neuroradiology and imaging-based diagnostics in general have a dire need for scan techniques with improved microstructural sensitivity for detection of subtle tissue alterations in early disease phases or for diagnostics of diseases that are currently simply radiologically invisible. Diseases in which this need is most outspoken are often neurodegenerative diseases such as Alzheimer's disease, multiple sclerosis, and Parkinson's disease but examples also include (mild, repetitive) trauma, addiction, and stroke. Less frequently reported but important nevertheless is the need for sensitive methods for diagnosis and monitoring of patients exposed to poisonous substances. In the industrialized parts of the world, the leading cause of poisoning is carbon monoxide (CO).[1] In the study by Zhang et al[2] in the present issue of the *American Journal of Neuroradiology* (*AJNR*), brain microstructure in CO-poisoned patients is assessed at 3 time points using diffusional kurtosis imaging (DKI) and is correlated to patient cognitive performance. It concluded that DKI metrics provide important information about the damage to the brain due to CO, and supplement cognitive scores. As a first, the study found kurtosis fractional anisotropy (KFA) to have the best diagnostic efficiency based on a standard area under the curve measure. Because this parameter is likely to be somewhat new to many working in the field of neuroradiology, this commentary aims to recapitulate the basis of KFA and what it might indicate about tissue microstructure.

Diffusion MR Imaging and Diffusional Kurtosis Imaging

Water is abundant in the brain, and the water molecules are thermally driven to move ceaselessly and randomly. The local environment of a water molecule determines its mobility. Therefore, water ensemble properties such as mean diffusivity, diffusion anisotropy, and diffusion distribution shape vary among tissues with different compositions. In neural tissue, diffusion variations are seen among tissue microdomains at the subcellular level,[3] the intra- or extracellular space, among cell types,[4] and therefore also on a coarser scale between gray and white matter tissue.[5] Noninvasive MR imaging–based measurements of brain-water diffusion, therefore, in principle, contain abundant information about the cellular-level tissue composition. Initially, the diffusion MR imaging (dMRI) signal description was based on a Gaussian (normal) diffusion probability distribution,[6] forming the basis for the familiar diffusion tensor imaging technique. In biologic tissue, however, the overall diffusion behavior observed from an MR imaging voxel is not Gaussian under clinically relevant measurement conditions. To account for non-Gaussian diffusion, a kurtosis term is added to the DTI signal equation, producing the diffusion DKI framework:[7]

$$1) \qquad \log S(b,\hat{n}) = -bD(\hat{n}) + \frac{1}{6}b^2\bar{D}^2W(\hat{n}).$$

Equation 1 describes the behavior of the (log of the) normalized dMRI signal from tissue with diffusion described by a 3 × 3 diffusion tensor D, and kurtosis is described by the 4D tensor W. As written here, the signal is measured along a direction $\hat{n}$ with diffusion weighting b. The first term on the right-hand side is the DTI signal term, so DTI is fully contained (and actually improved[8]) in DKI. The second term on the right-hand side of Equation 1 is the kurtosis term, with the kurtosis tensor W describing the non-Gaussian properties of the diffusion, which are not contained in D. As written here, $D(\hat{n})$is the apparent diffusivity and $W(\hat{n})$ is the apparent kurtosis, both observed along the diffusion gradient direction $\hat{n}$. Note that sometimes the apparent kurtosis is referred to as $K(\hat{n})$, where $K(\hat{n}) = W(\hat{n})\bar{D}^2/D(\hat{n})^2$ ($\bar{D}$ is mean diffusivity, see below). Simply put, the kurtosis term accounts for the signal deviation from log-linear DTI behavior along the diffusion-encoding direction $\hat{n}$.

The wealth of information available from DTI and DKI is contained in the diffusion tensor D and the kurtosis tensor W. From D, a number of parameters are available, with typical reported metrics being the apparent diffusion coefficient, $ADC = D(\hat{n})$; mean diffusivity ($\bar{D} \equiv \mathrm{Tr(D)}/3 = (\lambda_1 + \lambda_2 + \lambda_3)/3$, where λ_{1-3} is the diffusion tensor eigenvalues—that is, $D(\hat{x}')$, $D(\hat{y}')$, $D(\hat{z}')$ in the tensor eigenframe); radial and axial diffusivities; and fractional anisotropy (FA).[9] In white matter, the direction with the highest diffusivity (axial diffusivity) largely identifies the main fiber direction.[10-12] The pronounced anisotropy of brain white matter is due to the myelin sheath, the axonal membrane itself, and the cytoskeleton inside the axon,[13] which collectively cause WM FA to be high (typically >0.6, however see the example below). In DKI, D and W are used together to provide more

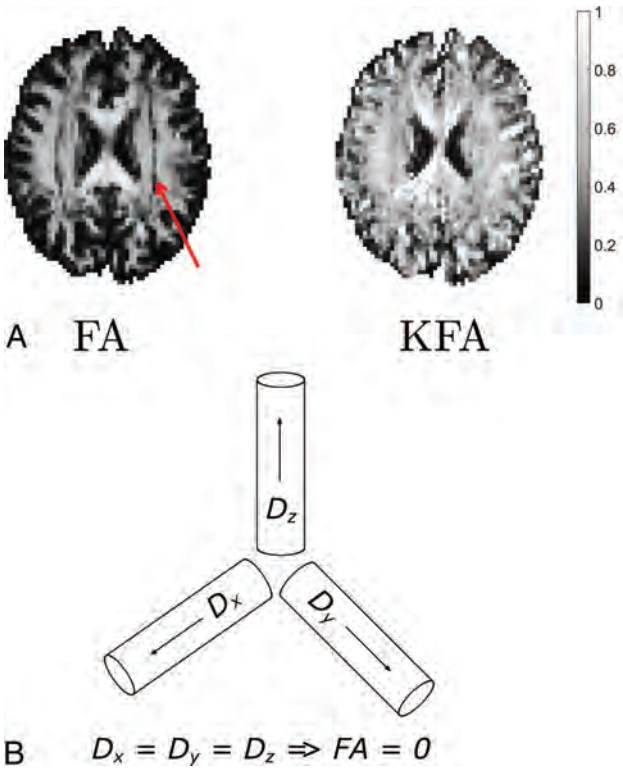

FIGURE. *A*, Maps of FA and KFA in the same section position in the normal human brain. The *color bar* on the right applies to both parameter maps. In the FA map in *A*, a band of low FA values is seen as a *dark band* in both hemispheres. The *red arrow* points to this feature. The same white matter region is seen to have KFA values similar to those of the surrounding white matter. *B*, The fiber arrangement causing this FA behavior is illustrated in a simplified thought experiment. Figure adapted with permission from Hansen and Jespersen.[17]

parameters. These tensors will behave very differently: For example, in a single fiber system, the observed diffusion is high along the fiber direction and low across the fiber direction. In contrast, the kurtosis would be higher across than along the fiber direction, mostly due to restriction effects. This added information improves the capability of dMRI to detect changes in brain and body organ microstructure.[14,15] From DKI, typically reported metrics are analogously the mean kurtosis (MK) and radial and axial kurtosis, and, for very aligned WM, a set of biomarkers from the WM tract integrity framework.[16] More recently, the KFA has been introduced.[17,18] These parameters, their estimation, and varying definitions are reviewed in Hansen and Jespersen.[19]

A comprehensive review of DKI in neuroimaging is outside the scope of this commentary, but to illustrate the potential of DKI, we list key neurologic disorders and neuroradiologic areas where DKI has already proved useful: addiction,[20] stroke,[21-23] Alzheimer's disease,[24] multiple sclerosis,[25] Parkinson's disease,[26-29] brain cancer (gliomas),[30,31] and head trauma/concussion.[32-36] While DKI is increasingly used, so far the relatively new KFA has not been given much attention in preclinical and clinical studies. It is, therefore, noteworthy that KFA features prominently in the article of Zhang et al.[2] Thus, KFA and its interpretation are the main focus of the remainder of this commentary.

dMRI Anisotropy Measures: FA and KFA

The DKI framework produces 2 scalar anisotropy measures: the FA from the diffusion tensor D and the KFA from the kurtosis tensor W. The FA is defined as

$$2)\ FA = \sqrt{\frac{3}{2}}\sqrt{\frac{(\lambda_1-\bar{D})^2+(\lambda_2-\bar{D})^2+(\lambda_3-\bar{D})^2}{(\lambda_1^2+\lambda_2^2+\lambda_3^2)}} = \sqrt{\frac{3}{2}}\frac{\|D-\bar{D}\mathbb{I}\|}{\|D\|},$$

where double bars denote the Euclidean tensor norm (the Frobenius norm), $\mathbb{I}$ is the 3×3 identity matrix, and the remaining parameters are defined above. The numeric front factor ensures that that the FA assumes values in the range from 0 (completely isotropic diffusion) to 1 (fully anisotropic, unidirectional diffusion). Although a few alternative definitions of the kurtosis anisotropy have been proposed (notably the one in Poot et al[37]), the agreed upon definition today is the one introduced in Hansen et al:[18]

$$3)\qquad KFA = \frac{\|\mathrm{W}-\bar{W}\mathrm{I}\|}{\|\mathrm{W}\|},$$

where W is the kurtosis tensor, $\bar{W}$ is the kurtosis tensor mean,[18,38,39] and I is the fully symmetric rank 4 isotropic tensor. Conveniently, this definition of KFA is analogous to the FA definition in Equation 2, with the only difference being due to tensor dimensions. We note the absence of a numeric front factor in Equation 3; KFA naturally assumes values in the 0–1 range. Interested readers are referred to early explorations of KFA in Hansen and Jespersen[17] and Glenn et al.[40] In these studies, simulations and experiments were used to investigate the information contained in the KFA. It was found that KFA contrast supplements the FA in important ways. This feature is illustrated in the Figure showing side-by-side maps of FA and KFA in the same image plane position in normal human brain (Fig 1*A*).

The red arrow points to a dark band in the FA map inside the WM. This band is seen in both hemispheres (note the symmetry). In each hemisphere, this band comprises voxels with low FA values, though the voxels are located in anatomic WM. Conversely, in the KFA map on the right in Fig 1*A*, we see that KFA in WM is high and notably retains its high value in the regions where FA fails as a reporter of anisotropy. These WM voxels assume low FA values because they contain a crossing-fiber arrangement in which WM fibers along 3 orthogonal directions weave between each other. This effectively produces the situation illustrated in the schematic in Fig 1*B*, which shows 3 separate WM fiber bundles that intersect at right angles. In this example, we ignore extra-axonal diffusion. We see that if diffusivities in the 3 fibers are similar (as they are likely to be), the mean diffusivity will be the same as the eigenvalues (ie, the diffusivities along 3 fiber directions $\bar{D} = (\lambda_1+\lambda_2+\lambda_3)/3 \approx \lambda_{1-3}$) causing the FA to vanish because, in this case, each term in the numerator in the middle expression in Equation 2 will be approximately zero. This

happens despite the diffusivity in this fiber arrangement being highly anisotropic. Although not particularly complex, the anisotropy in this fiber arrangement cannot be described by the diffusion tensor, resulting in the low FA constituting the dark band in this WM region.

In the interpretation of these metrics, it is crucial to remember that FA and KFA report on different features of the diffusion process. We, therefore, stress that FA summarizes the spatial variation of diffusion rates, whereas KFA summarizes the directional variation in the degree of non-Gaussian diffusion. Loosely speaking, another difference is that the KFA stems from the kurtosis tensor, which is a 4D tensor with much more "room" to capture, in detail, the spatial variation in kurtosis. Collectively, these factors contribute to the demonstrated behavior in which KFA continues to provide contrast in areas where FA does not. Both metrics can be difficult to interpret in strict terms of tissue properties, but on the basis of the simple example above, we can cautiously state that KFA reflects tissue-diffusion complexity. In the example above, we saw that the 2D diffusion tensor cannot resolve anisotropy in voxels with complex fiber composition. However, we also saw that areas with complex fiber arrangements may be distinguished from genuine low-anisotropy regions using FA and KFA in combination: If FA is low and KFA is high, then likely the diffusion is, in fact, anisotropic but the fiber arrangement is too complex to be captured by the diffusion tensor. Thus, the KFA is a good parameter to include in studies in which subtle remodeling is expected in complex tissue regions. While KFA may therefore prove to be a valuable marker of tissue microstructure, we nevertheless stress that no DKI parameter is specifically bound to a particular microscopic tissue component.

Discussion and Future Perspectives

DKI is sometimes omitted from clinical protocols due to longer acquisition and parameter estimation times than a simple DTI protocol. While strategies exist for fast estimation of most DKI parameters,[18,19,38-44] robust estimation of KFA still requires the full kurtosis tensor W to be determined by fitting on a pixel-by-pixel basis.[17] This requires multishell dMRI data with typically 30 directions and 2–3 nonzero b-values. With modern dMRI techniques, this is possible in clinically feasible scan times.[45] From such datasets, DKI parameter estimation is possible using any one of the many software packages that exist for dMRI data analysis such as MUSC's DKE software package (https://medicine.musc.edu/departments/centers/cbi/dki/dki-data-processing), which also computes the KFA as defined in Equation 3. As noted above, interpretation of DKI findings in terms of biophysical tissue properties is a difficult problem. In preclinical work, subsequent histology may be used to interpret DKI findings,[15,46,47] and insights gained from such efforts may aid in interpretation of clinical DKI.

In the discussion of the example in the Figure, we noted that KFA somehow reflects the diffusion anisotropy below the voxel level. Other techniques achieve similar sensitivity[48,49] but require nonstandard pulse sequences. Until such techniques reach the clinic in earnest, the KFA may serve as an indicator of the diagnostic potential of such sensitivity.

CONCLUSIONS

Imaging techniques with improved sensitivity to microstructure have utility in many areas of neuroimaging, including diagnosis and monitoring of patients exposed to toxic or poisonous substances. The study by Zhang et al[2] uses the microstructurally sensitive DKI framework to assess cerebral damage in CO-poisoned subjects. From DKI, the authors obtain measures of mean diffusivity, FA, MK, and the less explored KFA. These measures are then correlated to neuropsychiatric scores. The work presents a timely contribution to 2 avenues of neuroradiology: 1) the exploration of DKI and KFA in clinical practice, and 2) identification of sensitive markers for diagnostics of CO-intoxicated patients. Insights gained from this study may also benefit and inspire many other areas of neuroimaging where the same techniques could be used. With this commentary, we hope that the KFA will have become more familiar to readers of *AJNR* so that investigators will consider it a parameter of interest in their future work.

REFERENCES

1. Omaye ST. **Metabolic modulation of carbon monoxide toxicity.** *Toxicology* 2002;180:139–50 CrossRef Medline
2. Zhang Y, Wang T, Lei J, et al. **Cerebral damage after carbon monoxide poisoning: a longitudinal diffusional kurtosis imaging study.** *AJNR Am J Neuroradiol* 2019;40:1630–37
3. Lee CH, Flint JJ, Hansen B, et al. **Investigation of the subcellular architecture of L7 neurons of Aplysia Californica using magnetic resonance microscopy (MRM) at 7.8 microns.** *Sci Rep* 2015;5:11147 CrossRef Medline
4. Flint JJ, Hansen B, Portnoy S, et al. **Magnetic resonance microscopy of human and porcine neurons and cellular processes.** *Neuroimage* 2012;60:1404–11 CrossRef Medline
5. Flint JJ, Lee CH, Hansen B, et al. **Magnetic resonance microscopy of mammalian neurons.** *Neuroimage* 2009;46:1037–40 CrossRef Medline
6. Basser PJ, Mattiello J, LeBihan D. **Estimation of the effective self-diffusion tensor from the NMR spin-echo.** *J Magn Reson B* 1994;103:247–54 CrossRef Medline
7. Jensen JH, Helpern JA, Ramani A, et al. **Diffusional kurtosis imaging: the quantification of non-Gaussian water diffusion by means of magnetic resonance imaging.** *Magn Reson Med* 2005;53:1432–40 CrossRef Medline
8. Veraart J, Poot DHJ, Van Hecke W, et al. **More accurate estimation of diffusion tensor parameters using diffusion kurtosis imaging.** *Magn Reson Med* 2011;65:138–45 CrossRef Medline
9. Basser PJ. **Inferring microstructural features and the physiological state of tissues from diffusion-weighted images.** *NMR Biomed* 1995;8:333–44 CrossRef Medline
10. Flint JJ, Hansen B, Blackband SJ. **Diffusion tensor microscopy data (15.6 μm in-plane) of white matter tracts in the human, pig, and rat spinal cord with corresponding tissue histology.** *Data Brief* 2016;9:271–74 CrossRef Medline
11. Flint JJ, Hansen B, Fey M, et al. **Cellular-level diffusion tensor microscopy and fiber tracking in mammalian nervous tissue with direct histological correlation.** *Neuroimage* 2010;52:556–61 CrossRef Medline
12. Hansen B, Flint JJ, Heon-Lee C, et al. **Diffusion tensor microscopy in human nervous tissue with quantitative correlation based on direct histological comparison.** *Neuroimage* 2011;57:1458–65 CrossRef Medline
13. Beaulieu C. **The basis of anisotropic water diffusion in the nervous system: a technical review.** *NMR Biomed* 2002;15:435–55 CrossRef Medline
14. Rosenkrantz AB, Padhani AR, Chenevert TL, et al. **Body diffusion kurtosis imaging: basic principles, applications, and considerations**

for clinical practice. *J Magn Reson Imaging* 2015;42:1190–202 CrossRef Medline
15. Kjølby BF, Khan AR, Chuhutin A, et al. **Fast diffusion kurtosis imaging of fibrotic mouse kidneys.** *NMR Biomed* 2016;29:1709–19 CrossRef Medline
16. Fieremans E, Jensen JH, Helpern JA. **White matter characterization with diffusional kurtosis imaging.** *Neuroimage* 2011;58:177–88 CrossRef Medline
17. Hansen B, Jespersen SN. **Kurtosis fractional anisotropy, its contrast and estimation by proxy.** *Sci Rep* 2016;6:2399 CrossRef Medline
18. Hansen B, Lund TE, Sangill R, et al. **Experimentally and computationally fast method for estimation of a mean kurtosis.** *Magn Reson Med* 2013;69:1754–60 CrossRef Medline
19. Hansen B, Jespersen SN. **Recent developments in fast kurtosis imaging.** *Front Phys* 2017;5 CrossRef
20. Garza-Villarreal EA, Chakravarty MM, Hansen B, et al. **The effect of crack cocaine addiction and age on the microstructure and morphology of the human striatum and thalamus using shape analysis and fast diffusion kurtosis imaging.** *Transl Psychiatry* 2017;7:e1122 CrossRef Medline
21. Hui ES, Fieremans E, Jensen JH, et al. **Stroke assessment with diffusional kurtosis imaging.** *Stroke* 2012;43:2968–73 CrossRef Medline
22. Weber RA, Hui ES, Jensen JH, et al. **Diffusional kurtosis and diffusion tensor imaging reveal different time-sensitive stroke-induced microstructural changes.** *Stroke* 2015;46:545–50 CrossRef Medline
23. Bay V, Kjolby BF, Iversen NK, et al. **Stroke infarct volume estimation in fixed tissue: comparison of diffusion kurtosis imaging to diffusion weighted imaging and histology in a rodent MCAO model.** *PLos One* 2018;13:e019616 CrossRef Medline
24. Falangola MF, Jensen JH, Tabesh A, et al. **Non-Gaussian diffusion MRI assessment of brain microstructure in mild cognitive impairment and Alzheimer's disease.** *Magn Reson Imaging* 2013;31:840–46 CrossRef Medline
25. Inglese M, Bester M. **Diffusion imaging in multiple sclerosis: research and clinical implications.** *NMR Biomed* 2010;23:865–72 CrossRef Medline
26. Arab A, Ruda-Kucerova J, Minsterova A, et al. **Diffusion kurtosis imaging detects microstructural changes in a methamphetamine-induced mouse model of Parkinson's disease.** *Neurotox Res* 2019 Jun 18. [Epub ahead of print] CrossRef Medline
27. Khairnar A, Latta P, Drazanova E, et al. **Diffusion kurtosis imaging detects microstructural alterations in brain of alpha-synuclein overexpressing transgenic mouse model of parkinson's disease: a pilot study.** *Neurotox Res* 2015;28:281–89 CrossRef Medline
28. Wang JJ, Lin WY, Lu CS, et al. **Parkinson disease: diagnostic utility of diffusion kurtosis imaging.** *Radiology* 2011;261:210–17 CrossRef Medline
29. Zhang G, Zhang Y, Zhang C, et al. **Diffusion kurtosis imaging of substantia nigra is a sensitive method for early diagnosis and disease evaluation in Parkinson's disease.** *Parkinsons Dis* 2015;2015:207624 CrossRef Medline
30. Van Cauter S, Veraart J, Sijbers J, et al. **Gliomas: diffusion kurtosis MR imaging in grading.** *Radiology* 2012;263:492–501 CrossRef Medline
31. Bai Y, Lin Y, Tian J, et al. **Grading of gliomas by using monoexponential, biexponential, and stretched exponential diffusion-weighted MR imaging and diffusion kurtosis MR imaging.** *Radiology* 2016;278:496–504 CrossRef Medline
32. Grossman EJ, Ge Y, Jensen JH, et al. **Thalamus and cognitive impairment in mild traumatic brain injury: a diffusional kurtosis imaging study.** *J Neurotrauma* 2012;29:2318–27 CrossRef Medline
33. Grossman EJ, Jensen JH, Babb JS, et al. **Cognitive impairment in mild traumatic brain injury: a longitudinal diffusional kurtosis and perfusion imaging study.** *AJNR Am J Neuroradiol* 2013;34:951–57 CrossRef Medline
34. Næss-Schmidt E, Blicher JU, Eskildsen SF, et al. **Microstructural changes in the thalamus after mild traumatic brain injury: a longitudinal diffusion and mean kurtosis tensor MRI study.** *Brain Injury* 2017;31:230–36 CrossRef Medline
35. Østergaard L, Engedal TS, Aamand R, et al. **Capillary transit time heterogeneity and flow-metabolism coupling after traumatic brain injury.** *J Cereb Blood Flow Metab* 2014;34:1585–98 CrossRef Medline
36. Næss-Schmidt E, Blicher JU, Tietze A, et al. **Diffusion MRI findings in patients with extensive and minimal post-concussion symptoms after mTBI and healthy controls: a cross sectional study.** *Brain Inj* 2018;32:91–8 CrossRef Medline
37. Poot DH, den Dekker AJ, Achten E, et al. **Optimal experimental design for diffusion kurtosis imaging.** *IEEE Trans Med Imaging* 2010;29:819–29 CrossRef Medline
38. Hansen B, Lund TE, Sangill R, et al. **Experimental considerations for fast kurtosis imaging.** *Magn Reson Med* 2016;76:1455–68 CrossRef Medline
39. Hansen B, Lund TE, Sangill R, et al. **Erratum: Hansen, Lund, Sangill, and Jespersen. Experimentally and computationally fast method for estimation of a mean kurtosis.** *Mag Reson Med* 2014;71:2250
40. Glenn GR, Helpern JA, Tabesh A, et al. **Quantitative assessment of diffusional kurtosis anisotropy.** *NMR Biomed* 2015;28:448–59 CrossRef Medline
41. Alstrup AKO, Munk OL, Jensen TH, et al. **Magnetic resonance imaging and computed tomography as tools for the investigation of sperm whale (Physeter macrocephalus) teeth and eye.** *Acta Vet Scand* 2017;59:38 CrossRef Medline
42. Hansen B, Jespersen SN. **Data for evaluation of fast kurtosis strategies, b-value optimization and exploration of diffusion MRI contrast.** *Sci Data* 2016;3:160072 CrossRef Medline
43. Hansen B, Khan AR, Shemesh N, et al. **White matter biomarkers from fast protocols using axially symmetric diffusion kurtosis imaging.** *NMR Biomed* 2017;30 CrossRef Medline
44. Hansen B, Shemesh N, Jespersen SN. **Fast imaging of mean, axial and radial diffusion kurtosis.** *Neuroimage* 2016;142:381–93 CrossRef Medline
45. Setsompop K, Fan Q, Stockmann J, et al. **High-resolution in vivo diffusion imaging of the human brain with generalized slice dithered enhanced resolution: simultaneous multislice (gSlider-SMS).** *Magn Reson Med* 2018;79:141–51 CrossRef Medline
46. Khan AR, Chuhutin A, Wiborg O, et al. **Biophysical modeling of high field diffusion MRI demonstrates microstructural aberration in chronic mild stress rat brain.** *Neuroimage* 2016;142:421–30 CrossRef Medline
47. Khan AR, Hansen B, Wiborg O, et al. **Diffusion MRI and MR spectroscopy reveal microstructural and metabolic brain alterations in chronic mild stress exposed rats: a CMS recovery study.** *Neuroimage* 2018;167:342–53 CrossRef Medline
48. Lasicõ S, Szczepankiewicz F, Eriksson S, et al. **Microanisotropy imaging: quantification of microscopic diffusion anisotropy and orientational order parameter by diffusion MRI with magic-angle spinning of the q-vector.** *Front Phys* 2014;2 CrossRef
49. Avram AV, Ozarslan E, Sarlls JE, et al. **In vivo detection of microscopic anisotropy using quadruple pulsed-field gradient (qPFG) diffusion MRI on a clinical scanner.** *Neuroimage* 2013;64:229–39 CrossRef Medline

B. Hansen
Center of
Functionally Integrative Neuroscience
Aarhus University
Aarhus, Denmark

http://dx.doi.org/10.3174/ajnr.A6235

White Matter Abnormalities in Multiple Sclerosis Evaluated by Quantitative Synthetic MRI, Diffusion Tensor Imaging, and Neurite Orientation Dispersion and Density Imaging

A. Hagiwara, K. Kamagata, K. Shimoji, K. Yokoyama, C. Andica, M. Hori, S. Fujita, T. Maekawa, R. Irie, T. Akashi, A. Wada, M. Suzuki, O. Abe, N. Hattori, and S. Aoki

ABSTRACT

BACKGROUND AND PURPOSE: A number of MR-derived quantitative metrics have been suggested to assess the pathophysiology of MS, but the reports about combined analyses of these metrics are scarce. Our aim was to assess the spatial distribution of parameters for white matter myelin and axon integrity in patients with relapsing-remitting MS by multiparametric MR imaging.

MATERIALS AND METHODS: Twenty-four patients with relapsing-remitting MS and 24 age- and sex-matched controls were prospectively scanned by quantitative synthetic and 2-shell diffusion MR imaging. Synthetic MR imaging data were used to retrieve relaxometry parameters (R1 and R2 relaxation rates and proton density) and myelin volume fraction. Diffusion tensor metrics (fractional anisotropy and mean, axial, and radial diffusivity) and neurite orientation and dispersion index metrics (intracellular volume fraction, isotropic volume fraction, and orientation dispersion index) were retrieved from diffusion MR imaging data. These data were analyzed using Tract-Based Spatial Statistics.

RESULTS: Patients with MS showed significantly lower fractional anisotropy and myelin volume fraction and higher isotropic volume fraction in widespread white matter areas. Areas with different isotropic volume fractions were included within areas with lower fractional anisotropy. Myelin volume fraction showed no significant difference in some areas with significantly decreased fractional anisotropy in MS, including in the genu of the corpus callosum and bilateral anterior corona radiata, whereas myelin volume fraction was significantly decreased in some areas where fractional anisotropy showed no significant difference, including the bilateral posterior limb of the internal capsule, external capsule, sagittal striatum, fornix, and uncinate fasciculus.

CONCLUSIONS: We found differences in spatial distribution of abnormality in fractional anisotropy, isotropic volume fraction, and myelin volume fraction distribution in MS, which might be useful for characterizing white matter in patients with MS.

ABBREVIATIONS: AVF = axon volume fraction; EDSS = Expanded Disability Status Scale; FA = fractional anisotropy; ICVF = intracellular volume fraction; ISO = isotropic volume fraction; MNI = Montreal Neurological Institute; MVF = myelin volume fraction; NAWM = normal-appearing white matter; NODDI = neurite orientation dispersion and density imaging; ODI = orientation dispersion index; QRAPMASTER = quantification of relaxation times and proton density by multiecho acquisition of a saturation-recovery using turbo spin-echo readout

MS is a demyelinating disorder that mainly affects young individuals and involves inflammatory demyelination accompanied by axonal degeneration. Various quantitative metrics, including myelin water imaging,[1] quantitative synthetic MR imaging,[2,3] diffusion tensor imaging,[4] and neurite orientation dispersion and density imaging (NODDI),[5] have revealed abnormalities in both WM lesions and the WM that appears normal on conventional T2WI.

Quantitative synthetic MR imaging simultaneously measures longitudinal T1 and transverse T2 relaxation times (and their inverse, R1 and R2 relaxation rates) and proton density in

Received June 6, 2019; accepted after revision July 28.

From the Departments of Radiology (A.H., K.K., K.S., C.A., M.H., S.F., T.M., R.I., T.A., A.W., M.S., S.A.) and Neurology (K.Y., N.H.), Juntendo University School of Medicine, Tokyo, Japan; Department of Radiology (A.H., S.F., T.M., R.I., O.A.), Graduate School of Medicine, University of Tokyo, Tokyo, Japan; Department of Diagnostic Radiology (K.S.), Tokyo Metropolitan Geriatric Hospital, Tokyo, Japan; and Department of Radiology (M.H.), Toho University Omori Medical Center, Tokyo, Japan.

This work was supported by Japan Society for the Promotion of Science KAKENHI grant Nos. 19K17150, 19K17177, 18H02772, and 18K15643; grant No. JP16H06280, Grant-in-Aid for Scientific Research on Innovative Areas, resource and technical support platforms for promoting research "Advanced Bioimaging Support"; the Japanese Society for Magnetic Resonance in Medicine; and the program for Brain Mapping by Integrated Neurotechnologies for Disease Studies from the Japan Agency for Medical Research and Development.

Please address correspondence to Akifumi Hagiwara, MD, PhD, Department of Radiology, Juntendo University School of Medicine, 1-2-1, Hungo, Bunkyo-ku, Tokyo, Japan 113-8421; e-mail: a-hagiwara@juntendo.ac.jp

Indicates open access to non-subscribers at www.ajnr.org
Indicates article with supplemental on-line tables.
http://dx.doi.org/10.3174/ajnr.A6209

multiple slices,[6] with high repeatability and reproducibility across scanners.[7] It allows creation of any contrast-weighted image, including T1-weighted, T2-weighted, and FLAIR images,[8] without requiring additional scanning time. Furthermore, a 4-compartment model was developed to estimate myelin volume fraction (MVF) in each voxel in the brain, based on the measured R1, R2, and proton density.[9] The estimated myelin correlates with histology in healthy populations[10] and in patients with MS[11] and with other MR imaging–based myelin measurements.[12] Even though synthetic myelin maps have shown tissue abnormalities in plaques and periplaque WM in patients with MS,[2] the voxel-level difference in the estimated myelin between patients with MS and healthy controls has not been investigated to date.

Diffusion-weighted imaging also provides information on microstructure, such as fiber density and orientation, by altering the diffusion-sensitization strength and direction of the encoding gradients.[13] Although used as a standard diffusion MR imaging technique, diffusion tensor imaging lacks specificity for individual tissue microstructural features.[14] Advanced diffusion models have been developed to quantify specific neurite morphology,[13] such as NODDI, which assumes 3 compartments in the brain: an intracellular compartment with restricted anisotropic non-Gaussian diffusion (intracellular volume fraction [ICVF]), an extracellular compartment with hindered anisotropic Gaussian diffusion, and a water compartment with free isotropic Gaussian diffusion (isotropic volume fraction [ISO]).[15] ICVF is attributed to the axon and dendrite density and can be used for calculating axon volume fraction (AVF) when combined with myelin imaging.[16] Notably, the myelin signal is negligible in diffusion MR imaging, and an additional technique is required to retrieve information about axons and myelin.[16] NODDI provides directional neurite information as an orientation dispersion index (ODI).

Despite the recent development of multiple advanced MR imaging techniques, reports of combined analyses are scarce. Granberg et al[5] found that NODDI was more sensitive than myelin-sensitive imaging to changes in normal-appearing WM (NAWM) in patients with MS. However, they used the T1-weighted/T2-weighted ratio as a measure of myelin, which has been reported to be less than optimal for evaluating myelin in WM.[12,17] Moreover, no previous study has performed voxelwise whole-brain analysis of tissue-damage distribution in patients with MS using NODDI or myelin-imaging techniques. Even though our previous work[3] combined quantitative synthetic MR imaging and NODDI for evaluating WM damage in patients with MS, we did not compare quantitative values in patients with MS with those in healthy controls.

Therefore, this study aimed to evaluate the distribution of WM damage in patients with MS compared with healthy controls by combining quantitative synthetic MR imaging and NODDI. We used Tract-Based Spatial Statistics (TBSS; http://fsl.fmrib.ox.ac.uk/fsl/fslwiki/TBSS),[18] which allows voxelwise analysis of the whole brain within core WM tracts, to compare patients with MS and healthy controls, and we used ROI analysis to compare NAWM and lesions in patients with MS with WM in healthy controls.

MATERIALS AND METHODS

Study Participants

We prospectively recruited 24 patients with relapsing-remitting MS from August to November 2016 who were diagnosed according to the 2010 revised McDonald diagnostic criteria.[19] Disability was assessed using the Expanded Disability Status Scale (EDSS) score.[20] These patients were on stable disease-modifying treatment or no treatment for at least 3 months and had been free of clinical relapse within the 3 months and corticosteroid use within 1 year before MR imaging. As a control group, we also recruited 24 age- and sex-matched healthy subjects without neurologic and psychological symptoms or a history of neuropsychological disorders. Acquired images were confirmed not to include abnormalities such as moderate-to-severe WM ischemic lesions (Fazekas grade II or higher[21]), brain infarction, or tumor. This study was approved by the institutional review board of Juntendo University Hospital, Tokyo, Japan, and written informed consent was obtained from all participants. The patients in this study partially overlapped with a previously published study population.[22]

Image Acquisition and Processing

MR imaging was performed on a 3T scanner (Discovery MR750w; GE Healthcare, Milwaukee, Wisconsin) with a 19-channel head coil. All participants were scanned with a 2D axial quantification of relaxation times and proton density by multiecho acquisition of a saturation-recovery using turbo spin-echo readout (QRAPMASTER) pulse sequence and 2-shell diffusion MR imaging.

QRAPMASTER is a multislice, multiecho, multisaturation-delay saturation-recovery turbo spin-echo acquisition method in which images are collected with combinations of 2 TEs and 4 saturation-delay times. We used TEs of 16.9 and 84.5 ms and delay times of 146, 546, 1879, and 3879 ms. The other parameters were as follows: TR = 4.0 seconds, FOV = 240 × 240 mm, matrix = 320 × 320, echo-train length = 10, bandwidth = 31.25 kHz, section thickness/gap = 4.0 mm/1.0 mm, slices = 30, and acquisition time = 7 minutes 12 seconds. The 8 complex images acquired per section were postprocessed with SyMRI software (Version 8.0; SyntheticMR, Linköping, Sweden) to derive longitudinal R1 relaxation and transverse R2 relaxation rates and proton density and to estimate MVF per voxel. The myelin estimation model assumes 4 brain compartments: myelin, excess parenchymal water, cellular water, and free-water volume fractions.[9] The R1, R2, and proton density of each volume fraction in a voxel presumably contribute to the effective R1, R2, and proton density of the voxel as a whole. Synthetic FLAIR images and T1WI were also created with the same software using the R1, R2, and proton density maps, with the following postprocessing parameters: TR = 15,000 ms, TE = 100 ms, TI = 3000 ms for FLAIR, and TR = 500 ms, TE = 10 ms for T1WI.

Diffusion MR imaging was performed with single-shot echo-planar imaging along 30 and 60 motion-probing gradient directions for b-values of 1000 and 2000 s/mm^2, respectively. Additionally, a volume of non-diffusion-weighted images was also acquired. The other sequence parameters were the following: TR = 5000 ms, TE = 88.2 ms, FOV = 256 × 256 mm, matrix size =

256×256, echo-train length = 128, bandwidth = 1953.12 kHz, section thickness/gap = 4.0 mm/1.0 mm, slices = 30, and acquisition time = 7 minutes 40 seconds. All datasets were visually inspected for artifacts. We corrected in-plane and through-plane distortions of diffusion-weighted images caused by eddy currents and motion using affine brain registration to non-diffusion-weighted images.[23] Processed images were further denoised using multishell position-orientation adaptive smoothing based on the propagation-separation approach.[24,25] On denoising, diffusion data with b-values of 1000 and 2000 s/mm^2 were handled simultaneously to improve denoising stability.[25] Maps of fractional anisotropy (FA), mean diffusivity, axial diffusivity, and radial diffusivity were computed using diffusion data with b-values of 0 and 1000 s/mm^2 by fitting a tensor model. A NODDI model[15] was applied to the whole 2-shell diffusion data to produce ICVF, ISO, and ODI maps, while processing was accelerated using an Accelerated Microstructure Imaging via Convex Optimization algorithm.[26]

The AVF and g-ratio maps were acquired using the following equations:

$$AVF = (1 - MVF)(1 - ISO)ICVF,$$

$$g - ratio = \sqrt{\frac{AVF}{MVF + AVF}},$$

assuming that the signal of myelin is almost negligible in diffusion-weighted imaging but that the volume of myelin is not,[16]—that is, the volume fractions calculated by NODDI correspond to nonmyelinated tissues. Postprocessing was performed with an in-house program in Matlab (MathWorks, Natick, Massachusetts). Affine transformation was performed to register the acquired images using Statistical Parametric Mapping software (SPM12; http://www.fil.ion.ucl.ac.uk/spm/software/spm12).

TBSS Analysis

We performed whole-brain voxelwise analysis of the quantitative maps using TBSS implemented in the FMRIB Software Library (FSL; http://www.fmrib.ox.ac.uk/fsl).[18,27] First, FMRIB58_FA (https://fsl.fmrib.ox.ac.uk/fsl/fslwiki/FMRIB58_FA) in the Montreal Neurological Institute (MNI) common space was used as the target image for nonlinear registration of all subjects' FA maps, using the FMRIB Nonlinear Registration Tool (FNIRT; http://fsl.fmrib.ox.ac.uk/fsl/fslwiki/FNIRT/). The transformed FA images were averaged and skeletonized, representing the centers of all WM tracts common to all subjects. The mean FA skeleton was thresholded at 0.2 to include major WM tracts and to exclude peripheral tracts and gray matter.[18] Each participant's aligned FA map was then projected onto this skeleton by assigning to each voxel the maximum FA in a line perpendicular to the local skeleton. The R1, R2, proton density, MVF, mean diffusivity, axial diffusivity, radial diffusivity, ICVF, ISO, ODI, AVF, and g-ratio maps were projected onto the mean FA skeleton after applying the warping registration field of each subject to the standard space.

Comparisons between patients with MS and healthy controls were performed by voxelwise statistics of the skeletonized quantitative maps using nonparametric statistical thresholding (FSL Randomise permutation algorithm; https://fsl.fmrib.ox.ac.uk/fsl/fslwiki/Randomise). The thresholded mean FA skeleton was used as a mask. Five thousand permutations and statistical inference using threshold-free cluster enhancement were performed,[28] with P values $< .05$ after family-wise error correction for multiple comparisons considered significant. Age and sex were used as covariates. The anatomic locations of regions with significant group differences on the WM skeleton were identified from the Johns Hopkins University WM labels atlas.[29] For parameters showing significant differences, correlations with disease duration and EDSS were also examined using Randomise ($P < .05$, corrected for age and sex).

Lesion Maps

For all patients, hyperintense lesions were automatically segmented on synthetic FLAIR images using the lesion-prediction algorithm[30] implemented in the Lesion Segmentation Toolbox, Version 2.0.15 (http://www.applied-statistics.de/lst.html)[31] running in SPM 12. All lesion maps were visually inspected and manually corrected by an experienced neuroradiologist (A.H.). The whole-brain WM lesion volume in each patient was calculated by multiplying the lesion area by the section thickness. Synthetic T1WI in each patient was spatially normalized to MNI space, and warping fields were saved and subsequently applied to lesion maps. Because synthetic images derived from QRAPMASTER are inherently aligned,[32] no prior registration between synthetic T1WI and lesion maps created on synthetic FLAIR was required. Normalized lesion maps in all patients were aggregated to create group lesion maps.

ROI Analysis

To investigate tissue damage in NAWM and lesions separately, we performed ROI analysis using the WM skeleton and lesion maps. We registered the skeleton in the MNI space to each subject's space by applying the warping field created for TBSS analysis after inversion of the field. Next, we enlarged each patient's lesion map by 4 voxels. We segmented the synthetic T1WI for each subject to extract WM segmentation maps using FMRIB's Automated Segmentation Tool (FAST; http://fsl.fmrib.ox.ac.uk/fsl/fslwiki/fast). WM segmentation maps were then thresholded at 0.9 to minimize the partial volume effects and were used as WM masks. We created NAWM masks by subtracting the enlarged lesion maps from the thresholded WM masks for each patient. Overlapping areas between the warped skeleton and WM masks in healthy controls, NAWM masks in patients, or lesion maps in patients were used as ROIs to extract metrics from each quantitative map for the WM of healthy controls, the NAWM of patients with MS, or the lesion areas of patients with MS, respectively.

Statistical Analysis

Statistical analyses of demographic data were performed using a 2-sample t test for age and a χ^2 test for sex. For ROI data, nonnormality of synthetic MR imaging metrics has been reported previously[2,3]; therefore, we used the nonparametric Steel test for multiple comparisons to compare R1, R2, proton density, MVF,

FA, mean diffusivity, axial diffusivity, radial diffusivity, ICVF, ISO, ODI, AVF, and g-ratio values between the WM of healthy controls and the NAWM or lesion areas of patients with MS. A 2-sided $P < .05$ was considered statistically significant. These statistical analyses were performed with the software package R, Version 3.2.1 (http://www.r-project.org/).

RESULTS

The demographic and clinical data of patients with MS and of healthy controls are provided in the Table. Age and sex did not differ significantly between groups.

Demographic and clinical details of all participants

	MS	Healthy Control	*P* Values
No. of subjects	24	24	
Mean age (yr)	39.83 ± 8.25	39.50 ± 11.13	.91[a]
Sex (male/female)	5:19	5:19	1[b]
Disease duration (mean) (yr)	11.82 ± 5.99	NA	
EDSS score (range)	1 (0–7)	NA	
White matter lesion volume (mean) (mL)	10.05 ± 10.00	NA	

Note:—NA indicates not applicable.
[a] Two-sample *t* test.
[b] χ^2 test.

On TBSS analysis, patients with MS showed significantly lower FA and MVF and higher ISO values in the corpus callosum, cingulate gyri, and corona radiata (Fig 1 and On-line Table 1). The MVF differed between patients with MS and healthy controls in the most widespread areas, and only MVF showed significant differences (lower values in patients with MS) in the inferior longitudinal fasciculus, inferior fronto-occipital fasciculus, uncinate fasciculus, fornix, and external capsule. Conversely, only FA showed significantly different values (lower in patients with MS) in the genu of the corpus callosum and anterior corona radiata. All areas with significant ISO differences were included within areas that showed a significant FA difference. No significant correlation was found between EDSS or disease duration and FA, ISO, or MVF. R1, R2, proton density, mean diffusivity, axial diffusivity, radial diffusivity, ICVF, ODI, AVF, and g-ratio maps did not differ statistically significantly in the WM between patients and controls.

Figure 2 and On-line Table 2 show ROI analysis results. All quantitative metrics except ISO differed significantly between the healthy control WM and the WM lesions in patients with MS. R1, FA, mean diffusivity, radial diffusivity, ISO, ODI, and MVF differed significantly between healthy control WM and NAWM of patients with MS.

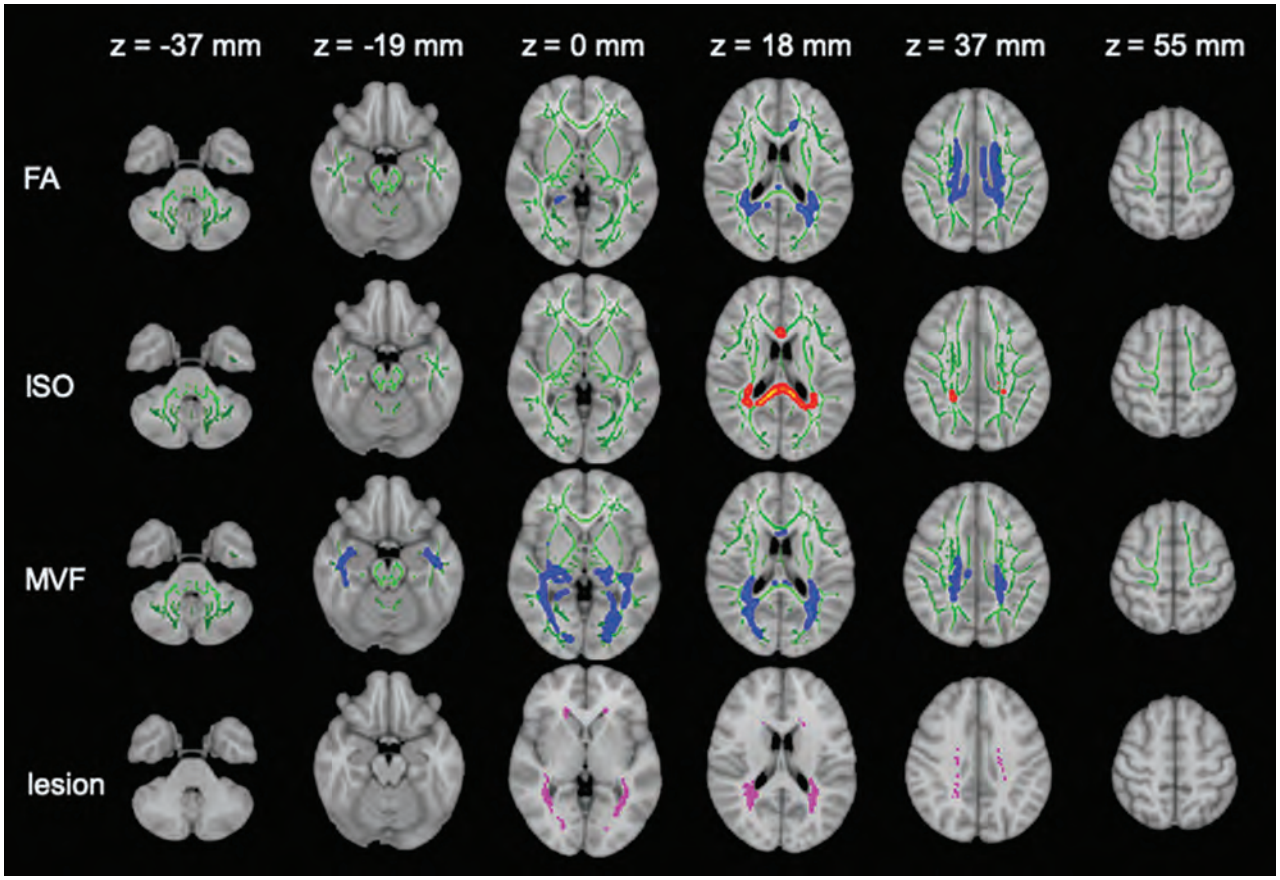

FIG 1. TBSS results are shown for FA, ISO, and MVF maps, which show significant differences between patients with MS and healthy controls. Green represents the mean FA skeleton of all participants thresholded at 0.2. Blue–light blue represents lower values in patients with MS compared with healthy controls in FA (*first row*) and MVF (*third row*) maps; red-yellow represents higher values in ISO maps (*second row*) (family-wise error-corrected $P < .05$). The significant regions are thickened for better visibility. The mean lesion probability distribution in patients with MS, thresholded at 20%, is shown in the *fourth row* in purple.

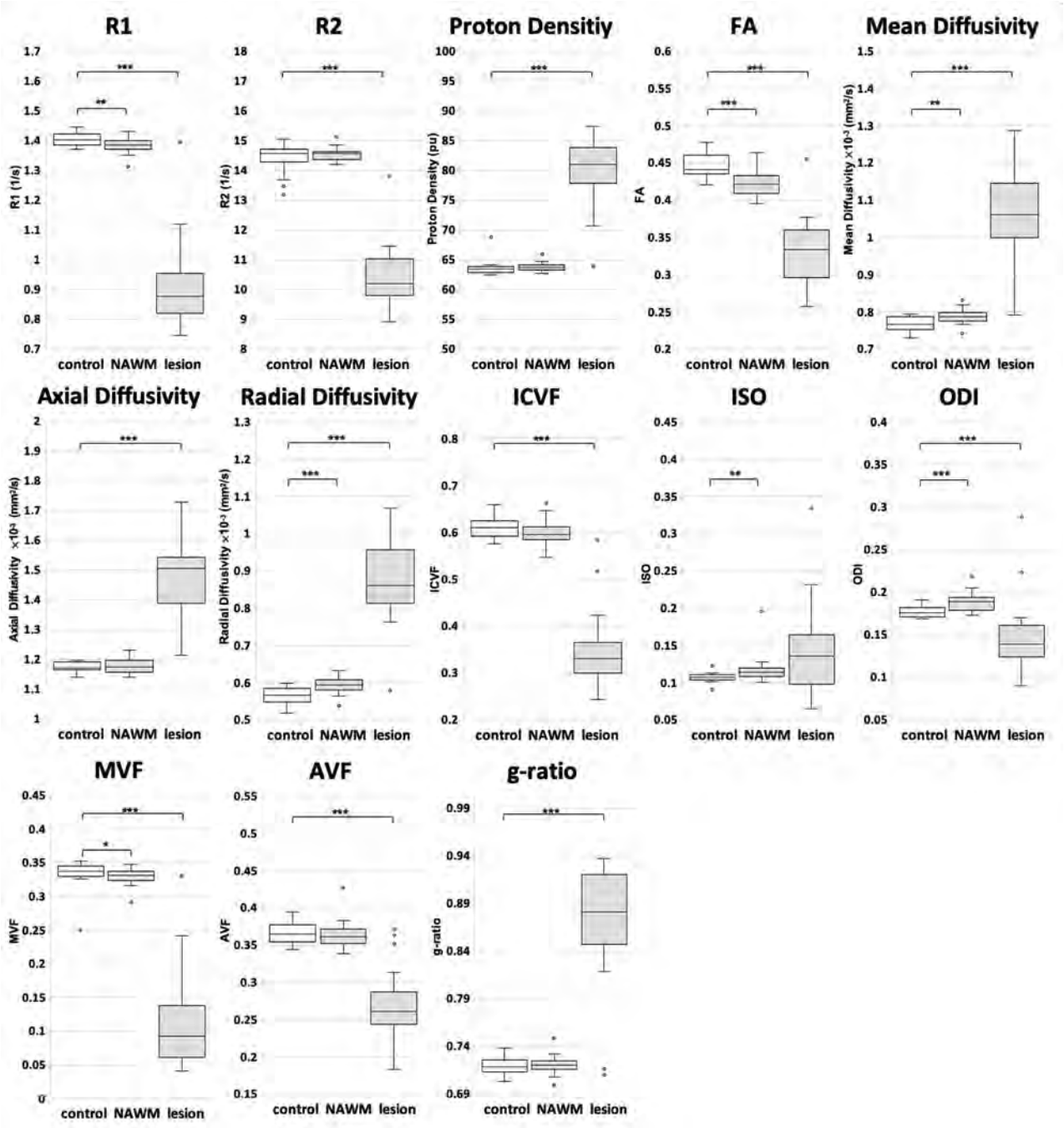

FIG 2. Quantitative metrics compared among the WM of healthy controls, NAWM of patients with MS, and WM lesions of patients with MS. The median and 25th and 75th percentiles are marked in *boxplots*, with outliers plotted by *open circles*. *Asterisks* indicate significant differences among the groups. The *asterisk* indicates $P < .05$; *double asterisks*, $P < .01$; *triple asterisks*, $P < .001$.

DISCUSSION

We here compared the WM of patients with MS and healthy controls using a combination of synthetic MR imaging and diffusion MR imaging by implementing TBSS and ROI analysis. To our knowledge, no previous study has performed voxelwise analysis of whole-brain WM using synthetic MVF or NODDI. We showed a lower FA in widespread WM areas in patients with MS, consistent with previous findings.[33-35] The distribution of abnormality in MVF value in patients differed from those of FA and ISO values. Even though the mechanisms underlying these differences are unclear, we can assume that various disease processes such as demyelination, axonal degeneration, gliosis, and edema[36] play a role. Because FA is nonspecific for demyelination and other pathologic processes[37] and ISO reportedly shows inflammatory free-water or edema,[5] this combination of synthetic MR imaging and diffusion MR imaging may allow more detailed evaluation than is achieved using FA only.

TBSS analysis did not show statistically significant differences in the AVF, ICVF, and g-ratio between patients with MS and healthy controls, while MVF differed significantly. Furthermore, in a comparison between the NAWM of patients and the WM of healthy controls, ROI analysis showed significant differences in MVF, but not in the AVF, ICVF, and g-ratio. These results agreed with those of our previous study[3] reporting that MVF was more sensitive than AVF to WM damage in plaque and periplaque WM than in NAWM. Even though TBSS analysis showed no significant difference in axial and radial diffusivity between patients with MS and healthy controls in our study, ROI analysis revealed higher radial diffusivity in the NAWM of patients with MS than in healthy control WM, whereas axial diffusivity did not differ significantly, even in ROI analysis. Our observation was consistent with previously reported findings that radial diffusivity showed more widespread abnormalities in the WM of patients with MS than axial diffusivity,[34] where radial diffusivity and axial diffusivity are considered surrogate markers for myelin and axon integrity, respectively. The widespread decrease in MVF, without a significant AVF decrease in this study, supported the notion that demyelination is a key pathologic element in MS and that MVF can be a biomarker for monitoring progression and treatment response in MS.

In ROI analysis, the ODI was higher in the NAWM of patients with MS than in the healthy control WM, but it was lower in WM lesions in patients with MS than in healthy control WM. This was congruent with the findings of Schneider et al[38] involving 5 patients with relapsing-remitting MS, which indicated a loss of fiber coherence (ie, increased dispersion) in the NAWM. They found a lower ODI in WM lesions, as in our study, even though another study involving early-stage MS (disease duration, <5 years) showed higher ODI in WM lesions.[5] These results might suggest that NAWM and early plaques show a loss of fiber coherence with relatively maintained neuronal fiber density, leading to an increase in ODI, whereas loss of neuronal fibers, with fewer signals from fibers, may cause a decrease in ODI in chronic plaques.

ISO values were higher in the WM of patients with MS on TBSS analysis and in the NAWM of patients with MS on ROI analysis, than in healthy control WM, possibly indicating edema with free diffusion in patients' NAWM. However, patients' WM lesion values were not significantly higher than those of healthy control WM, in contrast to the findings of Schneider et al.[38] This difference could be attributed to the high variability of ISO in lesions in our study (Fig 2), which is partly explained by the partial volume effects of lesion ROIs. Chung et al[39] previously revealed that NODDI metrics showed higher variability at tissue boundaries. Hence, future investigations with higher resolution are warranted.

In TBSS, R1, R2, and proton density, as opposed to the MVF derived from these metrics, did not differ significantly between the patients with MS and healthy controls, agreeing with a previous observation showing the higher sensitivity of MVF than R1, R2, and proton density for revealing WM damage in plaque and periplaque WM.[2] On ROI analysis, only R1 differed significantly between the NAWM of patients with MS and the WM of healthy controls. Previous reports have inconsistently reported differences between healthy WM and NAWM revealed by these metrics,[40-43] and 1 previous study showed significant differences in T2 and proton density, but not in T1, between healthy WM and NAWM.[43] These metrics are thus nonspecifically affected by pathologic processes; hence, MVF and AVF may be more suitable for capturing changes in tissue microstructure in patients with MS.

In our study, no correlation was found between quantitative metrics and EDSS or disease duration. This could be due to the small sample size and the low EDSS scores (median, 1). Larger studies including a wider range of clinical disabilities are needed.

This study had some limitations. First, the study design was cross-sectional. Future longitudinal studies are required to understand intraindividual variation and the trajectory of metric changes during disease progression. Second, we used a 4-mm section thickness with a 1-mm gap. A future combination of 3D synthetic MR imaging[44] and high-resolution diffusion-weighted imaging in a larger study population would facilitate a more robust analysis.

CONCLUSIONS

We compared the metrics acquired by synthetic MR imaging and NODDI in the WM between patients with MS and healthy controls. Compared with healthy controls, patients with MS showed significantly lower FA, lower MVF, and higher ISO in large WM areas. Furthermore, a decrease in FA and MVF showed different spatial distributions; combined, these quantitative values can facilitate better WM characterization in patients with MS.

Disclosures: Akifumi Hagiwara—*RELATED*: *Grant*: Japan Society for the Promotion of Science KAKENHI, *Comments*: grant No, 19K17150; *UNRELATED*: *Travel/Accommodations/Meeting Expenses Unrelated to Activities Listed*: GE Healthcare, *Comments*: SIGNA Masters Series Neuro Summit (Singapore) October 2018. Keigo Shimoji—*UNRELATED*: *Grants/Grants Pending*: MEXT KAKENHI, grant No. 18H02772. Shigeki Aoki—*RELATED*: *Grant*: Japan Society for the Promotion of Science KAKENHI, ABiS, Branding Project*; *UNRELATED*: *Grants/grants Pending*: Japan Society for the Promotion of Science KAKENHI, ABiS, Branding Project, Daiichi Sankyo, Mediphysics, Fuji Film RI, Eisai, Guerbet*; *Payment for Lectures Including Service on Speakers Bureaus*: GE Healthcare, Siemens, Canon, Bayer, Daiichi Sankyo, Mediphysics, FujiRI, Fujifilm Medical Systems, Eisai, Guerbet. *Money paid to institution.

REFERENCES

1. Vavasour IM, Huijskens SC, Li DK, et al. **Global loss of myelin water over 5 years in multiple sclerosis normal-appearing white matter.** *Mult Scler* 2018;24:1557–68 CrossRef Medline
2. Hagiwara A, Hori M, Yokoyama K, et al. **Utility of a multiparametric quantitative MRI model that assesses myelin and edema for evaluating plaques, periplaque white matter, and normal-appearing white matter in patients with multiple sclerosis: a feasibility study.** *AJNR Am J Neuroradiol* 2017;38:237–42 CrossRef Medline
3. Hagiwara A, Hori M, Yokoyama K, et al. **Analysis of white matter damage in patients with multiple sclerosis via a novel in vivo MR method for measuring myelin, axons, and g-ratio.** *AJNR Am J Neuroradiol* 2017;38:1934–40 CrossRef Medline
4. Guo AC, MacFall JR, Provenzale JM. **Multiple sclerosis: diffusion tensor MR imaging for evaluation of normal-appearing white matter.** *Radiology* 2002;222:729–36 CrossRef Medline
5. Granberg T, Fan Q, Treaba CA, et al. **In vivo characterization of cortical and white matter neuroaxonal pathology in early multiple sclerosis.** *Brain* 2017;140:2912–26 CrossRef Medline

6. Warntjes JB, Leinhard OD, West J, et al. **Rapid magnetic resonance quantification on the brain: optimization for clinical usage.** *Magn Reson Med* 2008;60:320–29 CrossRef Medline
7. Hagiwara A, Hori M, Cohen-Adad J, et al. **Linearity, bias, intrascanner repeatability, and interscanner reproducibility of quantitative multidynamic multiecho sequence for rapid simultaneous relaxometry at 3 T: a validation study with a standardized phantom and healthy controls.** *Invest Radiology* 2019;54:47–39 CrossRef Medline
8. Wallaert L, Hagiwara A, Andica C, et al. **The advantage of synthetic MRI for the visualization of anterior temporal pole lesions on double inversion recovery (DIR), phase-sensitive inversion recovery (PSIR), and myelin images in a patient with CADASIL.** *Magn Reson Med Sci* 2018;17:275–76 CrossRef Medline
9. Warntjes M, Engstrom M, Tisell A, et al. **Modeling the presence of myelin and edema in the brain based on multi-parametric quantitative MRI.** *Front Neurol* 2016;7:16 CrossRef Medline
10. Warntjes JBM, Persson A, Berge J, et al. **Myelin detection using rapid quantitative MR imaging correlated to macroscopically registered luxol fast blue-stained brain specimens.** *AJNR Am J Neuroradiol* 2017;38:1096–102 CrossRef Medline
11. Ouellette R, Warntjes M, Forslin Y, et al. **Rapid estimation of myelin for diagnostic imaging (REMyDI): a clinical and histopathological validation in multiple sclerosis.** *In: Proceedings of the Annual Meeting of the International Society for Magnetic Resonance in Medicine and the European Society for Magnetic Resonance in Medicine*, Paris, France, June 16-21, 2018;Abstract 1864
12. Hagiwara A, Hori M, Kamagata K, et al. **Myelin measurement: comparison between simultaneous tissue relaxometry, magnetization transfer saturation index, and T1w/T2w ratio methods.** *Sci Rep* 2018;8:10554 CrossRef Medline
13. Alexander DC, Dyrby TB, Nilsson M, et al. **Imaging brain microstructure with diffusion MRI: practicality and applications.** *NMR Biomed* 2019;32:e3841 CrossRef Medline
14. Pierpaoli C, Jezzard P, Basser PJ, et al. **Diffusion tensor MR imaging of the human brain.** *Radiology* 1996;201:637–48 CrossRef Medline
15. Zhang H, Schneider T, Wheeler-Kingshott CA, et al. **NODDI: practical in vivo neurite orientation dispersion and density imaging of the human brain.** *Neuroimage* 2012;61:1000–16 CrossRef Medline
16. Stikov N, Campbell JS, Stroh T, et al. **In vivo histology of the myelin g-ratio with magnetic resonance imaging.** *Neuroimage* 2015; 118:397–405 CrossRef Medline
17. Arshad M, Stanley JA, Raz N. **Test-retest reliability and concurrent validity of in vivo myelin content indices: myelin water fraction and calibrated T1 w/T2 w image ratio.** *Hum Brain Mapp* 2017;38:1780–90 CrossRef Medline
18. Smith SM, Jenkinson M, Johansen-Berg H, et al. **Tract-based spatial statistics: voxelwise analysis of multi-subject diffusion data**. *Neuroimage* 2006;31:1487–505 CrossRef Medline
19. Polman CH, Reingold SC, Banwell B, et al. **Diagnostic criteria for multiple sclerosis: 2010 revisions to the McDonald criteria.** *Ann Neurol* 2011;69:292–302 CrossRef Medline
20. Kurtzke JF. **A new scale for evaluating disability in multiple sclerosis.** *Neurology* 1955;5:580–83 CrossRef Medline
21. Fazekas F, Chawluk JB, Alavi A, et al. **MR signal abnormalities at 1.5 T in Alzheimer's dementia and normal aging.** *AJR Am J Roentgenol* 1987;149:351–56 CrossRef Medline
22. Andica C, Hagiwara A, Kamagata K, et al. **Gray matter alterations in early and late relapsing-remitting multiple sclerosis evaluated with synthetic quantitative magnetic resonance imaging.** *Sci Rep* 2019;9:8147 CrossRef Medline
23. Mohammadi S, Moller HE, Kugel H, et al. **Correcting eddy current and motion effects by affine whole-brain registrations: evaluation of three-dimensional distortions and comparison with slicewise correction.** *Magn Reson Med* 2010;64:1047–56 CrossRef Medline
24. Becker SM, Tabelow K, Voss HU, et al. **Position-orientation adaptive smoothing of diffusion weighted magnetic resonance data (POAS).** *Med Image Anal* 2012;16:1142–55 CrossRef Medline
25. Becker SM, Tabelow K, Mohammadi S, et al. **Adaptive smoothing of multi-shell diffusion weighted magnetic resonance data by msPOAS.** *Neuroimage* 2014;95:90–105 CrossRef Medline
26. Daducci A, Canales-Rodriguez EJ, Zhang H, et al. **Accelerated Microstructure Imaging via Convex Optimization (AMICO) from diffusion MRI data.** *Neuroimage* 2015;105:32–44 CrossRef Medline
27. Smith SM, Jenkinson M, Woolrich MW, et al. **Advances in functional and structural MR image analysis and implementation as FSL.** *Neuroimage* 2004;23(Suppl 1):S208–19 CrossRef Medline
28. Keihaninejad S, Ryan NS, Malone IB, et al. **The importance of group-wise registration in tract based spatial statistics study of neurodegeneration: a simulation study in Alzheimer's disease.** *PLoS One* 2012;7:e45996 CrossRef Medline
29. Mori S, Wakana S, Nagae-Poetscher LM, et al. *MRI Atlas of Human White Matter*. Amsterdam: Elsevier; 2005
30. Egger C, Opfer R, Wang C, et al. **MRI FLAIR lesion segmentation in multiple sclerosis: does automated segmentation hold up with manual annotation?** *Neuroimage Clin* 2017;13:264–70 CrossRef Medline
31. Schmidt P, Gaser C, Arsic M, et al. **An automated tool for detection of FLAIR-hyperintense white-matter lesions in multiple sclerosis.** *Neuroimage* 2012;59:3774–83 CrossRef Medline
32. Hagiwara A, Warntjes M, Hori M, et al. **SyMRI of the brain: rapid quantification of relaxation rates and proton density, with synthetic MRI, automatic brain segmentation, and myelin measurement.** *Invest Radiology* 2017;52:647–57 CrossRef Medline
33. Sbardella E, Tona F, Petsas N, et al. **DTI measurements in multiple sclerosis: evaluation of brain damage and clinical implications.** *Mult Scler Int* 2013;2013:671730 CrossRef Medline
34. Liu Y, Duan Y, He Y, et al. **Whole brain white matter changes revealed by multiple diffusion metrics in multiple sclerosis: a TBSS study.** *Eur J Radiology* 2012;81:2826–32 CrossRef Medline
35. Huang J, Liu Y, Zhao T, et al. **White matter microstructural alterations in clinically isolated syndrome and multiple sclerosis.** *J Clin Neurosci* 2018;53:27–33 CrossRef Medline
36. Miller DH, Barkhof F, Frank JA, et al. **Measurement of atrophy in multiple sclerosis: pathological basis, methodological aspects and clinical relevance.** *Brain* 2002;125:1676–95 CrossRef Medline
37. Inglese M, Bester M. **Diffusion imaging in multiple sclerosis: research and clinical implications**. *NMR Biomed* 2010;23:865–72 CrossRef Medline
38. Schneider T, Brownlee W, Zhang H, et al. **Sensitivity of multi-shell NODDI to multiple sclerosis white matter changes: a pilot study.** *Funct Neurol* 2017;32:97–101 CrossRef Medline
39. Chung AW, Seunarine KK, Clark CA. **NODDI reproducibility and variability with magnetic field strength: a comparison between 1.5 T and 3 T.** *Hum Brain Mapp* 2016;37:4550–65 CrossRef Medline
40. Barbosa S, Blumhardt LD, Roberts N, et al. **Magnetic resonance relaxation time mapping in multiple sclerosis: normal appearing white matter and the "invisible" lesion load.** *Magn Reson Imaging* 1994;12:33–42 CrossRef Medline
41. Davies GR, Hadjiprocopis A, Altmann DR, et al. **Normal-appearing grey and white matter T1 abnormality in early relapsing-remitting multiple sclerosis: a longitudinal study.** *Mult Scler* 2007;13:169–77 CrossRef Medline
42. Shepherd TM, Kirov II, Charlson E, et al. **New rapid, accurate T2 quantification detects pathology in normal-appearing brain regions of relapsing-remitting patients with MS.** *Neuroimage Clin* 2017;14:363–70 CrossRef Medline
43. Reitz SC, Hof SM, Fleischer V, et al. **Multi-parametric quantitative MRI of normal appearing white matter in multiple sclerosis, and the effect of disease activity on T2.** *Brain Imaging Behav* 2017;11:744–53 CrossRef Medline
44. Fujita S, Hagiwara A, Hori M, et al. **3D quantitative synthetic MRI-derived cortical thickness and subcortical brain volumes: scan-rescan repeatability and comparison with conventional T1-weighted images.** *J Magn Reson Imaging* 2019 Apr 10. [Epub ahead of print] CrossRef Medline

Perfusion MRI-Based Fractional Tumor Burden Differentiates between Tumor and Treatment Effect in Recurrent Glioblastomas and Informs Clinical Decision-Making

M. Iv, X. Liu, J. Lavezo, A.J. Gentles, R. Ghanem, S. Lummus, D.E. Born, S.G. Soltys, S. Nagpal, R. Thomas, L. Recht, and N. Fischbein

ABSTRACT

BACKGROUND AND PURPOSE: Fractional tumor burden better correlates with histologic tumor volume fraction in treated glioblastoma than other perfusion metrics such as relative CBV. We defined fractional tumor burden classes with low and high blood volume to distinguish tumor from treatment effect and to determine whether fractional tumor burden can inform treatment-related decision-making.

MATERIALS AND METHODS: Forty-seven patients with high-grade gliomas (primarily glioblastoma) with recurrent contrast-enhancing lesions on DSC-MR imaging were retrospectively evaluated after surgical sampling. Histopathologic examination defined treatment effect versus tumor. Normalized relative CBV thresholds of 1.0 and 1.75 were used to define low, intermediate, and high fractional tumor burden classes in each histopathologically defined group. Performance was assessed with an area under the receiver operating characteristic curve. Consensus agreement among physician raters reporting hypothetic changes in treatment-related decisions based on fractional tumor burden was compared with actual real-time treatment decisions.

RESULTS: Mean low fractional tumor burden, high fractional tumor burden, and relative CBV of the contrast-enhancing volume were significantly different between treatment effect and tumor ($P = .002$, $P < .001$, and $P < .001$), with tumor having significantly higher fractional tumor burden and relative CBV and lower fractional tumor burden. No significance was found with intermediate fractional tumor burden. Performance of the area under the receiver operating characteristic curve was the following: high fractional tumor burden, 0.85; low fractional tumor burden, 0.7; and relative CBV, 0.81. In comparing treatment decisions, there were disagreements in 7% of tumor and 44% of treatment effect cases; in the latter, all disagreements were in cases with scattered atypical cells.

CONCLUSIONS: High fractional tumor burden and low fractional tumor burden define fractions of the contrast-enhancing lesion volume with high and low blood volume, respectively, and can differentiate treatment effect from tumor in recurrent glioblastomas. Fractional tumor burden maps can also help to inform clinical decision-making.

ABBREVIATIONS: FTB = fractional tumor burden; HGG = high-grade glioma; ICC = intraclass correlation coefficient; rCBV = relative cerebral blood volume; TE = treatment effect

An important challenge in the care of patients with high-grade gliomas (HGGs) following conventional therapy with maximal safe surgical resection and chemoradiation is the differentiation of tumor and treatment effect (TE). The current practice standard, Response Assessment in Neuro-Oncology criteria, to determine the response to therapy of a tumor is largely based on the assessment of T2/FLAIR signal extent and the size of T1 gadolinium enhancement on MR imaging across time.[1] An increase in T2/FLAIR signal and contrast enhancement following treatment does not, however, always indicate tumor progression. Thus, perfusion imaging markers such as relative cerebral blood volume (rCBV) have been thoroughly investigated and used to differentiate tumor from TE.[2-4] More recent studies have demonstrated that another perfusion-derived metric, fractional tumor burden (FTB), which is defined as the volume fraction of tumor voxels above a specified rCBV threshold, has similar potential.[2,3,5]

Received May 9, 2019; accepted after revision August 1.

From the Departments of Neuroimaging and Neurointervention (M.I., N.F.), Pathology (J.L., R.G., S.L., D.E.B.), Medicine (Biomedical Informatics Research) (A.J.G.), Radiation Oncology (S.G.S.), and Neurology (Neuro-Oncology) (S.N., R.T., L.R.), Stanford University, Stanford, California; and Department of Neurosurgery (X.L.), Shengjing Hospital of China Medical University, Shenyang, China.

Michael Iv and Xiaobai Liu are co-first authors and contributed equally to this work.

Please address correspondence to Michael Iv, MD, Stanford University Medical Center, Department of Radiology, 300 Pasteur Dr, Grant Bldg, Room S031E, Stanford, CA 94305; e-mail: miv@stanford.edu; @Michael_Iv_MD

Indicates article with supplemental on-line photos.

http://dx.doi.org/10.3174/ajnr.A6211

Despite their promise, MR imaging perfusion–derived metrics have yet to be widely adopted. Reasons for this include interoperator subjectivity in producing rCBV values (often based on "hot spot" ROI analysis), lack of clinically validated parameters to differentiate tumor from TE, and lack of standardization of imaging-acquisition techniques and postprocessing software across different sites.[6] Specifically, the hot spot ROI methodology is largely based on manually placing an ROI in an area of tumor with the highest rCBV on a single image.[7-9] This method, however, underrepresents the entire volume and heterogeneity of the tumor. Assessment of whole-tumor perfusion, for example, with FTB mitigates this issue by providing per-voxel measurements rather than computing 1 value to represent the entire contrast-enhancing lesion. Even with this technique, however, an rCBV threshold defining tumor versus TE is needed. A previous study evaluating stereotactic biopsy specimens of recurrent glioblastoma demonstrated that rCBV of $\leq$1.0 distinguished tumor from TE with 100% accuracy.[2] Another study found similar findings, with a threshold of 1.13 yielding 82% sensitivity and 90% specificity.[3]

Apart from using rCBV to differentiate TE from tumor, higher rCBV thresholds have been used to identify more aggressive tumors. One of the earliest glioma studies using a single rCBV threshold found that tumors with an rCBV of >1.75 portended a worse prognosis.[8] Another study found that rCBV of ≥1.8 (despite rCBV being estimated by the negative enhancement integral on T2WI) best distinguished tumor burden when it was >20% of the entire tumor.[10] Discrepancies in previously reported rCBV thresholds,[2,3,8,10] therefore, are not always due to lack of standardized methodologies but may be related to the specific question being asked.

In this study, we evaluated the utility of quantitative FTB of the entire contrast-enhancing lesion volume in patients with suspected recurrent HGGs. We hypothesize that the use of 2 rCBV values (1.0, which has been found to effectively differentiate TE from tumor, and 1.75, which has been shown to indicate aggressive tumor) to define low and high fractional tumor burden, respectively, would be effective in distinguishing recurrent tumor from TE. We also assessed whether qualitative interpretation of FTB among 5 physicians agrees with the histopathologic diagnosis and whether FTB can be used to inform treatment-related decision-making.

MATERIALS AND METHODS

Patients

This retrospective study was approved by Stanford University's institutional review board. We evaluated adults with suspected HGG recurrence after previous surgical resection followed by standard chemoradiation between January 2007 to June 2018. Inclusion criteria were the following: 18 years of age or older with HGG initially treated with conventional therapy, enlarging or new contrast-enhancing mass on follow-up DSC-MR imaging, surgical resection or biopsy of the mass, and availability of tissue specimens for histopathologic examination. All patients who had a resection had >90% or gross total resection as determined qualitatively by the amount of residual contrast enhancement on immediate postsurgical T1WI. Exclusion criteria included non-contrast-enhancing tumor on MR imaging, marked susceptibility related to blood or surgical material on raw precontrast DSC images, low-grade gliomas, and any oligodendroglioma. Oligodendrogliomas were excluded because elevated intratumoral rCBV has been shown to relate to fine capillaries and is not necessarily indicative of aggressive tumor.[11] Patients on bevacizumab at the time of an operation for suspected recurrence were not excluded because the presence of an enlarging contrast-enhancing mass while on bevacizumab suggests a refractory response to antiangiogenic therapy.[12] After screening and assessment of eligibility, 47 patients were included (Online Fig 1). Clinical demographics, histopathologic and molecular information, and treatment history were obtained through the electronic medical record.

Perfusion MR Imaging Acquisition

MRIs were performed on a 1.5T (n = 28, Signa Explorer; GE Healthcare, Milwaukee, Wisconsin) or 3T (n = 19, Discovery MR750; GE Healthcare) scanner. Images were acquired as part of the brain tumor protocol of our institution, which varied across the years. However, all examinations included pre- and postgadolinium axial 2D-T1-weighted spin-echo or 3D-T1-weighted inversion recovery echo-spoiled gradient-echo BRAin VOlume (BRAVO) images (GE Healthcare). DSC imaging was performed in each patient, and during the study period, it was acquired with nonpreload single-echo gradient EPI (parameters: TR/TE =1800/35–40 ms, section thickness = 5 mm, 0 skip with 20 images covering the brain, flip angle = 60°, matrix = 96 × 128 mm, FOV = 220–240 mm). A dynamic bolus was acquired using a full dose of a gadolinium (0.1 mmol/kg), which was administered intravenously by a power injector at a rate of 4–5 mL/s.

Image Processing and Quantitative Analysis

We used a workstation equipped with OsiriX MD (Version 7.0; http://www.osirix-viewer.com) and a commercially available plug-in (IB Neuro, Version 2.0; Imaging Biometrics, Elm Grove, Wisconsin), which uses well-established and previously published methods, including a leakage-correction algorithm, to process perfusion data and calculate rCBV and FTB.[2,3,5,13-15] For semiautomated image analysis, we used IB Rad Tech (Version 2.0; Imaging Biometrics), which is a workflow engine that generates quantitative ΔT1 and FTB maps from the IB Delta Suite (Version 2.0; Imaging Biometrics), and IB Neuro plug-ins. The overall workflow, which has been described previously,[2] is highlighted as follows: 1) The volume of contrast enhancement was determined from ΔT1 maps, which are standardized difference maps computed from the difference of coregistered pre- and postcontrast T1-weighted images;[14-17] 2) postcontrast T1 images were coregistered to the raw DSC images; 3) the contrast-enhancing VOI was transferred to the rCBV map; 4) normalization was performed by drawing and taking the average of two 5 × 5 mm^2 ROIs in the contralateral normal appearing white matter; and 5) output rCBV and FTB maps, in which lesion mask voxels were used to classify areas of contrast enhancement on the basis of predefined rCBV thresholds, were subsequently generated. As previously stated, we selected thresholds of 1.0 and 1.75 to define 3 FTB classes: FTB_{low}, percentage of contrast-enhancing voxels with

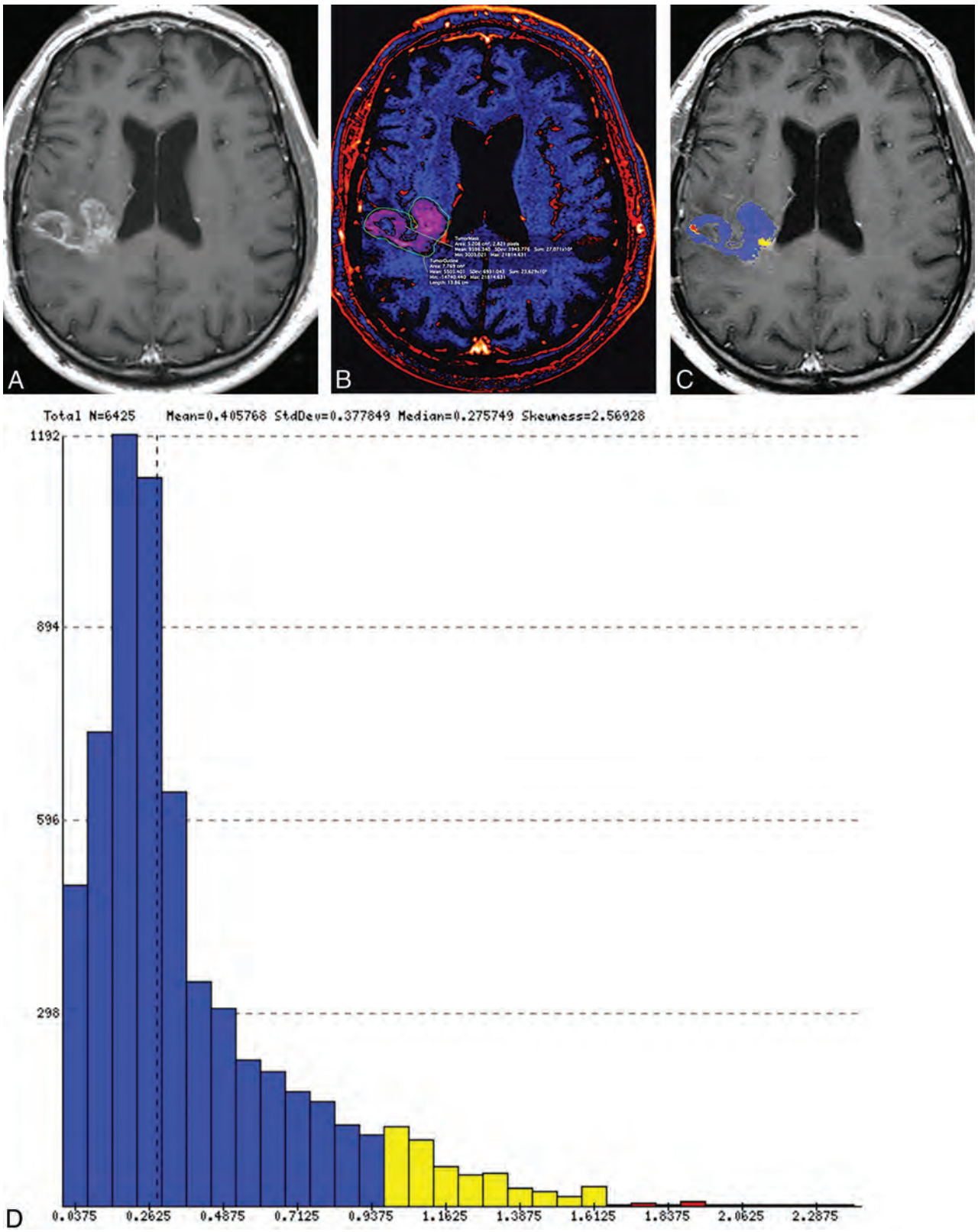

FIG 1. Representative examples of treatment effect (*A–D*) and recurrent tumor (*E–H*) in 2 patients with previously resected and irradiated glioblastomas. Contrast-enhancing lesions on postcontrast T1-weighted (*A* and *E*) and ΔT1 (*B* and *F*) images. Output FTB maps superimposed on the contrast-enhanced T1-weighted images (*C* and *G*). Blue represents areas of low blood volume (FTB_{low}), and red represents areas of high blood volume (FTB_{high}). Histograms (*D* and *H*) show all voxels of the contrast-enhancing volume classified into the respective FTB_{low}, FTB_{mid} (yellow), and FTB_{high} classes, which is based on the rCBV thresholds of 1.0 and 1.75.

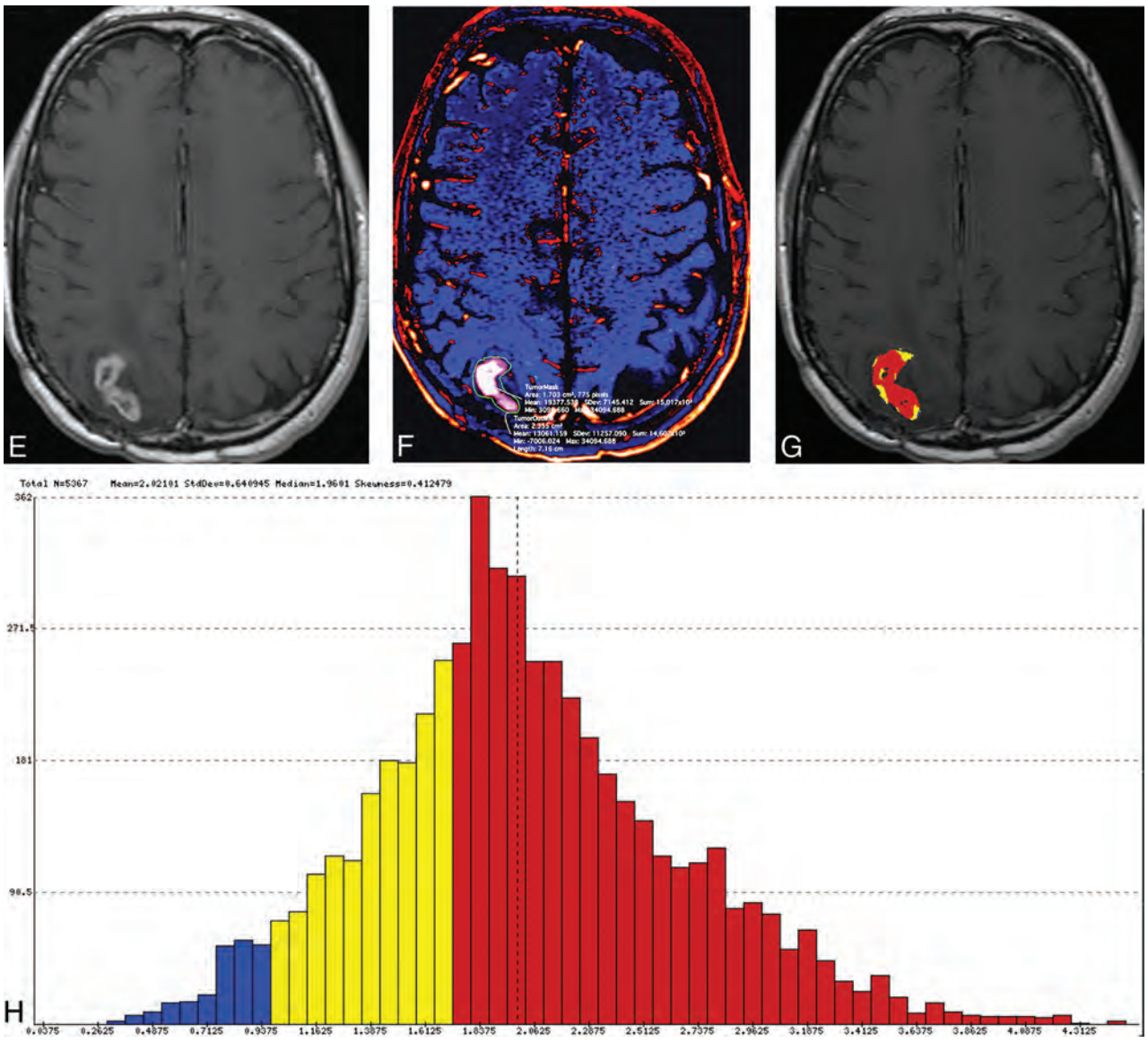

FIG 1. Continued.

rCBV of ≤1.0; FTB_{mid}, percentage of voxels with rCBV between 1.0 and 1.75; and FTB_{high}, percentage of voxels with rCBV of ≥1.75. Percentage values from the 3 FTB classes totaled 100%. Mean rCBV values of the contrast-enhancing VOIs were generated for each patient. Volumetric images of the contrast-enhancing lesion superimposed on the FTB map containing colored voxels of each class (FTB_{low} = blue; FTB_{mid} = yellow; FTB_{high} = red) and a histogram displaying voxels for the entire contrast-enhancing VOI were also produced (Fig 1).

Histopathologic Examination

A team of 2 neuropathologists with 2 (J.L.) and 21 (D.E.B.) years of neuro-oncology–pathology experience was blinded to clinical and MR imaging results. Histopathologic examination of tissue specimens was performed by consensus agreement in a single session, with the reviewers providing only a single assessment for each sample. From each resection or biopsy, sections from different areas of the entire tissue submitted for histopathology were evaluated. To determine a single histopathologic diagnosis for a given case, the team evaluated whether each section consisted of TE (defined as the absence of neoplastic cells or the presence of scattered infiltrating atypical cells but without a focal group or a solid sheet of neoplastic cells) or tumor (defined as the presence of any group or a solid sheet of neoplastic cells with or without superimposed treatment-related changes). For the purpose of this study, scattered atypical cells were classified as TE because it was not absolutely certain to the neuropathologists whether the atypical cells represented radiation effect or treated-but-viable glioma cells. Second, the resolution of today's perfusion MR imaging is not high enough to detect scattered atypical cells that are otherwise only identified microscopically.

Qualitative Analysis

Five physician raters who are involved in the care of patients with glioma, consisting of 3 neuro-oncologists (R.T., S.N., L.R.) with varying levels of experience (6, 8, and 35 years), a radiation

Table 1: Patient demographics and clinicopathologic information[a]

	TE ($n = 17$)	Tumor ($n = 30$)	Total ($n = 47$)
Age (yr)			
Mean (SD)	56 (10)	55 (13)	55 (12)
Range	38–77	20–80	20–80
Sex			
Male	11 (65%)	18 (60%)	29 (62%)
Female	6 (35%)	12 (40%)	18 (38%)
Interval time between end of radiation therapy and surgery (mo)			
Median (range)	11.4 (0.6–60.4)	10.7 (1.3–101.5)	10.9 (0.6–101.5)
Bevacizumab at time of surgery[b]	2 (12%)	3 (10%)	5 (11%)
Surgical procedure			
Biopsy	3 (18%)	4 (13%)	7 (15%)
>90% resection	3 (18%)	9 (30%)	12 (25%)
Gross total resection	11 (64%)	17 (57%)	28 (60%)
HGG histopathology			
Anaplastic astrocytoma, WHO grade III	2 (12%)	0	2 (4%)
Glioblastoma, WHO grade IV	15 (88%)	29 (97%)	44 (94%)
Gliosarcoma, WHO grade IV	0	1 (3%)	1 (2%)
HGG molecular features			
IDH wild-type	11 (65%)	11 (37%)	22 (47%)
IDH mutant	0	2 (7%)	2 (4%)
Unknown *IDH* status	6 (35%)	17 (56%)	23 (49%)
MGMT-unmethylated	6 (35%)	15 (50%)	21 (45%)
MGMT-methylated	6 (35%)	8 (27%)	14 (30%)
Unknown MGMT status	5 (30%)	7 (23%)	12 (25%)

Note:—*IDH* indicates *isocitrate dehydrogenase;* MGMT, O-6-methylguanine-DNA methyltransferase; WHO, World Health Organization.

[a] Percentage values in parentheses for sex, bevacizumab at time of the operation, surgical procedure, HGG histopathology, and HGG molecular features are percentages relative to the number of patients in each column.

[b] Patient received a dose of bevacizumab within 1 month of the surgical procedure for suspected recurrence.

oncologist (S.G.S.) with 14 years of experience, and a neuroradiologist (N.F.) with 25 years of experience, were blinded to clinical and histopathology information. Each rater was given a PowerPoint file (Microsoft, Redmond, Washington) consisting of representative MR images and numeric perfusion values of a patient's contrast-enhancing lesion (On-line Fig 2). The file consisted of 3 sample patients drawn from the total pool of 47 patients, one with histopathologically confirmed TE and the other 2 with histopathologically confirmed tumor. Anonymized data of the remaining 44 patients, who were presented in random order, followed the 3 sample patients. For all patients, 2 representative axial images of the segmented contrast-enhancing mass with 2 corresponding axial images of the color FTB map and the histogram and FTB percentages of the entire contrast-enhancing lesion were provided. Of note, although only 2 representative image slices of a patient's lesion were provided for visualization, the histogram data and percentage values, which represented the entire contrast-enhancing volume, were provided. Raters recorded whether they thought that the data represented TE or tumor and whether they would hypothetically change treatment on the basis of FTB. A change in treatment was defined as a change in surgical or medical management and excluded the option for shorter interval imaging surveillance. For qualitative image interpretation, we compared the consensus decision (representing most decisions among all raters) with the actual histopathologic diagnosis. For decisions of treatment change, we compared the consensus decision with the actual treatment decision that was made at the time of the patient's real-time care, which was largely based on histopathologic assessment.

Statistical Analyses

Descriptive statistics were used to report patient demographics and perfusion metrics. We used the nonparametric Mann-Whitney test to compare FTB classes and rCBV between the TE and tumor groups. The performance of each FTB class and rCBV to distinguish TE and tumor was evaluated with the area under the receiver operating characteristic curve. To determine whether the use of both FTB_{low} and FTB_{high} improved performance, we first used the Youden index to determine the percentage values that yielded the best sensitivity and specificity; then, we assigned a score of zero for cases that did not meet both conditions and a score of 1 for those that did. We subsequently used the Fisher exact test to assess significance between the groups and determined the sensitivity and specificity for this method. A $P < .05$ was considered statistically significant for all analyses.

For analysis of the qualitative data, we included only the 44 evaluated patients and excluded the 3 sample patients. The intraclass correlation coefficient (ICC) was used to assess agreement among the 5 raters for FTB interpretation and the decision to change treatment based on FTB. Agreement between the consensus scores for FTB interpretation and actual histopathologic diagnosis and between hypothetic and real-time treatment changes was also assessed with the ICC, using the following model of ICC interpretation: <0.40, poor; 0.40–0.75, fair-to-good; ≥0.75, excellent.[18]

All statistical analyses were performed with R statistical and computing software (Version 3.4.0; http://www.r-project.org/); graphs were created with GraphPad Prism software for illustrative purposes (Version 8.0.1; GraphPad Software, San Diego, California).

RESULTS

Patients

Table 1 summarizes patient demographics and histopathologic and molecular tumor information. Seven patients underwent a biopsy, while 40 had a resection (12 had >90% and 28 had gross total resection). Averages of 5 (range, 1–12) and 6 (range, 1–16) representative sections per the entire volume of submitted tissue specimen were analyzed in the biopsy and resection groups, respectively. On the basis of histopathologic examination, 17 were classified as TE (consisting of 4 samples with no tumor cells

Table 2: Mean values of FTB classes and normalized rCBV in histopathologically defined treatment effect and tumor groups[a]

	TE	Tumor	*P* Values
FTB_{low}	54.8 (22.3)	33.1 (20.8)	.002
FTB_{mid}	27.0 (15.4)	21.3 (11.3)	.16
FTB_{high}	18.2 (14.4)	45.5 (22.6)	<.001
rCBV	1.2 (0.6)	2.1 (1.0)	<.001

[a] Values are reported as mean (standard deviation), except for *P* values.

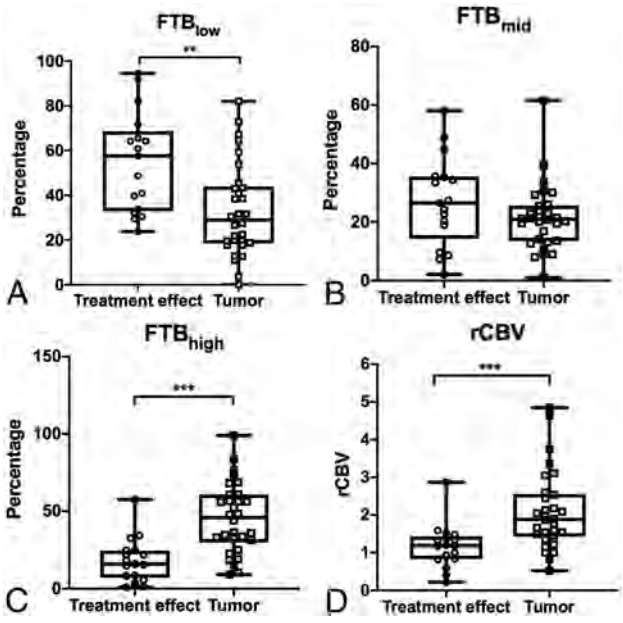

FIG 2. Boxplots of the relationship between FTB and normalized rCBV in 2 histopathologically defined groups: treatment effect and recurrent tumor. *Open circles* and *squares* represent individual measurements. The upper and lower limits of the *whiskers* represent the minimum and maximum of all of the data. *Double asterisks* indicate $P < .01$; *triple asterisks*, $P < .001$.

and 13 with scattered infiltrating atypical cells), and 30, as recurrent tumor.

Quantitative FTB and rCBV

Differences in mean FTB_{low}, FTB_{high}, and rCBV of the contrast-enhancing lesion volume were significant between TE and tumor ($P = .002$, <.001, and <.001, respectively), with tumor having higher FTB_{high} and rCBV and lower FTB_{low} than TE (Table 2 and Fig 2). No significance was found with FTB_{mid} ($P = .16$).

Areas under the receiver operating characteristic curve for using FTB and rCBV to distinguish TE and tumor were the following: 0.77 for FTB_{low} (95% CI, 0.64–0.90; $P = .002$), 0.63 for FTB_{mid} (95% CI, 0.44–0.81; $P = .16$), 0.85 for FTB_{high} (95% CI, 0.74–0.97; $P < .001$), and 0.81 for rCBV (95% CI, 0.69–0.94; $P < .001$) (Fig 3). The FTB_{high} cut-point of >24.9% yielded a sensitivity of 80% and a specificity of 82%, and the FTB_{low} cut-point of <28.5% yielded a sensitivity of 50% and specificity of 94% for tumor prediction. The use of both cut-points showed significance in differentiating tumor from TE ($P < .001$), with a sensitivity of 100% and specificity of 47%. The optimal rCBV cut-point for

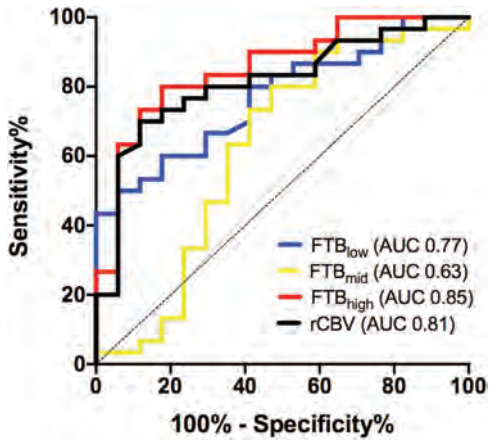

FIG 3. Receiver operating characteristic curves for the use of fractional tumor burden classes and normalized rCBV to differentiate tumor from treatment effect.

identifying tumor was found to be >1.53, yielding a sensitivity of 70% and specificity of 88%.

Qualitative Analysis

Agreement among the 5 physicians for the use of FTB to differentiate TE from tumor was fair-to-good (ICC = 0.48). When we compared the consensus decision with the actual histopathology, agreement improved (ICC = 0.70). Of the total number of cases with histopathologically confirmed tumor ($n = 28$) and TE ($n = 16$), there were disagreements in 7% (2/28) of tumor and 25% (4/16) of TE cases (Fig 4*A*).

Agreement among the raters when asked whether they would hypothetically change treatment on the basis of their interpretation of FTB was fair-to-good (ICC = 0.48). The consensus decision was to hypothetically change treatment in 93% (26/28) of tumor cases and not to change treatment in 75% (12/16) of TE cases. When we compared the consensus decision with the actual treatment plan, agreement was fair-to-good (ICC = 0.46). Of the histopathologically confirmed tumor and TE groups, there were disagreements in 7% (2/28) of tumor and 44% (7/16) of TE cases (Fig 4*B*). In this latter TE group, all disagreements occurred in cases in which the surgical specimen showed scattered atypical cells and none in which the specimen showed no tumor cells (Fig 4*C*).

DISCUSSION

Our results show that the use of 2 rCBV thresholds to define low and high fractional tumor burden of the contrast-enhancing volume allows differentiation of tumor and TE in the recurrent glioblastoma setting. Of the 3 FTB classes and rCBV parameters, FTB_{high} performed the best for this task. In addition, we found good consensus agreement among 5 physicians for the use of FTB to differentiate TE from tumor and to inform potential treatment-related decision-making.

Given the variability of previously published mean rCBV thresholds to differentiate TE from tumor (with a reported range of 0.9–2.15 based on a recent meta-analysis),[6] we selected predefined values on the low and high ends of the range to define

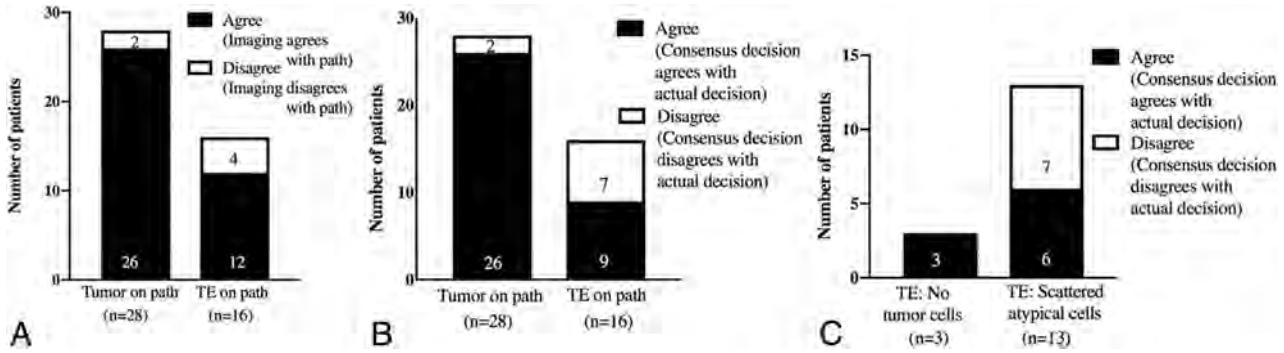

FIG 4. Agreement between the consensus (among 5 physician raters) qualitative interpretation of imaging and the actual histopathologic diagnosis (*A*). Agreement between the hypothetic consensus decision to change treatment plans and the actual (real-time) management plans (*B* and *C*).

fractions of the contrast-enhancing volume with low and high blood volume, respectively. On the basis of prior radiology-pathology correlative studies, areas of TE tend to have low blood volume and areas of tumor tend to have high blood volume on perfusion MR imaging.[2,3,19] We did not generate the optimal thresholds to use from our own dataset (to minimize institutional bias in generating the values) and opted to use values that have been tested or validated in prior studies: On the low end of the rCBV range, a threshold of 1.0 has been used to reliably distinguish TE and tumor,[2,3] and on the high end, a threshold of 1.75 has been used to identify aggressive tumors.[8,10] In our study, the use of 2 thresholds allowed the delineation of 3 FTB classes; we found that TE had significantly higher FTB_{low} than tumor and that tumor had significantly higher FTB_{high} than TE. In comparing these metrics, FTB_{high} performed better than FTB_{low} for tumor identification. The use of both FTB_{high} and FTB_{low} percentage cut-points improved the sensitivity of tumor diagnosis to 100%, but specificity remained low. We postulate that FTB_{high} is a more robust marker than FTB_{low} due to tumoral heterogeneity, in which previously treated tumors can have regional and interspersed areas of both high and low blood volume, presumably related to varying degrees of angiogenesis and necrosis, respectively.[20] In contrast, areas of pure TE and radiation necrosis tend to consistently show low blood volume.[21] Sampling error, which is further discussed in the limitations, may also help to explain the lower specificity found in this study. FTB_{mid}, which includes all rCBV values between 1.0 and 1.75, did not reliably differentiate TE from tumor, likely because of overlapping values in this range found in samples with both TE and tumor, which is consistent with findings in the study of Barajas et al.[20] Nonetheless, a strength of using FTB is that it is less dependent on the magnitude of rCBV values, except to classify voxels within a FTB class, and it has been shown to better approximate tumor volume fraction.[2]

We did not correlate perfusion results with prognostic clinical end points such as overall survival because there were insufficient patient numbers to perform a meaningful analysis. Rather, we assessed whether FTB data could be used to predict the histopathologic diagnosis and inform short-term management plans. Agreement between the consensus assessment of disease based on FTB and the actual histopathologic diagnosis was good. In keeping with the imaging interpretation, the consensus decision was to hypothetically change treatment in 93% (26/28) of tumor cases and not to change treatment in 75% (12/16) of TE cases. This is in the context of all patients undergoing surgical intervention in real-time because of concerns for tumor progression at the time of the clinical MR imaging and suggests the potential role of this approach to help triage patients who may or may not need an operation for diagnosis. Most of the disagreement in treatment changes occurred in the histopathologically defined TE group; upon further analysis, all disagreements in this group occurred in cases in which histopathology showed scattered atypical cells. This may be because, in real-time, the decision to change treatment considered the uncertainty of whether the atypical cells represented radiation-related change or treated-but-viable glioma cells and other clinical factors (such as patient age, Karnofsky Performance Status Scale, tumor molecular status, and patient desires) that were not incorporated in our study. Nonetheless, our findings are in keeping with those of Geer et al,[22] who showed that the addition of DSC and arterial spin-labeling perfusion imaging impacted and changed management plans in 8.5% (5/59) of patient care episodes and significantly increased physician confidence in treatment plans. In contrast to that study, which included only qualitative image interpretation, we show the potential of a combined approach using quantitative and qualitative data to inform treatment-related decision-making.

Limitations of this study should be considered. First, the retrospective nature of this study consisting of a single institutional dataset and small sample size limits the generalizability of our results. Second, acquisition of DSC-MR imaging during the study period was performed without preload dosing, which can confound rCBV estimates.[7,23] Of note, Hu et al[5] showed that the use of IB Neuro software, which was used in this study, generated rCBV metrics, including FTB, that were highly correlated even between nonpreload- and preload-dose-corrected conditions. Schmainda et al[15] also recently showed that DSC imaging using a low flip angle (30°) and no preload dose produces rCBV values similar to those of the conventional method of using an intermediate flip angle (60°) with preload and postprocessing leakage correction. Third, misregistration of VOIs

due to geometric distortion in DSC is another potential source of error. Finally and most important, we used histopathologic examination of available tissue specimens from both surgical resection and, to a smaller extent, biopsies for ground truth diagnoses. Although we evaluated different representative sections of the entire submitted samples to determine a diagnosis, we could not provide histopathologic correlation for every voxel of the contrast-enhancing volume available on FTB. Because glioblastomas are markedly heterogeneous tumors, histopathologic diagnosis of samples from separate locations may differ; even with a given sample, diagnostic agreement among pathologists can vary.[24] However, despite the real possibility of sampling error, histopathologic assessment remains the "criterion standard" for determining disease status and often influences treatment-related decision-making. Taking these issues into consideration, we show the potential of FTB to distinguish TE from tumor, and we have yet to fully explore its role as an alternative means to provide accurate diagnostic and prognostic information, particularly given the limitations of histopathologic evaluation.

CONCLUSIONS

The use of 2 rCBV thresholds (1.0 and 1.75) to define FTB_{low} and FTB_{high} provided good spatial visualization and quantification of contrast-enhancing volume fraction with low and high blood volume, respectively, and they performed well to differentiate tumor from TE in the recurrent glioblastoma setting. In addition, combining qualitative image interpretation with quantitative FTB data can help inform clinical decision-making, with such decisions closely mirroring actual treatment decisions made for groups with histopathologically confirmed tumor and no tumor cells. Larger prospective studies, however, are needed to validate this method for use in real-time clinical decision-making and for correlation with important clinical outcomes.

Disclosures: Scott G. Soltys—*UNRELATED: Consultancy*: Inovio Pharmaceuticals.

REFERENCES

1. Wen PY, Macdonald DR, Reardon DA, et al. **Updated response assessment criteria for high-grade gliomas: Response Assessment in Neuro-Oncology Working Group**. *J Clin Oncol* 2010;28:1963–72 CrossRef Medline
2. Hu LS, Eschbacher JM, Heiserman JE, et al. **Reevaluating the imaging definition of tumor progression: perfusion MRI quantifies recurrent glioblastoma tumor fraction, pseudoprogression, and radiation necrosis to predict survival**. *Neuro Oncol* 2012;14:919–30 CrossRef Medline
3. Prah MA, Al-Gizawiy MM, Mueller WM, et al. **Spatial discrimination of glioblastoma and treatment effect with histologically-validated perfusion and diffusion magnetic resonance imaging metrics**. *J Neurooncol* 2018;136:13–21 CrossRef Medline
4. Jain R, Scarpace L, Ellika S, et al. **First-pass perfusion computed tomography: initial experience in differentiating recurrent brain tumors from radiation effects and radiation necrosis**. *Neurosurgery* 2007;61:778–86; discussion 786–87 Medline
5. Hu LS, Kelm Z, Korfiatis P, et al. **Impact of software modeling on the accuracy of perfusion MRI in glioma**. *AJNR Am J Neuroradiol* 2015;36:2242–49 CrossRef Medline
6. Patel P, Baradaran H, Delgado D, et al. **MR perfusion-weighted imaging in the evaluation of high-grade gliomas after treatment: a systematic review and meta-analysis**. *Neuro Oncol* 2017;19:118–27 CrossRef Medline
7. Paulson ES, Schmainda KM. **Comparison of dynamic susceptibility-weighted contrast-enhanced MR methods: recommendations for measuring relative cerebral blood volume in brain tumors**. *Radiology* 2008;249:601–13 CrossRef Medline
8. Law M, Young RJ, Babb JS, et al. **Gliomas: predicting time to progression or survival with cerebral blood volume measurements at dynamic susceptibility-weighted contrast-enhanced perfusion MR imaging**. *Radiology* 2008;247:490–98 CrossRef Medline
9. Prager AJ, Martinez N, Beal K, et al. **Diffusion and perfusion MRI to differentiate treatment-related changes including pseudoprogression from recurrent tumors in high-grade gliomas with histopathologic evidence**. *AJNR Am J Neuroradiol* 2015;36:877–85 CrossRef Medline
10. Gasparetto EL, Pawlak MA, Patel SH, et al. **Posttreatment recurrence of malignant brain neoplasm: accuracy of relative cerebral blood volume fraction in discriminating low from high malignant histologic volume fraction**. *Radiology* 2009;250:887–96 CrossRef Medline
11. Cha S, Tihan T, Crawford F, et al. **Differentiation of low-grade oligodendrogliomas from low-grade astrocytomas by using quantitative blood-volume measurements derived from dynamic susceptibility contrast-enhanced MR imaging**. *AJNR Am J Neuroradiol* 2005;26:266–73 Medline
12. Boxerman JL, Zhang Z, Safriel Y, et al. **Early post-bevacizumab progression on contrast-enhanced MRI as a prognostic marker for overall survival in recurrent glioblastoma: results from the ACRIN 6677/RTOG 0625 Central Reader Study**. *Neuro Oncol* 2013;15:945–54 CrossRef Medline
13. Prah MA, Stufflebeam SM, Paulson ES, et al. **Repeatability of standardized and normalized relative CBV in patients with newly diagnosed glioblastoma**. *AJNR Am J Neuroradiol* 2015;36:1654–61 CrossRef Medline
14. Schmainda KM, Prah MA, Rand SD, et al. **Multisite concordance of DSC-MRI analysis for brain tumors: results of a National Cancer Institute quantitative imaging network collaborative project**. *AJNR Am J Neuroradiol* 2018;39:1008–16 CrossRef Medline
15. Schmainda KM, Prah MA, Hu LS, et al. **Moving toward a consensus DSC-MRI protocol: validation of a low-flip angle single-dose option as a reference standard for brain tumors**. *AJNR Am J Neuroradiol* 2019;40:626–33 CrossRef Medline
16. Bedekar D, Schmainda KM, Rand S, et al. **Delta T1 (dT1) method as a tool to evaluate tumor progression in patients with brain cancer**. *J Clin Oncol* 2011;29:e21056–56
17. Schmainda KM, Prah MA, Zhang Z, et al. **Quantitative delta T1 (dT1) as a replacement for adjudicated central reader analysis of contrast-enhancing tumor burden: a subanalysis of the American College of Radiology Imaging Network 6677/Radiation Therapy Oncology Group 0625 Multicenter Brain Tumor Trial**. *AJNR Am J Neuroradiol* 2019;40:1132–39 CrossRef Medline
18. Rosner B. *Fundamentals of Biostatistics*. Belmont: Thomson Brooks/Cole; 2006
19. Hu LS, Baxter LC, Smith KA, et al. **Relative cerebral blood volume values to differentiate high-grade glioma recurrence from posttreatment radiation effect: direct correlation between image-guided tissue histopathology and localized dynamic susceptibility-weighted contrast-enhanced perfusion MR imaging measurements**. *AJNR Am J Neuroradiol* 2009;30:552–58 CrossRef Medline
20. Barajas RF Jr, Chang JS, Segal MR, et al. **Differentiation of recurrent glioblastoma multiforme from radiation necrosis after external beam radiation therapy with dynamic susceptibility-weighted contrast-enhanced perfusion MR imaging**. *Radiology* 2009;253:486–96 CrossRef Medline

21. Li Z, Zhou Q, Li Y, et al. **Mean cerebral blood volume is an effective diagnostic index of recurrent and radiation injury in glioma patients: a meta-analysis of diagnostic test**. *Oncotarget* 2017;8:15642–50 CrossRef Medline
22. Geer CP, Simonds J, Anvery A, et al. **Does MR perfusion imaging impact management decisions for patients with brain tumors? A prospective study**. *AJNR Am J Neuroradiol* 2012;33:556–62 CrossRef Medline
23. Hu LS, Baxter LC, Pinnaduwage DS, et al. **Optimized preload leakage-correction methods to improve the diagnostic accuracy of dynamic susceptibility-weighted contrast-enhanced perfusion MR imaging in posttreatment gliomas**. *AJNR Am J Neuroradiol* 2010;31:40–48 CrossRef Medline
24. Holdhoff M, Ye X, Piotrowski AF, et al. **The consistency of neuropathological diagnoses in patients undergoing surgery for suspected recurrence of glioblastoma**. *J Neurooncol* 2019;141:347–54 CrossRef Medline

Regional Cerebral Blood Flow in the Posterior Cingulate and Precuneus and the Entorhinal Cortical Atrophy Score Differentiate Mild Cognitive Impairment and Dementia Due to Alzheimer Disease

B. Thomas, R. Sheelakumari, S. Kannath, S. Sarma, and R.N. Menon

ABSTRACT

BACKGROUND AND PURPOSE: Alzheimer disease is the most common degenerative dementia affecting humans and mild cognitive impairment is considered the forerunner of this devastating illness with variable progression. Differentiating between them has become all the more essential with the advent of disease-modifying medications. The aim of this study was to test the utility of the entorhinal cortical atrophy score in combination with quantitative CBF in the posterior cingulate and precuneus using arterial spin-labeling to differentiate mild cognitive impairment and early Alzheimer disease.

MATERIALS AND METHODS: We analyzed MR imaging from a prospective data base of 3 age-matched groups: 21 cognitively healthy controls, 20 patients with mild cognitive impairment, and 19 patients with early Alzheimer disease. The highest entorhinal cortical atrophy score and an atlas-based measurement of CBF in the posterior cingulate and precuneus were estimated in these groups. Statistical comparison was performed among the groups for disease-prediction probability with these parameters independently and in combination using a binary logistic regression model.

RESULTS: The entorhinal cortical atrophy score performed well in distinguishing AD from HC, with a predicted probability of .887 (area under the curve, $P < .001$). The mean CBF of the posterior cingulate and precuneus was also found to be a useful discriminator (area under the curve, 0.810, $P = < .001$). Combining the entorhinal cortical atrophy score and CBF was the best predictor (area under the curve, 0.957, $P < .001$). In distinguishing mild cognitive impairment and Alzheimer disease, entorhinal cortical atrophy also did well with an area under the curve of 0.838 ($P < .001$). However regional CBF was not useful in differentiating them (area under the curve = 0.589, $P = .339$). Entorhinal cortical atrophy scored poorly in distinguishing mild cognitive impairment from healthy controls (AUC = 0.571, $P = .493$), but CBF fared well, with an area under the curve of 0.776 ($P = .002$).

CONCLUSIONS: Combining entorhinal cortical atrophy and regional CBF could be a potential imaging biomarker in distinguishing mild cognitive impairment and Alzheimer disease.

ABBREVIATIONS: ACE-M = South Indian language of Malayalam version of Addenbrooke's Cognitive Examination; AD = Alzheimer disease; ASL = arterial spin-labeling; ERICA = entorhinal cortical atrophy; HC = healthy controls; MCI = mild cognitive impairment; PCG = posterior cingulate gyrus; PC = precuneus; ROI = region of interest

Alzheimer disease (AD) is the most common degenerative dementia affecting humans with marked socio-economic burden for care of the affected.[1,2] Mild cognitive impairment (MCI) is considered the forerunner of this devastating illness with variable progression.[3] With the advent of disease-modifying medications, early detection and classification of preclinical dementia have become essential. Exploration of possible biomarkers identifying individuals who are at high risk for developing AD is the focus of current research. Validated biomarkers for diagnosing MCI at risk of progression include Pittsburgh compound–based PET and CSF biomarkers, which are either not available in many centers worldwide or are prohibitively expensive.[4] The relevance of validating instruments from widely available multimodality imaging techniques has been demonstrated by our group previously.[5]

Received April 22, 2019; accepted after revision August 1.

From the Department of Imaging Sciences and Interventional Radiology (B.T., R.S., S.K.), Division of Cognitive and Behavioural Neurology (R.N.M.), and Achutha Menon Centre for Health Sciences Studies (S.S.), Sree Chitra Tirunal Institute for Medical Sciences and Technology, Thiruvananthapuram, Kerala, India.

This work was supported by CSI/90/2012, SATYAM/278/2015, and SERB N-PDF 2017 grants from the Government of India.

Please address correspondence to Bejoy Thomas, MD, DNB, PDCC, Department of Imaging Sciences and Interventional Radiology, Sree Chitra Tirunal Institute for Medical Sciences and Technology, Thiruvananthapuram, Kerala, India; e-mail: bejoy@sctimst.ac.in; @drbejoy2002

http://dx.doi.org/10.3174/ajnr.A6219

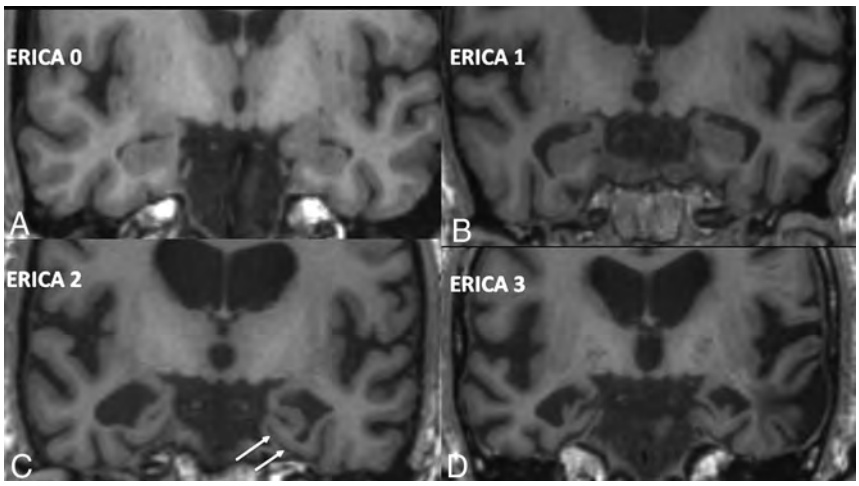

FIG 1. ERICA scoring. *A*, Score 0 with no parahippocampal atrophy. *B*, Score 1 with mild atrophy with prominence of collateral sulcus. *C*, Score 2 with moderate entorhinal cortical atrophy with tentorial cleft sign (*arrows*). *D*, Score 3 with marked parahippocampal atrophy. Adapted from Enkirch et al.[17]

Cerebral blood flow alterations in patients with AD and MCI have been identified as an important marker in understanding the neurophysiologic changes even before development of neuronal loss.[6] Arterial spin-labeling (ASL) uses tagged arterial blood as an endogenous contrast for detecting regional CBF perfusion changes. Many recent studies have highlighted its role in imaging AD and MCI, in which different brain regions have been found to show hypo- or hyperperfusion.[7-13] ASL is a noninvasive MR perfusion technique, without the use of any ionizing radiation, intravenous contrast agents, or radioactive isotopes, and it is considered a potential alternative to FDG-PET imaging.[14,15] Using ASL, many studies have consistently shown statistically significant hypoperfusion involving the posterior cingulate gyrus (PCG) and precuneus (PC), among many regions studied in MCI-AD.[10,11,13] Only a few studies have correlated quantitative CBF with neuropsychology in AD and MCI.[16] No consistent correlation has been established between CBF and gray matter volume changes in the corresponding regions in patients with AD and MCI in the existing literature.[13]

The entorhinal cortex has been shown to undergo graded atrophy in the MCI-AD complex and is thought to be one of the early areas of the brain that shows gray matter atrophy in AD.[17] A recently described numeric atrophy scale of the entorhinal cortex (ERICA) score has been shown to correlate well with the cognitive changes and the diagnosis of AD.[17] It has also been shown to be better than the previously described medial temporal lobe atrophy score in differentiating AD from subjectively reported cognitive impairment in patients.[17] The ERICA score is a 4-point atrophy rating scale from 0 to 3, where 0 indicates no evidence for atrophy of the entorhinal cortex, and 3, marked atrophy (Fig 1). This was shown to be handy because the scoring system is very simple, but powerful enough to be used for the distinction of these conditions. However, this scoring system has not yet been validated by further studies.

The aim of the present study was to test the hypothesis that the regional CBF changes measured in the posterior cingulate and precuneus (PCG + PC) region using the 3D fast spin-echo pseudocontinuous ASL sequence along with ERICA scoring of entorhinal cortical atrophy will be a better biomarker in differentiating patients with AD and MCI compared with healthy controls (HC).

MATERIALS AND METHODS

MR images from the data base of prospectively recruited consecutive subjects attending the Memory and Neurobehavioral Disorders Clinic of a tertiary referral teaching hospital in the South Indian state of Kerala, between 2016 and 2018, were included in this study. Age-matched control data were also collected during the period from the data base. Five subjects were excluded due to insufficient image quality. The final sample consisted of 21 controls, 20 patients with MCI, and 19 patients with AD. All subjects provided written consent according to procedures approved by the Institutional Ethics Committee of our institution. The diagnosis of MCI and AD was based on subjective cognitive symptoms verified by objective evidence of decline by a family member compared with the previous status and confirmed by evidence of a decline in $\geq$1 neuropsychological domain[4] as shown below. Participants with a global cognitive assessment score, as determined on the vernacular version (in the South Indian language of Malayalam of Addenbrooke's Cognitive Examination [ACE-M]), between 88 and 100; a Clinical Dementia Rating score of 0; with formal education of $>$10 years; no subjective memory symptoms; and with no serious neurologic/psychiatric issues were selected as healthy controls.[18,19] Participants with a Clinical Dementia Rating of $<$2 and an ACE-M score between 60 and 78 were confirmed as having AD according to standard National Institute of Neurological and Communicative Diseases and Stroke/Alzheimer's Disease and Related Disorders Association diagnostic criteria.[20]

Because we wanted to recruit patients with early AD who were largely independent for activities of daily living and capable of giving informed consent, we decided to include subjects with a Clinical Dementia Rating of only 0.5–1. Patients with MCI were diagnosed per the Modified Petersen Criteria with a Clinical Dementia Rating of $\leq$0.5 and an ACE-M score between 78 and 88 with evidence of impairment in $\geq$1 cognitive domain, defined as test performance on at least 2 tests (which also included the ACE-M subcomponent scores) for a given domain falling below a mean $-$1.5 SD of the normative scores for the corresponding age and education status.[21] Exclusion criteria included the presence of a major neurologic disorder (stroke), medical comorbidities (cardiovascular, renal), and psychiatric illness (clinically significant anxiety and depression [Hospital Anxiety Depression

Scale score should be <7], psychosis), similar to those in our previous study.[19]

Imaging Protocol

A 3T scanner (Discovery MR750w, GE Healthcare, Milwaukee, Wisconsin) with a 32-channel phased array head coil was used to acquire structural and ASL images. Structural images were obtained using a high-resolution 3D brain volume imaging sequence (3D-BRAVO) with the following parameters: TR/TE = 7/2.98 ms, section thickness = 1 mm, flip angle = 12°, matrix size = 256 × 256, and voxel size = 1 × 1 × 1 mm^3. A 3D fast spin-echo pseudocontinuous ASL sequence was performed with the following acquisition parameters: TR/TE = 4852/10.70 ms, flip angle = 111°, voxel size = 1.875 × 1.875 × 4, section thickness = 4 mm, NEX = 3, and postlabel delay = 2025 ms.

Data Analysis

Structural and ASL data were processed using an off-line PC workstation. For ASL processing, quantitative CBF maps with values measured in units of milliliters/100 g/min in each subject were used. All the structural images and CBF maps were oriented in the anterior/posterior commissure line using Statistical Parameter Mapping software (SPM12; http://www.fil.ion.ucl.ac.uk/spm/download/spm12/). CBF maps of all the participants were then normalized to a standard stereotactic space and spatially smoothed with an 8-mm isotropic Gaussian kernel to improve the signal-to-noise ratio. Second-level statistical procedures implemented in SPM12 were used to analyze the CBF maps. The value of total intracranial volume was used as a covariate in the statistical design to correct variability among groups. Information on regional perfusion values was extracted by means of an ROI analysis. Anatomic ROIs for the posterior cingulate and precuneus were defined by means of the WFU PickAtlas tool (https://www.nitrc.org/projects/wfu_pickatlas/) (Fig 2). Regional CBF was estimated using parameter extraction with MarsBaR (https://www.nitrc.org/projects/marsbar/). Values within ROIs of both sides were then averaged and tabulated for HC, MCI, and AD groups.

ERICA scoring was performed on coronally reformatted 3D-T1 BRAVO images in all subjects by 2 independent neuroradiologists (B.T. and S.K.) with 19 and 10 years of experience, respectively, at the level of the mamillary bodies as described by Enkirch et al.[17] The interobserver agreement was calculated using Cohen κ statistics. Values on the right and left sides were tabulated, and the highest ERICA score in consensus in each subject was used for further analysis.

Statistical Analysis

The χ^2 test was used for comparison of sex differences and vascular risk factors among groups (Table 1). The clinical differentiation scores are also summarized in the same table. For comparison of age, 1-way ANOVA was performed. The ERICA score and CBF measures in the ROI were used to derive the predicted probability of MCI and AD based on a binary logistic regression model. The derived measures were used for generating the receiver operating characteristic curves, and the area under the curve was used to compare them (Table 2 and Fig 3). Statistical analyses were performed using the software SPSS for Windows, Version 21.0 (IBM, Armonk, New York).

RESULTS

The demographics, clinical cognitive scores, and vascular risk factors of each group are summarized in Table 1. There was no significant difference in age, sex, or vascular risk factors among these 3 cohorts.

The average highest ERICA score was 0.71 ± 0.46 in HC, 0.90 ± 0.64 in MCI, and 2.15 ± 0.83 in AD. There was overall substantial interrater agreement for ERICA scoring (Cohen κ = 0.783 for the right side, 0. 777 for the left side, and 0.797 for the highest ERICA score). The mean CBF in PCG + PC was 46.64 ± 8.4, 39.08 ± 6.6, and 36.51 ± 8.4 mL/100/min in HC, MCI, and AD, respectively (Table 2).

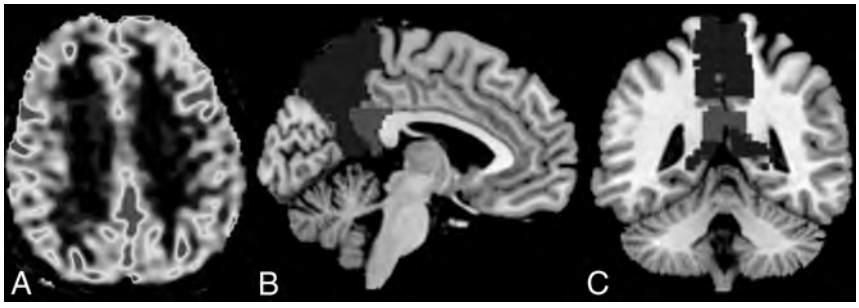

FIG 2. *A*, Axial ASL CBF gray-scale map. *B* and *C*, Sagittal and coronal representative images, respectively, of the template for automated segmentation and extraction of posterior cingulate (light gray) and precuneus (dark gray) ASL CBF perfusion maps.

Table 1: Demographic data, comorbidities, and clinical scores of subjects

Characteristic	HC (*n* = 21)	MCI (*n* = 20)	AD (*n* = 19)	*P* Value		
				MCI versus HC	AD versus HC	AD versus MCI
Sex (male/female)	11:10	11:9	11:8	.87	.77	.88
Age (mean ± SD) (yr)	64.57 ± 5.74	66.75 ± 4.08	66.68 ± 5.31	.37	.66	1.00
H/o hypertension	5/21	7/20	9/19	.33	.11	.32
H/o diabetes mellitus	5/21	8/20	10/19	.22	.06	.32
RAVLT cumulative learning score (mean)	48.52 ± 8.46	33.47 ± 10.07	25.21 ± 7.15	**<.001**	**<.001**	**.035**
RAVLT 20-min recall score (mean)	10.00 ± 2.82	5.41 ± 3.74	1.36 ± 1.73	**<.001**	**<.001**	**.001**
ACE-M	93.38 ± 4.11	81.12 ± 11.09	72.00 ± 11.09	**<.001**	**<.001**	**.020**

Note:—H/o indicates History of; RAVLT, Rey auditory verbal learning test; ACE-M, Addenbrooke's Cognitive examination. Significant *P* values are highlighted in bold.

Table 2: Performance of the ERICA score and CBF of PCG + PC in predicting HC, MCI, and AD

Parameters	HC (Mean)	MCI (Mean)	AD (Mean)	Predicted Probability of Diagnosis (Area under the Curve of ROC) with *P* Values in Parentheses		
				MCI vs HC	AD vs HC	AD vs MCI
ERICA (0–3)	0.71 ± 0.46	0.90 ± 0.64	2.15 ± 0.83	0.571 (.493)	0.887 (<**.001**)	0.838 (<**.001**)
CBF in PCG + PC (mL/100 g/min)	46.64 ± 8.4	39.08 ± 6.6	36.51 ± 8.4	0.776 (**.002**)	0.810 (<**.001**)	0.589 (.339)
Combined ERICA and CBF				0.781 (**.002**)	0.957 (<**.001**)	0.829 (<**.001**)

Note:—ROC indicates receiver operating characteristic. Significant *P* values are highlighted in bold.

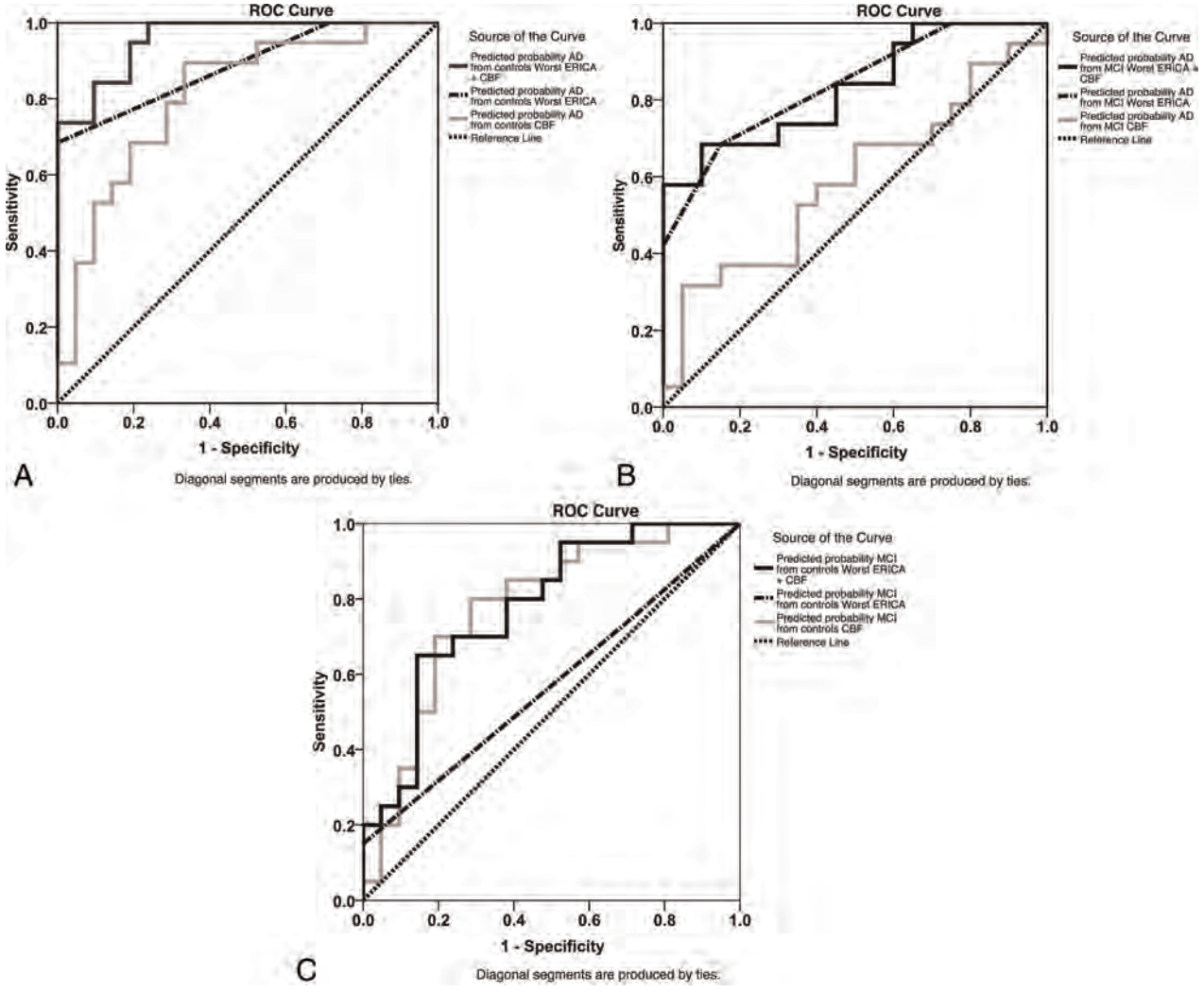

FIG 3. Receiver operating characteristic curves for predicted probability from ERICA (*dot-dash lines*) and regional CBF (*light gray continuous lines*) and a combination of both (*black continuous lines*). AD versus HC (*A*), AD versus MCI (*B*), MCI versus HC (*C*).

Both ERICA scores and mean CBF were highly predictive of distinguishing AD from HC, with a predicted probability of 0.887 ($P < .001$) and 0.810 ($P < .001$), respectively. How-ever, combining the ERICA score and mean CBF significantly increased the discriminatory power between AD and HC with the predicted probability of 0.957 ($P < .001$) (Fig 3*A*). While the ERICA score was found to be useful in distinguishing MCI from AD (predictive probability of 0.838, $P < .001$), regional mean CBF was not useful to differentiate these 2 groups (predictive probability of 0.589, $P = .339$). Marginal reduction of predictive probability (0.829, $P < .001$) was observed after a combination of ERICA scores and CBF without loss of discriminant ability (Fig 3*B*).

Significantly, the ERICA score was not found to be effective in distinguishing MCI from HC (predictive probability = 0.571, $P = .493$). On the contrary, regional CBF demonstrated a higher predictive probability of 0.776 ($P = .002$) to differentiate these groups. Combined ERICA scores and CBF maintained this predictive power, with a marginal increase of the predictive probability of 0.781 ($P = .002$). (Fig 3*C*).

The results are summarized in Table 2 and Fig 3.

DISCUSSION

ASL is a noninvasive technique for cerebral perfusion measurement using electromagnetically labeled arterial water as a diffusible tracer. Several ASL perfusion studies have highlighted regional hypo- and hyperperfusion in multiple areas of the brain in MCI-AD.[7-13] However, due to the variability of clinical subsets studied and the usage of nonreplicable sequences, these studies were not directly comparable.[13] In the past, differences in technical implementation schemes and lack of standardized protocols hindered the routine use of ASL as a robust perfusion method in the clinical setting. International consensus guidelines have been developed recently for standardized ASL acquisitions.[22] A 3D fast spin-echo pseudocontinuous ASL with a spiral readout is now generally considered the standard method of ASL in clinical research. In this study, we used a 3D fast spin-echo pseudocontinuous ASL technique on 3T MR imaging to investigate regional perfusion differences in patients with MCI and AD compared with HC. ROIs were extracted using atlas-based semiautomated techniques to avoid errors due to manual contouring.

Although several brain areas have been shown to be involved, one of the most consistent regions of hypoperfusion reported in MCI-AD is the PCG and anterior PC.[10,11,13] Identification of hypoperfusion in the PCG + PC has been reported to have a sensitivity of 91% and a specificity of 80% for diagnosing AD.[23] This method is in contrast to inclusion of a combination of different regions in subjects with amnestic and dysexecutive MCI, in which an accuracy of only 60%–70% was observed.[24] From the existing literature, it is not clear whether the hypoperfusion is the cause or consequence of the disease process.[25] In our study, the regional mean CBF in PCG + PC was 46.64, 39.08, and 36.51 mL/100/min in HC, MCI, and AD, respectively, and it performed well in distinguishing AD-HC and MCI-HC, but not between MCI and AD. This finding may be because the perfusion deficit in the PCG + PC occurs early in the course of this dementing illness spectrum, and this particular feature may be used as a reliable marker to delineate patients with MCI and AD from HC. However, from MCI to AD transformation, the perfusion reduction in these regions may be less remarkable and hence may not have significant diagnostic utility as a stand-alone measure.

There is no consistent correlation established between CBF and gray matter changes in the corresponding regions in patients with AD and MCI.[13] In the initial stages of AD, changes such as intraneuronal alterations in the form of neurofibrillary tangles and neuropil threads are observed more frequently in the entorhinal cortex compared with hippocampus.[26] This accumulation may be noted in other conditions, including normal aging, and when this is associated with neuronal loss, it leads to global cognitive decline. MR volumetric studies have also shown entorhinal cortex volume loss in dementia due to Alzheimer spectrum diseases.[27,28] It has been shown in studies that in early stages of AD, certain areas such as the prefrontal cortex or medial temporal lobe structures would eventually have the ability to compensate for the cognitive decline.[29] Simultaneously, perfusion deficits might also be present from the very early preclinical phases of AD, including MCI at risk of conversion, persisting into the advanced stages of the disease, demonstrating a progressive hypoperfusion with disease development, leading to brain atrophy and underlying neuronal loss that correlates with cognitive and functional decline.[13] With regard to the pathophysiologic interpretation of the regional hypoperfusion consistently found in the PCG + PC, in comparison with ERICA, controversy exists about whether this is a cause or consequence of the disease process.[25] It is well known that risk factors such as ischemic stroke, amyloid angiopathy, atherosclerosis, hypertension, diabetes, and cardiac disease are repeatedly implicated in the risk of MCI converting to AD.[30] While AD and vascular dementia have traditionally been considered as independent entities, there is growing evidence implicating vascular pathology in AD to the extent of suggesting an overlap between AD and vascular dementia.[31] Moreover, evidence from aging and stroke studies suggests that chronic brain hypoperfusion is the key pathophysiology that leads to neurodegeneration and consequent cognitive decline.[25] Neuropsychologic correlations have also been established between perfusion measures in the parieto-occipital region and the parietal cortex along with the PCG + PC.[32] Hypoperfusion may lead to changes in cortical thickness, as measured on structural MR imaging scans, in areas most vulnerable to aging (medial prefrontal and pericentral cortices) as well as in areas associated with amyloid aggregation (eg, occipitotemporal and basal temporal cortices), more so in *apolipoprotein E4* carriers.[33] Hence, there is the necessity to address disparate or nonconcordant topographic areas rather than looking at concordant brain volumes underlying areas of hypoperfusion while attempting to combine hypoperfusion and volumetric measures as with ERICA.

Compared with conventional MR imaging–medial temporal lobe atrophy scoring, which reported a sensitivity of 81% and a specificity of 67%, ERICA had a higher sensitivity of 83% and specificity of 98% in differentiating AD.[17,34] ERICA is also easier to comprehend and score compared with the more complex medial temporal lobe atrophy score. It is also reliable and reproducible as confirmed in our study. The tentorial cleft sign (Fig 1*C*), which indicated an ERICA score of ≥2, had a high diagnostic accuracy for AD.[17] In our study, the average ERICA score of patients with AD was 2.15. ERICA performed well in differentiating AD from MCI and AD from HC, but not MCI from HC. This performance may mean that significant parahippocampal atrophy does not happen early in MCI and probably is a much later occurrence compared with CBF reduction in PCG + PC in the course of progression of dementia. This hypothesis is further validated by the observations of neuropathology studies by Braak and Braak published in 1991.[26]

ASL hypoperfusion abnormality in PCG + PC and parahippocampal atrophy may be considered as complementary imaging biomarkers to distinguish MCI and AD. In our study combining the ERICA score with regional CBF in PCG + PC showed a promising trend to differentiate MCI, AD, and HC groups rather than individual parameters. However, MCI-AD is a more heterogeneous disease process, and not all patients with MCI are converters to AD.[17] Further prospective studies are needed to validate the usefulness of combined ERICA and regional CBF in predicting this conversion. Although the pattern of results in MCI-HC comparison indicates better utility of CBF PCG + PC as opposed to the ERICA score, nosologically, there are important considerations while stratifying MCI at risk of AD using

biomarkers. Per available criteria, to identify MCI at an intermediate or higher likelihood of AD requires combining biomarkers of -β amyloid accumulation (PET or CSF) with markers of neuronal injury (τ, FDG-PET, structural MR imaging).[35] A combined instrument using 2 MR imaging markers of neuronal injury rather than -β amyloid accumulation precludes prediction of the proportion of the MCI cohort who are likely to convert in our series.

One also needs to consider that MCI is a heterogeneous condition and potentially could be due to other causes like vascular cognitive impairment. There is evidence in the literature available from MCI negative for β amyloid, where common etiologies include vascular diseases and depression.[36] It is possible that a subset of our MCI cohort may, with time, evolve as vascular cognitive impairment or other alternative trajectories or may potentially remain stable without converting to AD. This possibility is perhaps part of the reason that the ERICA score did not show a significant difference between MCI and HC as opposed to the other 2 comparisons. Lack of longitudinal data to ascertain the trajectory of the MCI group with time precludes confirmation of the same in the present study and warrants future prospective follow-up studies. A relatively small sample size in our study also might have resulted in a lower ability to detect differences between MCI and AD using CBF alone at baseline. All these facts point to the relevance of including multiple MR imaging markers as implemented in one of our previous studies on multimodality neuroimaging.[37]

The study was performed on a prospectively acquired dataset with measurement of only 2 parameters, which could be easily reproduced in a clinical setting. We preferred to use computed segmentation of the ROI CBF to avoid any bias due to manual drawing of contours. However, this study had several limitations. Though ASL is a robust technique to measure cerebral perfusion, technical parameters and patient-specific factors could variably influence the CBF calculation and confound the results. Specific to dementia, one of the major confounders is the arterial transit time, which can be different for each subject due to associated vascular or nonvascular comorbidities. The possible vascular risk contributors like diabetes mellitus and hypertension were not considerably different in each subgroup in the present study (Table 1). Again, transit delay can be higher in some of the ROIs in dementia imaging like the posterior parietal lobes, leading to erroneous CBF measurements.[38] The appropriately increased postlabeling delay time could be used to reduce this error. Alternatively, a multidelay ASL can potentially solve this problem, but it is not ready for prime time imaging yet. Also, a small sample size and cross-sectional study design did not permit analyzing a causal relationship between the biomarkers and the development of MCI and AD, and further large longitudinal studies are needed to confirm its role in predicting progression of the disease. Additionally, head-to-head comparisons between Pittsburgh compound PET imaging and CSF biomarkers (which are currently not available at our center) and MR imaging markers would have enabled us to ascertain the sensitivity and specificity; however, this comparison remains a concern across many centers in the developing world, and only multicentric collaborative ventures can transcend the issue.

CONCLUSIONS

This study explored the utility of measuring structural and perfusion changes in specific and nonoverlapping ROIs in differentiating MCI and AD. Combining regional perfusion measurements in the PCG + PC using ASL along with the ERICA score on structural imaging has the potential to be a better imaging biomarker to distinguish among Alzheimer spectrum disorders. In centers that do not have access to nuclear imaging scans including FDG Pittsburgh compound PET, this study has shown the utility of objective multimodal imaging scores to distinguish MCI at risk of progression to AD. This use of scores has the potential to serve as a noninvasive tool to stratify MCI etiologically, which is a heterogeneous entity in itself. Future studies are needed to explore the longitudinal risk of cognitive decline in MCI due to AD (using markers of amyloid accumulation) as opposed to MCI due to non-AD pathology, including vascular cognitive impairment, in direct correlation with ERICA and regional CBF measures. This categorization should also account for confounding factors such as age, education status, hypertension, coronary artery disease, body mass index, dyslipidemia, and impaired glucose tolerance in these groups.

Disclosures: Bejoy Thomas—*RELATED*: *Grant*: Department of Science and Technology (DST), Government of India*; *Support for Travel to Meetings for the Study or Other Purposes*: DST, Government of India*; *UNRELATED*: *Grants/Grants Pending*: GE Healthcare, research grant*; *Patents (Planned, Pending or Issued)*: applied for Indian patent*; *Stock/Stock Options*: Minority stocks in Wipro India. Ramshekhar N. Menon—*RELATED*: *Grant*: Department of Science and Technology, *Comments*: grant numbers mentioned in the article*; *UNRELATED*: *Grants/Grants Pending*: Department of Science and Technology, *Comments*: Details are provided in terms of grant numbers in the article.* *Money paid to institution.

REFERENCES

1. Crous-Bou M, Minguillón C, Gramunt N, et al. **Alzheimer's disease prevention: from risk factors to early intervention.** *Alzheimers Res Ther* 2017;9:71 CrossRef Medline
2. Tolppanen A-M, Taipale H, Purmonen T, et al. **Hospital admissions, outpatient visits and healthcare costs of community-dwellers with Alzheimer's disease.** *Alzheimers Dement* 2015;11:955–63 CrossRef Medline
3. Petersen RC. **Mild cognitive impairment as a diagnostic entity.** *J Intern Med* 2004;256:183–94 CrossRef Medline
4. Apostolova LG. **Alzheimer disease.** *Continuum (Minneap Minn)* 2016;22:419–34 CrossRef Medline
5. Sheelakumari R, Kesavadas C, Lekha VS, et al. **Menon RN structural correlates of mild cognitive impairment: a clinicovolumetric study.** *Neurol India* 2018;66:370–36 CrossRef Medline
6. Hays CC, Zlatar ZZ, Wierenga C. **The utility of cerebral blood flow as a biomarker of preclinical Alzherimer's disease.** *Cell Mol Neurobiol* 2016;36:167–79 CrossRef Medline
7. Sandson TA, O'Connor M, Sperling RA, et al. **Noninvasive perfusion MRI in Alzheimer's disease: a preliminary report.** *Neurology* 1996; 47:1339–42 CrossRef Medline
8. Alsop DC, Detre JA, Grossman M. **Assessment of cerebral blood flow in Alzheimer's disease by spin-labeled magnetic resonance imaging.** *Ann Neurol* 2000;47:93–100 CrossRef Medline
9. Johnson NA, Jahng G-H, Weiner MW, et al. **Pattern of cerebral hypoperfusion in Alzheimer disease and mild cognitive impairment measured with arterial spin-labeling MR imaging: initial experience.** *Radiology* 2005;234:851–59 CrossRef Medline
10. Dai W, Lopez OL, Carmichael OT, et al. **Mild cognitive impairment and Alzheimer disease: patterns of altered cerebral blood flow at MR imaging.** *Radiology* 2009;250:856–66 CrossRef Medline

11. Binnewijzend MAA, Kuijer JPA, Benedictus MR, et al. **Cerebral blood flow measured with 3D pseudocontinuous arterial spin-labeling MR imaging in Alzheimer disease and mild cognitive impairment: a marker for disease severity.** *Radiology* 2013;267:221–30 CrossRef Medline
12. Bron EE, Steketee RME, Houston GC, et al. **Diagnostic classification of arterial spin labeling and structural MRI in presenile early stage dementia.** *Hum Brain Mapp* 2014;35:4916–31 CrossRef Medline
13. Sierra-Marcos A. **Regional cerebral blood flow in mild cognitive impairment and Alzheimer's disease measured with arterial spin labeling magnetic resonance imaging.** *Int J Alzheimer's Dis* 2017; 2017:5479597 CrossRef Medline
14. Verclytte S, Lopes R, Delmaire C, et al. **Optimization of brain perfusion image quality by cortical surface-based projection of arterial spin labeling maps in early-onset Alzheimer's disease patients.** *Eur Radiol* 2015;25:2479–84 CrossRef Medline
15. Tosun D, Schuff N, Jagust W, et al; Alzheimer's Disease Neuroimaging Initiative. **Discriminative power of arterial spin labeling magnetic resonance imaging and 18F-fluorodeoxyglucose positron emission tomography changes for amyloid-beta-positive subjects in the Alzheimer's disease continuum.** *Neurodegener Dis* 2016; 16:87–94 CrossRef Medline
16. Kaneta T, Katsuse O, Hirano T, et al. **Voxel-wise correlations between cognition and cerebral blood flow using arterial spin-labeled perfusion MRI in patients with Alzheimer's disease: a cross-sectional study.** *BMC Neurol* 2017;17:91 CrossRef Medline
17. Enkirch SJ, Traschütz A, Müller A, et al. **The ERICA score: an MR imaging-based visual scoring system for the assessment of entorhinal cortex atrophy in Alzheimer disease.** *Radiology* 2018;288:226–33 CrossRef Medline
18. Mathuranath PS, Hodges JR, Mathew R, et al. **Adaptation of the ACE for a Malayalam speaking population in southern India.** *Int J Geriat Psychiatry* 2004;19:1188–94 CrossRef Medline
19. Menon R, Lekha V, Justus S, et al. **A pilot study on utility of Malayalam version of Addenbrooke′s Cognitive Examination in detection of amnestic mild cognitive impairment: a critical insight into utility of learning and recall measures.** *Ann Indian Acad Neurol* 2014;17:420 CrossRef Medline
20. McKhann G, Drachman D, Folstein M, et al. **Clinical diagnosis of Alzheimer's disease: report of the NINCDS-ADRDA Work Group under the auspices of Department of Health and Human Services Task Force on Alzheimer's disease.** *Neurology* 1984; 34:939–44 CrossRef Medline
21. Petersen RC, Stevens JC, Ganguli M, et al. **Practice parameter: early detection of dementia: mild cognitive impairment (an evidence-based review)—report of the Quality Standards Subcommittee of the American Academy of Neurology.** *Neurology* 2001;56:1133–42 CrossRef Medline
22. Alsop DC, Detre JA, Golay X, et al. **Recommended implementation of arterial spin-labeled perfusion MRI for clinical applications: a consensus of the ISMRM Perfusion Study group and the European Consortium for ASL in Dementia.** *Magn Reson Med* 2015;73:102–16 CrossRef Medline
23. Yoshiura T, Hiwatashi A, Noguchi T, et al. **Arterial spin labelling at 3-T MR imaging for detection of individuals with Alzheimer's disease.** *Eur Radiol* 2009;19:2819–25 CrossRef Medline
24. Chao LL, Pa J, Duarte A, et al. **Patterns of cerebral hypoperfusion in amnestic and dysexecutive MCI.** *Alzheimer Dis Assoc Disord* 2009;23:245–52 CrossRef Medline
25. Austin BP, Nair VA, Meier TB, et al. **Effects of hypoperfusion in Alzheimer's disease.** *J Alzheimer's Dis* 2011;26(Suppl 3):123–33 CrossRef Medline
26. Braak H, Braak E. **Neuropathological stageing of Alzheimer-related changes.** *Acta Neuropathol* 1991;82:239–59 CrossRef
27. Jessen F, Feyen L, Freymann K, et al. **Volume reduction of the entorhinal cortex in subjective memory impairment.** *Neurobiol Aging* 2006;27:1751–56 CrossRef Medline
28. deToledo-Morrell L, Stoub TR, Bulgakova M, et al. **MRI-derived entorhinal volume is a good predictor of conversion from MCI to AD.** *Neurobiol Aging* 2004;25:1197–1203 CrossRef Medline
29. Chen W, Song X, Beyea S, et al. **Advances in perfusion magnetic resonance imaging in Alzheimer's disease.** *Alzheimers Dement* 2011; 7:185–96 CrossRef Medline
30. Mazza M, Marano G, Traversi G, et al. **Primary cerebral blood flow deficiency and Alzheimer's disease: shadows and lights.** *J Alzheimers Dis* 2011;23:375–89 CrossRef Medline
31. Zhang Q, Stafford RB, Wang Z, et al. **Microvascular perfusion based on arterial spin labeled perfusion MRI as a measure of vascular risk in Alzheimer's disease.** *J Alzheimers Dis* 2012;32:677–87 CrossRef
32. Alsop DC, Detre JA, Grossman M. **Assessment of cerebral blood flow in Alzheimer's disease by spin-labeled magnetic resonance imaging.** *Ann Neurol* 2000;47:93–100 CrossRef
33. Espeseth T, Westlye LT, Fjell AM, et al. **Accelerated age-related cortical thinning in healthy carriers of apolipoprotein E epsilon 4.** *Neurobiol Aging* 2008;29:329–40 CrossRef Medline
34. Scheltens P, Leys D, Barkhof F, et al. **Atrophy of medial temporal lobes on MRI in "probable" Alzheimer's disease and normal ageing: diagnostic value and neuropsychological correlates.** *J Neurol Neurosurg Psychiatry* 1992;55:967–72 CrossRef Medline
35. Albert MS, DeKosky ST, Dickson D, et al. **The diagnosis of mild cognitive impairment due to Alzheimer's disease: recommendations from the National Institute on Aging-Alzheimer's Association workgroups on diagnostic guidelines for Alzheimer's disease.** *Alzheimers Dement* 2011;7:270–79 CrossRef Medline
36. Landau SM, Horng A, Fero A, et al. Alzheimer's Disease Neuroimaging Initiative**. Amyloid negativity in patients with clinically diagnosed Alzheimer disease and MCI.** *Neurology* 2016;86:1377–85 CrossRef Medline
37. Sheelakumari R, Sarma SP, Kesavadas C, et al. **Multimodality neuroimaging in mild cognitive impairment: a cross-sectional comparison study.** *Ann Indian Acad Neurol* 2018;21:133–39 CrossRef Medline
38. Alsop DC, Dai W, Detre JA, et al. **Arterial spin labeling blood flow MRI: its role in the early characterization of Alzheimer's disease.** *J Alzheimers Dis* 2010;20:871–80 CrossRef Medline

Lateral Posterior Choroidal Collateral Anastomosis Predicts Recurrent Ipsilateral Hemorrhage in Adult Patients with Moyamoya Disease

J. Wang, Y. Yang, X. Li, F. Zhou, Z. Wu, Q. Liang, Y. Liu, Y. Wang, S. Na, X. Chen, X. Zhang, and B. Zhang

ABSTRACT

BACKGROUND AND PURPOSE: Choroidal collateral anastomosis is associated with hemorrhage recurrence in patients with Moyamoya disease. However, the relationship between recurrent ipsilateral hemorrhage and choroidal collateral anastomosis subtypes (anterior choroidal artery anastomosis, lateral posterior choroidal artery anastomosis, and medial posterior choroidal artery anastomosis) is unclear. This study aimed to assess this potential association in adult patients with Moyamoya disease.

MATERIALS AND METHODS: Patients angiographically diagnosed with Moyamoya disease who underwent conservative treatment between January 2008 and December 2018 were included in this retrospective study. Two readers assessed the angiographic images to identify choroidal collateral anastomosis subtypes, and Cox proportional hazard regression models were used to estimate the risk of recurrent hemorrhage associated with each subtype.

RESULTS: Thirty-nine patients (mean age = 45.2 years) were included in this study. During 52.4 ± 37.0 months of follow-up, recurrent ipsilateral hemorrhage occurred in 48.7% (19/39) of patients. Patients with recurrent hemorrhage had a higher prevalence of choroidal collateral (94.8% versus 60.0%; $P = .02$) and lateral posterior choroidal artery (78.9% versus 25.0%; $P < .01$) anastomoses than those without recurrent hemorrhage. Lateral posterior choroidal artery anastomosis was associated with recurrent hemorrhage before (hazard ratio = 6.66; 95% CI, 2.18–20.39; $P < .01$) and after (hazard ratio = 5.78; 95% CI, 1.58–21.13; $P < .01$) adjustments were made for age, sex, and other confounding factors.

CONCLUSIONS: Choroidal collateral anastomosis is responsible for most cases of recurrent hemorrhage in adult patients with Moyamoya disease; lateral posterior choroidal artery anastomosis is a significant risk factor for these recurrent events.

ABBREVIATIONS: AChA = anterior choroidal artery; ChCA = choroidal collateral anastomosis; HR = hazard ratio; LPChA = lateral posterior choroidal artery; MMD = Moyamoya disease; MPChA = medial posterior choroidal artery

Moyamoya disease (MMD) is an uncommon but potentially catastrophic cerebrovascular disorder characterized by progressive occlusion in the terminal portion of the internal carotid artery and its main branches within the circle of Willis.[1]

Received April 29, 2019; accepted after revision July 29.

From the Department of Neurosurgery (J.W., Z.W.), The Affiliated Changzhou No. 2 People's Hospital of Nanjing Medical University, Changzhou, China; Departments of Neurosurgery (J.W., Y.Y., Q.L., Y.W., S.N., X.C.) and Radiology (X.L., F.Z., X.Z., B.Z.), The Affiliated Drum Tower Hospital of Nanjing University Medical School, Nanjing, China; and Department of Neurosurgery (Y.L.), West China Hospital, Sichuan University, Chengdu, China.

J. Wang, Y. Yang, X. Li, F. Zhou, and B. Zhang contributed equally to this study.

This work was supported by the Natural Science Foundation of China (81720108022, B.Z.) and the Social Development Project of Science and Technology in Jiangsu Province (BE2016605, BE201707, B.Z.).

Please address correspondence to Bing Zhang, MD, PhD, Department of Radiology, The Affiliated Drum Tower Hospital of Nanjing University Medical School, Nanjing, China, 210008; e-mail: zhangbing_nanjing@vip.163.com

http://dx.doi.org/10.3174/ajnr.A6208

Intracranial hemorrhage accounts for half of initial manifestations of MMD in adult patients,[2,3] and the recurrence rate of hemorrhage can be as high as 17.1% per year during the natural course of the disease.[4,5] Patients with hemorrhage recurrence generally have poor outcomes such as life-long disabilities or even death.[4] Identifying risk factors for recurrent hemorrhage is therefore useful for clinical decision-making in terms of management and follow-up.

The occurrence of periventricular hemorrhage is a major clinical concern in adult patients with MMD who experience recurrent hemorrhage.[6] In brain hemispheres with recurrent hemorrhage, the hemorrhage is more likely to occur around the posterior territory, particularly in the periventricular area around the atrium or the posterior portion of the body of the lateral ventricle.[5,7] A previous postmortem study demonstrated that the subependymal collateral arteries supplying the above territories originate mainly from the lateral posterior choroidal arteries (LPChAs) but rarely from the anterior choroidal arteries

(AChAs) or medial posterior choroidal arteries (MPChAs).[8] Therefore, we suspect that the LPChAs may play a key role in the occurrence of recurrent hemorrhage. Choroidal collateral anastomosis (ChCA) has previously been shown to be associated with recurrent hemorrhage in this patient population.[5,9,10] However, the relationship between the subtypes of ChCA and recurrent ipsilateral hemorrhage is still unclear.

In this retrospective study, we therefore sought to assess the association between the subtypes of ChCA and recurrent ipsilateral hemorrhage in adult patients with MMD.

MATERIALS AND METHODS

Study Population

This study was approved by The Affiliated Drum Tower Hospital of Nanjing University Medical School with a waiver of informed consent. Consecutive patients with MMD who had experienced initial intracranial hemorrhage and received conservative treatment (no surgical intervention) and clinical follow-up between January 2008 and December 2018 were recruited for this retrospective study. We enrolled as many patients as possible with >5 years of clinical follow-up for nonrecurrent hemorrhage controls. Considering that the main purpose of our study was to evaluate the association between the ChCA subtypes and recurrent ipsilateral hemorrhage, the factors associated with non-MMD-related hemorrhage and influencing the target vessel evaluation were excluded in the present study. All cases of MMD had bilateral involvement and were diagnosed via angiography according to the guidelines proposed by the Ministry of Health, Labor, and Welfare of Japan.[11] Patients with autoimmune disease, meningitis, brain tumor, Down syndrome, neurofibromatosis type 1, or a history of head irradiation were excluded from the study. We also excluded patients who met any of the following 3 conditions: 1) age older than 65 years[12]; 2) the presence of factors influencing the evaluation of recurrent hemorrhage such as bleeding diathesis, uncontrolled diabetes mellitus (fasting blood glucose level of >300 mg/dL), or uncontrolled hypertension (systolic pressure of >180 mm Hg and/or diastolic pressure of >110 mm Hg); or 3) a history of intracranial hemorrhage. The occurrence of recurrent hemorrhage was recorded if there was an acute neurologic symptom during follow-up with a corresponding new intracranial hemorrhage on brain imaging. Demographic and clinical characteristics for all patients were collected from the medical records.

Imaging Techniques

For the initial hemorrhagic event, a cerebrovascular DSA examination was performed on an x-ray scanner (Allura Xper FD20/2D; Philips Healthcare, Best, the Netherlands); this examination included selective common, internal, and external carotid artery arteriography on both sides and vertebral arteriography on at least 1 side. The imaging parameters for this examination were as follows: 6 frames/s, injection pressure =300 psi/kg, and contrast medium administered at a rate of 3 mL/s. When a recurrent hemorrhage occurred, non-contrast-enhanced CT of the brain was performed to identify the intracranial hemorrhagic site. When diffuse ventricular hemorrhage occurred, SWI examinations were conducted within 2 months of the hemorrhagic event, with all scans obtained on a 3T MR imaging scanner (uMR 770; United Imaging Healthcare; Shanghai) with a 24-channel phased array head and neck coil. The MR images were acquired using the following parameters: TR/TE = 24.2/15 ms, flip angle = 15°, FOV = 190 × 190 mm^2, section thickness = 1.2 mm, voxel size = 0.6 × 0.6 × 1.2 mm^3, and acquisition time = 7 minutes 35 seconds.

Definitions and Analysis of Angiographic Variables

The definition of ChCA provided by Funaki et al[9] was adapted to the present study. For this study, the subtypes of ChCA were categorized into AChA anastomosis, LPChA anastomosis, and MPChA anastomosis.[9] AChA anastomosis is defined as anastomosis between the extreme dilation and extension of the AChA with sudden deviation from the shape of the lateral ventricle at its peripheral portion to connect the medial end of the medullary artery. LPChA anastomosis refers to the extreme extension of the LPChA beyond the atrium of the lateral ventricle to reach the body of the lateral ventricle. MPChA anastomosis is defined as the extreme extension of the MPChA beyond the level of the pericallosal artery to the corpus callosum. Schematic illustrations and representative examples of each subtype are shown in Fig 1. Other variables such as Suzuki stages[1] (stages I–VI), involvement of the posterior cerebral arteries (Mugikura stage II–IV),[13] thalamic collateral anastomosis,[9] the presence of an intracranial aneurysm, and the presence of a fetal posterior communicating artery at the time of initial hemorrhage were also evaluated. The initial angiographic images were reviewed in consensus by 2 neuroradiologists, both with >5 years' experience in neurovascular imaging and both blinded to the brain images. A third investigator with >10 years' experience in neurovascular imaging resolved any discrepancies.

Follow-Up

After the initial hemorrhagic event was investigated and conservative treatment was initiated, all patients underwent follow-up in the outpatient clinic every 3–6 months so that cases of hemorrhage recurrence could be identified. When hemorrhage reoccurred, the site of the hemorrhage was determined on CT within 1 week after the onset of the event. When diffuse ventricular hemorrhage occurred, the presumed origin of the recurrent hemorrhage was identified by SWI within 2 months of the event. The interval between the initial event and hemorrhage recurrence was also recorded.

Reproducibility

All angiographic data were interpreted by the 2 raters twice, with a 1-month time interval between sessions to minimize memory bias. Interrater and intrarater agreement values for the subtypes of ChCA were calculated.

Statistical Analysis

Continuous variables were described as mean ± SD, and categoric variables were presented as number and percentage. An independent t test, a Mann-Whitney U test, and a χ^2 or Fisher exact test were used to compare patients with and without recurrent

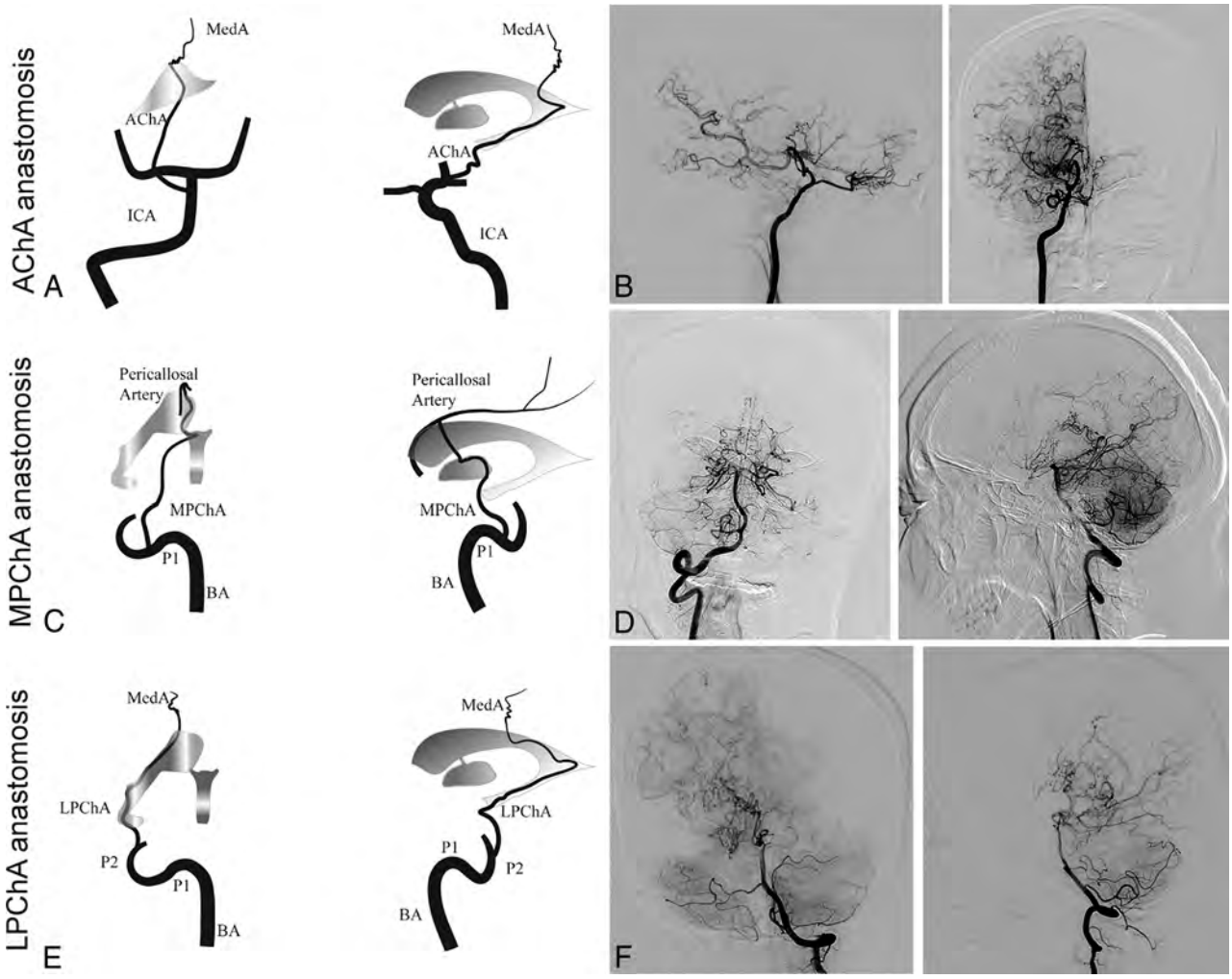

FIG 1. Schematic illustrations and angiographic findings from representative cases of each subtype of choroidal collateral anastomosis. *A* and *B*, Anterior-posterior and lateral right carotid artery angiograms show a dilated anterior choroidal artery extending beyond the lateral ventricle to the cortex (*arrows*). *C* and *D*, Anterior-posterior and lateral right vertebral artery angiograms show a medial posterior choroidal artery extending beyond the level of the pericallosal artery (*arrows*) to the corpus callosum. *E* and *F*, Anterior-posterior and lateral left vertebral artery angiograms show a lateral posterior choroidal artery extending beyond the body of the lateral ventricle to the cortex (*arrows*). MedA indicates the medullary artery; P1 and P2, the proximal portion of posterior cerebral artery; BA, the basilar artery.

hemorrhage and hemispheres with and without recurrent hemorrhage in terms of baseline characteristics. Univariate and multivariate Cox proportional hazard regression models were used to estimate the risk of recurrent ipsilateral events for each ChCA subtype. Interrater and intrarater agreement values for ChCA subtype evaluation were calculated using the unweighted Cohen κ. A P value $< .05$ was considered significant. All statistical analyses were performed using SPSS 22.0 (IBM, Armonk, New York).

RESULTS

From January 2008 to December 2018, a total of 68 patients presented with hemorrhagic MMD and underwent conservative treatment. Of these 68 patients, 9 (13.2%) were excluded for the following reasons: uncontrolled hypertension and diabetes mellitus ($n = 1$), age older than 65 years ($n = 2$), history of intracranial hemorrhage ($n = 5$), and equivocal initial hemorrhagic sites ($n = 1$). During the follow-up period, another 20 (29.4%) patients were excluded for the following reasons: equivocal recurrent hemorrhagic sites ($n = 2$), follow-up images of recurrent hemorrhage unknown ($n = 2$), presenting with recurrent hemorrhage in the contralateral hemispheres ($n = 3$), unrelated death from other medical causes (liver tumor, $n = 1$), and follow-up period of <5 years (patients without recurrent hemorrhage, $n = 12$). The remaining 39 (57.4%) patients (29 women; mean age at diagnosis = 45.2 ± 9.1 years) met the eligibility criteria for the final analysis (Fig 2). Of these 39 patients, 2 (5.1%) were smokers, 13 (33.3%) had hypertension, 8 (20.5%) had dyslipidemia, 3 (7.7%) had diabetes mellitus, and 3 (7.7%) had a history of ischemic stroke (defined as symptomatic infarctions confirmed on DWI). None of the study patients were treated with antiplatelets or anticoagulants. During 52.4 ± 37.0 months (range, 1–114 months) of follow-up, 48.7% (19/39) of patients

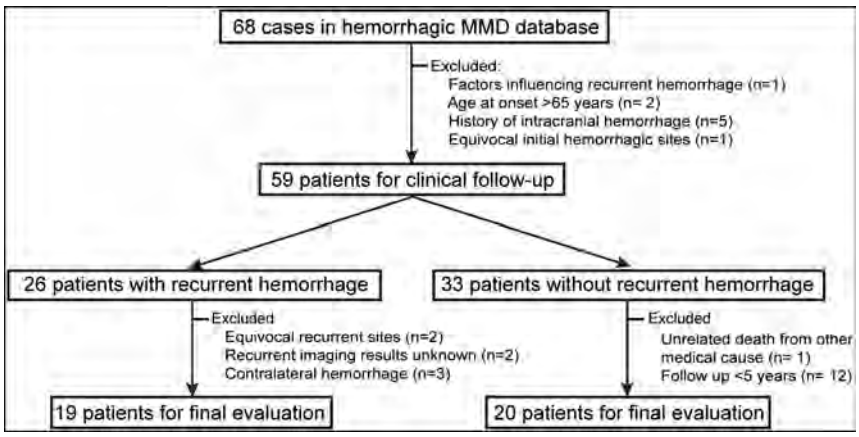

FIG 2. Flowchart of patient recruitment.

Table 1: Baseline characteristics in patients with MMD with and without recurrent ipsilateral hemorrhage

Characteristic	Patients without Recurrent Hemorrhage ($n = 20$)	Patients with Recurrent Hemorrhage ($n = 19$)	*P* Value
Women (No.) (%)	15 (75.0)	14 (73.7)	.93
Age (mean) (yr)	43.7 ± 10.6	46.9 ± 7.0	.27
Smokers (No.) (%)	1 (5.0)	1 (5.3)	>.99
Concurrent disease (No.) (%)			
Hypertension	8 (40.0)	5 (26.3)	.37
Dyslipidemia	4 (20.0)	4 (21.1)	>.99
Diabetes mellitus	2 (10.0)	1 (5.3)	>.99
History of ischemia (No.) (%)	1 (5.0)	2 (10.5)	.61
Hemorrhagic type (No.) (%)			
IVH	13 (65.0)	13 (68.4)	.82
Only IVH	6 (30.0)	10 (52.6)	.20
ICH + IVH	7 (35.0)	3 (15.8)	.46
SAH	0 (0.0)	4 (21.1)	.05
Only SAH	0 (0.0)	1 (5.3)	.49
SAH + IVH	0 (0.0)	3 (15.8)	.27
ICH	7 (35.0)	2 (10.5)	.13

Note:—IVH, intraventricular hemorrhage; ICH, intracerebral hemorrhage.

experienced recurrent ipsilateral hemorrhage. Of the baseline clinical risk factors assessed, only the number of subarachnoid hemorrhages in patients with recurrent events was significantly higher than in those without recurrent events (21.1% versus 0.0%; $P = .05$; Table 1).

Intracranial Hemorrhage

In 39 hemispheres, the initial hemorrhagic sites were in the subependymal area of the lateral ventricle in 21 hemispheres (53.8%), the insular lobe in 5 hemispheres (12.8%), the temporal lobe in 3 hemispheres (7.7%), the basal ganglia in 2 hemispheres (5.1%), the occipital lobe in 2 hemispheres (5.1%), the corpus callosum in 1 hemisphere (2.6%), the frontal lobe in 1 hemisphere (2.6%), and the subarachnoid in 4 hemispheres (10.2%). Of the 39 hemispheres with intracranial hemorrhage, 11 (28.2%) demonstrated recurrent hemorrhage at the initial hemorrhage site and 8 (20.5%) demonstrated recurrent hemorrhage at a different site in the same hemisphere. Comparisons of imaging features in hemispheres with and without recurrent hemorrhage are shown in Fig 3.

Analysis of Angiographic Variables

Of the 39 cases in the study, none demonstrated intracranial lesions at Suzuki stage I, one (2.6%) demonstrated lesions at stage II, nineteen (48.7%) demonstrated lesions at stage III, five (12.8%) demonstrated lesions at stage IV, twelve (30.8%) demonstrated lesions at stage V, and 2 (5.1%) demonstrated lesions at stage VI. In addition, 11 (28.2%) intracranial arteries were found to have stenotic-occlusive lesions involving the posterior cerebral arteries. The fetal posterior communicating artery and thalamic anastomosis were identified in 33.3% (13/39) and 15.4% (6/39) of cases, respectively. An intracranial aneurysm was identified in those 4 patients presenting with subarachnoid hemorrhage, including the posterior cerebral artery in 2 patients, the lenticulostriate artery in 1 patient, and the middle meningeal artery in 1 patient.

A ChCA was identified in 76.9% (30/39) of patients, including AChA in 13 patients, LPChA in 20 patients, and MPChA in 14 patients. Compared with hemispheres without hemorrhage recurrence, hemispheres with hemorrhage recurrence demonstrated a higher prevalence of ChCA (94.8% versus 60.0%; $P = .02$), LPChA anastomosis (78.9% versus 25.0%; $P < .01$), and intracranial aneurysms (21.1% versus 0.0%; $P = .03$). A representative case demonstrating LPChA anastomosis and recurrent ipsilateral hemorrhage is shown in Fig 4. No other significant differences were noted in baseline angiographic characteristics between hemispheres with and those without recurrent hemorrhage (Table 2).

Association between Subtypes of ChCA and Recurrent Ipsilateral Hemorrhage

Table 3 summarizes the radiographic characteristics of the 19 hemispheres in which recurrent hemorrhage was seen. In 14 hemispheres, ChCA was considered responsible for the recurrence because the recurrent hemorrhage occurred in the hemisphere containing a ChCA and corresponded to the distribution of the choroidal arteries: Five stemmed from the AChA, 7 stemmed from the LPChA, and 2 stemmed from the MPChA.

In univariate Cox regression analysis, a significant association was demonstrated between LPChA anastomosis and hemorrhage recurrence (hazard ratio [HR] = 6.66; 95% CI, 2.18–20.39; $P < .01$). In multivariate Cox regression analysis, after adjustments

were made for age, sex, a history of ischemia, Suzuki stage >III, involvement of the posterior cerebral arteries, thalamic anastomosis, the fetal posterior communicating artery, and intracranial aneurysm, the association between LPChA anastomosis and hemorrhage recurrence remained significant (HR = 5.78; 95% CI, 1.58–21.13; $P < .01$) (Table 4).

Reproducibility

The κ values for intrarater agreement in the identification of AChA, MPChA, and LPChA were 0.84, 0.71, and 0.69, respectively. The κ values for interrater agreement in the identification of AChA, MPChA, and LPChA were 0.76, 0.66, and 0.61, respectively.

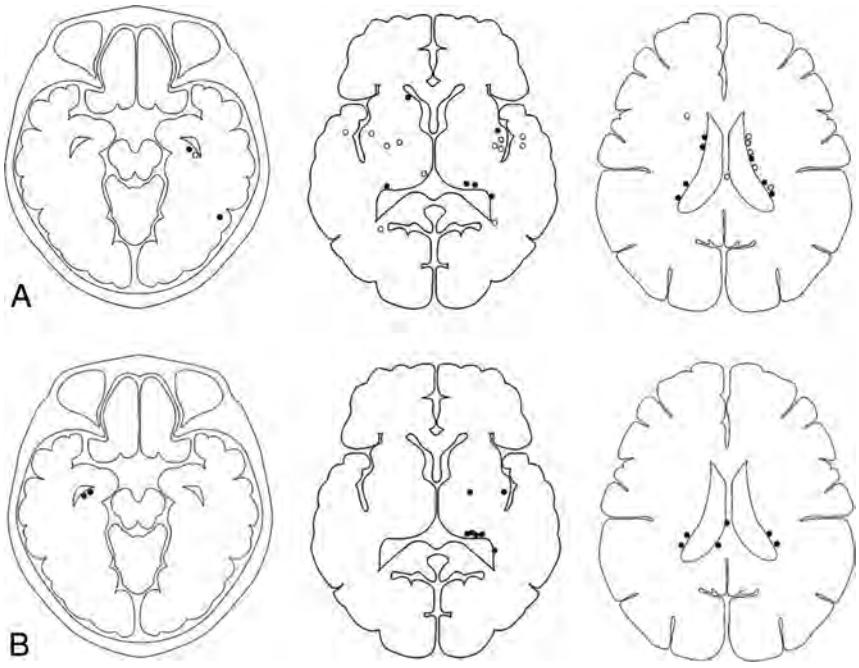

FIG 3. Topographic analysis showing the distribution of initial and recurrent hemorrhagic sites. *A*, Topographic analysis of initial hemorrhagic sites for those with (*black dots*) and those without (*white dots*) recurrent hemorrhage. *B*, Another topographic analysis shows the distribution of recurrent hemorrhagic sites (*black dots*). Four patients with recurrent hemorrhage attributable to intracranial aneurysm rupture are not shown in this analysis.

DISCUSSION

In this study, we found that recurrent ipsilateral hemorrhage was common among adult patients with MMD, and ChCA was responsible for most cases of hemorrhage recurrence in these patients. In addition, LPChA anastomosis was found to be an independent predictor of recurrent ipsilateral hemorrhage. Our findings suggest that serial imaging follow-up of LPChA anastomosis may provide additional information for risk stratification in patients with MMD.

Previous research has suggested that MMD-related intracranial hemorrhage may differ from primary intracranial hemorrhage in terms of location: MMD-related hemorrhage is more likely to present as intraventricular hemorrhage with or without intracerebral hemorrhage.[6] One study showed that the presence of intraventricular hemorrhage was significantly correlated with the occurrence of recurrent hemorrhage in patients with MMD.[14] Similarly, our study demonstrated that >50% of hemorrhage recurrence events presented as intraventricular hemorrhages; however, this result did not reach statistical significance. These differences in results between studies may be partially due to the different exclusion criteria used in different studies.

In the current study, ChCA was found to be more prevalent in hemispheres with recurrent hemorrhage among patients with MMD, findings consistent with previous results.[5,9] We also found that the subtypes of ChCA were more frequently observed in the hemispheres with recurrent hemorrhage, though this difference was not significant for AChA or MPChA anastomosis. The recurrent hemorrhagic sites were distributed mainly in the

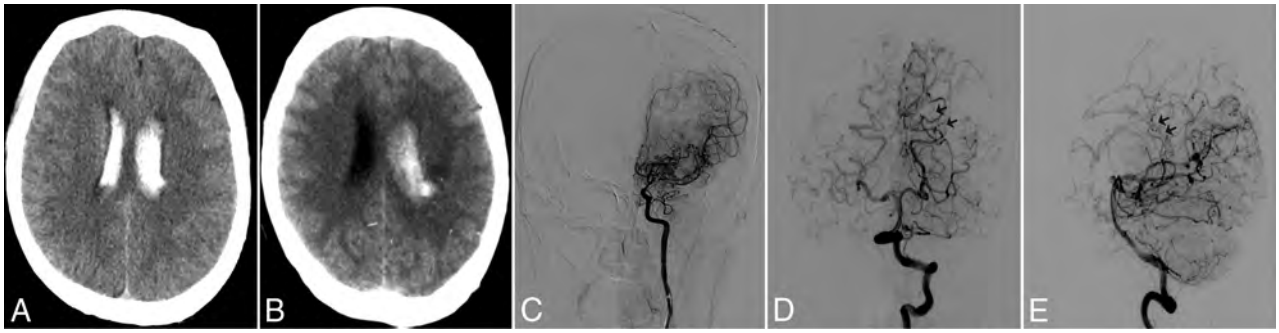

FIG 4. A 50-year-old man experienced a recurrent hemorrhage in the ipsilateral hemisphere. *A*, CT image indicates the initial hemorrhage in the posterior portion of the body of the left lateral ventricle. *B*, CT image obtained 49 months later reveals a recurrent hemorrhage in the initial hemorrhagic site. *C*. Left anterior-posterior carotid artery angiogram obtained at baseline demonstrates no obvious anterior choroidal anastomosis from the internal carotid artery. Anterior-posterior (*D*) and lateral (*E*) views of the left vertebral angiogram obtained at baseline reveal the typical finding of lateral posterior choroidal anastomosis responsible for recurrent hemorrhage (*black arrows*).

periventricular area around the atrium or the posterior portion of the body of the lateral ventricle, suggesting that fragile choroidal collateral vessels around the periventricular area are mainly derived from the posterior circulation, particularly for LPChA.

LPChA anastomosis was shown to be significantly correlated with recurrent ipsilateral hemorrhage in this study, suggesting that LPChA anastomosis plays a key role in the occurrence of recurrent hemorrhage in patients with MMD. However, the mechanism of this correlation is not fully understood. We propose 2 possible mechanisms to explain this relationship.

The first potential mechanism involves persistent hemodynamic stress of the collateral vessels in different periventricular regions. Yamamoto et al[15] demonstrated that the Moyamoya collateral vessels longitudinally shift from the anterior to posterior circulation during disease progression. In the current study, we found that recurrent hemorrhage was rarely observed in the insular lobe and basal ganglia but was more prevalent in the atrium and the posterior portion of the body of the lateral ventricle. The collateral anastomoses around the insular lobe and basal ganglia are mainly derived from the single blood supply of the anterior circulation, whereas the collateral anastomoses around the atrium and the posterior portion of the body of the lateral ventricle derive from the multiple blood supplies of both the anterior and posterior circulations. Persistent hemodynamic stress is thus added from both the anterior and posterior circulations, a potential trigger of recurrent hemorrhage.

The second potential mechanism is related to the development of ventricular microaneurysms in the LPChA. A previous study using 7T TOF MRA found that a high number of patients with MMD had ventricular microaneurysms in the periventricular region.[16] In the current study, excluding cases of intracranial aneurysm rupture, recurrent hemorrhage occurred in the initial hemorrhagic sites in 46.7% (7/15) of hemispheres. The coexisting anterior and posterior choroidal anastomoses in MMD indicate that ventricular microaneurysms may be present in choroidal collateral vessels, particularly in the LPChA. Future studies using high-resolution MR imaging to characterize the

Table 2: Baseline variables in hemispheres with and without recurrent hemorrhage in adult patients with MMD

Variables	Hemispheres without Recurrent Hemorrhage (*n* = 20)	Hemispheres with Recurrent Hemorrhage (*n* = 19)	*P* Value
Suzuki stage (No.) (%)			
I	0 (0.0)	0 (0.0)	
II	1 (5.0)	0 (0.0)	
III	10 (50.0)	9 (47.4)	
IV	3 (15.0)	2 (10.5)	
V	5 (25.0)	7 (36.8)	
VI	1 (5.0)	1 (5.3)	
Suzuki stage >III (No.) (%)	9 (45.0)	10 (52.6)	.63
Involved PCA (No.) (%)	4 (20.0)	7 (36.8)	.30
Fetal PcomA (No.) (%)	7 (35.0)	6 (31.6)	.82
IA (No.) (%)	0 (0.0)	4 (21.1)	.03
TC anastomosis (No.) (%)	2 (10.0)	4 (21.1)	.41
ChCA subtype (No.) (%)	12 (60.0)	18 (94.8)	.02
AChA anastomosis	5 (25.0)	8 (42.1)	.26
LPChA anastomosis	5 (25.0)	15 (78.9)	<.01
MPChA anastomosis	5 (25.0)	9 (47.4)	.15

Note:—PCA indicates posterior cerebral artery; PcomA, posterior communicating artery; IA, intracranial aneurysm; TC, thalamic collateral.

Table 3: Clinical features of adult patients with MMD who experienced recurrent ipsilateral hemorrhage

Case	Age (yr)/Sex	Hemorrhagic Site		Interval (mo)	Target ChCA		
		Site of Initial Hemorrhage	Site of Recurrent Hemorrhage		AChA	LPChA	MPChA
1	46/M	Right body of lateral ventricle	Right body of lateral ventricle	5		+	
2	43/M	Left atrium	Left atrium	10	+		
3	44/F	Right anterior body of lateral ventricle	Right temporal horn of lateral ventricle	2	+		
4	42/F	Right posterior body of lateral ventricle	Right posterior body of lateral ventricle	10	+		
5	50/M	Left posterior body of lateral ventricle	Left posterior body of lateral ventricle	49		+	
6	63/F	Left occipital horn of lateral ventricle	Left occipital horn of lateral ventricle	1		+	
7	46/M	Right frontal horn of lateral ventricle	Right splenium of corpus callosum	4			+
8	51/F	Left posterior horn of lateral ventricle	Left atrium	12		+	
9	51/F	Left atrium	Left atrium	5		+	
10	45/F	Left temporal horn of lateral ventricle	Left posterior body of lateral ventricle	58		+	
11	50/F	Left insular lobe	Left insular lobe	47	+		
12	58/F	Right anterior body of lateral ventricle	Right body of corpus callosum	14			+
13	36/F	Left body of lateral ventricle	Left atrium	59	+		
14	32/F	Right posterior horn of lateral ventricle	Right temporal horn of lateral ventricle	1		+	
15[a]	42/F	Left temporal-occipital lobe	Left putamen	25			
16[b]	56/M	Left perimesencephalic subarachnoid	Left perimesencephalic subarachnoid	39			
17[b]	45/F	Right insular lobe and subarachnoid	Right insular lobe and subarachnoid	1			
18[b]	57/F	Left quadrigeminal cistern	Left quadrigeminal cistern	57			
19[b]	42/F	Left temporal lobe and subarachnoid	Left temporal lobe and subarachnoid	2			

Note:—+ indicates present.

[a] Recurrent hemorrhage not attributable to choroidal anastomosis.

[b] Recurrent hemorrhage attributable to intracranial aneurysm rupture.

Table 4: Univariate and multivariate adjusted[a] analyses of the association between ChCA subtypes and recurrent ipsilateral hemorrhage in adult patients with MMD

	Presence of Recurrent Hemorrhage					
	Univariate Analysis			Multivariate Analysis		
ChCA Subtype	HR	95% CI	*P* Value	HR	95% CI	*P* Value
AChA anastomosis	1.77	0.71–4.41	.22	8.23	1.41–48.13	.02
MPChA anastomosis	2.14	0.86–5.29	.10	3.43	0.80–14.80	.10
LPChA anastomosis	6.66	2.18–20.39	<.01	5.78	1.58–21.13	<.01

[a] Multivariate analysis was adjusted for confounding factors including age, sex, a history of ischemia, Suzuki stage >III, involvement of posterior cerebral arteries, thalamic anastomosis, fetal posterior communicating artery, and intracranial aneurysm.

arteriopathy of the LPChA in patients with MMD are warranted.

This study is limited by its retrospective nature. In addition, because of the rarity of nonsurgical intervention in patients with hemorrhagic MMD and the large number of patients excluded, this study is limited by its small sample size. Furthermore, interrater and intrarater agreement values for the identification of LPChA were low due to technical flaws in angiographic imaging of some unilateral vertebral arteries and the use of a weak contrast agent for angiography in some cases. The relationship between subtypes of ChCA and recurrent hemorrhage was determined only via analysis of the initial angiographic images, with no follow-up angiographic validation. Therefore, the development of ChCA subtypes was unclear in our study. Nevertheless, this study remains one of the first to analyze the association between ChCA subtypes and recurrent ipsilateral hemorrhage in patients with MMD. Considering the unique collateral anastomosis seen in patients with MMD, multicenter prospective studies are needed to determine the natural course of these collateral vessels. MR imaging may be able to be used for serial imaging follow-up of LPChA anastomosis in patients with MMD. In a recent study, sliding thin-slab maximum-intensity-projection coronal MRA images were found to provide reliable follow-up of periventricular anastomosis.[17] Future studies are warranted to assess surgical revascularization in the area of the LPChA in nonsurgical patients and serial imaging follow-up of LPChA changes in surgical patients with MMD.

CONCLUSIONS

Recurrent ipsilateral hemorrhage is common in the natural course of hemorrhagic MMD, and LPChA anastomosis is associated with recurrent hemorrhage in this patient population. In light of these findings, LPChA anastomosis may serve as a marker of the risk of recurrent ipsilateral hemorrhage in patients with MMD.

ACKNOWLEDGMENTS

We thank Zhongzhi Jia, MD, The Affiliated Changzhou No. 2 People's Hospital of Nanjing Medical University, Changzhou, China, and Megan Griffiths, scientific writer, Cleveland, Ohio, for help with revising the manuscript.

REFERENCES

1. Suzuki J, Takaku A. **Cerebrovascular "Moyamoya" disease: disease showing abnormal net-like vessels in base of brain.** *Arch Neurol* 1969;20:288–99 CrossRef Medline
2. Kuroda S, Houkin K. **Moyamoya disease: current concepts and future perspectives.** *Lancet Neurol* 2008;7:1056–56 CrossRef Medline
3. Takahashi JC, Miyamoto S. **Moyamoya disease: recent progress and outlook.** *Neurol Med Chir (Tokyo)* 2010;50:824–32 CrossRef Medline
4. Kobayashi E, Saeki N, Oishi H, et al. **Long-term natural history of hemorrhagic Moyamoya disease in 42 patients.** *J Neurosurg* 2000;93:976–80 CrossRef Medline
5. Funaki T, Takahashi JC, Houkin K, et al. **High rebleeding risk associated with choroidal collateral vessels in hemorrhagic Moyamoya disease: analysis of a nonsurgical cohort in the Japan Adult Moyamoya trial.** *J Neurosurg* 2018 Feb 1:1–8 [Epub ahead of print] CrossRef Medline
6. Nah HW, Kwon SU, Kang DW, et al. **Moyamoya disease-related versus primary intracerebral hemorrhage: [corrected] location and outcomes are different [erratum in Stroke 2013;44:e119].** *Stroke* 2012;43:1947–50 CrossRef Medline
7. Takahashi J, Funaki T, Houkin K, et al; JAM Trial Investigators. **Significance of the hemorrhagic site for recurrent bleeding: prespecified analysis in the Japan Adult Moyamoya Trial.** *Stroke* 2016;47:37–43 CrossRef Medline
8. Marinković S, Gibo H, Filipović B, et al. **Microanatomy of the subependymal arteries of the lateral ventricle.** *Surg Neurol* 2005; 63:451–58; discussion 458 Medline
9. Funaki T, Takahashi JC, Houkin K, et al. **Angiographic features of hemorrhagic moyamoya disease with high recurrence risk: a supplementary analysis of the Japan Adult Moyamoya Trial.** *J Neurosurg* 2018;128:777–84 CrossRef Medline
10. Funaki T, Takahashi JC, Houkin K, et al. **Effect of choroidal collateral vessels on de novo hemorrhage in Moyamoya disease: analysis of nonhemorrhagic hemispheres in the Japan Adult Moyamoya Trial.** *J Neurosurg* 2019 Feb 8:1–7 [Epub ahead of print] CrossRef Medline
11. Research Committee on the Pathology and Treatment of Spontaneous Occlusion of the Circle of Willis; Health Labour Sciences Research Grant for Research on Measures for Infractable Diseases. **Guidelines for diagnosis and treatment of Moyamoya disease (spontaneous occlusion of the circle of Willis).** *Neurol Med Chir (Tokyo)* 2012;52:245–66 CrossRef Medline
12. Miyamoto S, Yoshimoto T, Hashimoto N, et al. **Effects of extracranial-intracranial bypass for patients with hemorrhagic Moyamoya disease: results of the Japan Adult Moyamoya Trial.** *Stroke* 2014;45:1415–21 CrossRef Medline
13. Mugikura S, Takahashi S, Higano S, et al. **Predominant involvement of ipsilateral anterior and posterior circulations in Moyamoya disease.** *Stroke* 2002;33:1497–500 CrossRef Medline
14. Kim KM, Kim JE, Cho WS, et al. **Natural history and risk factor of recurrent hemorrhage in hemorrhagic adult Moyamoya disease.** *Neurosurgery* 2017;81:289–96 CrossRef Medline
15. Yamamoto S, Hori S, Kashiwazaki D, et al. **Longitudinal anterior-to-posterior shift of collateral channels in patients with Moyamoya disease: an implication for its hemorrhagic onset.** *J Neurosurg* 2019;130:884–90 CrossRef Medline
16. Matsushige T, Kraemer M, Schlamann M, et al. **Ventricular microaneurysms in Moyamoya angiopathy visualized with 7T MR angiography.** *AJNR Am J Neuroradiol* 2016;37:1669–72 CrossRef Medline
17. Miyakoshi A, Funaki T, Takahashi JC, et al. **Restoration of periventricular vasculature after direct bypass for Moyamoya disease: intra-individual comparison.** *Acta Neurochir (Wien)* 2019;161:947–54 CrossRef Medline

Hemorrhagic Factors of Moyamoya Disease

In this issue, Liu et al[1] found that choroidal collateral anastomosis was a predictor of the recurrent hemorrhage of Moyamoya disease (MMD), especially lateral posterior choroidal artery anastomosis. This study will further deepen our understanding of the risk factors of MMD rebleeding.

The predominant feature of the pathology of MMD is now known to be progressive stenosis of the carotid artery terminations and the development of dilated, fragile perforating arteries, which are termed "Moyamoya vessels." Although MMD is an uncommon cerebrovascular disease, it is an important cause of stroke. Most pediatric patients have ischemic attacks, whereas adult patients can have ischemic attacks, bleeding attacks, or both. More than half of adult MMD presents with intracranial bleeding. Such bleeding attacks are potentially fatal and seriously affect the patients' prognoses. The common hemorrhage site of MMD is intraventricular hemorrhage, and it is also common in the paraventricular area of the posterior lateral ventricle (ie, the blood supply area of the lateral posterior choroidal artery). A previous case-control study found that the compensatory dilated anterior choroidal artery and posterior communicating–posterior cerebral artery were associated with bleeding manifestations of MMD, but not with recurrent bleeding of MMD.[2]

Pseudoaneurysms are often found in children's MMD by digital subtraction angiography after bleeding. Most of the aneurysms are located in the posterior choroidal artery. Encephalo-duro-arterio-synangiosis is often effective for these patients.[3,4] In other locations, if the aneurysm is accessible endovascularly, coils or Onyx (Covidien, Irvine, California) embolization is also an effective treatment.[5] The proliferation of dural vessels in the cavernous sinus can lead to a dural arteriovenous fistula, which tends to spontaneous occlusion.[6] A recent study by Cho et al[7] found that the risk of stroke was 4.5% per year in 241 cases of MMD. Intraventricular hemorrhage was associated with recurrent hemorrhage of MMD, and the risk of recurrent hemorrhage in hemorrhagic MMD was 4.3%. The risk of recurrent ischemic stroke in ischemic presentations was 3.0%; the risk of stroke in asymptomatic MMD was no less than in the former 2 groups. Thyroid disease and family history are both risk factors for stroke. A survey of 128 patients with conservatively managed hemorrhagic MMD provided a rebleeding rate of 4.5% per year.[8] The cumulative risk of rebleeding was 7.8% at 5 years, 22.6% at 10 years, and 35.9% at 15 years. The morbidity and mortality after rebleeding was 44.7%. Funaki et al[9] investigated 75 hemorrhagic hemispheres of 75 patients and found that choroidal anastomosis and posterior cerebral artery involvement were factors associated with posterior hemorrhage. They concluded that choroidal anastomosis might be considered a potential source of posterior hemorrhage at high risk of rebleeding.

There are 2 main causes of intracranial bleeding in MMD: rupture of dilated, fragile Moyamoya vessels (perforating arteries) and rupture of circle of Willis aneurysms. Another rare cause of bleeding in adult patients is rupture of the dilated collateral arteries on the brain surface. In this study,[1] the authors report that bleeding or posterior ventricle bleeding is caused by the Moyamoya vessels rupture. The choroidal arteries play an important role in providing collateral circulation in MMD, especially the lateral posterior choroidal artery. Although the authors found that lateral posterior choroidal artery anastomosis was a predictor of rebleeding of MMD, there was selection bias in this study because 43% of patients had been excluded.

REFERENCES

1. Wang J, Yang Y, Li X, et al. **Lateral posterior choroidal collateral anastomosis predicts recurrent ipsilateral hemorrhage in adult patients with Moyamoya disease.** *AJNR Am J Neuroradiol* 2019;40:1665–71 CrossRef
2. Liu P, Liu AH, Han C, et al. **Difference in angiographic characteristics between hemorrhagic and nonhemorrhagic hemispheres associated with hemorrhage risk of Moyamoya disease in adults: a self-controlled study.** *World Neurosurg* 2016;95:348–56 CrossRef Medline
3. Liu P, Han C, Li DS, et al. **Hemorrhagic Moyamoya disease in children: clinical, angiographic features, and long-term surgical outcome.** *Stroke* 2016;47:240–43 CrossRef Medline
4. Liu P, Lv XL, Liu AH, et al. **Intracranial aneurysms associated with Moyamoya disease in children: clinical features and long-term surgical outcome.** *World Neurosurg* 2016;94:513–20 CrossRef Medline
5. Liu P, Lv X, Li Y, et al. **Onyx embolization of a ruptured rotundum foreman artery aneurysm in a patient with Moyamoya disease: case report.** *World Neurosurg* 2015;84:1178.e1–3 CrossRef Medline
6. Liu P, Xu Y, Lv X, et al. **Progression of unilateral Moyamoya disease resulted in spontaneous occlusion of ipsilateral cavernous dural arteriovenous fistula: case report.** *Interv Neuroradiol* 2016;22:362–64 CrossRef Medline

7. Cho WS, Chung YS, Kim JE, et al. **The natural clinical course of hemodynamically stable adult Moyamoya disease.** *J Neurosurg* 2015; 122:82–89 CrossRef Medline
8. Kang S, Liu X, Zhang D, et al. **Natural course of Moyamoya disease in patients with prior hemorrhagic stroke.** *Stroke* 2019;50:1060–66 CrossRef Medline
9. Funaki T, Takahashi JC, Houkin K, et al. **Angiographic features of hemorrhagic Moyamoya disease with high recurrence risk: a supplementary analysis of the Japan Adult Moyamoya Trial.** *J Neurosurg* 2018;128:777–84 CrossRef Medline

X. Lv
Associate Professor
Neurosurgical Department
Beijing Tsinghua Changgung Hospital
School of Clinical Medicine, Tsinghua University
Beijing, China

http://dx.doi.org/10.3174/ajnr.A6217

Identification of the Bleeding Point in Hemorrhagic Moyamoya Disease Using Fusion Images of Susceptibility-Weighted Imaging and Time-of-Flight MRA

A. Miyakoshi, T. Funaki, Y. Fushimi, T. Kikuchi, H. Kataoka, K. Yoshida, Y. Mineharu, J.C. Takahashi, and S. Miyamoto

ABSTRACT

BACKGROUND AND PURPOSE: The location of intracerebral hemorrhage in Moyamoya disease is a prognostic factor for rebleeding and the degree of preventive effects obtainable with bypass surgery. We evaluated whether the bleeding point and responsible vessel were detectable using fusion images of SWI and time-of-flight MRA performed during chronic-phase hemorrhage.

MATERIALS AND METHODS: We retrospectively enrolled 42 patients with hemorrhagic Moyamoya disease (48 hemorrhagic events). Fusion images of SWI and MRA were made using workstations, and we defined the bleeding point as the point at which the signal of an abnormally extended artery on MRA overlapped the hypointense area on SWI. Two independent raters identified the bleeding point, and classified the location and responsible vessels.

RESULTS: The bleeding point was detectable at a frequency of 79.2% by rater 1. Agreement for the presence of a bleeding point was high (interrater κ = 0.83; 95% CI, 0.65–1; intrarater κ = 0.86; 95% CI, 0.68–1). The frequency of a periventricular location of the bleeding point was 65.8% by rater 1, and agreement on the location was again high (interrater κ = 0.92; 95% CI, 0.82–1; intrarater κ = 0.85; 95% CI, 0.72–0.99). The choroidal artery was the most frequent responsible vessel (57.9% by rater 1), and agreement on the responsible vessel was high (interrater κ = 0.84; 95% CI, 0.69–1; intrarater κ = 0.90; 95% CI, 0.78–1).

CONCLUSIONS: Detection of the bleeding point in hemorrhagic Moyamoya disease using SWI and MRA fusion images offers highly reproducible results.

ABBREVIATION: ICH = intracerebral hemorrhage

Intracerebral hemorrhage (ICH) is one of the major factors affecting prognosis for patients with Moyamoya disease.[1] ICH associated with Moyamoya disease is more common in adult patients and is mostly located in the parenchyma and ventricle.[2] Dilated perforating and choroidal arteries developing as part of the collateral network are supposed to represent 1 source of hemorrhage.[3,4] Direct bypass surgery for hemorrhagic-onset Moyamoya disease has been reported to contribute to the prevention of recurrent bleeding.[5-8] Furthermore, the hemorrhage location is associated with the incidence of rebleeding and the degree of preventative effect achievable with bypass surgery.[9] Accurate identification of the bleeding point and the vessel responsible for hemorrhage is thus clinically important.

Although some reports have investigated the distribution of microbleeds in Moyamoya disease,[10,11] no reports have addressed the bleeding point and vessels responsible for symptomatic hemorrhage related to Moyamoya disease, with the exception of 1 study using head CT.[12] Determining the site from which bleeding has occurred on CT and MR imaging performed during acute-phase hemorrhage is often difficult.

MRA performed using a 3T scanner has proved useful for evaluating the abnormally extended collateral networks in Moyamoya disease.[13] The present study evaluated the reproducibility of fusion images of SWI and TOF-MRA performed during the chronic phase of hemorrhage to detect the precise bleeding point. Furthermore, we created a distribution map of bleeding points and investigated the vessels responsible for hemorrhage.

MATERIALS AND METHODS

This cross-sectional study was approved by the ethics committee at Kyoto University Graduate School of Medicine.

Received February 18, 2019; accepted after revision July 29.

From the Departments of Neurosurgery (A.M., T.F., T.K., H.K., K.Y., Y.M, S.M.) and Diagnostic Imaging and Nuclear Medicine (Y.F.), Kyoto University Graduate School of Medicine, Kyoto, Japan; and Department of Neurosurgery (J.C.T.), National Cerebral and Cardiovascular Center, Osaka, Japan.

Please address correspondence to Akinori Miyakoshi, MD, Department of Neurosurgery, Kyoto University Graduate School of Medicine, 54 Kawahara-cho, Shogoin, Sakyo-ku, Kyoto 606-8507, Japan; e-mail: myks-knr@umin.ac.jp

http://dx.doi.org/10.3174/ajnr.A6207

Patients

We retrospectively enrolled consecutive patients diagnosed with symptomatic hemorrhagic Moyamoya disease who visited Kyoto University Hospital between January 2009 and April 2018. The diagnosis of Moyamoya disease was determined according to the proposed criteria.[14] Patients who had undergone emergent hematoma evacuation craniotomy during the acute stage of hemorrhage were excluded because the responsible vessel might have been blocked. Patients who presented with primary subarachnoid hemorrhage, had undergone specific treatments for peripheral aneurysms, or for whom SWI or TOF-MRA images were unavailable were excluded. Cases in which fusion images could not be constructed because of an error caused by image processing at scanning were also excluded.

Imaging Protocol and Postimaging Processing

A 3T MR scanner (Magnetom Trio; Skyra, Prisma; Siemens, Erlangen, Germany) using a 32-channel head coil, which successfully reveals abnormal collateral vessels in Moyamoya disease, was introduced to our institution in 2009. Imaging parameters for SWI and TOF-MRA in this study were as follows—SWI: TR, 28 ms; TE, 20 ms; flip angle, 15°; FOV, 230 × 179 mm; matrix, 320 × 250; section thickness, 1 mm; 128 slices; axial acquisition; acceleration factor of 2 using generalized autocalibrating partially parallel acquisition; scan time, 4 minutes 53 seconds; TOF-MRA: TR, 20–21 ms; TE, 3.69 ms; flip angle, 20°; FOV, 220 × 187 mm; matrix, 384 × 328; section thickness, 0.7 mm; generalized autocalibrating partially parallel acquisition of 3; scan time, 5 minutes 48 seconds. The imaging field extended from the level of the foramen magnum to beyond the upper margin of the body of the lateral ventricle. Since 2016, the imaging field has been extended to the top of the head.

With the use of SWI and TOF-MRA images scanned during the chronic phase of ICH (≥3 weeks since onset), we generated SWI and TOF-MRA axial fusion images on a workstation (Aquarius iNtuition Viewer, Version 4.4.12; TeraRecon, Foster City, California).

Identification of Bleeding Point and Vessel Responsible for Bleeding

We defined the bleeding point as that point at which the signal of the abnormally extended artery on TOF-MRA overlapped the hypointense area on SWI. We classified the bleeding point into 9 groups, distinguishing between left and right for all sites other than the corpus callosum: 1) thalamus, 2) basal ganglia and internal capsule, 3) periventricular area, 4) corpus callosum, and 5) others, using the minor revised classification of microbleeds (Microbleed Anatomical Rating Scale)[15] if a bleeding point was detectable (Fig 1). The basal ganglia included the caudate and lentiform nuclei, and the periventricular area was defined as the subependymal and white matter area located within 10 mm of the wall of the lateral ventricles, except for the thalamus, basal ganglia, and corpus callosum.[15] In cases of patients who had a history of multiple symptomatic hemorrhages, we referred to patient records and CT images obtained during acute-phase hemorrhage.

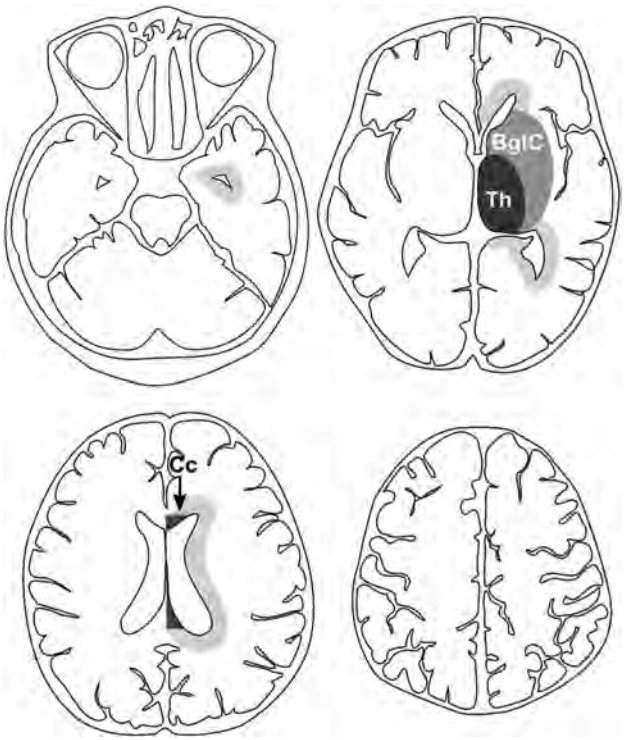

FIG 1. Diagram used for the classification of the site of bleeding. The periventricular area was defined as subependymal tissue and the white matter area located within 10 mm from the wall of the lateral ventricles except for the thalamus, basal ganglia, and corpus callosum. Th indicates thalamus; BgIC, basal ganglia and internal capsule; Cc, corpus callosum.

Furthermore, we classified the vessel responsible for hemorrhage into 4 types using axial TOF-MRA images and sliding-thin-slab maximum-intensity projection images:[13] 1) thalamic perforator (thalamotuberal artery, thalamoperforating artery or thalamogeniculate artery); 2) lenticulostriate artery; 3) choroidal artery (anterior choroidal artery, medial posterior choroidal artery, or lateral posterior choroidal artery); or 4) other. All bleeding points were drawn in an anatomic diagram showing the type of vessels responsible for bleeding.

Two independent raters (A.M. and T.F.) who were blinded to other clinical information, except for 3 patients with multiple concomitant hemorrhages, assessed whether the bleeding point was detectable and rated the location of bleeding points and responsible vessels. Rater 1 (A.M.) had 12 years of experience in neurosurgery, and rater 2 (T.F.) had 17 years of experience in neurosurgery. Rater 1 rated fusion images twice at an 8-week interval to determine intrarater reliability. Both raters had participated in a training session involving 5 representative cases in which the bleeding point had been confirmed. In cases of disagreement, we determined bleeding points and vessels as the consensus decision of the 2 raters (A.M. and T.F.) to create the distribution map. After evaluating inter- and intrarater reliability, we confirmed the accuracy of the fusion image in some cases using another workstation (Osirix X DICOM Viewer 10.0; http://www.osirix-viewer.com).

craniotomy, $n = 9$; embolization for peripheral anterior choroidal aneurysm, $n = 1$; diagnosis of localized primary subarachnoid hemorrhage, $n = 1$; patient not having undergone SWI, $n = 1$; and patient not being able to undergo construction of fusion images because of errors in imaging processing at scanning, $n = 1$). We investigated the remaining 42 patients, who had experienced 48 hemorrhagic events (3 patients had experienced repeat hemorrhage in different locations).

Seventeen male and 25 female patients with Moyamoya disease were included (median age, 37 years; range, 7–66 years). Of these 42 patients, 8 (19%) were diagnosed with hypertension and 5 (11.6%) were diagnosed with dyslipidemia. No patients showed comorbid diabetes mellitus. Twelve patients (28.6%) had a smoking habit, and 16 patients (38.1%) had undergone direct or indirect bypass surgery at the time of MR imaging. The median interval from onset to MR imaging was 323.5 days (range, 26–8683 days).

Intra- and interrater reliabilities for the presence of a bleeding point, site of bleeding, and origin of the responsible vessels are shown in the Table. The detection rate for a bleeding point was 79.2% (38/48) for rater 1 and 72.9% (35/48) for rater 2, and interrater reliability was high ($\kappa = 0.83$; 95% CI, 0.65–1). Intrarater reliability of rater 1 for detecting the bleeding point at a 2-month interval was also high ($\kappa = 0.86$; 95% CI, 0.68–1). Raters 1 and 2 classified the site of the bleeding point as follows: thalamus, 3 (7.9%) versus 4 (11.4%); basal ganglia and internal capsule, 9 (23.7%) versus 7 (20%); periventricular area, 25 (65.8%) versus 23 (65.7%); and corpus callosum, 1 (2.6%) versus 1 (2.9%), respectively. Interrater and intrarater reliabilities of rater 1 at a 2-month interval for classification of the site of bleeding were high (interrater: $\kappa = 0.92$; 95% CI, 0.82–1; intrarater: $\kappa = 0.85$; 95% CI, 0.72–0.99). Raters 1 and 2 determined the origin of the responsible vessel as follows: lenticulostriate artery, 9 (23.7%) versus 10 (28.6%); thalamic perforator, 7 (18.4%) versus 4 (11.4%); and choroidal artery, 22 (57.9%) versus 21 (55.3%), respectively. Interrater and intrarater reliabilities

Reliability of detection of the bleeding point and vessel-related hemorrhage[a]

	Rater 1 ($n = 48$)	Rater 2 ($n = 48$)	IE (95% CI)	IA (95% CI)
Presence of responsible vessel	38 (79.2%)	35 (72.9%)	0.83 (0.65–1)	0.86 (0.68–1)
Location of bleeding point	($n = 38$)	($n = 35$)	0.92 (0.82–1)	0.85 (0.72–0.99)
Thalamus	3 (7.9%)	4 (11.4%)		
Basal ganglia and internal capsule	9 (23.7%)	7 (20%)		
Periventricular area	25 (65.8%)	23 (65.7%)		
Corpus callosum	1 (2.6%)	1 (2.9%)		
Other	0	0		
Origin of responsible vessels	($n = 38$)	($n = 35$)	0.84 (0.69–1)	0.90 (0.78–1)
Lenticulostriate artery	9 (23.7%)	10 (28.6%)		
Thalamic perforator	7 (18.4%)	4 (11.4%)		
Choroidal artery	22 (57.9%)	21 (55.3%)		
Other	0	0		

Note:—IE indicates interrater; IA, intrarater.
[a] Data are κ-agreements and correlation coefficients.

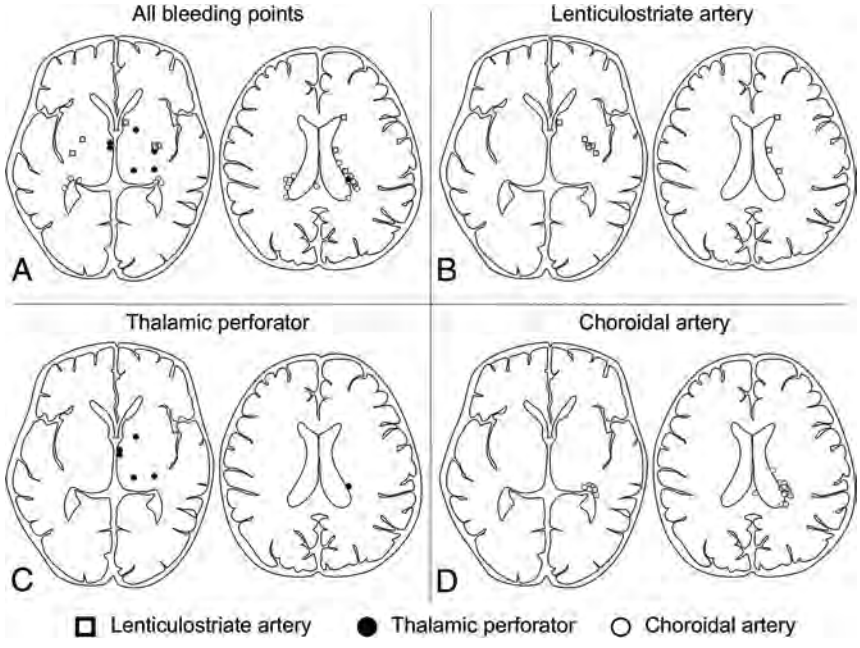

FIG 2. Diagrams show the distribution map of bleeding points and responsible vessels. *Squares* represent bleeding points derived from lenticulostriate arteries, *black circles* represent those from thalamic perforators, and *white circles* represent those from choroidal arteries. *A*, All bleeding points are drawn in a diagram. *B–D*, Diagrams show bleeding points derived from lenticulostriate arteries, the thalamic perforator, and choroidal artery, respectively. Bleeding points are on the left hemisphere.

Statistical Analysis

Intra- and interrater agreement for the presence or absence of a bleeding point was calculated using the unweighted κ statistic. Classifications of the bleeding point and the vessel responsible for hemorrhage were also calculated using unweighted κ statistics. All statistical analyses were conducted using JMP, Version 13 software (SAS Institute, Cary, North Carolina).

RESULTS

Between January 2009 and April 2018, a total of 55 patients with hemorrhagic Moyamoya disease visited our institution. Thirteen patients were excluded (due to hematoma-evacuation

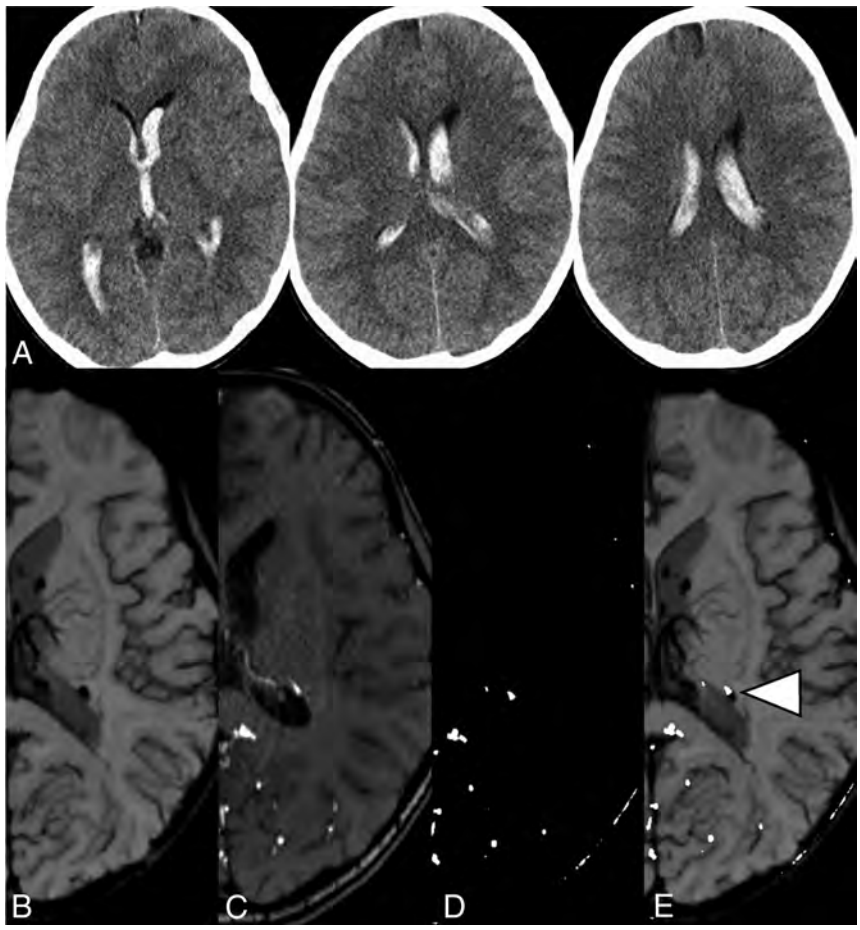

FIG 3. *A*, CT images from a 7-year-old boy with acute intraventricular hemorrhage. Images of SWI (*B*) and TOF-MRA (*C*), contrast-adjusted TOF-MRA (*D*), and a fusion image of contrast-adjusted TOF-MRA and SWI (*E*) for intraventricular hemorrhage in the same patient (chronic phase). The *arrowhead* shows the bleeding point at which the signal from the abnormally extended artery on TOF-MRA overlaps the hypointense spot on SWI. This point was defined as the bleeding point for the present case.

of rater 1 at a 2-month interval for the classification of the origin of responsible vessel were both high (interrater: κ = 0.84; 95% CI, 0.69–1; intrarater: κ = 0.90; 95% CI, 0.78–1). Distributions of bleeding points and vessels responsible for bleeding are depicted in Fig 2.

Sixteen patients had undergone direct or indirect bypass surgery before MR imaging. Twelve patients underwent bypass surgery between the initial hemorrhage and MR imaging, and 4 patients had undergone bypass before initial hemorrhage. In these 16 patients, the detection rate of responsible vessels was 75% (12 of 16 vessels). After excluding those cases that underwent bypass surgery, the detection rate improved to 84.4% (27 of 32 events).

Three patients experienced rebleeding twice. One patient developed right putaminal hemorrhage; then a second hemorrhage occurred in the left thalamus. She experienced the third hemorrhage in the right temporal lobe. Another patient developed left putaminal hemorrhage, and the second attack was intraventricular hemorrhage. She experienced the third hemorrhage in the left putamen again. The other patient developed intraventricular hemorrhage, and the second hemorrhage occurred in the right putamen. She presented with intraventricular hemorrhage again as the third attack.

Among the 38 cases in which rater 1 could have detected the bleeding point, 32 sets of angiographic data were obtained. Dilated or extended responsible vessels were confirmed in 30 of the 32 cases on angiograms. Our MR imaging findings corroborated well the results of angiography.

DISCUSSION

Bleeding points in hemorrhagic Moyamoya disease appeared to be identified with high reproducibility using fusion images of chronic-phase SWI and TOF-MRA. SWI images were created using a high-resolution gradient-echo method imaged with 3D and corrected flow velocity, and SWI has both high sensitivity for changes in magnetic susceptibility and higher spatial resolution than T2*WI.[16,17]

Detecting the bleeding point in Moyamoya disease using noncontrast or contrast-enhanced CT performed during acute-phase ICH is sometimes difficult (Figs 3*A*, 4*A*, and 5*A*), particularly in cases of intraventricular hemorrhage or a large hematoma. On the other hand, chronic-phase SWI and TOF-MRA fusion images demonstrated the bleeding point and responsible artery well (Figs 3*E*, 4*E*, and 5*F*). SWI for chronic-phase hemorrhage offers the advantage of being unaffected by any mass effect of the hematoma (Figs 4*B*, -5*C*), and evidence of small hematoma in the subependymal region is easily detected by being washed out of intraventricular hematoma (Fig 3*B*). In a case of ICH thought of as putaminal hemorrhage in which contrast-enhanced CT could not detect a bleeding point (Fig 5*A*), angiograms showed dilated lenticulostriate arteries and anterior choroidal artery, but determining the responsible vessel was difficult (Fig 5*B*). Chronic-phase SWI and TOF-MRA fusion images demonstrated the responsible vessel well; the dilated choroidal artery was thought to have collapsed in the periventricular area in this case (Fig 5*F*).

The bleeding point could not be detected on SWI or TOF-MRA fusion images in around 20%–30% of cases in the present study. Traces of old hemorrhage were detectable on SWI among each of the 10 cases in which rater 1 could not detect a bleeding point, whereas the signal from the vessels was faint (7 cases) or undetectable (3 cases) on TOF-MRA images. In some cases, an aneurysm had been observed on the dilated perforating artery

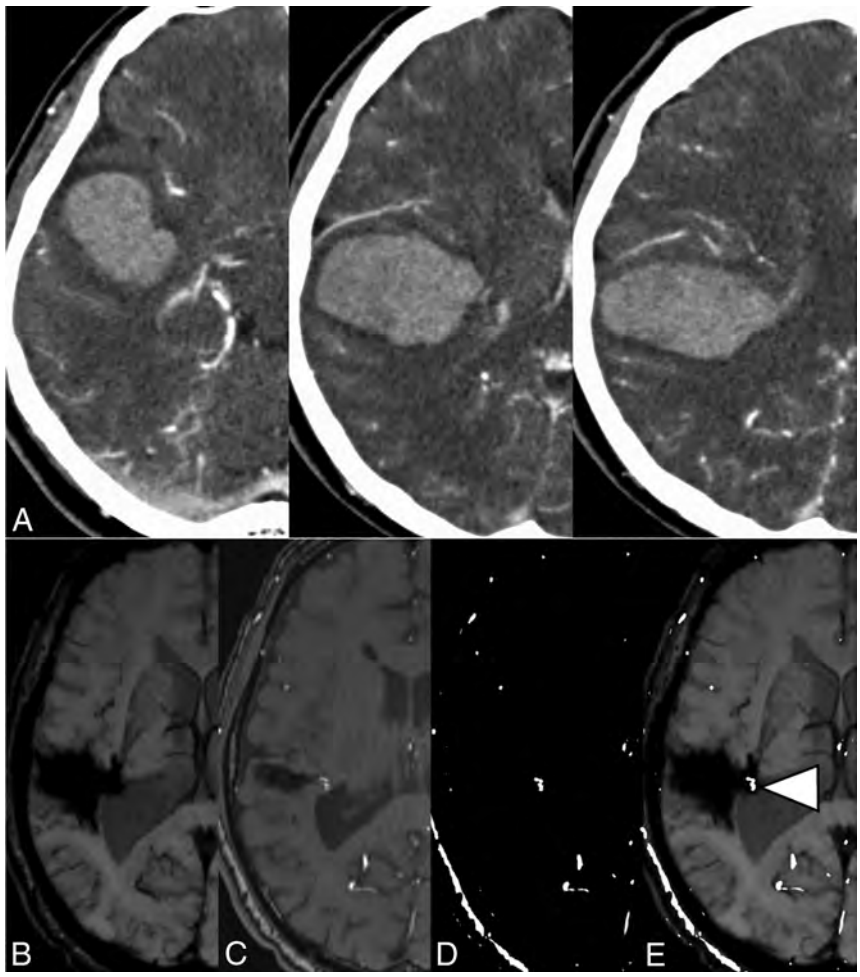

FIG 4. *A*, Contrast-enhanced CT of a 54-year-old man with acute lobar hemorrhage. Images of SWI (*B*) and TOF-MRA (*C*), contrast-adjusted TOF-MRA (*D*), and a fusion image of contrast-adjusted TOF-MRA and SWI (*E*) in the same patient (chronic phase). The *arrowhead* shows the signal of an abnormally dilated choroidal artery.

before the hemorrhagic events, but such aneurysms and the dilated perforating artery were not detectable on chronic-phase MRA. In such cases, the responsible vessel might have been blocked during vessel rupture or may have shrunk because the demand for blood flow decreased following damage to the cortex during hemorrhage. In addition, the detection ratio for responsible vessels might have decreased due to the effects of bypass surgery because direct or indirect bypass surgery improves abnormally dilated choroidal arteries and perforators of the posterior communicating artery.[3,18]

Bleeding points were concentrated around the subependymal region, particularly the trigon and posterior parts of the bodies of the lateral ventricles (Fig 2). On the other hand, bleeding points were distributed at the thalamus and putamen, similar to common hypertensive ICH. This distribution pattern corresponds to that described in a past study that investigated bleeding using acute-phase CT[12] and also resembles the distribution of microbleeds in Moyamoya disease.[10,11] Furthermore, the choroidal artery was most frequently detected as the responsible vessel in the periventricular area. Previous studies have shown dilation of the choroidal artery and posterior communicating artery as risk factors for ICH in Moyamoya disease.[18-20] The development of collateral anastomoses between the choroidal or perforating artery and medullary artery was significantly associated with a hemorrhagic presentation of Moyamoya disease.[12,13,21] This study suggested that the choroidal artery and perforating artery were at high risk of disruption in the subependymal area in Moyamoya disease. Baltsavias et al[22] demonstrated anastomotic connections between the lenticulostriate artery, choroidal artery, or thalamic artery and the medullary artery in the periventricular subependymal white matter using superselective angiography in pediatric patients with Moyamoya disease. That finding corresponds to the concept of periventricular anastomosis as previously reported by Funaki et al.[12,13] This connection is not present in the normal brain, and thus is speculated to lack the ordinary arterial wall structure at the subependymal area.[23-25] Hemodynamic stress at this point might lead to collapse of the fragile connection and cause ICH.

Rebleeding attacks were frequent among patients with hemorrhage and Moyamoya disease, and the risk of rebleeding increased with time for 5 years.[5] This finding suggests that patients with hemorrhage and Moyamoya disease are at risk of rebleeding for a long time. Precise detection and careful observation of the vessel responsible for hemorrhage might help prevent rebleeding. If the responsible vessel enlarges with time, tailored bypass may be able to shrink the vessel and prevent rebleeding.[26]

This study had several limitations that must be considered when interpreting the results. First, although we defined the bleeding point as the point at which the signal from abnormally extended vessel on TOF-MRA overlapped the area of hypointensity on SWI, demonstrating whether this vessel had actually been disrupted is difficult. This issue was mainly because we included only cases that had not undergone hematoma evacuation surgery. Second, gradient-echo imaging such as SWI shows blooming effects proportional to TE and local fields. Overestimation of bleeding size is thus 1 limitation of this study. Quantitative susceptibility imaging has been proposed to eliminate blooming artifacts dependent on gradient echo imaging parameters. Quantitative susceptibility imaging is reported to estimate the size without blooming effects by performing dipole kernel

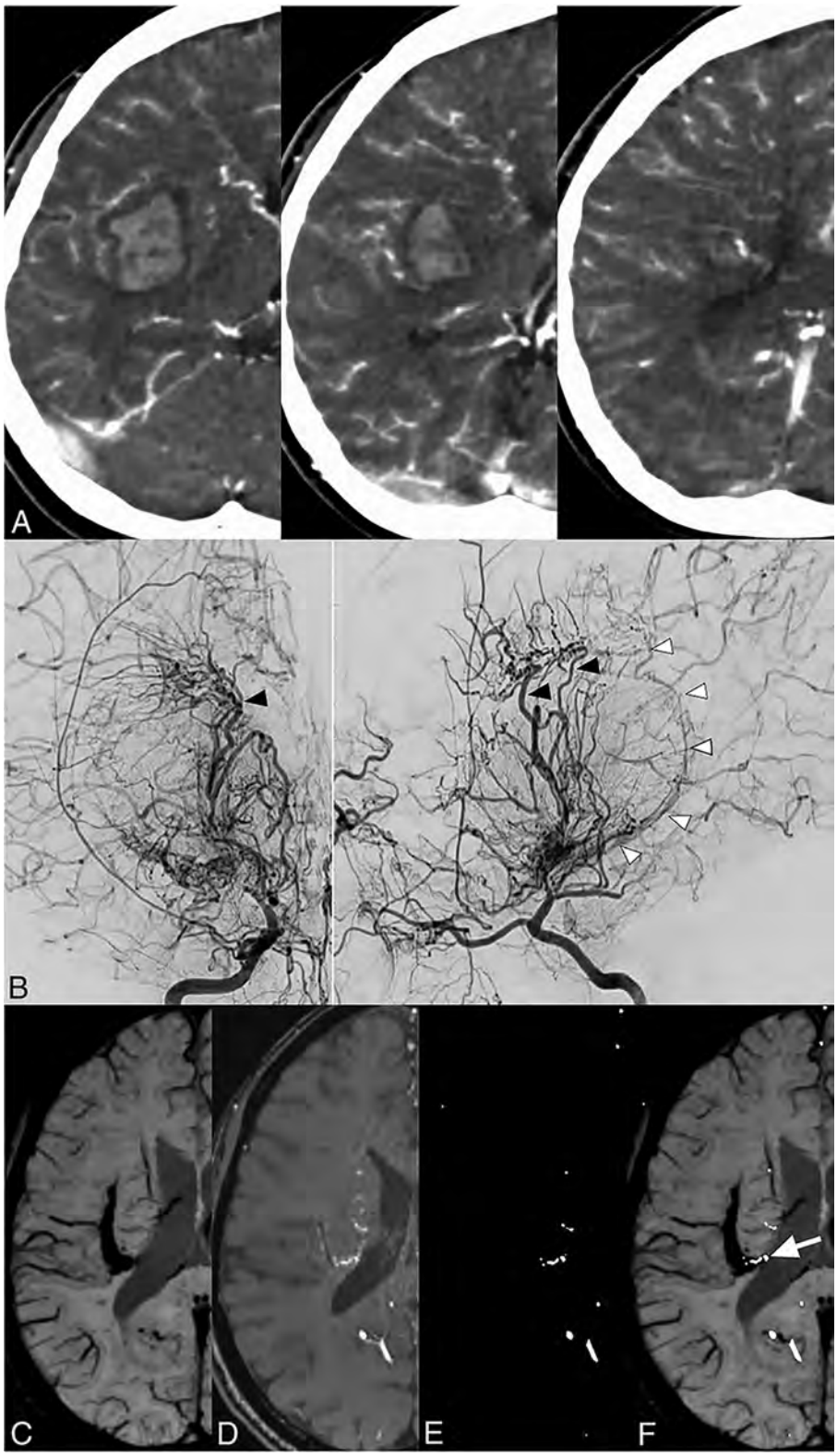

FIG 5. *A*, Contrast-enhanced CT of a 29-year-old woman with acute putaminal hemorrhage. *B*, Right internal carotid angiogram of the same patient (acute phase) shows abnormal dilation and extension of the lenticulostriate arteries (*black arrowheads*) and choroidal artery (*white arrowheads*). Images of SWI (*C*) and TOF-MRA *(D)*, contrast-adjusted TOF-MRA (*E*), and fusion image of contrast-adjusted TOF-MRA and SWI (*F*) in the same patient (chronic phase). The *arrow* shows the dilated choroidal artery, which might be disrupted in the periventricular area in this case.

deconvolution.[27] Third, several cases were seen in which multiple abnormal dilated vessel signs were detected in the low-intensity area on SWI when the hematoma was large. This was the main factor underlying disagreements between the 2 raters.

Chronic-phase SWI and TOF-MRA fusion images are useful to detect bleeding points and the responsible vessel in ICH-related Moyamoya disease. Further research is needed to establish optimal MR imaging protocols for detecting bleeding points and responsible arteries, and clarification of the features of the responsible artery for ICH might contribute to the prevention of ICH in Moyamoya disease.

CONCLUSIONS

Diagnosis using chronic-phase SWI and TOF-MRA fusion images offered good intra- and interrater reliabilities for detecting the bleeding point and responsible vessel. Abnormally dilated perforating and choroidal arteries might offer a key source of ICH in Moyamoya disease. This imaging technique might be clinically useful for accurate identification of the bleeding point, which is often difficult using only the initial CT.

REFERENCES

1. Han DH, Kwon OK, Byun BJ, et al; Korean Society for Cerebrovascular Disease. **A co-operative study: clinical characteristics of 334 Korean patients with Moyamoya disease treated at neurosurgical institutes (1976–1994).** *Acta Neurochir (Wien)* 2000;142:1263–73 CrossRef Medline
2. Nah HW, Kwon SU, Kang DW, et al. **Moyamoya disease-related versus primary intracerebral hemorrhage: location and outcomes are different.** *Stroke* 2012;43:1947–50 CrossRef Medline
3. Jiang H, Yang H, Ni W, et al. **Long-term outcomes after combined revascularization surgery in adult hemorrhagic Moyamoya disease.** *World Neurosurg* 2018;116:e1032–41 CrossRef Medline
4. Funaki T, Takahashi JC, Houkin K, et al. **High rebleeding risk associated with choroidal collateral vessels in hemorrhagic Moyamoya disease: analysis of a nonsurgical cohort in the Japan Adult Moyamoya Trial.** *J Neurosurg* 2018 Feb 1:1–8. [Epub ahead of print] CrossRef Medline
5. Miyamoto S, Yoshimoto T, Hashimoto N, et al. **Effects of extracranial-intracranial bypass for patients with hemorrhagic Moyamoya disease: results of the Japan Adult Moyamoya Trial.** *Stroke* 2014;45:1415–21 CrossRef Medline
6. Liu X, Zhang D, Shuo W, et al. **Long term outcome after conservative and surgical treatment of haemorrhagic Moyamoya disease.** *J Neurol Neurosurg Psychiatry* 2013;84:258–65 CrossRef Medline
7. Jang DK, Lee KS, Rha HK, et al. **Bypass surgery versus medical treatment for symptomatic Moyamoya disease in adults.** *J Neurosurg* 2017;127:492–502 CrossRef Medline
8. Ge P, Zhang Q, Ye X, et al. **Clinical features, surgical treatment, and long-term outcome in children with hemorrhagic Moyamoya disease.** *J Stroke Cerebrovasc Dis* 2018;27:1517–23 CrossRef Medline
9. Takahashi JC, Funaki T, Houkin K, Trial, et al. **Significance of the hemorrhagic site for recurrent bleeding: prespecified analysis in the Japan Adult Moyamoya Trial.** *Stroke* 2016;47:37–43 CrossRef Medline
10. Kazumata K, Shinbo D, Ito M, et al. **Spatial relationship between cerebral microbleeds, Moyamoya vessels, and hematoma in Moyamoya disease.** *J Stroke Cerebrovasc Dis* 2014;23:1421–28 CrossRef Medline
11. Wenz H, Wenz R, Maros M, et al. **Incidence, locations, and longitudinal course of cerebral microbleeds in European Moyamoya.** *Stroke* 2017;48:307–13 CrossRef Medline
12. Funaki T, Takahashi JC, Houkin K, et al. **Angiographic features of hemorrhagic Moyamoya disease with high recurrence risk: a supplementary analysis of the Japan Adult Moyamoya Trial.** *J Neurosurg* 2018;128:777–84 CrossRef Medline
13. Funaki T, Takahashi JC, Yoshida K, et al. **Periventricular anastomosis in Moyamoya disease: detecting fragile collateral vessels with MR angiography.** *J Neurosurg* 2016;124:1766–72 CrossRef Medline
14. Research Committee on the Pathology Treatment of Spontaneous Occlusion of the Circle of Willis. Health Labour Sciences Research Grant for Research on Measures for Infractable Diseases. **Guidelines for diagnosis and treatment of Moyamoya disease (spontaneous occlusion of the circle of Willis).** *Neurol Med Chir (Tokyo)* 2012;52:245–66 CrossRef Medline
15. Gregoire SM, Chaudhary UJ, Brown MM, et al. **The Microbleed Anatomical Rating Scale (MARS): reliability of a tool to map brain microbleeds.** *Neurology* 2009;73:1759–66 CrossRef Medline
16. Haacke EM, Xu Y, Cheng YC, et al. **Susceptibility weighted imaging (SWI).** *Magn Reson Med* 2004;52:612–18 CrossRef Medline
17. Sehgal V, Delproposto Z, Haacke EM, et al. **Clinical applications of neuroimaging with susceptibility-weighted imaging.** *J Magn Reson Imaging* 2005;22:439–50 CrossRef Medline
18. Morioka M, Hamada JI, Kawano T, et al. **Angiographic dilatation and branch extension of the anterior choroidal and posterior communicating arteries are predictors of hemorrhage in adult patients with Moyamoya disease.** *Stroke* 2003;34:90–95 CrossRef Medline
19. Liu W, Zhu S, Wang X, et al. **Evaluation of angiographic changes of the anterior choroidal and posterior communicating arteries for predicting cerebrovascular lesions in adult Moyamoya disease.** *J Clin Neurosci* 2011;18:374–78 CrossRef Medline
20. Liu P, Han C, Li DS, et al. **Hemorrhagic Moyamoya disease in children: clinical, angiographic features, and long-term surgical outcome.** *Stroke* 2016;47:240–43 CrossRef Medline
21. Fujimura M, Funaki T, Houkin K, et al. **Intrinsic development of choroidal and thalamic collaterals in hemorrhagic-onset Moyamoya disease: case-control study of the Japan Adult Moyamoya Trial.** *J Neurosurg* 2018 May 4:1–7. [Epub ahead of print] CrossRef Medline
22. Baltsavias G, Khan N, Valavanis A. **The collateral circulation in pediatric Moyamoya disease.** *Childs Nerv Syst* 2015;31:389–98 CrossRef Medline
23. Nelson MD Jr, Gonzalez-Gomez I, Gilles FH. **Dyke Award: the search for human telencephalic ventriculofugal arteries.** *AJNR Am J Neuroradiol* 1991;12:215–22 Medline
24. Mayer PL, Kier EL. **The controversy of the periventricular white matter circulation: a review of the anatomic literature.** *AJNR Am J Neuroradiol* 1991;12:223–28 Medline
25. Marinkovic S, Gibo H, Filipovic B, et al. **Microanatomy of the subependymal arteries of the lateral ventricle.** *Surg Neurol* 2005;63:451–58 CrossRef Medline
26. Sasagasako T, Funaki T, Tanji M, et al. **Intractable medial anastomotic branches from the lenticulostriate artery causing recurrent hemorrhages in Moyamoya disease.** *World Neurosurg* 2019;127:279–83 CrossRef Medline
27. Wang S, Lou M, Liu T, et al. **Hematoma volume measurement in gradient echo MRI using quantitative susceptibility mapping.** *Stroke* 2013;44:2315–17 CrossRef Medline

Paracoccidioidomycosis of the Central Nervous System: CT and MR Imaging Findings

M. Rosa Júnior, A.C. Amorim, I.V. Baldon, L.A. Martins, R.M. Pereira, R.P. Campos, S.S. Gonçalves, T.R.G. Velloso, P. Peçanha, and A. Falqueto

ABSTRACT

BACKGROUND AND PURPOSE: Paracoccidioidomycosis is a fungal infection mainly caused by the thermodimorphic fungus *Paracoccidioides*. The purpose of our study was to demonstrate the neuroimaging findings from 24 patients with CNS paracoccidioidomycosis.

MATERIALS AND METHODS: We performed a retrospective analysis focusing on the radiologic characteristics of CNS paracoccidioidomycosis. The 24 selected patients underwent MR imaging and/or CT, and the diagnosis was made by the presence of typical neuroimaging features, combined with fungus isolation, a serologic test, or the presence of disseminated disease.

RESULTS: Headache was the most common neurologic symptom, while the pseudotumoral form was the most common pattern. The number of lesions ranged from 1 to 11, with most localized on the frontal lobe with >2-cm lesions. CT showed mainly hypoattenuating lesions, whereas MR imaging demonstrated mainly hyposignal lesions on T1WI and T2WI. Furthermore, ring enhancement was present in most patients. The "dual rim sign" on SWI occurred in 100% of our patients with lesions of >2 cm.

CONCLUSIONS: The diagnosis of CNS paracoccidioidomycosis is difficult. Nevertheless, imaging examinations can play an important role in the diagnosis and evaluation of the disease.

ABBREVIATIONS: PCM = paracoccidioidomycosis; CT = computed tomography; MRI = magnetic resonance imaging; CNS = central nervous system; DSC = dynamic susceptibility contrast; DCE = dynamic contrast enhanced; rCBV = relative cerebral blood volume; Gd = gadolinium

Paracoccidioidomycosis (PCM) is a fungal infection, which is endemic in Latin America and is mainly caused by the thermodimorphic fungus *Paracoccidioides* spp, which primarily attacks the lungs and has a potential to disseminate to other organs.[1] Recently described are 4 other species of the genus *Paracoccidioides* apart from *P brasiliensis*: *P lutzii, P restrepiensis, P venezuelensis,* and *P Americana*.[2,3]

Paracoccidioides spp inhabits primarily the soil and causes autochthonous infection from southern Mexico to northern Argentina.[4-6] Most reported cases (approximately 80%) are from Brazil, and the rest are mainly from Venezuela, Colombia, and Argentina.[6-14]

The criterion standard for the diagnosis of PCM consists of demonstrating the presence of the fungus as multiple budding cells in clinical or tissue specimens. Nevertheless, serologic tests and imaging examinations such as CT, MR imaging, and x-rays also play an important role in the diagnosis and evaluation of the disease.[1,5-17]

CNS involvement is more common than it was once believed, and the disease can affect the CNS, ranging from 1% to 27.27% of cases.[18-25] Although the brain form of PCM is usually an outcome of hematogenous or lymphatic dissemination of a primary focus, it is not necessarily followed by disseminated PCM; in a few cases, it is the only location of the fungus in the body.[26]

Our purpose was to describe the clinical and radiologic data (CT and MR imaging) of 24 patients diagnosed with CNS PCM between 1978 and 2019. To the best of our knowledge, this is the largest imaging study of CNS PCM.

MATERIALS AND METHODS

This was a retrospective study, focusing on the radiologic characteristics of patients with CNS PCM attending the University Hospital Cassiano Antônio de Moraes, Federal University of

Received June 19, 2019; accepted after revision July 25.

From the Departments of Neuroradiology (M.R.J.) and Radiology (A.C.A., I.V.B., L.A.M., R.M.P.), Hospital Universitário Cassiano Antônio de Moraes da Universidade Federal do Espírito Santo, HUCAM/UFES/EBSERH, Vitória, Espírito Santo, Brazil; Department of Neuroradiology (R.P.C.), Hospital Meridional, Cariacica, Espírito Santo, Brazil; and Departments of Pathology (S.S.G.), Clinical Dentistry (T.R.G.V.), and Infectious Disease (P.P., A.F.), Universidade Federal do Espírito Santo, Vitória, Espírito Santo, Brazil.

Please address correspondence to Marcos Rosa Júnior, MD, PhD, Universidade Federal do Espírito Santo, UFES, Centro de Ciências da Saúde, Maruípe, 29043900, Vitória, Espírito Santo, Brazil; e-mail: marcosrosajr@hotmail.com

Indicates open access to non-subscribers at www.ajnr.org

http://dx.doi.org/10.3174/ajnr.A6203

Table 1: Epidemiologic and clinical characteristics

Characteristic	Value
Age	
Median (range) (yr)	54 (19–66)
Subgroup (No. of patients) (%)	
0–19	1 (4.1)
20–39	6 (25.0)
40–59	11 (45.8)
≥60	6 (25.0)
Male sex (No.) (%)	24 (100)
Neurologic symptoms (No. of patients) (%)	
Headache	8 (33.3)
Epilepsy	7 (29.1)
Focal neurologic signs	6 (25.0)
Paresis	5 (20.8)
Paresthesia	4 (16.6)
Plegia	2 (8.3)
Dysarthria	2 (8.3)
Mental confusion	2 (8.3)
Head lump	2 (8.3)
Diplopia	1 (4.1)
Chorea	1 (4.1)
Vertigo	1 (4.1)
Absence of neurologic symptom	2 (8.3)

Table 2: CT findings

Characteristic	Value
Patterns (No. of patients) (%)	
Pseudotumoral	21 (87.5)
Meningeal	1 (4.1)
Pseudotumoral + meningeal (combined)	2 (8.3)
Calcifications (No. of patients) (%)	0 (0)
Perilesional edema (No. of patients) (%)[a]	19 (90.4)
Hydrocephalus (No. of patients) (%)	6 (25.0)
Hemorrhage (No. of patients) (%)[b]	3 (13.0)
No. of lesions[b]	
Mean (range)	3.0 (1–11)
Subgroup (No. of patients) (%)	
Single lesions	9 (39.1)
2–5	11 (47.8)
6–10	2 (8.6)
>10	1 (4.3)
Lesion size (No. of patients) (%)[b]	
>2 cm	15 (65.2)
Larger axial diameter of the major lesion[b]	
Mean (range) (cm)	2.6 (0.3–5.6)
CT attenuation (No. of patients) (%)[c]	
Hyperattenuating lesions	11 (20.7)
Hypoattenuating lesions	30 (56.6)
Hypoattenuating center and hyperattenuating margin	12 (22.6)
CT or MR imaging contrast enhancement (No. of patients) (%)	
Ring enhancement	17 (70.8)
Nodular enhancement	3 (12.5)
Ring and nodular enhancement	3 (12.5)
Leptomeningeal enhancement	1 (4.1)

[a] This category considered only in the 21 patients with pseudotumoral form.
[b] These categories excluded the patient with the meningeal form isolated.
[c] Seven patients did not have CT scans and were eliminated from the calculations.

Table 3: Lesion sites

Characteristic	Value
Localization (No. of patients) (%)	
Basal meningitis	1 (4.1)
Pachymeningitis	1 (4.1)
Skull	2 (8.3)
Parietal lobe	7 (29.1)
Occipital lobe	6 (25.0)
Frontal lobe	9 (37.5)
Temporal lobe	5 (20.8)
Cerebellum	8 (33.3)
Cingulate gyrus	3 (12.5)
Thalamus	5 (20.8)
Basal ganglia	3 (12.5)
Striatum	1 (4.1)
Globus pallidus	1 (4.1)
Caudate nucleus	1 (4.1)
Putamen	1(4.1)
Corpus callosum	2 (8.3)
Hippocampus	1 (4.1)
Hypothalamus	1 (4.1)
Pons	2 (8.3)

Espirito Santo, between 1978 to 2019. The 24 selected patients had MR imaging and/or CT scans, and the diagnosis was made by the presence of typical neuroimaging features, combined with fungus isolation, a serologic test, or the presence of disseminated disease.

The CT scans were performed with Aquilion ONE 64-slice (Toshiba Medical Systems, Tokyo, Japan) or Asteion single-section (Toshiba Medical Systems) scanners. Patients were studied with 1-, 5-, or 10-mm axial slices before and/or after administration of an intravenous iodinated contrast agent in a peripheral vein at a total dose of 1.5 mL/kg. Fourteen patients underwent CT before and after contrast, and 3 patients, without contrast administration.

The MR images were obtained in a 1.5T Achieva (Philips Healthcare, Best, the Netherlands) or a 1.5T Brivo (GE Healthcare, Milwaukee, Wisconsin), with a specific head coil model with 8 channels, with T1-weighted, T2-weighted, FLAIR, DWI, T2*, and T1 postcontrast images. Intravenous administration of 0.1 mmol/kg of gadolinium-based contrast agent through the antecubital vein was performed for all patients. The MR imaging parameters were the following—Achieva: T1-weighted: TR = 547.8–623 ms, TE = 12.8–15 ms, section thickness = 5.0 mm, matrix = 528 × 528–328 × 271; T2-weighted: TR = 4572.5–4631 ms, TE = 100 ms, section thickness = 5.0 mm, matrix = 704 × 704–328 × 253; FLAIR: TR = 11,000 ms, TE = 140 ms, TI = 2800, section thickness = 5.0 mm, matrix = 640 × 640–256 × 156; DWI: TR = 4583–6596.3 ms, TE = 79–88.2 ms, section thickness = 3.5 mm, matrix = 512 × 512–192 × 114; T2*: TR = 588–609 ms, TE = 13.8 ms, section thickness = 5.0 mm, matrix = 512 × 512–232 × 183; SWI: TR = 22.6 ms, TE = 32.5 ms, section thickness = 2.0 mm, matrix = 448 × 448; T1 3D saggital postcontrast fast-field echo: TR = 12.4 ms, TE = 5946 ms, section thickness = 1 mm, matrix = 288 × 288; Brivo: T1-weighted: TR = 728 ms, TE = 3 ms, section thickness = 5.5 mm, matrix = 416 × 192; T2-weighted: TR = 3625 ms, TE = 122 ms, section thickness = 4.5 mm, matrix = 416 × 192; DWI: TR = 7309 ms, TE = 117 ms, section thickness = 4.5 mm, matrix = 128 × 128; T2*: TR = 434 ms, TE = 15.8 ms, section thickness = 4.5 mm, matrix = 320 × 224; FLAIR: TR = 10,000 ms, TE = 110 ms, section thickness = 4.5 mm, matrix = 288 × 192; T1 3D saggital postcontrast: TR = 7.9 ms, TE = 2.6 ms, section thickness = 2.0 mm, matrix = 288 × 224.

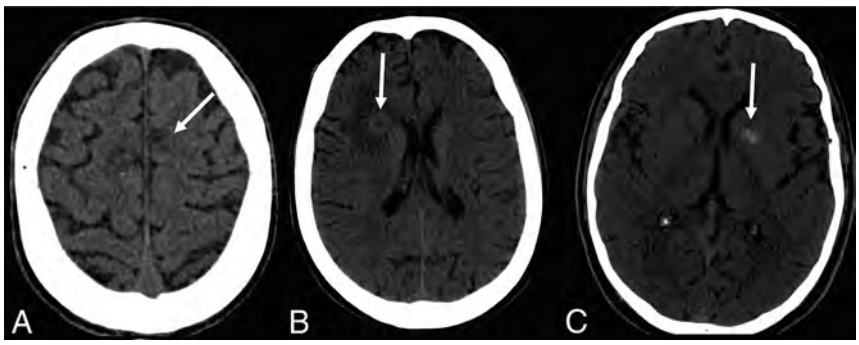

FIG 1. Brain CT showing different presentations of the lesions. *A*, Hypoattenuating lesions. *B*, Hypoattenuating lesions with a hyperattenuating halo. *C*, Hyperattenuating lesions.

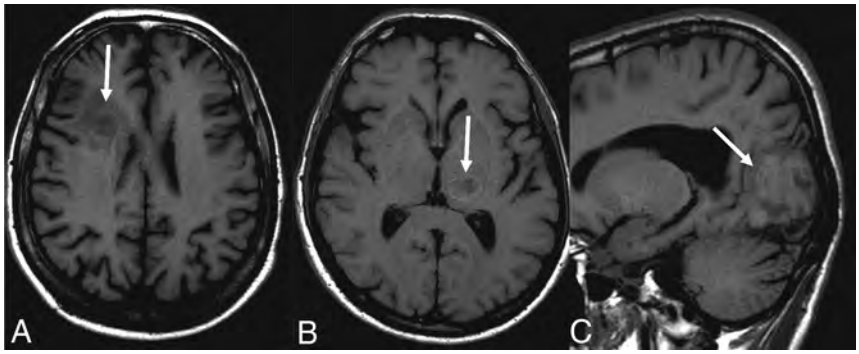

FIG 2. Signal on the TI-weighted images: hypointense lesion (*A*), lesion with hypointense center and hyperintense halo (*B*), and hyperintense lesion (*C*).

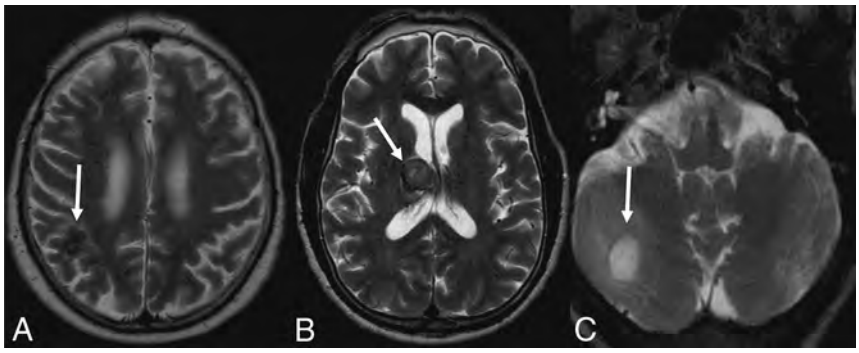

FIG 3. T2-weighted images show a hypointense lesion (*A*), a heterogeneous signal (*B*), and a hyperintense lesion (*C*).

Five patients also underwent SWI, 2 patients underwent perfusion DSC and dynamic contrast-enhanced imaging, and 2 patients underwent spectroscopy studies, only with qualitative analyses.

Dynamic Contrast-Enhanced MR Imaging

A power injector was used to administer a bolus of gadolinium-based contrast agent at a dose of 0.05 mmol/kg and rate of 5 mL/s. The kinetic enhancement of tissue before and after contrast injection was obtained using a 3D-T1-weighted fast-spoiled gradient-echo sequence (TR = 5.5 ms, TE = 1.3 ms, section thickness = 5 mm, flip angle = 12°, FOV = 240 × 177 × 125 cm, matrix = 108 × 100) and consisted of 25 images in the axial plane. Ten phases for preinjection time delay and 30 phases for postinjection were obtained.

DSC-PWI was performed with a gradient-recalled T2*-weighted echo-planar imaging sequence. The imaging parameters were as follows: TR/TE = 2085/40 ms, flip angle = 75°, section thickness = 5 mm, intersection gap = 0.5 mm, NEX = 1.0, FOV = 240 × 240 mm. During the first 3 phases, images were acquired before injecting the contrast material to establish a baseline. When the scan was in the fourth phase of DSC-PWI, a bolus of gadolinium-based contrast agent at a dose of 0.25 mmol/kg of body weight and 5 mL/s was injected intravenously with an MR imaging–compatible power injector. After we injected a bolus of the contrast material, a 20.0-mL bolus of saline was administered at the same injection rate. The series had 25 sections with 60 phases.

Single-voxel spectroscopy was acquired encompassing the annular enhancement area and the center nonenhancement area after contrast administration with the following parameters: point-resolved spectroscopy sequence, axial acquisition plane, TE = 35 and 144 ms, TR = 541 ms, number of acquisitions = 64, spectral resolution = 4096 points, voxel size = 8 cm^3 (2 × 2 × 2 cm).

We evaluated the following findings on head CT scans: density, the presence of calcifications, hydrocephalus, hemorrhage, perilesional edema, topography, number and size of lesions, and the contrast-enhancement pattern. We evaluated the following on MR imaging: T1 and T2 signals and diffusion, perfusion, and spectroscopy findings.

Similar to Toh et al,[27] who studied the "dual rim sign" on SWI in pyogenic abscesses, we also evaluated patients with SWI sequences for the presence of the dual rim sign, which is defined as 2 concentric rims around the central cavities at the margins of lesions, with the outer rim being hypointense, and the inner rim, hyperintense relative to the cavity contents. All imaging findings were assessed by 1 neuroradiologist with 8 years of experience. In addition, the clinical symptoms were accessed through systematic chart review.

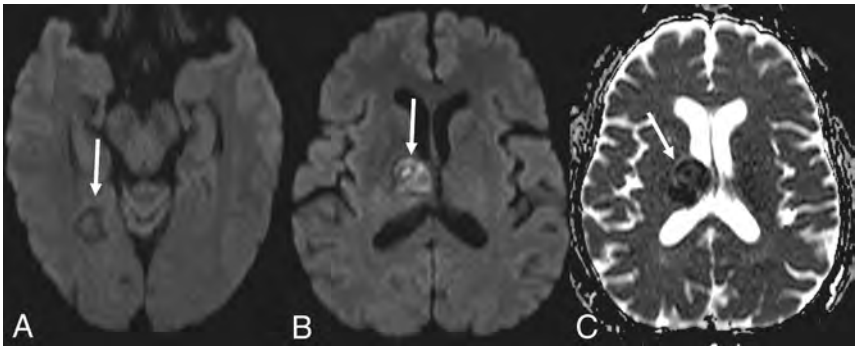

FIG 4. Demonstration that the lesions may not present with diffusion restriction (*A*) or diffusion restriction (*B*) with a low signal on the ADC map (*C*).

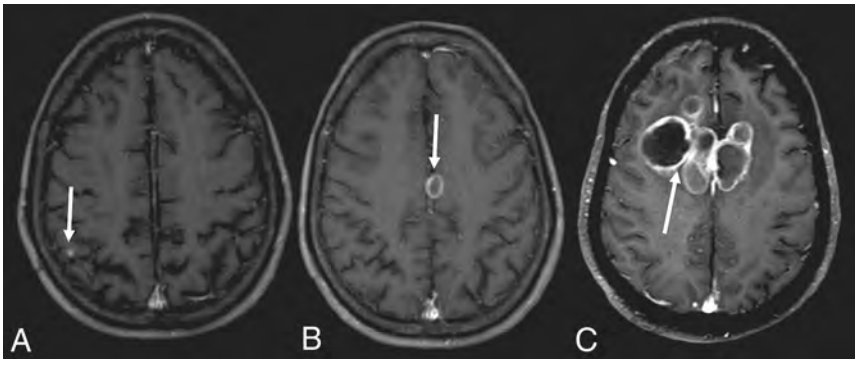

FIG 5. T1-weighted images after contrast administration demonstrating a small nodule in the cortical-subcortical transition (*A*), nodular lesion with annular enhancement (*B*), and multiple nodular lesions with annular enhancement and "daughter cysts" in a complex heterogeneous mass (*C*).

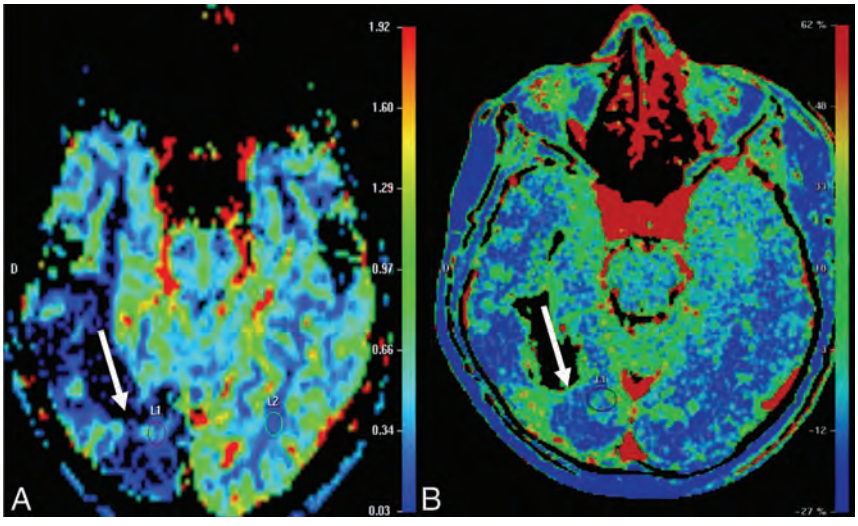

FIG 6. T2-weighted perfusion shows a lesion with low perfusion (*A*). T1-weighted perfusion shows the blood-brain barrier breakdown (*B*).

RESULTS

We describe 24 patients with a diagnosis of CNS PCM. All patients were men, ranging from 19 to 66 years of age. Approximately half of the patients were between 40 and 59 years of age. Headache was the most common neurologic symptom and was present in 33.3% of the cases. The epidemiology and clinical characteristics are summarized in Table 1.

Twenty-one patients had the pseudotumoral form, defined by the presence of parenchymal lesions with annular or nodular enhancement, while the meningeal pattern was observed in 1 case, and the combined form, in 2 cases. None of the patients had calcifications at the time of the initial neuroimaging. Perilesional edema was present in 90.4% of cases, whereas hydrocephalus and hemorrhage were found in 25% and 13% of cases, respectively. The number of lesions observed in each patient ranged from 1 to 11, with a mean of 3. Eleven patients had between 2 and 5 lesions (Table 2). Most were localized in the frontal lobe (37.5%), followed by the cerebellum (33.3%), parietal lobe (29.1%), occipital lobe (25%), and thalamus (20.8%) (Table 3). Furthermore, 65.2% of the lesions had an axial diameter of >2 cm, and the larger axial diameter of the major lesion ranged from 0.3 to 5.6 cm (Table 2).

Seventeen patients had CT scans showing a total of 53 lesions, of which 56.6% were hypoattenuating, 20.7% were hyperattenuating, and 22.6% had a hypoattenuating center with a hyperattenuating margin (Table 2 and Fig 1). On the other hand, 19 patients underwent MR imaging, in which a total of 61 lesions were observed. The T1-weighted sequence demonstrated that 50.8% were hypointense, 34.4% were hyperintense, and 14.7% were heterogeneous with a hypointense center with a hyperintense margin (Fig 2). On the T2-weighted sequence, 59% were hypointense, 9.8% were hyperintense, and 31.1% had heterogeneous lesions (hyperintense + hypointense) (Fig 3). Restricted diffusion was present in 47.3% (Fig 4), and the target sign was observed in 1 patient (5.2%). Ring contrast enhancement was observed in 70.8%; nodular enhancement, in 12.5%; both ring and nodular enhancement, in 12.5%; and

Furthermore, the study was approved by the Ethics Committee for Clinical Research of the University Hospital Cassiano Antônio de Moraes, Federal University of Espirito Santo, Espirito Santo, Brazil.

leptomeningeal enhancement, in 4.1% of the cases (Table 3 and Fig 5). Moreover, 3 patients underwent MR perfusion imaging, and 2 underwent proton spectroscopy. The perfusion demonstrated decreased relative CBV on DSC and slow and progressive ascending perfusion on dynamic contrast-enhanced imaging in all 3 patients (Fig 6). The spectroscopy demonstrated an increase of lipids and choline in both patients (Table 4 and Fig 7). Of the 5 patients in whom the SWI sequence was performed, 4 showed the dual rim sign on SWI (Fig 8). The patient who did not show the dual rim signal on SWI had a lesion <2 cm.

Thoracic imaging revealed that all patients presented with thoracic lesions in the form of pulmonary nodules, ground-glass opacities, consolidations, reversed halo sign, bronchiectasis, or lymph node enlargement.

Table 4: MR imaging findings

Characteristic	Value
MR imaging scans (No. of patients) (%)[a]	
T1-weighted[b]	
Hyperintense lesions	21 (34.4)
Hypointense lesions	31 (50.8)
Hypointense center and hyperintense margin	
T2-weighted[b]	
Hyperintense lesions	6 (9.8)
Hypointense lesions	36 (59.0)
Heterogeneous lesions (hyperintense + hypointense)	19 (31.1)
T1, perfusion[c]	
Slow and progressive ascending	3 (100)
T2, perfusion[c]	
Decreased rCBV	3 (100)
Spectroscopy[c]	
Decrease of NAA	2 (100)
Increase of choline	2 (100)
Increase of lipids	2 (100)
Diffusion-weighted (No. of patients) (%)[d]	
Restricted diffusion	9 (47.3)
Target sign	1 (5.2)

Note:—rCBV indicates relative CBV.
[a] Five patients did not have MR imaging scans and were eliminated from the calculations.
[b] The patient with the meningeal form was eliminated from the calculations.
[c] Only 3 patients underwent perfusion, and only 2 underwent spectroscopy.
[d] Five patients did not have diffusion and were eliminated from the calculations.

DISCUSSION

To the best of our knowledge, this study presents the largest imaging case series of CNS PCM until now (Fig 9). We describe the neuroimaging findings from 24 patients who were treated in a reference hospital in the State of Espirito Santo.

Peçanha et al[28] analyzed 546 patients in a reference hospital from 1978 to 2012 presenting with PCM. The historical case series revealed the involvement of the CNS in 4.5% (22 patients) with the chronic form and 3.3% (2 patients) with the acute/subacute form.

The main patterns of CNS PCM described are the pseudotumoral (90%) and meningeal (10%) forms.[19-21,29] Moreover, meningitis associated with the pseudotumoral form may occur in 17% of cases, or more rarely, it can be an isolated finding.[19] In our study, we also observed the predominance of the pseudotumoral form (87.5%), while the meningeal form was observed in 4.1%, and the combined form, in 8.3% of the cases.

The meningeal form is characterized by inflammation of the leptomeninges or pachymeninges, generally in the base of the skull, similar to what is observed in tuberculosis meningitis.[18,29-33] It may be diffuse or localized, isolated, or with dissemination to the parenchyma or nervous roots.

On the other hand, the pseudotumoral form consists of intraparenchymal granulomas, involving both the supratentorial and infratentorial compartments, which may mimic primary tumors, metastases, pyogenic abscesses, or viral and fungal etiologies.[20,34] The granulomas are frequently irregular (76%), ranging from 10

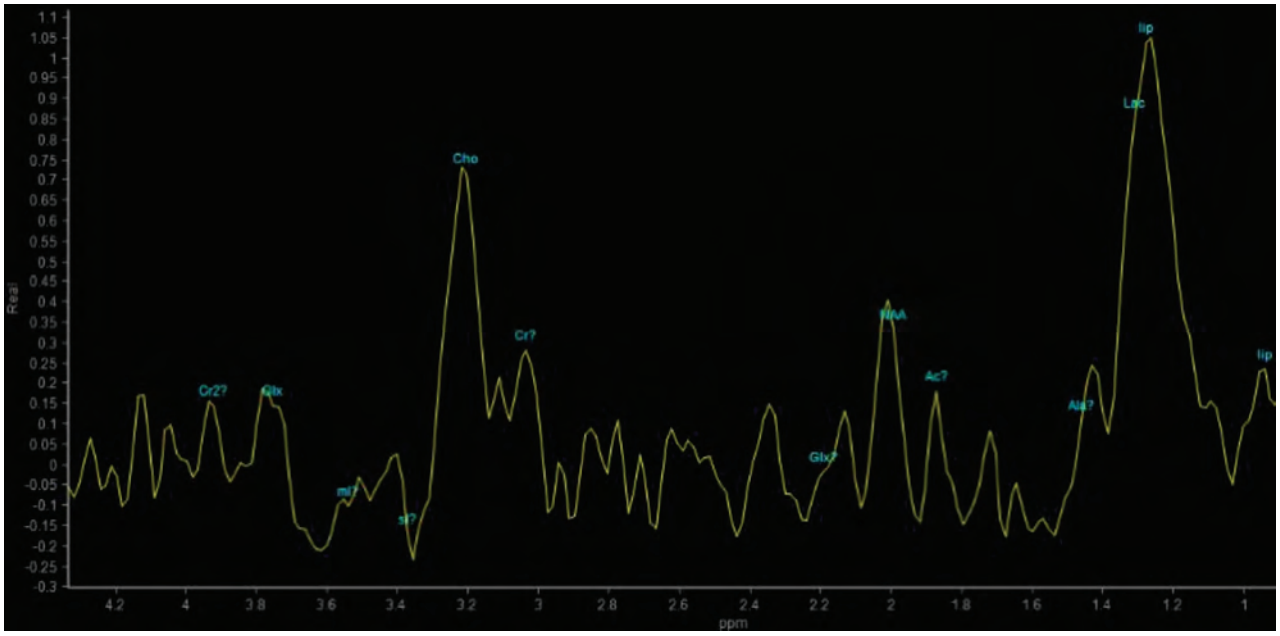

FIG 7. Proton spectroscopy with a TE = 144 ms showing increased lipid and choline peaks, with decreased NAA peaks.

to 45 mm, with mass effect, peripheral enhancement by contrast, and perilesional edema in 82% of the cases.[20,29,32] In our study, 65.2% of the patients had a granuloma larger than 2.0 cm; the mean diameter of the larger lesion was 2.3 cm with the range 0.3–5.6 cm, showing the same irregularity described in other studies. Similar to the studies described in the medical literature, perilesional edema was present in 90.4% of our patients.

The lesion can be situated in the cerebral hemispheres (67%), cerebellum (25%), brain stem (25%), and spinal cord (4%).[19,20] In our study, 62.5% of patients had lesions in the cerebral hemispheres; 33.3%, in the cerebellum; and 8.3%, in the brain stem; and no patient had a spinal cord lesion. Gasparetto et al[20] demonstrated that 47% of patients had a singular granuloma, 23% had 2 lesions, and 30% had ≥3 lesions. In our study, we observed a frequency similar to that of Gasparetto et al; 40.9% of the patients had a single granuloma. The mean number of lesions was 3, and the range was 1–11.

The location of the lesions determines the signals and symptoms in the patients.[29,35] The 5 most frequent symptoms were epilepsy, hemiparesis, cerebellar signs, headache, and hydrocephalus.[19,32] In our patients, the most common symptom was headache, followed by epilepsy.

The pseudotumoral form can assume a compact granulomatous pattern, which is completely solid, or it can have a necrotic center that explains the findings in the MR images. In addition, granulomas do not infiltrate or spread to the adjacent tissue.[20] Therefore, necrotic lesions in PCM may resemble pyogenic abscesses, and proton MR imaging with spectroscopy being a noninvasive technique can help distinguish the lesions.[36,37] Similar to Reis et al,[33] we found a high peak of the lipids and choline in all cases.

MR images show the pseudotumoral lesions consist of variable, hypo- or hyperintense lesions in T1 and T2 sequences. In particular, Reis et al[33] described the presence of a peripheral hyperintense halo in the T1 sequences without contrast in all 8 patients who were included in their research. In our study, this finding was in only 14.7%, demonstrating that it is not as frequent as reported in the above study.

Due to the variability of the composition of a granuloma, the diffusion-weighted sequence may exhibit lesions with or without restriction of water molecules. In our cases, 47.3% of patients had restriction on the diffusion imaging, showing variability as is described.

Similar to Toh et al,[27] who found the dual rim sign on SWI in 9 of 12 patients with pyogenic abscesses, we found this sign in all our 4 patients who presented with lesions >2 cm and underwent the SWI sequence, showing that this sign is not specific for pyogenic abscess. The contrast-enhancing rim of bacterial brain abscesses on MR imaging corresponds to the abscess capsule, and the magnetic susceptibility results from the free radicals produced by macrophages. There are a necrotic center and a zone of granulation tissue between the fibrocollagenous capsule and the center of the abscesses. With image coregistration,

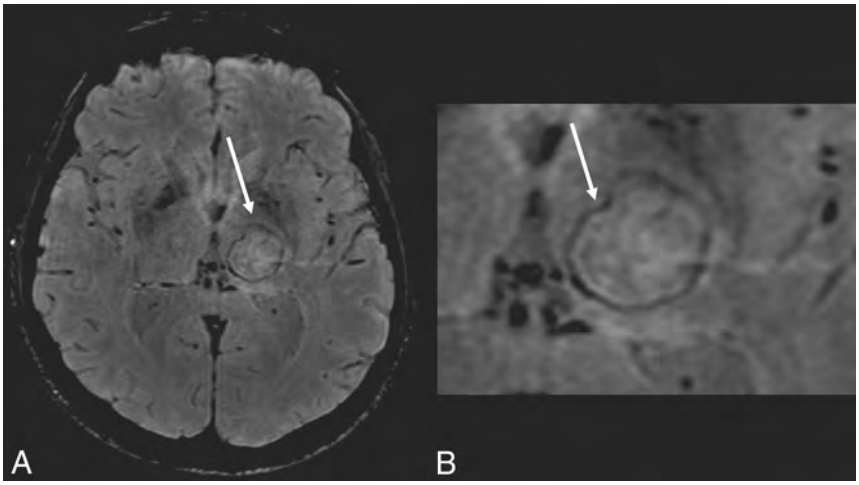

FIG 8. SWI sequence showing the dual rim sign. Note the external hypointense halo with an internal hyperintense halo.

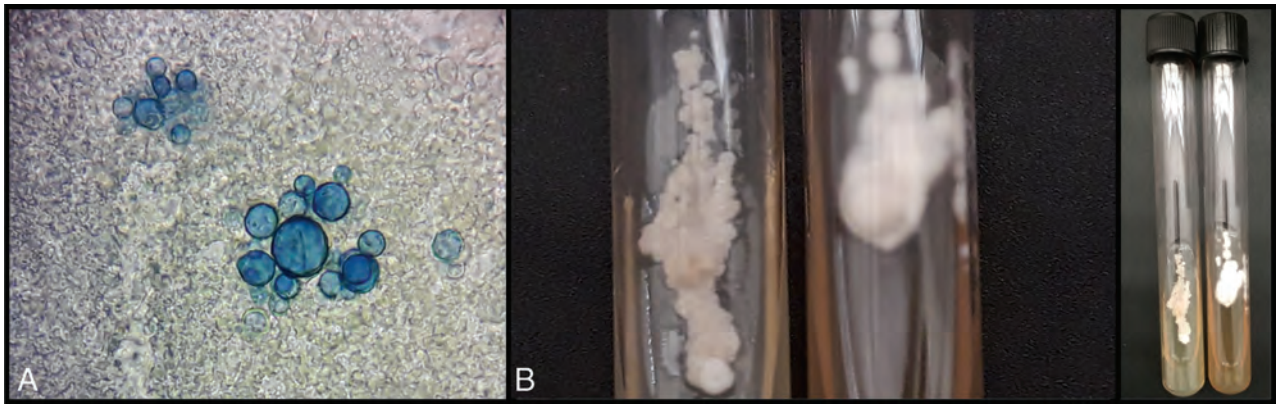

FIG 9. Laboratory diagnosis of paracoccidioidomycosis. Fresh examination in Parker-KOH stain shows yeast cells with multiple buds (*A*). Cultivation of *Paracoccidioides* spp. Left, yeast colonies to 37°C; and right, filamentous colonies to 25°C (*B*).

Toh et al[27] speculated that the hyperintense rims probably represent granulation tissue in pyogenic abscesses. We think this finding, the dual rim, occurs because PCM is also an infection. We suspect that this signal may occur in other infections, not only in bacterial abscesses as initially described by Toh et al. Because an antifungal is the treatment form, histopathologic examination of the margins may not be available in most cases. Thus, this finding is limited by a lack of direct histopathologic correlation with SWI findings, making it difficult to precisely define its origin.

CT images of the pseudotumoral form usually show hypoattenuating lesions with ring enhancement after contrast administration and surrounding edema. Calcifications or septations within the lesions might occur in up to 20% of cases.[20] With time, pseudotumoral CNS PCM gradually becomes more attenuating in noncontrast tomography and progressively becomes smaller.[20]

PCM shows a typical granulomatous reaction consisting of multinucleated giant cells mixed with extensive interstitial and conglomerate fibrosis, necrosis, and arterial intimal fibrosis. It subsequently may develop a central area of necrosis, and this may explain the heterogeneous image pattern. The central area of necrosis is initially solid and later may liquefy. On CT, the solid granuloma, without necrosis, may present as isoattenuated or slightly hyperattenuated to the brain parenchyma. On MR imaging, it is hypointense on both T1- and T2WI. The heterogeneity of imaging findings show homogeneous enhancement on postcontrast images. Because the granuloma shows necrosis of its central portion, the images show hypoattenuated lesions on CT, hyperintense on T2WI, with ring enhancement on postcontrast images. Liquid necrotic lesions show restricted diffusion, whereas solid necrotic lesions do not have restriction of diffusion.[15,20,33]

Similar to Reis et al,[33] all our cases presented with thoracic lesions. Gasparetto et al[20] also found thoracic alterations in most patients (88%), a finding that may help in the differential diagnosis.

This study has limitations. Few patients were studied with advanced MR imaging methods like DSC, dynamic contrast-enhancement, spectroscopy, and SWI, with only qualitative analyses, but it paves the way for new studies in the area that may contribute to additional findings in this disease.

CONCLUSIONS

CNS involvement has a variable frequency rate in PCM, and an increase in reports has been observed in recent years.[19,26] The diagnosis of PCM in the CNS is difficult because of the low sensitivity of diagnostic tests, the isolated forms of PCM in the CNS, the absence of previous systemic infection, and nonspecific symptoms that may be confused with other entities. Nevertheless, imaging examinations though nonspecific, when combined with the epidemiology and clinical manifestations, can play an important role in the diagnosis and evaluation of the disease. Therefore, it should be considered as a differential diagnosis for expansive lesions in the brain or meningitis, particularly in endemic areas.

REFERENCES

1. Kwon-Chung KJ, Bennett JE. **Medical mycology.** *Rev Inst Med Trop Sao Paulo* 1992;34:504–04 CrossRef
2. Marques-da-Silva SH, Rodrigues AM, de Hoog GS, et al. **Occurrence of Paracoccidioides lutzii in the Amazon region: description of two cases.** *Am J Trop Med Hyg* 2012;87:710–14 CrossRef Medline
3. Turissini DA, Gomez OM, Teixeira MM, et al. **Species boundaries in the human pathogen Paracoccidioides.** *Fungal Genet Biol* 2017;106:9–25 CrossRef Medline
4. Bagagli E, Theodoro RC, Bosco SM, et al. **Paracoccidioides brasiliensis: phylogenetic and ecological aspects.** *Mycopathologia* 2008;165:197–207 CrossRef Medline
5. Terçarioli GR, Bagagli E, Reis GM. **Ecological study of Paracoccidioides brasiliensis in soil: growth ability, conidia production and molecular detection.** *BMC Microbiol* 2007;7:92 CrossRef Medline
6. Wanke B, Aide MA. **Chapter 6: paracoccidioidomycosis.** *J Bras Pneumol* 2009;35:1245–49 CrossRef Medline
7. Coutinho ZF, Silva D, Lazera M, et al. **Paracoccidioidomycosis mortality in Brazil (1980-1995).** *Cad Saúde Pública* 2002;18:1441–54 CrossRef Medline
8. Ajello L, Polonelli L. **Imported paracoccidioidomycosis: a public health problem in non-endemic areas.** *Eur J Epidemiol* 1985;1:160–65 CrossRef Medline
9. Kamei K, Sano A, Kikuchi K, et al. **The trend of imported mycoses in Japan.** *J Infect Chemother* 2003;9:16–20 CrossRef Medline
10. Buitrago MJ, Cuenca-Estrella M. **Current epidemiology and laboratory diagnosis of endemic mycoses in Spain [in Spanish].** *Enferm Infecc Microbiol Clin* 2012;30:407–13 CrossRef Medline
11. Laccourreye O, Mirghani H, Brasnu D, et al. **Imported acute and isolated glottic paracoccidioidomycosis.** *Ann Otol Rhinol Laryngol* 2010;119:89–92 CrossRef Medline
12. Onda H, Komine M, Murata S, et al. **Letter: imported paracoccidioidomycosis in Japan.** *Dermatol Online J* 2011;17:11 Medline
13. Van Damme PA, Bierenbroodspot F, Telgtt DS, et al. **A case of imported paracoccidioidomycosis: an awkward infection in the Netherlands.** *Med Mycol* 2006;44:13–18 CrossRef Medline
14. Walker SL, Pembroke AC, Lucas SB, et al. **Paracoccidioidomycosis presenting in the U.K.** *Br J Dermatol* 2007;158:624–26 CrossRef Medline
15. Rosa Junior M, Baldon IV, Amorim AFC, et al. **Imaging paracoccidioidomycosis: a pictorial review from head to toe.** *Eur J Radiol* 2018;103:147–62 CrossRef Medline
16. Martinez R. **Epidemiology of paracoccidioidomycosis.** *Rev Inst Med Trop Sao Paulo* 2015;57:11–20 CrossRef Medline
17. Benard G. **An overview of the immunopathology of human paracoccidioidomycosis.** *Mycopathologia* 2008;165:209–21 CrossRef Medline
18. Finamor LP, Muccioli C, Martins MC, et al. **Ocular and central nervous system paracoccidioidomycosis in a pregnant woman with acquired immunodeficiency syndrome.** *Am J Ophthalmol* 2002;134:456–59 CrossRef Medline
19. de Almeida SM, Queiroz-Telles F, Teive HA, et al. **Central nervous system paracoccidioidomycosis: clinical features and laboratorial findings.** *J Infect* 2004;48:193–98 CrossRef Medline
20. Gasparetto EL, Liu CB, de Carvalho Neto A, et al. **Central nervous system paracoccidioidomycosis: imaging findings in 17 cases.** *J Comput Assist Tomogr* 2003;27:12–17 CrossRef Medline
21. Magalhaes AC, Bacheschi LA, Caramelli P, et al. **Paracoccidioidomycosis of the central nervous system: study of 5 cases by magnetic resonance [in Portuguese].** *Rev Hosp Clin Fac Med Sao Paulo* 1993;48:94–97 Medline
22. Duarte AL, Baruffa G, Terra HB, et al. **Systemic paracoccidioidomycosis with central nervous system involvement [in Portuguese].** *Rev Soc Bras Med Trop* 1999;32:439–42 CrossRef Medline
23. Correa RB, Puccioni-Sohler M, Artemenko SR, et al. **An uncommon neurologic presentation in the course of paracoccidioidomycosis: report of a case [in Portuguese].** *Arq Neuropsiquiatr* 1991;49:456–59 CrossRef Medline

24. de Moura LP, Raffin CN, del Negro GM, et al. **Paracoccidioidomycosis evidencing spinal cord involvement treated with success by fluconazole [in Portuguese].** *Arq Neuropsiquiatr* 1994;52:82–86 CrossRef Medline
25. Pereira WC, Tenuto RA, Raphael A, et al. **Brain localization of South American blastomycosis: considerations apropos of 9 cases [in Portuguese].** *Arq Neuropsiquiatr* 1965;23:113–26 CrossRef Medline
26. de Almeida SM. **Central nervous system paracoccidioidomycosis: an overview.** *Braz J Infect Dis* 2005;9:126–33 CrossRef Medline
27. Toh CH, Wei KC, Chang CN, et al. **Differentiation of pyogenic brain abscesses from necrotic glioblastomas with use of susceptibility-weighted imaging.** *AJNR Am J Neuroradiol* 2012;33:1534–38 CrossRef Medline
28. Peçanha PM, Batista Ferreira ME, Massaroni PM, et al. **Paracoccidioidomycosis: epidemiological and clinical aspects in 546 cases studied in the state of Espirito Santo, Brazil.** *Am J Trop Med Hyg* 2017;97:836–44 CrossRef Medline
29. Elias J Jr, dos Santos AC, Carlotti CG Jr, et al. **Central nervous system paracoccidioidomycosis: diagnosis and treatment.** *Surg Neurol* 2005;63(Suppl 1):S13–21; discussion S21 CrossRef Medline
30. Pedro RDJ, Branchini ML, de Lucca RS, et al. **Paracoccidioidomycosis of the central nervous system: apropos of 2 cases [in Portuguese].** *Rev Inst Med Trop Sao Paulo* 1980;22:269–74 Medline
31. Lorenzoni PJ, Chang MR, Paniago AM, et al. **Paracoccidioidomycosis meningitis: case report [in Portuguese].** *Arq Neuropsiquiatr* 2002;60:1015–18 CrossRef Medline
32. Francesconi F, Francesconi do Valle AC, Silva MT, et al. **International issues: meningoencephalitis due to Paracoccidioides brasiliensis.** *Neurology* 2008;71:e65–67 CrossRef Medline
33. Reis F, Collier PP, Souza TF, et al. **Neuroparacoccidioidomycosis (NPCM): magnetic resonance imaging (MRI) findings.** *Mycopathologia* 2013;175:181–86 CrossRef Medline
34. Rodacki MA, De Toni G, Borba LA, et al. **Paracoccidioidomycosis of the central nervous system: CT findings.** *Neuroradiology* 1995;37:636–41 CrossRef Medline
35. Teive HA, Zanatta A, Germiniani FM, et al. **Holmes' tremor and neuroparacoccidioidomycosis: a case report.** *Mov Disord* 2002;17:1392–94 CrossRef Medline
36. Faria AV, Dabus GC, Zanardi VA, et al. **Proton magnetic resonance spectroscopy and magnetic resonance imaging findings in a patient with central nervous system paracoccidioidomycosis.** *J Neuroimaging* 2004;14:377–79 CrossRef Medline
37. Magalhaes AC, Caramelli P, Silva ED, et al. **Magnetic resonance imaging in intracranial paracoccidioidomycosis.** *J Neuroimaging* 1993;3:216–19 CrossRef Medline

Multinodular and Vacuolating Posterior Fossa Lesions of Unknown Significance

A. Lecler, J. Bailleux, B. Carsin, H. Adle-Biassette, S. Baloglu, C. Bogey, F. Bonneville, E. Calvier, P.-O. Comby, J.-P. Cottier, F. Cotton, R. Deschamps, C. Diard-Detoeuf, F. Ducray, L. Duron, C. Drissi, M. Elmaleh, J. Farras, J.A. Garcia, E. Gerardin, S. Grand, D.C. Jianu, S. Kremer, N. Magne, M. Mejdoubi, A. Moulignier, M. Ollivier, S. Nagi, M. Rodallec, J.-C. Sadik, N. Shor, T. Tourdias, C. Vandendries, V. Broquet, and J. Savatovsky; for the ENIGMA Investigation Group (EuropeaN Interdisciplinary Group for MVNT Analysis)

ABSTRACT

SUMMARY: Multinodular and vacuolating neuronal tumor of the cerebrum is a rare supratentorial brain tumor described for the first time in 2013. Here, we report 11 cases of infratentorial lesions showing similar striking imaging features consisting of a cluster of low T1-weighted imaging and high T2-FLAIR signal intensity nodules, which we referred to as multinodular and vacuolating posterior fossa lesions of unknown significance. No relationship was found between the location of the lesion and clinical symptoms. A T2-FLAIR hypointense central dot sign was present in images of 9/11 (82%) patients. Cortical involvement was present in 2/11 (18%) of patients. Only 1 nodule of 1 multinodular and vacuolating posterior fossa lesion of unknown significance showed enhancement on postcontrast T1WI. DWI, SWI, MRS, and PWI showed no malignant pattern. Lesions did not change in size or signal during a median follow-up of 3 years, suggesting that multinodular and vacuolating posterior fossa lesions of unknown significance are benign malformative lesions that do not require surgical intervention or removal.

ABBREVIATIONS: IQR interquartile range; MVNT = multinodular and vacuolating neuronal tumor of the cerebrum; MV-PLUS = multinodular and vacuolating posterior fossa lesions of unknown significance

Multinodular and vacuolating neuronal tumor of the cerebrum (MVNT) is a rare brain tumor described for the first time in 2013 and added in the World Health Organization Classification of Tumors of the Central Nervous System in 2016.[1,2] Its prevalence and pathophysiology are unknown. It is often asymptomatic and discovered incidentally. It remains unclear whether MVNT should be considered a true neoplasm or a malformative lesion.[1-7]

MVNTs have been reported to show highly suggestive imaging features, especially with MR imaging.[8-16] MVNT consists of the coalescence of small T2-weighted imaging and T2-FLAIR

Received June 10, 2019; accepted after revision July 27.

From the Departments of Neuroradiology (A.L., J.B., L.D., J.-C.S., C.V., V.B., J.S.) and Neurology (R.D., A.M.), Fondation Ophtalmologique A. Rothschild, Paris, France; Department of Radiology (B.C., J.S.), Centre Hospitalier Régional Universitaire de Rennes, Rennes, France; Department of Pathology (H.A.-B.), Lariboisière Hospital, Paris Diderot, Paris-Cité-Sorbonne University, Paris, France; Department of Radiology (S.B., S.K.), University Hospital of Strasbourg, Strasbourg, France; Department of Neuroradiology (C.B.), Centre Hospitalier Universitaire Limoges, Limoges, France; Department of Neuroradiology (F.B.), Hôpital Pierre-Paul-Riquet, Centre Hospitalier Universitaire Purpan, Toulouse, France; Neurology Department (E.C., J.A.G.), Hôpital René et Guillaume-Laënnec, Centre Hospitalier Universitaire de Nantes, Saint-Herblain, France; Department of Vascular and Interventional Radiology (P.-O.C.), Image-Guided Therapy Center, François-Mitterrand University Hospital, Dijon Cedex, France; Department of Radiology (J.-P.C.), Centre Hospitalier Régional Universitaire de Tours, Tours, France; Brain and Imaging Laboratory (J.-P.C.), UMR U930, National Institute for Health and Medical Research, François-Rabelais University, Tours, France; Service de Radiologie (F.C.), Centre Hospitalier Lyon-Sud, Hospices Civils de Lyon, University Claude Bernard Lyon 1, Lyon, France; Centre de Recherche en Acquisition et Traitement de l'Image pour la Santé (CREATIS) (F.C.), National Institute for Health and Medical Research U1044/Centre National de la Recherche Scientifique (CNRS) Unité Mixte de Recherche (UMR) 5220, Lyon, France; Department of Neurology (C.D.-D.), CH Sainte-Périne, Paris, France; Department of Neuro-Oncology (F.D.), Lyon French Reference Center of Paraneoplastic Neurological Syndrome, Hospices Civils de Lyon, Hôpital Neurologique, Bron Cedex, France; Synatac Team (F.D.), NeuroMyoGene Institut, National Institute for Health and Medical Research U1217/Centre National de la Recherche Scientifique (CNRS) Unité Mixte de Recherche (UMR) 5310, Lyon, France; University Claude Bernard Lyon 1 (F.D.), Lyon, France; Institut National de Neurologie (C.D., S.N.), Service de Neuroradiologie, Université de Tunis El Manar, Faculté de Médecine de Tunis, Tunis, Tunisia; Pediatric Radiology Department (M.E.), Robert Debré Hospital, Paris, France; Jordi Radiologia C/de la Roda (J.F.), Andorra la Vella, Andorra; Department of Neuroradiology and MRI (E.G., N.M.), Rouen University Hospital, Rouen, France; Neuroradiologie Diagnostique et Interventionnelle et IRM Nord (S.G.), Centre Hospitalier et Universitaire de Alpes Grenoble, Grenoble, France; Department of Neurology (D.C.J.), Victor Babes University of Medicine and Pharmacy, Timisoara, Romania; Department of Neuroradiology (M.M.), University Hospital of Martinique, Fort-de-France, Martinique, France; Groupe Hospitalier Pellegrin (M.O.), Bordeaux, France; Clinique les Berges du Lac (S.N.), les Berges du Lac, Tunis, Tunisia; Centre d'Imagerie Centre Cardiologique du Nord (M.R.), CCN, Saint-Denis, France; Department of Neuroradiology (N.S.), Pitié-Salpêtrière Hospital, Paris, France; Service de Neuroimagerie Diagnostique et Thérapeutique (T.T.), Centre Hospitalier Universitaire de Bordeaux et National Institute for Health and Medical Research U1215, Université de Bordeaux, Bordeaux, France; Centre d'Imagerie Médicale Paris 15ème (C.V.), RMX, Paris, France; Department of Neuroradiology (V.B.), Centre Hospitalier Universitaire Lille, Lille, France; and Imagerie Paris 13 (J.S.), Paris, France.

Please address correspondence to Augustin Lecler, MD, PhD, Department of Neuroradiology, Fondation Ophtalmologique Adolphe de Rothschild, 25 rue Manin, 75019 Paris, France; e-mail: alecler@for.paris; @RothNeuroRad

Indicates article with supplemental on-line table.

Indicates article with supplemental on-line photo.

http://dx.doi.org/10.3174/ajnr.A6223

hyperintense nodules in subcortical and juxtacortical areas, with rare or no postcontrast enhancement. It is considered a "leave-me-alone" lesion because of the absence of malignancy criteria and the lack of evolutivity on follow-up MRIs.[8,9]

All MVNTs reported so far in the literature involved the supratentorial part of the brain. We report 11 patients from 24 international centers with lesions exhibiting a remarkably similar pattern of imaging findings in the posterior fossa, which we will refer to in this article as multinodular and vacuolating posterior fossa lesions of unknown significance (MV-PLUS).

The aim of our study was to describe the MR imaging characteristics at diagnosis and during follow-up.

CASE SERIES

Study Design

We conducted a multicenter retrospective study in 24 international centers specializing in neurologic diseases. This study was approved by our institutional Research Ethics Board (Fondation Ophtalmologique A.Rothschild) and adhered to the tenets of the Declaration of Helsinki. This study follows the Strengthening Reporting of Observational Studies in Epidemiology (STROBE) guidelines.

Patients

From July 2014 to February 2019, seventy-four patients with a suspicion of MVNT were identified and collected from the PACS of 24 international centers. Inclusion criteria were the following: 1) the presence of a lesion suggestive of MVNT on MR imaging, defined as a subcortical or juxtacortical lesion consisting of clusters of discrete or confluent high T2-FLAIR signal intensity small nodules; 2) the absence of an obvious differential diagnosis such as asymmetric enlargement of perivascular spaces, defined as smoothly demarcated fluid-filled cysts showing the same attenuation or intensity as CSF; cortical dysplasia, defined as a cortical thickening with general blurring at the white matter–gray matter junction; or a low-grade glial lesion defined as a cortically centered rounded mass with regular margins, with or without postcontrast enhancement; and 3) with a minimum patient follow-up of 12 months.

Among them, 12/74 (16%) were located in the posterior fossa, thus, they could not be strictly considered MVNT because MVNT refers, by definition, to lesions involving the cerebrum. One of these 12 patients had an associated brain stem glioblastoma and was excluded. The remaining 11 patients were included for analysis. Their lesions will be referred to as MV-PLUS throughout this article.

Clinical Charts

All patients' medical charts were systematically reviewed. Demographic features were recorded as well as symptoms prompting imaging and clinical reports, including a comprehensive neurologic examination and follow-up. The presence of a relationship between the location of MV-PLUS and extension and clinical symptoms was evaluated and assessed as follows: no relationship, possible relationship, or definite relationship.

MR Imaging

All MR imaging examinations were performed on 3T scanners with a 16- or a 32-channel head coil. The minimal common protocol included multiplanar or 3D-T1- and T2-FLAIR-weighted imaging. Depending on the centers, postcontrast T1WI, T2WI, high-resolution T2WI, DWI, T2*WI or SWI. PWI and proton MRS were acquired in 3 (27%) patients. A single-voxel point-resolved proton spectroscopy sequence with a short TE of 35 ms was used for all 3 patients. A single-voxel point-resolved proton spectroscopy sequence with a long TE of 135 ms was used for 2 patients. Voxel placement included both the lesion and normal tissue with a ratio of approximately 80%/20%, respectively.

Image Analysis

MR imaging examinations were anonymized and sent to a single core laboratory for reading. Three readers, 1 radiologist with 1 year of experience who had previously studied MVNT extensively prior this study and had acquired substantial expertise in MVNT (V.B.) and 2 neuroradiologists with 4 and 9 years of experience respectively (J.B. and A.L.) reviewed all MRIs in a consensus analysis. All reading sessions were completed on a dedicated workstation using Horos software (Nimble Co, Annapolis, Maryland).

The readers assessed the following characteristics of MV-PLUS at diagnosis and during follow-up:

- Precise locations in the posterior fossa, divided into the 6 following areas: vermis, left or right cerebellar hemisphere, left or right cerebellar peduncle, and brain stem. The center of the lesion and all areas involved were reported separately.
- Overall size defined by the longest diameter of the lesion on T2-FLAIR. The size of the nodules of each lesion was reported as well.
- Signal intensity on T1-, T2-, and T2-FLAIR-weighted imaging. Signal was compared with that of the normal-appearing cerebellar white matter.
- The presence of enhancement on postcontrast T1WI.
- The presence of a restriction of the diffusion on DWI.
- The presence of intratumoral susceptibility signal or a blooming on T2* or SWI.
- Measurement of the relative CBV and relative CBF on PWI. Two ROIs were drawn: the first one inside the largest nodule of a MV-PLUS, the second one in a healthy cerebellar white matter region. Both ROIs were equal in size.
- Quantification of MRS metabolites at 2 TEs (35 and 135 ms). We calculated 3 indices: choline/creatine, choline/*N*-acetyl aspartate, and *N*-acetyl aspartate/creatine.
- The presence of a T2-FLAIR central dot sign, defined as a T2-FLAIR hypointense punctiform signal at the center of at least 1 hyperintense nodule.
- The type of margins between the nodules and the adjacent normal-appearing white matter, defined as sharp or blurred.
- The presence of cortical involvement.
- The presence of a mass effect, defined as any shift in any of the intracranial structures, including ventricles.
- Associated imaging abnormalities.

The readers assessed the presence of a change in the size or the signal of MV-PLUS during follow-up. The size was defined

by the longest diameter of the lesion on FLAIR. 3D reformatting and coregistration were performed for readers to measure the lesion in the exact same plane as in the first MR imaging. A size change was defined as positive in the case of a change superior to or equal to 5% of initial size. A signal change was defined as positive in the case of a change of at least 1 component of the signal of the lesion on any of the sequences used, compared with the normal-appearing cerebellar white matter.

Statistical Analysis

Analyses were conducted using R software, Version 3.3.2.[17] Categoric data were reported as a number (percentage) as appropriate. Continuous data were reported as median with interquartile range or mean ± SD as appropriate.

Table 1: Patient characteristics and clinical data

	No. of Patients ($n = 11$)	Percentage (%)
Sex		
Male	5	45
Female	6	55
Age (mean) (yr)	37 ± 13	
Clinical symptoms prompting initial imaging		
Headache	4	36
Meningioma screening	2	18
Bilateral upper arm paresthesia	1	9
Hearing loss	1	9
Tinnitus	1	9
Dizziness	1	9
Aneurysm screening	1	9

RESULTS

Patient Characteristics and Clinical Data

Eleven patients were included (6 women and 5 men; mean age, 37 ± 13 years; range, 22–70 years). Headache was the most frequent symptom prompting initial imaging. No relationship was found between the location of MV-PLUS and clinical symptoms. Median follow-up was 3.6 years (interquartile range [IQR] = 1 year), No patient developed symptoms potentially related to the MV-PLUS. No patient underwent an operation during follow-up. Detailed patient characteristics are presented in Table 1.

MV-PLUS MR Imaging Characteristics at Diagnosis

Lesions were all located in the cerebellum. No lesion involved the brain stem. Almost all lesions centered on the vermis extended laterally to the cerebellar hemispheres: 5/7 (71%). Conversely, none of the lesions centered on a cerebellar hemisphere extended to the vermis (Fig 1).

Lesions were all hyperintense on T2-FLAIR and T2WI and all hypointense on T1WI except for 1. One patient presented with postcontrast enhancement of the nodule of 1 lesion (Fig 2). A central dot sign was visible in 9/11 (82%) patients (Online Figure). Cortical involvement was present in 2/11 (18%) patients. Detailed MR imaging characteristics are presented in Table 2 and the On-line Table.

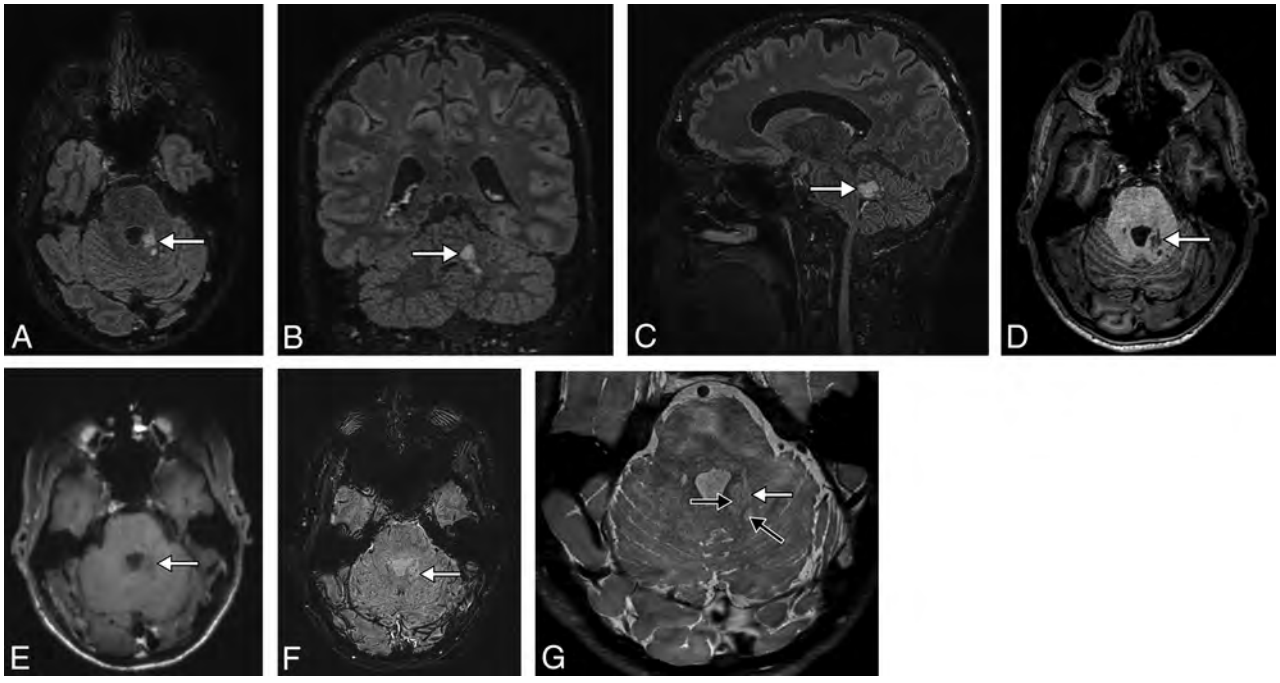

FIG 1. A 38-year-old man presenting with headache. 3D-T2-FLAIR reformatted in the axial (*A*), coronal (*B*), and sagittal (*C*) planes shows a high-signal intensity lesion (*white arrow*) of the posterior part of the left cerebellar peduncle, consisting of a coalescence of small nodules, highly suggestive of MV-PLUS. The lesion is hypointense on axial T1WI (*D*) and does not enhance on postcontrast T1WI (*E*). SWI (*F*) shows no blooming or intratumoral susceptibility signal. High-resolution T2WI (*G*) shows hypointensity in the center of hyperintense nodules (*black arrows*), consistent with a central dot sign. Note the small mass effect and distortion of the lateral margin of the fourth ventricle.

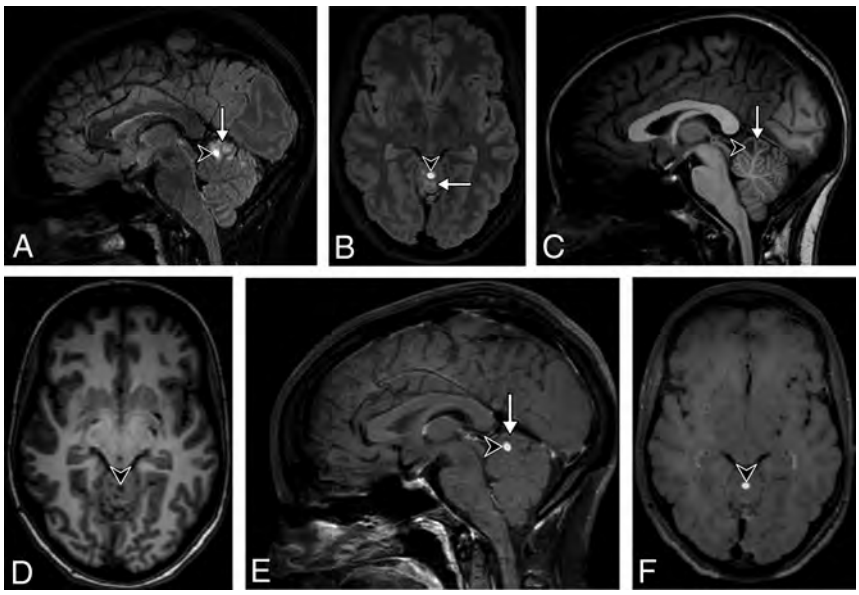

FIG 2. A 31-year-old woman presenting with headache. 3D-T2-FLAIR reformatted in the sagittal (*A*) and axial (*B*) planes shows a high signal intensity multinodular lesion (*arrow*) of the upper vermis, highly suggestive of an MV-PLUS. Almost all clustered nodules are hypointense on 3D-T1WI reformatted in the sagittal (*C*) and axial (*D*) planes and do not enhance on postcontrast 3D-T1WI reformatted in the sagittal (*E*) and axial (*F*) planes. One anterior nodule (*arrowhead*) shows a substantially higher T2-FLAIR and lower T1 signal intensity than all the others, with a marked enhancement after contrast injection. Note the T2-FLAIR hypointense central dot sign does not enhance on postcontrast T1WI.

MV-PLUS MR Imaging Characteristics during Follow-Up

The median follow-up was 3.1 years (IQR = 1 year). None of the described lesions changed size or signal during follow-up.

DISCUSSION

We describe the imaging characteristics of a new entity that we referred to as MV-PLUS. This entity has never been described in the literature to the best of our knowledge.

MV-PLUS imaging features consist of the coalescence of small T1WI hypointense and T2-FLAIR hyperintense nodules in subcortical and juxtacortical areas. They are very similar to those described in MVNT, a rare and recently described brain tumor,[8-14] which was added in the World Health Organization Classification of Tumors of the Central Nervous System in 2016.[1,2] None of the case reports and small series published in the literature so far have reported posterior fossa MVNT. Among 74 patients analyzed in 24 international centers showing MR imaging features highly suggestive of MVNT, we found only 11 (15%) posterior fossa lesions, suggesting that MV-PLUS might be 10 times rarer than MVNT.

Similar to MVNT, MV-PLUS showed no sign of malignancy on MR imaging and an absence of evolutivity during follow-up.[8,9] In our study, MR imaging showed neither restriction on DWI nor intratumoral susceptibility signal on T2* or SWI. PWI showed no increase in relative CBF or CBV. MRS showed no increase in choline peaks. There was no or only a small mass effect on the surrounding posterior fossa structures. Moreover, no changes in size or signal could be observed during follow-up, and no relationship was observed between the location of lesions and clinical symptoms. Only 1 nodule in 1 patient showed enhancement after contrast injection, which is similar to the low rate of enhancement reported for MVNT in the literature.[8,9] However, this nodule had a very distinct signal compared with other nodules throughout all sequences. Enhancing MVNTs were reported in the literature to show only faint enhancement, suggesting that it might be a distinct lesion.[8,9]

Differential diagnoses for posterior fossa intra-axial lesions encompass a wide range of diseases, such as ischemic lesions, inflammatory diseases like multiple sclerosis, infectious diseases, vascular malformations, neoplastic lesions, degenerative lesions like ataxias, toxic lesions, malformative lesions like dysplastic cerebellar gangliocytoma, or normal variants like enlargement of perivascular spaces.[18-20] However, both the location in juxtacortical or subcortical regions and typical features such as the presence of clusters of discrete or confluent high T2-FLAIR signal intensity small nodules make the diagnosis of MV-PLUS very likely. Moreover, we reported the presence of a T2-FLAIR hypointense central dot sign for most MV-PLUS lesions. This central dot sign was present in most nodules of >4 mm and was more conspicuous on high-resolution T2WI. It was missing in images of 2 patients with low-resolution imaging. This central dot sign was already reported in the literature in MVNT, but its prevalence is not known.[8,10] It might reflect the presence of a high protein or a solid component within the vacuolated areas, which is a typical pathology feature reported in MVNT histopathologic studies.[1,7] It might be an interesting imaging criterion that could increase readers' confidence when diagnosing MV-PLUS. This sort of evidence might help rule out differential diagnoses.

Two patients had very subtle cortical involvement on imaging, which has not been reported in MVNT.[8,9] However, these 2 patients had low-resolution images, with 2D-FLAIR images with a section thickness of 3 and 5 mm, respectively. Distinguishing cortical and subcortical areas is more challenging in the posterior fossa than in supratentorial regions. Thus, this appearance might be due to partial averaging rather than true cortical involvement and should be confirmed by other observations with high-resolution imaging.

MV-PLUS should probably be considered a leave-me-alone lesion, requiring no operation to confirm the diagnosis. Its nature remains unknown, and it is not clear whether it should be considered a neoplasm or a malformation. However, the absence of changes during follow-up, the absence of or only a small mass effect or malignant pattern on MR imaging, and the absence of a relationship with clinical symptoms might suggest that MV-

Table 2: MR imaging characteristics of multinodular and vacuolating posterior fossa lesions of unknown significance (MV-PLUS) at diagnosis and during follow-up

	No. of Patients	Percentage (%)
Location		
Center of the lesion		
Cerebellum		
Vermis	7/11	64
Left cerebellar hemisphere	1/11	9
Right cerebellar hemisphere	2/11	18
Left cerebellar peduncle	1/11	9
Right cerebellar peduncle	0/11	0
Brain stem	0/11	0
All areas involved		
Cerebellum		
Vermis	7/11	64
Left cerebellar hemisphere	3/11	27
Right cerebellar hemisphere	8/11	73
Left cerebellar peduncle	1/11	9
Right cerebellar peduncle	0/11	0
Brain stem	0/11	0
Overall size (median) (IQR) (mm)	27 (24)	
Size of the nodules (median) (IQR) (mm)	4 (5)	
DWI		
Restriction	0/11	0
T2* or SWI		
Presence of ITSS	0/11	0
Blooming	0/11	0
PWI		
rCBV (median) (IQR)	0.62 (0.06)	
rCBF (median) (IQR)	0.61 (0.06)	
MRS		
TE = 35 ms		
Choline/creatine (median) (IQR)	0.9 (0.2)	
Choline/*N*-acetyl aspartate (median) (IQR)	0.9 (0.1)	
N-acetyl aspartate/creatine (median) (IQR)	1 (0.2)	
TE = 135 ms		
Choline/creatine (median) (IQR)	1.2 (0)	
Choline/*N*-acetyl aspartate (median) (IQR)	1 (0)	
N-acetyl aspartate/creatine (median) (IQR)	1.2 (0)	
Type of margins		
Sharp	11/11	100
Blurred	0/11	0
Mass effect		
Yes	4/11	36
No	7/11	64
Associated imaging abnormalities		
None	7/11	64
Small-vessel disease	3/11	27
Colloid cyst	1/11	9
Cholesteatoma	1/11	9

Note:—ITSS indicates intratumoral susceptibility signal; rCBV, relative CBV; rCBF, relative CBF.

PLUS is a benign malformative lesion rather than a true neoplasm. However, we advise clinicians to perform a comprehensive protocol when characterizing possible MV-PLUS, including thin-millimetric T2- or T2-FLAIR sequences to detect the central dot sign, and MR spectroscopy as well as PWI to show the absence of malignant criteria. We also suggest long-term follow-up to assess any changes in size or signal.

Our study has some limitations: First, although we analyzed patients from 24 international centers, the results of the study are somewhat limited by the relatively small number of patients. Two asymptomatic patients underwent MR imaging for meningioma screening, representing 18% of our population, which is higher than expected and might be due to a selection bias. The first patient had a sibling recently diagnosed with a meningioma. The second patient had been taking cyproterone acetate for a long time, which had been reported to increase the chance of developing a meningioma.

Second, 2 centers contributed >1 case. Most of the 24 centers where clinicians were aware of MVNT had not identified any patients with similar imaging findings, suggesting that MV-PLUS might be very rare.

Third, none of our patients underwent an operation; thus, we do not have any histopathologic evidence showing that MV-PLUS might be, in fact, MVNT. The posterior fossa is a very challenging region for surgery, and none of our patients had clinical symptoms related to their lesions; thus, none of them became surgical candidates. This is why we chose to remain cautious and to refer to this entity as MV-PLUS instead of posterior fossa MVNT. Given the benign MR imaging characteristics of MV-PLUS and the absence of evolutivity with time, it might be extremely difficult to obtain pathologic details in the near future.

Fourth, the examinations were performed on various MR imaging devices from different vendors. Protocols were heterogeneous among the centers, mixing comprehensive multiparametric protocols and basic low-resolution MR imaging protocols. Therefore, our analysis of MV-PLUS might not be optimal. Some of the information we provide, such as the absence of a central dot sign or the involvement of the cortex, might be inaccurate because of low-resolution images in 2 patients. PWI and MRS were performed in only 3/11 (27%) patients; thus, the quantitative values we provided might be inaccurate. Moreover, only single-voxel spectroscopy was performed, which might have resulted in volume averaging with normal tissue.

CONCLUSIONS

We provided the first description of a new entity that we referred to as MV-PLUS. Our observation might help clinicians diagnose this entity, adapting their patient management and possibly avoiding an operation.

Disclosures: Fabrice Bonneville—*UNRELATED*: *Employment*: Année. Elisabeth Auffrey-Calvier—*UNRELATED*: *Board Membership*: optimizing the MRI practices of patient with Sclérose en Plaques (SEP) in the Hôpitaux Universitaires Grand Ouest (HUGO) inter-region; *Consultancy*: place of imaging in the differential diagnosis of neurologic pathologies, focus on multiple sclerosis. Roman Deschamps—*UNRELATED*: *Support for Travel to Meetings for the Study or Other Purposes*: Biogen. Julien Savatovsky—*UNRELATED*: *Payment for Lectures Including Service on Speakers Bureaus:* Novartis, Biogen, Medtronic, Philips Healthcare, Sanofi; *Travel/Accommodations/Meeting Expenses Unrelated to Activities Listed*: Bayer. Stéphane Kremer—*UNRELATED*: *Board Membership*: Bayer; *Payment for Lectures Including Service on Speakers Bureaus*: Bayer Healthcare, Novartis, Biogen, Roche; *Travel/Accommodations/Meeting Expenses Unrelated to Activities Listed*: Biogen.

ACKNOWLEDGMENT

Laura McMaster provided professional English-language medical editing of this article.

REFERENCES

1. Huse JT, Edgar M, Halliday J, et al. **Multinodular and vacuolating neuronal tumors of the cerebrum: 10 cases of a distinctive seizure-associated lesion: multinodular and vacuolating neuronal tumors.** *Brain Pathol* 2013;23:515–24 CrossRef Medline
2. Louis DN, Perry A, Reifenberger G, et al. **The 2016 World Health Organization Classification of Tumors of the Central Nervous System: a summary.** *Acta Neuropathol* 2016;131:803–20 CrossRef Medline
3. Choi E, Kim SI, Won JK, et al. **Clinicopathological and molecular analysis of multinodular and vacuolating neuronal tumors of the cerebrum.** *Hum Pathol* 2019;86:203–12 CrossRef Medline
4. Calderon-Garcidueñas AL, Mathon B, Lévy P, et al. **New clinicopathological associations and histoprognostic markers in ILAE types of hippocampal sclerosis.** *Brain Pathol* 2018;28:644–55 CrossRef Medline
5. Pekmezci M, Stevers M, Phillips JJ, et al. **Multinodular and vacuolating neuronal tumor of the cerebrum is a clonal neoplasm defined by genetic alterations that activate the MAP kinase signaling pathway.** *Acta Neuropathol* 2018;135:485–88 CrossRef Medline
6. Thom M, Liu J, Bongaarts A, et al. **Multinodular and vacuolating neuronal tumors in epilepsy: dysplasia or neoplasia?** *Brain Pathol* 2018;28:155–71 CrossRef Medline
7. Yamaguchi M, Komori T, Nakata Y, et al. **Multinodular and vacuolating neuronal tumor affecting amygdala and hippocampus: a quasi-tumor?** *Pathol Int* 2016;66:34–41 CrossRef Medline
8. Nunes RH, Hsu CC, da Rocha AJ, et al. **Multinodular and vacuolating neuronal tumor of the cerebrum: a new "leave-me-alone" lesion with a characteristic imaging pattern.** *AJNR Am J Neuroradiol* 2017;38:1899–904 CrossRef Medline
9. Alsufayan R, Alcaide-Leon P, de Tilly LN, et al. **Natural history of lesions with the MR imaging appearance of multinodular and vacuolating neuronal tumor.** *Neuroradiology* 2017;59:873–83 CrossRef Medline
10. Badat N, Savatovsky J, Charbonneau F, et al. **Multinodular vacuolating and neuronal tumor of the cerebrum.** *Neurology* 2017;89:304–05 CrossRef Medline
11. Shitara S, Tokime T, Akiyama Y. **Multinodular and vacuolating neuronal tumor: A case report and literature review.** *Surg Neurol Int* 2018;9:63. CrossRef Medline
12. Gonzalez-Quarante LH, Ruiz-Juretschke F, Sola Vendrell E, et al. **Multinodular and vacuolating neuronal tumor of the cerebrum: a rare entity—new case and review of the literature.** *Neurocirugia (Astur)* 2018;29:44–55 CrossRef Medline
13. Makrakis D, Veneris S, Papadaki E. **Multinodular and vacuolating neuronal tumor incidentally discovered in a young man: conventional and advanced MRI features.** *Radiol Case Rep* 2018;13:960–64 CrossRef Medline
14. Fukushima S, Yoshida A, Narita Y, et al. **Multinodular and vacuolating neuronal tumor of the cerebrum.** *Brain Tumor Pathol* 2015;32:131–36 CrossRef Medline
15. Monté A-S, D'Arco F, De Cocker L. **Multinodular and vacuolating neuronal tumor in an adolescent with Klinefelter syndrome.** *Neuroradiology* 2017;59:1187–88 CrossRef Medline
16. Johnson DR, Guerin JB, Giannini C, et al. **2016 updates to the WHO Brain Tumor Classification System: what the radiologist needs to know.** *Radiographics* 2017;37:2164–80 CrossRef Medline
17. **The R Project for Statistical Computing**, 2019. https://www.R-project.org. Accessed March 11, 2019
18. Loevner LA. **Imaging features of posterior fossa neoplasms in children and adults.** *Semin Roentgenol* 1999;34:84–101 CrossRef Medline
19. Gass A, Filippi M, Grossman RI. **The contribution of MRI in the differential diagnosis of posterior fossa damage.** *J Neurol Sci* 2000;172:(Suppl 1):S43–S49 CrossRef Medline
20. Shih Y-Y, De La Garza BH, Huang S, et al. **Comparison of retinal and cerebral blood flow between continuous arterial spin labeling MRI and fluorescent microsphere techniques.** *J Magn Reson Imaging* 2014;40:609–15 CrossRef Medline

Empty Sella Is a Sign of Symptomatic Lateral Sinus Stenosis and Not Intracranial Hypertension

A. Zetchi, M.-A. Labeyrie, E. Nicolini, M. Fantoni, M. Eliezer, and E. Houdart

ABSTRACT

BACKGROUND AND PURPOSE: Empty sella has been reported in patients with idiopathic intracranial hypertension and is thought to be a sign of elevation of intracranial pressure. However, it can also be found in patients with lateral sinus stenosis presenting with isolated pulsatile tinnitus without signs of intracranial hypertension. We hypothesized that the volume of the sella turcica would be similar in both groups of patients undergoing stent placement for lateral sinus stenosis.

MATERIALS AND METHODS: Consecutive patients with idiopathic intracranial hypertension or isolated venous pulsatile tinnitus and undergoing lateral sinus stent placement from January 2012 to December 2017 were included. The primary outcome was the estimated volume of the sella turcica based on preoperative CTA measurements. The ratio of the pituitary gland height/sellar height was calculated on preoperative MR imaging. Sellar volumes were compared among the 3 groups: pulsatile tinnitus, idiopathic intracranial hypertension, and a control group, matched by age and sex.

RESULTS: Eighty-eight patients underwent lateral sinus stent placement. The median age was 37 years, and 94% were women. No difference in age, sex, or body mass index was found among the groups. Patients undergoing venous stent placement had significantly higher sellar volumes than the control group ($P < 0.001$). There was no difference in the sellar volumes ($P = .63$) or gland/sellar height ratios ($P = .25$) between the pulsatile tinnitus and idiopathic intracranial hypertension groups.

CONCLUSIONS: Empty sella is found in 2 differing groups of patients undergoing lateral sinus stent placement, suggesting that it is a radiologic sign of symptomatic hemodynamic lateral sinus stenosis rather than elevated intracranial pressure.

ABBREVIATIONS: BMI = body mass index; GH/SH = ratio of pituitary gland height/sellar height; IIH = idiopathic intracranial hypertension; IPT = isolated venous pulsatile tinnitus

Empty sella is defined as a widening of the sella turcica associated with an intrasellar arachnoidocele. Secondary forms can follow a pituitary operation or trauma.[1] Empty sella is a radiologic sign that has been described in patients with idiopathic intracranial hypertension (IIH)[2-5] and is often reported as a chronic consequence of the elevation of intracranial pressure.[6,7] IIH is associated with a large number of cases with lateral sinus stenosis,[8,9] which is increasingly being treated by lateral sinus stent placement.[10-12] Pulsatile tinnitus may constitute 1 mode of presentation of IIH.[13] Lateral sinus stenosis may also be revealed by pulsatile tinnitus without evidence of intracranial hypertension.[14-17] When pulsatile tinnitus is disabling, stent placement for lateral sinus stenosis may be efficient for suppressing it.[18-20] We therefore hypothesized that an empty sella is a consequence not of the elevation of the intracranial pressure but of the venous sinus stenosis. This stenosis, when symptomatic, may present in the form of either IIH or isolated venous pulsatile tinnitus (IPT). In the current study, we measured and compared the volumes of the sella turcica in patients with sinus stenosis revealed by IIH or IPT and treated by sinus stent placement. We compared the results of these 2 groups with those obtained in a control group of subjects free of venous sinus stenosis.

MATERIALS AND METHODS

Study Population

Consecutive patients undergoing lateral sinus stent placement from January 2012 to December 2017 were screened using a local data base and by cross-referencing it with the data base of the neuroradiology department archives. Patients with the combination of IIH or IPT and radiologic evidence of lateral venous sinus stenosis were included. IPT was defined as a pulsatile tinnitus in

Received April 11, 2019; accepted after revision August 1.

From the Service de Neuroradiologie du Pr Houdart, Hôpital Lariboisière, Paris, France.

Please address correspondence to Akli Zetchi, MD, Service de Neuroradiologie du Pr Houdart, Hôpital Lariboisière, APHP, 2, rue Ambroise Paré, Paris 75010, France; e-mail: akli.zetchi@gmail.com

http://dx.doi.org/10.3174/ajnr.A6210

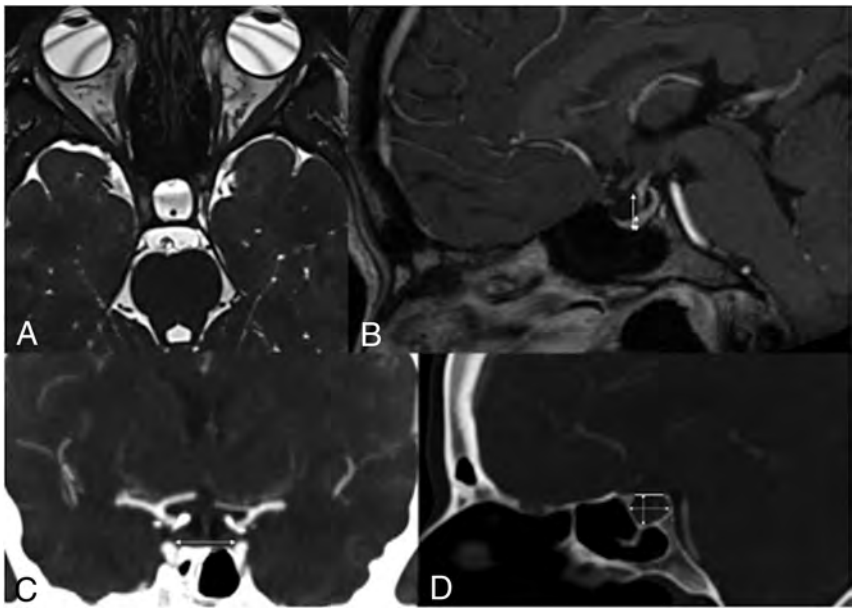

FIG 1. A 47-year-old female patient who presented with right-sided disabling pulsatile tinnitus disappearing on compression of the right jugular vein. MR imaging with an axial CISS sequence (*A*) shows enlargement and CSF infiltration of the sella turcica. Sagittal T1-weighted MR imaging with gadolinium shows flattening of the pituitary gland (*B*). Ratios of pituitary gland height/sellar height were calculated on sagittal reconstruction of a 3D gadolinium-enhanced T1 MRI sequence using the cut showing the thickest section of pituitary gland (*B*). Sellar volumes were estimated on the basis of dimensions measured on a preoperative CTA. The laterolateral dimension of the sella was measured on the coronal MPR of the preoperative CTA as shown in *C* using the longest measurement between the medial walls of the cavernous segments of the internal carotid arteries (*white arrow*). The sellar height and anterior-posterior diameter were measured on the 3D-MPR in the midsagittal plane as shown in *D*. Height was the longest measurement intersecting a line joining the tuberculum and dorsum sellae and the lowest point in the sella. The anterior-posterior measurement was defined as the longest measure on the midsagittal plane (*white arrows*).

relation to a lateral sinus stenosis (ie, disappearing after stent placement of the stenosis) and without clinical signs of IIH. Patients with a current or past history of spontaneous or traumatic CSF leak, sellar pathology including those who underwent transphenoidal surgery, and those who presented with another potential etiology for their pulsatile tinnitus were excluded. Patients with no available preoperative and/or postoperative imaging were also excluded. Patients in whom the venous stent placement procedure failed or was not completed were also excluded. This study was approved by the institutional review board.

Data Collection

Patients' baseline demographic data and body mass index (BMI) were collected. All imaging was independently reviewed by 2 authors, one experienced neurointerventionalist (A.Z.) and a fellow in interventional neuroradiology (E.N.). Trans-stenotic gradients derived from venous manometry and the type of stenosis were also recorded. The primary outcome was defined as the estimated volume of the sella turcica based on measurements on a preoperative CTA. Maximal anterior-posterior (*AP*) and height (*H*) measurements were obtained on midsagittal 3D-MPR reconstruction. Maximal laterolateral (*L*) measurements were obtained on coronal 3D-MPR reconstruction (Fig 1). The volume of the sella turcica (*V*) was estimated on the basis of the formula for an ellipsoid volume:

$$V = \frac{AP \times L \times H}{1,91}.$$

The ratio of the pituitary gland height/sellar height (GH/SH) was also calculated on the basis of preoperative 3D gadolinium-enhanced T1-weighted MR imaging with sagittal reconstruction (Fig 1). The section showing the thickest pituitary gland was chosen.

Diagnosis and Treatment

Most patients were assessed and treated by our senior author (E.H.). Patients presenting with symptoms of IIH according to the modified Dandy criteria[21] were studied by lumbar puncture with opening pressure measurements and an ophthalmologic assessment. Lumbar puncture was not performed on patients with IPT when they were free of any clinical sign of IIH, including headache, papilledema, or cranial nerve VI palsy. Patients with IIH or IPT were studied with CTA and cerebral MR imaging, including 3D-TOF, T1-weighted with gadolinium, and MRV sequences.

CT angiography was performed on Somatom Sensation 64 CT scanner (Siemens, Erlangen, Germany) using the following parameters: section thickness = 0.75 mm; 80 mAs; and 120 kV (peak) per section.

MR imaging examinations were performed on a 3T scanner (Magnetom Skyra; Siemens) with a 64-channel head-neck-spine coil after contrast media administration (0.2 mL/kg) (gadoterate megluimine, Dotarem; Guerbet, Aulnay-sous-Bois, France). We performed the 3D-TOF sequence with the following parameters: FOV = 200 × 200 mm, TR = 21 ms, TE = 3.69 ms, 384 × 278 mm, NEX = 1, and scan time = 4 minutes 40 seconds. We performed a 3D-T1 MPRAGE sequence with the following parameters: FOV = 270 × 270 mm, TR = 2000 ms, TE = 2.68 ms, 320 × 288 mm, NEX = 2, generalized autocalibrating partially parallel acquisition = 2, and scan time = 4 minutes 4 seconds. We also performed a 3D-T2 CISS sequence with the following parameters: FOV = 145 × 145 mm, TR = 6.6 ms, TE = 3.1 ms, 320 × 320 mm, flip angle = 57°, NEX = 1, and scan time = 4 minutes 30 seconds.

When stent placement of the lateral stenosis was considered, a catheter cerebral angiography was performed with the patient

under local anesthesia, and pressure measurements were performed in the lateral sinus proximal and distal to the stenosis. Trans-stenotic gradient measurements were obtained by microcatheter pressure transducer manometry and Verrata fractional flow reserve piezoelectric 0.014-inch microguidewire (Philips Volcano, San Diego, California) velocity and pressure measurements. The gradient was considered high if it was equal or superior to 8 mm Hg.

Patients with confirmed IIH were first treated medically with acetazolamide and lumbar puncture. In case of refractory or recurrent symptoms after a minimum of 4 months of medical treatment, lateral sinus stent placement was proposed. We selected the dominant sinus in IIH. For IPT, disability was assessed on a visual analog scale from 0 to 10. Stent placement was proposed when the score reached or exceeded 5. In this group, venous stent placement was performed on the symptomatic side. Our technique for venous sinus stent placement has been previously described.[22]

Data Analysis

Sellar volumes were compared among 3 groups: patients with IPT, patients with confirmed IIH, and a control group. The sample of control subjects comprised patients with normal findings on CTA after presentation to our emergency department, matched by age and sex. Control subjects were selected if they had no past or present intracranial pathology, no history of pulsatile tinnitus, no clinical sign of IIH, and no radiologic evidence of cerebral venous sinus stenosis. Kruskal-Wallis, ANOVA, and Dunn 2-tailed tests were used. A P value $< .05$ was considered statistically significant. The GH/SH and trans-stenotic gradients were compared between IPT and IIH groups using a Mann-Whitney 2-tailed test. The intraclass correlation coefficient was used to measure the interrater agreement for sellar volumes. An ANCOVA was used to test age, sex, the type of stenosis (intrinsic versus extrinsic), and BMI as potential confounding explanatory variables.

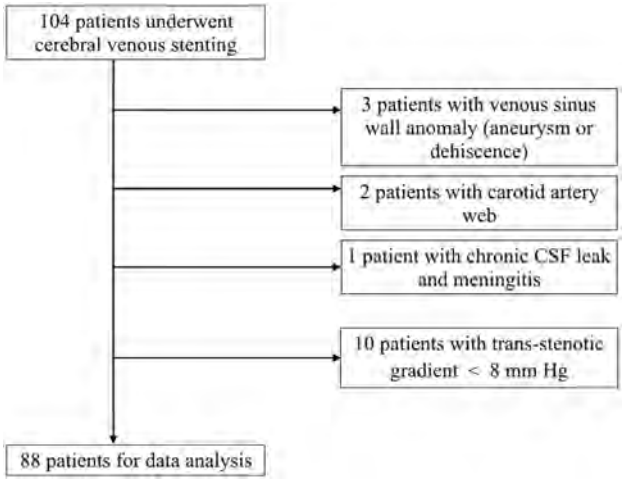

FIG 2. Study flow chart.

Patients' baseline characteristics

	IPT	IIH	Control	*P* Value
No.	34	54	39	
Age (median in years)	39 ± 15	35.5 ± 113	35 ± 14	.65
Women (No. and %)	32 (94.1)	51 (94.4)	36 (92.3)	.91
BMI (mean)	27.7 ± 5.3	31.9 ± 6.7	N/A	.06
Pulsatile tinnitus (%)	100	53.7	N/A	
Lumbar puncture opening pressure (cm H_2O, mean and range)	N/A	31.8 ± 10.6 (21–53)	N/A	

Note:—N/A indicates not available.

RESULTS

A total of 104 patients were screened between January 2012 and December 2017. Sixteen patients were excluded (see the flow chart in Fig 2). The median age of the 88 patients who underwent lateral sinus stent placement was 37 years (range, 20–75 years), and 94% were women. Patients' baseline characteristics are detailed in the Table. No significant difference in age or sex was noted among the 3 groups. The BMI did not differ between the 2 groups of patients with symptomatic sinus stenosis.

The mean sellar volume was 962 ± 317 mm^3 in the IPT group, 1079 ± 455 mm^3 in the IIH group, and 534 ± 118 mm^3 for the control group. Patients with IPT and IIH undergoing venous stent placement had significantly higher sellar volumes than the control group ($P < .001$). There was no difference in the sellar volumes between IPT and IIH groups ($P = .63$) (Fig 3). The intraclass correlation coefficient was 0.782 for sellar volumes between the independent reviewers.

The mean ratio of GH/SH was 0.436 ± 0.21 for the IPT group and 0.375 ± 0.18 for the IIH group ($P = .25$). There was a trend toward higher trans-stenotic gradients for the IIH group (mean, 11.3 ± 6.1 mm Hg) compared with the IPT group (mean, 8.9 ± 5.4 mm Hg) ($P = .07$), as depicted in Fig 4. The ANCOVA showed no association between sellar volumes or GH/SH and age, sex, trans-stenotic gradients, BMI, or the type of venous stenosis.

DISCUSSION

In the current study, we found that the sellar volumes and heights were significantly higher in patients with symptomatic lateral sinus stenosis compared with a sample of control subjects. There was no significant difference in sellar volumes or GH/SH between patients with IPT and IIH. These findings suggest that an empty sella is found in 2 differing groups of patients, both benefiting from venous sinus stent placement. To our knowledge, the sellar characteristics of patients with IPT, but not satisfying the Dandy criteria, have not previously been reported or compared with patients with elevated intracranial pressure and with control subjects. An empty or partially empty sella has been reported in patients with both IPT and no elevated intracranial pressure[23] and patients with IIH.[24] Patients with IIH can present with IPT,[25] and venous sinus stenosis has been observed and treated in both instances.[26,27] However, an empty sella is less commonly observed in

other causes of chronic elevation of intracranial pressure or after venous thrombosis.[28,29] Eisenman et al[30] also observed a high rate of empty sella and transverse sinus stenosis in a series of 40 patients presenting with pulsatile tinnitus who underwent transtemporal surgical reconstruction of sigmoid sinus wall anomalies.

On the basis of our results, we suggest that the arachnoidocele of the sella is not the consequence of an elevation of the intracranial pressure but rather a consequence of a disorder of CSF resorption following the elevation of venous pressure.

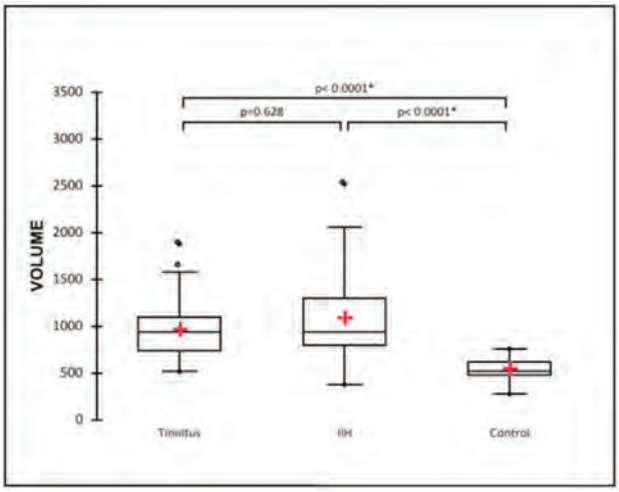

FIG 3. Estimated sellar volumes (cubic millimeters) based on preoperative CTA measurements for patients with isolated venous pulsatile tinnitus and idiopathic intracranial hypertension.

The potential mechanism of pulsatile tinnitus in the context of a cerebral venous sinus stenosis with a significant transstenotic gradient has been previously discussed.[18,30] Flow turbulence secondary to acceleration through the stenosis, combined with the rhythmicity of the additional compression during the systole of venous structures in the vicinity of the inner ear, is hypothesized to explain the pulsatile nature of the tinnitus.

On the other hand, the physiopathology of IIH may be complex, and proposed mechanisms remain to be demonstrated. The default in CSF reabsorption at the arachnoid granulations of the superior sagittal sinus is increasingly being linked to an increased endoluminal pressure in the superior sagittal sinus in the context of hemodynamic stenosis.[31]

Various theories have been suggested to explain the physiopathology of the empty sella: congenital absence or insufficiency of the diaphragm sellae, induced enlargement of the bony sellar compartment, or necrosis of a previous pituitary adenoma.[32-34] More recent work on animal models of CSF turnover pointed out the role of cervical lymphatics.[35-37] CSF that is not reabsorbed through arachnoid granulations at the superior sagittal sinus may reach the cervical lymphatics by tracking along the cranial nerves[38] or the Virchow-Robin spaces.[39] Increased CSF spaces and infiltration of the sella may occur once these compensatory mechanisms are exceeded, and this may explain the radiologic findings in patients with venous sinus stenosis, including an empty sella syndrome.

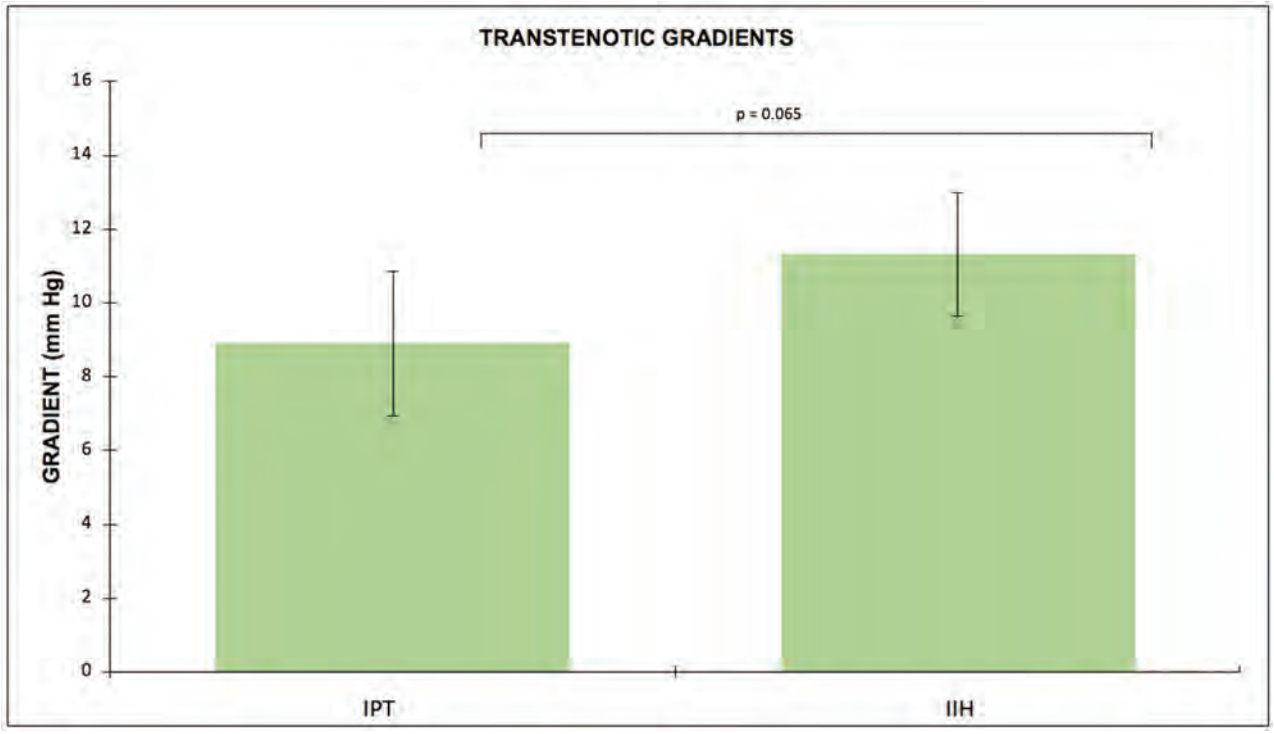

FIG 4. Trans-stenotic gradients (millimeters of mercury) based on local anesthesia venous manometry measurements for patients with isolated venous pulsatile tinnitus and IIH.

We propose that enlarged CSF spaces found in patients with either intracranial hypertension or pulsatile tinnitus are the consequence of a common mechanism—a hemodynamic venous sinus stenosis. The hemodynamic stenosis of the lateral sinuses would, therefore, be a pathologic entity in itself, leading to a disruption of the CSF drainage at the origin of specific radiologic signs of this entity, regardless of the intracranial pressure. We would propose a new name for this entity: "symptomatic lateral sinus stenosis." Levitt et al[20] reported the results of 9 patients without IIH who underwent venous stent placement and grouped them under the terminology "symptomatic venous sinus stenosis." Demonstration of causality remains, however, beyond the scope of the current study.

The reason that some patients with lateral sinus stenosis go on to develop isolated IPT versus IIH remains unclear. We did not find a significant correlation among age, sex, and the type of sinus stenosis. In the current study, we observed a trend to indicate a graded clinical spectrum for symptomatic cerebral venous sinus stenosis. Our study was not primarily designed to and lacks the power to study explanatory variables for the difference between patients with IIH and IPT. Obesity, hormonal factors, brain volumes, associated venous sinus anomalies, and reversibility of the enlarged sella would be additional variables to explore in future research. We elected to exclude patients with associated sigmoid sinus wall anomalies in the current study because endovascular therapy can also be effective in dealing with this etiology of pulsatile tinnitus.[19]

One of the limitations of our study lies in its retrospective nature. Discrimination between patients with IIH and IPT relied on retrospective chart review and on chart annotation or lumbar puncture opening pressures, ophthalmologic assessments, and clinical histories. However, the main outcome was based on prospectively collected radiologic data by 2 independent reviewers. Because lumbar puncture is not part of our routine work-up for patients with IPT, it is possible that some patients in this group had an unrecognized intracranial hypertension. Lumbar puncture was performed in the first 2 patients with IPT considered for venous stent placement. Neither had headache, papilledema, nor sixth cranial nerve palsy. The opening pressures were, respectively, 14 and 16 cm H_2O. Both patients developed a cerebral hypotension syndrome following the lumbar puncture and required a blood patch.

We considered, at that time, that submitting the IPT group to lumbar punctures strictly for academic purposes was unethical, though this choice limits interpretation of the current study. We have since restricted the lumbar punctures to the group of patients presenting with papilledema or otherwise suspected of having IIH. Future research should consider lumbar puncture in patients with IPT as long as the ethical aspects have been debated. Even though MR imaging with a sella turcica protocol would have provided a more accurate estimation of sellar volumes, we elected to use the CTA performed in our institution to help standardize the measurements. We did not repeat an MR imaging at our institution for patients who already had one in another center. Dedicated sella turcica sequences were, therefore, not available for all patients. This method may overestimate the volume of CSF in the sella turcica, but we were more interested in the relative value of sellar volumes among the 3 samples of subjects than the absolute value. Moreover, the intraclass coefficient was good between the 2 reviewers. The accuracy of volume estimation may also have been limited by the differing sellar shapes. Software calculation may be considered in future work. We did not look at the reversibility of the sinus stenosis after treatment. Controversy surrounding the cause-and-effect relationship of venous stenosis and elevated intracranial pressure[40-43] should, nevertheless, be explored in future research.

CONCLUSIONS

The current study supports our hypothesis that sellar volumes are comparable in between patients treated for a symptomatic venous sinus stenosis and are larger than in a control group. We suggest that the empty sella is a radiologic sign of hemodynamic lateral sinus stenosis rather than elevated intracranial pressure. Various clinical presentations may thus be regrouped under a new clinical entity: the symptomatic lateral sinus stenosis. Future research should prospectively look at the long-term radiologic and clinical outcomes of untreated or asymptomatic patients with a lateral sinus stenosis. The concept of a clinical spectrum for symptomatic cerebral venous stenosis may be explored by studying factors that may differentiate IIH from IPT.

REFERENCES

1. Naing S, Frohman LA. **The empty sella.** *Pediatr Endocrinol Rev* 2007;4:335–42 Medline
2. Davis S, Tress B, King J. **Primary empty sella syndrome and benign intracranial hypertension.** *Clin Exp Neurol* 1978;15:248–57 Medline
3. Bidot S, Saindane AM, Peragallo JH, et al. **Brain imaging in idiopathic intracranial hypertension.** *J Neuroophthalmology* 2015;35:400–11 CrossRef Medline
4. Agid R, Farb RI, Willinsky RA, et al. **Idiopathic intracranial hypertension: The validity of cross-sectional neuroimaging signs.** *Neuroradiology* 2006;48:521–27 CrossRef Medline
5. Brodsky MC, Vaphiades M. **Magnetic resonance imaging in pseudotumor cerebri.** *Ophthalmology* 1998;105:1686–93 CrossRef Medline
6. de Vries-Knoppert WA. **Primary empty sella syndrome and benign intracranial hypertension.** *Doc Ophthalmol* 1986;61:319–25 Medline
7. Foley KM, Posner JB. **Does pseudotumor cerebri cause the empty sella syndrome?** *Neurology* 1975;25:565–69 CrossRef Medline
8. Degnan AJ, Levy LM. **Pseudotumor cerebri: brief review of clinical syndrome and imaging findings.** *AJNR Am J Neuroradiol* 2011;32:1986–93 CrossRef Medline
9. Rohr AC, Riedel C, Fruehauf MC, et al. **MR imaging findings in patients with secondary intracranial hypertension.** *AJNR Am J Neuroradiol* 2011;32:1021–29 CrossRef Medline
10. Ahmed RM, Wilkinson M, Parker GD, et al. **Transverse sinus stenting for idiopathic intracranial hypertension: a review of 52 patients and of model predictions.** *AJNR Am J Neuroradiol* 2011;32:1408–14 CrossRef Medline
11. Higgins JNP, Owler BK, Cousins C, et al. **Venous sinus stenting for refractory benign intracranial hypertension.** *Lancet* 2002;359:228–30 CrossRef Medline
12. Dinkin MJ, Patsalides A. **Venous sinus stenting in idiopathic intracranial hypertension.** *J Neuroophthalmol* 2017;37:113–21 CrossRef Medline
13. Sismanis A. **Otologic manifestations of benign intracranial hypertension syndrome: diagnosis and management.** *Laryngoscope* 1987;97:1–17 CrossRef Medline

14. Reardon MA, Raghavan P. **Venous abnormalities leading to tinnitus: imaging evaluation.** *Neuroimaging Clin N Am* 2016;26:237–45 CrossRef Medline
15. Dong C, Zhao PF, Yang JG, et al. **Incidence of vascular anomalies and variants associated with unilateral venous pulsatile tinnitus in 242 patients based on dual-phase contrast-enhanced computed tomography.** *Chin Med J (Engl)* 2015;128:581–85 CrossRef Medline
16. Dietz RR, Davis WL, Harnsberger HR, et al. **MR imaging and MR angiography in the evaluation of pulsatile tinnitus.** *AJNR Am J Neuroradiol* 1994;15:879–89 Medline
17. Krishnan A, Mattox DE, Fountain AJ, et al. **CT arteriography and venography in pulsatile tinnitus: preliminary results.** *AJNR Am J Neuroradiol* 2006;27:1635–68 Medline
18. Lenck S, Labeyrie MA, Vallee F, et al. **Stent placement for disabling pulsatile tinnitus caused by a lateral sinus stenosis: a retrospective study.** *Oper Neurosurg (Hagerstown)* 2017;13:560–65 CrossRef Medline
19. Yang I-H, Pereira VM, Lenck S, et al. **Endovascular treatment of debilitating tinnitus secondary to cerebral venous sinus abnormalities: a literature review and technical illustration.** *J Neurointerv Surg* 2019;11:841–46 CrossRef Medline
20. Levitt MR, Albuquerque FC, Gross BA, et al. **Venous sinus stenting in patients without idiopathic intracranial hypertension.** *J Neurointerv Surg* 2017;9:512–15 CrossRef Medline
21. Smith JL. **Whence pseudotumor cerebri?** *J Clin Neuroophthalmol* 1985;5:55–66 Medline
22. Lenck S, Vallée F, Labeyrie M-A, et al. **Stenting of the lateral sinus in idiopathic intracranial hypertension according to the type of stenosis.** *Neurosurgery* 2017;80:393–400 CrossRef Medline
23. Weissman JL, Hirsch BE. **Imaging of tinnitus: a review.** *Radiology* 2000;216:342–49 Medline
24. Silbergleit R, Junck L, Gebarski SS, et al. **Idiopathic intracranial hypertension (pseudotumor cerebri): MR imaging.** *Radiology* 1989;170:207–09 CrossRef Medline
25. Sismanis A, Butts FM, Hughes GB. **Objective tinnitus in benign intracranial hypertension: an update.** *Laryngoscope* 1990;100:33–36 CrossRef Medline
26. Bracard S, Schmitt E, Klein O, et al. **"Benign" intracranial hypertension: neuroradiology and endovascular treatments (in French).** *Neurochirurgie* 2008;54:721–73 CrossRef Medline
27. Puffer RC, Mustafa W, Lanzino G. **Venous sinus stenting for idiopathic intracranial hypertension: a review of the literature.** *J Neurointerv Surg* 2013;5:483–86 CrossRef Medline
28. Kesavadas C, Thomas B, Kapilamoorthy T, et al. **Imaging signs in idiopathic intracranial hypertension: are these signs seen in secondary intracranial hypertension too?** *Ann Indian Acad Neurol* 2013;16:229 CrossRef Medline
29. Ridha MA, Saindane AM, Bruce BB, et al. **Magnetic resonance imaging findings of elevated intracranial pressure in cerebral venous thrombosis versus idiopathic intracranial hypertension with transverse sinus stenosis.** *Neuroophthalmology* 2013;37:1–6 CrossRef Medline
30. Eisenman DJ, Raghavan P, Hertzano R, et al. **Evaluation and treatment of pulsatile tinnitus associated with sigmoid sinus wall anomalies.** *Laryngoscope* 2018;128:S1–13 CrossRef Medline
31. Markey KA, Mollan SP, Jensen RH, et al. **Understanding idiopathic intracranial hypertension: mechanisms, management, and future directions.** *Lancet Neurol* 2016;15:78–91 CrossRef Medline
32. Weisberg LA, Housepian EM, Saur DP. **Empty sella syndrome as complication of benign intracranial hypertension.** *J Neurosurg* 1975;43:177–80 CrossRef Medline
33. Kyung SE, Botelho JV, Horton JC. **Enlargement of the sella turcica in pseudotumor cerebri.** *J Neurosurg* 2014;120:538–42 CrossRef Medline
34. Bjerre P. **The empty sella: a reappraisal of etiology and pathogenesis.** *Acta Neurol Scand, Suppl* 1990;130:1–25 Medline
35. Johnston M, Zakharov A, Papaiconomou C, et al. **Evidence of connections between cerebrospinal fluid and nasal lymphatic vessels in humans, non-human primates and other mammalian species.** *Cerebrospinal Fluid Res* 2004;1:2 CrossRef Medline
36. Brinker T, Stopa E, Morrison J, et al. **A new look at cerebrospinal fluid circulation.** *Fluids Barriers CNS* 2014;11:10 CrossRef Medline
37. Bulat M, Klarica M. **Recent insights into a new hydrodynamics of the cerebrospinal fluid.** *Brain Res Rev* 2011;65:99–112 CrossRef Medline
38. McComb JG. **Recent research into the nature of cerebrospinal fluid formation and absorption.** *J Neurosurg* 1983;59:369–83 CrossRef Medline
39. Cherian I, Beltran M, Kasper E, et al. **Exploring the Virchow-Robin spaces function: a unified theory of brain diseases.** *Surg Neurol Int* 2016;7(Suppl 26):S711–14 CrossRef Medline
40. Bateman GA. **Stenoses in idiopathic intracranial hypertension: to stent or not to stent?** *AJNR Am J Neuroradiol* 2008;29:215 CrossRef Medline
41. Fraser JA, Leung AE. **Reversibility of MRI features of pseudotumor cerebri syndrome.** *Can J Neurol Sci* 2014;41:530–32 Medline
42. Rohr A, Dörner L, Stingele R, et al. **Reversibility of venous sinus obstruction in idiopathic intracranial hypertension.** *AJNR Am J Neuroradiol* 2007;28:656–59 Medline
43. De Simone R, Ranieri A, Montella S, et al. **The role of dural sinus stenosis in idiopathic intracranial hypertension pathogenesis: the self-limiting venous collapse feedback-loop model.** *Panminerva Med* 2014;56:201–09 Medline

Diagnostic Impact of Intracranial Vessel Wall MRI in 205 Patients with Ischemic Stroke or TIA

J.D. Schaafsma, S. Rawal, J.M. Coutinho, J. Rasheedi, D.J. Mikulis, C. Jaigobin, F.L. Silver, and D.M. Mandell

ABSTRACT

BACKGROUND AND PURPOSE: Secondary prevention of ischemic stroke depends on determining the cause of the initial ischemic event, but standard investigations often fail to identify a cause or identify multiple potential causes. The purpose of this study was to characterize the impact of intracranial vessel wall MR imaging on the etiologic classification of ischemic stroke.

MATERIALS AND METHODS: This was a single-center, retrospective study of 205 consecutive patients who were referred for vessel wall MR imaging to clarify the etiology of an ischemic stroke or TIA. An expert panel classified stroke etiology before and after incorporating vessel wall MR imaging results using a modified Trial of Org 10172 in Acute Stroke Treatment system. We measured the proportion of patients with an altered etiologic classification after vessel wall MR imaging.

RESULTS: The median age was 56 years (interquartile range = 44–67 years), and 51% (106/205) of patients were men. Vessel wall MR imaging altered the etiologic classification in 55% (112/205) of patients. The proportion of patients classified as having intracranial arteriopathy not otherwise specified decreased from 31% to 4% (64/205 versus 9/205; $P < .001$) and the proportion classified as having intracranial atherosclerotic disease increased from 23% to 57% (48/205 versus 116/205; $P < .001$). Conventional work-up classification as intracranial arteriopathy not otherwise specified was an independent predictor of vessel wall MR imaging impact (OR = 8.9; 95% CI , 3.0–27.2). The time between symptom onset and vessel wall MR imaging was not a predictor of impact.

CONCLUSIONS: When vessel wall MR imaging is performed to clarify the etiology of a stroke or TIA, it frequently alters the etiologic classification. This is important because the etiologic classification is the basis for therapeutic decision-making.

ABBREVIATION: VW = vessel wall

Secondary prevention of ischemic stroke depends on determining the cause of the initial stroke or TIA. However, for 25% of patients, standard investigations fail to identify a cause;[1] and investigations sometimes identify multiple potential causes.

Conventional imaging of the intracranial arteries (using CTA, MRA, or conventional angiography) shows the contour of the arterial lumen, but not the arterial wall itself. This approach fails to detect nonstenotic intracranial atherosclerotic disease[2-4] and to differentiate disorders such as vasculitis and reversible cerebral vasoconstriction syndrome.[5] It also incompletely characterizes disease activity, contributing to uncertainty about whether a particular vascular abnormality is incidental or the culprit etiology.

High-resolution vessel wall (VW) MR imaging is an adjunct to conventional vascular imaging. VW-MR imaging shows the arterial wall directly and enables the diagnosis of nonstenotic arterial disease,[2-4] differentiation of diseases that have a similar appearance on conventional vascular imaging,[6-8] and assessment of vascular disease activity.[9] Studies have described the VW-MR imaging appearance of several stroke etiologies[6,9,10] and measured the diagnostic accuracy of specific vessel wall findings.[8,11,12] There are practice guidelines for clinical use of VW-MR imaging,[9,13] and the technique has been increasingly adopted on a clinical basis.

However, there remains a broader question. When intracranial VW-MR imaging is performed to clarify the etiology of a stroke or TIA, how often and in what circumstances does this supplementary examination have an impact on the etiologic classification?

Received May 9, 2019; accepted after revision July 24.

From the Division of Neurology, Department of Medicine (J.D.S., J.R., C.J., F.L.S.), and Division of Neuroradiology, Department of Medical Imaging (S.R., J.M.C., D.J.M., D.M.M.), University Health Network, Toronto, Ontario, Canada; and Department of Neurology (J.M.C.), Academic Medical Center, Amsterdam, the Netherlands.

This study was supported by the Ontario Academic Health Science Centres Innovation Fund.

Please address correspondence to Daniel Mandell, MD, PhD, Medical Imaging, 3MCL-426, Toronto Western Hospital, 399 Bathurst St, Toronto, ON M5T2S8, Canada; e-mail: danny.mandell@uhn.ca

Indicates article with supplemental on-line table.

http://dx.doi.org/10.3174/ajnr.A6202

Table 1: Framework for diagnostic categorization of vessel wall MR imaging findings[a]

VW-MR Imaging Category	Findings
Normal	Arterial wall is thin or imperceptible; no wall enhancement other than ± proximal intracranial internal carotid and vertebral arteries attributed to vasa vasorum
Intracranial atherosclerotic disease	Arterial wall is focally, eccentrically thickened; T2 prolongation ± enhancement immediately adjacent to the lumen and T2 shortening within the wall more peripherally; markers of disease activity include plaque enhancement and intraplaque hemorrhage
Arterial dissection	Arterial wall is eccentrically thickened; thickened wall has the signal characteristics of blood products; marker of disease activity is intramural signal characteristics of acute or subacute blood product
Vasculitis	Arterial wall is concentrically, homogeneously thickened and enhancing
Reversible cerebral vasoconstriction syndrome	Arterial wall is concentrically, homogeneously thickened with no (or mild) enhancement

[a] Adapted from the consensus recommendations of the Vessel Wall Imaging Study Group of the American Society of Neuroradiology.[9]

To answer this question, we studied 205 consecutive patients who had VW-MR imaging performed to clarify the etiology of a stroke or TIA. We interpreted the VW-MR imaging according to consensus guidelines and used expert-panel adjudication to characterize the impact of VW-MR imaging on the etiologic classification.

MATERIALS AND METHODS

Patients

This was a single-center, retrospective study at the University Health Network, Toronto, Ontario, Canada. We included consecutive patients referred from the hospital stroke service between 2006 and 2014 for intracranial VW-MR imaging to clarify the etiology of an ischemic stroke or TIA. We excluded patients scanned after 2014 to enable a separate analysis of long-term clinical follow-up. The institutional review board approved the study.

High-Resolution Intracranial Vessel Wall MR Imaging

VW-MR imaging on a 3T MR imaging system (Signa HDx; GE Healthcare, Milwaukee, Wisconsin) with an 8-channel receive-only head coil included time-of-flight MRA of the intracranial arteries (3D with FOV = 22 × 22 cm, acquired matrix = 512 × 512, acquired section thickness = 1 mm, section overlap = 50%, 145 slices, TR = 21 ms, TE = 2.7 ms), a T2-weighted VW-MR imaging sequence (2D fast spin-echo with FOV = 22 × 22 cm, acquired matrix = 512 × 512, section thickness = 2 mm, no interslice gap, acquired voxel = 0.4 × 0.4 × 2.0 cm, 15–25 slices, TR = 3250 ms, TE = 89 ms), and a T1-weighted VW-MR imaging sequence (single inversion recovery-prepared, 2D fast spin-echo with identical voxel dimensions, TR = 2263 ms, TI = 860 ms, TE = 13 ms) before and immediately after a 5-mL intravenous injection of gadobutrol (Gadovist; Bayer Schering Pharma, Berlin, Germany). Each VW-MR imaging sequence took 3–7 minutes, depending on the number of slices. A neuroradiologist monitored each examination to target the vessels of interest in both short- and long-axis planes, which were axial, sagittal, or coronal planes or obliques of these depending on the orientation of the vessels of interest. When conventional vascular imaging findings were normal, the VW-MR imaging target was the vessels supplying the territory of the ischemic event.

Panel Adjudication Stage 1: Conventional Work-Up

The panel included 2 neurologists with subspecialization in stroke, and 2 neuroradiologists with expertise in cerebrovascular disease. A stroke neurologist blinded to VW-MR imaging results reviewed the clinical history and physical examination notes, laboratory results, and conventional imaging reports for each patient. The neurologist categorized stroke etiology for each patient using a modification of the Trial of Org 10172 in Acute Stroke Treatment (TOAST)[14] categories. We used the TOAST categories of cardioembolism, small-artery occlusion, other determined etiology, and undetermined etiology. We limited use of the TOAST category "large artery atherosclerosis" to the cervical arteries and categorized intracranial atherosclerotic disease separately. We supplemented these categories with 4 additional categories: intracranial arterial dissection, vasculitis, reversible cerebral vasoconstriction syndrome, and intracranial arteriopathy not otherwise specified. The undetermined category includes the subcategories negative evaluation, incomplete evaluation, and ≥2 causes identified. The second stroke neurologist independently categorized stroke etiology for 50 randomly selected patients in the study to assess interobserver variability.

Panel Adjudication Stage 2: Incorporating VW-MR Imaging

A neuroradiologist reviewed the VW-MR imaging for each patient and flagged any examinations that were completely nondiagnostic due to poor technical quality. The neuroradiologist categorized VW-MR imaging findings using the framework described in the Consensus Recommendations of the Vessel Wall Imaging Study Group of the American Society of Neuroradiology,[9] which is summarized in Table 1. We followed the recommendations for interpretation of VW-MR imaging,[9] including the need to confirm vessel wall findings in multiple planes and with multiple tissue weightings, with accurate determination of the inner and outer boundaries of the vessel wall, to confirm that vessel wall findings were indeed within the vessel wall and not thrombus within the lumen or outside the vessel. Using the same framework, the neuroradiologist also recorded whether there were VW-MR imaging findings to suggest active rather than quiescent disease. A second neuroradiologist independently categorized VW-MR imaging findings for 50 randomly selected patients in the study to assess interobserver variability.

Table 2: Conventional investigations performed to determine the etiology of TIA or stroke in 205 patients

Investigation	Proportion of Patients
Brain imaging	
MR imaging (± CT)	92% (189/205)
CT only	8% (16/205)
Conventional vascular imaging (cervical-cerebral)	
CTA only	18% (36/205)
MRA only	37% (75/205)
CTA and MRA	23% (47/205)
CTA and DSA	5% (11/205)
MRA and DSA	10% (20/205)
CTA, MRA, and DSA	8% (16/205)
Cardiac investigations	
Electrocardiography	100% (205/205)
Rhythm monitoring ≥24 hours	29% (59/205)
Transthoracic echocardiography	68% (140/205)
Transesophageal echocardiography	6% (30/205)
Laboratory investigations	
Serology screen for vasculitis	25% (51/205)
Serology screen for hypercoagulability	34% (69/205)
CSF analysis	14% (28/205)
Brain biopsy	2% (4/205)

The 2 stroke neurologists then reviewed the VW-MR imaging interpretation for each case they had previously classified, and considering the VW-MR imaging findings in the context of the entire conventional stroke work-up, they each independently either confirmed or reclassified the stroke etiology for each patient.

Statistical Analysis

Analysis software was SPSS, Version 24 (IBM, Armonk, New York). We calculated an unweighted Cohen κ statistic to measure interobserver agreement for categorization of VW-MR imaging findings, classification based on conventional work-up, and classification incorporating VW-MR imaging. We calculated the overall proportion of patients with etiologic classifications altered by intracranial VW-MR imaging and then compared the proportion of patients in each etiologic category based on conventional work-up versus conventional work-up supplemented with VW-MR imaging and used the McNemar test to identify significant differences. To identify factors from the conventional work-up (age, sex, time from symptom onset to VW-MR imaging, etiologic classification) that were associated with a change in etiologic classification after VW-MR imaging, we performed univariate logistic regression analysis with "change in diagnosis after VW-MR imaging" as the dependent variable, followed by an exploratory multivariate logistic regression.

RESULTS

Patients Characteristics and Conventional Work-Up

The study included 205 patients: 187 (91%) with stroke and 18 (9%) with TIA. Ischemic events were in the anterior circulation in 123 patients (60%), the posterior circulation in 64 patients (31%), and both in 18 patients (9%). The median age was 56 years (interquartile range = 44–67 years), and 51% of patients (106/205) were men. Table 2 describes the conventional stroke investigations. The median time from symptom-onset to VW-MR imaging was 14 days (interquartile range = 5–120 days). VW-MR imaging quality was nondiagnostic in 3/205 (1.5%) patients. All 205 patients were included in the analysis.

Expert Panel Interobserver Agreement

Neuroradiologists' categorizations of VW-MR imaging findings had good[15] interobserver agreement (Cohen κ = 0.75; 95% CI, 0.59–0.91). Neurologists' classifications of stroke etiology had good interobserver agreement before incorporating VW-MR imaging (Cohen κ = 0.76; 95% CI, 0.61–0.90) and very good interobserver agreement after incorporating VW-MR imaging (Cohen κ = 0.87; 95% CI, 0.74–0.99).

Impact of VW-MR Imaging on Etiologic Classificaion

The etiologic classification was altered by intracranial VW-MR imaging in 55% (112/205) of patients. The On-line Table provides details. The most common etiologic classification based on the conventional work-up was intracranial arteriopathy not otherwise specified, and 92% (59/64) of patients in this subgroup had an altered etiologic classification after VW-MR imaging.

VW-MR imaging led to a decrease in the proportion of patients classified as having "intracranial arteriopathy not otherwise specified" from 31% to 4% (64/205 versus 9/205; $P < .001$) and an increase in the proportion of patients classified as having "intracranial atherosclerotic disease" from 23% to 57% (48/205 versus 116/205; $P < .001$). VW-MR imaging led to a decrease in the proportion classified as "etiology undetermined due to 2 or more potential causes" from 4% to 1% (9/205 versus 2/205; $P = .016$), and a decrease in the proportion classified as having "small-vessel occlusion" from 3% to 0% (7/205 versus 1/205; $P = .031$). The Figure shows a representative case.

Predictors of Impact

In the multivariate analysis, the 1 factor that independently predicted a change in etiologic classification after VW-MR imaging was the conventional work-up classification of intracranial arteriopathy not otherwise specified (odds ratio = 8.9; 95% CI, 3.0–27.2). Factors that independently predicted no change were the conventional work-up classification of intracranial atherosclerotic disease (OR = 0.2; 95% CI, 0.1–0.4) or cardioembolism (OR = 0.1; 95% CI, 0–0.6). Table 3 provides details.

DISCUSSION

The objective of our study was not to measure the diagnostic accuracy of intracranial VW-MR imaging but to apply the current guidelines for interpretation of VW-MR imaging and measure the impact of the technique on the etiologic classification in patients with recent ischemic stroke or TIA. We found that VW-MR imaging substantially increased the proportion of strokes attributed to intracranial atherosclerotic disease. VW-MR imaging did not change the overall proportion of strokes attributed to vasculitis, but it altered which particular strokes were attributed to vasculitis. VW-MR imaging was most likely to have a

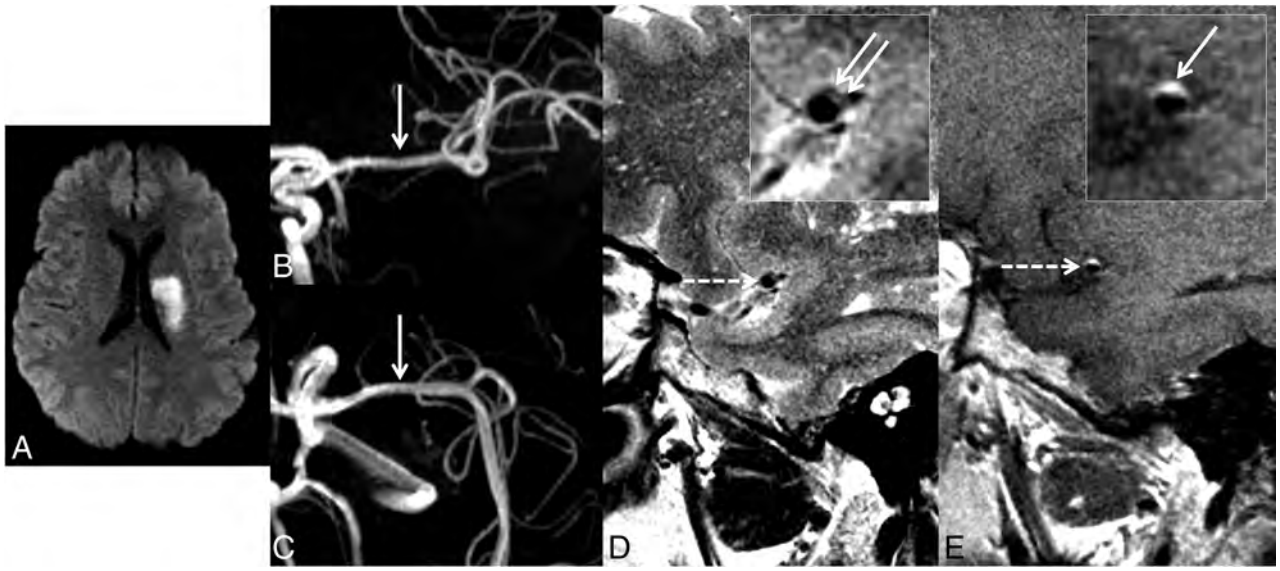

FIGURE. Representative case with conventional stroke work-up with negative findings and altered etiologic classification after VW-MR imaging. Diffusion-weighted MR imaging (*A*) shows an acute infarct in the left MCA lenticulostriate territory. MRA anterior-posterior (*B*) and craniocaudal (*C*) projections show no/minimal narrowing of the left MCA (*arrows*). Sagittal T2-weighted VW-MR imaging (*D*) shows a cross-section through the left MCA (*dashed arrow*), and a magnified view (*inset box*) shows focal, eccentric, thickening of the superior-posterior wall of the left MCA (*solid arrows*). Sagittal contrast-enhanced T1-weighted VW-MR imaging (*E*) shows the same vessel (*dashed arrow*) with corresponding wall enhancement (*solid arrow*). The VW-MR imaging appearance is consistent with atherosclerotic plaque, and the enhancement is a finding more common in recently symptomatic plaque. Adapted with permission from Schaafsma et al.[23]

Table 3: Factors associated with revised etiologic classification when conventional stroke work-up is supplemented with VW-MR imaging

	OR (95% CI) for Change in Etiologic Classification when Conventional Work-Up is Supplemented with VW-MR Imaging	
	Univariate Logistic Regression	Multivariate Logistic Regression
Age	0.97[a] (0.95–0.99)	0.99 (0.97–1.01)
Sex	1.05 (0.61–1.82)	1.14 (0.55–2.39)
Time interval between symptom onset and VW-MR imaging (days)	1.00 (1.00–1.00)	NA
Etiologic classification based on conventional stroke work-up		
Intracranial arteriopathy not otherwise specified	19.59[a] (7.39–51.91)	8.94[a] (2.95–27.19)
Intracranial atherosclerotic disease	0.09[a] (0.04–0.20)	0.15[a] (0.05–0.41)
Undetermined etiology	0.86 (0.41–1.82)	NA
Vasculitis	1.58 (0.56–4.45)	1.39 (0.42–4.55)
Cardioembolism	0.10[a] (0.23–0.46)	0.12[a] (0.02–0.57)
Other determined etiology	0.48 (0.11–2.08)	0.43 (0.09–21.83)
Small-vessel occlusion	5.21 (0.62–44.06)	4.92 (0.54–44.73)
Cervical atherosclerotic disease	0.55 (0.09–3.33)	NA
Arterial dissection	1.39E + 9 (0.001 to ∞)	NA
Reversible cerebral vasoconstriction syndrome	0.41 (0.04–4.95)	0.39 (0.03–4.83)

Note:—NA indicates not applicable as a factor; not included in the multivariate logistic regression.
[a] Statistically significant.

diagnostic impact for patients who already had categorization as having intracranial arteriopathy based on the conventional work-up. The length of time between symptom onset and VW-MR imaging was not a predictor of impact.

We were not surprised to find strokes newly attributed to intracranial atherosclerotic disease after VW-MR imaging. VW-MR imaging can detect plaque that is occult on conventional vascular imaging, and previous studies have shown plaque on VW-MR imaging in patients with cryptogenic lacunar infarction.[3,4] This is important because symptomatic intracranial plaque portends a high risk of recurrent stroke and can prompt specific treatment such as dual antiplatelet drug therapy and optimization of blood pressure and lipid profile.[16] However, the presence of intracranial atherosclerotic plaque does not alone imply that intracranial plaque is the culprit, and we will return to this point later in this discussion.

VW-MR imaging did not alter the proportion of strokes attributed to vasculitis, but it altered which particular strokes were attributed to vasculitis. Among patients categorized as having vasculitis based on conventional work-up, only two-thirds were categorized as having vasculitis after VW-MR imaging. Most of these patients had a vessel wall lesion with typical characteristics of atherosclerotic plaque. Conversely, among patients categorized as having vasculitis after VW-MR imaging, only one-third had been categorized as having vasculitis based on conventional work-up alone. Most of these patients had been

categorized as having intracranial arteriopathy not otherwise specified rather than a specific condition by conventional work-up alone.

The definitive test for central nervous system vasculitis is brain biopsy. A limitation of biopsy is undersampling due to spatially heterogeneous disease or the need to avoid eloquent regions.[5] Also, vasculitis may predominate in the larger intracranial arteries rather than the smaller vessels that are usually biopsied.[17] VW-MR imaging is a noninvasive means to assess arterial wall inflammation, and this can help discriminate between vasculitis and mimics such as reversible cerebral vasoconstriction syndrome and atherosclerotic disease.[7,8,12,18]

We had few patients categorized as having etiology undetermined due to ≥2 potential causes, but VW-MR imaging significantly decreased the proportion of patients in this category. VW-MR imaging can be useful in this context because it provides information on disease activity.

The factor that independently predicted a change in the etiologic classification after VW-MR imaging was the conventional work-up classification as intracranial arteriopathy not otherwise specified. This was not unexpected, but the high odds ratio (OR = 8.9; 95% CI, 3.0–27.2) emphasizes that a pre-existing abnormality on conventional imaging increases the likelihood of impact from VW-MR imaging. We found that the time between symptom onset and VW-MR imaging was not a predictor of impact from VW-MR imaging in our study, which had a median delay of 2 weeks, but it may be best to perform VW-MR imaging within weeks rather than months of symptom onset because findings such as atherosclerotic plaque enhancement may wane after several weeks to months.[19,20]

There is no single, ideal reference standard for determining stroke etiology. Therefore, we modelled our study design on clinical practice and used an expert panel to categorize stroke etiology. The stroke neurologists integrated multiple clinical, laboratory, and imaging factors to decide on the categorization. For example, 1 patient had both a patent foramen ovale and an intracranial atherosclerotic plaque, so the neurologists had to decide which one was the likely etiology. For this case, the plaque was designated as the likely etiology because contrast echocardiography had characterized the patent foramen ovale as "low-risk," intracranial plaque was only evident in the artery supplying the territory of the stroke, and the plaque was intensely enhancing (a feature that the VW-MR imaging framework views as a feature of recently symptomatic plaque).[19,20] We believe this use of an expert panel, with independent assessments and measurement of in-terobserver agreement, is a re-asonable approach to measure the diagnostic impact of VW-MR imaging. However, it is important to recognize the potential for confirmation bias: interpreting the additional information provided by VW-MR imaging as overly definitive.

This study used T1-, T2-, and contrast-enhanced T1-weighted VW-MR imaging sequences, and the interpreting neuroradiologists used the multiple tissue-weighting and multiple imaging planes to confirm the vessel wall findings as recommended.[9] Some centers use only T1-weighted VW-MR imaging sequences. Our local preference has been to routinely include a T2-weighted sequence as well because it can help confirm that a finding is within the vessel wall rather than within the lumen and can contribute to the characterization of vessel wall lesions (eg, identification of hyperintensity within the fibrous cap of atherosclerotic plaque).

We evaluated patients who were referred for VW-MR imaging to clarify the cause of a stroke or TIA. We believe this is a clinically relevant patient group because it likely approximates the types of patients who will have intracranial VW-MR imaging at other centers. However, relying on the referral patterns of multiple stroke neurologists who have different thresholds for requesting intracranial VW-MR imaging does introduce a selection bias, and the proportion of patients with altered etiologic classifications after VW-MR imaging may differ at other institutions.

We used a modified TOAST[14] classification system because this system is well-known and reflects the kind of etiologic classification often used in clinical practice, but there are other systems we could have used,[21,22] and these may have led to different proportions of patients with a revised etiologic classification. Also, we did not attempt to stratify the level of diagnostic confidence within each particular etiologic category, but changes in the level of confidence within categories may affect therapeutic decision-making, too.

All patients had electrocardiography and many (74%) had echocardiography, but fewer (29%) had Holter rhythm monitoring for >24 hours. This scenario likely reflects the high proportion of patients who had intracranial arteriopathy not otherwise specified or a working diagnosis based on conventional work-up rather than completely cryptogenic stroke.

CONCLUSIONS

We found that when VW-MR imaging is performed to clarify the etiology of a stroke or TIA, it can have a substantial impact on etiologic classification. Because this impact is substantial, intracranial VW-MR imaging has the potential to improve therapeutic decision-making for many patients. The contrary is also true: Improper application of the interpretive framework or limitations of the framework itself have the potential to misinform therapeutic decision-making for many patients. Physicians who are performing and interpreting VW-MR imaging should familiarize themselves with technical recommendations and interpretive pitfalls for VW-MR imaging and recognize that there remain gaps in knowledge and that research is ongoing.

ACKNOWLEDGMENTS

We appreciate the dedication and skill of the Toronto Western Hospital MR imaging technologists involved in this work, especially Nicole Bennett, Holly Chun, Colleen Grace, Mary Hatchard, Olga Ioffina, Nisha James, Mahnaz Miraftabi, Asma Naheed, Jessica Pinto, Keith Ta, and Danfeng Zhao.

Disclosures: Daniel M. Mandell—*RELATED*: *Grant*: Ontario Academic Health Science Centers Innovation Fund.* *Money paid to the Institution.

REFERENCES

1. Saver JL. **Cryptogenic stroke.** *N Engl J Med* 2016;374:2065–74 CrossRef Medline

2. Chung JW, Kim BJ, Sohn CH, et al. **Branch atheromatous plaque: a major cause of lacunar infarction (high-resolution MRI study).** *Cerebrovasc Dis Extra* 2012;2:36–44 CrossRef Medline
3. Yoon Y, Lee DH, Kang DW, et al. **Single subcortical infarction and atherosclerotic plaques in the middle cerebral artery: high-resolution magnetic resonance imaging findings.** *Stroke* 2013;44:2462–67 CrossRef Medline
4. Klein IF, Lavallée PC, Mazighi M, et al. **Basilar artery atherosclerotic plaques in paramedian and lacunar pontine infarctions: a high-resolution MRI study.** *Stroke* 2010;41:1405–09 CrossRef Medline
5. Powers WJ. **Primary angiitis of the central nervous system: diagnostic criteria**. *Neurol Clin* 2015;33:515–26 CrossRef Medline
6. Swartz RH, Bhuta SS, Farb RI, et al. **Intracranial arterial wall imaging using high-resolution 3-Tesla contrast-enhanced MRI.** *Neurology* 2009;72:627–34 CrossRef Medline
7. Mandell DM, Matouk CC, Farb RI, et al. **Vessel wall MRI to differentiate between reversible cerebral vasoconstriction syndrome and central nervous system vasculitis: preliminary results.** *Stroke* 2012;43:860–62 CrossRef Medline
8. Mossa-Basha M, Hwang WD, De Havenon A, et al. **Multicontrast high-resolution vessel wall magnetic resonance imaging and its value in differentiating intracranial vasculopathic processes.** *Stroke* 2015;46:1567–73 CrossRef Medline
9. Mandell DM, Mossa-Basha M, Qiao Y, et al. **Intracranial vessel wall MRI: principles and expert consensus recommendations of the American Society of Neuroradiology.** *AJNR Am J Neuroradiol* 2017;38:218–29 CrossRef Medline
10. Lindenholz A, van der Kolk AG, Zwanenburg JJM, et al. **The use and pitfalls of intracranial vessel wall imaging: how we do it.** *Radiology* 2018;286:12–28 CrossRef Medline
11. Mossa-Basha M, de Havenon A, Becker KJ, et al. **Added value of vessel wall magnetic resonance imaging in the differentiation of Moyamoya vasculopathies in a non-Asian cohort.** *Stroke* 2016; 47:1782–88 CrossRef Medline
12. Mossa-Basha M, Shibata DK, Hallam DK, et al. **Added value of vessel wall magnetic resonance imaging for differentiation of nonocclusive intracranial vasculopathies.** *Stroke* 2017;48:3026–33 CrossRef Medline
13. Dieleman N, van der Kolk AG, Zwanenburg JJ, et al. **Imaging intracranial vessel wall pathology with magnetic resonance imaging: current prospects and future directions.** *Circulation* 2014;130:192–201 CrossRef Medline
14. Adams HP Jr, Bendixen BH, Kappelle LJ, et al. **Classification of subtype of acute ischemic stroke: definitions for use in a multicenter clinical trial—TOAST. Trial of Org 10172 in Acute Stroke Treatment.** *Stroke* 1993;24:35–41 CrossRef Medline
15. Brennan P, Silman A. **Statistical methods for assessing observer variability in clinical measures.** *BMJ* 1992;304:1491–94 CrossRef Medline
16. Qureshi AI, Caplan LR. **Intracranial atherosclerosis.** *Lancet* 2014; 383:984–98 CrossRef Medline
17. Rossi CM, Di Comite G. **The clinical spectrum of the neurological involvement in vasculitides.** *J Neurol Sci* 2009;285:13–21 CrossRef Medline
18. Singhal AB, Topcuoglu MA, Fok JW, et al. **Reversible cerebral vasoconstriction syndromes and primary angiitis of the central nervous system: clinical, imaging, and angiographic comparison.** *Ann Neurol* 2016;79:882–94 CrossRef Medline
19. Gupta A, Baradaran H, Al-Dasuqi K, et al. **Gadolinium enhancement in intracranial atherosclerotic plaque and ischemic stroke: a systematic review and meta-analysis.** *J Am Heart Assoc* 2016;5 CrossRef Medline
20. Skarpathiotakis M, Mandell DM, Swartz RH, et al. **Intracranial atherosclerotic plaque enhancement in patients with ischemic stroke.** *AJNR Am J Neuroradiol* 2013;34:299–304 CrossRef Medline
21. Amarenco P, Bogousslavsky J, Caplan LR, et al. **The ASCOD phenotyping of ischemic stroke (updated ASCO phenotyping).** *Cerebrovasc Dis* 2013;36:1–5 CrossRef
22. Ay H, Benner T, Arsava EM, et al. **A computerized algorithm for etiologic classification of ischemic stroke: the Causative Classification of Stroke System.** *Stroke* 2007;38:2979–84 CrossRef Medline
23. Schaafsma JD, Mikulis DJ, Mandell DM. **Intracranial vessel wall MR imaging: an emerging technique with a multitude of uses.** *Top Magn Reson Imaging* 2016;25:41–47 CrossRef Medline

Impact of Vessel Wall MR Imaging in the Work-Up for Ischemic Stroke

Interest in the diagnostic utility of intracranial vessel wall MR imaging (VW-MR imaging) has increased during the past 2 decades. Many studies have shown that VW-MR imaging provides supplemental anatomic information to existing lumen-based imaging techniques.[1,2] Yet, the diagnostic utility of VW-MR imaging in the work-up of ischemic stroke still remains investigative, and questions remain about whether it provides diagnostic information that ultimately improves patient outcomes.

In a comprehensive study design, the authors take the first step in addressing this question. In this single-center retrospective case series from 2006 to 2014, the authors measure the impact of VW-MR imaging to see whether supplementing the conventional diagnostic work-up with inclusion of multicontrast VW-MR imaging changed the stroke neurologist's working diagnosis in 205 cases. Stroke etiologies were classified using a modified version of the Trial of ORG 10172 in Acute Stroke Treatment (TOAST)[3] classification scheme by a stroke neurologist before and after incorporating information from VW-MR imaging reviewed by an experienced neuroradiologist. The authors report that VW-MR imaging frequently altered the etiologic classification. In particular, a higher proportion of cases were attributed to intracranial atherosclerotic disease and fewer cases were categorized as "intracranial arteriopathy, not otherwise specified," "etiology undetermined due to 2 or more potential causes," and "small vessel occlusion." On the basis of these results, the authors conclude that VW-MR imaging has substantial impact in the work-up of stroke etiologies.

The results are interesting for several reasons: First, the study attempts to measure the value of VW-MR imaging by assessing the frequency in the change of the working diagnosis of stroke etiologies if additional vessel wall imaging information is made available to the stroke neurologist. At the authors' institution under the direction of expert panels, a measurable impact was detected. It would be most interesting to know whether in a prospective design, if a change in therapeutic management would follow, indicating confidence in the diagnostic interpretation or in a retrospective study including diagnostic follow-up information to assess diagnostic accuracy. In a slightly different study design, Kesav et al[4] also assessed the potential impact of VW-MR imaging by measuring the reclassification of stroke etiologies with the addition of VW-MR imaging. Kesav et al also suggest that VW-MR imaging impacts the diagnostic evaluation with diagnostic etiology reclassification in cases originally classified as "undetermined" etiologies and large (intracranial) artery atherosclerosis.

This leads to a second interesting aspect of the study. The study results suggest that intracranial atherosclerosis could be a more common ischemic stroke etiology than previously thought. Among the 205 cases, 116 were reclassified as "intracranial atherosclerosis" following VW-MR imaging. One possible explanation may be the ability of VW-MR imaging to detect prestenotic or angiographically occult atherosclerotic lesions.[5-7] The detection of such culprit lesions may, in part, decrease the expensive downstream work-up costs of cryptogenic stroke.

Third, in the analysis, the time interval between symptom onset and VW-MR imaging was not significantly associated with a change in etiologic classification. This could be explained by the possibility of the studied sample comprising largely of chronic or long-standing diseases such as atherosclerosis as opposed to more acute vasculopathies such as reversible cerebral vasoconstriction syndrome. Moreover, in cases such as artery-to-artery embolism within the intracranial arterial vasculature, timing may be key to detecting enhancing culprit lesions with plaque surface irregularity.[8] As a future direction, it would be informative to examine the importance of the timing of VW-MR imaging to address its impact in acute primary treatment decisions, which, in turn, would also address secondary prevention.

Finally, the results of this study give rise to optimism, given the improved techniques of VW-MR imaging since 2006 and could potentially be more impactful than reported. For instance, VW-MR imaging using 3D techniques with whole-brain coverage suggest improved assessment of vasculitis as well as intracranial atherosclerosis.[9,10]

As the field of stroke continues to advance, intracranial VW-MR imaging has diagnostic potential but, as the authors cautiously acknowledge, remains an area of active research. Next, it would be most informative to show diagnostic accuracy, which

could be achieved by incorporating data from clinical and imaging follow-up to assess clinical improvement. Such an analysis would yield results that would help persuade one that VW-MR imaging provides diagnostic information that may ultimately improve patient outcomes.

REFERENCES

1. Song JW, Obusez EC, Raymond SB, et al. **Vessel wall MRI added to MR angiography in the evaluation of suspected vasculopathies.** *J Neuroimaging* 2019;29:454–57 CrossRef Medline
2. Mossa-Basha M, Shibata DK, Hallam DK, et al. **Added value of vessel wall magnetic resonance imaging for differentiation of nonocclusive intracranial vasculopathies.** *Stroke* 2017;48:3026–33 CrossRef Medline
3. Adams HP, Jr, Bendixen BH, Kappelle LJ, et al. **Classification of subtype of acute ischemic stroke. Definitions for use in a multicenter clinical trial. TOAST. Trial of Org 10172 in Acute Stroke Treatment.** *Stroke* 1993;24:35–41
4. Kesav P, Krishnavadana B, Kesavadas C, et al. **Utility of intracranial high-resolution vessel wall magnetic resonance imaging in differentiating intracranial vasculopathic diseases causing ischemic stroke.** *Neuroradiology* 2019;61:389–96 CrossRef Medline
5. Song JW, Rafla SD, Obusez EC, et al. **High-resolution vessel wall MR imaging in prestenotic intracranial atherosclerotic disease.** *J Clin Neurosci* 2019;63:278–80 CrossRef Medline
6. Chung J, Kim BJ, Sohn CH, et al. **Branch atheromatous plaque: a major cause of lacunar infarction (high-resolution MRI study).** *Cerebrovasc Dis Extra* 2012;2:36–44 CrossRef Medline
7. Klein IF, Lavallée PC, Mazighi M, et al. **Basilar artery atherosclerotic plaques in paramedian and lacunar pontine infarctions: a high-resolution MRI study.** *Stroke* 2010;41:1405–09 CrossRef Medline
8. Wu F, Song H, Ma Q, et al. **Hyperintense plaque on intracranial vessel wall magnetic resonance imaging as a predictor of artery-to-artery embolic infarction.** *Stroke* 2018;49:905–11 CrossRef Medline
9. Eiden S, Beck C, Venhoff N, et al. **High-resolution contrast-enhanced vessel wall imaging in patients with suspected cerebral vasculitis: prospective comparison of whole-brain 3D T1 SPACE versus 2D T1 black blood MRI at 3 Tesla.** *PLoS One* 2019;14:e0213514 CrossRef Medline
10. Wu F, Ma Q, Song H, et al. **Differential features of culprit intracranial atherosclerotic lesions: a whole-brain vessel wall imaging study in patients with acute ischemic stroke.** *J Am Heart Assoc* 2018;7 CrossRef Medline

J.W. Song
Department of Radiology
University of Pennsylvania
Philadelphia, Pennsylvania

http://dx.doi.org/10.3174/ajnr.A6241

Effect of Time Elapsed since Gadolinium Administration on Atherosclerotic Plaque Enhancement in Clinical Vessel Wall MR Imaging Studies

A. de Havenon, H.J. Muhina, D.L. Parker, J.S. McNally, and M.D. Alexander

ABSTRACT

SUMMARY: Vessel wall MR imaging is a useful tool for the evaluation of intracranial atherosclerotic disease. Enhancement can be particularly instructive. This study investigated the impact of the duration between contrast administration and image acquisition. The cohort with the longest duration had the greatest increase in signal intensity change. When using vessel wall MR imaging to assess intracranial atherosclerotic disease, protocols should be designed to maximize the duration between contrast administration and image acquisition to best demonstrate enhancement.

ABBREVIATIONS: DANTE = delay alternating with nutation for tailored excitation; vwMRI = vessel wall MR imaging; ICAD = intracranial atherosclerotic disease; SPACE = sampling perfection with application-optimized contrasts by using different flip angle evolutions

Development of vessel wall MR imaging (vwMRI) protocols has improved the evaluation of intracranial atherosclerotic disease (ICAD) by providing direct visualization of the vessel wall and the plaque itself.[1-6] In the evaluation of ICAD with vwMRI, an important diagnostic finding is plaque enhancement, a characteristic widely believed to reflect inflammation.[7,8] Inconsistencies in acquisition parameters and image interpretation have limited progress in the development of these promising MR imaging techniques.[6,7,9-12]

Reproducible quantitative interpretation techniques could help overcome these limitations, particularly with respect to enhancement, but standardization of acquisition parameters is also needed.[6] Duration between contrast administration and image acquisition affects the degree of measured enhancement in other pathologies.[13,14] This study examined the impact of time intervals on enhancement measured in ICAD plaques and reference structures.

MATERIALS AND METHODS

Following an institutional review board–approved protocol, retrospective analysis was performed of patients undergoing vwMRI for the evaluation of ischemic stroke at a major academic medical center. In this protocol, vwMRI studies are performed for patients with confirmed new infarcts suspected of being due to ICAD or not attributed to another etiology. All patients in this study were evaluated with vwMRI within 14 days of the infarct.

Studies were performed with dedicated head coils on Prisma, Trio, or Verio 3T MR imaging scanners (Siemens, Erlangen, Germany). Two blinded neuroradiologists assessed the arterial tree upstream from the new infarct. The reviewers were notified about which artery to assess by the vascular neurologist, who adjudicated the stroke parent artery status according to diffusion-weighted imaging lesions within the vascular territory of a major artery with ICAD. Reviewers were blinded to clinical data and other MR imaging findings, most notably DWI. Reviewers noted the lesion that had most likely caused the downstream infarction. The culprit lesions were determined by each reviewer and confirmed between them to be the same lesion for each patient. Each reviewer was blinded to measurements made by the other reviewer. Patients in whom multiple ICAD lesions in the same vascular bed could be considered culprit were excluded to avoid bias.

After we confirmed the consensus on the culprit lesion, maximum signal intensity values were recorded on 3D T1-weighted sampling perfection with application-optimized contrasts by using different flip angle evolutions (SPACE; Siemens) with delay alternating with nutation for tailored excitation (DANTE) flow suppression pre- and postcontrast.[5] Patients were given gadobenate dimeglumine (MultiHance; Bracco Diagnostics, Princeton, New Jersey) at a dose of 0.2 mL/kg (0.1 mmol/kg). Additionally, structures known to normally enhance were included, including the low infundibulum, defined as the lowest segment distinguishable from the pituitary gland on axial images; muscle, chosen

Received May 20, 2019; accepted after revision July 17.

From the Departments of Radiology and Imaging Sciences (M.D.A., D.L.P., J.S.M.), Neurosurgery (M.D.A.), Neurology (A.d.H.), and the School of Medicine (H.J.M.), University of Utah, Salt Lake City, Utah.

This study was funded, in part, by National Institutes of Health grants NIH S10OD018482, NIH R01HL127582, NIH/NINDS K23NS105924, and the American Heart Association (19TPA34910194 and 17SDG33460420).

Please address correspondence to Matthew D. Alexander, MD, 30 North 1900 East, Room 1A071, Salt Lake City, UT 84132; e-mail: Matthew.Alexander@hsc.utah.edu

http://dx.doi.org/10.3174/ajnr.A6191

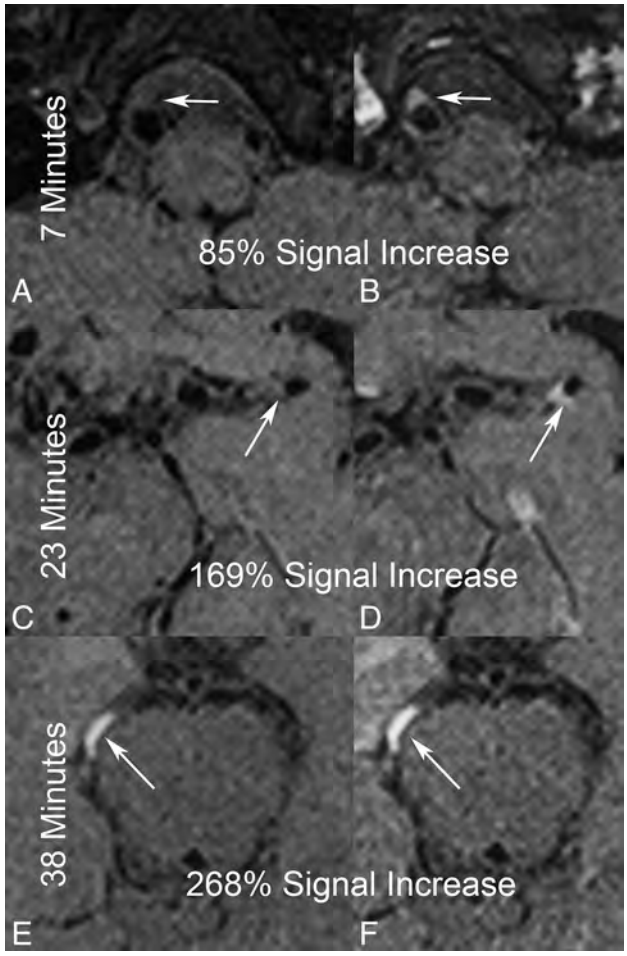

FIG 1. Representative images of vwMRI studies of symptomatic ICAD lesions (*arrows*) in each of the 3 timing cohorts, <20 minutes (*A* and *B*), 20–30 minutes (*C* and *D*), and 30–40 minutes (*E* and *F*). For each study, pre- (*A*, *C*, and *E*) and postcontrast (*B*, *D*, *F*) images are shown of lesions in the right V4 segment (*A* and *B*), distal left M1 segment (*E* and *F*).

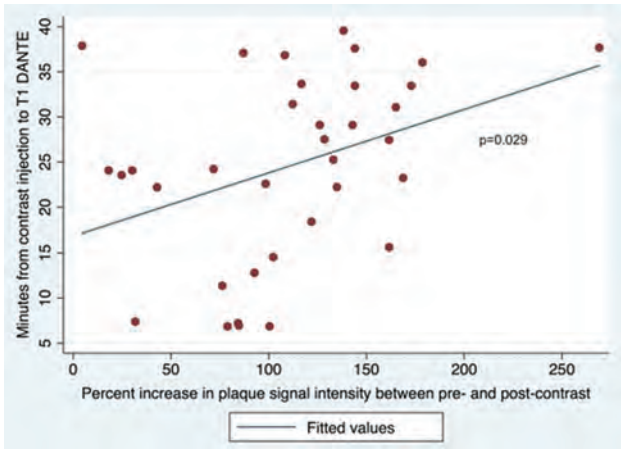

FIG 2. Linear regression between the minutes from contrast injection to T1 DANTE and the percentage increase in plaque signal intensity between pre- and postcontrast.

within the temporalis muscle medial to its midbelly fibrous band; cavernous sinus, measuring a segment clearly representing only blood; and the choroid plexus.[6,15] Three data points were measured for each site assessed, and the mean was calculated.

Times were tabulated for contrast administration and acquisition of postcontrast images. To exclude outlier data during early development of the vwMRI protocol that could introduce bias, we excluded studies with >40 minutes between contrast injection and T1 DANTE acquisition. Correlation coefficients were calculated among variables as well as *P* values to assess the significance of associations. For further analysis, the cohort was divided into 3 different time intervals from contrast injection to T1 DANTE: 0–20 minutes, 20–30 minutes, and 30–40 minutes. Comparison was made of the variance of pre- to postcontrast measurements across these time periods using the Levene test of the equality of variance. All analyses were performed in STATA 15.1 (StataCorp, College Station, Texas).

RESULTS

Studies from 54 patients were evaluated. Thirty-five patients met all the inclusion criteria (10 studies in the 0- to 20-minute group, 13 at 20–30 minutes, and 12 at 30–40 minutes). Representative studies from each time group are provided in Fig 1. The mean ± SD time from contrast injection to T1 DANTE was 24.5 ± 10.4 minutes (range, 6.9–39.5 minutes). In culprit plaques, the percentage increase in signal intensity from pre- to postcontrast was 110.2% ± 54.7%, which was significantly associated with the time from contrast injection to T1 DANTE (Fig 2, $P = .029$). For the reference structures, there was no association between the time from contrast injection to T1 DANTE and the change in signal intensity between pre- and postcontrast (Table). Creating a ratio of percentages in increased T1 signals of plaque over the lower infundibulum demonstrates a stronger correlation with timing than plaque alone ($r^2 = 0.410$, $P = .016$). If one introduces a pituitary signal increase into the model for plaque as a covariate, plaque maintains the association with time ($P < .05$). Additionally, there is no direct association between the plaque and infundibulum changes ($r^2 = -0.103$, $P = .561$).

DISCUSSION

Evaluation of ICAD can be aided by vwMRI studies.[1-3,6,8] While these techniques have proved useful, broad clinical use is impeded by heterogeneous acquisition and interpretation methods. Standardized methodologies can mitigate such issues, particularly when quantitative analyses are used.[6] Enhancement of ICAD plaques is a particularly instructive feature, and this characteristic, in particular, is prone to variability.[6-8] These results confirm our early clinical observation that lesion enhancement was accentuated by increased duration between contrast administration and acquisition of postcontrast DANTE images. The association between time and T1 signal changes is independent of changes in the pituitary gland. Standardizing plaque signal change to change measured in the pituitary gland is even more dependent on time from contrast administration. In response to these findings, we have standardized a vwMRI protocol that maximizes this duration within the accepted temporal confines for these studies by acquiring sequences not impacted by contrast (T2, FLAIR) after contrast administration and before postcontrast DANTE imaging.

Correlation between time from contrast injection to T1 DANTE and measurements of change in signal intensity between pre- and postcontrast

Variable	Correlation Coefficient	Coefficient of Determination (r^2)	*P* Value
Time from contrast injection to T1 DANTE			
Plaque (% increase)	0.370	0.137	.029
Low infundibulum (% increase) (*n* = 34)	−0.314	0.099	.071
Cavernous sinus (% increase) (*n* = 32)	−0.054	0.003	.770
Muscle (% increase) (*n* = 33)	−0.011	<0.001	.951
Choroid plexus (% increase) (*n* = 33)	0.049	0.002	.788
Change in signal intensity between pre- and postcontrast			
Plaque (% increase)	0.370	0.137	.029
Low infundibulum (% increase) (*n* = 34)	−0.314	0.099	.071
Cavernous sinus (% increase) (*n* = 32)	−0.054	0.003	.770
Muscle (% increase) (*n* = 33)	−0.011	<0.001	.951
Choroid plexus (% increase) (*n* = 33)	0.049	0.002	.788

This study has several limitations that warrant mention. Visualized enhancement may reflect variables other than timing such as differences in plaques, patient age or sex, or other factors. Additionally, elapsed time after contrast may be confounded, which cannot be determined without imaging the same person multiple times or doing a dynamic study. Such factors can be assessed in future investigations. Despite these limitations, it appears that future studies using vwMRI might benefit from defined time intervals between contrast administration and postcontrast T1 imaging.

Disclosures: J. Scott McNally—*RELATED*: *Grant*: American Heart Association, *Comments*: American Heart Association Scientist Development Grant (17SDG33460420) supports a portion of my research time.* *Money paid to the institution.

REFERENCES

1. Mossa-Basha M, Alexander M, Gaddikeri S, et al. **Vessel wall imaging for intracranial vascular disease evaluation.** *J Neurointerv Surg* 2016;8:1154–59 CrossRef Medline
2. de Havenon A, Mossa-Basha M, Shah L, et al. **High-resolution vessel wall MRI for the evaluation of intracranial atherosclerotic disease.** *Neuroradiology* 2017;59:1193–1202 CrossRef Medline
3. Mandell DM, Mossa-Basha M, Qiao Y, et al. **Intracranial vessel wall MRI: principles and expert consensus recommendations of the American Society of Neuroradiology.** *AJNR Am J Neuroradiol* 2017;38:218–29 CrossRef Medline
4. Li L, Chai JT, Biasiolli L, et al. **Black-blood multicontrast imaging of carotid arteries with DANTE-prepared 2D and 3D MR imaging.** *Radiology* 2014;273:560–69 CrossRef Medline
5. Li L, Miller KL, Jezzard P. **DANTE-prepared pulse trains: a novel approach to motion-sensitized and motion-suppressed quantitative magnetic resonance imaging.** *Magn Reson Med* 2012;68:1423–38 CrossRef Medline
6. Alexander MD, de Havenon A, Kim SE, et al. **Assessment of quantitative methods for enhancement measurement on vessel wall magnetic resonance imaging evaluation of intracranial atherosclerosis.** *Neuroradiology* 2019;61:643 CrossRef
7. Gupta A, Baradaran H, Al-Dasuqi K, et al. **Gadolinium enhancement in intracranial atherosclerotic plaque and ischemic stroke: a systematic review and meta-analysis.** *J Am Heart Assoc* 2016;5 CrossRef
8. Alexander MD, Yuan C, Rutman A, et al. **High-resolution intracranial vessel wall imaging: imaging beyond the lumen.** *J Neurol Neurosurg Psychiatry* 2016;87:589–97 CrossRef Medline
9. Kim JM, Jung KH, Sohn CH, et al. **Middle cerebral artery plaque and prediction of the infarction pattern.** *Arch Neurol* 2012;69:1470–75 CrossRef Medline
10. Qiao Y, Zeiler SR, Mirbagheri S, et al. **Intracranial plaque enhancement in patients with cerebrovascular events on high-spatial-resolution MR images.** *Radiology* 2014;271:534–42 CrossRef Medline
11. Skarpathiotakis M, Mandell DM, Swartz RH, et al. **Intracranial atherosclerotic plaque enhancement in patients with ischemic stroke.** *AJNR Am J Neuroradiol* 2013;34:299–304 CrossRef Medline
12. Vakil P, Vranic J, Hurley MC, et al. **T1 gadolinium enhancement of intracranial atherosclerotic plaques associated with symptomatic ischemic presentations.** *AJNR Am J Neuroradiol* 2013;34:2252–58 CrossRef Medline
13. Tofts PS, Kermode AG. **Measurement of the blood-brain barrier permeability and leakage space using dynamic MR imaging, 1: fundamental concepts.** *Magn Reson Med* 1991;17:357–67 CrossRef Medline
14. Alexander MD, Hughes N, Cooke DL, et al. **Revisiting classic MRI findings of venous malformations: changes in protocols may lead to potential misdiagnosis.** *Neuroradiol J* 2018;31:5095–12 CrossRef Medline
15. Smirniotopoulos JG, Murphy FM, Rushing EJ, et al. **Patterns of contrast enhancement in the brain and meninges.** *Radiographics* 2007;27:525–51 CrossRef Medline

Increased Diameters of the Internal Cerebral Veins and the Basal Veins of Rosenthal Are Associated with White Matter Hyperintensity Volume

A.L. Houck, J. Gutierrez, F. Gao, K.C. Igwe, J.M. Colon, S.E. Black, and A.M. Brickman

ABSTRACT

BACKGROUND AND PURPOSE: White matter hyperintensities on T2-weighted MR imaging are typical in older adults and have been linked to several poor health outcomes, including cognitive impairment and Alzheimer disease. The presence and severity of white matter hyperintensities have traditionally been attributed to occlusive arteriopathy, but recent evidence also implicates deep medullary venule collagenosis and associated vasogenic edema. Historically, postmortem analyses have been the sole way to analyze cerebral veins, but SWI can be now used to examine cortical veins in vivo. The aim of the current study was to determine whether there is an association between the diameters of the large draining cerebral veins/sinuses and white matter hyperintensity volume.

MATERIALS AND METHODS: T2-weighted FLAIR and SWI were performed in 682 older adults without dementia (mean age, 73.9 ± 5.9 years; 59.1% women). Total and regional white matter hyperintensity volume was derived. We measured the diameters of 5 regions of the cerebral venous draining system: internal cerebral veins, basal veins of Rosenthal, superior sagittal sinus, vein of Galen, and straight sinus terminus.

RESULTS: Increased diameter of the internal cerebral veins was associated with greater total white matter hyperintensity volume (β = 0.09, P = .02) and regionally in the parietal (β = 0.10, P = .006), frontal (β = 0.09, P = .02), and temporal (β = 0.09, P = .02) lobes. Increased diameter of the basal veins of Rosenthal was associated with greater total (β = 0.10, P = .01), frontal (β = 0.11, P = .003), and temporal (β = 0.09, P = .02) white matter hyperintensity volume.

CONCLUSIONS: Our results suggest that the caliber of the internal cerebral veins and of the basal veins of Rosenthal relates to regional white matter disease.

ABBREVIATIONS: AD = Alzheimer disease; WHICAP = Washington Heights–Inwood Columbia Aging Project; WMH = white matter hyperintensity; ICC = intraclass correlation coefficient

Received May 31, 2019; accepted after revision August 1.

From the Taub Institute for Research on Alzheimer's Disease and the Aging Brain (A.L.H., K.C.I., J.M.C., A.M.B.) and Department of Neurology (J.G., A.M.B.), College of Physicians and Surgeons, Columbia University, New York, New York; and Hurvitz Brain Sciences Research Program (F.G., S.E.B.), Sunnybrook Research Institute, University of Toronto, Toronto, Ontario, Canada.

Data collection and sharing for the project were supported by the Washington Heights–Inwood Columbia Aging Project (WHICAP, P01AG07232, R01AG037212, RF1AG054023, R01AG034189, R01AG054520, and R56AG034189) funded by the National Institute on Aging and the National Center for Advancing Translational Sciences, National Institutes of Health, through grant No. UL1TR001873.

This article has been reviewed by Washington Heights–Inwood Columbia Aging Project investigators for scientific content and consistency of data interpretation with previous Washington Heights–Inwood Columbia Aging Project study publications.

Please address correspondence to Adam M. Brickman, PhD, Taub Institute for Research on Alzheimer's Disease and the Aging Brain, Department of Neurology, College of Physicians and Surgeons, Columbia University, 630 West 168th St, P&S Box 16, New York, NY 10032; e-mail: amb2139@columbia.edu

http://dx.doi.org/10.3174/ajnr.A6213

Chronic ischemia of the white matter of the brain can result in demyelination and axonal loss, manifesting primarily as white matter hyperintensities (WMHs), or "leukoaraiosis," on T2-weighted MR imaging.[1,2] Increased WMH volume is associated with a number of suboptimal health outcomes, including cognitive decline, elevated Alzheimer disease (AD) risk, AD-related genetic profiles, bipolar disorder, and stroke risk.[3-8]

The importance of vascular dysfunction and AD is increasingly appreciated, but the underlying mechanisms behind this relationship remain unclear.[9] Although periventricular venous collagenosis was linked to WMHs > 20 years ago,[10] the clinical observations associating vascular disease with WMHs typically assume that they are solely arterial in origin. The idea that venous pathology contributes to the radiologic manifestation of WMHs is now being revisited, and contemporary hypotheses suggest that the pathology of the veins and venules may at least partially mediate the association between WMHs and AD.[11] Periventricular

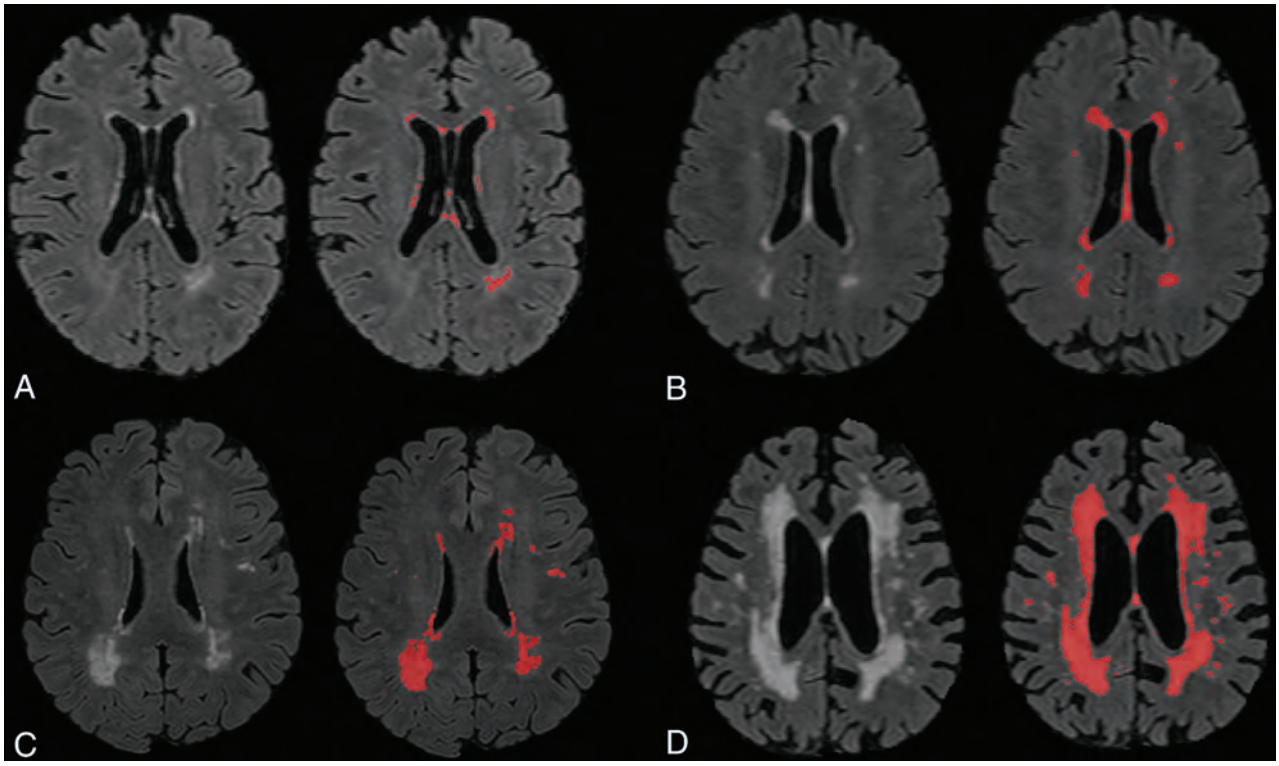

FIG 1. Four sample images of WMH on T2 FLAIR, labeled for quantification using an intensity threshold with our software. *A*, Minimal WMHs. *B*, Mild WMHs. *C*, Moderate WMHs. *D*, Severe WMHs.

venous collagenosis and large-caliber venous stenosis may be 1 mechanism through which WMHs and AD are associated, and venous collagenosis may increase overall resistance in the veins, leading to reduced blood flow to the deep white matter.[12] Venous outflow obstruction may also lead to decreased clearance of metabolic by-products and toxic misfolded proteins as seen in AD, resulting in ischemic stress.[12]

Cerebral veins have typically been distinguished from the arterial and capillary systems by postmortem analysis with complex immunostaining. Studies of postmortem tissue noted that concentric collagen deposition in the deep medullary venular system (eg, luminal stenosis or occlusion) correlates with WMH severity.[10,13] Historically, the cortical veins have been difficult to distinguish on brain imaging, but SWI can detect cortical veins that are difficult to visualize on T2-weighted or proton density images. With this technique, venous vessels become hypointense due to the magnetic susceptibility differences between oxygenated and deoxygenated blood. Even without contrast administration, SWI is particularly sensitive to the visualization of periventricular veins.[14] In this study, we used SWI to visualize and measure the diameters of large draining veins in the brain to test the hypothesis that cerebral basal vein dilation is related to WMH volume.

MATERIALS AND METHODS

Study Subjects

The Washington Heights–Inwood Columbia Aging Project (WHICAP) is an ongoing epidemiologic study of cognitive aging and dementia in the racially/ethnically diverse community surrounding Columbia University Medical Center in upper Manhattan. It includes randomly sampled adults 65 years or older; there were no specific inclusion/exclusion criteria other than age. More than 6000 participants have been recruited into WHICAP since its inception in 1992. Neuropsychological, medical, neurologic, demographic, and psychosocial data are collected on all active participants at approximately 24-month intervals. Neuroimaging was incorporated into WHICAP in 2 waves, beginning in 2004 and in 2009. For the neuroimaging substudies, participants were enrolled who did not meet the diagnostic criteria for dementia at their previous or closest longitudinal visit. In the current study, we analyzed participants with MR imaging data from the second wave, which included 3T scans with T1-weighted, T2-weighted FLAIR, and SWI sequences. We ascertained vascular risk history based on chart review and participant interview and self-reported history of heart disease, hypertension, and type 2 diabetes. Each vascular risk factor was established by a diagnostic history and/or documentation or report of treatment for the condition, including medication or other medical intervention. These 3 dichotomous variables were added to create a vascular risk factor summary score that ranged from 0 to 3, as we have done in past studies.[15-17] The study was approved by the Columbia University Medical Center ethics committee; all participants gave written informed consent.

MR Imaging

MR imaging was performed using a 3T Intera scanner (Philips Healthcare, Best, the Netherlands). Images included T1-weighted (TR = 6.6 ms, TE = 3.0 ms, flip angle = 8°, FOV = 256 × 256 × 165 mm, section thickness =1.0 mm), T2-

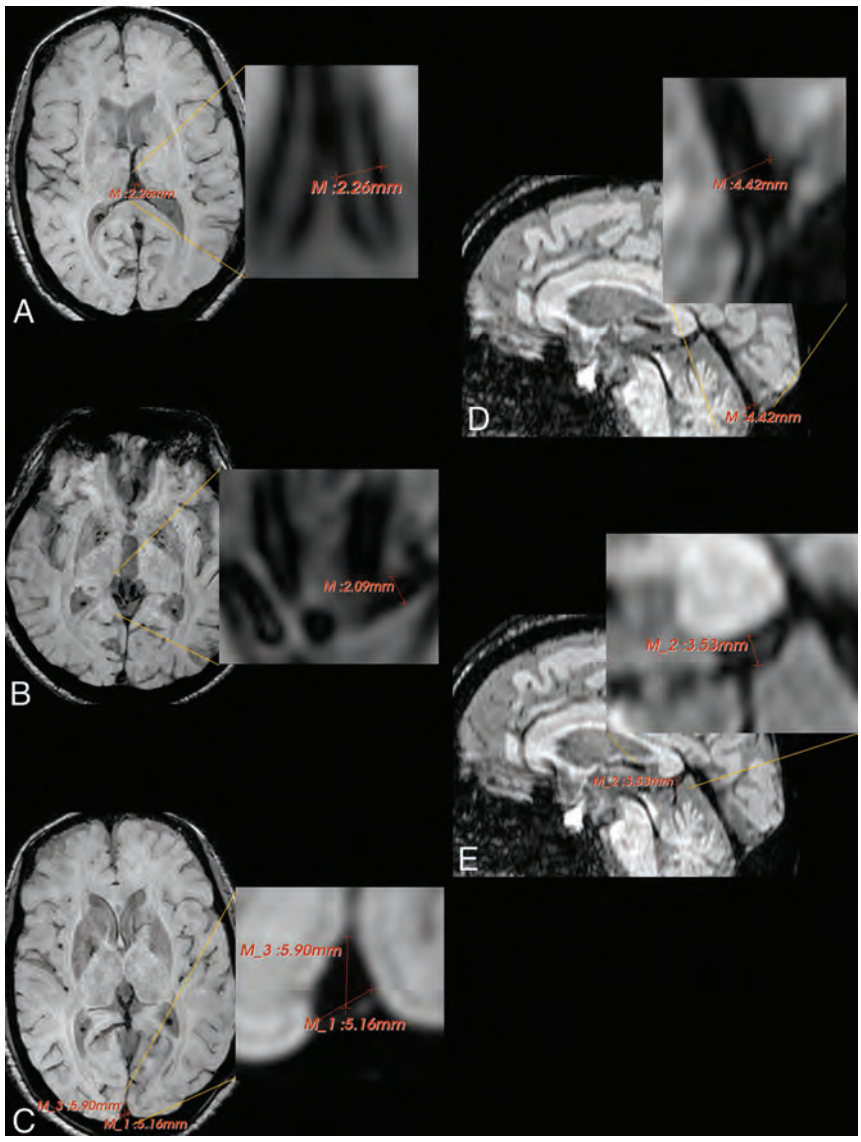

FIG 2. Sample depiction of vein/sinus measurement on SWI using 3D Slicer. *A*, The diameters of the left and right internal cerebral veins were measured in the axial plane and then averaged. *B*, The diameters of the left and right basal veins of Rosenthal were measured at their termini in the axial plane and then averaged. *C*, The base and anterior-posterior diameters of the superior sagittal plane were measured in the axial plane and then averaged. *D*, The straight sinus terminus was measured in the sagittal plane. *E*, The vein of Galen was measured inferior to the splenium in the sagittal plane.

weighted FLAIR (TR = 8000 ms, TE = 337 ms, inversion recovery time = 2400 ms, flip angle = 90°, FOV = 240 × 240 × 180 mm, section thickness =2.0 mm), and SWI (TR = 16 ms, TE = 22 ms, flip angle = 15°, FOV = 512 × 512 × 150 mm, section thickness = 1.0 mm) sequences.

T1-weighted images were used to estimate total intracranial volume using FreeSurfer (Version 6.0; http://surfer.nmr.mgh.harvard.edu). FLAIR sequencing was used to derive total WMH volume using previously described techniques developed in our laboratory (Fig 1).[18,19] In short, FLAIR images were skull-stripped and normalized, and a Gaussian curve was fit to map the voxel intensity values. If the voxels were >2.1 SDs above the mean FLAIR image, they were labeled as WMHs. This threshold of 2.1 SDs was selected on the basis of the greatest sensitivity and specificity of detection across participants, as determined by trained experts. White matter hyperintensity volume in cubic centimeters was calculated as the sum of labeled voxels multiplied by voxel dimensions. All labeled images were visually checked for errors, and manual corrections were made in the case of false-positive errors. The most common false-positive errors were small "speckles" of voxels labeled as hyperintense in the cortex, likely due to subtle intensity inhomogeneity that is common on T2-weighted images. The major lobes of the brain were derived by applying a standard spatial "lobar" atlas, and regional WMHs were defined as the intersection of labeled voxels and each segmented cerebral lobe.

Vein and Sinus Measurements

3D Slicer 4.8.1 (www.slicer.org) was used to measure the veins and sinuses on SWI (Fig 2).[20] In the axial plane, the ruler function was used to measure the diameters of the left and right internal cerebral veins in millimeters. Due to variations in venous morphology and image quality, we visually identified the region of the vein that appeared most continuously linear and measured the diameter of the vein there. In each image, the measurements for the left and right internal cerebral veins were averaged for 1 value. Also, in the axial plane, the base and the anterior-posterior diameter of the superior sagittal sinus were measured immediately above the confluence of sinuses. These measurements were then averaged for 1 value. We also measured the widths of the left and right basal veins of Rosenthal in the axial plane just before they converged with the internal cerebral veins into the vein of Galen. These values were averaged for a singular measurement. In the sagittal plane, the vein of Galen was measured directly inferior to the splenium, where the width of the vein appeared most consistent. In addition, in the sagittal plane, the straight sinus was measured at its terminus immediately anterior to the confluence of sinuses. Intrarater reliability of all measurements was confirmed with intraclass correlation coefficients (ICCs; see the following section).

Statistical Analyses

Descriptive statistics were generated for participant demographic data. To test for intrarater reliability of the vein and sinus

measurements, we randomly selected 40 subjects and remeasured their veins and sinuses without knowledge of the previous measurement. Of the 10 forms of ICCs, a single-rating, absolute-agreement, 2-way random-effects model was chosen on the basis of recently described selection and reporting guidelines.[21,22]

Linear regression was used to test the primary hypotheses of this study. Each vein/sinus measurement was entered as the independent variable, and total WMH volume was set as the dependent variable. We performed another linear regression with the same variables, adjusting for age at the time of the scan, estimated intracranial volume, and the aforementioned vascular risk factor score. These linear models were run again separately for each cerebral lobe (frontal, temporal, parietal, and occipital) as dependent variables. After that, all regression analyses were repeated separately for all of the measured vein/sinus diameters. *Z* scores were also derived for all variables, and these values were used to calculate confidence intervals for the standardized β values.

Table 1: Study sample characteristics and mean values for measured vein/sinus diameters and WMH volume

Characteristics	
No., overall	682
Age at scan (mean) (SD) (yr)	73.9 (5.93)
Women (No.) (% total)	403 (59.1)
Race/ethnicity (No.) (% within race/ethnicity)	
White	185 (27.1)
Black	243 (35.6)
Hispanic	236 (34.6)
Other	18 (2.6)
Vascular risk factors (No.) (% total)	
Heart disease	130 (19.1)
Hypertension	434 (63.6)
Diabetes	166 (24.3)
Diameter, based on SWI (mean) (SD (mm)	
Internal cerebral veins	1.73 (0.26)
Basal veins of Rosenthal	1.64 (0.26)
Superior sagittal sinus	6.18 (0.87)
Vein of Galen	2.72 (0.57)
Straight sinus	3.80 (0.90)
WMH volume (mean) (SD) (mm^3)	
Total	5.21 (6.64)
Frontal lobe	2.27 (3.46)
Temporal lobe	0.32 (0.57)
Parietal lobe	1.44 (2.46)
Occipital lobe	0.42 (0.56)

RESULTS

Sample Characteristics

Six hundred eighty-two participants from the WHICAP study had complete SWI, WMH, and demographic data. Participants had a mean age at scanning of 73.9 ± 5.9 years, and 59.1% were women. There was a fairly even distribution of race/ethnicity among whites, blacks, and Hispanics. The median time interval between the closest clinical follow-up visit and MR imaging was 38 days. Complete demographic data, including vascular disease and primary MR imaging measurements, are shown in Table 1.

Intrarater Reliability

All 5 measurements had ICC values indicating either moderate or good reliability (internal cerebral veins: 0.81 [95% CI, 0.67–0.90], basal veins of Rosenthal: 0.73 [95% CI, 0.54–0.85], superior sagittal sinus: 0.68 [95% CI, 0.37–0.84], vein of Galen: 0.76 [95% CI, 0.50–0.88], and straight sinus: 0.76 [95% CI, 0.60–0.87]).[22]

Relationship between Vein/Sinus Measurements and WMH Volumes

In the unadjusted model, increased diameters of the internal cerebral vein, basal veins of Rosenthal, and the superior sagittal sinus were associated with higher total WMH volume (Table 2). Regionally, the internal cerebral vein diameter was associated with greater WMH volume across all brain lobes; the basal veins of Rosenthal were associated with greater WMH volume in the frontal, temporal, and parietal lobes; and the superior sagittal sinus was associated with greater WMH volume in the temporal, parietal, and occipital lobes.

When we controlled for age, estimated intracranial volume, and vascular risk factors in the adjusted model, the association between the internal cerebral veins and occipital lobe WMH volume was attenuated, the association between the basal veins of Rosenthal and parietal lobe WMH volume was attenuated, and all associations pertaining to the superior sagittal sinus were attenuated (Table 3). We found that the increased diameter of the

Table 2: Unadjusted associations (using standardized β values and corresponding 95% CI) between sinus/vein diameters and WMH volume[a]

	Total WMH	Frontal Lobe	Temporal Lobe	Parietal Lobe	Occipital Lobe
Internal cerebral veins					
β (95% CI)	0.11 (0.03–0.18)	0.10 (0.03–0.18)	0.11 (0.03–0.18)	0.12 (0.05–0.20)	0.09 (0.02–0.17)
P	.006	.007	.006	.001	.02
Basal veins of Rosenthal					
β (95% CI)	0.13 (0.06–0.20)	0.15 (0.08–0.22)	0.13 (0.05–0.20)	0.10 (0.02–0.17)	0.06 (−0.01–0.13)
P	.001	<.001	.001	.009	.11
Superior sagittal sinus					
β (95% CI)	0.09 (0.01–0.16)	0.07 (−0.01–0.14)	0.12 (0.05–0.20)	0.09 (0.02–0.17)	0.11 (0.04–0.19)
P	.02	.08	.002	.02	.003
Vein of Galen					
β (95% CI)	0.02 (−0.05–0.10)	0.05 (−0.03–0.12)	-0.01 (−0.08–0.07)	0.01 (−0.06–0.09)	0.00 (−0.08–0.07)
P	.55	.25	.84	.72	.95
Straight sinus					
β (95% CI)	0.00 (−0.08–0.07)	0.00 (−0.08–0.07)	-0.01 (−0.08–0.07)	0.00 (−0.07–0.08)	0.00 (−0.08–0.07)
P	.98	.97	.88	.96	.93

[a]Model 1: unadjusted; model 2: age-adjusted; model 3: adjusted for age and estimated intracranial volume.

Table 3: Associations (using standardized β values and corresponding 95% CI) between sinus/vein diameters and WMH volume after adjusting for age, estimated intracranial volume, and vascular risk factors

	Total WMH	Frontal Lobe	Temporal Lobe	Parietal Lobe	Occipital Lobe
Internal cerebral veins					
β (95% CI)	0.09 (0.02–0.16)	0.09 (0.01–0.16)	0.09 (0.02–0.17)	0.10 (0.03–0.18)	0.07 (−0.01–0.14)
P	.02	.02	.02	.006	.09
Basal veins of Rosenthal					
β (95% CI)	0.10 (0.02–0.17)	0.11 (0.04–0.19)	0.09 (0.01–0.17)	0.07 (−0.01–0.14)	0.00 (−0.07–0.08)
P	.01	.003	.02	.09	.95
Superior sagittal sinus					
β (95% CI)	0.04 (−0.4–0.12)	0.01 (−0.07–0.09)	0.08 (−0.001–0.16)	0.05 (−0.03–0.12)	0.04 (−0.04–0.12)
P	.33	.75	.05	.26	.35
Vein of Galen					
β (95% CI)	0.01 (−0.07–0.08)	0.03 (−0.05–0.10)	−0.02 (−0.10–0.06)	0.00 (−0.07–0.08)	−0.02 (−0.10–0.05)
P	.85	.51	.61	.93	.54
Straight sinus					
β (95% CI)	-0.01 (−0.08–0.07)	-0.01 (−0.08–0.06)	−0.01 (−0.09–0.06)	-0.003 (−0.08–0.07)	-0.02 (−0.10–0.05)
P	.83	.79	.71	.93	.55

internal cerebral veins maintained associations with higher total, frontal, temporal, and parietal WMH volume. An increased diameter of the basal veins of Rosenthal maintained associations with higher total, frontal, and temporal WMH volume. The diameters of the vein of Galen and straight sinus terminus were not associated with WMH volume in any of our analyses, either globally or regionally.

DISCUSSION

Strong evidence links cerebrovascular disease with WMH. Although current models do not typically implicate veins or venules in the development of WMH, recent data suggest that they may play a role.[11] In this cross-sectional study of older adults, we hypothesized that increased venous diameter would be associated with increased WMH volume. We found that increased diameters of the internal cerebral veins and the basal veins of Rosenthal were associated with greater WMH volume (Table 3). The strongest association for the internal cerebral veins was in the parietal lobe, the brain region where past studies have most consistently identified a correlation between WMH and AD.[23] The strongest association for the basal veins of Rosenthal was in the frontal lobe.

Our study builds on past studies that identified a relationship between periventricular venous collagenosis and WMHs.[10,12] In the first description of this phenomenon >20 years ago, Moody et al[10] studied 22 postmortem brains from older adults and showed that 65% had periventricular venous collagenosis of the small deep venules identified by trichrome staining; of these, 77% had severe WMH, as detected on antemortem scans. More recently, Keith et al[12] extended these results, primarily implicating the large caliber (>200 μm in diameter) deep penetrating venules in a postmortem sample of 24 patients with dementia known to have periventricular white matter disease and 18 controls without dementia. While collagenosis of venules (small- and medium-caliber deep medullary venules) and myelin pallor (a marker of demyelination) also correlated with WMH volume, in a multivariate analysis, stenosis of the large-diameter venules best predicted WMH volumes. The same lab group also previously corroborated these results in vivo, using novel imaging techniques to visualize intraparenchymal venules or perivascular spaces, similarly describing an association between enlargement of these vessels and WMH volume.[24]

Yan et al[25] used susceptibility-weighted MR imaging to quantify venulopathy of the deep medullary veins on the basis of voxel-intensity projection images. They found a relationship between WMH volume and large-caliber deep medullary vein visibility, which may be a manifestation of venous collagenosis. In a follow-up study, this same group created a visual grading score of deep medullary veins based on the venous continuity and homogeneity and found that scores were higher in subjects with higher WMH volume.[26]

Our study is the first to find an association between WMH and larger cerebral veins, namely the internal cerebral veins and the basal veins of Rosenthal. In the brain, the veins are valveless, and the draining system begins in the postcapillary venule and drains into venules, collecting veins, major parenchymal veins, the extraparenchymal veins, and finally the major dural sinuses. In particular, the periventricular veins drain into both the deep medullary veins and the internal cerebral veins and basal veins of Rosenthal. Moody et al[10] hypothesized that periventricular venous collagenosis increases venous pressure, thus shunting blood away from these larger veins. Understanding the pathophysiology underlying the association between venous diameter and increased WMH, a traditional marker of small artery disease, may help us broaden the vascular contributions to AD and related dementias. We must interpret this association cautiously because we do not have histologic data to provide evidence as to what may be contributing to this increased diameter.

It is likely that venous collagenosis in aging is driven by chronic ischemia in the periventricular white matter from chronic occlusive arteriopathies, resulting from vascular risk factors such as hypertension and diabetes, but also possibly amyloid angiopathy, arteriolar tortuosity related to age, and other arterial pathologies.[27,28] Arterial occlusive diseases exacerbate the gradient of diminishing cerebral blood flow toward the periventricular white matter, and this is especially evident in the watershed zones at the frontal and posterior horns of the ventricles.[29] This chronic ischemia leads to venous collagenosis,

which makes the deep medullary venules leaky and less able to absorb fluid. Collagenosis also increases venous resistance, which can further impair perfusion and interstitial flow and may also impede perivascular clearance of toxic proteins such as amyloid.[12] The resulting venous hypertension could also increase pressure in the adjacent internal cerebral veins and basal veins, enlarging their diameters, thus causing them to become dilated in some individuals. This effect may be dampened in the vein of Galen because it is much larger and drains venous blood from a number of other regions, including the basal ganglia, thalamus, and occipital regions. The straight sinus and superior sagittal sinus are lined by the dura and would, therefore, not be expected to change in size with increased venous pressure.

Typically, cerebral venous dilatory anomalies are described as developmental in nature, usually resulting in severe complications that present neonatally or in early childhood. To our knowledge, the only descriptions of enlarged internal cerebral veins or basal veins of Rosenthal in the older population have been in cases of cerebral venous thrombosis, a clinically symptomatic condition that often presents with headache, stroke symptoms, and seizures.[30-32] Some type of pathology downstream of the veins, such as increased resistance, stenosis, or vessel tortuosity, could result in reflux and subsequent dilation, similar to what is seen in varicose veins. Vein of Galen malformations and aneurysmal dilations, for example, both congenital anomalies, result in dilation of the internal cerebral veins and basal veins of Rosenthal due to reflux.[33]

Another possibility is that a larger vein diameter may result from the dilated perivascular space around it. An enlarged perivascular space has been described as a feature of cerebral small-vessel disease, with specific association with lacunar ischemic stroke and WMHs.[34] Likewise, a strong association has been observed between the severity of dilation of perivascular spaces and the severity of AD, and this relationship correlates to β amyloid load in the cortex.[35] Most interesting, venous collagenosis in the deep white matter has been observed in CADASIL,[28] a syndrome that also exhibits dilated perivascular spaces.[36] Furthermore, perivascular spaces are thought to be involved in the clearing of interstitial solutes such as β amyloid via the glymphatic system.[37] Thus, if venous dilation were a surrogate marker of dilated perivascular spaces, the associations that we found would have biologic plausibility as suggested by current literature. We are currently developing techniques for perivascular space quantification, which we hope to use in future studies.

The issue of multiple comparisons is a potential limitation to the study, but most of the observed effects were similar in magnitude and predicted direction; therefore, we do not believe that they were merely a result of a type I error. SWI is a noninvasive technique that allows vein visualization in vivo. The "blooming effect" is a phenomenon known to occur in SWI scans, in which certain hypointense signals become amplified. Although blooming may have played a role in the absolute values that we were able to measure, all SWI scans were acquired under identical, controlled parameters and any blooming impact should be consistent across all subjects.

CONCLUSIONS

Overall, this study provides evidence of the relationship between WMHs and both the internal cerebral veins and the basal veins of Rosenthal. It is unclear whether this association is merely correlative or if there is a causation between these pathologies. There are many avenues that can expand on this research in the future. As mentioned above, our lab is in the process of developing methods for perivascular space quantification, which could be used to determine whether these spaces relate to cerebral venous diameter. Longitudinal comparative analyses and/or comparisons across age groups could provide evidence of a temporal relationship. We could also examine specific CSF biomarkers of AD to see whether there is an association between vein/sinus diameter and CSF amyloid and τ. Our cohort consists of randomly recruited individuals without dementia diagnoses; an analysis of subjects with MCI and AD could provide a more nuanced understanding of this relationship. Other techniques such as angiography could depict what is happening internally within the vasculature to help delineate the pathology, though costs and physical risks could provide limitations. With the aging population, the clinical implications are clear: Understanding the etiology of this relationship might lead to therapeutic and preventative techniques to combat vascular disease and its downstream effects.

ACKNOWLEDGMENTS

We acknowledge the WHICAP study participants and the WHICAP research and support staff for their contributions to this study.

Disclosures: Jose Gutierrez—*RELATED*: *Grant*: National Institute on Aging*; *UNRELATED*: *Consultancy*: specialist on call, law firm for medical litigation; *Employment*: Columbia University; *Grants/Grants Pending*: National Institute on Aging.* Sandra E. Black—*UNRELATED*: *Consultancy*: Novartis, Merck, Eli Lilly, Pfizer, Roche, *Comments*: ad hoc consultancy; *Grants/Grants Pending*: GE Healthcare, Eli Lilly, Biogen Idec, Novartis, Genentech, Optina, Roche*; *Payment for Lectures Including Service on Speakers Bureaus*: Medscape/Biogen, Eli Lilly, Novartis, *Comments*: Continuing Medical Education. *Money paid to the institution.

REFERENCES

1. Pantoni L, Garcia JH, Gutierrez JA. **Cerebral white matter is highly vulnerable to ischemia.** *Stroke* 1996;27:1641–47 CrossRef Medline
2. Prins ND, Scheltens P. **White matter hyperintensities, cognitive impairment and dementia: an update.** *Nat Rev Neurol* 2015;11:157 CrossRef
3. Brickman AM, Provenzano FA, Muraskin J, et al. **Regional white matter hyperintensity volume, not hippocampal atrophy, predicts incident Alzheimer disease in the community.** *Arch Neurol* 2012;69:1621–27 CrossRef Medline
4. Lo RY, Jagust WJ; Alzheimer's Disease Neuroimaging Initiative. **Vascular burden and Alzheimer disease pathologic progression.** *Neurology* 2012;79:1349–55 CrossRef Medline
5. Brickman AM, Schupf N, Manly JJ, et al. **APOE ε4 and risk for Alzheimer's disease: do regionally distributed white matter hyperintensities play a role?** *Alzheimers Dement* 2014;10:619–29 CrossRef Medline
6. Lee S, Viqar F, Zimmerman ME, et al. **White matter hyperintensities are a core feature of Alzheimer's disease: evidence from the dominantly inherited Alzheimer network.** *Ann Neurol* 2016;79:929–39 CrossRef Medline

7. Ahn KH, Lyoo IK, Lee HK, et al. **White matter hyperintensities in subjects with bipolar disorder.** *Psychiatry Clin Neurosci* 2004;58:516–21 CrossRef Medline
8. Kuller LH, Longstreth W, Jr, Arnold AM, et al. **White matter hyperintensity on cranial magnetic resonance imaging: a predictor of stroke.** *Stroke* 2004;35:1821–25 CrossRef Medline
9. Snyder HM, Corriveau RA, Craft S, et al. **Vascular contributions to cognitive impairment and dementia including Alzheimer's disease.** *Alzheimers Dement* 2015;11:710–17 CrossRef Medline
10. Moody DM, Brown WR, Challa VR, et al. **Periventricular venous collagenosis: association with leukoaraiosis.** *Radiology* 1995;194:469–76 CrossRef Medline
11. Black S, Gao F, Bilbao J. **Understanding white matter disease: imaging-pathological correlations in vascular cognitive impairment.** *Stroke* 2009;40:S48–52 CrossRef Medline
12. Keith J, Gao F-Q, Noor R, et al. **Collagenosis of the deep medullary veins: an underrecognized pathologic correlate of white matter hyperintensities and periventricular infarction?** *J Neuropathol Exp Neurol* 2017;76:299–312 CrossRef Medline
13. Moody DM, Brown WR, Challa VR, et al. **Cerebral microvascular alterations in aging, leukoaraiosis, and Alzheimer's disease.** *Ann NY Acad Sci* 1997;826:103–16 CrossRef Medline
14. Mittal S, Wu Z, Neelavalli J, et al. **Susceptibility-weighted imaging: technical aspects and clinical applications, Part 2.** *AJNR Am J Neuroradiol* 2009;30:232–52 CrossRef Medline
15. Brickman AM, Schupf N, Manly JJ, et al. **Brain morphology in older African Americans, Caribbean Hispanics, and whites from northern Manhattan.** *Arch Neurol* 2008;65:1053–61 CrossRef Medline
16. Luchsinger J, Reitz C, Honig LS, et al. **Aggregation of vascular risk factors and risk of incident Alzheimer disease.** *Neurology* 2005;65:545–51 CrossRef Medline
17. Piriz A, Reyes D, Narkhede A, et al. **Cerebrovascular disease and neurodegeneration in Alzheimer's disease with and without a strong family history: a pilot magnetic resonance imaging study in Dominican Republic.** *J Alzheimers Dis* 2018;66:1519–28 CrossRef Medline
18. Brickman AM, Muraskin J, Zimmerman ME. **Structural neuroimaging in Alzheimer's disease: do white matter hyperintensities matter?** *Dialogues Clin Neurosci* 2009;11:181–90 Medline
19. Brickman AM, Sneed JR, Provenzano FA, et al. **Quantitative approaches for assessment of white matter hyperintensities in elderly populations.** *Psychiatry Res* 2011;193:101–06 CrossRef Medline
20. Fedorov A, Beichel R, Kalpathy-Cramer J, et al. **3D Slicer as an image computing platform for the Quantitative Imaging Network.** *Magn Reson Imaging* 2012;30:1323–41 CrossRef Medline
21. McGraw KO, Wong SP. **Forming inferences about some intraclass correlation coefficients.** *Psychological Methods* 1996;1:30 CrossRef
22. Koo TK, Li MY. **A guideline of selecting and reporting intraclass correlation coefficients for reliability research.** *J Chiropr Med* 2016;15:155–63 CrossRef Medline
23. Brickman AM, Zahodne LB, Guzman VA, et al. **Reconsidering harbingers of dementia: progression of parietal lobe white matter hyperintensities predicts Alzheimer's disease incidence.** *Neurobiol Aging* 2015;36:27–32 CrossRef Medline
24. Gao F, van Gaal S, Levy-Cooperman N, et al. **P2-010: does variable progression of incidental white matter hyperintensities in Alzheimer's disease relate to venous insufficiency?** *Alzheimer's & Dementia* 2008;4:T368-T9 CrossRef Medline
25. Yan S, Wan J, Zhang X, et al. **Increased visibility of deep medullary veins in leukoaraiosis: a 3-T MRI study.** *Front Aging Neurosci* 2014;6:144 CrossRef Medline
26. Zhang R, Zhou Y, Yan S, et al. **A brain region-based deep medullary veins visual score on susceptibility weighted imaging.** *Front Aging Neurosci* 2017;9:269 CrossRef Medline
27. Thore CR, Anstrom JA, Moody DM, et al. **Morphometric analysis of arteriolar tortuosity in human cerebral white matter of preterm, young, and aged subjects.** *J Neuropathol Exp Neurol* 2007;66:337–45 CrossRef Medline
28. Pettersen JA, Keith J, Gao F, et al. **CADASIL accelerated by acute hypotension arterial and venous contribution to leukoaraiosis.** *Neurology* 2017;88:1077–80 CrossRef Medline
29. Makedonov I, Black SE, MacIntosh BJ. **BOLD fMRI in the white matter as a marker of aging and small vessel disease.** *PLoS One* 2013;8:e67652 CrossRef Medline
30. Bousser M, Chiras J, Bories J, et al. **Cerebral venous thrombosis–a review of 38 cases.** *Stroke* 1985;16:199–13 CrossRef Medline
31. Krayenbühl HA. **Cerebral venous and sinus thrombosis.** *Neurol Med Chir (Tokyo)* 1968;10:1–24 CrossRef Medline
32. Leach JL, Fortuna RB, Jones BV, et al. **Imaging of cerebral venous thrombosis: current techniques, spectrum of findings, and diagnostic pitfalls.** *Radiographics* 2006;26:S19–41 CrossRef Medline
33. Boldrey E, Miller ER. **Arteriovenous fistula (aneurysm) of the great cerebral vein (of Galen) and the circle of Willis: report on two patients treated by ligation.** *Arch Neurol Psychiatry* 1949;62:778–83 CrossRef Medline
34. Doubal FN, MacLullich AM, Ferguson KJ, et al. **Enlarged perivascular spaces on MRI are a feature of cerebral small vessel disease.** *Stroke* 2010;41:450–54 CrossRef Medline
35. Roher AE, Kuo Y-M, Esh C, et al. **Cortical and leptomeningeal cerebrovascular amyloid and white matter pathology in Alzheimer's disease.** *Mol Med* 2003;9:112 CrossRef Medline
36. Cumurciuc R, Guichard JP, Reizine D, et al. **Dilation of Virchow-Robin spaces in CADASIL.** *Eur J Neurol* 2006;13:187–90 CrossRef Medline
37. Iliff JJ, Wang M, Liao Y, et al. **A paravascular pathway facilitates CSF flow through the brain parenchyma and the clearance of interstitial solutes, including amyloid β.** *Sci Transl Med* 2012;4:147ra111 CrossRef Medline

The Internal Cerebral Vein: New Classification of Branching Patterns Based on CTA

K. Brzegowy, M.P. Zarzecki, A. Musiał, H.M. Aziz, T. Kasprzycki, R.S. Tubbs, T. Popiela, and J.A. Walocha

ABSTRACT

BACKGROUND AND PURPOSE: The internal cerebral vein begins at the foramen of Monro by the union of the thalamostriate and the anterior septal veins. The lateral direct vein is its other major tributary. Numerous researchers have reported differences in internal cerebral vein branching patterns but did not classify them. Hence, the objectives of this study were to evaluate the anatomy of the internal cerebral vein and its primary tributaries and classify them depending on their course patterns using CTA.

MATERIALS AND METHODS: Head CTAs of 250 patients were evaluated in this study, in which we identified the number and termination of the anterior septal vein and the lateral direct vein. The course of the lateral direct vein and its influence on the number of thalamostriate veins and their diameters and courses were assessed. The anterior septal vein–internal cerebral vein junctions and their locations in relation to the foramen of Monro also were evaluated.

RESULTS: We classified internal cerebral vein branching patterns into 4 types depending on the presence of an extra vessel draining the striatum. Most commonly, the internal cerebral vein continued further as 1 thalamostriate vein (77%). The lateral direct veins were identified in 22% of the hemispheres, and usually they terminated at the middle third of the internal cerebral vein (65.45%). The most common location of the anterior septal vein–internal cerebral vein junction was anterior (57.20%), with the anterior septal vein terminating at the venous angle.

CONCLUSIONS: Detailed knowledge of the anatomy of the deep cerebral veins is of great importance in neuroradiology and neurosurgery because iatrogenic injury to the veins may result in basal nuclei infarcts. A classification of internal cerebral vein branching patterns may aid clinicians in planning approaches to the third and lateral ventricles.

ABBREVIATIONS: ASV = anterior septal vein; ICV = internal cerebral vein; LDV = lateral direct vein; TSV = thalamostriate vein

The internal cerebral vein (ICV), together with the basal vein of Rosenthal and their tributaries, form the deep cerebral venous system. The ICV begins at the union of the anterior septal vein (ASV) and the thalamostriate vein (TSV) at the posterior margin of the foramen of Monro.[1] Other major tributaries that join the ICV include the lateral direct vein (LDV) and the medial atrial vein. The deep cerebral veins have received little attention in comparison with the cerebral arteries. However, because of their high inter- and intraindividual variability, they are of particular interest to neuroradiologists and neurosurgeons. Detailed anatomic knowledge of both the normal and variant anatomy of the ICV branching patterns is crucial to develop optimal surgical strategies to access the third and lateral ventricles, and the large number of diagnostic head studies available currently allows us to conduct an assessment of anatomic variations on a great number of subjects.

The thalamostriate vein is usually the largest tributary of the ICV. The TSV receives several transverse caudate veins, and overall, it collects blood from the caudate nucleus, internal capsule, lentiform nucleus, claustrum, extreme capsule, and the white matter of the frontoparietal lobes.[1,2] The U-shaped angle where the junction of the TSV and the ICV forms is called the venous angle[1] and is an anatomic landmark for access to the third ventricle via the lateral ventricle.[3,4] A true venous angle is adjacent to the posterior margin of the foramen of Monro, while a false venous angle lies behind it.[3] Another important clinical aspect is the ASV termination at the ICV because the location of the ASV–ICV junction determines the limit of posterior enlargement of

Received April 10, 2019; accepted after revision July 25.

From the Department of Anatomy (K.B., M.P.Z., A.M., H.M.A., T.K., J.A.W.), Jagiellonian University Medical College, Krakow, Poland; Seattle Science Foundation (R.S.T.), Seattle, Washington; and Departments of Radiology and Rescue Medicine and Multiorgan Trauma (T.P.), University Hospital, Krakow, Poland.

Please address correspondence to Karolina Brzegowy, Department of Anatomy, Jagiellonian University Medical College, Krakow, Poland, 12 Kopernika St, 31–034 Krakow, Poland; e-mail: karolina.brzegowy@gmail.com

Indicates article with supplemental on-line tables.

http://dx.doi.org/10.3174/ajnr.A6200

Table 1: The termination points of the ASV[a]

ASV Termination Type	ASV Termination	Total (531 ASVs)	
Type A	Venous angle	383	72.13%
Type B	ICV: anterior third	76	14.31%
	ICV: middle third	52	9.79%
	ICV: posterior third	1	0.19%
	ICV elongation (absent TSV)	20	3.77%
	LDV	5	0.94%
	MAV	15	2.82%
	Cavernous sinus	1	0.19%

Note:—MAV indicates medial atrial vein.

[a] Types A and B refer to the classification of ASV–ICV junction proposed by Türe et al (1997),[3] and they differentiate between the ASV located at the venous angle (anteriorly) or beyond it (posteriorly).[11]

the foramen of Monro. An ASV terminating at the ICV at the venous angle is a disadvantage, while an ASV joining the trunk of the ICV is an advantage because it allows greater surgical exposure of the third ventricle. Türe et al,[3] in 1997, subclassified the true (type I) and false (type II) venous angles further into subtypes: A, in which the ASV–ICV junction is located at the venous angle, and B, in which the ASV joins the main stem of the ICV beyond the venous angle, with a total of 4 venous angle types (IA, IB, IIA, IIB).

The LDV, or the thalamocaudate vein,[5,6] is located on the floor of the body of the lateral ventricle and enters the ICV at various levels.[1] A prominent LDV drains blood from the lateral part of the body of the lateral ventricle and receives tributaries from the caudate nucleus. As the LDV takes over the area the TSV usually drains, the TSV may be insufficiently developed when it is present.[6,7]

The increasing use of micro-operative techniques to approach the cerebral areas through which the deep cerebral veins course necessitates a thorough understanding of their course and drainage patterns. An injury to an important deep cerebral vein may result in hemorrhage or basal nuclei infarcts that could lead to severe functional impairment.[8] The ICV tributaries should be preoperatively investigated via diagnostic imaging studies specifically when these veins would undergo surgical manipulation during access to the third and lateral ventricles.

Hence, the objective of this study was to evaluate the anatomy of the internal cerebral vein and its main tributaries, including the ASV, TSV, and LDV, and to classify the veins depending on their course patterns using CTA.

MATERIALS AND METHODS

Evaluation of the ICV anatomy in this retrospective study was conducted on adult Polish patients who underwent a head CTA at the Department of Radiology, Department of Rescue Medicine and Multiorgan Trauma, University Hospital in Krakow, Poland, between June 2017 and July 2018. The exclusion criteria included the following: hydrocephalus; cerebral lesions (intracranial hematoma, tumors, vascular malformations); posttraumatic, postsurgical, and poststroke defects that affect the presence and course of the veins; significant imaging artifacts (such as low quality or illegible images); postcraniotomy state; and incomplete cross-sections. Of the initial 292 patients with CTA scans available, a total of 42 were excluded because of significant imaging artifacts (n = 22), incomplete cross-sections (n = 2), massive hydrocephalus (n = 3), cerebral lesions (n = 14), and repeat studies (n = 1). The remaining 250 patients were included in this study, of whom 84 were men (33.6%) and 166 were women (66.4%).

The study was performed using a multidetector row CT scanner (Optima CT 660; GE Healthcare, Milwaukee, Wisconsin), and a nonionic contrast agent iomeprol (70 mL administered; Iomeron 350; 350 mg iodine/mL; Bracco Imaging, Milan, Italy) was injected. After the bolus reached the common carotid artery at a level of C3–C4, the scanning procedure initiated automatically. The scanner settings were as follows: 120 kV, 200 mA, and 64 × 0.625 mm section collimation. Axial 0.625-mm slices at increments of 1.25 mm were reconstructed using a 512 × 512 matrix, with a standard kernel applied. The data were analyzed on a dedicated workstation (Advantage Workstation AW4.5; GE Healthcare) equipped with software for MIP and 3D volume-rendering postprocessing of images. The analysis was performed primarily on the MIP cross-sectional images (axial, sagittal, coronal). The statistical analysis was conducted with SPSS, Version 25, 2000–2016 (IBM, Armonk, New York). The χ^2 independence test was applied for the dichotomous and nominal variables, and P was set at $<.05$.

The Anatomical Quality Assurance Checklist of the International Evidence-Based Anatomy Working Group, Department of Anatomy, Jagiellonian University Medical College in Krakow, Poland, was used to ensure high-quality reporting of anatomic variants in this study.[9] The Bioethical Committee of the Jagiellonian University, Krakow, Poland, approved the study (No. 1072.6120.121.2018).

RESULTS

We evaluated 84 men and 166 women whose average age was 52.3 ± 16.6 years (range, 19–89 years). A total of 250 CTA images were deemed eligible for the study.

In the total research material, we observed the following number of ASVs present: no ASV present in 3 hemispheres (3 on the right side), 1 present (the most common) in 464 hemispheres (234 right and 230 left hemispheres), 2 present in 32 hemispheres (13 right, 19 left), and last, the least common, 3 ASVs in just 1 hemisphere (left). The number of ASVs that predominated in both right and left hemispheres among patients of both sexes was 1 (95.24% of right and 91.67% of left male hemispheres, and 92.77% right and 92.17% left female hemispheres). No statistically significant differences were found between the number of ASVs present and the hemispheres in the sample overall ($P = .16$), in the male patients ($P = .27$), in the female patients ($P = .36$), or while comparing the variant presence of the ASV in the different hemispheres and both sexes ($P = .16$). The terminations of the ASV encountered in the study material is presented in Table 1. The most common was termination at the venous angle (71.15% of the right and 73.06% of the left hemispheres).

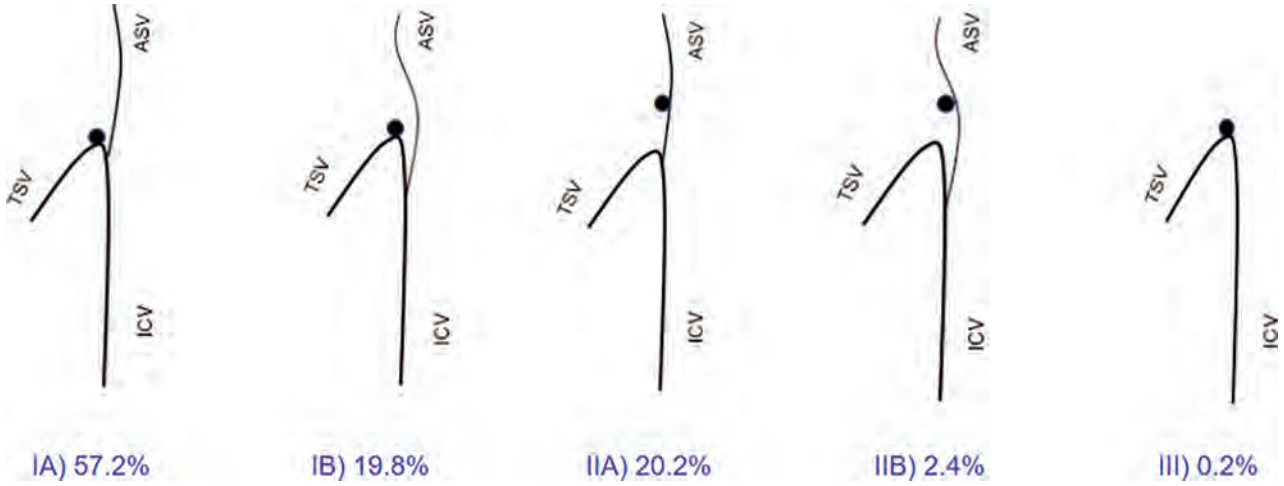

FIG 1. Variations of the ASV–ICV junction and its relation to the foramen of Monro. There are a total of 5 venous angle types (IA, IB, IIA, IIB, III).[3] Types I and II refer to the relation of the venous angle to the foramen of Monro (adjacent to or located behind, respectively), whereas types A and B differentiate the ASV located at the venous angle (anteriorly) or beyond it (posteriorly). In type III, the ASV is absent.

Table 2: The termination points of the lateral direct vein[a]

Branching Type	LDV Termination	Total (110 LDV)	
Type 2 (a suprathalamic LDV)	ICV: anterior third	8	7.27%
	ICV: middle third	70	63.64%
	ICV: middle third, as a common stem with an MAV	2	1.82%
Type 3 (a retrothalamic LDV)	ICV: posterior third	18	16.36%
	ICV: posterior third, as a common stem with an MAV	8	7.27%
	Great cerebral vein	2	1.82%

Note:—MAV indicates medial atrial vein.
[a] The presence of the LDV characterizes types 2 and 3 of the ICV branching patterns.

The ASV–ICV junction was divided into 5 types[3] and was present as follows: type IA: 286 hemispheres (147 right and 139 left hemispheres); type IB: 99 hemispheres (52 right, 47 left); type IIA: 101 hemispheres (41 right, 60 left); and type IIB: 12 hemispheres (8 right, 4 left) (Fig 1). Type III, ASV absent, was found only in 2 hemispheres (both on the right side). Type IA predominated in both men (50% of the right and 54.76% of the left hemispheres) and women (63.25% of the right and 56.02% of the left hemispheres). No statistically significant differences were found between the type of ASV–ICV junction present and the hemispheres in the sample overall ($P = .12$), in the male patients ($P = .06$), in the female patients ($P = .28$), or while comparing the variant presence of the ASV–ICV junction on the different hemispheres and sexes combined ($P = .12$). Two distinctly different types (asymmetric) of the ASV–ICV junction in both hemispheres were found in 41 men and 89 women.

The number of TSVs found was as follows: no TSVs in 17 hemispheres (9 right, 8 left), 1 TSV in 480 hemispheres (239 right, 241 left), and 2 TSVs in only 3 hemispheres (2 right, 1 left). One TSV predominated in both hemispheres in both sexes. No statistically significant differences were found between the number of TSVs present and the hemispheres in the sample overall ($P = .82$), in the male patients ($P = .27$), in the female patients ($P = .57$), or while comparing the variant presence of the TSV in the different hemispheres and the sexes combined ($P = .82$). Bifurcation of the TSV was noted in 23 right and 15 left hemispheres with the TSV present.

The LDV was present in 110 hemispheres (62 right, 48 left). No statistically significant differences were found between the presence of the LDV and the hemispheres in the sample overall ($P = .13$), in the male patients ($P = .47$), in the female patients ($P = .18$), or while comparing the variable presence of the LDV in the different hemispheres and sexes combined ($P = .13$). Only single LDVs were observed. The various points of termination of the LDVs are presented in Table 2. The most common termination point was found to be the middle third of the ICV (64.52% of the right and 66.67% of the left hemispheres).

Classification

We classified ICV tributaries into 4 types, depending on the main veins draining the basal nuclei (Fig 2). In type 1, only the thalamostriate vein collects blood from the basal nuclei and the LDV is absent. The presence of the LDV located above or behind the thalamus characterizes types 2 and 3, respectively. Type 2 comprises all suprathalamic LDVs terminating at the anterior and middle thirds of the ICV. Type 2 includes retrothalamic LDVs, terminating at the posterior third of the ICV or the great cerebral vein. In type 4, the basal vein takes an unusual course and drains the basal nuclei. In these hemispheres, the branches from the caudate nucleus join the basal vein, which further forms a loop in the atrium of the lateral ventricle and terminates at the ICV or great cerebral vein. The prevalence of each type is presented in On-line Table 1. Detailed characteristics of deep cerebral veins within types 2 and 3, including the influence of the presence of an LDV on the TSV presence, TSV length, TSV diameter, and the ICV diameter are presented in On-line Table 2.

Type 1 was the most common type present in this study (77% of all hemispheres), while type 4 was present least often (1% of all hemispheres). The same was true for men and women when considered independently. Statistically significant differences were found neither between the hemispheres and the types in general ($P = .23$) nor between the types and sexes in general ($P = .41$). Furthermore, statistically insignificant results were also obtained in the presence of the particular types in specific hemispheres only in men ($P = .67$) or women ($P = .24$). Last, no statistically significant differences were found in the combined analysis of sex, hemisphere, and type ($P = .25$). Symmetric types were found between the 2 hemispheres in 50 men and 110 women (59.5% and 66.3%, respectively). Notwithstanding, the discrepancies were not statistically significant ($P = .29$).

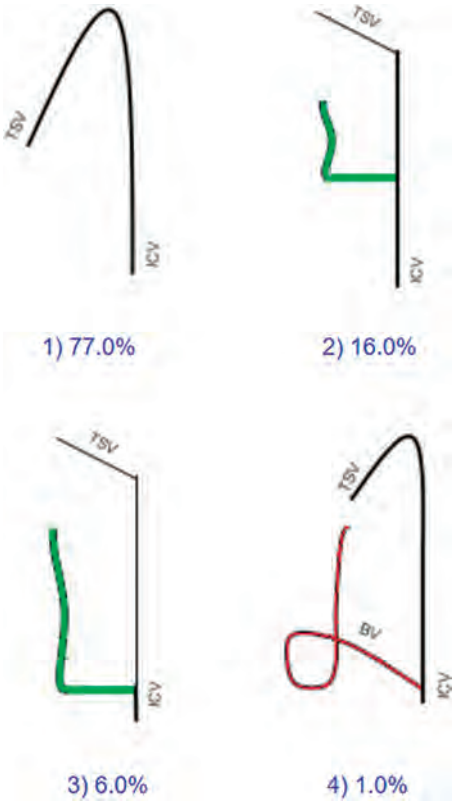

FIG 2. Types of ICV branching patterns. We classified ICV tributaries into 4 types with respect to the main veins draining the basal nuclei. In type 1, only the thalamostriate vein collects blood from the basal nuclei. Types 2 and 3 are characterized by the presence of a suprathalamic or retrothalamic LDV, respectively, which receives tributaries from the striatum. In type 4, the basal vein takes an unusual course and drains the basal nuclei.

DISCUSSION

Previous studies on the deep cerebral veins have focused on the venous anatomy only in the region of the foramen of Monro, and currently existing classifications focus solely on the location of the ASV–ICV junction.[7,10,11] Numerous researchers have reported differences in ICV branching patterns but did not classify them.[10,12] This study describes variations in the major veins joining the entire trunk of the ICV and classifies them. It is vital to explore detailed anatomic characteristics of all the tributaries of the ICV, especially the LDV, because a surgical strategy may require altering when it is present.

The primary tributary of the ICV is either the TSV or the LDV. Our study found that the TSV was the only tributary draining the striatum in 77% of the hemispheres; thus, we consider this type to be a normal anatomy (type 1) (Fig 3*A*). We found an LDV in 22% of the hemispheres, which is less than reported previously in a cadaveric study (35%) and a radiologic study on MRA (36%).[6,7] In 18.6% of the hemispheres included in our study, both the TSV and the LDV drained the striatum. When the LDV was present, the TSV had a reduced diameter compared with the ipsilateral TSV in 38.95% of the hemispheres. The literature suggests that the size of the LDV may be proportionally inverse to that of the TSV.[6] The TSV was absent in 3.4% of the hemispheres, and the LDV was the only tributary draining the striatum (Fig 4). The LDV may drain most blood for the ICV; therefore, the ICV diameter is visibly smaller anterior to the LDV. Identification of the major tributary of the ICV is of immense importance because a surgical occlusion or an injury to the vein draining the basal ganglia may result in a venous infarction.[13]

Our results show that 64% of the patients had different types of patterns of ICV tributaries in the left and right hemispheres. Therefore, before a surgical approach in the region of the third and the lateral ventricles, the appearance and size of the ICV tributaries should be investigated for each individual patient.

Another important clinical aspect is the relation of an LDV to the thalamus and the lateral ventricles.[1] In our study, a suprathalamic LDV (type 2: 16.00%) was more prevalent than the retrothalamic LDV (type 3: 6.00%) (Fig 3*B*, -*C*). The findings of our study are also valuable for an operation on the lateral ventricles. Removal of a mass located in the body of the lateral ventricle exposes vascular structures localized beneath the

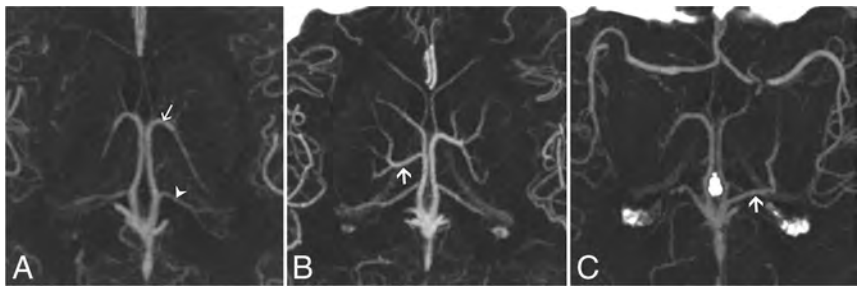

FIG 3. CTA MIP axial cross-sections of the ICV branching patterns. *A*, Normal ICV anatomy (type 1) in both the left and right hemispheres. The *arrow* indicates the TSV; the *arrowhead*, the medial atrial vein. *B*, The suprathalamic variants of the lateral direct vein (right hemisphere). The *arrow* indicates the LDV. Type 1 is present in the left hemisphere. *C*, The retrothalamic LDV (left hemisphere). The *arrow* indicates the LDV. Type 1 is shown in the right hemisphere.

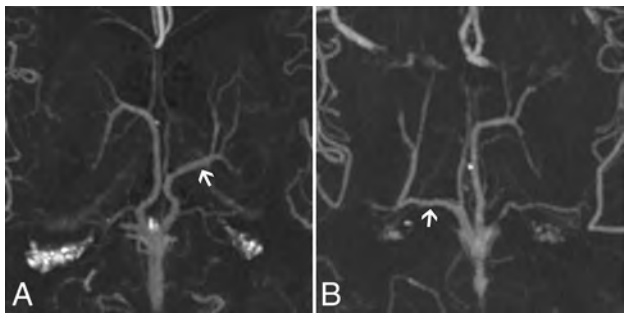

FIG 4. CTA MIP axial cross-sections of the ICV branching patterns with an LDV and an absent thalamostriate vein. *Arrows* indicate LDVs. *A*, The suprathalamic LDV (type 2; left hemisphere). *B*, The retrothalamic LDV (type 3; right hemisphere).

lesion, and an LDV originating from the anterior or middle portion of the ICV courses farther in this area. Preoperative assessment of veins coursing in the body of the lateral ventricle would help in the development of a dissection plan that minimizes the risk of vascular complications.[14]

As stated above, the anatomy of the ICV tributaries is particularly important in minimally invasive procedures such as deep brain stimulation because placing an electrode properly ensures that no vessel is injured. It has been proved that a minor change in the deep brain stimulation electrode location may make a major difference between penetrating or avoiding a vessel; thus, it can lead to an important difference for the patient's outcome.[15,16] Furthermore, the venous anatomy of the brain is of great importance to neuroradiologists who perform endovascular interventions in deep brain AVMs and dural arteriovenous fistulas.

An operation on the third ventricle poses a major challenge for neurosurgeons because it is surrounded by vital neural and vascular structures. The foramen of Monro serves as a natural opening from the lateral ventricle to the anterior and middle portions of the third ventricle.[6,17] However, when a lesion has not widened the foramen of Monro, it can be enlarged surgically as far as the ASV–ICV junction.[11,17] Successful application of approaches to the third ventricle depends on the surgeon's knowledge of the venous variations of this region.[18]

Our study concluded that the anterior location of the ASV–ICV junction (type IA: 58.8% of the hemispheres) is more common than its posterior location (types IB + IIA + IIB: 40.4% of the hemispheres). These findings are consistent with those of other radiologic studies. Two MRA studies found type IA in 53.9% and 63.4% of hemispheres,[11,14] while a cadaveric study found it in 52.2% of the hemispheres.[3] Furthermore, our study revealed that nearly half of the patients (48%) had an ASV–ICV junction asymmetry between 2 hemispheres. This is particularly clinically important in planning a third ventricle operation because the ventricle can be accessed more easily via the side on which the ASV–ICV junction is located posteriorly. In the event of bilateral ASV–ICV junctions located at the venous angles, posterior enlargement of the foramen of Monro is prevented on both sides and the third ventricle has to be accessed via the interforniceal approach.[19] Preoperative assessment of the location and symmetry of the ASV–ICV junction may facilitate developing optimal surgical strategies to access the third ventricle and decrease the risk of iatrogenic injury.

Our study was limited by the technique with which the ICV evaluation was conducted. CTA may not have detected small veins terminating at the ICV because of insufficient resolution of this imaging method. However, our goal in this study was to provide general information on the largest of the ICV tributaries as well as their frequencies. Several studies have been conducted on high-field (3T, 9.4T), SWI MRA that focused on the small deep medullary veins.[17,20] Second, we performed only a qualitative analysis of vessel diameters by comparing the LDV with the ipsilateral TSV and 1 TSV with the contralateral one. Last, we analyzed only white patients; thus, no interracial differences were investigated. Future studies should attempt to investigate the morphometric lengths of the veins to enhance patient outcomes.

CONCLUSIONS

We found that the TSV alone was the main ICV tributary draining the striatum in 77% of the hemispheres; therefore, we considered this pattern the normal anatomy (type 1). The LDV as the additional vein draining the striatum was present in 18.6% of the hemispheres and replaced the TSV in 3.4%. The ASV–ICV junction usually was located at the foramen of Monro (57.2%). We also developed a new classification system of the deep cerebral veins draining into the ICV to increase the safety and quality of treatment and diagnosis provided by neuroradiologists and neurosurgeons worldwide.

- Types 2 and 3 warrant consideration during surgical approaches to the body of the lateral ventricle because a sacrifice of a major vein draining the basal nuclei may result in serious complications, such as venous infarction.
- A suprathalamic LDV (type 2) and a retrothalamic LDV (type 3) outline the superior and posterior surfaces of the thalamus, respectively, and require attention during a thalamic operation.
- Type 4 should be identified prior to managing lesions situated in the atrium of the lateral ventricle.

A thorough preoperative understanding of the variation in the patterns of deep cerebral veins may help reduce the risk of iatrogenic injury to those vessels.

Disclosures: Michał P. Zarzecki—*UNRELATED*: *Grants/Grants Pending*: Polish Ministry of Science and Higher Education, *Comments*: "The Best of the Best! 3.0" grant for the young researchers to assist with costs of international competitions and conferences.* Tadeusz Popiela—*UNRELATED*: *Employment*: Specjalistyczna Praktyka Lekarska. *Money paid to the institution.

REFERENCES

1. Salamon G, Huang YP, Michotey P, et al. **Deep cerebral veins.** In: Salamon G, Huang YP, Michotey P, et al. *Radiologic Anatomy of the Brain*. Berlin: Springer-Verlag; 1976:210–61
2. Zhang X, Li J, Wen X, et al. **Susceptibility-weighted imaging of the anatomic variation of thalamostriate vein and its tributaries.** *PLoS One* 2015;10:e0141513 CrossRef
3. Türe U, Yaşargil MG, Al-Mefty O. **The transcallosal-transforaminal approach to the third ventricle with regard to the venous variations in this region.** *J Neurosurg* 1997;87:706–15 CrossRef Medline

4. Sindou M. **The "dangerous" intracranial veins.** In: Sindou M. *Practical Handbook of Neurosurgery*. Vienna:Springer-Verlag; 2009: 71–83
5. Sindou M, Auque J. **The intracranial venous system as a neurosurgeon's perspective.** *Adv Tech Stand Neurosurg* 2000;26:131–216 Medline
6. Ono M, Rhoton AL, Peace D, et al. **Microsurgical anatomy of the deep venous system of the brain.** *Neurosurgery* 1984;15:621–57 CrossRef Medline
7. Wang J, Wang J, Sun J, et al. **Evaluation of the anatomy and variants of internal cerebral veins with phase-sensitive MR imaging.** *Surg Radiology Anat* 2010;32:669–74 CrossRef Medline
8. Sindou MP, Auque J, Jouanneau E. **Neurosurgery and the intracranial venous system.** In: Yonekawa Y, Sakurai Y, Keller E, et al eds. *New Trends of Surgery for Stroke and its Perioperative Management*. Vienna: Springer-Verlag; 2005:167–75
9. Tomaszewski KA, Henry BM, Kumar Ramakrishnan P, et al. **Development of the Anatomical Quality Assurance (AQUA) Checklist: guidelines for reporting original anatomical studies.** *Clin Anat* 2017;30:14–20 CrossRef Medline
10. Mokrohisky JF, Paul RE, Lin PM, et al. **The diagnostic importance of normal variants in deep cerebral phlebography.** *Radiology* 1956;67:34–47 CrossRef Medline
11. Fujii S, Kanasaki Y, Matsusue E, et al. **Demonstration of cerebral venous variations in the region of the third ventricle on phase-sensitive imaging.** *AJNR Am J Neuroradiol* 2010;31:55–59 CrossRef Medline
12. Lang J. **Surgical anatomy of the hypothalamus.** *Acta Neurochir (Wien)* 1985;75:5–22 CrossRef Medline
13. Elhammady MS, Heros RC. **Cerebral veins: to sacrifice or not to sacrifice, that is the question.** *World Neurosurg* 2015;83:320–24 CrossRef Medline
14. Çagatay Çimsit N, Türe U, Ekinci G, et al. **Venous variations in the region of the third ventricle: the role of MR venography.** *Neuroradiology* 2003;45:900–04 CrossRef Medline
15. Nowinski WL, Chua BC, Marchenko Y, et al. **Three-dimensional reference and stereotactic atlas of human cerebrovasculature from 7 Tesla.** *Neuroimage* 2011;55:986–98 CrossRef Medline
16. Mahvash M, Pechlivanis I, Charalampaki P, et al. **Visualization of small veins with susceptibility-weighted imaging for stereotactic trajectory planning in deep brain stimulation.** *Clin Neurol Neurosurg* 2014;124:151–55 CrossRef Medline
17. Chen Z, Qiao H, Guo Y, et al. **Visualization of anatomic variation of the anterior septal vein on susceptibility-weighted imaging.** *PLoS One* 2016;11:e0164221 CrossRef Medline
18. Schijman E. **Microsurgical anatomy of the transcallosal approach to the ventricular system, pineal region and basal ganglia.** *Childs Nerv Syst* 1989;5:212–19 CrossRef Medline
19. Greenberg MS. *Handbook of Neurosurgery*. 7th ed. New York: Thieme Medical Publishers; 2010:168–72
20. Budde J, Shajan G, Hoffmann J, et al. **Human imaging at 9.4 T using T2*-, phase-, and susceptibility-weighted contrast.** *Magn Reson Med* 2011;65:544–50 CrossRef Medline

Cerebral Venous Thrombosis: MR Black-Blood Thrombus Imaging with Enhanced Blood Signal Suppression

G. Wang, X. Yang, J. Duan, N. Zhang, M.M. Maya, Y. Xie, X. Bi, X. Ji, D. Li, Q. Yang, and Z. Fan

ABSTRACT

BACKGROUND AND PURPOSE: The residual blood flow artifact is a critical confounder for MR black-blood thrombus imaging of cerebral venous sinus thrombosis. This study aimed to conduct a validation of a new MR black-blood thrombus imaging technique with enhanced blood signal suppression.

MATERIALS AND METHODS: Twenty-six participants (13 volunteers and 13 patients) underwent conventional imaging methods followed by 2 randomized black-blood thrombus imaging scans, with a preoptimized delay alternating with nutation for tailored excitation (DANTE) preparation switched on and off, respectively. The signal intensity of residual blood, thrombus, brain parenchyma, normal lumen, and noise on black-blood thrombus images were measured. The thrombus volume, SNR of residual blood, and contrast-to-noise ratio for residual blood versus normal lumen, thrombus versus residual blood, and brain parenchyma versus normal lumen were compared between the 2 black-blood thrombus imaging techniques. Segmental diagnosis of venous sinus thrombosis was evaluated for each black-blood thrombus imaging technique using a combination of conventional imaging techniques as a reference.

RESULTS: In the volunteer group, the SNR of residual blood (11.3 ± 2.9 versus 54.0 ± 23.4, $P < .001$) and residual blood-to-normal lumen contrast-to-noise ratio (7.5 ± 3.4 versus 49.2 ± 23.3, $P < .001$) were significantly reduced using the DANTE preparation. In the patient group, the SNR of residual blood (16.4 ± 8.0 versus 75.0 ± 35.1, $P = .002$) and residual blood-to-normal lumen contrast-to-noise ratio (12.4 ± 7.8 versus 68.8 ± 35.4, $P = .002$) were also significantly lower on DANTE-prepared black-blood thrombus imaging. The new black-blood thrombus imaging technique provided higher thrombus-to-residual blood contrast-to-noise ratio, significantly lower thrombus volume, and substantially improved diagnostic specificity and agreement with conventional imaging methods.

CONCLUSIONS: DANTE-prepared black-blood thrombus imaging is a reliable MR imaging technique for diagnosing cerebral venous sinus thrombosis.

ABBREVIATIONS: BTI = black-blood thrombus imaging; CE = contrast-enhanced; CNR = contrast-to-noise ratio; CVT = cerebral venous sinus thrombosis; DANTE = delay alternating with nutation for tailored excitation; TSE = turbo spin-echo; SPACE = sampling perfection with application-optimized contrasts by using different flip angle evolution

Cerebral venous sinus thrombosis (CVT) is a potentially life-threatening cerebrovascular disorder that most often affects young individuals.[1] MR imaging is currently the best noninvasive imaging technique for the diagnosis of CVT.[2] A series of MR images, such as T1- and T2-weighted turbo spin-echo (TSE), T2*-weighted gradient recalled-echo, and MRV, are usually combined to confirm the diagnosis and stage of CVT. However, technical limitations associated with each of these methods may

Received May 10, 2019; accepted after revision July 29.

From the Department of Biomedical Sciences (G.W., N.Z., Y.X., D.L., Q.Y., Z.F.), Biomedical Imaging Research Institute, and Department of Imaging (M.M.M.), Cedars-Sinai Medical Center, Los Angeles, California; Department of Radiology (G.W.), The First Affiliated Hospital of China Medical University, Shenyang, China; Departments of Emergency (J.D., X.J.) and Radiology (X.Y., Q.Y.) Xuanwu Hospital, Capital Medical University, Beijing, China; Paul C. Lauterbur Research Center for Biomedical Imaging (N.Z.), Shenzhen Institutes of Advanced Technology, Chinese Academy of Sciences, Shenzhen, China; MR R&D (X.B., D.L.), Siemens Healthineers, Los Angeles, California; and Departments of Medicine (D.L., Z.F.) and Bioengineering (Z.F.), University of California, Los Angeles, California.

G. Wang and X. Yang have contributed equally to this work.

This work was supported by National Institutes of Health/National Heart, Lung, and Blood Institute 1 R01 HL147355 and Beijing Natural Science Foundation (No. 17L20253), The National Science Foundation of China (No. 91749127 and 81830056), and Beijing Municipal Administration of Hospitals Clinical Medicine Development of Special Funding Support. (ZYLX201706).

Please address correspondence to Zhaoyang Fan, PhD and Qi Yang, MD, PhD, 8700 Beverly Blvd, Pacific Theatres Suite 400, Los Angeles, CA 90048, e-mail: Zhaoyang.Fan@csmc.edu; yangyangqiqi@gmail.com

Indicates open access to non-subscribers at www.ajnr.org
Indicates article with supplemental on-line appendix.
Indicates article with supplemental on-line photos.
http://dx.doi.org/10.3174/ajnr.A6212

result in an equivocal diagnosis.[3] Moreover, inconsistent spatial coverage and resolution among these 2D and 3D scans along with their potential misregistration would preclude precise characterization of CVT in, for example, its location, extent, and the degree of recanalization. Detailed knowledge of these aspects is, however, relevant to treatment decision-making and therapeutic response monitoring.[4,5]

Recently, an MR black-blood thrombus imaging (BTI) method based on a T1-weighted 3D variable-flip angle TSE sequence was proposed for early detection of CVT.[6] The sequence has an inherent black-blood effect and superior SNR performance.[7] The black-blood image contrast in BTI allows thrombi to be visually isolated within the dark lumen of the venous sinuses. Configured as a T1-weighted acquisition, BTI is particularly useful for the detection of subacute CVT, which is rich in short-T1 methemoglobins and thus appears hyperintense with respect to surrounding brain parenchyma and sinus lumen.

Despite the high sensitivity and specificity reported for the detection of subacute CVT,[6] BTI is potentially limited in accurately characterizing acute (particularly hyperacute) or chronic CVT due to the presence of residual blood flow artifacts. Residual signal intensity was observed in the venous sinuses, which has been attributed to slow flow velocity and inadequate blood signal attenuation of the sequence.[6] While such artifacts have a negligible influence on the detection of subacute CVT, they may pose a diagnostic challenge in the detection of thrombi in chronic and acute CVT because thrombi and venous blood have similar signal intensities on T1-weighted images.[8]

The goal of this work was to present an MR BTI technique with enhanced blood signal attenuation and perform a clinical study to validate its improved performance in imaging of CVT and to demonstrate the feasibility of CVT characterization.

MATERIALS AND METHODS

Study Population

Twenty-six participants, including 13 healthy volunteers (9 women; 35–65 years of age; mean age, 53 years) and 13 patients (7 women; 19–54 years of age; mean age, 35 years), were recruited to undergo MR BTI studies. The inclusion criteria were no history of cerebrovascular diseases for healthy controls and CVT diagnosed on the basis of clinical symptoms and conventional imaging techniques (CT, TSE, SWI, contrast-enhanced [CE]-MRV, and TOF-MRV) for patients. Exclusion criteria included contraindications for MR imaging and intolerance to additonal MR images. Xuanwu Hospital institutional review committee approval and patients' informed consent were obtained.

Imaging System

Imaging was performed on a 3T whole-body system (Magnetom Verio; Siemens, Erlangen, Germany). A standard head-neck 12-channel coil was used for receiving signals from a volume ranging from the superior sagittal sinus to the internal jugular veins.

MR Imaging Sequence

The sequence used for MR BTI was designed on the basis of sampling perfection with application-optimized contrasts by using different flip angle evolution (SPACE sequence; Siemens).[7] A previously proposed black-blood preparation method, delay alternating with nutation for tailored excitation (DANTE),[9] was used to improve the suppression of venous flow signals while introducing minimal T2 weighting.[10,11] The DANTE module consists of a train of short, hard radiofrequency pulses interspersed with dephasing gradients that are applied simultaneously in all 3 orthogonal directions. The module is followed by chemically selective fat saturation and a T1-weighted SPACE readout. Whole-head spatial coverage is achieved using nonselective hard radiofrequency pulses for excitation, which averts the need for multiple signal averages to suppress free-induction-decay artifacts.[7] A saggitally oriented imaging volume is prescribed, which requires fewer partitions than other imaging orientations, to further reduce the imaging time. Three 40-mm-wide spatial presaturation bands are applied immediately before excitation to suppress the signals from the nose and ears if they are located outside the prescribed imaging volume. The parameters of the DANTE preparation were optimized for adequate flow signal suppression in a separate volunteer study (detailed in the On-line Appendix).

Imaging Protocol

All participants underwent conventional MR imaging sequences followed by 2 randomized BTI scans, with DANTE preparation switched on (DANTE+) and off (DANTE−), respectively. The major imaging parameters used in the SPACE readout were the following: TR/TE = 600/14 ms; FOV = $300 \times 206 \times 162$ mm^3; matrix size = $384 \times 264 \times 208$; spatial resolution = 0.78 mm isotropic; 6/8 partial Fourier in the partition-encoding direction; echo-train length = 36; parallel imaging (generalized autocalibrating partially parallel acquisition) acceleration factor = 2 in the phase-encoding direction; elliptic *k*-space sampling; scan time = 5 minutes 40 seconds.

Image Analysis

Image review and signal intensity measurements were performed on a workstation (syngo MultiModality Workplace; Siemens), where multiplanar reformation, maximum intensity projection, and minimum intensity projection functionalities were available to image reviewers. The venous system was divided into the following 16 segments: superior sagittal sinus, inferior sagittal sinus, straight sinus, confluence of sinuses, right transverse sinus, left transverse sinus, right sigmoid sinus, left sigmoid sinus, vein of Galen, internal cerebral vein, basal vein of Rosenthal, vein of Labbé, right cortical vein, left cortical vein, right internal jugular vein, and left internal jugular vein.

For the healthy volunteer group, both BTI DANTE+ and DANTE− image sets of each subject were reviewed side by side by a radiologist (G.W.) with 8 years of experience in MR image interpretation to identify residual blood signals in individual segments. When residual blood was observed in a segment, mean signal intensity was measured. The mean signal intensity of the adjacent brain parenchyma and normal lumen and noise (σ, SD of signal intensity in the adjacent air space) were also measured. The contrast-to-noise ratio (CNR) (A-to-B CNR = $[SI_A - SI_B]/\sigma$), where SI indicates signal intensity, was calculated for residual blood versus normal lumen (indicating the blood-suppressing

performance of DANTE) and for brain parenchyma versus normal lumen (indicating the overall sacrifice in the black-blood contrast caused by DANTE), respectively.

For the patient group, 2 radiologists with 13 years (Q.Y.) and 8 years (G.W.) of experience in MR image interpretation, respectively, performed consensus reading. Combined conventional sequences from the 13 subjects were blindly reviewed for segment-level diagnosis of CVT. One month later, diagnostic review was also performed on the randomized 26 BTI image sets (2 sets per subject). Visible signals within the dark sinus lumens were deemed "apparent thrombi," unless they were of granule shape (highly indicative of arachnoid granulations) or appeared as floating patches (highly indicative of residual blood rather than thrombi). Furthermore, the total volume of apparent thrombi was quantified in the superior sagittal sinus by manually contouring the thrombi section by section using commercial software (Vessel Analysis, Beijing Sirui Star Technology Co., Ltd.).

The 2 BTI image sets from each patient were then reviewed side by side to scrutinize the actual incidence of residual blood and true thrombus by the same 2 radiologists. The finalized true thrombi were individually categorized into hyperintense, isointense, or hybrid types on the basis of their appearance with respect to adjacent normal brain parenchyma. Signal intensity measurement was performed, respectively, for the regions of residual blood and residual blood nearest isointense and hyperintense thrombus, normal lumen, and brain parenchyma on both image sets. The CNRs of residual blood or thrombus to other tissues were calculated.

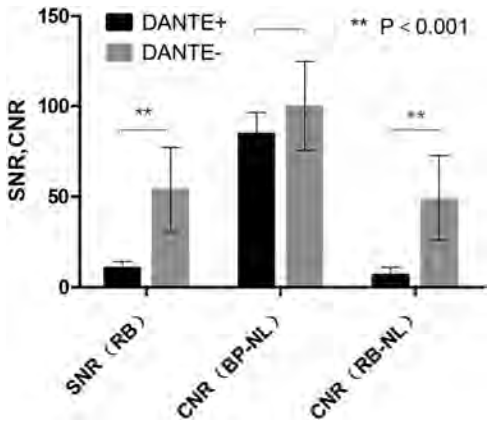

FIG 1. SNR of residual blood (RB), CNR between brain parenchyma (BP) and normal lumen (NL), and CNR between RB and NL in the healthy volunteer group. SNR of RB and RB-to-NL CNR were significantly reduced on BTI DANTE+ images compared with those on BTI DANTE- images. *Double asterisks* denote $P < .001$.

Statistical Analysis

Statistical analysis was performed using SPSS (Version 16.0; IBM, Armonk, New York). A 2-tailed Wilcoxon signed rank test was used to determine the difference in the thrombus volume, SNR, and CNR between the 2 BTI techniques. A Cohen κ test was used to determine the agreement in the diagnosis of CVT at the per-segment level between BTI and conventional imaging techniques. Conventional imaging techniques were used as the reference standard for assessing the sensitivity, specificity, and negative and positive predictive values of BTI techniques. Statistical significance was defined as $P < .05$.

RESULTS

All 26 participants successfully underwent both BTI scans. In the volunteer group, the SNR of residual blood (11.3 ± 2.9 versus 54.0 ± 23.4, $P < .001$) and residual blood-to-normal lumen CNR (7.5 ± 3.4 versus 49.2 ± 23.3, $P < .001$) were significantly reduced on BTI DANTE+ images compared with BTI DANTE− images, whereas there was no significant difference in brain parenchyma-to-normal lumen CNR (85.4 ± 11.2 versus 100.2 ± 24.7, $P = .060$ (Fig 1).

The clinical characteristics of patients are listed in Table 1. Two patients were clinically diagnosed with acute CVT (0–7 days after symptom onset); 2 patients, with subacute CVT (7–14 days); and 9 patients, with chronic CVT (≥15 days). CVT was detected in 11 subjects and 72 segments on conventional images. Blinded review of BTI reported apparent thrombi in 11 subjects and 77 segments on BTI DANTE+ but in 13 subjects and 94 segments on BTI DANTE− (Table 2). The agreement at the per-segment level between BTI and conventional imaging techniques was excellent for BTI DANTE+ ($\kappa = 0.964$) but moderate for BTI DANTE− ($\kappa = 0.770$). The specificities of CVT detection at the per-segment level were 96.3% and 83.8%, respectively, for the 2 different BTI techniques (Table 3). Representative cases are shown in Fig 2. In the 9 patients who were diagnosed with apparent thrombi in the superior sagittal sinus, the thrombus

Table 1: Clinical characteristics of patients with CVT

Patient	Sex	Age (yr)	Symptom	Duration	Conventional Imaging Methods
1	F	47	Headache	2 days	TSE, SWI, CE-MRV, TOF-MRV, CT
2	M	19	Headache	10 days	TSE, TOF-MRV, CT
3	M	54	Focal neurologic deficit	13 days	TSE, SWI, CE-MRV, TOF-MRV, CT
4	M	30	Headache, focal neurological deficit	20 days	TSE, CE-MRV, TOF-MRV, CT
5	M	44	Seizures	25 days	TSE, TOF-MRV
6	F	53	Headache	27 days	TSE, SWI, CE-MRV, TOF-MRV, CT
7	M	42	Headache	1 mo	TSE, CE-MRV, TOF-MRV
8	F	32	Headache	1 mo + 22 days	TSE, SWI, CE-MRV, TOF-MRV, CT
9	M	19	Headache	2 mo	TSE, TOF-MRV, CT
10	F	28	Headache	4 mo	TSE, TOF-MRV, CT
11	F	45	Headache, papilledema	4 mo	SWI, TOF-MRV, CT
12	F	36	Headache	1 year	TSE, CE-MRV, TOF-MRV, CT
13	F	19	Headache	2 days	TSE, TOF-MRV, CE-MRV

Table 2: Locations of thrombi and residual flow artifacts identified on BTI with and without DANTE preparation[a]

	Segments															
Pt. No.	SSS	ISS	VG	SS	CS	RTS	LTS	RSS	LSS	ICV	BVR	VL	RC	LC	RJV	LJV
1	=				=		=						=	=		
2						=		=								
3	+/=		=		+	=	=							+	+	
4	=		=	=	+/=	=	=	+	=				=	=	=	
5																
6	=		=			=	=	=	=				=	=		
7	=				=	=	=	+/=					=	=		
8	+/=		+	+/=	+/=	+/=	=	=	=	=	+				+/=	+/=
9	=	=			=	=	=	=	=					=	=	
10	+/=			+/=	+/=		+/=		+/=							=
11																
12	=				=	=	=	=	=							=
13							=		=							=

Note:—SSS indicates superior sagittal sinus; ISS, inferior sagittal sinus; VG, vein of Galen; SS, straight sinus; CS, confluence of sinus; RTS, right transverse sinus; LTS, left transverse sinus; RSS, right sigmoid sinus; LSS, left sigmoid sinus; ICV, internal cerebral vein; BVR, basal vein of Rosenthal; VL, vein of Labbé; RC, right cortical vein; LC, left cortical vein; RJV, right jugular vein; LJV, left jugular vein; =, iso-intense thrombus; +, hyperintense thrombus; +/=, hybrid thrombus.

[a] Shadow indicates that residual flow artifacts are present in the segment on BTI without DANTE preparation but not on BTI with DANTE preparation.

volume was significantly lower (4.814 ± 2.278 mL versus 6.341 ± 2.302 mL, $P = .008$) when using the DANTE preparation (Fig 3).

Table 3: Diagnostic performance of BTI with/without DANTE for the detection of CVT on the per-segment level

	Dante+	Dante−
Sensitivity	100%	100%
Specificity	96.3%	83.8%
PPV	93.5%	76.6%
NPV	100%	100%
FP	3.7%	16.2%

Note:—PPV indicates positive predictive value; NPV, negative predictive value; FP, false-positive.

Residual blood signals in patients with CVT were also dramatically suppressed using the DANTE preparation. The SNR of residual blood (16.4 ± 8.0 versus 75.0 ± 35.1, $P = .002$) and residual blood-to-normal lumen CNR (12.4 ± 7.8 versus 68.8 ± 35.4, $P = .002$) were significantly reduced on BTI DANTE+. Furthermore, the thrombus-to-residual blood CNR was improved, which was significant for isointense thrombi (hyperintense thrombi: 208.5 ± 81.3 versus 154.9 ± 68.0, $P = .068$; isointense thrombi: 59.4 ± 21.7 versus 19.0 ± 31.5, $P = .001$) (Fig 4*A*). On the other hand, the use of the DANTE preparation had negligible impact on the contrast between thrombi and surrounding tissues (Fig 4*B*).

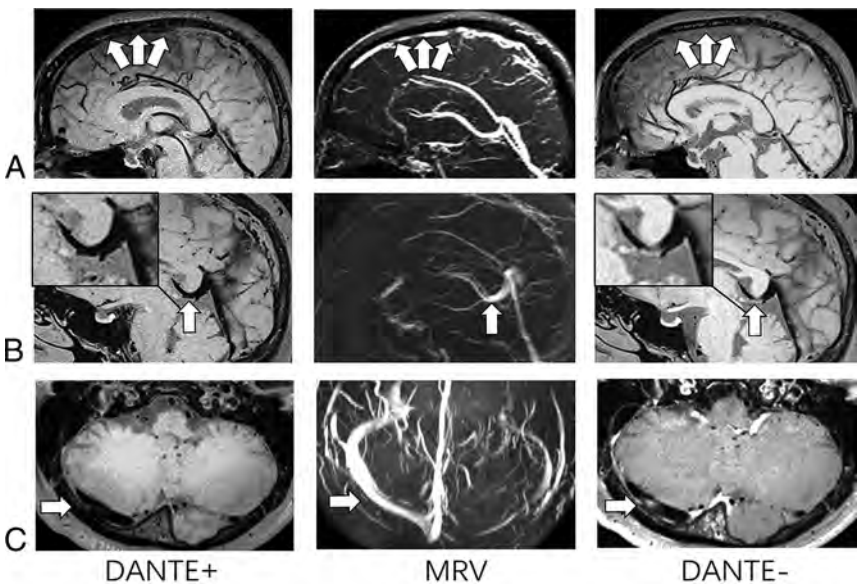

FIG 2. BTI (with/without DANTE preparation) images and MRV images of 3 patients with CVT. On BTI DANTE− images, isointense signals appear in the superior sagittal sinus (*arrows, A*), vein of Galen (*arrow, B*), and right transvers sinus (*arrow, C*). However, they are not shown on the BTI DANTE+ images (*arrows*). MRVs for these 3 patients demonstrate no filling defects on corresponding segments (*arrows*).

DISCUSSION

Our work presents a further refinement in blood signal suppression for MR BTI. This is the first study to evaluate the effectiveness and clinical practicability of BTI with the DANTE preparation in healthy subjects and those with CVT, to our knowledge. Our initial results demonstrate improved performance of the technique in the detection of thrombi and the feasibility of quantifying the thrombus volume and assessing the degree of recanalization.

Blood signal suppression is the most important contributing factor for the improved accuracy of MR BTI in the detection of CVT, regardless of its stage. While the SPACE sequence used in the original BTI technique has inherent black-blood contrast, residual blood flow signals were observed here in both healthy subjects and patients. This suggests

that its blood-suppressing capacity is insufficient for slow or even stagnant venous blood flow in the sinuses. Such image artifacts can mimic thrombus (isointense), resulting in false-positives or overestimation of CVT. Additional blood signal suppression is therefore indispensable. Previous work has reported that the DANTE preparation is sensitive to blood flow over a broad range of velocities above approximately 1 mm/s.[9] In our study, this approach demonstrated the effectiveness of eliminating residual flow signals as evidenced by significantly reduced SNR of residual blood and residual blood-to-normal lumen CNR compared with that measured from the original BTI. On the other hand, this approach did not substantially sacrifice the CNR of thrombi to the normal sinus lumen and brain parenchyma, indicating its minimal effect on static tissues. As a result, the diagnosis of CVT was remarkably improved, with combined conventional imaging techniques as the reference.

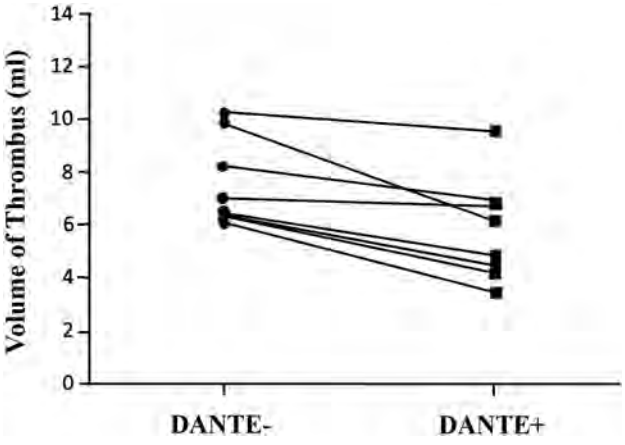

FIG 3. Thrombus volumes on BTI DANTE+ and BTI DANTE− images. In the 8 patients who were diagnosed with apparent thrombi in the superior sagittal sinus, the measured thrombus volume was significantly lowered (4.814 ± 2.278 mL versus 6.341 ± 2.302 mL, $P = .008$) when using the DANTE preparation.

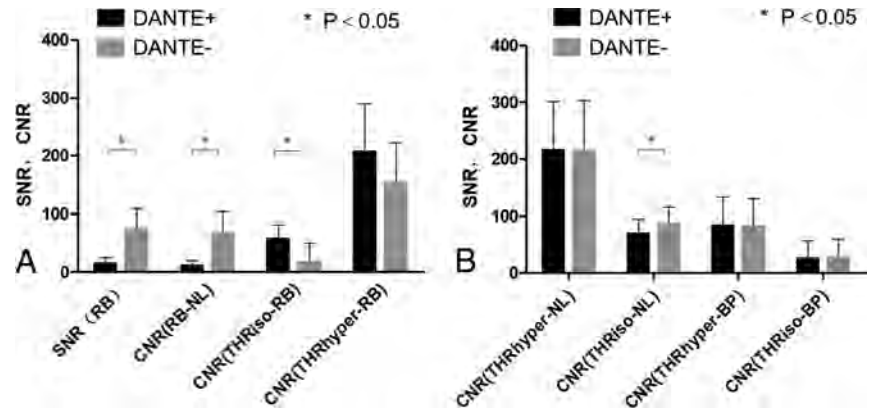

FIG 4. *A*, SNR of residual blood (RB), CNR between RB and normal lumen (NL), and CNR between RB and thrombus in the patient group. SNR of RB and RB-to-NL CNR was significantly reduced on BTI DANTE+ images compared with BTI DANTE− images. RB-to-thrombus CNR was significantly improved for the isointense thrombus type. *B*, CNR between thrombus and NL and CNR between thrombus and brain parenchyma (BP). When one used the DANTE preparation, the CNR between thrombus and NL or BP was not significantly sacrificed except for the CNR between isointense thrombus and NL. THRiso indicates isointense thrombus; THRhyper, hyperintense thrombus; *asterisk*, $P < .05$.

The feasibility of quantifying thrombus volumes is shown in our study. Thrombus volume was manually measured and demonstrated significant reduction in BTI when the DANTE preparation was used. Although quantification of thrombus volume is not yet a common clinical practice, presumably due to the lack of reliable thrombus-depicting approaches, this quantitative marker could be useful for following up the effect of clinical treatment and guiding treatment decisions on dose and duration. Conventional methods such as MRV and TSE are indirect approaches by detecting filling defects, which are susceptible to many factors related to the anatomy and imaging protocol.[12-14] BTI allows direct differentiation of CVT from other tissues, thus facilitating the quantification procedure. In this study, in a manual method, we demonstrated significantly reduced thrombus volume in DANTE-prepared MR BTI. In the future, MR BTI with DANTE is potentially helpful to quantitatively assess the recanalization effect of different clinical treatments as well as to compare the relationship between thrombus quantification and outcome.

The imaging protocol used in this study also incorporates additional features that will facilitate the translation of MR BTI into clinical practice. Specifically, a whole-brain imaging volume with isotropic high spatial resolution can be acquired within <6 minutes. This is advantageous over the protocol presented by Yang et al,[6] whereby spatial coverage and spatial resolution were compromised to maintain the reasonably short scan time. Moreover, a standard head-neck coil is used so that jugular veins can also be examined along with the cerebral venous system within the same scan. With these features combined, MR BTI could readily be integrated into the diagnostic work-up.

There were several limitations in the present study. First, this was a single-center study with a relatively small sample size. A multicenter trial with a large patient cohort is desirable, though the recruitment is relatively difficult because CVT is a rare disease with life-threatening potential. Second, MRV is currently considered the noninvasive test of choice for the evaluation of the dural sinus. CE-MRV (relative to time-of-flight MRV) more accurately depicts the degree of patency of thrombosed segments,[3,15] though not all patients in our study underwent CE-MRV. However, flow-related and susceptibility artifacts as well as the bolus-timing issues can impair the evaluation of the venous structures. The more invasive arterial DSA is still the standard of reference but is not routinely performed in our institution.[16]

CONCLUSIONS

The DANTE preparation significantly enhances the black-blood contrast in black-blood thrombus imaging, making the technique more accurate for the diagnosis of cerebral venous sinus thrombosis.

Disclosures: Zhaoyang Fan—*RELATED*: *Grant*: National Institutes of Health/National Heart, Lung, and Blood Institute 1 R01 HL147355. Qi Yang—*RELATED*: *Grant*: Beijing Natural Science Foundation (No. 17L20253), National Science Foundation of China (No. 91749127 and 81830056), Beijing Municipal Administration of Hospitals Clinical Medicine Development of Special Funding Support (ZYLX201706). Guan Wang—*RELATED*: China Medical University as a visiting scholar.

REFERENCES

1. Bousser MG, Ferro JM. **Cerebral venous thrombosis: an update.** *Lancet Neurol* 2007;6:162–70 CrossRef Medline
2. Bianchi D, Maeder P, Bogousslavsky J, et al. **Diagnosis of cerebral venous thrombosis with routine magnetic resonance: an update.** *Eur Neurol* 1998;40:179–90 CrossRef Medline
3. Leach JL, Fortuna RB, Jones BV, et al. **Imaging of cerebral venous thrombosis: current techniques, spectrum of findings, and diagnostic pitfalls.** *Radiographics* 2006;26:S19 CrossRef Medline
4. Leach JL, Wolujewicz M, Strub WM. **Partially recanalized chronic dural sinus thrombosis: findings on MR imaging, time-of-flight MR venography, and contrast-enhanced MR venography.** *AJNR Am J Neuroradiol* 2007;28:782–89 Medline
5. Saposnik G, Barinagarrementeria F, Brown RD, et al. **Diagnosis and management of cerebral venous thrombosis: a statement for healthcare professionals from the American Heart Association/American Stroke Association.** *Stroke* 2011;42:1158–92 Medline
6. Yang Q, Duan J, Fan Z, et al. **Early detection and quantification of cerebral venous thrombosis by magnetic resonance black-blood thrombus imaging.** *Stroke* 2016;47:404–09 CrossRef Medline
7. Mugler JP 3rd. **Optimized three-dimensional fast-spin-echo MRI.** *J Magn Reson Imaging* 2014;39:745–67 CrossRef Medline
8. Moody AR. **Magnetic resonance direct thrombus imaging.** *J Thromb Haemost* 2003;1:1403–09 CrossRef
9. Li L, Miller KL, Jezzard P. **DANTE-prepared pulse trains: a novel approach to motion-sensitized and motion-suppressed quantitative magnetic resonance imaging.** *Magn Reson Med* 2012;68:1423–38 CrossRef Medline
10. Li L, Chai JT, Biasiolli L, et al. **Black-blood multicontrast imaging of carotid arteries with DANTE-prepared 2D and 3D MR imaging.** *Radiology* 2014;273:560–69 CrossRef Medline
11. Xie Y, Yang Q, Xie G, et al. **Improved black-blood imaging using DANTE-SPACE for simultaneous carotid and intracranial vessel wall evaluation.** *Magn Reson Med* 2016;75:2286–94 CrossRef Medline
12. Long B, Koyfman A, Runyon MS. **Cerebral venous thrombosis: a challenging neurologic diagnosis.** *Emerg Med Clin North Am* 2017;35:869–78
13. Poon CS, Chang JK, Swarnkar A, et al. **Radiologic diagnosis of cerebral venous thrombosis: pictorial review.** *Am J Radiology* 2007;189:S64–75 CrossRef Medline
14. Leach JL, Jones BV, Tomsick TA, et al. **Normal appearance of arachnoid granulations on contrast-enhanced CT and MR of the brain: differentiation from dural sinus disease.** *AJNR Am J Neuroradiol* 1996;17:1523–32 Medline
15. Stam J. **Thrombosis of the cerebral veins and sinuses.** *N Engl J Med* 2005;352:1791–98 CrossRef Medline
16. Karthikeyan D, Vijay S, Kumar T, et al. **Cerebral venous thrombosis-spectrum of CT findings.** *Indian Journal of Radiology and Imaging* 2004;14:129–37

Carotid Intraplaque-Hemorrhage Volume and Its Association with Cerebrovascular Events

L. Saba, G. Micheletti, W. Brinjikji, P. Garofalo, R. Montisci, A. Balestrieri, J.S. Suri, J.K. DeMarco, G. Lanzino, and R. Sanfilippo

ABSTRACT

BACKGROUND AND PURPOSE: Our aim was to assess the relationship between volume and percentage of intraplaque hemorrhage measured using CT and the occurrence of cerebrovascular events at the time of CT.

MATERIALS AND METHODS: One-hundred-twenty-three consecutive subjects (246 carotid arteries) with a mean age of 69 years who underwent CTA were included in this retrospective study. Plaque volume of components and subcomponents (including intraplaque hemorrhage volume) was quantified with dedicated software.

RESULTS: Forty-six arteries were excluded because no plaque was identified. In the remaining 200 carotid arteries, a statistically significant difference was found between presentation with cerebrovascular events and lipid volume ($P = .002$), intraplaque hemorrhage volume ($P = .002$), percentage of lipid ($P = .002$), percentage of calcium ($P = .001$), percentage of intraplaque hemorrhage ($P = .001$), percentage of lipid-intraplaque hemorrhage ($P = .001$), and intraplaque hemorrhage/lipid ratio ($P = .001$). The highest receiver operating characteristic area under the curve was obtained with the intraplaque hemorrhage volume with a value of 0.793 ($P = .001$), percentage of intraplaque hemorrhage with an area under the curve of 0.812 ($P = .001$), and the intraplaque hemorrhage/lipid ratio with an area under the curve value of 0.811 ($P = .001$).

CONCLUSIONS: Results of our study suggest that Hounsfield unit values <25 have a statistically significant association with the presence of cerebrovascular events and that the ratio intraplaque hemorrhage/lipid volume represents a strong parameter for the association of cerebrovascular events.

ABBREVIATIONS: AUC = area under the curve; IPH = intraplaque hemorrhage; ROC = receiver operating characteristic

Several studies have demonstrated, in recent years, that the degree of stenosis should not be considered the only parameter to identify carotid plaque at risk of distal embolization and that additional plaque features can increase or reduce risk of plaque rupture and embolic events.[1-4] In particular, intraplaque hemorrhage (IPH) has been convincingly associated with a higher risk of ipsilateral cerebrovascular events.[5,6]

Although MR imaging has been widely used to identify IPH,[7-9] recent evidence suggests that CT,[10] using a threshold of attenuation values of <25 HU in the carotid artery, can consistently identify the presence of IPH. Moreover, with improved algorithmic and hardware evolution, there has been an increasing role of volumetric quantification of tissue components for plaque characterization.[11-14]

In the present study, we assessed the relationship between volume and the percentage of IPH measured using software analysis in volumetric CT and the occurrence of cerebrovascular events (stroke and TIA).

MATERIALS AND METHODS

Study Design and Patient Population

Institutional review board approval for this study was obtained, and patient consent was waived because of the retrospective nature. On the basis of a power calculation (type I error, $\alpha = .05$;

Received April 7, 2019; accepted after revision July 15.

From the Departments of Radiology (L.S., G.M., P.G., A.B.) and Vascular Surgery (R.M., R.S.), Azienda Ospedaliero Universitaria, Monserrato (Cagliari), Italy; Departments of Radiology (W.B.) and Neurosurgery (G.L.), Mayo Clinic, Rochester, Minnesota; Stroke Monitoring and Diagnostic Division (J.S.S.), AtheroPoint, Roseville, California; Point-of-Care Devices (J.S.S.), Global Biomedical Technologies, Roseville, California; Department of Electrical Engineering (J.S.S.), University of Idaho, Moscow, Idaho (Affiliated); and Department of Radiology (J.K.D.), Walter Reed Medical Center, Bethesda, Maryland.

The views expressed in this article are those of the author and do not reflect the official policy of the Department of Army/Navy/Air Force, Department of Defense, or US Government.

The identification of specific products or scientific instrumentation does not constitute endorsement or implied endorsement on the part of the author, Department of Defense, or any component agency.

Please address correspondence to Luca Saba, MD, Department of Radiology, Azienda Ospedaliero Universitaria, di Cagliari—Polo di Monserrato s.s. 554 Monserrato (Cagliari) 09045, Italy; e-mail: lucasaba@tiscali.it

http://dx.doi.org/10.3174/ajnr.A6189

type II error, $\beta = 0.1$; area under the curve [AUC] null hypothesis value = 0.5; AUC significant value = 0.7, pooled group), we estimated that a sample size of at least 130 (with a 30% IPH prevalence) carotid arteries would be sufficient to investigate the potential effect of CT-detected IPH versus the occurrence of cerebrovascular events. We decided to also include a correction factor of 10%, yielding a necessary sample size of 143 carotid arteries. Moreover, because in each subject, there are 2 carotid arteries and this determined a bias in the model, we decided to study 200 carotid arteries to avoid the inference determined by the 2 carotid arteries in each patient.

Consecutive subjects who underwent CT of the carotid arteries in our hospital from March 2013 were included until the threshold of 200 carotid arteries was reached (January 2014) for a total of 246 carotid arteries in 123 subjects (94 men, 29 women; mean age, 69 years; age range, 45–86 years). For each subject, when both carotid arteries showed atherosclerotic plaque, the left and right sides were included. Plaque was defined according to the Mannheim consensus[15] as a carotid wall thickness of $>1500\,\mu$m.

In cases in which only 1 carotid artery was pathologic, the normal side (46 carotid arteries) was excluded from analysis, leaving 200 arteries with an atherosclerotic plaque for analysis.

Quantification of the degree of stenosis and plaque analysis was performed using CTA according to previously published criteria.[16,17] Carotid sonography is used as a screening tool to identify carotid stenosis, and CTA was performed under the following circumstances: 1) Carotid sonography showed a pathologic stenosis (>50% measured with the NASCET criteria[18]) or features related to plaque vulnerability (ulcerations, irregular surface); 2) sonography could not adequately assess the degree of stenosis and plaque characteristics because of anatomic conditions; 3) diabetes screening; and 4) presurgery analysis. Moreover, all subjects with cerebrovascular events underwent CTA of the carotid arteries. The neurologic status at the time of CT was classified as symptomatic or asymptomatic according to the neurologic assessment documented in the clinical chart review using the Trial of Org 10172 in Acute Stroke Treatment (TOAST) criteria.[19,20] The maximum timing between events and imaging to consider a subject as symptomatic was 1 week. In the case of >1 week between ischemic symptoms and CTA of carotid arteries, the patient was excluded. We defined as symptomatic those patients with TIA or stroke, considering TIA as a brief (<24-hour) episode of neurologic dysfunction such as dysarthria, dysphasia, hemiparesis, or hemiparesthesia and monocular blindness. If the episodes of neurologic dysfunction lasted >24 hours, the patient was considered to have a stroke. In case of doubt with other pathologies (eg, hypoglycemia, migraine, postparoxysmal neurologic dysfunction), we excluded patients from the analysis. Asymptomatic patients had no history of either remote or recent symptoms at the time of the examination. Clinical classification into symptomatic and asymptomatic was based on the assessment of the clinician evaluating the patient and ordering the diagnostic study and was extracted from the chart. We considered symptomatic patients those who had plaque in the carotid artery ipsilateral to the cerebrovascular event.

Moreover, we excluded patients with the following conditions: 1) concomitant intracranial pathology such as brain tumor, abscess, and encephalitis; and 2) the presence of a cardioembolic source documented by a cardiologist.

CTA Technique

Patients were studied using a 16–detector row CT system (Brilliance; Philips Healthcare, Best, the Netherlands). CT images were obtained with coverage from the aortic arch to the carotid siphon in a caudocranial direction, and examinations were performed before and after the administration of contrast material. An angiographic phase was obtained with the administration of 80 mL of prewarmed contrast medium, Ultravist 370 (iopromide; Bayer HealthCare, Berlin, Germany) into a cubital vein using a power injector at a flow rate of 4–5 mL/s and a 16-ga intravenous catheter followed by 30 mL of saline flush. CT technical parameters included the following: section thickness = 0.6 mm, section interval = 0.3 mm, matrix size = 512 × 512 pixels, FOV = 14–19 cm. A C-filter algorithm of reconstruction was applied.

IPH and Plaque Volume Component Analysis Quantification

Two radiologists (L.S. and A.B. with 11 and 8 years of experience in CTA, respectively) blinded to clinical information regarding symptomatic status performed all measurements of Hounsfield units using as window/level settings, W = 850:L = 300.[21] Volume analysis was performed with dedicated software (Elucid Bioimaging, Wenham, Massachusetts) to semi-automatically quantify the subcomponent volume.[22,23] With this software, it is possible to identify attenuation values of all the voxels within a volume, and by means of applying some thresholds, it is possible to classify the tissues according to the attenuation values (Fig 1). For this analysis, we considered 5 classes: 3, as suggested by de Weert et al[24] in which voxels identifying lipid tissues were <60 HU, fibrous tissue between 60 and 130 HU, and calcium tissue >130 HU.[10,24] Two additional classes (4 and 5) were added by splitting the lipid: the fourth class was the IPH for values <25 HU according to the findings by Saba et al,[10] whereas the fifth class was the lipid-IPH, which included all the voxels with Hounsfield unit values between 26 and 59 HU.

We also calculated the percentages of these components, and finally, a ratio was introduced as the ratio of IPH/lipid volume (with values between 0, if no IPH was present, and 1, if all the lipid plaque component was due to IPH).

IPH Volume Dichotomization

After the volume calculation of the IPH, 5 thresholds were selected to obtain a dichotomization and subsequently test the effect of the presence/absence of IPH versus symptoms using a 6-hypothesis scenario. We considered the following 6 thresholds of IPH volume: 10, 50, 100, 150, 200, and 250 mm^3.

Statistical Analysis

In this study, continuous data were described as the mean ± SD. Receiver operating characteristic (ROC) curve analysis was performed between volume and volume subcomponents (lipid, mixed, calcified, IPH, lipid-IPH tissue), percentage of variable of

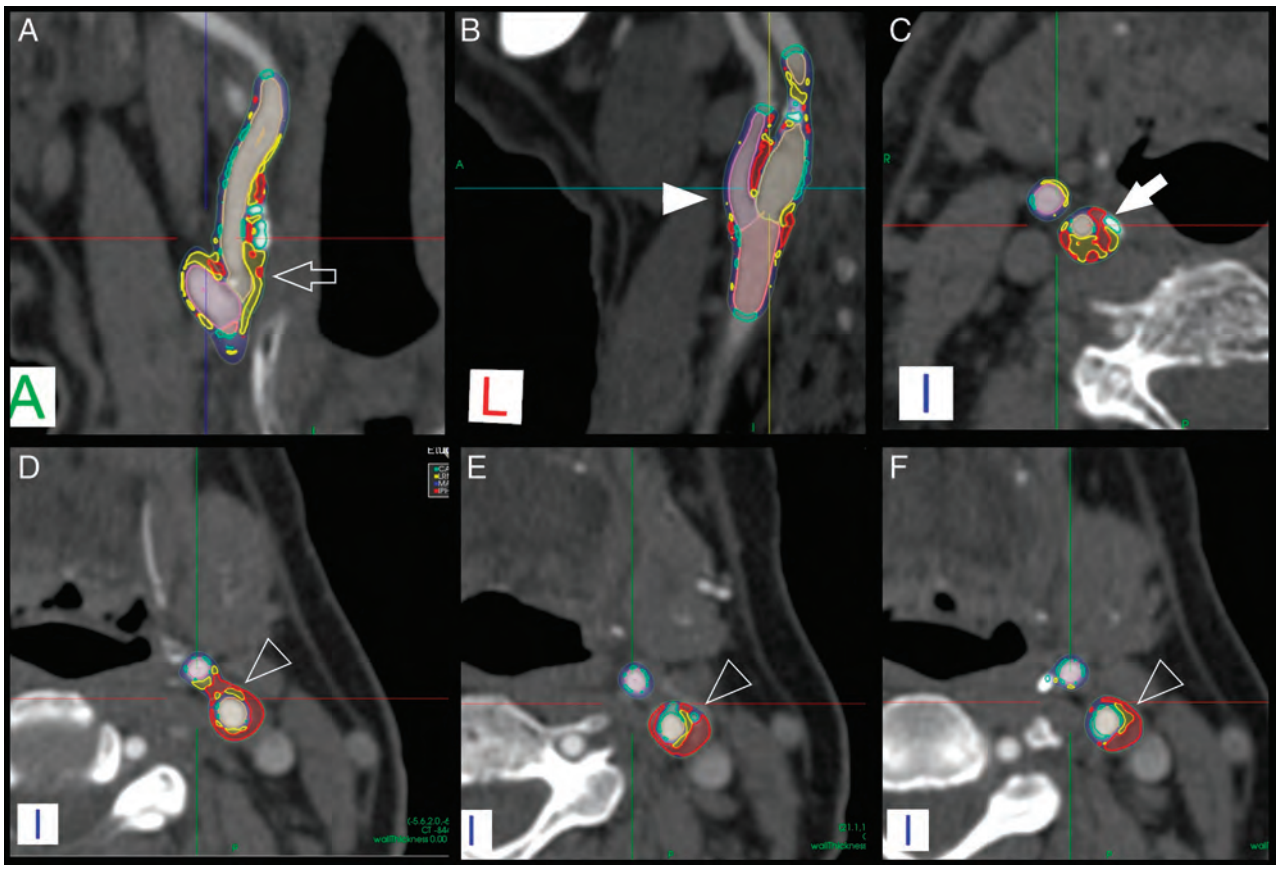

FIG 1. The first case is a 69-year-old male patient with right stroke who underwent CTA that showed a large IPH component of 107 mm^3 (*A–C*). *A*, The coronal view of the carotid CTA is given with the segmentation of the software (*white open arrow*). *B*, A coronal cut of the postprocessed carotid arteries is shown (*white arrowhead*). *C*, The *white arrow* indicates the internal carotid artery in the axial selected section. The legend of the chromatic scale is the following: red = IPH; yellow = lipid-IPH component; blue = mixed component; green = calcified component. The second case is a 73-year-old male patient with left MCA stroke with an IPH/lipid ratio of 0.93 (*D–F*). *D–F*, Three axial slices from the bifurcation upward were selected showing the presence of a large IPH and the small amount of lipid-IPH (*white arrowheads*).

the subcomponents, ratio of IPH/lipid, and the presence of cerebrovascular events. The normality of each continuous group was tested using the Kolmogorov-Smirnov *Z*-test, and different values in groups with and without cerebrovascular symptoms were compared using the Mann-Whitney test. The dichotomized IPH values according to the thresholds were tested versus the presence/absence of cerebrovascular events using a χ^2 test. A *P* value $< .05$ indicated a statistically significance association, and all values were calculated using a 2-tailed significance level. Statistical analysis was performed with the SPSS 13.0 Statistical Package (IBM, Armonk, New York). Graphics were plotted with MedCalc 15.0 software (MedCalc Software, Mariakerke, Belgium).

RESULTS

General Results

No patients were excluded due to suboptimal image quality. Of the 123 patients, 46 were symptomatic (15 strokes, 31 transient ischemic attacks) and 77 were asymptomatic. General plaque characteristics and their subcomponent volume and percentages are summarized in Table 1. No statistically significant difference was found for the common cerebrovascular risk factors between symptomatic and asymptomatic patients. However, there were statistically significant differences in the lipid volume ($P = .002$), IPH volume ($P = .001$), percentage of lipid ($P = .002$), percentage calcium ($P = .001$), percentage of IPH ($P = .0001$), percentage of lipid-IPH ($P = .0001$), and the IPH/lipid ratio ($P = .001$). Boxplots are given in Fig 2.

ROC Curve Analysis

The ROC curve analysis for the total plaque component and subcomponent volume versus the presence of cerebrovascular symptoms is given in Fig 3*A*. Table 2 summarizes general ROC results from the volume analysis. The best ROC AUC was obtained with the IPH volume, with a value of 0.793 ($P = .001$).

The ROC curve analysis was also performed for the percentage of plaque components versus the presence of cerebrovascular symptoms, and the ROC plot is shown in Fig 3*B*. Table 2 also summarizes the general ROC results from volume analysis. The best performance was obtained by the percentage of IPH with an AUC of 0.812; $P = .001$). Also, the IPH/lipid ratio showed a very good AUC, with a value of 0.811 ($P = .001$).

IPH Volume Dichotomization

In Table 3, the χ^2 results for the different threshold volumes of IPH and cerebrovascular symptoms are summarized. The best

Table 1: Demographic and plaque characteristic summary table

Cerebrovascular Symptoms	Yes	No	*P* Value	Test
Demographics				
Age (mean) (95% CI) (yr)	70 (66–74)	68 (65–71)	.37	Paired Student *t*
Sex (male = 93)	80% (37/46)	74% (57/77)	.55	χ^2
Hypertension	26% (12/46)	27% (42/154)	.98	χ^2
CAD	50% (23/46)	45% (70/154)	.71	χ^2
Smoking status	43% (20/46)	30% (46/154)	.12	χ^2
Diabetes	7% (3/43)	7% (11/154)	.85	χ^2
Dyslipidemia	28% (13/46)	32% (49/154)	.79	χ^2
Plaque composition				
Total plaque volume (mm^3)	793 (565–984)	560 (503–669)	.105	Mann-Whitney
Lipid volume (mm^3)	187 (132–240)	79 (63–101)	.002[a]	Mann-Whitney
Mixed volume (mm^3)	471 (400–544)	318 (290–367)	.062	Mann-Whitney
Calcified volume (mm^3)	103 (70–150)	128 (109–156)	.16	Mann-Whitney
IPH volume (mm^3)	115 (74–160)	2 (0–9)	.001[a]	Mann-Whitney
Lipid-IPH volume (mm^3)	61 (37–110)	67 (60–87)	.14	Mann-Whitney
% of lipid	23 (21–30)	17 (14–18)	.002[a]	Mann-Whitney
% of mixed	58 (56–63)	59 (56–61)	.51	Mann-Whitney
% of calcium	13 (12–17)	21 (18–22)	.001[a]	Mann-Whitney
% of IPH	15 (12–18)	1 (0–3)	.001[a]	Mann-Whitney
% of lipid-IPH	8 (6–11)	13 (12–14)	.001[a]	Mann-Whitney
IPH/lipid ratio	0.69 (0.59–0.73)	0.019 (0–0.064)	.001[a]	Mann-Whitney

Note:—CAD indicates coronary artery disease.
[a] Significant.

association was found by considering a threshold of 50 mm^3 (P = .001, χ^2 = 43.913, contingency coefficient = 0.424).

DISCUSSION

Several studies have recently shown that carotid artery plaque characteristics are associated with a risk of rupture and subsequent distal embolization.[2,3,5,24] In this study, we assessed the relationship between volume and percentage of IPH and other plaque components in the carotid artery detected with CT and their association with symptomatic status. We observed a significant association between the presence of ipsilateral cerebrovascular events and the absolute volume of IPH as well as plaque lipid content. Moreover, the ratio of IPH/lipid volume was strongly associated with cerebrovascular events.

Among factors involved with plaque rupture, IPH is one of the most dangerous, and its noninvasive identification is an important step for correct risk stratification.[5-8] MR imaging is considered the best technique for the detection of IPH, while the value of CT is debated. However, a recent study[10] suggests that a threshold of ≤25 HU is strongly associated with the presence of IPH on CT.

One of the main limitations of carotid plaque analysis was the fact that various imaging techniques do not account for the heterogeneous composition of the atherosclerotic tissue where several components can coexist in the same plaque.[25,26] In the carotid artery plaque, coexistence of several components is frequent with changes across time. Volumetric analysis of the plaque could offer important insights because it allows us to quantify different plaque components and provides a more complete analysis.[13,14,27,28] The introduction of a new CT criterion (≤25 HU of attenuation) for the detection of IPH applied to the use of volumetric quantification analysis systems could allow one to extrapolate the real impact of the IPH component. Recently published articles in 2019[29,30] have demonstrated that the volumetric analysis of the carotid artery plaques obtained by CT data is a reliable technique and that small changes in plaque composition can also be detected.[30]

In past years, the classic division of the carotid artery plaque type according to the attenuation values was based on the seminal study by de Weert et al,[24] in which 3 classes were identified: lipid (<60 HU), mixed (between 60 and 130 HU), and calcified (>130 HU). With the demonstration that attenuation values of <25 HU are due to IPH,[10] we tried to test the effect of the volumes for this component; therefore, the lipid class was divided into IPH (<25 HU) and lipid-IPH (from 26 to 59 HU). By comparing symptomatic with asymptomatic subjects, we found a statistically significant difference in volume for the lipid (P = .002), and in particular for the IPH volume (P = .001). These findings confirm that IPH volume is higher in plaques causing cerebrovascular events.[2,3,5,6,31,32] Of interest, there was no difference in lipid-IPH volume tissue, whereas the total lipid volume showed a statistically significant difference. This finding can be explained because in the old classification the lipid volume class included all the voxels <60 HU (and therefore also the IPH component); these results suggest that tissues with an attenuation between 26 to 59 HU, namely fatty components, are not associated with the presence of cerebrovascular events.

Further information can be gathered from the difference in the relative percentages of various tissue components. It is not only the volume threshold that can trigger plaque rupture but also the relative percentage, suggesting that the biomechanical structure of plaque is fundamental. In particular, in subjects with cerebrovascular symptoms, there is an increased percentage of IPH components and lipid (also including the IPH class). Conversely, in subjects without cerebrovascular symptoms, an increased percentage of calcium and lipid-IPH was found. The protective effect of the calcium was already demonstrated by

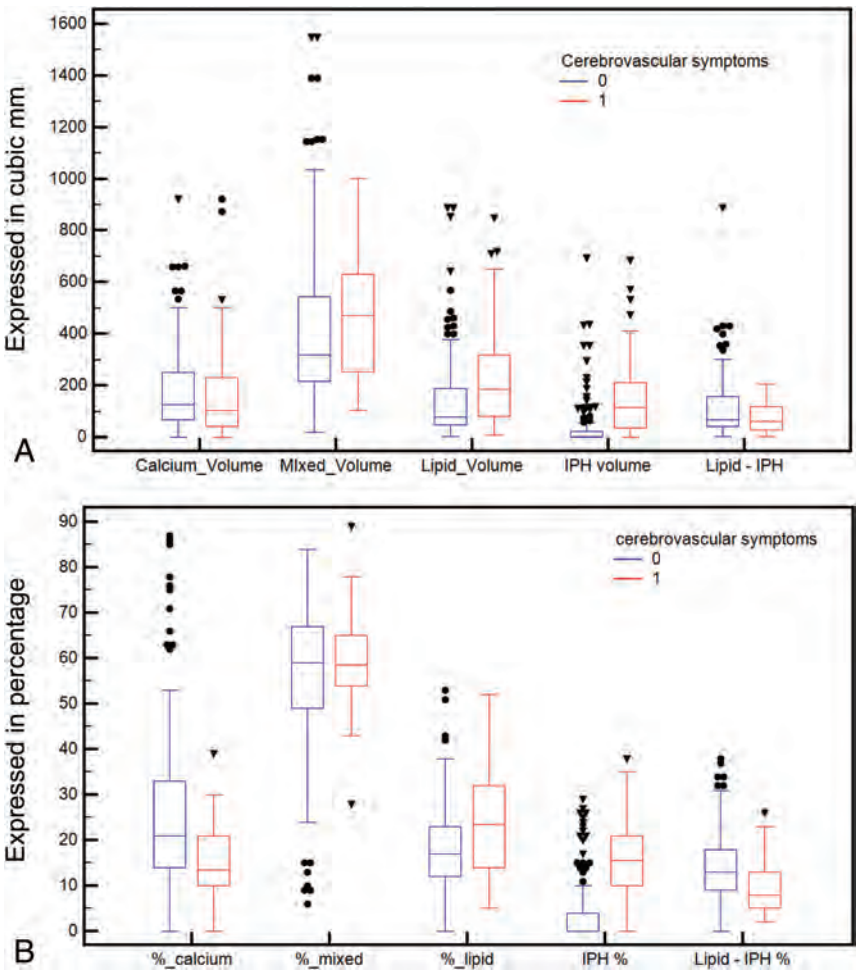

FIG 2. Boxplot of the volume components of the carotid artery plaque according to the presence or absence of cerebral symptoms (*A*) and boxplot of the percentages of the components according to the presence or absence of cerebrovascular symptoms (*B*).

Nandalur et al,[33] whereas the finding that the lipid-IPH percentage is lower in symptomatic subjects could support the histopathologic observation that lipid tissue within plaques is not active and not related to the risk of rupture.[34] The ROC curve analysis confirms these results by showing the highest area under the curve with the IPH volume (AUC of 0.793, $P = .001$) and percentage of IPH (AUC of 0.812, $P = .001$). To assess the effect of some volumetric thresholds, we created 6 different models by considering the following thresholds: 10, 50, 100, 150, 200, and 250 mm^3, and the best association was found by considering a threshold of 50 mm^3 ($P = .001$, $\chi^2 = 43.913$, contingency coefficient = 0.424).

Our study has some limitations. It is a retrospective analysis, and we did not explore the association between the presence of IPH (and its volume or percentage) and the risk of new/recurrent cerebrovascular events. Instead, IPH was assessed in patients who already had cerebrovascular events, and this may have introduced a bias because some plaques may have theoretically changed in structure and composition in the interval between symptom onset and the time of CTA detection. However, we think that the limited time between the symptomatic event and the CTA reduces this potential effect. Our

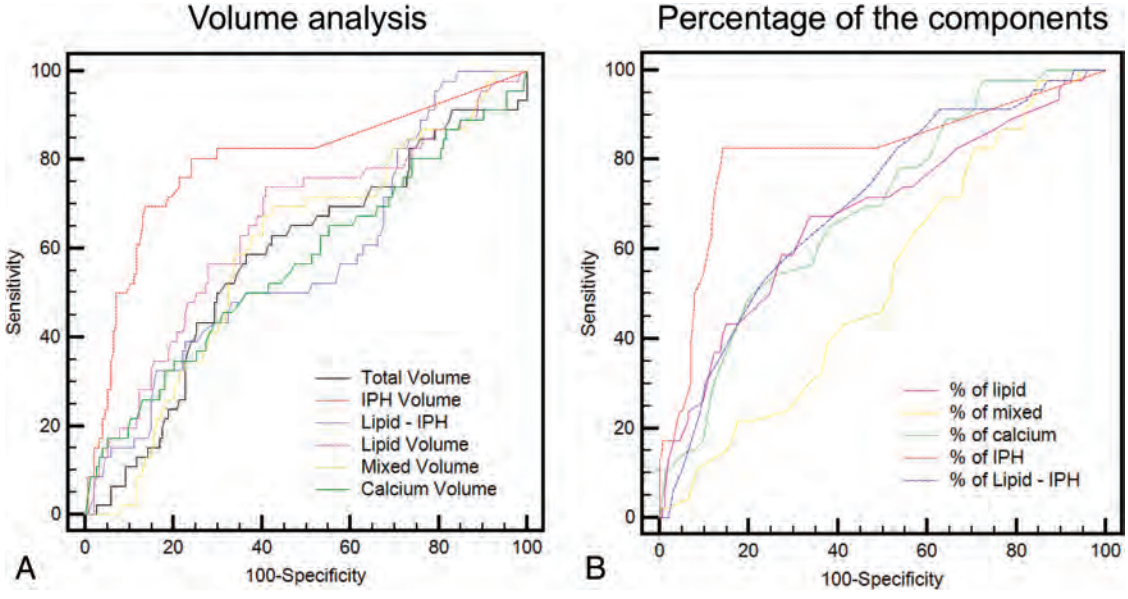

FIG 3. ROC curve analysis of the volume components of the carotid artery plaque according to the presence or absence of cerebral symptoms (*A*) and ROC curve analysis of the percentages of the components according to the presence or absence of cerebral symptoms (*B*).

Table 2: ROC curve analysis between symptoms and volume/percentage of plaque tissues

	AUC	SE	95% CI	*P* Value
Plaque volume	0.579	0.049	0.507–0.648	.108
IPH volume	0.793	0.0421	0.730–0.847	.001
Lipid minus IPH	0.574	0.0486	0.502–0.643	.129
Lipid volume	0.648	0.0486	0.577–0.714	.002
Mixed volume	0.594	0.0465	0.523–0.663	.043
Calcium volume	0.568	0.0517	0.497–0.638	.186
% of lipid	0.679	0.0476	0.609–0.743	.001
% of mixed	0.532	0.0459	0.460–0.602	.489
% of calcium	0.591	0.0426	0.522–0.654	.135
% of IPH	0.812	0.0413	0.751–0.863	.001
% of lipid minus IPH	0.702	0.0428	0.633–0.764	.001
IPH/lipid radio	0.811	0.0424	0.751–0.863	.001

Note:—SE indicates standard error.

Table 3: χ^2 test between symptoms and different volume thresholds of IPH

	χ^2	Contingency Coefficient	*P* Value
IPH, 10 mm^3	12.527	0.243	.001
IPH, 50 mm^3	43.913	0.424	.001
IPH, 100 mm^3	37.478	0.397	.001
IPH, 150 mm^3	34.763	0.385	.001
IPH, 200 mm^3	14.935	0.264	.001
IPH, 250 mm^3	7.944	0.195	.048

findings are based on a relatively small cohort, and these data will need to be validated in a larger and preferentially prospective cohort. Nevertheless, these data provide a valuable framework on which further confirmatory cohorts can be based.

CONCLUSIONS

The results of this study confirm that the value of <25 HU has a statistically significant association with the presence of cerebrovascular events and that the ratio between IPH and lipid volume represents a strong parameter for the association of cerebrovascular events.

Disclosures: Jasjit S. Suri—*UNRELATED*: *Other*: member of AtheroPoint LLC (owner). James Kevin DeMarco—*UNRELATED*: *Grants/Grants Pending*: Department of Defense*; *Payment for Lectures Including Service on Speakers Bureaus*: Baptist Neurological Institute, Jacksonville, Florida; *Payment for Development of Educational Presentations*: International Society for Magnetic Resonance in Medicine.* Waleed Brinjikji—*UNRELATED*: *Consultancy*: Superior Medical Editing (<$5000); *Grants/Grants Pending*: National Institutes of Health, *Comments*: Johnson and Johnson*; *Patents (Planned, Pending or Issued)*: Marblehead Medical, *Comments*: patents pending for stroke intervention devices*; *Stock/Stock Options*: Marblehead Medical, *Comments*: cofounder of the company. *Money paid to the Institution.

REFERENCES

1. Saba L, Yuan C, Hatsukami TS, et al. **Carotid artery wall imaging: perspective and guidelines from the ASNR Vessel Wall Imaging Study Group and Expert Consensus Recommendations of the American Society of Neuroradiology.** *AJNR Am J Neuroradiol* 2018;39:E9–31 CrossRef Medline
2. Lu M, Peng P, Cui Y, et al. **Association of progression of carotid artery wall volume and recurrent transient ischemic attack or stroke: a magnetic resonance imaging study.** *Stroke* 2018;49:614–20 CrossRef Medline
3. Saba L, Saam T, Jäger HR, et al. **Imaging biomarkers of vulnerable carotid plaques for stroke risk prediction and their potential clinical implications.** *Lancet Neurol* 2019;18:559–72 CrossRef Medline
4. Hellings WE, Peeters W, Moll FL, et al. **Composition of carotid atherosclerotic plaque is associated with cardiovascular outcome: a prognostic study.** *Circulation* 2010;121:1941–50 CrossRef Medline
5. Altaf N, MacSweeney ST, Gladman J, et al. **Carotid intraplaque hemorrhage predicts recurrent symptoms in patients with high-grade carotid stenosis.** *Stroke* 2007;38:1633 CrossRef
6. Turc G, Oppenheim C, Naggara O, HIRISC study investigators, et al. **Relationships between recent intraplaque hemorrhage and stroke risk factors in patients with carotid stenosis.** *Arterioscler Thromb Vasc Biol* 2012;32:492–99 CrossRef Medline
7. Parmar JP, Rogers WJ, Mugler JP, 3rd, et al. **Magnetic resonance imaging of carotid atherosclerotic plaque in clinically suspected acute transient ischemic attack and acute ischemic stroke.** *Circulation* 2010;122:2031–38 CrossRef Medline
8. Demarco JK, Ota H, Underhill HR, et al. **MR carotid plaque imaging and contrast-enhanced MR angiography identifies lesions associated with recent ipsilateral thromboembolic symptoms: an in vivo study at 3T.** *AJNR Am J Neuroradiol* 2010;31:1395–402 CrossRef Medline
9. Horie N, Morikawa M, Ishizaka S, et al. **Assessment of carotid plaque stability based on the dynamic enhancement pattern in plaque components with multidetector CT angiography.** *Stroke* 2012;43:393-98 CrossRef Medline
10. Saba L, Francone M, Bassareo PP, et al. **CT attenuation analysis of carotid intraplaque hemorrhage.** *AJNR Am J Neuroradiol* 2018;39:131–37 CrossRef Medline
11. Cheng J, Chen Y, Yu Y, et al. **Carotid plaque segmentation from three-dimensional ultrasound images by direct three-dimensional sparse field level-set optimization.** *Comput Biol Med* 2018;94:27–40 CrossRef Medline
12. Ball S, Rogers S, Kanesalingam K, et al. **Carotid plaque volume in patients undergoing carotid endarterectomy.** *Br J Surg* 2018;105:262–69 CrossRef Medline
13. Spence JD. **Approaching automated 3-dimensional measurement of atherosclerotic plaque volume.** *J Am Coll Cardiol* 2017;70:314–17 CrossRef Medline
14. Saba L, Raz E, Anzidei M, et al. **Differences in plaque morphology and correlation of stenosis at the carotid artery bifurcation and the carotid siphon.** *AJR Am J Roentgenol* 2013;201:1108–14 CrossRef Medline
15. Touboul PJ, Hennerici MG, Meairs S, et al. **Mannheim carotid intima-media thickness and plaque consensus (2004-2006-2011): an update on behalf of the advisory board of the 3rd, 4th and 5th watching the risk symposia, at the 13th, 15th and 20th European Stroke Conferences, Mannheim, Germany, 2004, Brussels, Belgium, 2006, and Hamburg, Germany, 2011.** *Cerebrovasc Dis* 2004;34:290–96 Medline
16. Saba L, Sanfilippo R, Montisci R, et al. **Agreement between multidetector-row CT angiography and ultrasound echo-color Doppler in the evaluation of carotid artery stenosis.** *Cerebrovasc Dis* 2008;26:525–32 CrossRef Medline
17. Saba L, Sanfilippo R, Pascalis L, et al. **Carotid artery wall thickness and ischemic symptoms: evaluation using multi-detector-row CT angiography.** *Eur Radiology* 2008;18:1962–71 CrossRef Medline
18. Alexandrov AV, Bladin CF, Maggisano R, et al. **Measuring carotid stenosis: time for a reappraisal.** *Stroke* 1993;24:1292–96 CrossRef Medline
19. de Paiva Bezerra R, de Miranda Alves MA, Conforto AB, et al. **Etiological classification of stroke in patients with Chagas Disease using TOAST, Causative Classification System TOAST, and ASCOD phenotyping.** *J Stroke Cerebrovasc Dis* 2017;26:2864–69 CrossRef Medline

20. Xin XY, Cheng L, Yang Z, et al. **Comparison study of ASCO and TOAST classification system in Chinese minor stroke patients.** *Cerebrovasc Dis* 2019;47:95–100 CrossRef Medline
21. Saba L, Mallarin G. **Window settings for the study of calcified carotid plaques with multidetector CT angiography.** *AJNR Am J Neuroradiol* 2009;30:1445–50 CrossRef Medline
22. Rozie S, de Weert TT, de Monyé C, et al. **Atherosclerotic plaque volume and composition in symptomatic carotid arteries assessed with multidetector CT angiography; relationship with severity of stenosis and cardiovascular risk factors.** *Eur Radiology* 2009;19:2294–301 CrossRef Medline
23. Sheahan M, Ma X, Paik D, et al. **Atherosclerotic plaque tissue: noninvasive quantitative assessment of characteristics with software-aided measurements from conventional CT angiography.** *Radiology* 2018;286:622–31 CrossRef Medline
24. de Weert TT, de Monyé C, Meijering E, et al. **Assessment of atherosclerotic carotid plaque volume with multidetector computed tomography angiography.** *Int J Cardiovasc Imaging* 2008;24:751–59 CrossRef Medline
25. Baroncini LA, Filho AP, Ramos SG, et al. **Histological composition and progression of carotid plaque.** *Thromb J* 2007;5:4 CrossRef Medline
26. Carr S, Farb A, Pearce WH, et al. **Atherosclerotic plaque rupture in symptomatic carotid artery stenosis.** *J Vasc Surg* 1996;23:755–65 CrossRef Medline
27. Miralles M, Arrébola M, Bruguer S, et al. **Volumetric assessment of the carotid bifurcation: an alternative concept to stenosis grading.** *Ann Vasc Surg* 2015;29:411–18 CrossRef Medline
28. Saba L, Raz E, di Martino M, et al. **Is there an association between asymmetry of carotid artery wall thickness (ACAWT) and cerebrovascular symptoms?** *Int J Neurosci* 2015;125:456–63 CrossRef Medline
29. Zhu G, Li Y, Ding V, et al. **Semiautomated characterization of carotid artery plaque features from computed tomography angiography to predict atherosclerotic cardiovascular disease risk score.** *J Comput Assist Tomogr* 2019 May 6 [Epub ahead of print] CrossRef Medline
30. Chrencik MT, Khan AA, Luther L, et al. **Quantitative assessment of carotid plaque morphology (geometry and tissue composition) using computed tomography angiography.** *J Vasc Surg* 2019 Mar 5. [Epub ahead of print] CrossRef Medline
31. Ajduk M, Pavić L, Bulimbasić S, et al. **Multidetector-row computed tomography in evaluation of atherosclerotic carotid plaques complicated with intraplaque hemorrhage.** *Ann Vasc Surg* 2009;23:186–93 CrossRef Medline
32. Liu Y, Wang M, Zhang B, et al. **Size of carotid artery intraplaque hemorrhage and acute ischemic stroke: a cardiovascular magnetic resonance Chinese atherosclerosis risk evaluation study.** *J Cardiovasc Magn Reson* 2019;21:36
33. Nandalur KR, Baskurt E, Hagspiel KD, et al. **Calcified carotid atherosclerotic plaque is associated less with ischemic symptoms than is noncalcified plaque on MDCT.** *AJR Am J Roentgenol* 2005; 184:295–28 CrossRef Medline
34. Bentzon JF, Otsuka F, Virmani R, et al. **Mechanisms of plaque formation and rupture.** *Circ Res* 2014;114:1852–66 CrossRef Medline

Carotid Artery Tortuosity Is Associated with Connective Tissue Diseases

J.P. Welby, S.T. Kim, C.M. Carr, V.T. Lehman, C.H. Rydberg, J.T. Wald, P.H. Luetmer, D.M. Nasr, and W. Brinjikji

ABSTRACT

BACKGROUND AND PURPOSE: There is a general assumption in the cerebrovascular literature that there is an association between carotid artery tortuosity and connective tissues disease; however, this has not been firmly established. The purpose of this study was to determine the prevalence of carotid artery tortuosity in patients with connective tissue diseases relative to matched controls.

MATERIALS AND METHODS: Patients with previous CTA or MRA and a diagnosis of connective tissue diseases were identified and compared with a cohort of age-matched controls. Radiologists blinded to the diagnosis reviewed the images and evaluated the presence of carotid artery tortuosity (including loops, kinks, or coils). Continuous variables were compared using the Student *t* test, and categoric variables with χ^2 tests.

RESULTS: One hundred forty-three patients with connective tissue disease and 143 controls were included in this study. Specific diagnoses included Marfan ($n = 33$), nonvascular Ehlers-Danlos ($n = 36$), Ehlers-Danlos vascular-type ($n = 32$), neurofibromatosis type 1 ($n = 26$), and Loeys-Dietz ($n = 16$) syndromes. The presence of carotid tortuosity was 44% in connective tissue disease and 16% in controls ($P < .001$). Of tortuosity manifestations, coils were most prevalent (23% versus 3%; $P < .001$). Among the various connective tissue diseases, the rates of any carotid tortuosity were 88% for Marfan syndrome, 63% for Loeys-Dietz syndrome, 42% for neurofibromatosis type 1, and 19% for both vascular- and nonvascular-type Ehlers-Danlos syndrome. The positive predictive value of the combination of aortic aneurysm and carotid tortuosity being associated with connective tissue disease was 95.4%. The specificity was 98.6%.

CONCLUSIONS: Carotid artery tortuosity is highly associated with connective tissue diseases, particularly Marfan syndrome, Loeys-Dietz syndrome, and neurofibromatosis type 1. Such findings are relevant in risk assessment for vascular complications in connective tissue disease, endovascular treatment planning, and in understanding the pathomechanisms of vascular tortuosity in general.

ABBREVIATIONS: CTD = connective tissue disease; EDS = Ehlers-Danlos syndrome; LDS = Loeys-Dietz syndrome; NF1 = neurofibromatosis type 1

Carotid artery tortuosity is defined as vascular elongation leading to redundancy or an altered course. Recent evidence suggests that the prevalence of carotid tortuosity is higher than conventionally expected ranging from 18% to 34%.[1,2] While often an incidental finding, carotid tortuosity has been known to contribute to cases of vertigo, tinnitus, and stroke secondary to dissection.[2,3] Furthermore, carotid tortuosity has been known to complicate access to the cranial vasculature in neuroendovascular procedures and has anecdotally been associated with a higher risk of iatrogenic dissection.[4]

The mechanisms underlying carotid artery tortuosity remain unclear.[5] Studies suggest that tortuous carotid arteries exhibit histopathologic changes, including degeneration of the tunica media and elastic lamina.[6] Reported risk factors include hypertension, elevated body mass index, advanced age, and atherosclerotic disease.[3,7-9] It is often assumed that patients with tortuosity may have some underlying collagenopathy as well; however, to our knowledge this has yet to be studied in connective tissue diseases (CTDs). Previous study has demonstrated a relationship between CTDs and neurovascular abnormalities. Through varied mechanisms such as altered fibrillin 1 structure in Marfan syndrome,

Received May 5, 2019; accepted after revision July 31.

From the Mayo Clinic Alix School of Medicine (J.P.W.) and Departments of Radiology (C.M.C., V.T.L., C.H.R., J.T.W., P.H.L., W.B.), Neurology (D.M.N.), and Neurosurgery (W.B.), Mayo Clinic, Rochester, Minnesota; and Department of Radiology (S.T.K.), University of California, San Francisco, San Francisco, California.

Please address correspondence to John P. Welby, MD, Mayo Clinic Alix School of Medicine, 200 1st St SW, Rochester, MN 55905; e-mail: Welby.John@mayo.edu

Indicates article with supplemental on-line tables.

http://dx.doi.org/10.3174/ajnr.A6218

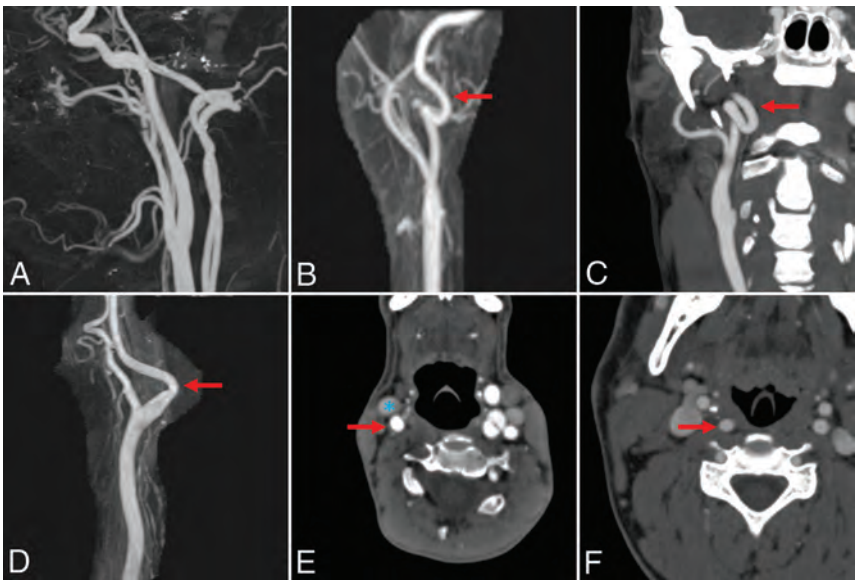

FIGURE. Examples of carotid artery tortuosity and path alterations. *A*, Sagittal CTA reconstruction shows normal bilateral carotid and vertebral arteries. *B*, Anterior reconstruction MRA of a patient with Marfan syndrome shows a carotid loop (*red arrow*). *C*, Coronal MIP CTA of a patient with Marfan syndrome shows bilateral carotid coils (*red arrow*). *D*, Sagittal–reconstruction MRA of a patient with EDS shows a carotid artery (*red arrow*) kink. *E*, Axial CTA of a patient with LDS shows a retrojugular carotid artery (carotid artery, *red arrow*; jugular vein, *blue asterisk*). *F*, Axial CTA of a patient with Marfan syndrome demonstrates a retropharyngeal carotid artery (*red arrow*) course.

collagen mutations in Ehlers-Danlos syndrome (EDS), or transforming growth factor-β signaling abnormalities in Loeys-Dietz syndrome (LDS), CTDs are demonstrated to alter vessel makeup and lead to vascular abnormalities, including aneurysms and dissections.[10] To date, no studies have rigorously determined whether CTDs are, in fact, associated with carotid artery tortuosity. Demonstrating this association could be important for identifying patients who could benefit from screening for CTDs as well as understanding the pathomechanisms behind cervical carotid tortuosity. To better understand whether there is an association between CTDs and carotid artery tortuosity, we performed an age- and sex-matched case-control study of patients with and without CTD including Marfan syndrome, EDS, neurofibromatosis type 1 (NF1), and LDS, and carotid artery tortuosity.

MATERIALS AND METHODS

Patient Identification

Following institutional review board approval, we identified all patients with prior CTA or MRA of the cervical vasculature and a history of CTD, including Marfan syndrome, EDS, LDS, or NF1 from July 1998 to January 2017. All patients had a clinically confirmed diagnosis of these syndromes as determined by a medical geneticist at Mayo Clinic. Patients who had other forms of unconfirmed CTDs were excluded; any patients with a history or suspicion of other connective tissue diseases (ie, spontaneous coronary artery dissection and so forth) were excluded from the control group. We then identified a group of 143 age-matched controls who had carotid CTA or MRA performed as part of emergency department work-ups for various indications, including trauma, stroke, dizziness, vertigo, and so forth.

Imaging Analysis

Radiologists blinded to each patient's medical history reviewed the CTA or MRA imaging to evaluate the presence of tortuosity within the cervical segment of the internal carotid artery per previously described methods.[2] Radiologists had access to multiplanar reformatted images and 3D reconstructions as available. Carotid artery tortuosity was defined as the presence of shape deformations including coils, loops, and kinks. Specifically, shape deformations were assessed using the following criteria: 1) The presence of loops was defined by findings of C- or S-shaped deformities wherein the vessel exhibited 2 turns with angles of $\leq$90°; 2) coils exhibited complete, 360°, turns in the vessel; and 3) kinks were observed as singular ≥90° bends in the vessel. Furthermore, we explored path alterations including retrojugular and retropharyngeal anatomy. Path alterations were defined by the following criteria: 1) A retrojugular carotid path was defined as >50% of the internal carotid artery by cross-sectional area traveling posterior to the internal jugular vein; and 2) a retropharyngeal path was defined as >50% of the ICA traveling behind (medially to) the lateral edge of the pharynx. Examples of tortuosity and path alterations can be found in the Figure. Additionally, the presence of atherosclerotic changes and fibromuscular dysplasia was assessed.

Clinical Variables

Secondary clinical and demographic information including age and sex were pulled from patient charts as available. Diagnoses of hypertension, dyslipidemia (including hyperlipidemia, hypercholesterolemia, and hypertriglyceridemia), diabetes, smoking history, stroke history, coronary artery disease history, and other history of dissection, aortic root dilation, or aneurysm were identified using the medical record search function and assessed categorically by the presence or nonpresence in physician notes and radiologic reads. Common synonyms and abbreviations were included.

Sensitivity Analysis

In addition to studying the association between CTD and carotid tortuosity, we also examined the association between the combination of both an aortic dilation/aneurysm and carotid tortuosity and connective tissue diseases.

Table 1: Demographics

	CTD		Control		
	Mean	SD	Mean	SD	*P*
Age (yr)	42.19	16.48	38.84	20.14	0.13
	No.	%	No.	%	
Sex (female)	92	64.3%	102	71.3%	0.21
Imaging technique					
CTA	42	39.4%	143	100%	
MRA	116	81.1%	44	30.8%	

Table 2: Baseline characteristics

	CTD ($n = 143$)		Control ($n = 143$)		
	No.	%	No.	%	*P*
Dyslipidemia	30	21%	31	22%	.89
HTN	38	27%	43	30%	.51
DM	3	2%	15	10%	.004[a]
Smoking	44	31%	50	35%	.45
Stroke history	20	14%	21	15%	.87
CAD history	8	6%	15	10%	.13
Other aneurysm/dissection/ FMD history	85	59%	28	20%	<.001[a]
CNS	12	8%	8	6%	.35
Carotid	19	13%	3	2%	<.001[a]
Vertebral	11	8%	5	3%	.12
Aortic	58	41%	7	5%	<.001[a]
Subclavian/brachial	5	3%	0	0%	.02[a]
Coronary	8	6%	0	0%	.004[a]
Abdominal (mesenteric, celiac, splenic, hepatic)	18	13%	0	0%	<.001[a]
Renal	10	7%	0	0%	.001[a]
Iliac/femoral/popliteal	15	10%	0	0%	<.001[a]

Note:—DM indicates diabetes mellitus; FMD, fibromuscular dysplasia; HTN, hypertension; CAD, coronary artery disease.
[a] Significant.

Statistical Analysis

Obtained data were analyzed using JMP, Version 13 (SAS Institute, Cary, North Carolina, 1989–2007). Data were analyzed on a per-patient basis. Continuous variables were compared using a 2-tailed Student *t* test, and categoric variables, using χ^2 tests. Multivariate logistic regression analysis was performed on demographic information, clinical variables, and association with tortuosity. Continuous variables are reported as per-unit change. Any ICA tortuosity was defined as the presence of any left or right kink, coil, or loop. Laterality, including the presence of any tortuosity on the left, right, or bilateral carotid arteries, was also included in the analysis. Distinct pathway alterations, including retropharyngeal and retrojugular, were analyzed independently. Statistical significance was determined with a threshold α $P < .05$. We performed subgroup analyses based on each individual connective tissue disease population relative to the control population as well.

RESULTS

Patient Population and Baseline Characteristics

We identified 143 patients with CTD (median age, 42 years; interquartile range, 29–54 years; 64.3% female) including Marfan syndrome ($n = 33$), EDS ($n = 68$), NF1 ($n = 26$), and LDS ($n = 16$) and available CTA or MRA. These individuals were paired with 143 matched controls without a diagnosis of CTD (median age, 40 years; interquartile range, 22–59 years; 71.3% female). Univariate analysis did not reveal a statistically significant difference in age or sex of the CTD group relative to controls. A summary of demographic characteristics is provided in Table 1. In patients with CTD, study indications most commonly included CTD screening (38%), whereas controls included trauma (20%) and headache (19%). A summary of study indications is included in On-line Table 1.

Baseline characteristics including relevant underlying vascular risk factors were assessed (Table 2). Patients with CTD exhibited a nonsignificant difference in the history of smoking (31% versus 35%; $P = .45$), stroke (14% versus 15%; $P = .87$), and coronary artery disease (6% versus 10%; $P = .13$), in addition to dyslipidemia (21% versus 22%, $P = .89$) and hypertension (27% versus 30%; $P = .51$). Controls had an increased prevalence of diabetes (2% versus 10%; $P = .004$). Assessment of other aneurysm or dissection history revealed a significantly increased prevalence of carotid, aortic, subclavian/brachial, renal, and other visceral vascular pathologies in patients with CTD relative to controls.

To explore previously published associations of carotid tortuosity with the above demographic and clinical variables in the general population, we performed analysis on the presence of any ICA tortuosity within the control group alone (On-line Table 2). Age, stroke history, diabetes, dyslipidemia, and hypertension were significantly associated with tortuosity on univariate analysis. On multivariate analysis, smoking history, stroke history, and hypertension were found to be significantly associated with tortuosity.

Carotid Artery Tortuosity

Comparison of patients with CTD with controls demonstrated significant differences in the prevalence of carotid artery tortuosity between these 2 groups. Patients with CTD exhibited increased prevalence of any ICA tortuosity (44% versus 16%; OR, 4.11; 95% CI, 2.36–7.16; $P < .001$), loops (21% versus 10%; OR, 2.27; 95% CI, 1.16–4.42; $P = .015$), and coils (23% versus 3%; OR, 10.43; 95% CI, 3.59–30.31; $P < .001$) reaching statistical significance. Patients with CTD had increased prevalence of bilateral tortuosity (30% versus 10%; OR, 3.67; 95% CI, 1.93–6.98; $P < .001$). Of patients with CTD with any ICA tortuosity, bilateral tortuosity was present in 68% ($n = 43/63$). While the presence of any left or right tortuosity was significant in patients with CTD relative to controls, right-sided pathologies were noted to be more common than left-sided ones in patients with CTD (40% versus 34%; $P < .001$). No significant difference was found in the prevalence of carotid kinks or alterations in the carotid route, including retrojugular or retropharyngeal paths relative to controls. There was no significant difference in rates of fibromuscular dysplasia (3% versus 1%; $P = .25$); however, there was a significantly lower rate of atherosclerosis in patients with CTD (5% versus 26%; $P < .001$; Table 1).The aforementioned findings are summarized in Table 3.

To better explore the extent of the association of CTD status and carotid artery tortuosity, we performed multivariate

Table 3: Carotid anatomy by CTD

	CTD ($n = 143$)		Controls ($n = 143$)			
	No.	%	No.	%	OR (95% CI)	*P*
Any ICA tortuosity	63	44%	23	16%	4.11 (2.36–7.16)	<.001[a]
Bilateral	43	30%	15	10%	3.67 (1.93–6.98)	<.001[a]
Left	49	34%	21	15%	3.03 (1.70–5.40)	<.001[a]
Right	57	40%	17	12%	4.91 (2.68–9.01)	<.001[a]
Loop	30	21%	15	10%	2.27 (1.16–4.42)	.015[a]
Coil	33	23%	4	3%	10.43 (3.59–30.31)	<.001[a]
Kink	13	9%	10	7%	1.33 (0.56–3.14)	.51
Pathway alterations						
Retrojugular	36	25%	29	20%	1.32 (0.76–2.31)	.32
Retropharyngeal	6	4%	5	3%	1.21 (0.36–4.05)	.76
Other						
Any carotid FMD	5	3%	2	1%	2.55 (0.49–13.39)	.25
Any carotid atheromatous disease	7	5%	37	26%	0.15 (0.06–0.34)	<.001[a]

Note:—FMD indicates fibromuscular dysplasia.
[a] Significant.

Table 4: Multivariate model for any ICA tortuosity by demographic and baseline characteristics

	Any ICA Tortuosity		
Variable	Adjusted OR	95% CI	Adjusted *P*
CTD status	5.24	2.78–9.90	<.001[a]
HTN	2.75	1.30–5.84	.008[a]
Stroke history	1.76	0.78–4.01	.18
DM	1.67	0.49–5.78	.41
Dyslipidemia	1.67	0.77–3.64	.19
CAD history	1.45	0.48–4.40	.51
Age	1.00	0.98–1.02	.99
Smoking	0.89	0.45–1.78	.65
Sex (female)	0.52	0.28–0.98	.04[a]

Note:—CAD indicates coronary artery disease; HTN, hypertension; DM, diabetes mellitus.
[a] Significant.

analysis of the association of demographic and clinical characteristics with any ICA tortuosity (Table 4). CTD status was highly associated with any ICA tortuosity (adjusted OR, 5.24; 95% CI, 2.78–9.90; $P < .001$). Additionally, hypertension (adjusted OR, 2.75; 95% CI, 1.30–5.84; $P = .008$) and female sex (adjusted OR, 0.52; 95% CI, 0.28–0.98; $P = .04$) were found to be significantly associated. The remaining variables, did not reach significance.

Analysis by CTD Type

Given the above findings, we sought to delineate the prevalence of carotid abnormalities within specific CTDs (On-line Table 3). Compared with the control group, patients with Marfan syndrome exhibit increased prevalence of any ICA tortuosity, loops, and coils. Patients with Marfan syndrome demonstrated marked prevalence of bilateral tortuosity (64% versus 10%; OR, 14.93; 95% CI, 6.14–36.30; $P < .001$). Notably, the prevalence of carotid kinking was not found to be significantly increased relative to the control population. Furthermore, analysis revealed an increased prevalence of retrojugular carotid course (48% versus 20%; OR, 3.70; 95% CI, 1.67–8.19; $P < .001$).

Patients with NF1 had an increased prevalence of any ICA tortuosity, specifically, carotid coils (15% versus 3%; OR, 6.32; 95% CI, 1.47–27.13; $P = .005$) relative to controls. Similarly, patients with LDS had significantly increased total vessel tortuosity with coils making up most observed abnormalities (50% versus 3%; OR, 34.75; 95% CI, 8.60–140.33; $P < .001$). Additionally, patients with LDS had a significantly increased prevalence of bilateral carotid tortuosity compared with controls (44% versus 10%; OR, 6.64; 95% CI, 2.16–20.41; $P < .001$). The prevalence of any vascular anomaly in patients with EDS, vascular and non–vascular types, was not significantly different from that in controls (On-line Table 3).

Sensitivity Analysis

A total of 43 patients had both aortic aneurysms and carotid tortuosity. Among patients with CTDs, 41 patients (28.7%) had aortic aneurysms and carotid tortuosity, and among patients without CTD, 2 patients (1.4%) had aortic aneurysms and tortuosity (OR, 28.3; 95% CI, 6.7–119.8; $P < .001$). The positive predictive value of the combination of aortic aneurysm or dilation and carotid tortuosity being associated with connective tissue disease was 95.4%. The specificity was 98.6%.

DISCUSSION

This study finds that the prevalence of carotid artery tortuosity is increased in CTD, particularly in patients with Marfan syndrome, LDS, and NF1. Specifically, carotid artery tortuosity was found in 44% of patients with CTD, 3–fold the prevalence in controls. Such tortuosity was frequently bilateral; 30% of all patients with CTD exhibited bilateral ICA tortuosity. Among CTDs, patients with Marfan syndrome had the highest prevalence of tortuosity, followed by LDS and NF1. Meanwhile, rates of carotid tortuosity were similar to those in controls among patients with both vascular and nonvascular types of EDS. One interesting finding from our study was that the combination of an ascending aortic aneurysm and any carotid artery tortuosity was highly associated with connective tissue disease with an odds ratio of 28 and a specificity of nearly 99%. These findings are important because they indicate that carotid artery tortuosity, especially when associated with an ascending aortic aneurysm or dilation, is highly associated with connective tissue disease.

There have been no studies, to our knowledge, evaluating the prevalence of carotid artery tortuosity among patients with CTDs outside of limited descriptive cases.[11] However, carotid tortuosity has been associated with connective tissue–related pathologies, such as cervical carotid dissection.[1,2,12] Additionally, retrospective studies found the prevalence of ICA tortuosity to be 53%–63% in patients with dissection and 20%–34% in controls.[2,13] Most interesting, Kim et al[2] further found that a retrojugular carotid course was significantly associated with dissection; 35% of dissections were associated with a retrojugular course relative to 16% in controls. Compared with the present study demonstrating a significantly increased prevalence of retrojugular course in patients with Marfan syndrome, such a finding may help explain the risk of dissection in this patient population.

We note a stark difference in the prevalence of carotid tortuosity across CTD types. The prevalence of any ICA tortuosity was 88% in Marfan syndrome, 63% in Loeys–Dietz syndrome, 42% in NF1, and 19% in patients with both vascular and nonvascular types of EDS. Marfan syndrome is due to a defect in the structure of fibrillin–1, while LDS is due to mutations in the transforming growth factor β protein receptor. Loss of microfibrils as a result of a defective fibrillin–1 results in aberrant transforming growth factor β signaling, which is essential to the proper formation of the extracellular matrix, including the biogenesis and maintenance of elastic fibers. Meanwhile, both vascular and nonvascular forms of EDS result in abnormal collagen structure rather than elastin. A previous hypothesis states that the extracranial ICA may be susceptible as a transition zone from an elastic vessel to muscular vessel.[6,14] Given the higher prevalence of carotid tortuosity in Marfan syndrome and patients with LDS and the fact that the respective mutated proteins in these 2 disorders are part of the same pathway affecting the biogenesis and maintenance of elastic fibers, we hypothesize that aberrations in elastic fiber structure rather than collagen structure are greater contributors to the development of tortuous vasculature.

Notably, little is known about subtypes of carotid tortuosity and their potential downstream effects. A study using in vitro and in vivo physiologic techniques found a significant pressure differential across carotid kinks; however, whether this is significant in other forms of tortuosity is unknown.[7,15] Here, carotid coils were significantly more prevalent in those with CTD (23% versus 3%). This finding is in line with the suggestion that carotid coils represent consequences of embryologic origins, whereas other tortuosity may be indicative of acquired risk factors.[6] Notably, the definition of tortuosity itself is wide-ranging, with some studies, including ours, following the descriptive Weibel-Fields and Metz modified criteria and others expanding this to include linear measurements of tortuosity.[1,2,9,16] Given possible differences in etiology and pathology, continued use of descriptive criteria alongside other measures is important toward evolving our understanding of tortuosity.

Numerous factors including hypertension, elevated BMI, advanced age, and atherosclerotic disease have been variably associated with tortuosity.[3,7-9,16,17] Atherosclerosis and age were noted as significant risks in early studies on carotid tortuosity.[3] In contrast, using sonographic assessment of 345 patients, Togay-Isikay et al[16] found no clear association with carotid tortuosity and stroke risk factors, including stenosis and atherosclerosis. Furthermore, a previous report suggests that hypertension is more prevalent in patients with tortuosity.[7] However, a recent study ultimately failed to find such a result, instead finding body mass index as a significant factor.[7,9] Other previously found associations include laterality[1,9,16,17] and sex differences,[9,12,16-18] though, notably, these remain discrepant and of uncertain significance. Using multivariate analysis, here we found hypertension, stroke history, and smoking history to be associated with tortuosity. We did not find an association between age, sex, diabetes, coronary artery disease and any ICA tortuosity. Contrary to previous suggestions, though tortuosity was increased in CTD, these patients had decreased carotid atherosclerosis compared with controls. Regarding laterality, we found bilateral tortuosity to be significantly increased in CTD. Additionally, right–sided predominance was noted among all CTD types, with Marfan syndrome exhibiting the most marked prevalence. Such a finding could suggest manifestation of tortuosity associated with proximity to the brachiocephalic trunk, in addition to known aortic pathologies. Outside of the aforementioned, tortuosity risk factors have been documented. Intriguing studies report carotid tortuosity in those with sickle cell anemia, thus suggesting an alternative mechanism to direct vascular structure abnormalities. Given the broad array of associations found and not found, future meta–analysis would be of benefit.

CTDs are associated with other vascular tortuosities. For example, the association of Marfan syndrome with aortic root dilation is well–established. Furthermore, recent evidence finds other cervical vasculature tortuosities in CTD. Vertebral artery tortuosity was found to be associated with earlier vascular interventions and worse outcomes in a young cohort of patients with CTD, particularly those with Marfan syndrome or LDS.[19] Here, we found a significantly increased prevalence of aortic, carotid, subclavian/brachial, abdominal, and renal pathology in patients with CTD. While this finding indicates a larger proportion of vascular abnormalities in those with CTD, the extent of such an effect may be exaggerated. Follow–up and the presence of other diagnostic imaging was not controlled for in this secondary analysis. Furthermore, some forms of tortuosity may be transient. A retrospective study has found retropharyngeal carotid course to change with time across patients, thus lending evidence that pathway alterations and tortuosity are dynamic processes.[20] Future prospective research exploring the temporal relationship among these risk factors, tortuosity, and ultimate disease pathology is needed.

Our study has some practical implications and also potentially paves the way for further study of connective tissue abnormalities for patients with ecstatic or dissected carotid arteries. Given the relatively high prevalence of carotid artery tortuosity in the general population and the rarity of CTDs, we certainly do not call for all patients with carotid tortuosity to be screened for CTDs. However, in the correct clinical context and in the presence of additional abnormal imaging findings (ie, dilated aortic root, dural ectasia, multiple aneurysms, multiple arterial ectasias, and so forth), carotid tortuosity could be an additional finding encouraging clinicians to think

about the possibility of CTD. This is especially true given that we found that the presence of aortic root dilation or an aneurysm in combination with carotid artery tortuosity was highly associated with CTDs, with a specificity of nearly 99% and a positive predictive value of >95%. Regarding future studies, it may be interesting to determine the prevalence of carotid dissections in patients with CTD with and without tortuosity. It is possible that vascular tortuosity is an important phenotypic component of patients with CTD who are at risk for dissection, thus making it an indication for regular cervical vascular screening.

Limitations

This study has limitations. These include limited patients with specific CTD subtypes identified for inclusion in this study. Strict sex and age matching were not applied. This study looked at imaging across a 20-year period with varied scanners and imaging protocols. The selection of patients with CTD with available cervical vasculature imaging may lead to incorporation bias of those with suspected disease and may not represent the larger CTD population. The case-control study design precludes the accurate determination of the incidence of CTD in those with tortuosity. Similarly, secondary data points, including the prevalence of other vascular abnormalities, may be subject to inclusion bias increased availability of other in patients with CTD relative to controls. Furthermore, inter- and intraobserver concordance of vessel tortuosity identification was not studied.

CONCLUSIONS

Tortuosity of the cervical internal carotid arteries is highly prevalent in patients with CTDs, particularly patients with Marfan syndrome or LDS. The finding of an ascending aortic aneurysm or dilation in combination with any carotid tortuosity is highly specific for the presence of a connective tissue disease. Such findings are relevant for risk assessment for vascular complications in CTD, endovascular treatment planning, and in understanding the pathomechanisms of vascular tortuosity in general.

REFERENCES

1. Saba L, Argiolas GM, Sumer S, et al. **Association between internal carotid artery dissection and arterial tortuosity.** *Neuroradiology* 2015;57:149–53 CrossRef Medline
2. Kim ST, Brinjikji W, Lehman VT, et al. **Association between carotid artery tortuosity and carotid dissection: a case–control study.** *J Neurosurg Sci* 2018;62:413–17 CrossRef Medline
3. Del Corso L, Moruzzo D, Conte B, et al. **Tortuosity, kinking, and coiling of the carotid artery: expression of atherosclerosis or aging?** *Angiology* 1998;49:361–71 CrossRef Medline
4. Lam RC, Lin SC, DeRubertis B, et al. **The impact of increasing age on anatomic factors affecting carotid angioplasty and stenting.** *J Vasc Surg* 2007;45:875–80 CrossRef Medline
5. Han HC. **Twisted blood vessels: symptoms, etiology and biomechanical mechanisms.** *J Vasc Res* 2012;49:185–97 CrossRef Medline
6. La Barbera G, La Marca G, Martino A, et al. **Kinking, coiling, and tortuosity of extracranial internal carotid artery: is it the effect of a metaplasia?** *Surg Radiology Anat* 2006;28:573–80 CrossRef Medline
7. Pancera P, Ribul M, Presciuttini B, et al. **Prevalence of carotid artery kinking in 590 consecutive subjects evaluated by echocolor Doppler: is there a correlation with arterial hypertension?** *J Intern Med* 2000;248:7–12 CrossRef Medline
8. Thomas JB, Antiga L, Che SL, et al. **Variation in the carotid bifurcation geometry of young versus older adults: implications for geometric risk of atherosclerosis.** *Stroke* 2005;36:2450–56 CrossRef Medline
9. Wang HF, Wang DM, Wang JJ, et al. **Extracranial internal carotid artery tortuosity and body mass index.** *Front Neurol* 2017;8:508 CrossRef Medline
10. Kim ST, Brinjikji W, Lanzino G, et al. **Neurovascular manifestations of connective–tissue diseases: a review.** *Interv Neuroradiol* 2016;22:624–37 CrossRef Medline
11. Kondo M, Itoh S, Nagano K, et al. **A 10–year–old boy with Marfan syndrome exhibiting cerebrovascular abnormalities.** *Brain Dev* 2001;23:251–54 Medline
12. Kim BJ, Yang E, Kim NY, et al. **Vascular tortuosity may be associated with cervical artery dissection.** *Stroke* 2016;47:2548–52 CrossRef Medline
13. Barbour PJ, Castaldo JE, Rae–Grant AD, et al. **Internal carotid artery redundancy is significantly associated with dissection.** *Stroke* 1994;25:1201–06 CrossRef Medline
14. Albanese V, Spadaro A, Iannotti F, et al. **Elastic tissue dysplasia of coiled internal carotid artery in an adult: case report.** *J Neurosurg* 1983;58:781–85 CrossRef Medline
15. Wang L, Zhao F, Wang D, et al. **Pressure drop in tortuosity/kinking of the internal carotid artery: simulation and clinical investigation.** *BioMed Res Int* 2016;2016:2428970 CrossRef Medline
16. Togay–Işikay C, Kim J, Betterman K, et al. **Carotid artery tortuosity, kinking, coiling: stroke risk factor, marker, or curiosity?** *Acta Neurol Belg* 2005;105:68–72 Medline
17. Macchi C, Gulisano M, Giannelli F, et al. **Kinking of the human internal carotid artery: a statistical study in 100 healthy subjects by echocolor Doppler.** *J Cardiovasc Surg (Torino)* 1997;38:629–37 Medline
18. Choudhry FA, Grantham JT, Rai AT, et al. **Vascular geometry of the extracranial carotid arteries: an analysis of length, diameter, and tortuosity.** *J Neurointerv Surg* 2016;8:536–40 CrossRef Medline
19. Morris SA, Orbach DB, Geva T, et al. **Increased vertebral artery tortuosity index is associated with adverse outcomes in children and young adults with connective tissue disorders.** *Circulation* 2011;124:388–96 CrossRef Medline
20. Lukins DE, Pilati S, Escott EJ. **The moving carotid artery: a retrospective review of the retropharyngeal carotid artery and the incidence of positional changes on serial studies.** *AJNR Am J Neuroradiol* 2016;37:336–41 CrossRef Medline

Safety and Efficacy of Transvenous Embolization of Ruptured Brain Arteriovenous Malformations as a Last Resort: A Prospective Single-Arm Study

Y. He, Y. Ding, W. Bai, T. Li, F.K. Hui, W.-J. Jiang, and J. Xue

ABSTRACT

BACKGROUND AND PURPOSE: The efficacy and safety of transvenous embolization for brain arteriovenous malformations remains unclear, given the very limited number of cases reported. This prospective study was performed to assess this technique in ruptured AVMs.

MATERIALS AND METHODS: Twenty-one consecutive patients with ruptured brain AVMs who underwent transvenous embolization were prospectively followed between November 2016 and November 2018. The Spetzler-Martin grade was I in 3 AVMs (14.3%), II in four (19.0%), III in eleven (52.4%), and IV in three (14.3%). The complete AVM occlusion rate was calculated from 6-month follow-up DSA images. Occurrence of hemorrhage and infarction after embolization was evaluated using CT and MR imaging within 1 month after the operation. The mRS was used to assess the functional outcomes.

RESULTS: Complete AVM nidus obliteration was shown in 16 (84%) of 19 patients with technically feasible AVMs immediately after embolization. One (5%) patient with a small residual nidus after treatment showed complete obliteration at 13-month follow-up. There were 5 hemorrhages and 1 infarction; 4 patients' symptoms improved gradually. The percentage of cases with mRS $\leq$ 2 rose from 57.1% (12/21) before embolization to 66.7% (14/21) at 1-month follow-up. Both the morbidity and mortality rates were 4.8% (1/21).

CONCLUSIONS: Transvenous embolization can be performed only in highly selected hemorrhagic brain AVMs with high complete obliteration rates, improved functional outcomes, and acceptable morbidity and mortality rates, but it should not be considered as a first-line treatment.

Brain arteriovenous malformations are characterized by an intervening plexus of abnormal vessels (nidus) between feeding arteries and draining veins. The most common presentations of AVMs include hemorrhages, seizures, headaches, and progressive neurologic deficits due to chronic vascular steal.[1] Hemorrhage can occur because of an inherent lack of normal smooth-muscle properties in the vascular architecture of AVMs. A first hemorrhagic event is associated with an increased risk of a new bleeding. Morbidity of AVM hemorrhage is estimated to be between 13% and 50%, and the mortality rate after intracranial hemorrhage from AVM rupture ranges from 12% to 67%.[2]

Treatment strategies (microsurgery, radiosurgery, and endovascular embolization) are chosen on the basis of angioarchitecture, location, and presentation of AVMs.[3,4] Elimination of hemorrhage risk by extirpation or endoluminal closure of the nidus remains the primary goal of AVM treatment. Surgical resection of an AVM can be challenging in deep, inaccessible locations and eloquent areas. Radiosurgery may not be ideal in hemorrhagic AVMs as the first choice because of the long latency between treatment and AVM involution. Endovascular embolization through arterial routes may not be curative for AVMs in many situations, especially in cases with indirect feeders and extreme vessel tortuosity.[5] Transvenous embolization can overcome these disadvantages.[6-14] Current indications for transvenous embolization of AVMs include

Received May 17, 2019; accepted after revision July 23.

From the Department of Interventional Neuroradiology (Y.H., W.B., T.L., J.X.), Henan Provincial People's Hospital, Zhengzhou University People's Hospital, Henan University People's Hospital, and Henan Provincial Neurointerventional Engineering Research Center, Zhengzhou, China; Department of Radiology (Y.D.), Mayo Clinic, Rochester, Minnesota; Department of Radiology (F.K.H.), Johns Hopkins Hospital, Baltimore, Maryland; and Department of Vascular Neurosurgery (W.-J.J.), the PLA Rocket Force General Hospital, Beijing, China.

Y. He, Y. Ding, and W. Bai contributed equally to this work.

The study was funded by the National Natural Science Foundation of China (No. 81601583), the Scientific and Technological Project (No. 2018020424), and Aboard Research Project (2016054) of Henan Provincial Health Commission.

Please address correspondence to Tianxiao Li, MD, Department of Interventional Neuroradiology, Henan Provincial People's Hospital, Zhengzhou University and Henan University, No. 7, Weiwu Rd, Zhengzhou, China; e-mail: dr.litianxiao@henu.edu.cn

Indicates open access to non-subscribers at www.ajnr.org

Indicates article with supplemental on-line video.

http://dx.doi.org/10.3174/ajnr.A6197

Table 1: Baseline characteristics of the 21 patients in this study

Variable	Value
Age (yr)	
Mean	29.9
Median	29
Range	8–59
SD	17.0
Sex (No.) (%)	
Male	14 (66.7)
Female	7 (33.3)
mRS before embolization (No.) (%)	
0–2	12 (57.1)
3–5	9 (42.9)
Location (No.) (%)	
Deep	18 (85.7)
Superficial	3 (14.3)
Size (No.) (%)	
≤3 cm	12 (57.1)
>3 cm	9 (42.9)
Eloquent (No.) (%)	
Yes	15 (71.4)
No	6 (28.6)
Venous pattern (No.) (%)	
Superficial	11 (52.4)
Deep	9 (42.9)
Deep (main) + superficial	1 (4.8)
No. of veins (%)	
Single	20 (95.2)
Multiple	1 (4.8)
Angioarchitecture (No.) (%)	
Aneurysms in the feeding artery or intranidus	9 (42.9)
Venous stenosis	4 (19.0)
Localized venous ectasia	2 (9.5)
Spetzler-Martin grade (No.) (%)	
I	3 (14.3)
II	4 (19.0)
III	11 (52.4)
IV	3 (14.3)
V	0 (0)

Table 2: Safety and efficacy outcomes

Variable	Value
Procedure	
Patients (No.)	21
Patients with technically feasible AVMs (No.) (%)	19 (90.5%)
Procedure-related complications (No.) (%)	6 (28.6)
Transient	4 (19.0)
Permanent, nondisabling	0 (0)
Permanent, disabling	1 (4.8)
Death	1 (4.8)
Non-neurologic	0 (0)
Follow-up	
Immediate obliteration after procedure (No.) (%)	
In 19 patients with technically feasible AVMs	16 (84.2)
In all 21 patients	16 (76.2)
Imaging follow-up of patients (No.)	14
Follow-up time (median) (range)	5.5 (3–15)
Obliteration at follow-up (No.) (%)	13 (92.9)
Stable	1 (7.1)
Recanalization	0 (0)
Clinical follow-up of patients within 1 mo (No.)	21
Events	6
Stroke	6
Others	0
Clinical follow-up of patients beyond 1 mo (No.)	20
The latest follow-up time (median) (range)	15 (2–26)
Events (No.)	1
Epilepsy	1
Others	0
The latest mRS	
0–2	19
3–5	1
6	0

deep location, unfavorable arterial access, a small nidus, and a single draining vein.[6-14] Because there are only a limited number of cases reported using this approach, the effectiveness and safety remain unclear. In this study, we tried to further validate this method.

MATERIALS AND METHODS

The Medical Ethics Committee of Henan Provincial People's Hospital approved this study. Key inclusion criteria were as follows: 1) patients with a ruptured brain AVM; 2) patients not suitable for intra-arterial embolization due to the absence of arterial access, narrow arterial feeders, extremely tortuous course, too many feeders, and so forth; and 3) patients in whom lesions were not amenable to surgery or radiosurgery or patients who refused to undergo surgery or radiosurgery (AVMs not amendable to surgery or radiosurgery are defined as cases with modified Spetzler-Martin grades of III+, IV, and V based on modification of the Spetzler-Martin scale[15] and those with scores of >1.5 based on Pollock-Flickinger grading scale,[16] which are proved have high rates of iatrogenic complications); and 4) patients with favorable venous angioarchitecture and a single main draining vein.

Key exclusion criteria were as follows: 1) multiple AVMs, 2) patients with ≥2 main draining veins, 3) a history of severe allergies to contrast or nonadhesive embolic agents, and 4) uncontrolled active bleeding.

Twenty-one consecutive patients with ruptured brain AVMs underwent transvenous embolization between November 2016 and November 2018. Thirteen patients experienced brain AVM ruptures with intracranial hematoma and intraventricular hemorrhage, 6 patients had intracranial hematoma without intraventricular involvement, 1 patient had subarachnoid hemorrhage, and another one had intraventricular hemorrhage. The mean AVM size was 2.76 ± 1.24 cm, ranging from 1.2 to 5.5 cm. A summary of patient characteristics is shown in Table 1.

All the embolization procedures were performed with the patient under general anesthesia. A 6F sheath was placed in the internal jugular vein followed by a 6F guiding catheter, which was advanced to the main draining vein of the brain AVMs. One or 2 microcatheters (Marathon, Covidien, Irvine, California; Apollo, Covidien; Echelon, Covidien; or Headway DUO, MicroVention, Tustin, California) were placed as close as possible to the nidus of the AVMs. A vascular sheath was placed in the right femoral artery followed by guide catheter placement though which a microcatheter was advanced into the feeding artery of the AVMs. Arterial inflow of the feeding

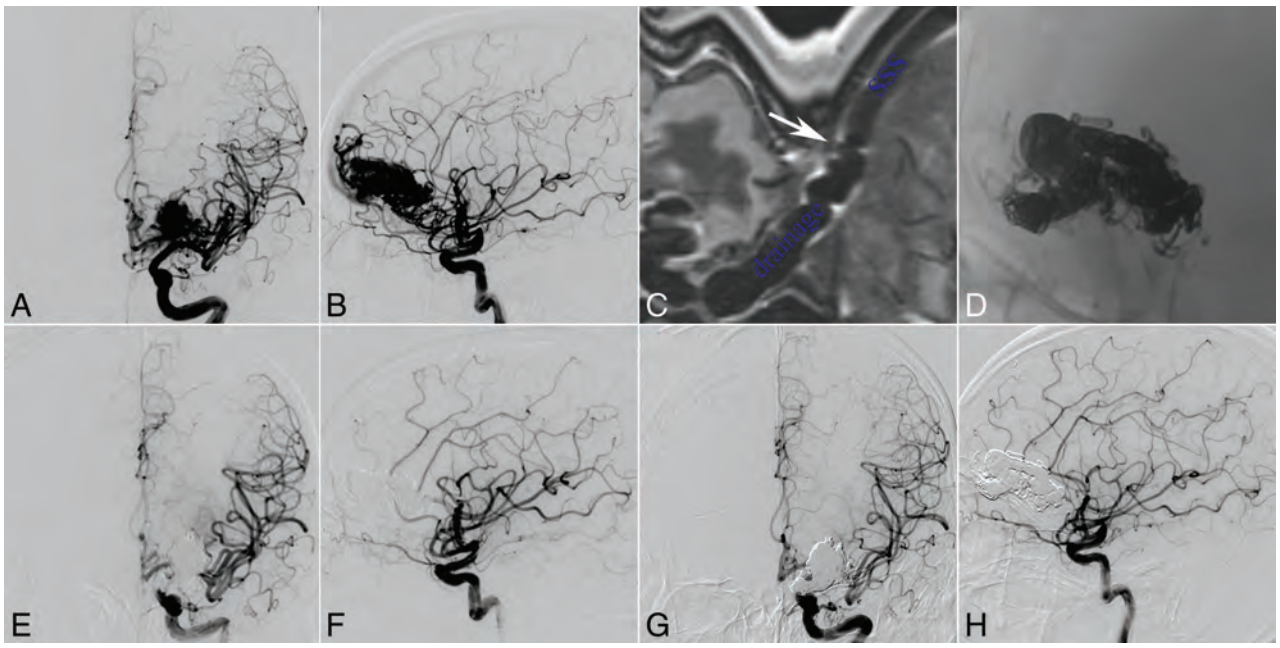

FIG 1. A 31-year-old man with intraparenchymal hemorrhage. Selective DSA of the left ICA (anteroposterior [*A*] and lateral [*B*] views) demonstrates that the AVM located at the frontal lobe is fed by the branches and perforators of anterior cerebral artery, MCA, and ICA and drains a single venous outlet via the cortical vein to the superior sagittal sinus (SSS). The high-resolution MR imaging shows that there is no severe stenosis or valvelike chordae in the connection part of the draining vein and superior sagittal sinus (*C*, *white arrow*). The nidus cast is through the transvenous embolization (*D*, unsubtracted image of the DSA), and the AVM is completely angiographically obliterated at the end of the operation (anteroposterior [*E*] and lateral [*F*] views) and at the 5-month follow-up (anteroposterior [*G*] and lateral [*H*] views).

artery was reduced by transarterial coil or liquid embolization or balloon inflation. Transvenous embolization was initiated by injecting ethylene-vinyl alcohol copolymer (Onyx; Covidien) into the nidus through the venous access route. Transvenous partial coiling in the draining vein through 1 microcatheter (known as the transvenous pressure cooker technique) was used to prevent reflux of Onyx.[17-19] At the completion of the procedure, the microcatheter injecting Onyx was cut at the level of the jugular sheath.[14]

Preoperative baseline functional status was determined using the mRS score. The same evaluation was performed on postoperative days 2, 7, and 30 and at 3, 6, and 12 months. Occlusion of the AVM nidus was categorized as complete (no residual nidus) and near-complete obliteration (residual nidus of <3 mm in diameter). Comparison of the degree of occlusion was classified as progressive, stable, or recanalized.

Procedural safety was evaluated by assessing the periprocedural complications occurring within 1 month after embolization.[20] Any deficit that resolved within the first 30 days was characterized as transient. Any deficit that persisted beyond 30 days was considered permanent. An mRS score of ≤2 indicated a nondisabling deficit. An mRS score of ≥3 indicated a disabling deficit. Periprocedural-related death was defined as any death occurring within 30 days after the procedure.

Statistical Analysis

Categoric variables are presented as numbers and percentages, and continuous variables are presented as mean and SD. A 2-sided *P* value < .05 was considered significant.

RESULTS

Procedural/Technical Specifications

The median time between hemorrhage and transvenous treatment was 47 days (range, 9–164 days). The procedure was technically feasible in 19 (90.5%) cases (Table 2). There was failure of microcatheter placement into the draining vein via the nidus in 2 cases.

For the 19 embolization procedures, access included the straight sinus in 9 cases, the cortical veins via the superior sagittal sinus in 6 cases, and the cortical veins via the transverse sinus in 4 cases.

The transvenous pressure cooker technique and Onyx injection were accomplished using 1 microcatheter in 3 patients and 2 microcatheters in 16 patients. The microcatheters for Onyx injection were retained in all patients except one.

The mean procedural time of all 21 patients from puncture onset to puncture closing was 251.6 ± 73.1 minutes. The mean volume of Onyx used for embolization was 3.79 ± 3.30 mL (range, 0 –13 mL).

AVM Nidus Obliteration

Immediately after the procedure, complete obliteration was achieved in 16 cases (Table 2), with an obliteration rate of 84.2% in the 19 technically feasible cases and 76.2% in all 21 cases. A postoperative small residual nidus was present in 3 patients after transvenous embolization. Follow-up angiography was performed from 1 to 15 months after embolization. Stable obliteration was confirmed in 18 patients. No recurrence was noted (Fig 1). One AVM located in the parietal lobe and basal ganglia showed progressive occlusion (Fig 2).

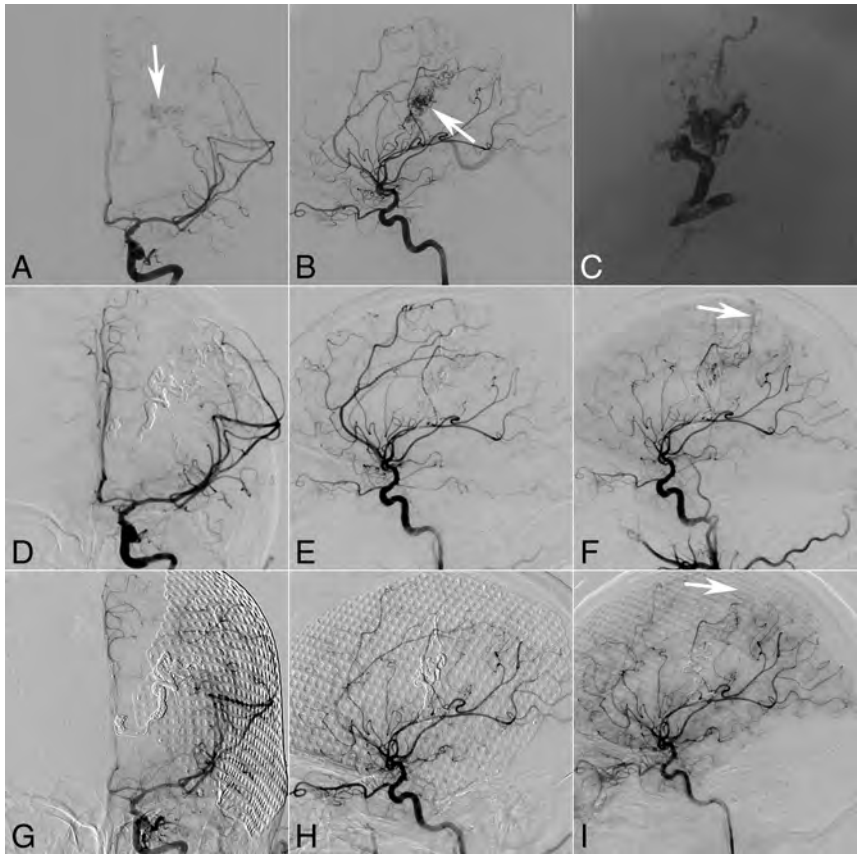

FIG 2. A 28-year-old man with intraparenchymal and intraventricular hemorrhage. Ventriculostomy, decompressive craniectomy, and transarterial embolization were performed at the local hospital. Three months later, the selective DSA of the left ICA (anteroposterior [A] and lateral [*B*] views, both *white arrows* referring to the nidus) demonstrates that the parietal lobe and basal ganglia arteriovenous malformation are fed by the branches of the MCA and drain a single venous outlet via the deep vein to the straight sinus. The nidus cast was through transvenous embolization (*C*, unsubtracted image of the DSA), but there is a small residual AVM (anteroposterior [*D*] and lateral [*E*] views at the median arterial phase) with drainage via a cortical vein (*F, white arrow)* to the superior sagittal sinus, which appeared at the late arterial phase of DSA. Thirteen-month angiography follow-up confirms the complete occlusion of the residual AVM (anteroposterior [*G*] and lateral [*H*] views at the median arterial phase and lateral view [*I*] at the late arterial phase).

Procedural Safety

Procedure-related complications occurred in 6 patients, including 4 intraventricular hemorrhages, 1 intraparenchymal hemorrhage with combined intraventricular hemorrhage (Fig 3), and 1 cerebral infarction (Fig 4). Three of these patients underwent ventriculostomy, 1 of whom also underwent lumbar drainage; the other patients just had conservative management. Good outcomes (mRS $\leq$ 2) at the 1-month evaluation were achieved in 4 patients following the above therapies. The clinical outcome was poor (mRS = 5) in 1 patient (Fig 4) at the 1-month evaluation, and another patient died.

Among the above complications, 5 occurred in small-sized AVMs, 5 in eloquent areas, 5 with deep venous drainage, 9 in deep locations, 4 with Spetzler-Martin III, 4 with aneurysms in the feeding artery or AVM nidus, and 1 with venous outflow stenosis. The Fisher exact test indicated no significant difference among these factors (Table 3).

The mRS scores at the latest follow-up for all surviving patients were as follows: 0 for 15 patients, 1 for 2 patients, 2 for 2 patients, and 5 for 1 patient. The percentage of good outcome (mRS $\leq$ 2) increased from 57.1% (12/21) before embolization to 66.7% (14/21) at 1-month follow-up and 100% (19/19) at 6-month follow-up, respectively (Fig 5).

DISCUSSION

Transvenous Obliteration

Total occlusion of AVMs with detachable or nondetachable microcatheters in transarterial procedures is difficult to achieve, mostly due to a variety of challenges, including microcatheter navigation, multiplicity of arterial feeders, and achieving deep and complete Onyx penetration of the AVM nidus.[5] In these challenging situations, transvenous embolization may be a viable alternative with total occlusion rates as high as 92.6%,[21] which is comparable with ours in this study. Transvenous microcatheter navigation, which occurred in 2 of our cases, might be difficult. However, this issue might be resolved by balloon-assisted microcatheter navigation techniques[22] or hybrid surgical techniques.[23,24]

The high occlusion rates of AVMs may be due to the small, compact architecture, which is more easily penetrated.

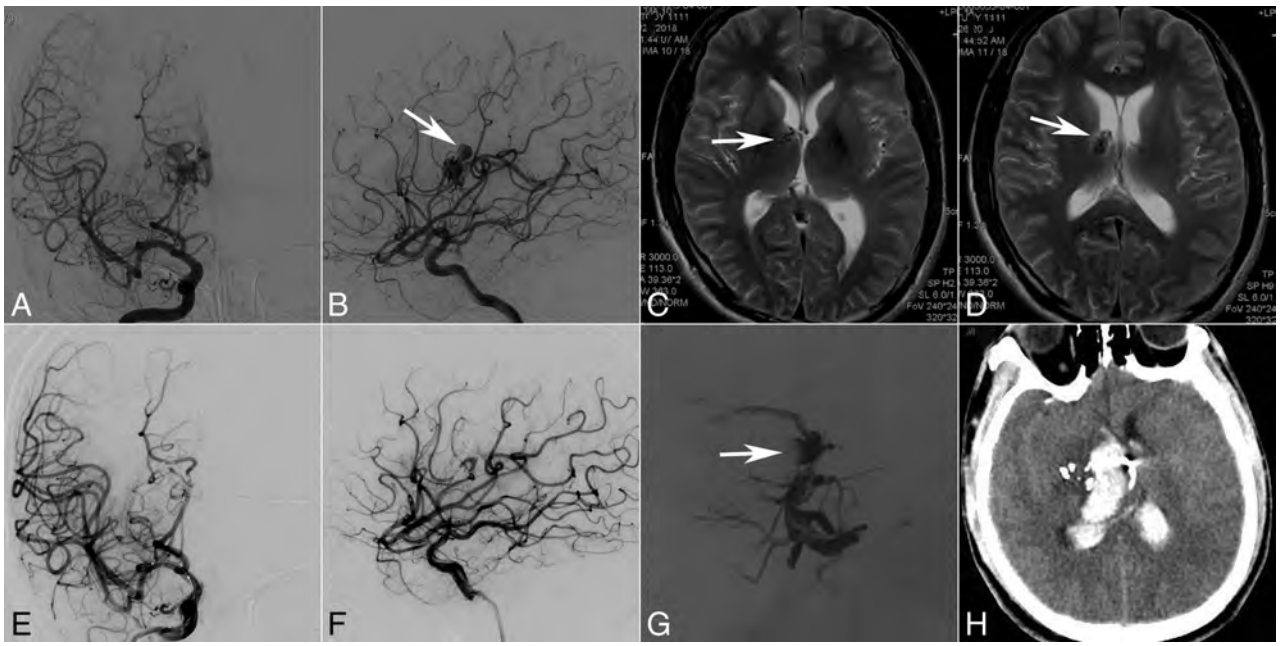

FIG 3. A 28-year-old man with intraventricular hemorrhage. Selective DSA of the right ICA (anteroposterior [*A*] and lateral [*B*] views) demonstrates that the AVM with an intranidal aneurysm (*B*, *white arrow*) is fed by perforators of the MCA and ICA and drains a single venous outlet via the deep vein to the straight sinus. Axial MR image indicates a basal ganglia arteriovenous malformation (*C*, *white arrow*) with the intranidus aneurysm next to the ventricle (*D*, *white arrow*). At the end of the operation, the AVM does not appear at the last angiography (anteroposterior [*E*] and lateral [*F*] views), but the cast image shows that the aneurysm does not have complete penetration by the embolic agent (*G*, *white arrow*) after transarterial and transvenous embolization. Two days later, intraventricular hemorrhage occurred (*H*, CT).

Additionally, the single, embolized draining vein may, in turn, induce the occlusion of many shunts in the nidus. Because arteriovenous fistulas compose most brain AVMs with plexiform nidi and upstream shunts, arterial occlusion without obliteration of the venous drainage of brain AVMs can lead to recurrence.[25] In the report of Viana et al,[26] 1 patient in whom immediate angiographic occlusion was not achieved showed spontaneous occlusion at the 6-month follow-up,[26] which was also observed in this study.

Brain AVM–related events can be controlled once the AVM nidus has been obliterated. A case series demonstrated no events occurring in the 6-month follow-up in 11 patients.[26] Another report indicated that only 1 (2.5%) patient had significant disability at the 6-month follow-up, but unfortunately, no detailed information was provided.[21] In this study, 1 seizure occurred 3 months after the operation.

Procedural Safety

Previous reports on the transvenous embolization of AVMs showed low rates of periprocedural complications, disability, and morbility.[21,27] In contrast, the complication rate was relatively high in our study. There are several possible reasons: First, the present study enrolled only patients with ruptured AVMs (100%), which had a higher risk for rebleeding.[1] In the report of Mendes et al,[21] the rate of ruptured AVMs was only 67.5%. Second, we enrolled more patients with higher Spetzler-Martin grades, and 66.7% of our patients were classified as Spetzler-Martin grade III or even higher. The percentage of higher Spetzler-Martin grades was 58.5% in the report of Mendes et al,[21] and only 25% in the report of Trivelato et al,[11] which are architecturally more complex.

Infarctions caused during transvenous embolization are supposed to be related to either penetration of Onyx into the feeding artery of the normal brain tissue or hyperemia and edema caused by draining vein occlusion. The outcome may depend on the local collateral circulation.[2,28] In this study, 1 cerebral infarct that caused disability was thought to be due to the occlusion of the feeding artery with Onyx. Trivelato et al[11] and Mendes et al[21] reported 2 cases each of postprocedural parenchymal edema thought to be related to venous outflow obstruction, one of which caused a disability.

Hemorrhagic complications might occur in different locations. Among the 5 hemorrhagic complications, 4 occurred in the eloquent area and 4 with deep venous drainage, which are also the risk factors for transarterial embolization.[29] All 5 AVMs with hemorrhagic complications were located in deep brain structures and around ventricles and bled into the ventricles, which is not a usual complication of transarterial embolization. Periventricular location has been cited as a risk factor for hemorrhage.[30] These hemorrhages may be related to the following reasons:[18] high arterial input pressure and venous outflow restriction in the deep AVMs; not enough brain tissue around the ventricle; and a large pressure gradient between the nidus and ventricle. Premature occlusion of draining veins during transvenous embolization before complete occlusion of the nidus can increase the pressure in the

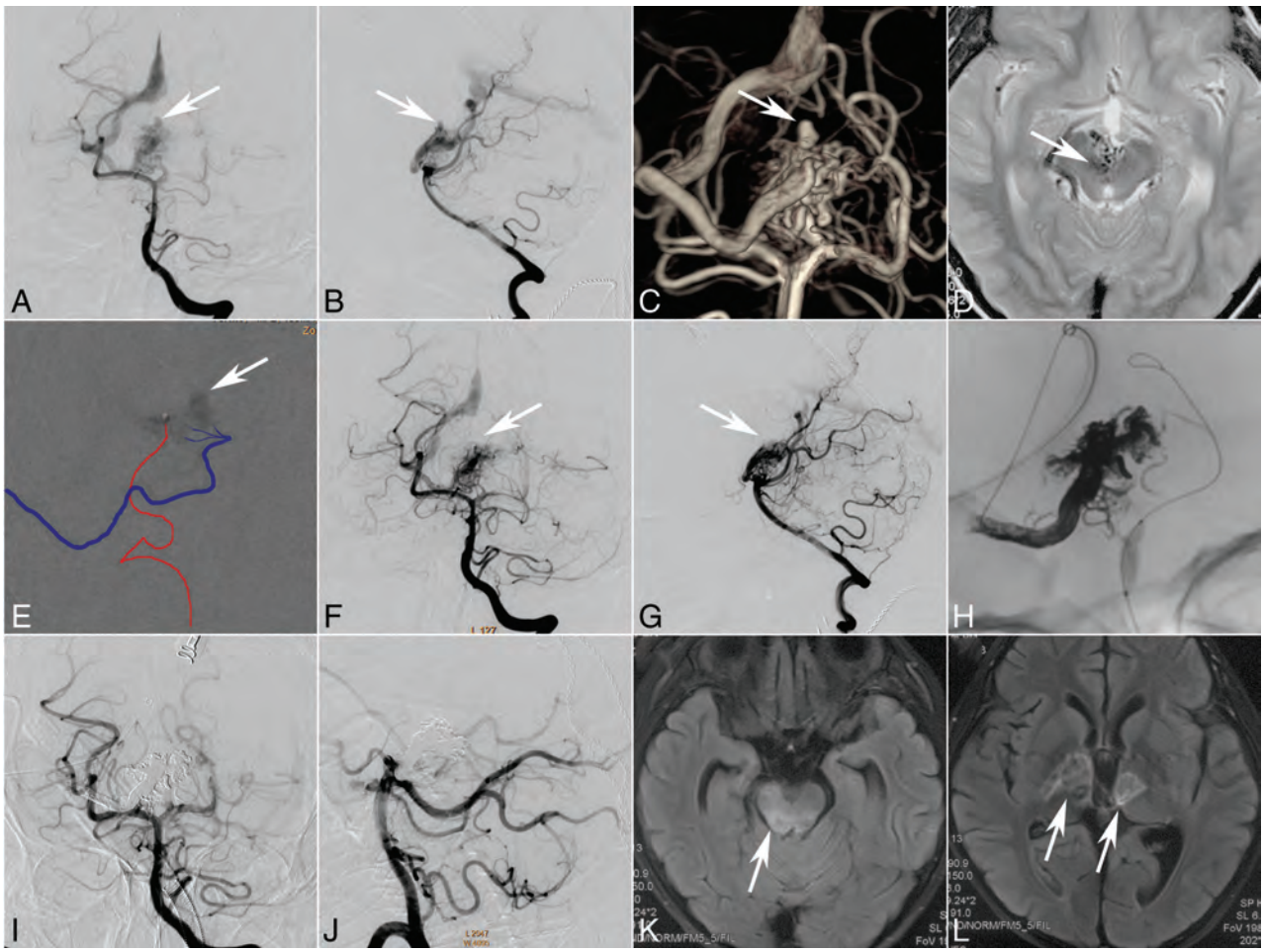

FIG 4. An 8-year-old boy who presented with sudden headache and vomiting. CT shows intraventricular hemorrhage. Selective DSA of the left vertebral artery (anteroposterior [*A*] and lateral [*B*] views, *white arrow*) demonstrates that the AVM with an intranidus aneurysm (*C*, 3D reconstruction, *white arrow*) is fed by the perforators of the posterior cerebral artery and drains a single venous outlet via the deep vein to the straight sinus. Axial MR image indicates a diencephalon arteriovenous malformation (*D*, *white arrow*). Transarterial ethanol sclerotherapy (80% ethanol in iohexol, Omnipaque 300 [GE Healthcare, Piscataway, New Jersey]) was performed to occlude the aneurysm (*E*, *white arrow*, the injection course can be seen in the On-line Video). Both the immediate angiography after sclerotherapy and the 2-month follow-up angiography (anteroposterior [*F*] and lateral [*G*] views, *white arrow*) demonstrate occlusion of the aneurysm. At 2-month follow-up, transvenous embolization was performed under transarterial balloon blocking (*H*). The last angiography (anteroposterior [*I*] and lateral [*J*] views) shows complete occlusion of the AVM. The intraprocedure electroencephalography monitoring did not show an abnormality, but the patient presented with light coma or lethargy. The MR imaging performed 12 days after the operation shows multiple infarctions in the mesencephalon (*K*, *white arrow*) and thalamus (*L*, *white arrows*).

Table 3: Relative analysis for the complications in 19 patients with technically feasible AVMs

Variable	Complication		*P* Value
	+	−	
Spetzler-Martin grade			.801
I–II	1	5	
III	4	6	
IV–V	1	2	
Size			.141
≤3 cm	5	5	
>3 cm	1	8	
Eloquent			.605
+	5	8	
−	1	5	
Deep venous drainage			.057
+	5	4	
−	1	9	

Note:—+ indicates yes; −, no.

AVM nidus,[31] which has been reported as one of the main causes of hemorrhagic complications.[32] Therefore, transvenous embolization is considered an "all-or-nothing" technique. In this study, 3 AVMs had residual nidi postembolization, with hemorrhages occurring in 2. The 1 AVM with a residual that did not bleed had continued drainage through a cortical vein after the deep drainage vein had been occluded, which may explain the lack of hemorrhage postprocedure.

Most of the patients in this study with complications (4/6) had good outcomes after receiving appropriate treatment. For the ischemic complications, the outcome depends on the location and size of the infarction, especially whether it is in an eloquent area. In this study, the patient with infarction involving the midbrain and thalamus did not recover well. For the other 5 hemorrhagic complications, 4

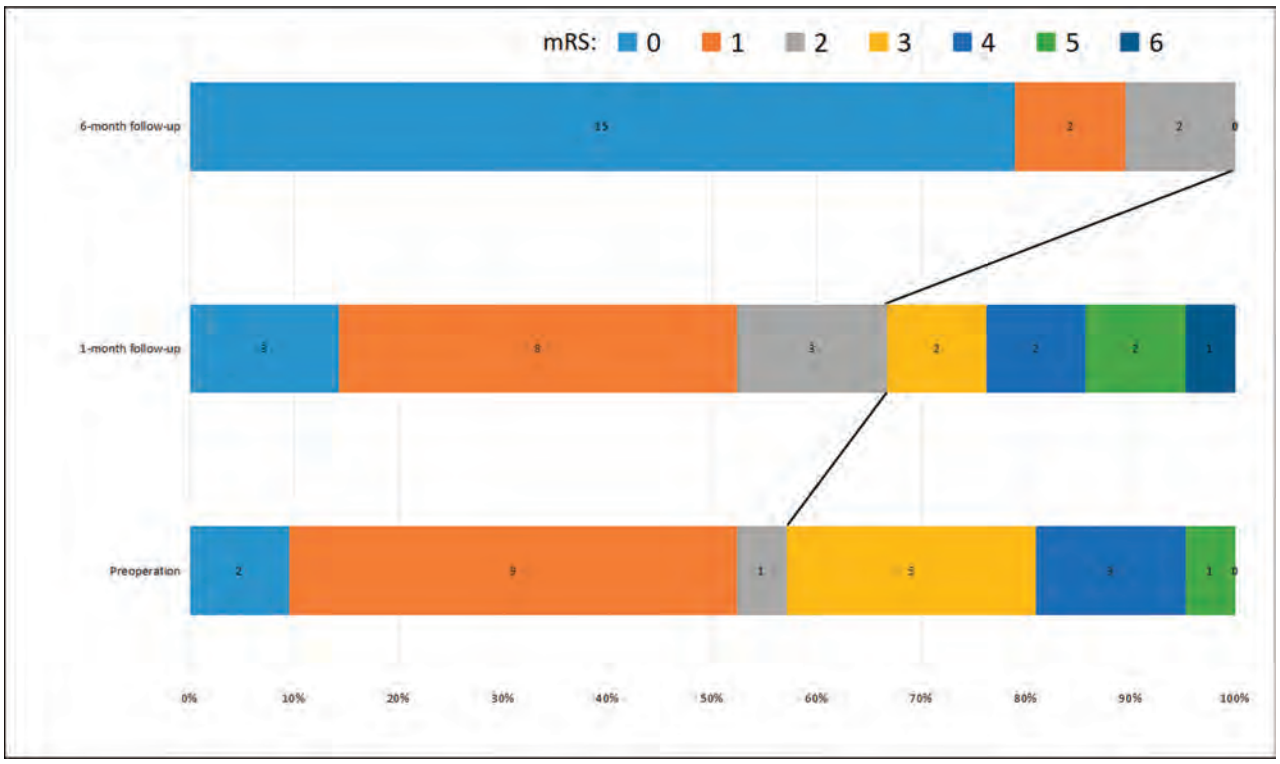

FIG 5. The good functional outcome (mRS $\leq$ 2) ratios improved from 57.1% (12/21) before the operation to 66.7% (14/21) at 1-month follow-up and 100% (19/19) at 6-month follow-up, respectively.

patients had good outcomes and 1 died due to severe intracranial infection after hemorrhage. This might be related to several factors: First, intraparenchymal hemorrhage often occurs in the same area as prior hemorrhage and is less likely to immediately damage healthy brain; second, the subarachnoid hemorrhage can be treated by drugs or ventriculostomy; and finally, the patients were relatively young in this study.

Limitations

Although the number of cases in this study was the second largest in all the publications currently available,[21] the sample size was still small. The patients were carefully selected and were selected for salvage procedures due to lack of good microsurgical, transarterial, and radiosurgical options, which may imply greater propensity for procedural risk than in other studies. Treatment strategy, patient factors, and doctors' experience are highly individualized and variable worldwide; thus, the findings of our study may not be consistent with other centers.

CONCLUSIONS

Transvenous embolization with high complete obliteration rates, improved functional outcomes, and acceptable morbidity and mortality rates can be performed in only carefully selected brain AVMs. However, more experience is necessary to discern the role of this technique in the management of ruptured AVMs, and it should not be considered a first-line treatment.

ACKNOWLEDGMENTS

The authors thank Yanyan He, Bin Xu, Xiaoyu Kang at Henan Provincial People's Hospital for data collection; Jingge Zhao at Henan Provincial People's Hospital for statistical analyses; Ajmal Zemmar and Juha Hernesniemi at Henan Provincial People's Hospital for their English editing assistance; and David F. Kallmes, Ramanathan Kadirvel, Daying Dai, and Kimberly Collins at the Mayo Clinic for their help in providing learning office and reference material.

REFERENCES

1. Solomon RA, Connolly EJ. **Arteriovenous malformations of the brain**. *N Engl J Med* 2017;376:1859–66 CrossRef Medline
2. Chen W, Choi EJ, McDougall CM, et al. **Brain arteriovenous malformation modeling, pathogenesis, and novel therapeutic targets.** *Transl Stroke Res* 2014;5:316–29 CrossRef Medline
3. Derdeyn CP, Zipfel GJ, Albuquerque FC, et al; American Heart Association Stroke Council. **Management of Brain Arteriovenous Malformations: a Scientific Statement for Healthcare Professionals from the American Heart Association/American Stroke Association.** *Stroke* 2017;48:e200–24 CrossRef Medline
4. Cenzato M, Boccardi E, Beghi E, et al. **European consensus conference on unruptured brain AVMs treatment (supported by EANS, ESMINT, EGKS, and SINCH).** *Acta Neurochir (Wien)* 2017;159:1059–64 CrossRef Medline
5. Elsenousi A, Aletich VA, Alaraj A. **Neurological outcomes and cure rates of embolization of brain arteriovenous malformations with**

n-butyl cyanoacrylate or Onyx: a meta-analysis. *J Neurointerv Surg* 2016;8:265–72 CrossRef Medline
6. Nguyen TN, Chin LS, Souza R, et al. **Transvenous embolization of a ruptured cerebral arteriovenous malformation with en-passage arterial supply: initial case report.** *J Neurointerv Surg* 2010;2:150–52 CrossRef Medline
7. Kessler I, Riva R, Ruggiero M, et al. **Successful transvenous embolization of brain arteriovenous malformations using Onyx in five consecutive patients.** *Neurosurgery* 2011;69:184–93; discussion 193 CrossRef Medline
8. Pereira VM, Marcos-Gonzalez A, Radovanovic I, et al. **Transvenous embolization of a ruptured deep cerebral arteriovenous malformation: a technical note.** *Interv Neuroradiol* 2013;19:27–34 CrossRef Medline
9. Consoli A, Renieri L, Nappini S, et al. **Endovascular treatment of deep hemorrhagic brain arteriovenous malformations with transvenous Onyx embolization.** *AJNR Am J Neuroradiol* 2013;34:1805–11 CrossRef Medline
10. Ahmed AZ. **Endovascular venous approach in the treatment of ruptured intra-cerebral arterio-venous malformation.** *The Egyptian Journal of Radiology and Nuclear Medicine* 2014;45:439–41 CrossRef
11. Trivelato FP, Manzato LB, Rezende MT, et al. **Transitory brain stem edema following successfully transvenous embolization of a posterior fossa arteriovenous malformation.** *Clin Neuroradiol* 2014; 24:151–53 CrossRef Medline
12. Choudhri O, Ivan ME, Lawton MT. **Transvenous approach to intracranial arteriovenous malformations: challenging the axioms of arteriovenous malformation therapy?** *Neurosurgery* 2015;77:644–52 CrossRef Medline
13. Renieri L, Limbucci N, Consoli A, et al. **Transvenous embolization: a report of 4 pediatric cases.** *J Neurosurg Pediatr* 2015;15:445–50 CrossRef Medline
14. Iosif C, Mendes GA, Saleme S, et al. **Endovascular transvenous cure for ruptured brain arteriovenous malformations in complex cases with high Spetzler-Martin grades.** *J Neurosurg* 2015;122:1229–38 CrossRef Medline
15. Lawton MT; UCSF Brain Arteriovenous Malformation Study Project. **Spetzler-Martin Grade III arteriovenous malformations: surgical results and a modification of the grading scale.** *Neurosurgery* 2003;52:740–49 CrossRef Medline
16. Pollock BE, Flickinger JC. **A proposed radiosurgery-based grading system for arteriovenous malformations.** *J Neurosurg* 2002;96:79–85 CrossRef Medline
17. Zhang G, Zhu S, Wu P, et al. **The transvenous pressure cooker technique: a treatment for brain arteriovenous malformations.** *Interv Neuroradiol* 2017;23:194–99 CrossRef Medline
18. He Y, Bai W, Li T, et al. **Curative transvenous embolization for ruptured brain arteriovenous malformations: a single-center experience from China.** *World Neurosurg* 2018;116:e421–28 CrossRef Medline
19. Chapot R, Stracke P, Velasco A, et al. **The pressure cooker technique for the treatment of brain AVMs.** *J Neuroradiol* 2014;41:87–91 CrossRef Medline
20. Jayaraman MV, Meyers PM, Derdeyn CP, et al. **Reporting standards for angiographic evaluation and endovascular treatment of cerebral arteriovenous malformations.** *J NeuroIntervent Surg* 2012;4:325–30 CrossRef Medline
21. Mendes G, Kalani M, Iosif C, et al. **Transvenous curative embolization of cerebral arteriovenous malformations: a prospective cohort study.** *Neurosurgery* 2018;83:957–64 CrossRef Medline
22. Mendes GA, Silveira EP, Saleme S, et al. **Balloon-assisted microcatheter navigation for AVM embolization: technical note.** *J Neurosurg* 2015;123:1120–24 CrossRef Medline
23. Wang MZ, Qiu HC, Wang S, et al. **A new technique for transvenous embolization of brain arteriovenous malformations in hybrid operation.** *Chin Med J (Engl)* 2018;131:2993–96 CrossRef Medline
24. Kulcsar Z, Machi P, Schaller K, et al. **Trans-venous embolization of a basal ganglia ruptured arteriovenous malformation with open surgical arterial control: a hybrid technique.** *J Neuroradiol* 2018;45:202–05 CrossRef Medline
25. Houdart E, Gobin YP, Casasco A, et al. **A proposed angiographic classification of intracranial arteriovenous fistulae and malformations.** *Neuroradiology* 1993;35:381–85 CrossRef Medline
26. Viana DC, de Castro-Afonso LH, Nakiri GS, et al. **Extending the indications for transvenous approach embolization for superficial brain arteriovenous malformations.** *J NeuroIntervent Surg* 2017; 9:1053–59 CrossRef Medline
27. Lv X, Song C, He H, et al. **Transvenous retrograde AVM embolization: indications, techniques, complications and outcomes.** *Interv Neuroradiol* 2017;23:504–09 CrossRef Medline
28. Stüer C, Ikeda T, Stoffel M, et al. **Evidence for a predominant intrinsic sympathetic control of cerebral blood flow alterations in an animal model of cerebral arteriovenous malformation.** *Transl Stroke Res* 2010;1:210–19 CrossRef Medline
29. Pan J, He H, Feng L, et al. **Angioarchitectural characteristics associated with complications of embolization in supratentorial brain arteriovenous malformation.** *AJNR Am J Neuroradiol* 2014;35:354–59 CrossRef Medline
30. Ma L, Huang Z, Chen XL, et al. **Periventricular location as a risk factor for hemorrhage and severe clinical presentation in pediatric patients with untreated brain arteriovenous malformations.** *AJNR Am J Neuroradiol* 2015;36:1550–57 CrossRef Medline
31. D'Aliberti G, Talamonti G, Piparo M, et al. **Venous flow rearrangement after treatment of cerebral arteriovenous malformations: a novel approach to evaluate the risks of treatment.** *World Neurosurg* 2014;82:160–69 CrossRef Medline
32. Baharvahdat H, Blanc R, Termechi R, et al. **Hemorrhagic complications after endovascular treatment of cerebral arteriovenous malformations.** *AJNR Am J Neuroradiol* 2014;35:978–83 CrossRef Medline

Application of High-Resolution C-Arm CT Combined with Streak Metal Artifact Removal Technology for the Stent-Assisted Embolization of Intracranial Aneurysms

T.-F. Li, J. Ma, X.-W. Han, P.-J. Fu, R.-N. Niu, W.-Z. Luo, and J.-Z. Ren

ABSTRACT

BACKGROUND AND PURPOSE: Metal artifacts from coils and stents limit the level of detail in C-arm CT images of stent attachment and coiling attenuation in the aneurysm neck. We evaluated the utility of high-resolution C-arm CT combined with streak metal artifact removal technology for stent-assisted embolization of intracranial aneurysms.

MATERIALS AND METHODS: From October 2017 to July 2018, the First Affiliated Hospital of Zhengzhou University treated 107 patients with intracranial aneurysms (118 aneurysms in total) with stent-assisted embolization. Conventional C-arm CT and high-resolution C-arm CT scanning of the stented area were performed during and after treatment. 3D images were reconstructed with and without streak metal artifact removal techniques. Subsequently, the image quality was compared. The reconstructed images indicated the stent deployment degree and packing density. Follow-up assessments included clinical and angiographic outcomes and complications.

RESULTS: In total, 118 aneurysms were successfully embolized using 118 stents. Image quality was significantly higher ($P < .05$) with high-resolution C-arm CT combined with streak metal artifact removal reconstruction. Streak metal artifact removal reconstruction and 2D angiography at working angles showed incomplete deployment of 6 stents and incomplete aneurysm embolization of 15 patients, which were subsequently resolved. One case of hemorrhage was noted postoperatively. Follow-up of 93 patients at 6–13 months indicated 3 cases of aneurysm recurrence.

CONCLUSIONS: High-resolution C-arm CT combined with the streak metal artifact removal technique effectively reduced metal artifacts from stents and coils during aneurysm embolization. This method can help physicians determine the extent of stent deployment and the packing density of coils and thus potentially reduce complications and aneurysm recurrence.

ABBREVIATIONS: ISAT = International Subarachnoid Aneurysm Trial; MAR = metal artifact removal; MRRC = modified Raymond-Roy occlusion classification; SMART = streak metal artifact reduction technology

Stent-assisted embolization is an important treatment method for wide-neck intracranial aneurysms, and its use is becoming more widespread.[1-3] The successful embolization of intracranial aneurysms depends on the surgeon's understanding of intracranial blood vessel anatomy and the relationship among target blood vessels, interventional devices (stents and coils), and the surrounding tissues. The introduction of C-arm CT has helped resolve several problems associated with invisible structures during interventions. DynaCT Micro (Siemens, Erlangen, Germany) is a new generation of high-resolution C-arm CT developed by Siemens in 2016. Compared with traditional C-arm CT (DynaCT; Siemens), its local spatial resolution is higher. Moreover, in combination with the metal artifact removal (MAR) technique, this new technique improves the visibility of stents.[4] In October 2016, Zhengzhou University First Affiliated Hospital introduced China's first flat panel detector DSA system (Artis Zeego; Siemens) with DynaCT Micro function and used it to treat patients with aneurysms. Image reconstruction in those cases used the latest generation of MAR technology (streak metal artifact reduction technology [SMART]; Siemens). In an in vitro aneurysm model, we observed that this new technique significantly improved the postprocessing quality of images of stents and coils, such as

Received April 23, 2019; accepted after revision July 16.

From the Departments of Interventional Radiology (T.-F.L., J.M., X.-W.H., P.-J.F., J.-Z.R.), Neurology (R.-N.N.), and Neurosurgery (W.-Z.L.), The First Affiliated Hospital of Zhengzhou University, Zhengzhou, China; and Interventional Institute of Zhengzhou University (T.-F.L., J.M., X.-W.H., P.-J.F., J.-Z.R), Zhengzhou, China.

T.-F. Li and J. Ma contributed equally to this work.

This work was supported by a grant from the National Natural Science Foundation of China (No. 81801806).

Please address correspondence to X.-W. Han, MD, No. 1 Jianshe Road, Zhengzhou City, Henan Province, China; e-mail: xinwei_han@163.com

http://dx.doi.org/10.3174/ajnr.A6190

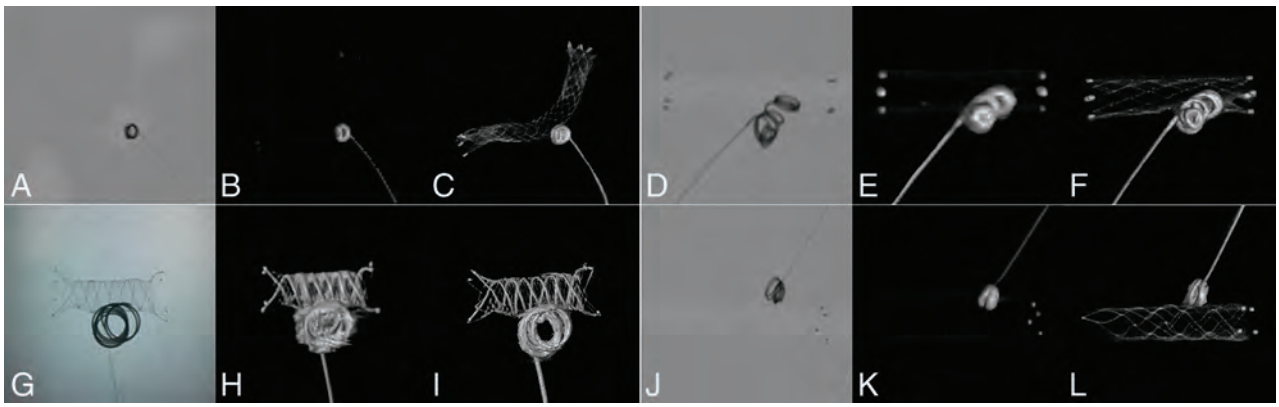

FIG 1. Different types of stents and coils in fluoroscopy, DynaCT, and DynaCT Micro combined with SMART image. *A–C*, Enterprise stent. *D–F*, Neuroform EZ stent. *G–I*, LVIS stent. *J–L*, Solitarie AB stent.

stent skeleton development and wire and coil metal artifact reduction (Fig 1). However, research on the use of this technique in aneurysms remains scarce. In the present study, we analyzed the reconstruction images of conventional C-arm CT (DynaCT) and high-resolution C-arm CT (DynaCT Micro) combined with SMART following the stent-assisted embolization of 118 intracranial aneurysms in 107 patients from October 2017 to July 2018 in the eastern district of our hospital. We assessed image quality, imaging characteristics, utility for guiding intravascular treatment, and the clinical value of high-resolution C-arm CT (DynaCT Micro) combined with SMART for the stent-assisted embolization of intracranial aneurysms.

MATERIALS AND METHODS

Ethics Statement

Written informed consent was obtained from each patient for the publication of this article and any accompanying images. This study was approved by the Ethics Committee of Zhengzhou University. The procedures followed were in accordance with the Helsinki Declaration of 1975, as revised in 1983.

Patient Selection

From October 2017 to July 2018, one hundred seven patients who were treated with stent-assisted embolization and met the following eligibility criteria were recruited for this study: 1) use of simple intracranial aneurysm stent-assisted (Neuroform EZ, Stryker Neurovascular, Kalamazoo, Michigan; Low Profile Visualized Intraluminal Support [LVIS], MicroVention, Tustin, California; Enterprise, Codman & Shurtleff, Raynham, Massachusetts; Solitarie AB, Covidien, Irvine, California) coil embolization; 2) no use of a liquid embolic agent (Onyx; Covidien) or other embolic material; 3) no indications for surgery or refusal to undergo surgery; and 4) no use of a flow diverter. Moreover, the exclusion criteria were as follows: 1) use of only coil- or balloon-assisted embolization; 2) use of embolic material other than metal coils, such as Onyx or Woven EndoBridge (WEB; Sequent Medical, Aliso Viejo, California); 3) use of surgical aneurysm clipping alone or in combination with embolization; 4) use of a flow diverter; and 5) refusal of study participation.

Table 1: Aneurysm measurements

	Mean (mm)
Dome width	5.6 ± 3.7
Dome-to-neck ratio	1.2 ± 0.7
Proximal parent artery diameter	3.6 ± 1.6
Distal parent artery diameter	3.4 ± 1.5

Among the 107 patients in the present study, 63 were men and 44 were women, and the mean age was 52.7 ± 12.4 years. Moreover, 68 patients (62 patients with 1 aneurysm and 6 patients with 2 aneurysms) had no symptoms and were found to have aneurysms during a routine health checkup. The other 39 patients developed headaches, nausea, and vomiting. CT or CSF examination or both were used for the diagnosis of SAH. CTA and/or MRA showed 34 cases with single aneurysms and 5 cases with 2 aneurysms. The clinical severity of subarachnoid hemorrhage was assessed using the Hunt and Hess scale. Hunt and Hess grade 1 was detected in 9 cases, grade 2 was detected in 24 cases, grade 3 was detected in 4 cases, and grade 4 was detected in 2 cases.

Aneurysms

Of the 118 aneurysms, 87 were detected in the anterior circulation, including 5 in the internal carotid artery cavernous sinus segment, 8 in the internal carotid artery clinoid segment, 19 in the ocular artery segments, 28 in the posterior communicating segments, 3 in the anterior cerebral artery A1 segments, 17 in the anterior communicating segments, and 7 in the middle cerebral artery bifurcation. Moreover, 31 aneurysms were detected in the posterior circulation, including 17 vertebral artery aneurysms, 10 basal artery stem aneurysms, and 4 basal artery top aneurysms. The spatial relationship between the aneurysms and the parent artery and its branches was confirmed via DSA and its 3D reconstruction function (Table 1).

Procedures, DynaCT Micro Scan, and Image Reconstruction

The procedures for perioperative management and stent-assisted embolization were similar to those described in previous reports.[1-3,5,6] Immediately after stent-assisted embolization,

conventional DynaCT was performed to rule out intraprocedural bleeding, and DynaCT Micro was performed to confirm stent deployment and apposition. The high-resolution DynaCT parameters were as follows: 20-second DynaCT Micro (x-ray voltage: 109 kV; electric current: 460 mA); FOV, 22 cm; maximum rotation range, 200°; rotation time, 20 seconds; and number of frames, 496. After completing data collection, the image data were automatically transferred to syngo X Workplace (4D, Siemens), and 3D reconstruction with or without SMART was performed respectively.

Evaluating Image Quality of DynaCT and DynaCT Micro Combined with SMART

The image was independently evaluated by 2 experienced neurointerventionists (J.M., with 12 years of experience; T.-F.L., with 10 years of experience). The evaluation criteria were as follows—a platinum mark or double helical strands: invisible or fuzzy (0 points) or clear (1 point); nickel-titanium wire: invisible or fuzzy (0 points) or clear (1 point); coil metal artifacts: extensive or moderate (0 points) or mild or no artifacts (1 point); and nickel-titanium wire artifacts: extensive or moderate (0 points) or mild or no artifacts (1 point).

Postoperative Evaluation and Follow-Up

The degree of aneurysmal occlusion was evaluated using DSA immediately after the procedure and at the 3-month follow-up. Angiographic examinations were performed by 2 senior professional physicians (J.M., with 12 years of experience; X.-W.H., with 35 years of experience), and the findings were subsequently scored using the modified Raymond-Roy occlusion classification (MRRC) system.[7] Complete occlusion was defined as the absence of contrast agent within the aneurysm intracavity; neck remnant was defined as the presence of contrast agent in the aneurysm neck; and aneurysm remnant was defined as the presence of contrast agent in a part of the aneurysm. Clinical outcomes were assessed at discharge and at 6 months using the mRS. Any death within 30 days after endovascular treatment was designated as a treatment-related death.

Statistical Analysis

All statistical analyses were performed using SPSS software, Version 19.0 (IBM, Armonk, New York). The measurement data are presented as mean ± SD. Moreover, the χ^2 or Fisher exact test was used for image-quality evaluation, and $P < .05$ was used to indicate statistical significance. The consistency between the 2 doctors in measuring the values of each indicator was tested using the κ test, and $\kappa \geq 0.75$ was considered good.

RESULTS

Technical and Anatomic Postoperative Results

A total of 118 intracranial stents were successfully used for the embolization of 118 aneurysms. The choice of stent type and size primarily depended on aneurysm morphology, as well as the diameter and morphology of the parent artery. Among the stents used, 35 were Neuroform EZ stents, including four 2.5 × 15 mm stents, four 2.5 × 20 mm stents, four 3.0 × 15 mm stents, six 3.0 × 20 mm stents, one 3.5 × 20 mm stent, three 3.5 × 30 mm stents, eight 4.0 × 20 mm stents, and five 4.5 × 20 mm stents; 72 were LVIS stents, including sixteen 3.5 × 15 mm stents, thirty 3.5 × 20 mm stents, six 4.5 × 15 mm stents, ten 4.5 × 20 mm stents, seven 4.5 × 30 mm stents, and three 5.5 × 25 mm stents; and 11 were Enterprise stents, including nine 4.5 × 22 mm stents and two 4.5 × 28 mm stents.

On the basis of the findings of the high-resolution DynaCT Micro scan in the stent area in combination with multiple 2D angiography at selected working angles, 6 stents (5 LVIS stents, 1 Enterprise stent) exhibited incomplete deployment. After microguidewire looping dilation and balloon dilation, the stent apposition improved. In 15 patients, the coil embolization in the aneurysm neck was not dense (9 with Neuroform EZ, 4 with LVIS, and 2 with Enterprise stents). After adjusting the microcatheter head position, embolization was continued until dense packing was observed. In 1 case, during the embolization of an unruptured aneurysm in the C4 section, the microcatheter head detached from the aneurysm cavity, and re-superselective catheterization was not successful due to the small size of the residual portion of the aneurysm and the inability of the guidewire to pass through the LVIS stent mesh. Immediately after surgery, MRRC embolization grading was performed, and 97 (82.2%) were categorized as class I, seventeen (14.4%) were categorized as class II, and 4 (3.4%) were categorized as class III (Figs 2*A*–*C* and 3*A*–*C*).

Evaluating Image Quality of DynaCT Micro Combined with SMART

There was good consistency in the evaluation results between the 2 physicians (κ value = 0.85, $P < .05$). A comparison of normal DynaCT reconstruction and DynaCT Micro reconstruction indicated that DynaCT Micro combined with SMART more clearly displayed the stent nickel-titanium wire and more effectively reduced coil metal artifacts. Moreover, the image quality was significantly improved ($P < .05$; Tables 2–5, Figs 2*D*–*F* and 3*D*–*F*).

Follow-Up

A total of 107 patients were followed up for 9.7 ± 2.4 months. Among these, 93 patients (101 aneurysms) were followed via DSA for 6–13 months. The MRRC results were as follows: 90 (89.1%) aneurysms as class I, nine (8.9%) aneurysms as class II, and II (2.0%) aneurysms as class III. In 3 cases with MRRC class I (2 cases with a Neuroform EZ and 1 case with an Enterprise stent), the coils were compressed, and the necks of aneurysms recurred (MRRC class II). Two of these cases underwent repeat embolization, and the other case underwent close observation. The mRS score during follow-up was 0 in 97 cases, 1 in 4 cases, 2 in 3 cases, 3 in 2 cases, and 4 in 1 case.

Perioperative Complications

A total of 5 patients had intraoperative complications, including various degrees of cerebral vasospasm (follow-up mRS score: 0 in 3 cases and 1 in 2 cases). No cases of intraoperative aneurysm rupture or stent thrombosis were noted. During the follow-up period, 2 patients developed subacute hydrocephalus (mRS scores of 2 and 3, respectively) and 2 patients developed a new cerebral infarction (caused by nonaneurysmal artery stenosis). None of these new conditions were related to the treatment of aneurysms.

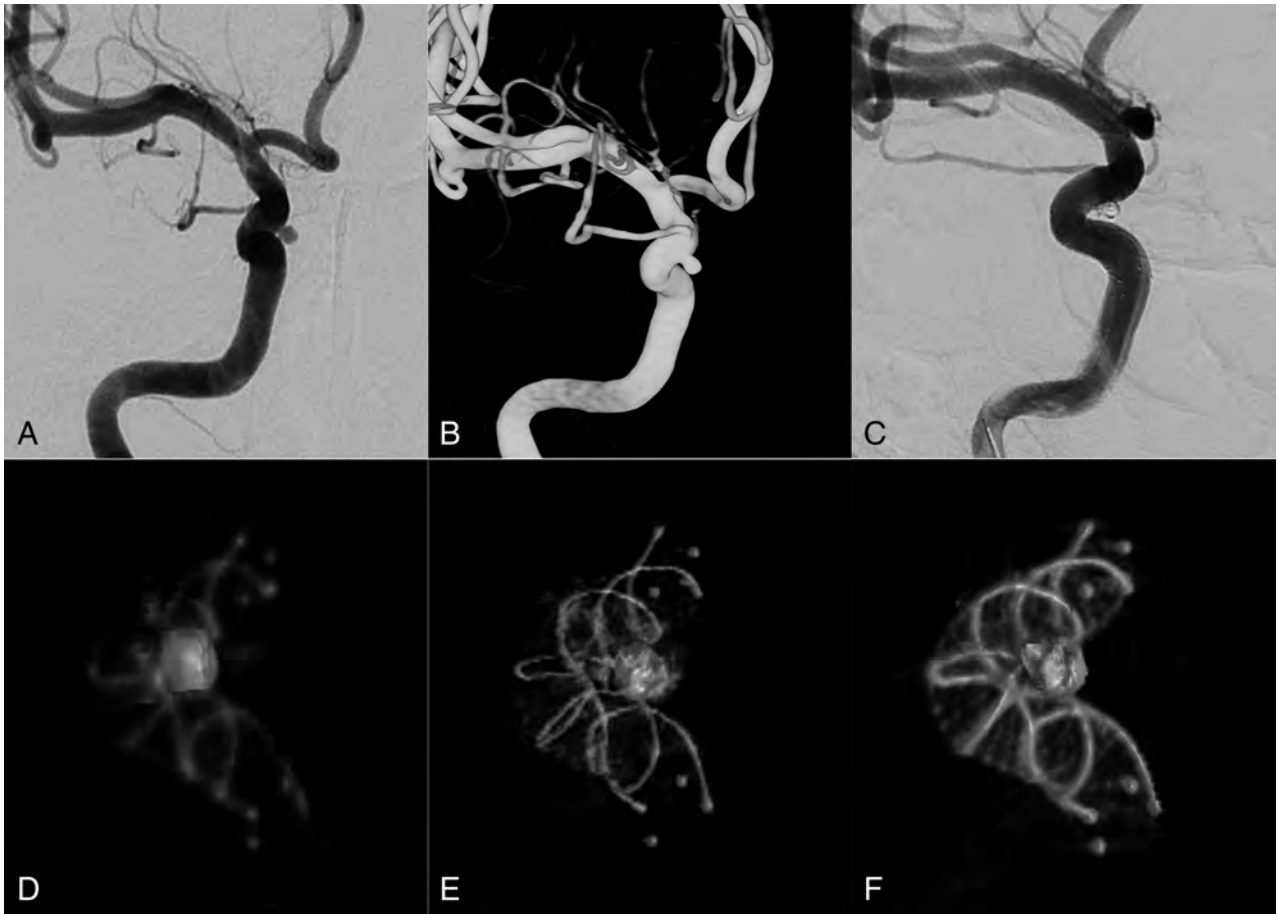

FIG 2. LVIS stent-assisted embolization of an unruptured aneurysm in the right ocular artery segments. *A* and *B*, DSA and 3D images show a wide-neck aneurysm in the right ocular artery segments (1.6 × 2.1 mm). *C*, LVIS stent-assisted complete embolization (4.5 × 20 mm) of an aneurysm classified as Raymond embolism class I. *D*, Normal DynaCT reconstructed images immediately after intervention show that the double helical marker wires of the stent are well developed, the nickel-titanium wires are poorly developed, and the coil metal artifacts are large. *E*, Immediate postoperative DynaCT Micro reconstructed images show that the double helical marker of the stent is well developed, but the nickel-titanium wire is still poorly developed. However, the appearance of metal wire and coil metal artifacts is significantly improved relative to normal DynaCT. *F*, Immediately after the operation, DynaCT Micro combined with SMART-reconstructed images shows that the double helix marker wires and nickel-titanium wire are well developed, the metal artifacts of the nickel-titanium wire and coils are significantly reduced, and the overall image quality is significantly improved.

DISCUSSION

Endovascular embolization has become an important method for the treatment of intracranial aneurysms. The International Subarachnoid Aneurysm Trial (ISAT) has confirmed the safety and effectiveness of endovascular embolization for the treatment of intracranial aneurysms.[8] However, the use of coil embolization alone for intracranial wide-neck aneurysms (aneurysm neck >4 mm or aneurysm neck/aneurysm body >1:2) remains technically challenging. The use of stents could not only assist the embolization but also promote the healing of the aneurysm neck. However, the diameter of the nickel-titanium wire in the currently available aneurysm stents is close to the detection limit of radiographs (including 0.0024 inches for the LVIS stent and 0.01 inches for the Neuroform EZ stent). Although platinum marks or double helixes may be observed in some cases during intervention, local distortion or incomplete stent expansion may be difficult to determine in other cases. Moreover, some aneurysms with a serious neck embolism may be overlooked due to a limited angiographic angle or the presence of coil metal artifacts.[9,10] This is an important potential risk factor for stent thrombosis, penetrating vascular occlusion, and prolonged stent re-endothelialization time.[11] Moreover, due to the impact of metal artifacts of the coil and the stent wire, conventional C-arm CT devices, such as DynaCT, VasoCT (Philips Healthcare, Best, the Netherlands), or Innova CT (GE Healthcare, Milwaukee, Wisconsin), may not be able to fully clarify the relationship between the stent and the aneurysm neck, as well as the relationship between the stent and the embolized coils. This issue may lead to the misjudgment of the degree of packing density of the aneurysm neck by the surgeon and could lead to postoperative aneurysm recurrence.[4,12]

Compared with conventional C-arm CT, the high-resolution C-arm CT (DynaCT Micro) used the nonbinning technique rather than the regular 2 × 2 pixel binning, adapted the acquisition parameters to include only a small FOV for small object visualization, and optimized the exposure parameters and image-processing algorithm to obtain enhanced image quality. The DynaCT Micro enabled the visualization of local lesions/devices

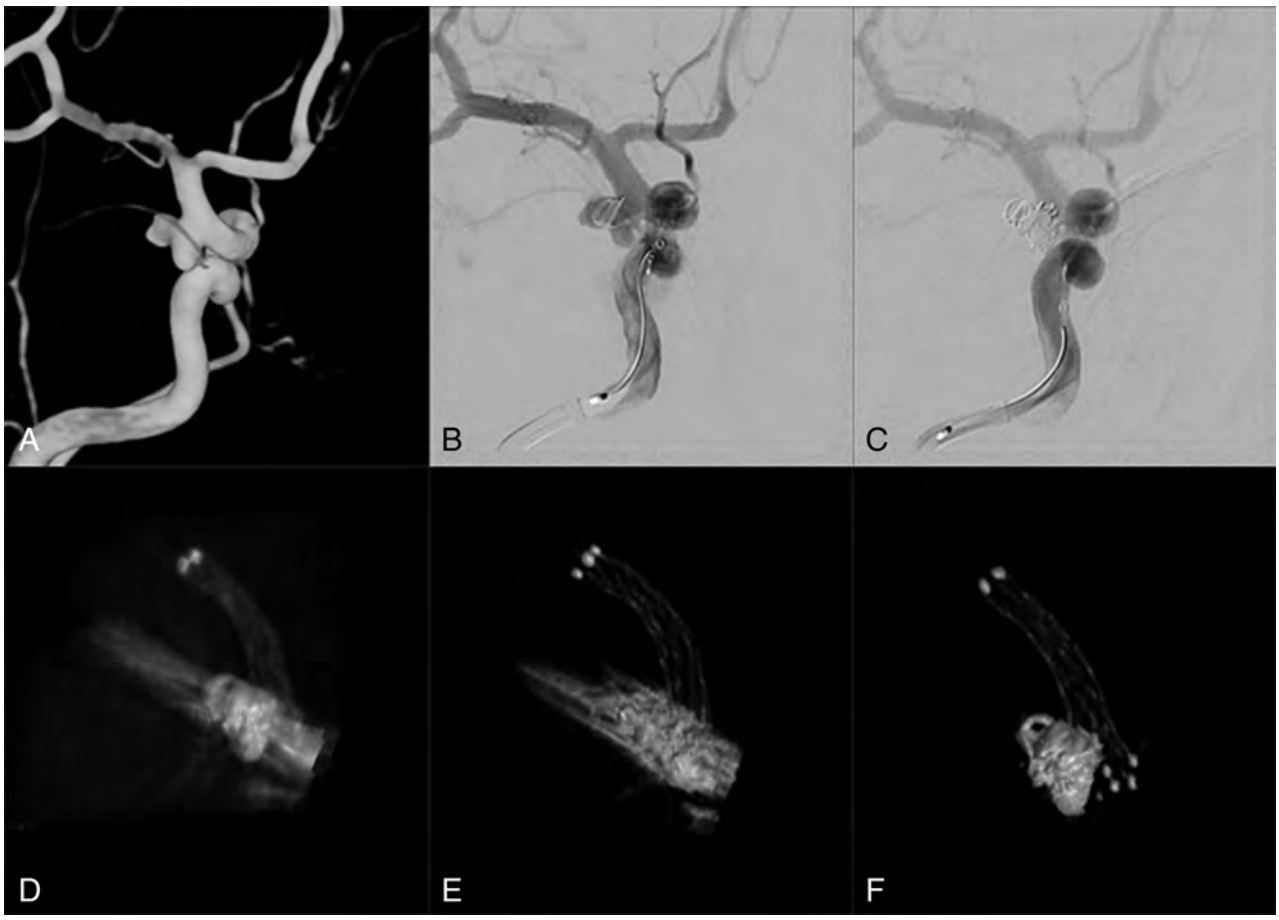

FIG 3. Neuroform EZ stent-assisted embolization of a ruptured aneurysm in the right posterior communicating artery. *A* and *B*, DSA and 3D reconstructed images show a right posterior communicating wide-neck aneurysm with an irregular petal shape (tumor neck: 3.4 mm; 2 daughter sacs of 2.8 × 3.6 and 2.4 × 3.1 mm). *C*, Complete aneurysm embolization with the Neuroform EZ stent (3.5 × 30 mm) while maintaining artery patency. *D*, Normal DynaCT reconstructed images immediately after the operation show that the stent mark is clearly developed, the stent wire is poorly developed, and the coil metal artifacts are large. *E*, DynaCT Micro reconstructed images immediately after the operation show that the mark at the 2 ends of the stent is well developed, the stent wire is significantly well developed (relative to normal DynaCT), and the coil metal artifacts are still large; *F*, Reconstructed images of DynaCT Micro combined with SMART immediately after the operation show that the marks of the stent and the nickel-titanium wire are well developed, the metal artifacts of the stent wire and coils are significantly reduced, and the overall image quality is significantly improved.

Table 2: Evaluation of images obtained with DynaCT, DynaCT Micro, and DynaCT Micro combined with SMART (Neuroform EZ stent, *n* = 35)

Methods	Platinum Marks		Nickel-Titanium Wire		Coil Metal Artifacts		Nickel-Titanium Wire Artifacts	
	0	1	0	1	0	1	0	1
DynaCT	0	35	35	0	35	0	35	0
DynaCT Micro	0	35	32	3	27	8	28	7
DynaCT Micro combined with SMART	0	35	8	27	7	28	6	29

with enhanced spatial resolution, with and without the use of diluted contrast agents. MAR techniques are widely used in spiral CT and MR imaging to reduce artifacts generated by metal implants and improve the overall image quality. However, their application in C-arm CT is still in its infancy, and only a few reports are found in the literature. Van der Bom et al[12] reported 25 cases of stent-assisted coil embolization using high-resolution VasoCT combined with MAR. They found that although the technology significantly improved the image quality, it still could not eliminate the metal artifacts produced by the embolism coils. In the aforementioned study, the MAR algorithm was based on the method proposed by Prell et al.[13] Thus, the matrix dimension (512^3 versus 256^3) obtained in volume reconstruction was significantly improved, and higher image resolution[4] was obtained. Innovations and combinations of SMART and high-resolution C-arm CT have theoretically contributed to the improvement of local image quality; however, at present, only a few reports have cited the clinical applications of high-resolution C-arm CT

Table 3: Evaluation of images obtained with DynaCT, DynaCT Micro, and DynaCT Micro combined with SMART (LVIS stent, *n* = 72)

Methods	Double Helix Marker Wires		Nickel-Titanium Wire		Coil Metal Artifacts		Nickel-Titanium Wire Artifacts	
	0	1	0	1	0	1	0	1
DynaCT	0	72	72	0	72	0	72	0
DynaCT Micro	0	72	66	6	65	7	65	7
DynaCT Micro combined with SMART	0	72	21	51	26	46	29	43

Table 4: Evaluation of images obtained with DynaCT, DynaCT Micro, and DynaCT Micro combined with SMART (Enterprise stent, *n* = 11)

Methods	Platinum Marks		Nickel-Titanium Wire		Coil Metal Artifacts		Nickel-Titanium Wire Artifacts	
	0	1	0	1	0	1	0	1
DynaCT	0	11	11	0	11	0	11	0
DynaCT Micro	0	11	10	1	8	3	9	2
DynaCT Micro combined with SMART	0	11	3	8	4	7	3	8

Table 5: Comparison of the image quality in different groups (*P* values)

Comparison Groups	Neuroform EZ Stent			LVIS Stent			Enterprise Stent		
	Nickel-Titanium Wire	Coil Metal Artifacts	Nickel-Titanium Wire Artifacts	Nickel-Titanium Wire	Coil Metal Artifacts	Nickel-Titanium Wire Artifacts	Nickel-Titanium Wire	Coil Metal Artifacts	Nickel-Titanium Wire Artifacts
DynaCT vs DynaCT Micro	.239	.050	.050	.028	.013	.013	1	.214	.476
DynaCT vs DynaCT Micro combined with SMART	<.001	<.001	<.001	<.001	<.001	<.001	.001	<.004	.001
DynaCT Micro vs DynaCT Micro combined with SMART	<.001	<.001	<.001	<.001	<.001	<.001	.008	.199	.030

combined with MARs.[4,12] In the present study, we observed 3 different types of stents (Neuroform EZ, LVIS, and Enterprise) using 3 different C-arm CT techniques—ie, conventional C-arm CT, high-resolution C-arm CT, and high-resolution C-arm CT with SMART. High-resolution C-arm CT combined with SMART had the highest image quality among all 3 imaging methods.

Unlike previously reported studies that used high-resolution C-arm CT with diluted contrast agents, our study focused on high-resolution C-arm CT without the use of any contrast agent. For stent-assisted coiling, the observation of stent deployment, packing density at the aneurysm neck, and the coil-stent relationship is more crucial to the surgeon than stent/vessel wall apposition. Nonenhanced high-resolution C-arm CT is a more convenient and quicker method for surgeons to confirm stent/coil deployment, without the need for a high-pressure injection or other complex procedures for diluting the contrast agent. For our future studies on flow-diverter visualization, enhanced C-arm CT will be used for the direct evaluation of the flow diverter/vessel wall relationship.

In the present study, based on the results of reconstruction with high-resolution DynaCT combined with SMART and multiple 2D angiography at selected working angles, we confirmed that 6 stents had mild incomplete expansion and that the wall condition had improved after microguidewire looping dilation and balloon dilation. On the basis the results of DynaCT Micro combined with 2D angiography at working angles, we found that the embolization of the aneurysm neck in 15 patients was unsatisfactory; therefore, we adjusted the microcatheter head to continue coil embolization and achieve the required density in the aneurysm neck. In these patients, due to the influence of vascular angles as well as coil and stent metal artifacts, it was difficult for conventional DynaCT and angiography to directly determine whether the coils in the aneurysm neck were dense, whether the coils protruded out of the aneurysm cavity or protruded into the stent, and whether the stent was completely expanded at the neck of the aneurysm. Caroff et al[14] used VasoCT to observe the stent-assisted embolization of intracranial aneurysms and reported that the use of high-resolution flat panel CT could reduce the incidence of thromboembolic events. This finding was supported by the fact that no serious complications, such as acute thrombosis or ruptured aneurysm, were observed in the present study. However, the results of DSA immediately after the operation and during the follow-up period indicated a greater proportion of patients with a Raymond I classification than previously reported (82.2% versus 36.4%–75.6%; 89.1% versus 81.8%–88%).[15-17]

Although there are differences in the inclusion criteria among the studies as well as the technical proficiency of the surgeons involved at the different centers, we clearly found that DynaCT Micro combined with SMART reconstruction could help

surgeons determine whether the stent has completely expanded and attached to the vascular wall and whether embolization of the aneurysm neck is satisfactory. Theoretically, this would improve the effect of stent-assisted aneurysm embolization and reduce the incidence of complications.

CONCLUSIONS

DynaCT Micro combined with SMART could improve the visualization of stent deployment and coil packing at the aneurysm neck in the stent-assisted embolization of intracranial aneurysms. This novel imaging technique could potentially reduce the incidence of postoperative complications and the recurrence of aneurysms. However, this is a single-center study, and the sample size is small; hence, our findings have certain limitations. A long-term study with a large sample size, as well as a multicenter, double-blind controlled study will be needed to confirm the reliability and long-term efficacy of this method.

REFERENCES

1. Santillan A, Boddu S, Schwarz J, et al. **LVIS Jr. stent for treatment of intracranial aneurysms with parent vessel diameter of 2.5 mm or less.** *Interv Neuroradiol* 2018;24:246–53 CrossRef Medline
2. Iosif C, Piotin M, Saleme S, et al. **Safety and effectiveness of the Low Profile Visualized Intraluminal Support (LVIS and LVIS Jr) devices in the endovascular treatment of intracranial aneurysms: results of the TRAIL multicenter observational study.** *J NeuroIntervent Surg* 2018;10:675–81 CrossRef Medline
3. Li TF, Shui SF, Han XW, et al. **The use of Solitaire AB stents in coil embolization of wide-necked cerebral aneurysms.** *PLoS One* 2015;10:e0139714 CrossRef Medline
4. Yuki I, Kambayashi Y, Ikemura A, et al. **High-resolution C-arm CT and metal artifact reduction software: a novel imaging modality for analyzing aneurysms treated with stent-assisted coil embolization.** *AJNR Am J Neuroradiol* 2016;37:317–23 CrossRef Medline
5. Ulfert C, Pham M, Sonnberger M, et al. **The Neuroform Atlas stent to assist coil embolization of intracranial aneurysms: a multicenter experience.** *J NeuroIntervent Surg* 2018;10:1192–96 CrossRef Medline
6. Ge H, Lv X, Yang X, et al. **LVIS Stent versus Enterprise stent for the treatment of unruptured intracranial aneurysms.** *World Neurosurg* 2016;91:365–70 CrossRef Medline
7. Roy D, Milot G, Raymond J. **Endovascular treatment of unruptured aneurysms.** *J Stroke* 2001;32:1998–2004 CrossRef Medline
8. Molyneux A, Kerr R, International Subarachnoid Aneurysm Trial (ISAT) Collaborative Group, et al. **International Subarachnoid Aneurysm Trial (ISAT) of neurosurgical clipping versus endovascular coiling in 2143 patients with ruptured intracranial aneurysms: a randomized trial.** *J Stroke Cerebrovasc Dis* 2002; 11:304–14 CrossRef Medline
9. Struffert T, Lang S, Adamek E, et al. **Angiographic C-arm CT visualization of the Woven EndoBridge cerebral aneurysm embolization device (WEB): first experience in an animal aneurysm model.** *Clin Neuroradiol* 2014;24:43–49 CrossRef Medline
10. Pfaff J, Struffert T, Gölitz P, et al. **Angiographic CT for intraprocedural monitoring of complex neuroendovascular procedures.** *AJNR Am J Neuroradiol* 2013;34:E77–80 CrossRef Medline
11. Foin N, Gutiérrez-Chico JL, Nakatani S, et al. **Incomplete stent apposition causes high shear flow disturbances and delay in neointimal coverage as a function of strut to wall detachment distance: implications for the management of incomplete stent apposition.** *Circ Cardiovasc Interv* 2014;7:180–89 CrossRef Medline
12. van der Bom IM, Hou SY, Puri AS, et al. **Reduction of coil mass artifacts in high-resolution flat detector conebeam CT of cerebral stent-assisted coiling.** *AJNR Am J Neuroradiol* 2013;34:2163–70 CrossRef Medline
13. Prell D, Kalender WA, Kyriakou Y. **Development, implementation and evaluation of a dedicated metal artefact reduction method for interventional flat-detector CT.** *Br J Radiol* 2010;83:1052–62 CrossRef Medline
14. Caroff J, Mihalea C, Neki H, et al. **Role of C-arm VasoCT in the use of endovascular WEB flow disruption in intracranial aneurysm treatment.** *AJNR Am J Neuroradiol* 2014;35:1353–57 CrossRef Medline
15. Wang CC, Li W, Feng ZZ, et al. **Preliminary experience with stent-assisted coiling of aneurysms arising from small (<2.5 mm) cerebral vessels using the Low-Profile Visualized Intraluminal Support Device.** *AJNR Am J Neuroradiol* 2017; 38:1163–68 CrossRef Medline
16. Wang CC, Fang YB, Zhang P, et al. **Reconstructive endovascular treatment of vertebral artery dissecting aneurysms with the Low-Profile Visualized Intraluminal Support (LVIS) device.** *PLoS One* 2017;12:e0180079 CrossRef Medline
17. Qin F, Li Z, Fang X, et al. **Therapeutic effect of Enterprise stent-assisted embolization for very small ruptured intracranial aneurysms.** *Medicine (Baltimore)* 2017;96:e7832 CrossRef Medline

A Multicenter Pilot Study on the Clinical Utility of Computational Modeling for Flow-Diverter Treatment Planning

B.W. Chong, B.R. Bendok, C. Krishna, M. Sattur, B.L. Brown, R.G. Tawk, D.A. Miller, L. Rangel-Castilla, H. Babiker, D.H. Frakes, A. Theiler, H. Cloft, D. Kallmes, and G. Lanzino

ABSTRACT

BACKGROUND AND PURPOSE: Selection of the correct flow-diverter size is critical for cerebral aneurysm treatment success, but it remains challenging due to the interplay of device size, anatomy, and deployment. Current convention does not address these challenges well. The goals of this pilot study were to determine whether computational modeling improves flow-diverter sizing over current convention and to validate simulated deployments.

MATERIALS AND METHODS: Seven experienced neurosurgeons and interventional neuroradiologists used computational modeling to prospectively plan 19 clinical interventions. In each patient case, physicians simulated 2–4 flow-diverter sizes that were under consideration based on preprocedural imaging. In addition, physicians identified a preferred device size using the current convention. A questionnaire on the impact of computational modeling on the procedure was completed immediately after treatment. Rotational angiography image data were acquired after treatment and compared with flow-diverter simulations to validate the output of the software platform.

RESULTS: According to questionnaire responses, physicians found the simulations useful for treatment planning, and they increased their confidence in device selection in 94.7% of cases. After viewing the simulations results, physicians selected a device size that was different from the original conventionally planned device size in 63.2% of cases. The average absolute difference between clinical and simulated flow-diverter lengths was 2.1 mm. In 57% of cases, average simulated flow-diverter diameters were within the measurement uncertainty of clinical flow-diverter diameters.

CONCLUSIONS: Physicians found computational modeling to be an impactful and useful tool for flow-diverter treatment planning. Validation results showed good agreement between simulated and clinical flow-diverter diameters and lengths.

ABBREVIATION: FD = flow diverter

Flow diverters (FDs) are being used with increasing frequency for the treatment of cerebral aneurysms. The immediate goal of FD treatment is to promote hemodynamic stasis and thrombus formation within the aneurysmal sac via flow diversion. Several studies have shown impressively effective use of FD devices in treating small-to-large aneurysms.[1-3] Recently, the FDA also approved the expanded indication for FD products for a much wider range of aneurysm sizes and locations, paving the way for additional FD entries into the market.[4] Nevertheless, selection of the correct FD size remains challenging and is an important consideration in the context of treatment success. Oversizing FDs can lead to in-stent stenosis or poor device expansion,[5,6] while undersizing can lead to device migration, prolapse into the aneurysm, and/or poor vessel coverage.[7,8] Deploying FDs in highly curved vessels can also present a number of technical challenges.[9]

The conventional approach to sizing FDs begins with measuring vessel diameters in images at the desired proximal and distal landing points. Specifically, lines projected onto 2D images are used to quantify the diameters. Next, the vessel length between

Received April 1, 2019; accepted after revision August 5.

From the Department of Neurosurgery (B.W.C., B.R.B., C.K., M.S.), Mayo Clinic, Phoenix, Arizona; Department of Neurosurgery (B.L.B., R.G.T., D.A.M.), Mayo Clinic, Jacksonville, Florida; Department of Neurosurgery (L.R.-C., A.T., H.C., D.K., G.L.), Mayo Clinic, Rochester, Minnesota; Endovantage, LLC (H.B.), Phoenix, Arizona; and Department of Biological and Health Systems Engineering (B.W.C., D.H.F.), Arizona State University, Tempe, Arizona.

This study was funded by the Mayo Clinic Office of Translation to Practice.

Paper previously presented, in part, at: Western Neuroradiological Society Annual Meeting, October 11–14, 2018, Dana Point, California; and SNIS 15TH Annual Meeting, July 23–26, 2018, San Francisco, California.

Please address correspondence to Brian W. Chong, MD, Mayo Clinic Hospital, Clinical Studies Unit, 5777 East Mayo Blvd, Phoenix, AZ 85017; e-mail: Chong.Brian@mayo.edu

Indicates article with supplemental on-line video.

Indicates article with supplemental on-line tables.

http://dx.doi.org/10.3174/ajnr.A6222

the 2 points is estimated. These collective measurements are used to select an FD size that will hopefully appose well to the vessel wall and cover the deployment region. However, this approach to sizing can be challenging because vessel diameters may vary considerably along the trajectory of a vessel. FDs can also elongate by >50% of the nominal length indicated by labeling.[10] Furthermore, measurements of vessel size taken from angiographic image data can be operator-dependent and are prone to measurement error. A recent study on intra- and interobserver variability when measuring cerebral aneurysm size in CT and MR angiography images showed a standard difference range of 12%–18% in size measurements.[11] A similar range in measurement variability during pretreatment planning can potentially lead to substantial FD undersizing or oversizing.

At present, there is no established method for predicting FD behavior in a patient's anatomy.

The physician's experience plays a primary role in understanding the interplay between device size, anatomy, and deployment. Different techniques for repairing suboptimal deployments have also been reported in the literature, including the use of catheter maneuvers, balloons, and additional FDs.[8,12,13] Needless to say, avoiding complications and suboptimal FD deployments through better planning and sizing is preferable to compensating for poor outcomes.

Computational modeling can help predict FD deployment behavior and thereby improve planning and selection of the optimal predicted FD size for a given patient. The use of computational modeling in clinical practice has grown widely during the past few years.[14,15] Here we present a pilot study that investigates the use of a computational modeling platform for the planning of FD treatments. The goals of the study were to determine whether computational modeling improves the selection of FD sizes over current convention and to validate the simulated deployments. The study surveys 7 experienced neurosurgeons and neurointerventional radiologists who used the proposed software platform to prospectively plan clinical interventions, and it validates the output of the process against rotational angiography scans of the actual clinical deployments.

MATERIALS AND METHODS

Patient Demographics

Mayo Clinic review board approval was obtained for the study protocol and patient recruitment. Eligible patients who provided written informed consent and met the inclusion criteria were included in the study. The study was conducted according to the Health Insurance Portability and Accountability Act. The primary inclusion criterion was patients approved for treatment with the Pipeline Embolization Device (PED; Covidien, Irvine, California). The major exclusion criteria were contraindications to 3D rotational angiography, insufficient time for treatment planning (at least 48 hours were required in the study), and poor image quality for vessel reconstruction (eg, poor contrast in the vessel or major artifacts near the aneurysm including prior coiling). Forty-three unruptured intracranial aneurysms that were approved for treatment with the Pipeline device at 3 Mayo Clinic institutions between January 2017 and July 2019 were included as eligible cases in the study. However, 16 cases were withdrawn due to clinical or administrative reasons (eg, the Pipeline device was not used, or forms were not received), 4 were withdrawn because of artifacts in the image data or poor image quality, and 4 were withdrawn due to an insufficient time for the computational modeling process (eg, when patient care needs precluded a 48-hour simulation time). The remaining 19 cases were included in the study. Each patient case represented a single aneurysm that was treated.

Table 1: Number of cases simulated and validated by physicians

Physician	Institution	No. of Cases Simulated/Validated
1	A	1/1
2	A	7/6
3	A	6/5
4	B	1/1
5	B	1/0
6	B	1/0
7	C	2/1

In total, 7 neurosurgeons and interventional neuroradiologists participated in the study. Five of the physicians had >15 years of experience in endovascular cerebral aneurysm treatments, while 2 had between 5 and 7 years of experience. Table 1 presents the number of cases performed by each physician. Patient demographics, clinical presentation, aneurysm location and size, pretreatment image data, and procedural information were acquired for each patient case.

Treatment-Planning Workflow

The SurgicalPreview computational modeling software (Endovantage, Phoenix, Arizona) was used for FD planning. The software is cleared by the FDA for computational modeling of the placement and deployment of neurointerventional devices.[16] Rotational angiography image data were acquired for each case before treatment and uploaded to the SurgicalPreview Web portal for vessel reconstruction and translation into a computational model. The reconstruction process was performed by trained Endovantage personnel using a thresholding-based, semiautomated image-segmentation technique. The 3D reconstructed models were uploaded back to the SurgicalPreview portal after reconstruction. The physician treating the case then indicated a distal landing point on the 3D vessel model in the portal for FD simulations and selected 2–4 Pipeline sizes for consideration from a list of all commercially available Pipeline sizes. Physicians used conventional vessel measurements on the patient's image data to identify potential FD sizes. They were also required to identify a preferred device size before viewing the simulation results. Selecting a single device in this way aligns with the current convention and facilitates later evaluations of the impact of computational modeling on final device selection.

FD simulations were performed automatically in SurgicalPreview on a high-performance computing cluster. The simulations use the finite element method and clinical deployment strategy to simulate deployment.[17] In summary, the software models a virtual catheter with the same diameter as the Pipeline delivery system and a linear-elastic material model to characterize the mechanical characteristics of the microcatheter. The geometry of all Pipeline FD sizes is modeled according to manufacturer's

specifications, and linear-elastic material models are used to characterize the material properties of the cobalt-chromium and platinum-tungsten alloy wires in the devices. Physical radial-compression mechanical tests were performed by Endovantage for each Pipeline FD size to calibrate the linear-elastic material models. The vessel model is assumed to be rigid, and the deployment procedure is assumed to be quasi-static. The software virtually deploys the FD into a vessel using an explicit finite element simulation. A feedback loop is used during the simulation to automatically adjust the deployment according to the vessel diameter and the diameter of the unsheathed region of the FD. This virtual feedback loop models the clinical deployment strategy of "painting the vessel wall" with the FD and promotes favorable apposition during deployment.

Results of simulating different FD sizes were then disseminated to each physician for feedback before treatment. The results included 3D models of the simulated FDs inside the pretreatment vessel, a deployment video showing unsheathing of the FD, and quantitative plots showing cross-sections of the vessel and FD at points that are uniformly spaced by 0.2 mm along the vessel centerline. A sample simulation result for 1 FD size is provided in Fig 1. An On-line Video of a simulated deployment showing unsheathing of the FD is also provided. Evaluations of the simulation results were performed by physicians at their offices, in their reading rooms, or before treatment in the operating room.

Each physician completed a questionnaire immediately after treatment that detailed procedural notes, devices used, and procedural time. The questionnaire also contained 5 questions on the impact of computational modeling on the procedure. Those questions are provided in Table 2. A clinical coordinator ensured that all fields were filled out.

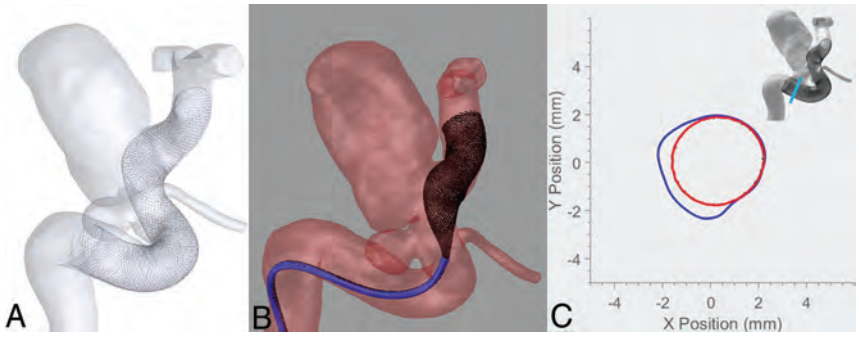

FIG 1. Sample simulation result from the SurgicalPreview computational modeling software showing a 3D model of the FD inside a pretreatment vessel (*A*), a frame from a deployment video (*B*), and a cross-section of the FD (red) and vessel (blue) at a position along the vessel centerline (*C*).

Deployment Validations

To validate the simulation results, we acquired a rotational angiography scan after each procedure. In total, posttreatment data were acquired for 15 of the 19 cases that were prospectively planned. The image data were used to reconstruct the clinically deployed FD devices and compare them with simulated deployments. Mimics (Materialise, Leuven, Belgium) was used to perform the reconstruction. An additional FD simulation was performed in the pretreatment vessel using the device model of the actual FD size used in the procedure, deployed at the exact distal landing point observed in the posttreatment reconstructions. The additional simulations addressed cases in which the physician used feedback from the simulation results to select a different device size and/or cases characterized by large discrepancies between the physician's desired and actual distal landing points.

A centerline that was discretized with 0.1-mm resolution was generated for each simulated and reconstructed FD using the Vascular Modeling Toolkit (VMTK, www.vmtk.org). At each point along the centerline, VMTK also computed the maximal inscribed sphere that could be fit at that location. FD length was calculated by measuring the total length of each simulated and clinical FD centerline. The average FD diameter was calculated by averaging the diameters of all maximal inscribed spheres along the length of each centerline.

The calculation of the average FD diameter was made using the outer surfaces of the reconstructed clinical and simulated FDs (ie, the inner lumen was ignored). In the reconstructed deployments, the outer FD surface is affected by the spatial image resolution and blooming artifact that is introduced by the actual FD in the posttreatment image data. The artifact expands device thickness beyond the actual thickness of the device and adds uncertainty to the measurement of FD diameter.[18,19] To quantify that uncertainty, we made 15 measurements of FD wire thickness (inner lumen to outer surface) at random locations along the entire length of each clinical FD using a digital caliper in Geomagic Studio (3D Systems, Rock Hill, South Carolina). The 15 measurements were averaged in each deployment and used to define the uncertainty range in measuring the clinical FD diameter. The true clinical FD diameter was assumed to be near the center of that uncertainty range.

Table 2: Survey questionnaire results on the impact of computational modeling

Survey Questions	Responses		
	Yes	No	Somewhat
Were the simulations useful for your planning?	18	0	1
Did the simulations give you greater confidence in your device selection?	18	0	1
Did the simulations change your device selection?	12	6	1
Do you think the simulations reduced the number of devices that you used?	2	14	3
Do you think the simulations reduced your operative time?	4	13	2

After the calculation of clinical and simulated FD lengths and diameters, a statistical analysis was performed to evaluate the differences between the deployments. Specifically, the mean, SD, and 95% confidence interval of the average difference and average absolute difference between deployments were calculated.

RESULTS

Patient Demographics

Of the 19 cases that were simulated in the study, 4 had presented with a different cerebral aneurysm previously. Nine patients were current or previous smokers. Most aneurysms were located on the internal carotid artery, and only 2 of the 19 aneurysms were fusiform, while the remaining were saccular. Regarding the sizes of the 17 saccular aneurysms, 6 were <7 mm, 9 were 7–10 mm, and 2 were >10 mm, while the measurement in millimeters refers to the largest dimension of the aneurysm. The average saccular aneurysm size was 8.4 ± 4.0 mm. The largest dimensions of the 2 fusiform aneurysms were 8.3 and 7.0 mm.

Physician Responses

Table 2 presents the results of the surgical-planning questionnaire. Physicians found the simulations useful for treatment planning in 94.7% of cases (ie, 18/19). Their comments on simulation utility in the questionnaire said that the simulations were specifically useful for the following: 1) rehearsing the deployment strategy and positioning of the device, 2) predicting how the device would behave around curved regions in the vessel, and 3) narrowing the list of device sizes being considered. Responses also indicated that the simulations increased perceived confidence in device selection in 94.7% of cases (ie, 18/19). Some physicians commented that they became more confident that the selected device size would span the desired proximal and distal landing points after viewing the simulation results.

After viewing the simulation results, physicians selected a device size that was different from the originally planned device size in 63.2% of cases (ie, 12/19). In most of those cases (9/12), physicians selected a device diameter or length that was 1 size smaller or larger than the originally planned device size. Furthermore, a different device diameter was selected in half of the cases (6/12), while only a different device length was selected in the remaining half. According to some questionnaire comments, physicians chose a different device length after viewing the simulated proximal landing point or chose a different device diameter on the basis of the simulated FD coverage of the vessel wall.

Physicians perceived that the simulations reduced the number of devices used and operative time in 10.5% (ie, 2/19) and 21.1% of cases (ie, 4/18), respectively. Seventeen of the 19 cases were treated with a single Pipeline device, while only 2 cases were treated with 2 Pipeline devices (ie, telescoping configuration). Balloon angioplasty was used in 2 cases, once to expand the proximal end of the FD after it did not fully open and once to expand the device to achieve better wall apposition. Procedural complications occurred in 2 cases. In 1 case, complete occlusion of the internal carotid artery with recanalization was observed, and in the second case, cerebral vasospasm was encountered. Regarding the procedural times of the 19 cases (quantified at the time from puncture until complete deployment), 6 cases were <30 minutes, 9 cases were 30–60 minutes, and 4 cases were >60 minutes. The average procedural time was 41.5 ± 19.4 minutes.

Deployment Validations

Fifteen of the 19 cases had posttreatment image data that could be used for validation analysis. However, 1 case was excluded because balloon angioplasty was used to expand the FD to achieve better wall apposition. Accordingly, 14 cases were considered in the validation analysis. Figure 2 shows 6 pairs of clinical and simulated deployments and presents them in ascending order according to their difference in device length. The figure shows similarity between predicted and actual FD deployments based on device length and diameter.

Figure 3 presents Bland-Altman plots that compare FD lengths and diameters between clinical and simulated deployments, and Table 3 presents the statistical analysis of the difference between deployments. On average, the simulations were 1.1 mm longer and 0.1 mm larger in diameter than clinical deployments. A 95% confidence interval indicated that the true average absolute difference in FD length was between 1.3 and 2.9 mm. The 95% confidence interval for the true average absolute difference in FD diameter was between 0.18 and 0.37 mm, which is close to the range of image spatial resolutions for rotational angiography data[11] and the range of the measured uncertainty in FD diameter measurements (0.13–0.39 mm). Figure 4 shows that in 57% of cases, the simulations had an average diameter that was within the uncertainty of the clinical FD diameter measurement. Note that wire thickness was used to quantify the uncertainty in clinical FD diameter measurements due to blooming artifacts and the spatial resolution of the posttreatment image data.

Additional detail on patient demographics, physician responses, and deployment validation are provided in the On-line Tables 1–4.

DISCUSSION

Technical complications such as malapposition, prolapse, migration, and incomplete expansion are common during FD deployment. Reports of such complications have increased recently due to the frequent use of FDs and improvement to the imaging technology used to visualize the devices after deployment.[20,21] To date, the rate of technical complications has ranged from 12% to 18%.[13,20,21] The recommended strategy for avoiding these complications is to select a FD size that will appose well to the vessel wall and cover at least 2–3 mm of the parent vessel beyond the aneurysm region.[22] Good wall apposition is also crucial for vessel remodeling and aneurysmal occlusion and may be a key factor for achieving complete occlusion as well as avoiding thrombosis of perforator branches.[23,24] Accordingly, proper FD sizing is critical for interventional success.

This study found computational modeling to be clinically useful for FD sizing and procedural planning. The participating physicians were able to experiment with different device sizes before interventions and select the predicted best option for a given patient's anatomy. According to questionnaire responses, physicians not only thought that modeling was useful for sizing but also found that it improved their confidence in device

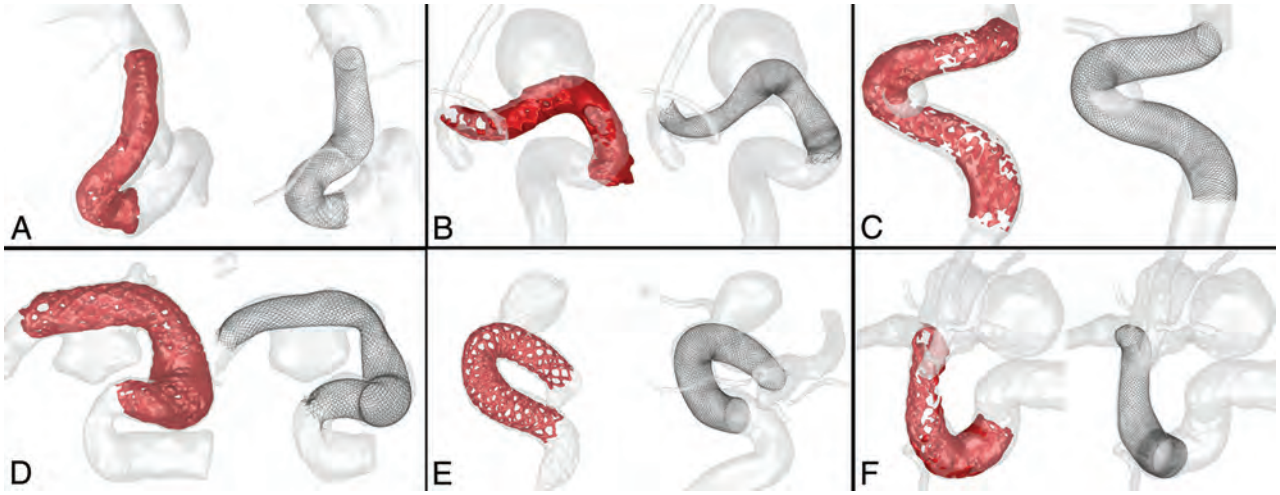

FIG 2. Examples of posttreatment clinical reconstructions (*red/left*) and pretreatment simulation results (*black/right*) for the same FD sizes. The deployment pairs are sorted in ascending order according to the difference between actual and simulated device lengths, which ranged from 1.58 to 4.06 mm.

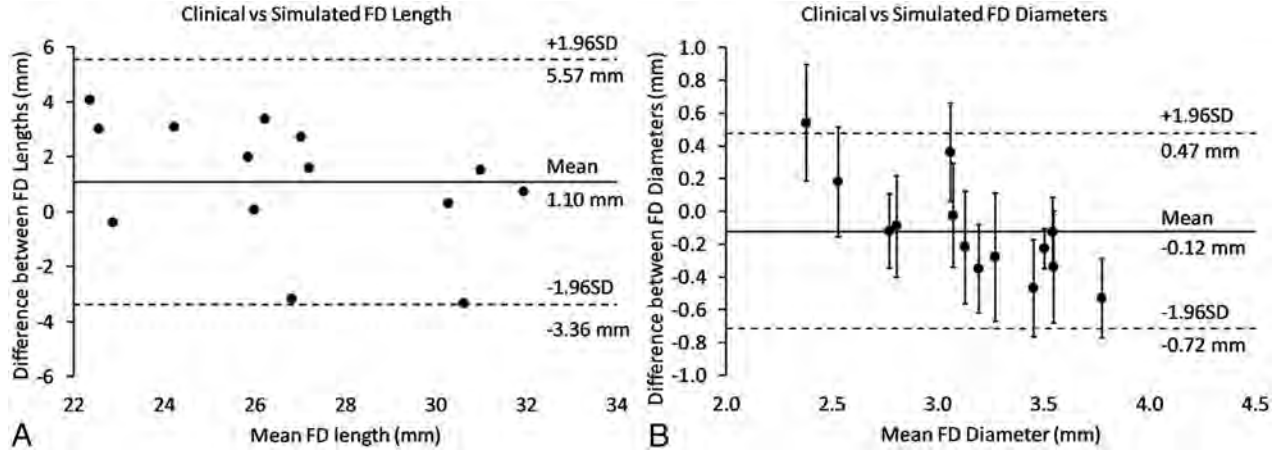

FIG 3. Bland-Altman plots showing *dots* that represent differences between the actual clinical and simulated deployments in FD length (*A*) and FD diameter (*B*). The plots show the means for the deployment pairs on the x-axis and the differences between pairs on the y-axis.

Table 3: Statistical analysis of the difference between clinical and simulated FD lengths and diameters for the 14 validated cases

	Difference			Absolute Difference		
	Mean (mm)	SD (mm)	95% CI (mm)	Mean (mm)	SD (mm)	95% CI (mm)
FD length	1.10	2.28	[−0.21, 2.42]	2.09	1.34	[1.32, 2.86]
FD diameter	−0.12	0.30	[−0.30, 0.05]	0.28	0.16	[0.18, 0.37]

placement. This effect was observed for both small (<7 mm) and large (>7 mm) aneurysms. Deployment videos of FD simulations helped some physicians to mentally rehearse the procedure and visualize the behavior of FDs around tortuous vessels. After viewing simulation results, the participating physicians changed their device size selections in 63.2% of the cases. This result highlights the impact of computational modeling on treatment planning.

Physician responses indicated that the effects of computational modeling on the number of devices used and on procedural time were limited to a small percentage of cases. However, such effects may be difficult to observe on the basis of a questionnaire, given a small sample size. A planned future study will use a larger patient population and a control group to better elucidate the influence of computational modeling on the number of devices used and procedural time.

Validation analysis showed good agreement between simulated and actual clinical FD diameters and lengths. Most of the simulations had average FD diameters that were within the uncertainty of the clinical FD diameter measurements, and in some cases, dissimilarity between the deployment technique of the software and the physician's technique led to FD length differences of >3 mm. Nevertheless, an average absolute difference of only 2.1 mm in FD length was observed over all cases examined.

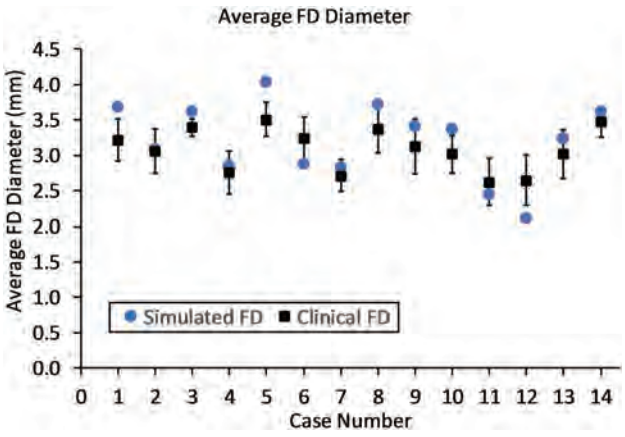

FIG 4. Average FD diameters for the actual clinical and simulated deployments. *Error bars* in the clinical FD diameter measurements were calculated by averaging 15 random measurements of FD thickness along the length of each reconstructed FD model.

Many studies have been reported in the literature on the application of computational device modeling to treatment planning.[10,25-27] Previous retrospective studies that evaluated the application of computational modeling to FD sizing have demonstrated the potential benefits of the technology for improving FD size selection.[10,25] To date, few, if any, studies have exclusively focused on both the utility and predictive fidelity of computational device modeling in a prospective case series. Yet, evaluations under typical clinical workflows are essential for understanding the contribution of the technology to clinical practice and its potential for adoption. This study presents an early evaluation of the impact of the technology on FD treatment planning.

Several limitations of this pilot study are noteworthy. First, the study included a small sample of patient cases and a small number of physicians. The small sample size was a reflection of the fact that several cases were referred from outside hospitals and these patients already had a recent CTA or catheter angiograms of their aneurysms. We did not think that it was justified to repeat the imaging and thereby expose the patients to additional unnecessary radiation. Therefore, these patients were excluded from enrollment. Furthermore, the primary goal of the study was to gauge the impact of computational modeling on clinical workflows, and a sample size of 19 was deemed appropriate for this purpose. Future work will include evaluating the impact of computational modeling on a larger patient population with a control group. Second, the distribution of cases among physicians was skewed, and most cases (73.6%) were performed by physicians operating at one of three sites (all part of the same healthcare organization). This distribution is proportional to the size of the site and the volume of Pipeline cases that the site receives. Therefore most cases were performed by the physicians from the largest and highest volume site. Third, the study did not evaluate short- and long-term patient outcomes such as aneurysmal occlusion, which is another goal of future work. Fourth, the study used a self-assessment questionnaire to evaluate the perceived usefulness of the technology. Self-assessment alone may not be an accurate measure of the usefulness or the improvement of the technology over convention and should be supported by performance metrics from a larger study with a control group.

CONCLUSIONS

Computational modeling of FDs was found to be an impactful clinical tool for interventional planning. Experienced interventional neuroradiologists and neurosurgeons at 3 centers found the modeling to be useful for FD sizing, FD placement, and case rehearsal. Use of the modeling platform led to device selection changes in 63.2% of cases. Validation analysis showed good agreement between simulated and actual clinical FD diameters and lengths. The proposed computational modeling approach has the potential to reduce technical complications during FD treatment and improve patient outcomes. To our knowledge, this is the first study that evaluates the utility of computational device modeling in a prospective case series.

Disclosures: Brian W. Chong—*RELATED*: *Board Membership*: Endovantage LLC; *Patents (Planned, Pending, Or Issued)*: Mayo Clinic, *Comments*: patent pending on intellectual property related to work on the article; *Royalties*: Mayo Clinic, *Comments*: royalty sharing with Mayo Clinic; *Stock/Stock Options*: Endovantage LLC; *Support for Travel to Meetings for the Study or Other Purposes*: Endovantage LLC, *Comments*: travel (airfare and hotel) to present at a scientific meeting. Haithem Babiker—*RELATED*: *Employment*: Endovantage LLC; *Patents (Planned, Pending or Issued)*: Endovantage LLC; *Stock/Stock Options*: Endovantage LLC. David Kallmes—*UNRELATED*: *Consultancy*: Medtronic, *Comments*: Safety Board for flow-diverter clinical trial*; *Grants/Grants Pending*: Medtronic, Sequent, MicroVention, NeuroSigma, *Comments*: support for preclinical and clinical research*; *Stock/Stock Options*: Superior Medical Experts, *Comments*: founder and stockholder of a medical editing and writing business. Giuseppe Lanzino—*UNRELATED*: *Consultancy*: Superior Medical Editing. Rabih G. Tawk—*UNRELATED*: *Stock/Stock Options*: Medtronic, *Comments*: $5000–$10,000. *Money paid to institution.

REFERENCES

1. Briganti F, Delehaye L, Leone G, et al. **Flow diverter device for the treatment of small middle cerebral artery aneurysms.** *J NeuroIntervent Surg* 2016;8:287–94 CrossRef Medline
2. Bhogal P, Pérez MA, Ganslandt O, et al. **Treatment of posterior circulation non–saccular aneurysms with flow diverters: a single-center experience and review of 56 patients.** *J NeuroIntervent Surg* 2017;9:471–81 CrossRef Medline
3. Saatci I, Yavuz K, Ozer C, et al. **Treatment of intracranial aneurysms using the Pipeline flow-diverter embolization device: a single-center experience with long-term follow-up results.** *AJNR Am J Neuroradiol* 2012;33:1436–46 CrossRef Medline
4. U.S. Food and Drug Administration. **P100018/S015, Pipeline™, Flex Embolization Device approval letter.** https://www.accessdata.fda.gov/cdrh_docs/pdf10/P100018S015A.pdf. Accessed May 22, 2019
5. Caroff J, Tamura T, King RM, et al. **Phosphorylcholine surface modified flow diverter associated with reduced intimal hyperplasia.** *J NeuroIntervent Surg* 2018;10:1097–1101 CrossRef Medline
6. Laurent E, Makoyeva A, Darsaut TE, et al. **In vitro reproduction of device deformation leading to thrombotic complications and failure of flow diversion.** *Interv Neuroradiol* 2013;19:432–37 CrossRef
7. Tsai YH, Wong HF, Hsu SW. **Endovascular management of spontaneous delayed migration of the flow-diverter stent.** *J Neuroradiol* 2018 Dec 1. [Epub ahead of print] CrossRef Medline
8. Al-Mufti F, Amuluru K, Cohen ER, et al. **Rescue therapy for procedural complications associated with deployment of flow-diverting devices in cerebral aneurysms.** *Oper Neurosurg (Hagerstown)* 2018;15:624–33 CrossRef Medline

9. Sindeev S, Prothmann S, Frolov S, et al. **Intimal hyperplasia after aneurysm treatment by diversion.** *World Neurosurg* 2019;122:e577–83 CrossRef Medline
10. Narata AP, Blasco J, Roman LS, et al. **Early results in flow diverter sizing by computational simulation: quantification of size change and simulation error assessment.** *Oper Neurosurg (Hagerstown)* 2018;15:557–66 CrossRef Medline
11. Kim HJ, Yoon DY, Kim ES, et al. **Intraobserver and interobserver variability in CT angiography and MR angiography measurements of the size of cerebral aneurysms.** *Neuroradiology* 2017;59:491–97 CrossRef Medline
12. Martínez–Galdámez M, Ortega–Quintanilla J, Hermosín A, et al. **Novel balloon application for rescue and realignment of a proximal end migrated Pipeline Flex embolization device into the aneurysmal sac: complication management.** *BMJ Case Rep* 2016;2016 CrossRef Medline
13. Kühn AL, Rodrigues KDM, Wakhloo AK, et al. **Endovascular techniques for achievement of better flow diverter wall apposition.** *Interv Neuroradiol* 2019;25:344–47 CrossRef Medline
14. Pontone G, Patel MR, Hlatky MA, et al. **Rationale and design of the prospective longitudinal trial of FFRCT: outcome and resource impacts study.** *Am Heart J* 2015;170:438–44 CrossRef Medline
15. Brouwer J, Gheorghe L, Nijenhuis VJ, et al. **Insight on patient specific computer modeling of transcatheter aortic valve implantation in patients with bicuspid aortic valve disease.** *Catheter Cardiovasc Interv* 2019;93:1097–1105 CrossRef Medline
16. U.S. Food and Drug Administration. **K171534, Surgical Preview. clearance letter.** https://www.accessdata.fda.gov/cdrh_docs/pdf17/K171534.pdf. Accessed May 16, 2019
17. Babiker H, Kalani Y, Levitt M, et al. **Clinical validations of simulated neurovascular braided stent deployments.** *Ann Biomed Eng* 2016;44:3719–49 CrossRef
18. Zwarzany Ł, Poncyljusz W, Burke TH. **Flat detector CT and its applications in the endovascular treatment of wide-necked intracranial aneurysms: a literature review.** *Eur J Radiol* 2017;88:26–31 CrossRef Medline
19. Ott S, Struffert T, Saake M, et al. **Influence of different reconstruction parameters in the visualization of intracranial stents using C-arm flat panel CT angiography: experience in an animal model.** *Acta Radiology* 2016;57:233–40 CrossRef Medline
20. Kizilkilic O, Kocer N, Metaxas GE, et al. **Utility of VasoCT in the treatment of intracranial aneurysm with flow-diverter stents: clinical article.** *J Neurosurg* 2012;117:45–49 CrossRef Medline
21. Clarençon F, Di Maria F, Gabrieli J, et al. **Clinical impact of flat panel volume CT angiography in evaluating the accurate intraoperative deployment of flow-diverter stents.** *AJNR Am J Neuroradiol* 2017;38:1966–72 CrossRef Medline
22. Al–Mufti F, Cohen ER, Amuluru K, et al. **Bailout strategies and complications associated with the use of flow-diverting stents for treating intracranial aneurysms.** *Interv Neuroradiol* 2019;8:38–54 CrossRef
23. Rouchaud A, Ramana C, Brinjikji W, et al. **Wall apposition is a key factor for aneurysm occlusion after flow diversion: a histologic evaluation in 41 rabbits.** *AJNR Am J Neuroradiol* 2016;37:2087–91 CrossRef Medline
24. Aquarius R, de Korte A, Smits D, et al. **The importance of wall apposition in flow diverters.** *Neurosurgery* 2019;84:804–10 CrossRef Medline
25. Ospel JM, Gascou G, Costalat V, et al. **Comparison of Pipeline embolization device sizing based on conventional 2D measurements and virtual simulation using the Sim&Size software: an agreement study.** *AJNR Am J Neuroradiol* 2019;40:524–30 CrossRef Medline
26. Karády J, Ntalas I, Prendergast B, et al. **Transcatheter mitral valve replacement in mitral annulus calcification: the art of computer simulation.** *J Cardiovasc Comput Tomogr* 2018;12:153–57 CrossRef Medline
27. Derycke L, Perrin D, Cochennec F, et al. **Predictive numerical simulations of double branch stent–graft deployment in an aortic arch aneurysm.** *Ann Biomed Eng* 2019;47:1051–62 CrossRef Medline

Low-Profile Intra-Aneurysmal Flow Disruptor WEB 17 versus WEB Predecessor Systems for Treatment of Small Intracranial Aneurysms: Comparative Analysis of Procedural Safety and Feasibility

L. Goertz, T. Liebig, E. Siebert, M. Herzberg, L. Pennig, M. Schlamann, J. Borggrefe, B. Krischek, F. Dorn, and C. Kabbasch

ABSTRACT

BACKGROUND AND PURPOSE: The Woven EndoBridge 17 has recently been introduced to the market for facilitated endovascular treatment of small bifurcation aneurysms (≤7 mm) with low-profile microcatheters. We compared the Woven EndoBridge 17 with its predecessor versions in terms of procedural safety and feasibility.

MATERIALS AND METHODS: This was a multicenter review of aneurysms ranging from 3 to 7 mm treated with the Woven EndoBridge between 2011 and 2019. Aneurysm characteristics, procedural parameters, and complications were retrospectively compared between treatment with the Woven EndoBridge 17 and a control group that was treated with its predecessor versions, using inverse probability of treatment weighting.

RESULTS: Thirty-eight aneurysms treated with a Woven EndoBridge 17 (mean size, 4.9 ± 1.5 mm) and 70 treated with a predecessor version of the Woven EndoBridge 17 (mean size, 5.6 ± 1.4 mm) were included. The predecessor version of the Woven EndoBridge 17 had a higher failure rate (10.3%) than the Woven EndoBridge 17 (0%, $P = .05$). Additional stent placement was performed more often with the predecessor version of the Woven EndoBridge 17 (10.0%) than with the Woven EndoBridge 17 (2.6%, adjusted $P = .005$). The predecessor version of the Woven EndoBridge 17 was associated with a higher thromboembolic event rate (14.3%) than the Woven EndoBridge 17 (5.3%, adjusted $P = .002$). Neurologic complications (Woven EndoBridge 17: 2.6%; predecessor version of the Woven EndoBridge 17: 2.9%, adjusted $P = 1.0$) and immediate complete aneurysm occlusion rates (Woven EndoBridge 17: 57.9%; predecessor version of the Woven EndoBridge 17: 54.3%, adjusted $P = .21$) did not differ significantly between groups.

CONCLUSIONS: In the current study, the Woven EndoBridge 17 was associated with a potentially lower thromboembolic event rate than the predecessor version of the Woven EndoBridge 17, without compromising the immediate aneurysm occlusion rate. Long-term clinical and angiographic outcome analysis will be necessary to draw a definite conclusion.

ABBREVIATIONS: AcomA = anterior communicating artery; IPTW = inverse probability of treatment weighting; pWEB = predecessor version of the Woven EndoBridge 17; SL = Single-Layer; WEB = Woven EndoBridge

Intrasaccular flow disruption is a cutting-edge treatment option for intracranial aneurysms, in particular for wide-neck and bifurcation aneurysms, which are typically difficult to treat by standard endovascular techniques.[1-3] The Woven EndoBridge (WEB; Sequent Medical, Aliso Viejo, California) is a self-expanding flow disruptor that is placed in the aneurysm sac and seals the aneurysm neck without the compelling need for supporting devices.[4-6] Its safety and efficacy have been demonstrated in several large, multicenter studies.[7-13] For instance, in the Woven EndoBridge Intrasaccular Therapy (WEB-IT) study, the adverse event rate was 0.7% among 148 patients, achieving adequate aneurysm occlusion in 84.6% at 1-year follow-up.[14]

Since the introduction of the Dual-Layer WEB in 2010, the WEB has been progressively refined and new systems such as the Single-Layer (SL) and Single-Layer Sphere WEBs have been introduced to the market, mainly to facilitate device deployment while maintaining good neck coverage and reducing procedural complications.[1,15-18] Whereas the early-generation WEBs could be delivered through only 0.027- to 0.033-inch microcatheters,

Received May 21, 2019; accepted after revision July 14.

From the Department of Neuroradiology (L.G., L.P., M.S., J.B., C.K.), University Hospital of Cologne, Cologne, Germany; Center for Neurosurgery (L.G., B.K.), University of Cologne, Faculty of Medicine and University Hospital, Cologne, Germany; Department of Neuroradiology (T.L., M.H., F.D.), University Hospital Munich, Munich, Germany; and Department of Neuroradiology (E.S.), University Hospital of Berlin (Charité), Berlin, Germany.

L. Goertz and T. Liebig contributed equally to this work.

Please address correspondence to Lukas Goertz, MD, Department of Neuroradiology, University Hospital of Cologne, Kerpener Str 62, 50937 Cologne, Germany; e-mail: lukas.goertz@uk-koeln.de

http://dx.doi.org/10.3174/ajnr.A6183

newer versions of the Single-Layer and Single-Layer Sphere types up to 7 mm in diameter were redesigned for delivery through a 0.021-inch microcatheter (WEB 21).

The WEB 17 is the latest generation. It is composed of fewer and thinner nitinol wires than the WEB 21 (72–108 versus 144–216 wires) and comes with a new delivery wire, which has been reduced from 0.020 to 0.015 inches.[19] Due to these modifications, the WEB 17 is compatible with a 0.017-inch inner-diameter microcatheter. The aim of this modification was to widen the range of applicability of the WEB, in particular for small and distally located aneurysms. To date, the WEB 17 system is available as the WEB Single-Layer (size range, 3 × 2 to 7 × 4 mm), which is oblong, and as the WEB Single-Layer Sphere (size range, 4–7 mm), which is more spherical.

Because the introduction of the WEB 17 system is relatively recent, clinical data on its safety and feasibility profile are still limited. The objective of the current study was to present our multicenter experience in treating small aneurysms with the WEB 17 and to compare the complication rates and procedural aspects with predecessor WEB systems. To address a potential selection bias, we performed an inverse probability of treatment weighting approach using propensity scores.

MATERIALS AND METHODS

The authors retrospectively reviewed consecutive patients who underwent WEB embolization at 3 German high-volume neurovascular centers (University Hospital Cologne, University Hospital Munich and University Hospital Berlin, Charité) between January 2011 and February 2019. In accordance with the institutional guidelines, ethics committee approval was not required for this retrospective study.

Inclusion and Exclusion Criteria

All patients treated with the WEB at the 3 institutions were retrospectively reviewed. Exclusion criteria were defined as follows: 1) WEB size >7 mm, 2) aneurysm size >7 mm, 3) previously treated aneurysms, and 4) treatment of multiple aneurysms with the WEB device during a single procedure. We report on patients with failed WEB implantations; however, these aneurysms were excluded from comparative analysis of complications and procedural aspects. The enrolled patients were divided into WEB 17 and predecessor version of the WEB 17 (pWEB) groups, on the basis of whether they were treated with the WEB 17 or with predecessor WEB versions.

Procedure

After diagnosis of a ruptured or unruptured intracranial aneurysm, the case was discussed within a multidisciplinary team among vascular neurosurgeons and interventional neuroradiologists and treatment decisions were made in consensus. The use of the WEB was left to the discretion of the neurointerventionalist. In general, the WEB was used for wide-neck and bifurcation aneurysms with unfavorable configuration for endovascular coiling as a treatment alternative for stent-assisted procedures or microsurgical clipping. At all 3 centers, the neurointerventionalists were initially trained and later proctored by the same neurointerventionalist (T.L.); this procedure ensured a homogeneous treatment technique across centers.

All procedures were performed via a transfemoral approach with the patient under general anesthesia in a biplane angiosuite (Philips AlluraClarity FD 20/15, Philips Healthcare, Best, the Netherlands and Siemens Axiom Artis, Siemens, Erlangen, Germany). The WEB 17 was delivered through the dedicated VIA 17 microcatheter (Sequent Medical), and the pWEB, through dedicated larger VIA microcatheters.

The appropriate WEB size was selected according to the aneurysm width and height as measured on 2D DSA images. Implant sizes were chosen to be slightly larger than the maximum aneurysm diameter as recommended in the instructions for use. We aimed to treat all aneurysms of <7 mm with the WEB only, without the use of additional intraluminal devices such as stents or flow diverters to avoid long-term antiplatelet medication. However, if the WEB tended to protrude into the parent vessel, an intracranial stent was additionally implanted at the operator's discretion. Adjunctive coiling was used in selected cases to provide optimal aneurysm occlusion.

Anti-Aggregation Therapy

For treatment of unruptured aneurysms, a bolus of heparin (5000 IU) was administered after groin puncture, followed by aliquots of 1000 IU/h. Heparin was discontinued at the end of the procedure. In all patients with unruptured aneurysms, acetylsalicylic acid, 100 mg/day, was administered 5–7 days before the procedure and continued for a minimum of 4–6 weeks. If additional stent implantation was necessary, dual antiplatelet therapy with acetylsalicylic acid, 100 mg, and clopidogrel, 75 mg, was administered for at least 4 months after the procedure. Thereafter, acetylsalicylic acid monotherapy was continued life-long. In patients with ruptured aneurysms treated with the WEB only, no antiplatelets were administered.

In scheduled cases, platelet inhibition was tested with acetylsalicylic acid and accessory P2Y12 assays when required (VerifyNow; Accumetrics, San Diego, California). A platelet inhibition level between 350 and 550 acetylsalicylic acid response units and 30%–90% for clopidogrel was requested. An insufficient response to either drug was counteracted by dose escalation (eg, clopidogrel, 150 mg/day) or substitution with prasugrel (60-mg bolus, 10 mg/day).

Data Collection

The following variables were collected retrospectively from the medical charts: patient age, sex, rupture status, World Federation of Neurosurgical Societies grading scale score, Fisher score, treatment duration, fluoroscopy time, radiation exposure, and amount of applied contrast. Procedural complications were recorded by 2 researchers (L.G., M.H.) who were not involved in aneurysm treatment. We report both symptomatic and asymptomatic events. All thromboembolic and hemorrhagic events are reported. The severity of ischemic stroke was assessed by the National Institutes of Health Stroke Scale, and any change of ≥1 point was considered a complication. Adverse events associated

Table 1: Baseline patient and aneurysm characteristics[a]

	WEB 17 (*n* = 38)	pWEB (*n* = 70)	*P* Value	Adjusted *P* Value
Patient age (yr)	55.7 ± 12.7	57.3 ± 12.2	.54	.72
Female sex	25 (65.8%)	52 (74.3%)	.35	.61
Ruptured aneurysms	10 (26.3%)	24 (34.3%)	.39	.59
WFNS I	2 (5.3%)	10 (14.3%)	.82	.06
WFNS II	2 (5.3%)	3 (4.3%)		
WFNS III	2 (5.3%)	4 (5.7%)		
WFNS IV	1 (2.6%)	2 (2.9%)		
WFNS V	3 (7.9%)	5 (7.1%)		
Fisher 1	1 (2.6%)	2 (2.9%)	.77	.30
Fisher 2	0 (0%)	2 (2.9%)		
Fisher 3	3 (7.9%)	5 (7.1%)		
Fisher 4	6 (15.8%)	13 (18.6%)		
Aneurysm location				
AcomA	14 (36.8%)	15 (21.4%)	.08	.92
Pericallosal	0 (0%)	1 (1.4%)	1.0	.24
MCA	4 (10.5%)	15 (21.4%)	.19	.60
ICA				
Paraophthalmic	1 (2.6%)	7 (10.0%)	.26	.06
PcomA	4 (10.5%)	5 (7.1%)	.72	.55
Terminus	3 (7.9%)	0 (0%)	.04	.25
BA	9 (23.7%)	24 (34.3%)	.25	.82
SUCA	1 (2.6%)	0 (0%)	.35	.01
PICA	2 (5.3%)	3 (4.3%)	1.0	.53
Anterior circulation	26 (68.4%)	43 (61.4%)	.47	.63
Posterior circulation	12 (31.6%)	27 (38.6%)		
Bifurcation location	27 (71.1%)	54 (77.1%)	.49	.72
Aneurysm size (mm)	4.9 ± 1.5	5.6 ± 1.4	.007	.55
Neck width (mm)	3.6 ± 1.1	4.2 ± 1.3	.04	.95
D/N ratio	1.4 ± 0.5	1.4 ± 0.4	.56	.90
Wide neck	35 (92.1%)	65 (92.9%)	1.0	.66

Note:—WFNS indicates World Federation of Neurosurgical Societies grading scale; D/N ratio, dome-to-neck ratio; PcomA, posterior communicating artery; BA, basilar apex; SUCA, superior cerebellar artery.
[a] Data are number and percentage of means.

with persisting neurologic deficits at discharge were defined as neurologic complications.

Angiography

Baseline conventional 4-vessel DSA scans were reviewed to determine aneurysm size, aneurysm neck width, and dome-to-neck ratio. Wide-neck aneurysms were defined as having a neck width of ≥4 mm and/or a dome-to-neck ratio of ≤2.

The Raymond-Roy occlusion classification was used to evaluate immediate aneurysm occlusion after WEB implantation: 1) complete occlusion, 2) neck remnant, and 3) aneurysm remnant. Complete occlusion and neck remnants were defined as adequate occlusion. Immediate aneurysm occlusion was assessed independently on the basis of 2D-DSA by 3 consultant neuroradiologists (C.K., E.S., F.D.). Discrepancies were resolved in consensus.

Statistical Analysis

Quantitative data were presented as numbers and percentages and analyzed with the χ^2 and Fisher exact tests. Quantitative data were presented as means with SDs and tested for normality using the Shapiro-Wilk test. Groups were compared using the unpaired *t* test (normally distributed data) or the Mann-Whitney *U* test (non-normally distributed data). Bivariate correlation analysis was performed using the Pearson and Spearman correlation coefficients. To account for a potential selection bias, we performed an inverse probability of treatment weighting (IPTW) approach based on the propensity score model. IPTW was used as a statistical technique to create 2 synthetic study groups with comparable propensity scores, in which treatment assignment was independent of measured baseline characteristics. This method aimed to minimize a potential selection bias and to obtain comparative estimates of treatment effects. Propensity scores were calculated using a multivariate logistic regression model with the WEB 17 treatment as the response and the following covariates: patient age, sex, ruptured/unruptured status, aneurysm location, aneurysm size, and neck width. Statistical analysis was performed using SPSS Statistics for Windows, Version 25.0 (IBM, Armonk, New York). A *P* value < .05 was considered as statistically significant.

RESULTS

Patient and Aneurysm Characteristics

Among 165 aneurysms treated during the study period, 108 aneurysms in 108 patients met our inclusion criteria and were enrolled. Fifty-seven aneurysms were excluded for the following reasons: WEB size of >7 mm (*n* = 30), aneurysm size of >7 mm (*n* = 11), failed WEB implantation (*n* = 8), treatment of recurrent aneurysms (*n* = 6), and treatment of multiple aneurysms with the WEB during 1 procedure (*n* = 2). The mean patient age was 56.7 ± 12.3 years (range, 21–87 years), and 77 patients (71.3%) were women. Thirty-four patients (31.5%) were treated for ruptured aneurysms, and 74 (68.5%), for unruptured aneurysms. The aneurysms were most frequently located at the basilar artery tip (33, 30.6%), followed by the anterior communicating artery (AcomA) (29, 26.9%), and the middle cerebral artery (19, 17.6%). The mean aneurysm size was 5.3 ± 1.5 mm (range, 3–7 mm), and the mean neck width was 4.0 ± 1.2 mm (range, 1.5–7.2 mm). A total of 100 aneurysms (92.6%) were classified as wide-neck.

Of 108 aneurysms, 38 were treated with the WEB 17 (35.2%) and 70 with pWEBs (64.8%). In the pWEB group, 64 patients were treated with a 0.021-inch microcatheter, and 6, with a 0.027-inch microcatheter. Baseline patient and aneurysm characteristics were comparable between the 2 groups, except for a larger aneurysm size (WEB 17: 4.9 ± 1.5 mm; pWEB: 5.6 ± 1.4 mm, *P* = .007) and a wider neck (WEB 17: 3.6 ± 1.1 mm; pWEB: 4.2 ± 1.3 mm, *P* = .042) in the pWEB group, as outlined in Table 1. To address this selection bias, we performed an IPTW adjustment approach based on the

Table 2: Procedural specifics[a]

	WEB 17 (*n* = 38)	pWEB (*n* = 70)	*P* Value	Adjusted *P* Value
WEB type				
DL	0 (0%)	6 (8.6%)	.09	.003
SL	31 (81.6%)	46 (65.7%)	.08	.001
SLS	7 (18.4%)	18 (25.7%)	.39	.02
WEB only	36 (94.7%)	62 (88.6%)	.49	.02
Additional coiling	1 (2.6%)	1 (1.4%)	1.0	1.0
Additional stents	1 (2.6%)	7 (10.0%)	.26	.005
Treatment duration (min)	122 ± 67	133 ± 67	.48	.007
Fluoroscopy time (min)	25.4 ± 20.1	27.6 ± 23.3	.77	.02
Radiation dose (cGy × cm^2)	10,319 ± 7108	11,899 ± 9142	.55	.03
Contrast (mL)	151 ± 68	145 ± 72	.59	.70

Note:—DL indicates Dual-Layer; SLS, Single-Layer Sphere.
[a] Data are number and percentage of means.

Table 3: Immediate angiographic results

	WEB 17 (*n* = 38)	pWEB (*n* = 70)	*P* Value	Adjusted *P* Value
Complete occlusion (RROC 1)	22 (57.9%)	38 (54.3%)	.55	.21
Neck remnant (RROC 2)	8 (21.1%)	11 (15.7%)		
Aneurysm remnant (RROC 3)	8 (21.1%)	21 (30.0%)		

Note:—RROC indicates Raymond-Roy occlusion classification.

Table 4: Procedure-related complications

	WEB 17 (*n* = 38)	pWEB (*n* = 70)	*P* Value	Adjusted *P* Value
Thromboembolic events	2 (5.3%)	10 (14.3%)	.21	.002
Ischemic stroke	1 (2.6%)	5 (7.1%)	.42	.06
Hemorrhagic complications	2 (5.3%)	1 (1.4%)	.28	.37
Neurologic complications	1 (2.6%)	2 (2.9%)	1.0	1.0

propensity score model, achieving comparable groups regarding all baseline characteristics (Table 1).

Aneurysm Treatment

Procedural specifics are detailed in Table 2. Implantation of the WEB 17 was technically successful in all aneurysms (38/38, 100%), compared with 8 treatment failures in the pWEB group (8/78, 10.3%, $P = .052$). Failed WEB implantation was recorded at the anterior communicating artery ($n = 3$), paraophthalmic regions of the internal carotid artery ($n = 3$), middle cerebral artery bifurcation ($n = 1$), and basilar apex ($n = 1$). The mean aneurysm size ranged from 3.3 to 6.9 mm. Reasons for failed implantation were WEB protrusion with impeded blood flow ($n = 3$), WEB malposition ($n = 3$), and delivery failure due to a sharp aneurysm angle in sidewall aneurysms ($n = 2$). Aneurysms with failed WEB implantation were excluded from further analysis as stated above. Of 108 included aneurysms, 98 (90.7%) were treated by the WEB only, 36 (94.7%) were in the WEB 17 group, and 62 (88.6%) were in the pWEB group ($P = .489$). In both groups, adjunctive coils were used in 1 patient to achieve immediate complete aneurysm occlusion, respectively. Additional stent placement was performed more often after implantation of predecessor WEBs (7/70, 10.0%) than after embolization with the WEB 17 (1/38, 2.6%). This difference was not significant in the unweighted analysis ($P = .256$) but became significant after IPTW adjustment ($P = .005$).

The smallest WEB 17 version, the WEB SL 3 × 2 mm, was used for treatment of 3 small wide-neck aneurysms with a maximum diameter ranging from 3 to 3.3 mm. The aneurysms were located at the AcomA, the basilar apex, and the M1 segment of the MCA, respectively. Navigation and delivery of the WEB were smooth in all cases, resulting in immediate complete occlusion in 2 cases and 1 neck remnant, without any incidence of adverse events. In a fourth case, a 7-mm large, bilobed AcomA aneurysm was treated, and the WEB SL 3 × 2 was used to occlude 1 aneurysm lobe, while the second lobe was embolized with 3 coils.

The average treatment duration was 128 ± 67 minutes, 122 ± 67 minutes for the WEB 17 and 133 ± 67 minutes for WEB controls ($P = .475$). The mean fluoroscopy time was 26.8 ± 22.2 minutes, 25.4 ± 20.1 minute for the WEB 17 and 27.6 ± 23.3 minutes for the pWEB ($P = .765$). The mean radiation dose was 11331 ± 8466 cGy × cm^2, 10319 ± 7108 cGy × cm^2 for the WEB 17 and 11899 ± 9142 cGy × cm^2 for the pWEB ($P = .552$). On average, 146 ± 70 mL of contrast was used, 151 ± 68 mL for the WEB 17 and 145 ± 72 mL for the pWEB ($P = .585$). After IPTW adjustment, treatment with the WEB 17 was associated with significantly shorter treatment duration ($P = .007$), shorter fluoroscopy time ($P = .016$), and reduced radiation exposure ($P = .031$) compared with predecessor WEBs.

Bivariate correlation analysis showed no significant correlation between treatment date and treatment duration ($r = -0.08$, adjusted $P = .36$) and radiation exposure ($r = -0.05$, adjusted $P = .5$).

Angiographic Outcome

Immediate complete occlusion after WEB implantation was obtained in 60 aneurysms (55.6%); neck remnants, in 19 (17.6%); and aneurysm remnants, in 29 (26.9%). Immediate occlusion rates were not significantly different between both treatment groups, either in the unweighted ($P = .55$) or the weighted analysis ($P = .21$) (Table 3).

Complications

Procedural complications are detailed in Table 4. In the WEB 17 group, there were 2 thromboembolic events (5.3%). In the first

case, a patient was treated for a ruptured PICA aneurysm. After the procedure, the patient had transient hemianopsia. The CT scan showed a partial posterior infarction of the posterior cerebral artery, which occurred most likely due to thromboembolism during WEB placement. In the second patient, implantation of a WEB into an unruptured AcomA aneurysm resulted in stenosis of the left A2 segment, which could be reopened by additional stent implantation. The patient did not have any symptoms after the procedure.

Furthermore, there were 2 hemorrhagic events (5.3%) related to the WEB 17 implantation. The first patient was treated for an unruptured aneurysm and had a subarachnoid hemorrhage from a proximal perforating artery, which probably ruptured due to manipulation of the microwire. The patient was discharged to a rehabilitation center with persisting mild hemiparesis. In the second case, perforation of an unruptured AcomA aneurysm occurred during device delivery; however, the bleeding was stopped immediately by WEB implantation and the patient did not have any symptoms.

The overall neurologic complication rate after WEB 17 implantation was 2.6%, and there was no procedure-related mortality.

The WEB 17 was associated with a lower thromboembolic event rate (5.3%) compared with the pWEB (14.3%, $P = .208$). After adjustment for the propensity score, this difference was statistically significant ($P = .002$). Moreover, there was a borderline significant trend toward a higher ischemic stroke rate after pWEB placement in the weighted analysis ($P = .055$). In the subgroup analysis of the pWEB group, thromboembolic events occurred tendentially more often in ruptured aneurysms (25%, 6/24) than in unruptured aneurysms (8.9%, 4/46, $P = .08$). The neurologic complication rate was similar between both groups (WEB 17: 2.6%; pWEB: 2.9%; $P = 1.0$, adjusted $P = 1.0$).

DISCUSSION

In the current study, we evaluated the treatment of small aneurysms ($\leq$7 mm) with the new low-profile WEB 17 and compared the results with predecessor WEB systems. To produce reliable results and to address a potential selection bias, we performed a separate IPTW analysis using propensity scores.

Small aneurysms located at a bifurcation represent a technical challenge for endovascular therapy, even when using the WEB device.[20] Moreover, the WEB is difficult to deliver to distally located aneurysms because it requires deployment by a relatively large microcatheter.

The WEB 17 consists of a reduced number of nitinol wires and can be delivered through a VIA 17 microcatheter, which is less rigid than the predecessor VIA 21. The flexible design of the WEB 17 system facilitates navigation through tortuous vessels and sharp-angled branching points. Besides navigation to more distally located aneurysms, reducing the delivery diameter of the WEB system may also facilitate the treatment of sidewall aneurysms, which can be difficult to treat with the more rigid 0.021-inch system. In a previous study on ICA sidewall aneurysms, we reported deployment failure due to malrotation of the device after delivery of the pWEB in 2 aneurysms with sharp aneurysm angles.[21] Because WEB positioning could not be improved, the WEBs were finally removed and the aneurysms were treated with standard coiling. We speculate that treatment of these aneurysms would have been possible with the low-profile WEB 17.

In our study, WEB 17 implantation was technically successful in all cases. In contrast, there were 8 treatment failures in the WEB 21 group (10.3%). Although this difference might be partially related to increased operator experience during WEB 17 implantation, it indicates the high feasibility of WEB 17 treatment.

To date, there are 2 available studies on the WEB 17. Van Rooij et al[19] analyzed 46 aneurysms and reported a technical success rate of 100%. Similar technical success was reported by Mihalea et al[22] in a study of 28 aneurysms. Both authors reported that handling the WEB 17 was smoother compared with predecessor versions and required less push and pull forces. However, the authors also acknowledged that the WEB 17 is more susceptible to deformation during delivery because it has fewer and thinner nitinol wires, resulting in a weaker structure and shape retention. These properties can result in malposition and neck remnants after delivery, which may require WEB repositioning and repeat deployment. Thus, Mihalea et al recommended validating the WEB position with VasoCT (Philips Healthcare) immediately after deployment.[22]

Our data corroborate the subjective ease of navigation and deployment of the WEB 17. Generally, positioning the WEB 17 was feasible, as reflected by a 100% technical success rate and a reduced use of intracranial stents, which were typically implanted if a WEB protruded into the parent vessel lumen. In our experience, repositioning the WEB 17 was not generally necessary, and immediate angiographic results were comparable with those with the predecessor WEB systems. Our results indicated that treatment with the WEB 17 was associated with reduced treatment duration, fluoroscopy time, and radiation exposure, which became significant after IPTW adjustment. Although we could not show a significant correlation between treatment date and treatment duration or radiation exposure, the differences in additional stent implantation and shorter treatment duration may be, in part, attributed to increasing operator experience during the study period, thus potentially favoring the WEB 17 group. However, in our experience, the WEB 17 system is more flexible and has a better conformability than the predecessor versions. Due to a comparably rigid design of the nitinol wires, the predecessor WEBs might have been more likely to protrude into the parent artery, in particular in cases in which the aneurysm axis deviates greatly from the vessel axis. In contrast, we observed that the WEB 17 generally adapts to the aneurysm wall very smoothly, showing a lower tendency to alter aneurysm geometry and to cause parent artery stenosis. Although a direct statistical comparison is difficult, our data support the impression that navigation and deployment of the WEB 17 may be smoother than in the predecessor WEB versions.

In the present study, we treated 3 very small aneurysms on the order of 3 mm with the new WEB SL 3 $\times$ 2 mm. Two were located at a bifurcation; and 1, at the M1 segment. In all cases, the device could be deployed smoothly, and adverse events did not occur. Immediate angiographic control showed complete occlusion in 2 cases and a neck remnant in the third case.

Thromboembolism is considered the most prevalent event related to WEB implantation.[18] Muskens et al[23] performed a meta-analysis on 718 aneurysms treated with the WEB before the introduction of the WEB 17 system and reported a thromboembolic event rate of 10.3%. Because most thromboembolic events remain asymptomatic, the WEB constitutes a safe treatment option with major morbidity and mortality as low as 3% and 2%, respectively.[24] In the current study, the safety results of the WEB control group are within the range cited previously, with thromboembolic events occurring in 14.3% and neurologic complications in 2.9%.[15,18,23]

In the comparative analysis, the thromboembolic event rate in the WEB 17 group was 5.3% and thus was much lower than in the WEB control group. This might be, in part, related to a smaller portion of aneurysms treated in combination with intracranial stents. Beyond that, a lower profile of all materials used, ease of use, and shorter procedure times associated with the WEB 17 system favor reducing the potential for thromboembolic events. Among intracranial stents and flow diverters, several in vivo and ex vivo studies have already suggested that miniaturization of the stent design and the delivery system may reduce the thrombogenicity of the device.[25-28] Hence, miniaturization of the WEB system might also contribute to reduced thrombogenicity of the system. Moreover, we observed that the WEB 17 showed a reduced tendency to protrude into the parent vessel, though we did not quantify this aspect. Finally, a slightly higher portion of ruptured cases in the pWEB group may also contribute to a higher thromboembolic event rate.[29]

In previous studies, similar results were obtained. The thromboembolic event rate was 4% in the study by Mihalea et al[22] and 5% in the study by van Rooij et al.[19]

These findings collectively suggest a high procedural safety profile of the WEB 17 system. Because treatment of small bifurcation aneurysms proved to be highly efficacious and could be achieved more smoothly than with predecessor WEB versions, we believe the WEB 17 system is a highly valuable adjunct to the neurointerventional armamentarium, and we have been using the WEB 17 exclusively for small aneurysms of <7 mm. Additional studies will be required to further expand the indications of the WEB 17.

Limitations

Our study has several limitations. Although we performed a multicenter study, the sample size was only moderate and data were collected retrospectively, making a generalization of the data difficult. To mitigate this limitation in part and to minimize a potential selection bias, we performed an IPTW approach based on propensity scores. Patients were not consecutive but were selected on the basis of the mentioned inclusion criteria and the anticipated suitability for WEB treatment. Because the introduction of the WEB 17 is relatively recent, angiographic follow-up is incomplete and was not reported in the current study. A further limitation is that aneurysm occlusion was not determined by a core laboratory, which might bias the interpretation of the angiographic results.[30] To reduce this potential bias at least in part, all angiographic images were assessed blinded and independently by 3 experienced consultant neurointerventionalists (C.K., F.D., E.S.). Discrepancies were resolved by consensus. Finally, increased operator experience may have favored the WEB 17 group in terms of complication rates and treatment duration.

CONCLUSIONS

Deployment of the new low-profile WEB 17 in small aneurysms was generally smooth and required less stent assistance than the predecessor WEB versions. The VIA 17 facilitates microcatheter navigation toward the target vessel, especially in situations with a complex vascular anatomy. If procedural time and the amount of radiation exposure can be used as surrogate parameters to measure ease of use, then the WEB 17 is a definite improvement over the pWEB. Finally, the thromboembolic event rate of the WEB 17 was lower compared with predecessor WEBs, seemingly without compromising treatment efficacy. These features make the WEB 17 a valuable adjunct to the existing WEB range and expand indications to very small aneurysms.

REFERENCES

1. Sivan-Hoffmann R, Gory B, Riva R, et al. **One-year angiographic follow-up after WEB-SL endovascular treatment of wide-neck bifurcation intracranial aneurysms.** *AJNR Am J Neuroradiol* 2015;36:2320–24 CrossRef Medline
2. Lubicz B, Mine B, Collignon L, et al. **WEB device for endovascular treatment of wide-neck bifurcation aneurysms.** *AJNR Am J Neuroradiol* 2013;34:1209–14. CrossRef Medline
3. Pierot L, Klisch J, Liebig T, et al. **WEB-DL endovascular treatment of wide-neck bifurcation aneurysms: long-term results in a European series.** *AJNR Am J Neuroradiol* 2015;36:2314–19 CrossRef Medline
4. Ding Y, Lewis D, Kadirvel R, et al. **The Woven EndoBridge: a new aneurysm occlusion device.** *AJNR Am J Neuroradiol* 2011;32:607–11 CrossRef Medline
5. Kabbasch C, Goertz L, Siebert E, et al. **WEB embolization versus stent-assisted coiling: comparison of complication rates and angiographic outcomes.** *J Neurointerv Surg* 2019;11:812–16 CrossRef Medline
6. Kabbasch C, Goertz L, Siebert E, et al. **Comparison of WEB embolization and coiling in unruptured intracranial aneurysms: safety and efficacy based on a propensity score analysis.** *World Neurosurg* 2019 Mar 9. [Epub ahead of print] CrossRef Medline
7. Fiorella D, Molyneux A, Coon A, et al. **Demographic, procedural and 30-day safety results from the WEB Intra-saccular Therapy Study (WEB-IT).** *J NeuroIntervent Surg* 2017;40:1191–96 CrossRef Medline
8. Pierot L, Gubucz I, Buhk J, et al. **Safety and efficacy of aneurysm treatment with the WEB: results of the WEBCAST 2 study.** *AJNR Am J Neuroradiol* 2017;38:1151 CrossRef Medline
9. Pierot L, Costalat V, Moret J, et al. **Safety and efficacy of aneurysm treatment with WEB: results of the WEBCAST study.** *J Neurosurg* 2016;124:1250–56 CrossRef Medline
10. Pierot L, Moret J, Turjman F, et al. **WEB treatment of intracranial aneurysms: clinical and anatomic results in the French Observatory.** *AJNR Am J Neuroradiol* 2016;37:655–59 CrossRef Medline
11. Goertz L, Liebig T, Siebert E, et al. **Risk factors of procedural complications related to Woven EndoBridge (WEB) embolization of intracranial aneurysms.** *Clin Neuroradiol* 2019 Feb 7. [Epub ahead of print] CrossRef Medline
12. Kabbasch C, Goertz L, Siebert E, et al. **Factors that determine aneurysm occlusion after embolization with the Woven EndoBridge (WEB).** *J Neurointerv Surg* 2018 Feb 7. [Epub ahead of print] CrossRef Medline

13. Kabbasch C, Goertz L, Siebert E, et al. **Treatment strategies for recurrent and residual aneurysms after Woven Endobridge implantation.** *J Neurointerv Surg* 2018;11:390–95 CrossRef Medline
14. Arthur AS, Molyneux A, Coon AL, et al. **The safety and effectiveness of the Woven EndoBridge (WEB) system for the treatment of wide-necked bifurcation aneurysms: final 12-month results of the pivotal WEB Intrasaccular Therapy (WEB-IT) Study.** *J Neurointerv Surg* 2019 Apr 16. [Epub ahead of print] CrossRef Medline
15. Lawson A, Molyneux A, Sellar R, et al. **Safety results from the treatment of 109 cerebral aneurysms using the Woven EndoBridge technique: preliminary results in the United Kingdom.** *J Neurosurg* 2018;128:144–53 CrossRef Medline
16. Pierot L, Moret J, Turjman F, et al. **WEB treatment of intracranial aneurysms: feasibility, complications, and 1-month safety results with the WEB DL and WEB SL/SLS in the French Observatory.** *AJNR Am J Neuroradiol* 2015;36:922–27 CrossRef Medline
17. Popielski J, Berlis A, Weber W, et al. **Two-center experience in the endovascular treatment of ruptured and unruptured intracranial aneurysms using the WEB device: a retrospective analysis.** *AJNR Am J Neuroradiol* 2018;39:111–17 CrossRef Medline
18. Tau N, Sadeh-Gonik U, Aulagner G, et al. **The Woven EndoBridge (WEB) for endovascular therapy of intracranial aneurysms: update of a systematic review with meta-analysis.** *Clin Neurol Neurosurg* 2018;166:110–15 CrossRef Medline
19. van Rooij S, Peluso J, Sluzewski M, et al. **The new low-profile WEB 17 system for treatment of intracranial aneurysms: first clinical experiences.** *AJNR Am J Neuroradiol* 2018;39:859–63 CrossRef Medline
20. Asnafi S, Rouchaud A, Pierot L, et al. **Efficacy and safety of the Woven EndoBridge (WEB) device for the treatment of intracranial aneurysms: a systematic review and meta-analysis.** *AJNR Am J Neuroradiol* 2016;37:2287–92 CrossRef Medline
21. Goertz L, Liebig T, Siebert E, et al. **Extending the indication of Woven EndoBridge (WEB) embolization to internal carotid artery aneurysms: a multicenter safety and feasibility study.** *World Neurosurg* 2019 Mar 12. Epub ahead of print] CrossRef Medline
22. Mihalea C, Caroff J, Pagiola I, et al. **Safety and efficiency of the fifth generation Woven EndoBridge device.** *J NeuroInterv Surg* 2019; 11:511–15 CrossRef Medline
23. Muskens IS, Senders JT, Dasenbrock HH, et al. **The Woven Endobridge device for treatment of intracranial aneurysms: a systematic review.** *World Neurosurg* 2017;98:809–17.e1 CrossRef Medline
24. Lv X, Zhang Y, Jiang W. **Systematic review of Woven EndoBridge for wide-necked bifurcation aneurysms: complications, adequate occlusion rate.** *World Neurosurg* 2018;110:20–25 CrossRef Medline
25. Kraus B, Goertz L, Turowski B, et al. **Safety and efficacy of the Derivo Embolization Device for the treatment of unruptured intracranial aneurysms: a multicentric study.** *J NeuroInterv Surg* 2019;11:68–73 CrossRef Medline
26. Ley D, Mühl-Benninghaus R, Yilmaz U, et al. **The Derivo embolization device, a second-generation flow diverter for the treatment of intracranial aneurysms, evaluated in an elastase-induced aneurysm model.** *Clin Neuroradiol* 2017;27:335–43 CrossRef Medline
27. Jankowitz BT, Hanel R, Jadhav AP, et al. **Neuroform Atlas Stent System for the treatment of intracranial aneurysm: primary results of the Atlas Humanitarian Device Exemption cohort.** *J NeuroInterv Surg* 2019;11:801–06 CrossRef Medline
28. Brassel F, Grieb D, Meila D, et al. **Endovascular treatment of complex intracranial aneurysms using Acandis Acclino stents.** *J Neurointerv Surg* 2017;9:854–59 CrossRef Medline
29. Liebig T, Kabbasch C, Strasilla C, et al. **Intrasaccular flow disruption in acutely ruptured aneurysms: a multicenter retrospective review of the use of the WEB.** *AJNR Am J Neuroradiol* 2015;36:1721–27 CrossRef Medline
30. Rezek I, Lingineni R, Sneade M, et al. **Differences in the angiographic evaluation of coiled cerebral aneurysms between a core laboratory reader and operators: results of the Cerecyte Coil Trial.** *AJNR Am J Neuroradiol* 2014;35:124–27 CrossRef Medline

Predicting Factors of Angiographic Aneurysm Occlusion after Treatment with the Woven EndoBridge Device: A Single-Center Experience with Midterm Follow-Up

F. Cagnazzo, R. Ahmed, R. Zannoni, C. Dargazanli, P.-H. Lefevre, G. Gascou, I. Derraz, C. Riquelme, A. Bonafe, and V. Costalat

ABSTRACT

BACKGROUND AND PURPOSE: Flow disruption with the Woven EndoBridge is increasingly used for the treatment of intracranial aneurysms. We examined factors leading to aneurysm occlusion and Woven EndoBridge shape change during a midterm follow-up.

MATERIALS AND METHODS: Patients with a minimum 12-month angiographic follow-up were included. Through a univariate and multivariate analysis, independent predictors of adequate occlusion (Raymond-Roy 1/Raymond-Roy 2) and Woven EndoBridge shape change (decrease of the height of the device) were assessed.

RESULTS: Eighty-six patients/aneurysms were included. The aneurysm mean size was 5.5 mm (range, 3–11.5 mm). The most common locations were the MCA (43/86 = 50%), basilar tip (13/86 = 15.1%), and anterior communicating artery (12/86 = 14%). Twenty-one patients (21/86 = 24%) had acute SAH. Immediate and long-term Raymond-Roy 1/Raymond-Roy 2 occlusion rates were 49% (42/86) and 80% (68/86), respectively. Woven EndoBridge shape change was detected among 22% (19/86) of cases. At binary logistic regression, wide ostium (≥4 mm) (OR = 0.2; 95% CI, 0.01–1; $P = .04$) and regular aneurysm morphology (OR = 5.9; 95% CI, 1.4–24; $P = .01$) were independent factors of incomplete and adequate aneurysm occlusion, respectively. In addition, irregular morphology (OR = 5.4; 95%CI , 1.4–19; $P = .01$) and a wide ostium (OR = 9.8; 95% CI, 1.6–60; $P = .03$) significantly increased the probability of the Woven EndoBridge shape change. Decrease of the Woven EndoBridge height was more common among incompletely occluded aneurysms (6/12 = 50% versus 13/74 = 17.5%), but it was not an independent prognosticator of occlusion at the multivariate model.

CONCLUSIONS: The likelihood of good occlusion was 5 times lower in the presence of a wide ostium, whereas aneurysms with regular morphology were 6 times more likely to be occluded. Woven EndoBridge shape modification was strongly influenced by the aneurysm shape and ostium size, and it was not independently associated with the angiographic occlusion.

ABBREVIATIONS: AcomA = anterior communicating artery; BT = basilar tip; RR = Raymond-Roy

The efficacy and safety of the Woven EndoBridge device (WEB; Sequent Medical, Aliso Viejo, California) have been largely evaluated by several multicentric trials.[1] Treatment with the WEB resulted in approximately 80% of complete/near-complete occlusion in many published series.[1-3] However, as reported in some recent studies,[2,4] aneurysm recurrence and WEB compaction may occur in nearly 8% and 40% of patients, respectively. Despite the increased operator experience and the better patient selection, factors leading to aneurysm occlusion, recanalization, or WEB shape modification are not fully understood. Very few studies explored patient and aneurysm characteristics potentially associated with the angiographic results after WEB implantation. Our study aimed to investigate independent predictors of adequate aneurysm occlusion and WEB shape modification among 86 patients/aneurysms available during midterm angiographic follow-up.

MATERIALS AND METHODS

Patient Selection

Our hospital institutional review board approved this retrospective study. A prospectively maintained data base of WEBs (2014–2019) was retrospectively reviewed by 2, and in case of inconsistency, by 3 investigators independently. We included patients with aneurysms (unruptured or ruptured) treated with the WEB and available at midterm angiographic follow-up (at least 12 months). To assess factors associated with midterm aneurysm

Received June 10, 2019; accepted after revision August 5.

From the Neuroradiology Department, University Hospital Güi-de-Chauliac, Centre Hospitalier Universitaire de Montpellier, Montpellier, France.

Please address correspondence to Federico Cagnazzo, MD, Neuroradiology Department, CHU Gui De Chauliac, 80 Ave Augustin Fliche, 34000 Montpellier, France; e-mail: f.cagnazzo86@gmail.com

Indicates article with supplemental on-line appendix and tables.

http://dx.doi.org/10.3174/ajnr.A6221

occlusion, we excluded patients with a radiologic follow-up of <12 months. Recanalized aneurysms for which the WEB was used as retreatment strategy were excluded. Indications for treatment were made by multidisciplinary consensus (vascular neurosurgeons, interventional neuroradiologists).

Indications for WEB

The selection of aneurysms treated with the WEB was performed by interventional neuroradiologists according to aneurysm characteristics and available sizes of the device. The main indications for WEB treatment were the following: 1) unruptured and ruptured wide-ostium aneurysms difficult to treat with simple coiling; 2) aneurysms located at bifurcation points not amenable to treatment with coiling or balloon-assisted coiling and where a flow diverter may lead to the risk of covering bifurcation branches or perforators. In addition, due to the progressive enlargement of WEB indications[5] and on the basis of our own positive results, some small-neck or small-sized aneurysms were treated with the WEB.

Antiplatelet Therapy

For unruptured aneurysms, patients were premedicated with dual antiplatelet therapy in case of a strategy shift to stent-assisted technique (aspirin, 75 mg, and clopidogrel, 75 mg, starting 5 days before treatment). Daily aspirin administration was continued for 1 month. In case of additional stent placement, the dual antiplatelet therapy was maintained for 3 months, and on the basis of the clinical and radiologic evaluation, the patients were switched to aspirin. The VerifyNow P2Y12 assay (Accumetrics, San Diego, California) was used to test the platelet inhibition (P2Y12 reaction unit). Concurrent with the procedure, intravenous heparinization was performed (activated clotting time of >250 seconds).

For ruptured aneurysms, apart from heparin in the pressure bags for flushing (1000 IU/L), no antiplatelet therapy was used. In case of stent placement, an intravenous bolus of abciximab (0.125 mg/kg) was administered before stent deployment, and standard dual antiplatelet therapy was started the day after.

Description of Technique

With the patient under general anesthesia, via a transfemoral approach, access to the aneurysm was obtained in a triaxial fashion. Through a long femoral sheath, a 6F guiding catheter was advanced into the carotid artery. The WEB was delivered under roadmap guidance through the dedicated VIA microcatheter (Sequent Medical). Most of the implanted WEBs were single-layer (SL): accordingly, we included only SL devices. VasoCT (Philips Healthcare, Best, the Netherlands) with diluted iodinated contrast medium was used to assess WEB apposition.

Selection of WEB Size

Size selection derived from the measurements of the aneurysm on 3D rotational angiography (width and height of the dome outside of additional blebs and daughter aneurysms). In general, on the basis of the rule of the manufacturer, the device was chosen adding 1 mm to the average width (to ensure good wall apposition) and subtracting 1 mm from the average height of the aneurysm (to adjust for the longitudinal increase caused by the horizontal compression).[6] Starting in 2017, WEB devices were selected using a computer-based-simulation modeling tool (Sim&Size software; Sim&Cure; Grabels, France).

Imaging Assessment

Anatomic and angiographic results were independently evaluated by 2 interventional neuroradiologists not directly involved in patient treatment. A senior interventional neuroradiologist solved discrepancies.

Aneurysm occlusion and WEB shape modification were evaluated on the DSA performed at least at 12-month follow-up. The aneurysm occlusion rate was defined on the basis of the Raymond-Roy (RR) classification: complete occlusion (class 1), residual ostium (class 2), and residual aneurysm (class 3).[7]

After WEB deployment, the size of the device was evaluated as "adequate" or "undersized." There were no cases of oversized devices resulting in WEB protrusion over the ostium. A detailed definition of undersized and adequately sized devices is reported in the On-line Appendix.

Aneurysm shape was dichotomized into regular (when the surface was smooth and regular in the 3D angiography) and irregular (in case of blebs or multilobular shape).

WEB shape change (also called "compaction") was defined as a decrease in the height of the device or a deepening of the proximal and distal concave recesses during follow-up:[8] It was analyzed on nonsubtracted images. Methods to evaluate WEB changes are reported in the On-line Appendix.

Statistical Analysis

Categoric data were described by frequency, whereas quantitative data, by means and SDs. We assessed the following: 1) long-term angiographic aneurysm occlusion ("adequate occlusion" [RR 1/RR 2] versus "incomplete occlusion"[RR 3]); and 2) WEB shape modification (yes versus no) during midterm follow-up. A χ^2 test was used to evaluate qualitative factors: vascular risk factors, location, ruptured status, bifurcation point versus sidewall, aneurysm shape, wide ostium (≥4 versus <4 mm), vessel coming from the aneurysm, additional stent placement, WEB shape modification, immediate aneurysm occlusion, and correctly sized versus undersized devices. The *t* test (2-tailed) was applied to assess quantitative factors (age, aneurysm dome size, dome/ostium ratio, aspect ratio). The independent variables significantly associated ($P \leq .1$ in the univariate analysis) with adequate occlusion or WEB shape modifications were analyzed together in a binary logistic regression to assess the independent contribution of each factor. The results of the regression model were calculated with the Wald test and expressed using a *P* value and related odds ratio. All statistical analyses, descriptive and inferential, were performed with SPSS, Version 24 (IBM, Armonk, New York).

RESULTS

Baseline Population and Aneurysm Characteristics

In the 5-year period, 130 consecutive aneurysms/patients were treated with the WEB (detailed data in On-line Table 1). We extracted 86 patients (58 women, 28 men; mean age, 61 years; range, 35–76 years) available at midterm angiographic follow-up. Twenty-one patients (24%) were treated in the setting of acute

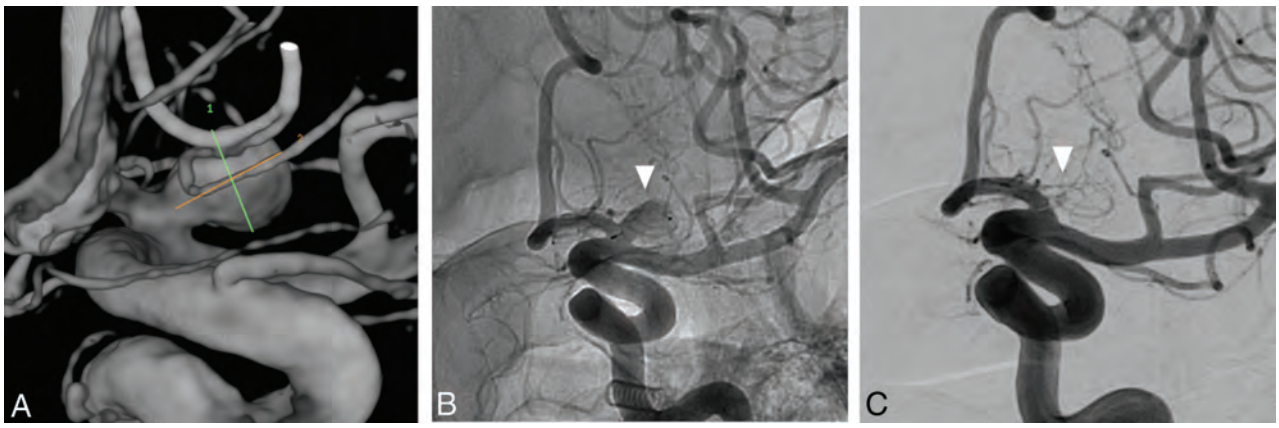

FIG 1. *A*, Left ICA angiography depicting an unruptured saccular aneurysm with regular morphology originating from the proximal A1 segment. The aneurysm dome, height, and ostium diameters were 6, 7, and 3 mm (small ostium), respectively. Accordingly, this aneurysm had all the predicting factors of adequate occlusion. *B*, A WEB-SLS (7 mm) was opened inside the sac, with a good aneurysm wall apposition (*white arrowhead*). *C*, Twelve-month DSA follow-up shows complete occlusion of the aneurysm (*white arrowhead*).

SAH. The mean aneurysm dome size was 5.5 ± 1.9 mm; range, 3–11.5 mm), and the most common location was the MCA bifurcation (43/86 = 50%), followed by the basilar tip (BT) (13/86 = 15%) and the anterior communicating artery (AcomA) (12/86 = 13.9%).

Treatment Characteristics and Technical Results

The WEB-SL was used in all cases (On-line Table 2). The WEB-SL and WEB-Single-Layer Sphere (SLS) were used in 90.6% (78/86) and 8.4% (8/86) of patients, respectively. Additional stent placement was performed in 13 cases (13/86 = 15%).

Successful WEB deployment was achieved in all cases. The mean intervention and fluoroscopy times were 66 ± 17 minutes (range, 50–103 minutes) and 30 ± 12 minutes (range, 18–60 minutes), respectively.

Angiographic Outcome of Aneurysms

The mean angiographic follow-up was 17 ± 11.5 months; range, 12–32 months) (On-line Table 2). Immediately after treatment, RR 1/RR 2 occlusion was 48.8% (42/86). At 12-month follow-up, 49/86 (57%) and 19/86 (22%) aneurysms presented with complete occlusion and ostium remnants, respectively. The proportion of RR 1 and RR 2 occlusion was close to 49% and 33% at the 24-month follow-up (60 patients available), respectively. Overall, 51/86 (59%) WEBs were defined as adequately sized, whereas 35/86 (41%) were classified as undersized devices.

WEB shape change was detected among 22% of cases (19/86): 7% (6/86), 15% (13/86), and 0% (0/60) at 6-, 12-, and 24-month follow-up, respectively. Retreatment with additional stent and coiling was required in 11/86 recanalized aneurysms (13%).

Predictors of Adequate Occlusion and WEB Shape Change

Significant predictors of occlusion and WEB shape change at univariate analysis were further analyzed in multivariable logistic regression (On-line Tables 3 and 4). Regular shape (OR = 5.9; 95% CI, 1.4–24; $P = .01$) was an independent predictor of good occlusion, whereas a wide ostium (OR = 0.2; 95% CI, 0.01–1; $P = .04$) was an independent factor in incomplete occlusion.

Irregular shape (OR = 5.4; 95% CI, 1.4–19; $P = .01$) and a wide ostium (OR = 9.8; 95% CI, 1.6–60; $P = .03$) independently influenced the likelihood of WEB shape change at follow-up. Higher aneurysm dome size (continuous variable) showed a trend toward greater WEB shape modification (OR = 1.39; 95% CI, 0.9–1.6; $P = .06$).

DISCUSSION

Predictors of Angiographic Occlusion

Consistent with the literature of WEB devices reporting 80% adequate occlusion at 1 year,[3,9] in our series, RR 1/RR 2 occlusion was 79% and 81% after 12- and 24-month DSA follow-up. Kabbasch et al,[10] evaluating a series of 98 aneurysms treated with the WEB, reported dome size, intra-aneurysmal thrombosis, and additional coiling as factors associated with lower occlusion at 6-month follow-up. Another recent series of 24 aneurysms reported that ostium size and dome-to-ostium ratio were significantly related to the angiographic results after WEB treatment.[2] To our knowledge, there are no studies investigating independent predictors of occlusion after treatment with WEB devices. In our series of 86 patients, eliminating the influence of potential confounders using the regression model showed that ostium diameter and aneurysm shape were the only independent predictors of occlusion. Among the subgroup of adequately occluded aneurysms, 60% had a diameter of the ostium <4 mm (Fig 1), whereas 40% had a diameter of the ostium ≥4 mm. In addition, wide-ostium lesions represented 91% of the incompletely occluded aneurysms (Fig 2). Therefore, the binary logistic regression revealed that a wide ostium indicated 80% reduction in the probability of achieving long-term good occlusion after WEB treatment (OR = 0.2; 95% CI, 0.01–1; $P = .04$).

Lower occlusion rates among lesions with a wide ostium are likely related to the following reasons: 1) Ostium coverage might be more difficult among large-ostium lesions; and 2) the higher hemodynamic impact of blood flow may decrease the intrasaccular thrombosis or may promote WEB displacement toward the aneurysm fundus. Hemodynamic studies showed that intra-

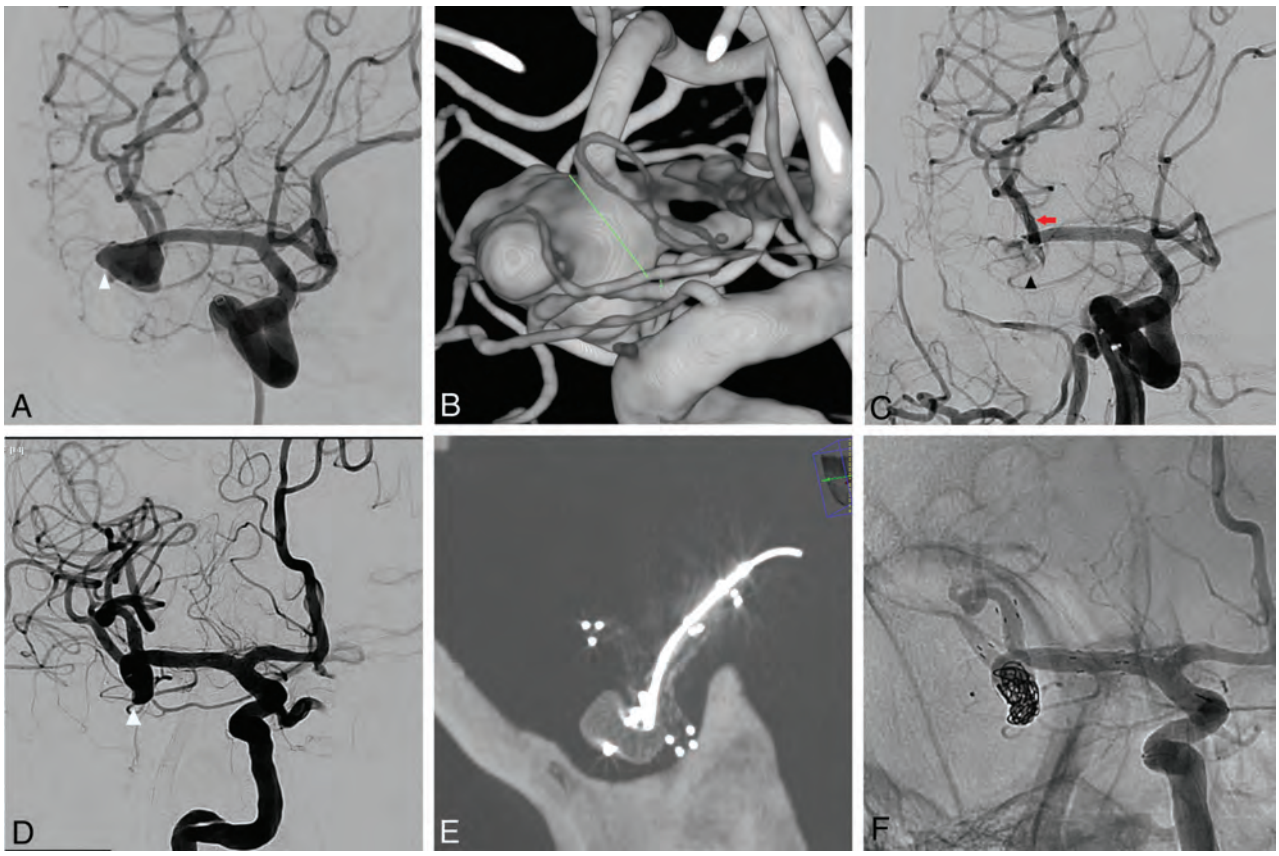

FIG 2. *A*, Right ICA angiography showing an irregular 9 (dome) × 5 mm (height) MCA unruptured aneurysm (*white arrowhead*) with a wide ostium (6 mm) (*B*). *C*, A WEB-SL (10 × 5) was delivered inside the sac (*black arrowhead*). Subsequently, in the same treatment session, a Neuroform Atlas (Stryker Neurovascular, Kalamazoo, Michigan) 3 × 20 (*red arrow*) was implanted from the M1 to the M2 (superior division branch) due to a small WEB protrusion into the vessel. *D*, Twelve-month DSA follow-up shows aneurysm recanalization (*white arrowhead*). This aneurysm presented with all the risk factors (wide ostium and irregular shape) for incomplete occlusion. *E*, Flat panel CT reconstruction depicts WEB shape modification (compaction) and the deployment of a second Neuroform Atlas 3 × 20 with a jailed microcatheter inside the sac. *F*, The residual aneurysm was completely occluded after Y-stent placement assisted coiling.

aneurysmal blood flow was faster when the aneurysm neck was wider.[11] The presence of a wide neck has been previously reported as a factor associated with lower occlusion rates after coiling.[12] Accordingly, higher intra-aneurysmal blood flow among lesions with a wide ostium may contribute, at least in theory, to the lower occlusion rate after WEB treatment. When one investigates the literature about other treatment options, a wide ostium appears significantly associated with aneurysm recanalization after coiling,[13] whereas aneurysm size and incorporation of a branch vessel predicted persistence after flow diversion.[14] Most interesting, in our analysis, aneurysm size and vessels coming from the aneurysm were not predictors of recanalization after WEB treatment. It is likely that size did not influence the angiographic occlusion due to the relatively small range of aneurysm dome size in our study (from 3 to 11 mm). Conversely, Bender et al[14] reported a larger size as a predictor of lower occlusion after flow diversion, including a larger range of aneurysm diameters (from 1 to 31 mm). Finally, the distal hemodynamic demand through the branching vessel will likely maintain the flow across the ostium, lowering the occlusion in case of flow-diverter devices, but not impacting intrasaccular thrombosis after WEB implantation.

The second independent predictor of occlusion was aneurysm shape: Aneurysms with regular morphology were 6 times more likely to be occluded at 12-month follow-up (Fig 1), compared with lesions presenting with an irregular sac (OR = 5.9; 95% CI, 1.4%–24%; $P = .01$) (Fig 2). Our study is the first highlighting shape as prognosticator of occlusion after the WEB treatment. In our experience, among irregular lesions, the more difficult selection of the appropriate WEB dimension, together with the incomplete apposition of the device on the aneurysm wall and ostium, may decrease the likelihood of good occlusion.

Although undersized WEBs were more represented among the group of incompletely occluded aneurysms (58% versus 34%), adequate sizing and undersizing were not significant predictors of the angiographic outcome. However, most of the WEBs were just slightly undersized, often in case of branching vessels coming from the aneurysm. Accordingly, the impact of this factor can be underestimated in our series. However, other authors also found similar results: Herbreteau et al,[15] in a prospective series of 39 aneurysms treated with WEB, reported statistically comparable rates of complete occlusion among undersized and appropriately sized WEB devices.

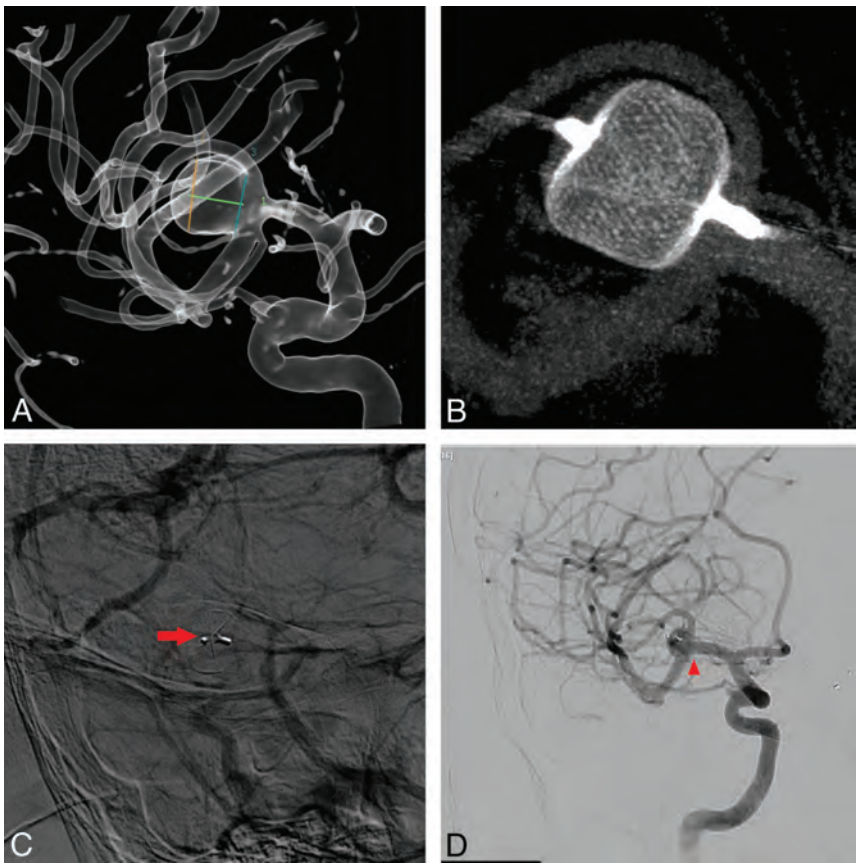

FIG 3. *A*, Right MCA saccular and unruptured aneurysm (dome size, 8 mm; ostium size, 5.5 mm; height, 7 mm). *B*, The aneurysm was treated with a WEB-SL 9 × 5, and the flat panel CT reconstruction showed the correct WEB deployment inside the sac. *C*, The WEB presented with an evident reduction of the height at the 14-month DSA angiography follow-up (*red arrow*). *D*, However, despite the evident WEB shape modification, the aneurysm was still adequately occluded, having a residual ostium (*red arrowhead*).

Another important point was that WEB shape change, though higher among the incompletely occluded aneurysms (50% versus 17.5%), was not an independent prognosticator of occlusion in the multivariate model (Fig 3). As discussed in the following paragraph, these data corroborate the theory that WEB shape modifications (sometimes called "WEB compaction") are more of an epiphenomenon of the aneurysm thrombosis process rather than a reflection of the treatment failure.

Finally, consistent with recent publications,[16] the use of the WEB with stent placement was feasible and effective, but additional devices did not significantly influence the final occlusion rate: Ruptured and unruptured lesions presented comparable rates of good angiographic results.

Predictors of WEB Shape Modification

WEB shape modification has been called, in some reports, "compression" or "compaction," and it is relative to the reduction of the height of the WEB on the angiographic follow-up.[4] This feature has been reported in up to 65% of patients, and whether WEB compaction is directly associated with aneurysm recanalization is still debated.[1,2] Recent series reported similar rates of adequate occlusion, among the group of lesions both with and without WEB modifications.[2,4] Herbreteau et al[15] reported WEB shape modification among 31% of aneurysms, stressing the absence of a relationship between the sizing of the device and its height reduction. The WEB shape change was associated with an increase of the ostium remnants, without impacting the overall rate of adequate occlusion. Our results were in accordance with this study, showing no statistically significant correlation between sizing and the risk of WEB shape modification at follow-up. Most interesting, aneurysm shape and ostium dimensions were significant predictors of WEB compaction. Irregular aneurysms were 63% and 28% among the group of lesions with and without WEB shape modification, respectively, increasing the probability of this phenomenon at follow-up (OR = 5.4; 95% CI, 1.4–19; $P = .01$) (On-line Table 4) >5 times, while the presence of a wide ostium increased the likelihood of compaction (OR = 8; 95% CI, 1.6–60; $P = .03$) by 10 times.

However, this phenomenon is still a matter of debate. First, as reported in the article of Cognard and Januel,[17] and in the response to this article by Pierot,[8] the term "compression" is probably not appropriate because it indicates only a "water-hammer" mechanism that is not yet demonstrated. Pierot et al[3] suggested that clot organization and retraction may contribute to both the intrasaccular occlusion and the shrinkage of the WEB. This effect has also been described in experimental models of coiled aneurysms, which observed that fibrosis increased coil retraction and compaction.[18] However, we still do not have a full explanation for this event, and mechanisms underlying WEB compaction are probably multifactorial. In our series, we demonstrated that WEB shape modifications were not associated with lower aneurysm occlusion, supporting the theory of a retraction of the marker recesses related to thrombus evolution/fibrosis.

Reasons behind the association between irregular shape and WEB shape change are difficult to explain, and it has never been investigated before. Cognard and Januel,[17] having reported this phenomenon for the first time, stressed that a large ostium and irregular shape were likely the main reasons for aneurysm remnants and cage compaction in their series. The authors questioned whether the cage must occupy the entire volume to obtain complete and stable occlusion, minimizing the risk of cage modifications by clot formation or cage displacement.[19]

Finally, as we previously reported, WEB shape modification was unlikely to be observed among small-ostium lesions (<4

mm), while a wide ostium was independently associated with this phenomenon. Accordingly, hemodynamic factors related to a larger diameter of the ostium may at least participate in the complex mechanism leading the decrease of the height of the device.[20]

Limitations of the Study

Our study has limitations intrinsic to single-center series. The data were analyzed retrospectively, and the number of patients was relatively small. The WEB shape modification was not quantitatively evaluated. Finally, due to the relatively small number of patients, some variables may not reach statistical significance in the multivariate analysis.

CONCLUSIONS

In our study, approximately 80% of aneurysms were adequately occluded after WEB implantation, whereas nearly 20% of the devices showed shape modification at follow-up. The likelihood of good occlusion was 5 times less in the presence of a wide ostium, whereas aneurysms with regular morphology were about 6 times more likely to be occluded. WEB shape change, though more prevalent among incompletely occluded lesions, was not independently associated with angiographic occlusion, and it was strongly dependent on aneurysm shape and ostium size.

Disclosures: Pierre-Henri Lefevre—*UNRELATED*: *Payment for Development of Educational Presentations*: Medtronic. Alain Bonafe—*UNRELATED*: *Consultancy*: Medtronic, Stryker, MicroVention.* Vincent Costalat—*UNRELATED*: *Consultancy*: Balt, Medtronic, MicroVention, Balt Stryker, Cerenovus; *Grants/Grants Pending*: Stryker, Medtronic; *Payment for Development of Educational Presentations*: Stryker, Medtronic. *Money paid to institution.

REFERENCES

1. Pierot L, Moret J, Barreau X, et al. **Safety and efficacy of aneurysm treatment with WEB in the cumulative population of three prospective, multicenter series.** *J Neurointerv Surg* 2018;10:553–59 CrossRef Medline
2. Limbucci N, Leone G, Rosi A, et al. **Endovascular treatment of unruptured intracranial aneurysms by the Woven EndoBridge device (WEB): are there any aspects influencing aneurysm occlusion?** *World Neurosurg* 2018;109:e183–93 CrossRef Medline
3. Pierot L, Gubucz I, Buhk JH, et al. **Safety and efficacy of aneurysm treatment with the WEB: results of the WEBCAST 2 study.** *AJNR Am J Neuroradiol* 2017;38:1151–55 CrossRef Medline
4. Janot K, Herbreteau D, Amelot A, et al. **Quantitative evaluation of WEB shape modification: a five-year follow-up study.** *J Neuroradiol* 2019 Mar 7. [Epub ahead of print] CrossRef Medline
5. Pierot L, Biondi A, Narata AP, et al. **Should indications for WEB aneurysm treatment be enlarged? Report of a series of 20 patients with aneurysms in "atypical" locations for WEB treatment.** *J Neuroradiol* 2017;44:203–09 CrossRef Medline
6. Lescher S, Du Mesnil de Rochemont R, Berkefeld J. **Woven Endobridge (WEB) device for endovascular treatment of complex unruptured aneurysms: a single center experience.** *Neuroradiology* 2016;58:383–90 CrossRef Medline
7. Roy D, Milot G, Raymond J. **Endovascular treatment of unruptured aneurysms.** *Stroke* 2001;32:1998–2004 CrossRef Medline
8. Pierot L. **Letter: WEB aneurysm treatment: occlusion stability and "compression."** *Neurosurgery* 2015;77:E666–67 CrossRef Medline
9. Asnafi S, Rouchaud A, Pierot L, et al. **Efficacy and safety of the Woven EndoBridge (WEB) device for the treatment of intracranial aneurysms: a systematic review and meta-analysis.** *AJNR Am J Neuroradiol* 2016;37:2287–92 CrossRef Medline
10. Kabbasch C, Goertz L, Siebert E, et al. **Factors that determine aneurysm occlusion after embolization with the Woven EndoBridge (WEB).** *J Neurointerv Surg* 2019;11:503–10 CrossRef Medline
11. Tateshima S, Chien A, Sayre J, et al. **The effect of aneurysm geometry on the intra-aneurysmal flow condition.** *Neuroradiology* 2010; 52:1135–41 CrossRef Medline
12. Hope JK, Byrne JV, Molyneux AJ. **Factors influencing successful angiographic occlusion of aneurysms treated by coil embolization.** *AJNR Am J Neuroradiol* 1999;20:391–99 Medline
13. Tan IY, Agid RF, Willinsky RA. **Recanalization rates after endovascular coil embolization in a cohort of matched ruptured and unruptured cerebral aneurysms.** *Interv Neuroradiol* 2011;17:27–35 CrossRef Medline
14. Bender MT, Colby GP, Lin LM, et al. **Predictors of cerebral aneurysm persistence and occlusion after flow diversion: a single-institution series of 445 cases with angiographic follow-up.** *J Neurosurg* 2018;130:259–67 CrossRef Medline
15. Herbreteau D, Bibi R, Narata AP, et al. **Are anatomic results influenced by WEB shape analysis in a prospective, single-center series of 39 patients with aneurysms treated with the WEB.** *AJNR Am J Neuroradiol* 2016;37:2280–86 CrossRef Medline
16. Cagnazzo F, Ahmed R, Dargazanli C, et al. **Treatment of wide-neck intracranial aneurysms with the Woven EndoBridge device associated with stenting: a single-center experience.** *AJNR Am J Neuroradiol* 2019;40:820-26 CrossRef Medline
17. Cognard C, Januel AC. **Remnants and recurrences after the use of the WEB intrasaccular device in large-neck bifurcation aneurysms.** *Neurosurgery* 2015;76:522–30; discussion 530 CrossRef Medline
18. Rouchaud A, Brinjikji W, Dai D, et al. **Autologous adipose-derived mesenchymal stem cells improve healing of coiled experimental saccular aneurysms: an angiographic and histopathological study.** *J Neurointerv Surg* 2018;10:60–65 CrossRef Medline
19. Cognard C, Januel AC. **In reply: WEB aneurysm treatment: occlusion stability and "compression."** *Neurosurgery* 2015;77:E667–69 CrossRef Medline
20. Caroff J, Mihalea C, Da Ros V, et al. **A computational fluid dynamics (CFD) study of WEB-treated aneurysms: can CFD predict WEB "compression" during follow-up?** *J Neuroradiol* 2017;44:262–68 CrossRef Medline

Comparison of [^{18}F] FDG-PET/MRI and Clinical Findings for Assessment of Suspected Lumbar Facet Joint Pain: A Prospective Study to Characterize Candidate Nonanatomic Imaging Biomarkers and Potential Impact on Management

V.T. Lehman, F.E. Diehn, S.M. Broski, M.A. Nathan, B.J. Kemp, N.B. Larson, R.A. Shelerud, J.S. Brault, M.P. Halasy, and T.P. Maus

ABSTRACT

BACKGROUND AND PURPOSE: Prior retrospective studies have suggested that both T2 hyperintensity and gadolinium enhancement on fat-suppressed MR imaging are associated with lumbar facet joint pain, but prospective evaluation of FDG-PET/MR imaging with a standardized protocol and correlation to clinical findings are lacking. The primary aim was to prospectively assess a standardized FDG-PET/MRI protocol in patients with suspected facetogenic low back pain, with determination of the concordance of imaging and clinical findings.

MATERIALS AND METHODS: Ten patients with clinically suspected facetogenic low back pain were prospectively recruited with a designation of specific facet joints implicated clinically. Subsequently, patients underwent an FDG-PET/MR imaging examination with gadolinium. Each facet joint was graded for perifacet signal change on MR imaging and FDG activity. The frequency and correlation of MR imaging, FDG-PET, and clinical findings were determined.

RESULTS: FDG activity showed high concordance with high overall MR imaging scores (concordance correlation coefficient = 0.79). There was concordance of the clinical side of pain with the side of high overall MR imaging scores and increased FDG activity on 12/20 (60%) sides. Both a high overall MR imaging score (concordance correlation coefficient = 0.12) and FDG-PET findings positive for increased activity (concordance correlation coefficient = 0.10) had low concordance with the specific clinically implicated facet joints. Increased FDG activity or high MR imaging scores or both were present in only 10/29 (34%) facet joints that had been clinically selected for percutaneous intervention. Eleven (11%) facet joints that had not been selected for treatment demonstrated these imaging findings.

CONCLUSIONS: There was low concordance of perifacet signal change and FDG activity with clinically implicated facet joints. This could indicate either the potential to change patient management or a lack of biomarker accuracy. Therefore, additional larger randomized studies with the use of comparative medial branch blocks would be useful to further investigate the clinical utility of these findings.

ABBREVIATIONS: MBB = medial branch block; ρ_{CCC} = concordance correlation coefficient; SUVmax = standard uptake value maximum

Facet joints have been implicated in 15%–45% of cases of low back pain, but diagnosis remains challenging.[1] Anatomic imaging findings of facet joint arthropathy or clinical findings are not considered reliable indicators of individual lumbar facet joints to target for treatment.[1,2] Current standards for identification of a painful facet joint require sequential blinded comparative medial branch blocks (MBBs) with local anesthetic and >80% pain relief.[3] While percutaneous treatments exist, more effective and more durable options are needed for many patients. Investigation of new treatment agents and modalities is already underway.[4,5] Thus, identification of nonanatomic facet joint imaging biomarkers to facilitate diagnosis, direct individualized target-specific treatment, and help assess response to existing and experimental treatments is highly desirable.

Recently, combined PET/MR imaging units have become clinically available, enabling simultaneous technique assessment that minimizes differences due to temporal fluctuation of findings or anatomic misregistration. Several retrospective

Received January 23, 2019; accepted after revision August 6.

From the Departments of Radiology (V.T.L., F.E.D., S.M.B., M.A.N., B.J.K., T.P.M.), Health Science Research (N.B.L.), and Physical Medicine and Rehabilitation (R.A.S., J.S.B., M.P.H.), Mayo Clinic, Rochester, Minnesota

Paper previously presented, in part, at: Spine Interventional Society Annual Meeting, August 14–17, 2019; New York, New York.

Please address correspondence to Vance T. Lehman, MD, Department of Radiology, Mayo Clinic, 200 First St SW, Rochester, MN 55905, e-mail: lehman.vance@mayo.edu

Indicates article with supplemental on-line tables.

Indicates article with supplemental on-line photos.

http://dx.doi.org/10.3174/ajnr.A6224

studies have suggested that facet/perifacet findings on fat-suppressed MR imaging are more prevalent in patients with low back pain, but prospective clinical investigations with standardized correlation of imaging findings to specifically implicated facet joints or MBBs have not been performed to evaluate and fully characterize these findings.[6-10] [^{18}F] FDG is the most widely available PET radiotracer, has been used to assess inflammation in a variety of conditions, allows quantitative uptake analysis, and has the potential to reflect inflammatory facet joint arthropathy.[11] Such facet joint FDG activity has been described in a prevalence study, a study of the cervical spine, and a case report in the lumbar spine,[12] but there is little prospective information addressing lumbar facet joints.[13,14]

The primary aim of this pilot study was to prospectively assess a standardized FDG-PET/MR imaging protocol with gadolinium in patients with suspected facetogenic axial low back pain. This includes assessment of the concordance of nonanatomic MR imaging FDG-PET and clinical findings on a patient and facet joint level. A secondary aim was to obtain concordance, prevalence, and descriptive information of these potential biomarkers for planning of large future studies using comparative MBBs.

MATERIALS AND METHODS

Patient Selection and Initial Clinical Evaluation

Institutional review board approval was obtained for this Health Insurance Portability and Accountability Act–compliant study. This study was registered under clinicaltrials.gov (NCT02921490). Subjects were identified primarily or referred to a spine or pain clinic and evaluated by a pain or spine specialist. Patients with unilateral or bilateral axial low back pain were assessed for inclusion criteria: 1) minimum 60% likelihood of facet joint–related axial low back pain based on clinical history, pain location and character, tenderness to palpation, and positive facet joint loading maneuvers; 2) no substantial pain or tenderness below the iliac crest/sacroiliac joint region or predominant pain radiating to the lower extremities; and 3) clinically a 60%–80% or 81%–100% confidence that pain was facetogenic for each side of the back with pain. These percentages were determined by the overall clinical impression using all available history and physical examination information based on the clinician's cumulative clinical experience compared with all other patients he or she had ever evaluated. Also documented were the response to facet joint loading maneuvers and tenderness to palpation on each side; the duration and severity of pain, with the latter being rated on the numeric rating scale; and the presence of known inflammatory arthropathy.

Exclusion criteria included younger than 50 years of age, a procedure within the preceding 2 months (lumbar spine injection, lumbar spine surgery, or facet joint intervention [MBB, radiofrequency ablation, or steroid injection]), history of major trauma to the lumbar spine, metastatic malignancy, conditions with increased radiosensitivity, pregnancy, compression fracture, and contraindication to MR imaging.

Before FDG-PET/MR imaging, the specialist clinician indicated which specific facet joints she or he was planning to target with percutaneous treatment (either steroid injection or MBB and radiofrequency ablation) on the basis of clinical evaluation alone as a representation of implicated facet joints. Treatment based on PET/MR imaging results was not mandated, and the clinical response to any injection was not recorded. Because the PET/MR imaging examination was performed before any treatment, clinicians were ultimately free to recommend interventions based on the initial plan and/or PET/MR imaging results using their best clinical judgment.

Imaging Protocol

Images were acquired on a fully integrated simultaneous 3T PET/MR imaging scanner (Signa PET/MR imaging; GE Healthcare, Milwaukee, Wisconsin) with TOF capability. Weight, height, and blood glucose levels were recorded for all patients. All patients fasted for >4 hours, had a blood glucose level of <200 mg/dL, and were injected with 10 mCi of [^{18}F] FDG (mean, 10.4 mCi). PET acquisition was limited to a single bed position centered over the lumbar spine. The PET scan was acquired for 15 minutes after an uptake period of 60 minutes (mean, 62 minutes). PET images were reconstructed with 3D ordered subset expectation maximization with TOF, 2 iterations, 28 subsets, and a 5-mm Gaussian postfilter into a 192 × 192 matrix covering a 50-cm FOV. PET attenuation correction was performed using a 3D dual-echo radiofrequency spoiled gradient recalled-echo sequence; scatter, randoms, deadtime, and decay corrections were also applied. MR imaging sequences obtained of the lumbar spine and acquired simultaneously with the PET scan included sagittal T1, sagittal T2, sagittal T2 with chemical fat saturation, axial T1, and axial T2 with chemical fat saturation without gadolinium. After gadolinium administration, axial and sagittal postgadolinium T1-weighted images were obtained with chemical fat saturation. These axial images covered the L1–L2 through L5–S1 facet joints with a straight axial pack. All sequences were performed as 2D fast spin-echo. Specific scan parameters are provided in On-line Table 1.

MR Imaging Analysis

Both radiologists interpreting MR imaging (T.P.M., F.E.D.) have extensive experience in spine imaging interpretation and pain management intervention, with Certificates of Added Qualification in neuroradiology. MR imaging readers were blinded to FDG-PET data and all clinical data. Images were viewed anonymously on an Advantage Workstation (GE Healthcare). MR images of each facet joint were scored twice, first using all available noncontrast MR images (including T2-weighted fat-suppressed images) and then a second time with the addition of gadolinium contrast-enhanced sequences.

Each lumbar facet joint L1–L2 through L5–S1 was individually graded for the following features: osseous signal change/enhancement and soft-tissue perifacet edema/enhancement. The grading scale represented a more granular modification of that used by Czervionke and Fenton,[6] which combined perifacet and bone features into a single grading scale.

Osseous signal change was graded on a I–III scale for T2 hyperintensity or enhancement: grade 0 (normal), none; grade I, present in 1 articular process; grade II, present in both articular

processes; and grade III, extending into the pedicle, transverse process, or lamina.

Soft-tissue perifacet signal change was graded on a I–IV scale for edema and enhancement: grade 0 was normal; grade I (minimal), thin and curvilinear confined to the posterior facet joint capsule without further extension; grade II (mild), in soft tissue extending beyond the facet joint capsule encompassing <50% of the facet joint perimeter; grade III (moderate to high), in soft tissue beyond the facet joint capsule encompassing 51%–100% of the facet joint perimeter; and grade IV (high), extending into the neural foramen, ligamentum flavum, and/or radial extension equal or >1 cm from the facet joint margin in any direction.

Each instance of a discrepant score between the 2 MR imaging readers was resolved with a tie-breaking grading by a third reader with a Certificate of Added Qualification in neuroradiology (V.T.L.), who was also blinded to all clinical and FDG-PET information at the time of interpretation. The tie-breaking radiologist was instructed to choose 1 of the 2 original scores.

FDG-PET Imaging Analysis

FDG-PET/MR images were rated independently by 2 radiologists, one with a Certificate of Added Qualification in nuclear medicine (S.M.B.) and one with double board certification by the American Board of Radiology and American Board of Nuclear Medicine (M.A.N.). MIM software was used for image review (MIM Software, Cleveland, Ohio). Both unfused PET and fused PET/MR images were available for review, but only the noncontrast sagittal and axial T1-weighted images without fat saturation were available for image coregistration. The readers remained blinded to all clinical information.

The readers graded the FDG activity subjectively on a 0–3 scale: 0 = normal, 1 = mildly increased, 2 = moderately increased, or 3 = markedly increased activity. Consensus grades for locations with an initial discrepancy were determined during a second review by both nuclear medicine radiologists. Additionally, the standard uptake value maximum (SUVmax) was determined at each facet joint by drawing a VOI to encompass the entire osseous facet joint. The SUVmax of the bone marrow within the L3 vertebral body and the blood pool activity within the abdominal aorta at the L3 level were both determined by placement of a 1-cm-diameter ROI on axial images. In addition to the facet joint SUVmax, ratios normalized by values from the L3 vertebral body and aorta were also considered for analysis.

Data Analysis

MR Imaging and FDG-PET Data. To facilitate comparison with FDG and clinical findings, we combined the perifacet and osseous grades into an overall MR imaging score: normal (bone or perifacet grade of 0); low MR imaging score (bone grade of 1–2 or perifacet grade I–2); or high MR imaging score (bone grade III or soft-tissue perifacet grade of 3–4). The highest of the consensus grades (osseous T2 signal, soft-tissue perifacet T2 signal, osseous enhancement, or soft-tissue perifacet enhancement) was used for this overall MR imaging score. To facilitate comparison with MR imaging and clinical findings, we assigned each joint an overall FDG-PET score of either normal or increased (grades 1–3) FDG activity.

The effect of gadolinium on grade and score assignments was determined by the rate at which these differed from the addition of gadolinium-enhanced images. The rates of high overall score designation on the basis of perifacet grade versus osseous grade were also determined.

Comparison of the Clinical Side of Pain and Implicated Facet Joints with Imaging Results. Comparison of clinical findings with imaging results had 2 main components: First, the imaging findings were evaluated for concordance with clinical findings on a patient side (right or left). For this evaluation, any side with pain that also had at least 1 facet joint with high-grade MR imaging findings and/or increased FDG activity was considered concordant, regardless of specific facet joint levels. Similarly, the absence of both pain and these imaging findings was considered concordant. Sides with a high overall MR imaging score and/or increased FDG activity without pain or pain without such imaging findings were considered discordant. The rationale was that determination of the precise level of facet joint pain clinically is thought to be difficult, but pain generators typically produce ipsilateral rather than contralateral pain.[2]

Statistical Analysis. Binary and categoric variables (eg, PET grade) were summarized as counts and percentages, while continuous measures were summarized by means and SDs or medians and interquartile ranges. Distributional assumptions for continuous-valued traits were assessed, and appropriate transformations were considered, as necessary. All analyses were conducted using the R statistical and computing software (http://www.r-project.org/), and statistical significance was declared at an α level of .05.

Concordance measures were used to quantify agreement among overall high MR imaging scores, increased FDG activity, and facet joints that had been selected for treatment on the basis of clinical evaluation. To account for the multiple lumbar levels per given patient, we applied the repeated-measures concordance correlation coefficient (ρ_{CCC}) using the *cccrm* R package[15] (https://www.rdocumentation.org/packages/cccrm/versions/1.2.1) to generate point estimates and 95% confidence intervals.

We tested whether the SUV measurements significantly differed by positive PET grade level using likelihood ratio tests based on a random-intercept linear mixed-model for each of the 3 SUV measurements. The reduced model used the dichotomized PET grade coding (0 versus 1–3), whereas the full model considered each positive grade as a separate factor level. For each model, SUV measurements were log-transformed to satisfy assumptions of normality.

We quantified discrimination of dichotomous PET grade coding by each SUV measurement using area under the receiver operating characteristic curve statistics. We applied the pooled repeated-measures approach[16] in the cvAUC R package (https://cran.r-project.org/web/packages/cvAUC/index.html) to account for within-patient correlation structure, providing point estimates and corresponding 95% CIs.

Given the ordinal nature of the grades, the ordinal Krippendorf α was used to determine the interrater reliability. The 95% confidence interval was estimated using the grouped

bootstrap to account for within-patient clustering, and the intervals were constructed using the percentile approach.

RESULTS

Participant Demographics, Lumbar Enumeration, and Clinical Characteristics

The study cohort consisted of 10 subjects including 7 (70%) women, with a mean age of 63 years (range, 50–79 years). This allowed evaluation of 100 facet joints on 20 sides (left or right) of the lumbar spine. Pain duration was >12 months (9/10 subjects, 90%) and 6–12 months (1/10, 10%). One (10%) subject had been diagnosed with underlying undifferentiated inflammatory arthropathy (patient 1).

The mean severity of pain on the numeric rating scale was 5 (range, 3–8) at the time of clinical evaluation. Four (40%) patients had unilateral pain, whereas 6 (60%) had bilateral pain. Of the 16 sides with pain, the clinical confidence that the pain was due to facet joint origin before imaging was in the 60%–80% range for 8 (50%) sides and 81%–100% range for 8 (50%) sides. Clinical features are detailed in On-line Table 2.

MR Imaging Scores

On MR imaging, 21 (21%) of 100 facet joints demonstrated a high overall MR imaging score, more frequently due to soft-tissue perifacet findings rather than osseous findings, specifically, 2/21 (10%) on the basis of osseous findings (grade III/III), 12/21 (57%) on the basis of soft-tissue perifacet findings (grades III–IV/IV), and 7/21 (33%) due to both perifacet and osseous findings. Of the 19 facet joints with high overall scores and grade III–IV soft tissue perifacet signal, 13 (68%) had a grade of III, and 6 (32%) had a grade of IV.

The use of gadolinium increased the number of facet joints with high over all MR imaging scores, predominantly due to an increased grade of soft-tissue perifacet signal change. Specifically, 10/21 (48%) joints were upgraded to a high MR imaging score with the addition of gadolinium-enhanced images compared with T2 fat-saturated images alone, whereas 11/21 (52%) were assigned a high overall MR imaging score with both T2-weighted and gadolinium-enhanced images. One of the 10 (10%) upgraded facet joints was on the basis of osseous enhancement, whereas 9/10 (90%) were upgraded on the basis of soft-tissue perifacet enhancement.

In the subset of 19 facet joints with high overall MR imaging scores due to grade III–IV soft-tissue perifacet signal change with gadolinium, the perifacet signal grades on fat-suppressed T2-weighted images were variable but frequently low-grade with the following frequencies: grade 0 (n = 1); grade I (n = 5); grade II (n = 7); grade III (n = 5); and grade IV (n = 1). Eight of 9 (89%) joints with high-grade bone signal (grade III) had the finding on both T2-weighted and gadolinium-enhanced images, whereas 1/9 (11%) had high-grade change on gadolinium-enhanced images alone.

Fifty-three of 100 (53%) facet joints were designated normal on T2-weighted images, but only 10 (10%) were scored as normal on both T2-weighted fat-suppressed and gadolinium-enhanced images (On-line Fig 1). Sixty-nine (69%) facet joints had a low overall MR imaging score. This includes 43/69 (62%) joints that were normal on T2 fat-saturated images alone but demonstrated low-grade findings on gadolinium-enhanced images due to the presence of low-grade capsular enhancement with or without mild perifacet extension. The other 26/69 (38%) had low-grade findings on both T2 fat-suppressed images and gadolinium-enhanced images.

FDG-PET Imaging Scores

On PET, 17/100 (17%) facet joints demonstrated increased FDG activity overall scores, 10 (10%) low-grade (grade I) and 7 (7%) moderate-to-high grade (grade II–III). All 17 (100%) FDG-positive facet joints demonstrated a high MR imaging overall score. Two patients (20%) had no (0%) facet joints with increased FDG activity; these were also the only 2 patients without high-grade MR imaging change. Increased FDG activity was highly correlated with the presence of a high overall MR imaging score within a specific facet joint (ρ_{CCC} = 0.78; 95% CI, 0.68–0.85). Furthermore, 12/12 (100%) sides with facet joints with high overall MR imaging scores also had increased FDG activity. Comparisons of the clinical features and major imaging findings are presented in On-line Tables 2 and 3.

The median (interquartile range) SUVmax for the 83 facet joints visually graded as 0 was 1.50 (0.55), compared with 1.85 (1.50) for the 17 facet joints with increased FDG activity (grades I–III). Comparison of SUVmax, SUVmax/aorta ratio, and SUVmax/L3 vertebral body ratios also demonstrated a trend of increasing SUVmax values with visually assigned grades ($P < .001$ for all analyses). There were also instances of overlapping values, in particular between grade 0 and grade I. The SUVmax values considered here include only a VOI of the osseous facet joint itself for consistency and reproducibility, whereas the visually assigned scores also considered perifacet soft-tissue and other osseous activity if present.

The area under the curve values for dichotomous discrimination between normal and abnormal (any grade) facet joints using the SUVmax, SUVmax/aorta ratio, or SUVmax/L3 vertebral body ratio were relatively comparable given overlapping CIs, with the SUVmax/L3 vertebral body ratio corresponding to the highest point estimate. Specifically, the area under the curve values were 0.72 (95% CI, 0.57–0.88) for SUVmax, 0.84 (95% CI, 0.73–0.96) for SUVmax/aorta, and 0.87 (95% CI, 0.74–0.99) for the SUVmax/L3 vertebral body.

Interrater Reliability

The interrater reliability of overall MR imaging scores was moderate, with an α estimate of 0.77 (95% CI, 0.52–0.92). The interrater reliability of the PET scores was high, with an α estimate of 0.85 (95% CI, 0.65–0.98).

Concordance of Facet Joint Imaging Findings to Side of Pain and Specific Facet Joints Implicated Clinically

There was concordance of the clinical side of pain, the side of the high overall MR imaging score, and the side of increased FDG activity on 12/20 (60%) sides (On-line Table 3). This includes 10 sides (50%) with imaging findings positive for concordance and 2 sides (10%) with imaging findings negative for concordance and the absence of suspected facet joint pain.

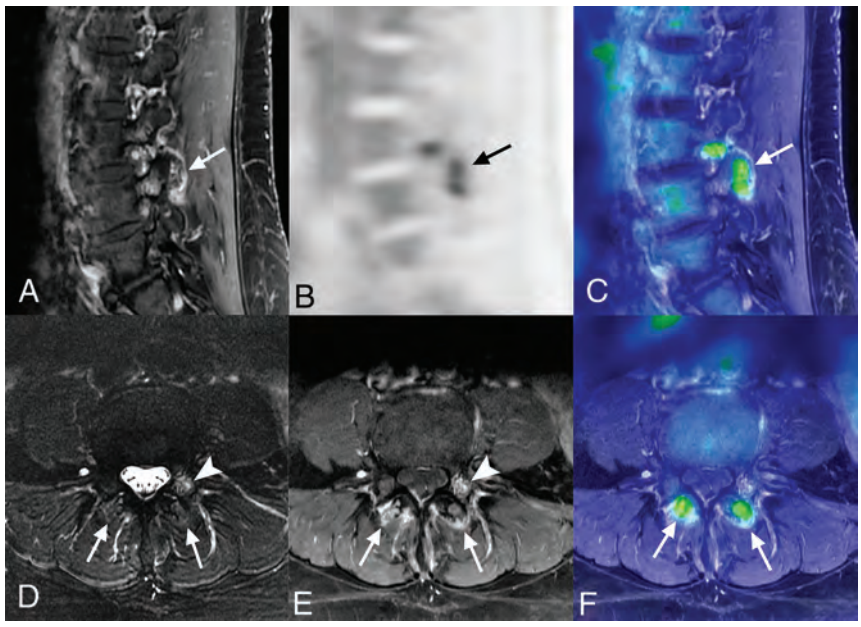

FIGURE. Clinical concordance of the sides of pain and imaging findings, but discordance of specific implicated facet joints. Clinically, this patient had bilateral low back pain and had been prescribed bilateral L4–L5 and L5–S1 facet joint injections. There were high-grade MR imaging scores and increased FDG activity of the bilateral L3–L4 facet joints, but not of the bilateral L4–L5 or L5–S1 facet joints. Sagittal fat-suppressed T1-weighted image with gadolinium demonstrates high-grade perifacet enhancement of the left L3–L4 facet joint (*arrow*), but not of the L4–L5 or L5–S1 facet joints (*A*). Sagittal FDG-PET and fused PET/MR images (*B* and *C*) also demonstrate increased L3–L4 perifacet FDG activity (*arrows*). Note that the FDG activity is distinguishable from areas of vascular enhancement but is not visually increased in the area of L3 pedicle enhancement (*arrowhead* in *D* and *E*). The perifacet signal change of the bilateral L3–L4 facet joints on axial fat-suppressed T2-weighted images is identified (*arrows*, *D*) but is more apparent on axial fat-suppressed T1-weighted images with gadolinium (*arrows*, *E*). An axial fused PET/MR image also demonstrates increased perifacet FDG activity of the bilateral L3–L4 facet joints (*arrows*, *F*).

Eight (40%) sides were discordant, including 5/20 (25%) sides with pain without a high overall MR imaging score or increased FDG activity and 3/20 (15%) sides with such imaging findings and no clinically suspected facet joint pain.

Tenderness to palpation was reported on 14/20 (70%) sides. Nine of 14 (64%) sides with tenderness had ipsilateral high overall MR imaging scores or increased FDG activity, while 5/14 (36%) sides with tenderness lacked these imaging findings. Conversely, a high overall MR imaging score and FDG activity were identified in 3/6 (50%) sides without tenderness to palpation.

Facet joints that had been selected for treatment before imaging demonstrated low correlation with those with either a high overall MR imaging score (ρ_{CCC} = 0.12; 95% CI, 0.002–0.23) or increased FDG activity (ρ_{CCC} = 0.10; 95% CI, −0.04–0.24). Treatment directed toward 29/100 (29%) facet joints was indicated on initial clinical evaluation before the PET/MR imaging. Increased FDG activity or high overall MR imaging scores or both were present in 10 of these 29 (34%) facet joints. Additionally, increased FDG activity or a high MR imaging score or both were present in 11 facet joints that were not initially prescribed treatment. Therefore, 10/21 (48%) facet joints with high overall MR imaging scores and/or FDG activity corresponded to facet joints specifically planned for targeted percutaneous intervention.

Moreover, specific facet joints with high-grade overall MR imaging scores and/or increased FDG activity completely differed from those facet joints originally prescribed treatment in 4/10 (40%) subjects, partially overlapped in 5/10 (50%) subjects, and completely corresponded in only 1 (10%) subject. A comparison of the facet joints originally selected for treatment with those with increased FDG activity or high-grade MR imaging scores is presented in On-line Table 3. Examples comparing the sides and specific facet joints implicated clinically with those demonstrating positive imaging findings are provided in the Figure and On-line Fig 2.

The most marked consensus MR imaging and FDG findings (grades II–III FDG findings, grade III osseous MR imaging signal, grade IV soft-tissue perifacet signal) were less frequent but were found on sides with concordant pain. Of the subgroup of 7 facet joints that had moderate (n = 4) or high-grade (n = 3) FDG activity, all 7 (100%) were on sides (n = 7 sides) with clinically concordant pain. Of the subset of 9 facet joints that had high-grade (grade III) osseous MR imaging signal, all 9 (100%) were on a side (n = 5 sides) of clinically concordant pain. Of the subset of 6 facet joints that had high-grade (grade IV) perifacet signal, all 6 (100%) were on a side (n = 6 sides) of clinical pain.

DISCUSSION

The primary result of this study was a low concordance between perifacet signal change or FDG activity with clinically implicated facet joints. This finding could indicate the potential of imaging findings to substantially change management if these prove to be predictive of facet joint pain. Alternatively, this low concordance could indicate a lack of sensitivity or specificity of imaging findings. In either case, further investigation seems warranted to facilitate appropriate interpretation of imaging findings and assess the utility (or lack thereof) for selection of joints for treatment. Most important, future study would benefit from the use of dual or triple comparative MBBs (multiple injections) to support/refute facet joint pain because a single intervention such as a steroid injection has an unacceptably high placebo rate and is not considered the standard of diagnosis in the pain medicine community.[3] As with this study, prior lumbar spine facet joint studies with MR imaging or FDG-PET have not incorporated such comparative MBBs.[6,9,10,13] Unlike the current study, these prior studies have not incorporated a standardized imaging protocol with

prospective clinical evaluation. We believe it will be useful if future investigations with multiple interventions are predicated on pilot data with standardized imaging protocols and image scoring such as in this study. Indeed, our results help provide justification for and facilitate planning of future investigations.

Specifically, the high correlation of FDG activity with MR imaging signal indicates that these findings are likely close surrogates for initial assessment, and the use of a single technique (MR imaging or FDG-PET) may be sufficient. However, comparison of MR imaging and FDG findings as possible biomarkers of treatment response would require additional study with FDG-PET/MR imaging at multiple time points. While not well-studied in the facet joints, there is evidence that FDG activity can indicate an early response to systemic treatment in other inflammatory conditions, including inflammatory arthritis.[17,18] We found that high-grade perifacet findings were more common with gadolinium, supporting the assertion that further investigation with MR imaging protocols including gadolinium, rather than fat-suppressed T2 images alone, would be reasonable. The results also provide initial assessment of the approximate frequency and concordance of potential imaging biomarkers on multiplane fat-suppressed T2, fat-suppressed T1 gadolinium-enhanced, and FDG-PET images using a standardized protocol.

In many instances, imaging findings were concordant with the side of pain but indicate partially or completely different facet joints for targeted treatment in nearly every patient and in more than half of all implicated facet joints. Complete concordance of imaging and clinical findings and clinical confidence would indicate that use of imaging biomarkers is unlikely to change the targets for treatment. Conversely, complete discordance of the imaging and clinical findings would raise doubt that the candidate biomarkers actually indicate facet joint pain at all. If either of these scenarios were observed, the utility of future investigation of these imaging findings could be questioned.

The instances of positive imaging findings in the absence of ipsilateral pain and vice versa raise the possibility that these candidate biomarkers may have limited specificity and sensitivity. The lack of imaging findings on the side of clinically suspected facet joint pain in some instances could either represent a limitation of imaging biomarker sensitivity or could potentially indicate non-facet joint origin of pain.

Because the facet joints with the most marked MR imaging signal and FDG activity were always correlated with the side of pain, future studies will ideally be large enough to determine the significance of this subset. Low-grade perifacet enhancement was nearly ubiquitous, however, raising caution of overinterpretation of this finding in clinical practice or research studies.

Unlike in the current study, Czervionke and Fenton[6] retrospectively reported that back and/or leg pain was always present on the side of unilateral high-grade facet joint signal change, perhaps due to methodologic differences of study design, clinical assessment, and standardization of imaging protocol. The correlation of back pain and imaging findings was not otherwise reported, and clinically implicated facet joints were not determined.[6] Sawicki et al[14] reported that FDG-PET/MR imaging–directed cervical facet joint steroid injections were associated with improved clinical pain scores relative to clinically selected facet joints in patients without imaging findings positive for increased activity, though MBBs were not used and gadolinium was not administered. They also found that MR imaging T2 hyperintensity and FDG activity may be surrogates.[14]

One prior study suggested that FDG-PET/MR imaging findings of the lumbar spine may help identify various causes of sciatica, including inflamed facet joints.[19] Limited evidence indicates that muscular or nerve FDG activity may be present in a painful lower extremity.[19,20] Future studies can build on these results and those of the current study to investigate the utility of FDG-PET/MR imaging in assessing other causes of axial and radicular lumbar pain.

This study has some limitations. The number of patients was small, and the study was performed at a single institution. However, the degree of concordance of MR imaging signal change and FDG was high enough and the lack of concordance between facet joints originally implicated with the imaging findings was marked enough to be statistically salient. Recruitment of patients specifically being evaluated by back pain specialists could introduce selection bias and could limit generalization of the results to other patient populations. Furthermore, each patient was evaluated by only a single clinician and subjective assignment of the likelihood of facet joint origin of pain, even with standardized items on the clinical examination, could potentially differ among clinicians. Finally, invasive tests such as MBBs to provide more definitive evidence to support or refute facet joint origin of pain were not used in this pilot study.

CONCLUSIONS

Although the most marked imaging findings were always found on a side with pain, there was low concordance of perifacet signal change and FDG activity with clinically implicated facet joints overall. This could indicate either a potential to change patient management or a lack of biomarker accuracy. Therefore, additional larger randomized studies with the use of comparative MBBs are needed to clarify the clinical utility of these findings. There was a high concordance of MR imaging and FDG-PET findings, suggesting that a single technique (MR imaging or FDG-PET) design may be reasonable for future studies.

ACKNOWLEDGMENTS

The authors acknowledge the assistance of study coordinators Susan Walsh and Caleb Hammel, MR imaging technologist Cynthia Lange, and Sonia Watson for assistance with manuscript preparation.

Disclosures: Brad J. Kemp—*UNRELATED*: *Grants/Grants Pending*: GE Healthcare, *Comments*: industry-sponsored trial, "Clinical Evaluation of MP26 Features in Adults"; involved data collection of brain and chest imaging on the GE Signa PET/MRI system; the project started in November 2016 and was closed on June 8, 2018.* Timothy P. Maus—*UNRELATED: Board Membership*: Spine Intervention Society (nonprofit), *Comments*: travel reimbursement for board meetings and speaking; *Travel/Accommodations/Meeting Expenses Unrelated to Activities Listed*: Spine Intervention Society, American Academy of Pain Medicine, New

Jersey Physical Medicine and Rehabilitation Society, Mayo Clinic, Cleveland Clinic, American University of Beirut, *Comments*: travel reimbursement for speaking. *Money paid to the institution.

REFERENCES

1. Schwarzer AC, Aprill CN, Derby R. **Clinical features of patients with pain stemming from the lumbar zygapophysial joints: is the lumbar facet syndrome a clinical entity?** *Spine (Phila Pa 1976)* 1994;19:1132–37 Medline
2. McCall IW, Park WM, O'Brien JP. **Induced pain referral from posterior lumbar elements in normal subjects.** *Spine (Phila Pa 1976)* 1979;4:441–46 Medline
3. Bogduk N. *ISIS Practice Guidelines for Spinal Diagnostic and Treatment Procedures*. 2nd ed. International Spine Intervention Society, San Francisco; 2014
4. Weeks EM, Platt MW, Gedroyc W. **MRI-guided focused ultrasound (MRgFUS) to treat facet joint osteoarthritis low back pain–case series of an innovative new technique.** *Eur Radiol* 2012;22:2822–35 CrossRef Medline
5. Wu J, Zhou J, Liu C, et al. **A prospective study comparing platelet-rich plasma and local anesthetic (LA)/corticosteroid in intra-articular injection for the treatment of lumbar facet joint syndrome.** *Pain Pract* 2017;17:914–24 CrossRef Medline
6. Czervionke LF, Fenton DS. **Fat-saturated MR imaging in the detection of inflammatory facet arthropathy (facet synovitis) in the lumbar spine.** *Pain Med* 2008;9:400–06 CrossRef Medline
7. D'Aprile P, Tarantino A, Lorusso V, et al. **Fat saturation technique and gadolinium in MRI of lumbar spinal degenerative disease.** *Neuroradiol J* 2006;19:654–71 CrossRef Medline
8. Friedrich KM, Nemec S, Peloschek P, et al. **The prevalence of lumbar facet joint edema in patients with low back pain.** *Skeletal Radiol* 2007;36:755–60 CrossRef Medline
9. Lakadamyali H, Tarhan NC, Ergun T, et al. **STIR sequence for depiction of degenerative changes in posterior stabilizing elements in patients with lower back pain.** *AJR Am J Roentgenol* 2008;191:973–79 CrossRef Medline
10. Suri P, Dharamsi AS, Gaviola G, et al. **Are facet joint bone marrow lesions and other facet joint features associated with low back pain? A pilot study.** *PM R* 2013;5:194–200 CrossRef Medline
11. Wu C, Li F, Niu G, et al. **PET imaging of inflammation biomarkers.** *Theranostics* 2013;3:448–66 CrossRef Medline
12. Houseni M, Chamroonrat W, Zhuang H, et al. **Facet joint arthropathy demonstrated on FDG PET.** *Clin Nucl Med* 2006;31:418–19 Medline
13. Rosen RS, Fayad L, Wahl RL. **Increased 18F-FDG uptake in degenerative disease of the spine: characterization with 18F-FDG PET/CT.** *J Nucl Med* 2006;47:1274–80 Medline
14. Sawicki LM, Schaarschmidt BM, Heusch P, et al. **Value of (18) F-FDG PET/MRI for the outcome of CT-guided facet block therapy in cervical facet syndrome: initial results.** *J Med Imaging Radiat Oncol* 2017;61:327–33 CrossRef Medline
15. Carrasco JL, Phillips BR, Puig-Martinez J, et al. **Estimation of the concordance correlation coefficient for repeated measures using SAS and R.** *Comput Methods Programs Biomed* 2013;109:293–304 CrossRef Medline
16. LeDell E, Petersen ML, van der Laan MJ. **Computationally efficient confidence intervals for cross-validated area under the ROC curve estimates.** *Electron J Stat* 2015;9:1583–1607 CrossRef Medline
17. Fosse P, Kaiser MJ, Namur G, et al. **(18)F- FDG PET/CT joint assessment of early therapeutic response in rheumatoid arthritis patients treated with rituximab.** *Eur J Hybrid Imaging* 2018;2:6 CrossRef Medline
18. Nguyen BJ, Burt A, Baldassare RL, et al. **The prognostic and diagnostic value of 18F-FDG PET/CT for assessment of symptomatic osteoarthritis.** *Nucl Med Commun* 2018;39:699–706 CrossRef Medline
19. Cipriano PW, Yoon D, Gandhi H, et al. **(18)F-FDG PET/MRI in chronic sciatica: early results revealing spinal and nonspinal abnormalities.** *J Nucl Med* 2018;59:967–72 CrossRef Medline
20. Biswal S, Behera D, Yoon DH, et al. **[18F]FDG PET/MRI of patients with chronic pain alters management: early experience.** *EJNMMI Phys* 2015;2:(Suppl 1):A84 CrossRef Medline

Transforaminal Insertion of a Thermocouple on the Posterior Vertebral Wall Combined with Hydrodissection during Lumbar Spinal Radiofrequency Ablation

R. Lecigne, J. Garnon, R.L. Cazzato, P. Auloge, D. Dalili, G. Koch, and A. Gangi

ABSTRACT

SUMMARY: The purpose of the present article is to describe the technique of transforaminal insertion of an ultrathin thermosensor in the anterior epidural space in 13 patients treated by radiofrequency ablation. The mean time taken to position the thermosensor was 10.6 minutes (range, 5–38 minutes). Technical success was 93% (correct positioning in 13/14 levels). Additional hydrodissection was performed through the same access in 11 cases. No postoperative neural deficit was elicited in any of the cases.

ABBREVIATION: RFA = radiofrequency ablation

Inadvertent thermal ablation of neural structures located in the lumbar canal is a rare but potentially debilitating complication following percutaneous thermal ablation of lesions located in the vertebral body, if the expected ablation zone abuts the posterior wall of the vertebra.[1-3] Using a thermosensor, one can monitor local temperatures to ensure that threshold temperatures are not breached in a critical area.[4,5] However, precise positioning of the thermometer at an ideal interface between the lumbar spine and the dural sac can be challenging. We herein aim to describe the technique of transforaminal insertion of an ultrathin thermocouple into the anterior epidural space while performing radiofrequency ablation of spinal metastases to monitor the temperature at the interface between the posterior part of the vertebral body and the dura.

MATERIALS AND METHODS

This is a single-center retrospective study. All patients gave informed consent for the procedure. Institutional review board approval was waived.

Received May 31, 2019; accepted after revision August 1.

From the Department of Radiology (R.L.), Pôle d'imagerie, Centre Hospitalier Universitaire, Cedex, France; Department of Interventional Radiology (J.G., R.L.C., P.A., G.K., A.G.), Hopitaux Universitaires de Strasbourg, Strasbourg, France; and Department of Radiology and Radiological Science (D.D.), Johns Hopkins University School of Medicine, Baltimore, Maryland.

Please address correspondence to Lecigne Romain, Department of Radiology, Pôle d'imagerie, Centre Hospitalier Universitaire, 47 rue Cognacq Jay, 51092 Reims Cedex, France; e-mail: romainlecigne@hotmail.fr

http://dx.doi.org/10.3174/ajnr.A6233

Study Population and Procedures

Between April 2015 and August 2018, thirteen patients (7 women, 6 men; mean age, 60.8 years) with 14 lumbar tumors were treated in our institution using radiofrequency ablation (RFA) and associated planned local temperature monitoring using the transforaminal approach. Patient, lesion, and RFA characteristics are listed in Table 1.

All procedures were performed with the patient under general anesthesia in the prone position, with either conebeam CT guidance ($n = 7$ patients) or combined CT and fluoroscopic guidance ($n = 1$), depending on room availability at the time of treatment. Thermal ablation was conducted according to the manufacturer's recommendations. If the temperature exceeded 45° and was not controllable with active hydrodissection, RFA was stopped. After completion of the ablation, additional cementoplasty was performed to ensure bone consolidation and reduce the risk of secondary postablation fracture.

Technique of the Double-Oblique Transforaminal Approach

Optimal insertion of the thermometer requires a double-oblique approach; the ideal trajectory is from cranial to caudal and from lateral to medial (Figs 1 and 2). First, an 18-ga spinal needle is advanced in the very medial part of the foramen. Subsequently, a 20-cm-long, 28-ga reusable monopolar nitinol radiofrequency electrode (MultGen; Stryker, Kalamazoo, Michigan) is inserted coaxially through the spinal needle and gently advanced. Although little resistance can be felt, the electrode should be advanced until it reaches the posterior vertebral wall/posterior part of the tumor. The electrode is used only for its capacity to display the temperature (and is

Table 1: Patients, lesions, and RFA characteristics

Patient	Age (yr)	Primary Cancer	Lesion No.	Level	Posterior Cortex Disruption	Epidural Involvement	RFA Type (Device, Company)
1	55	Colon	1	L1	No	No	Bipolar RFA (OsteoCool; Medtronic)[a]
2	78	Bladder	1	L2	No	No	Bipolar RFA (OsteoCool; Medtronic)
3	46	Breast	1	L1	No	No	Monopolar RFA (Cool-tip; Medtronic)
4	66	Kidney	1	L2	No	Yes	Bipolar RFA (OsteoCool; Medtronic)
5	52	Breast	1	L3	No	No	Bipolar RFA (OsteoCool; Medtronic)
			2	L4	No	No	Bipolar RFA (OsteoCool; Medtronic)
6	73	Lung	1	L1	No	No	Bipolar RFA (STAR; Merrit Medical)[b]
7	70	Melanoma	1	L1	No	Yes	Bipolar RFA (OsteoCool; Medtronic)
8	76	Lung	1	L2	Yes	Yes	Bipolar RFA (OsteoCool; Medtronic)
9	64	Breast	1	L1	No	No	Bipolar RFA (OsteoCool; Medtronic)
10	63	Lung	1	L4	No	No	Bipolar RFA (OsteoCool; Medtronic)
11	67	Rectum	1	L3	No	No	Bipolar RFA (OsteoCool; Medtronic)
12	41	Lung	1	L1	No	No	Bipolar RFA (OsteoCool; Medtronic)
13	40	Breast	1	L3	Yes	Yes	Bipolar RFA (OsteoCool; Medtronic)

[a] Medtronic, Minneapolis, Minnesota.
[b] Merit Medical, South Jordan, Utah.

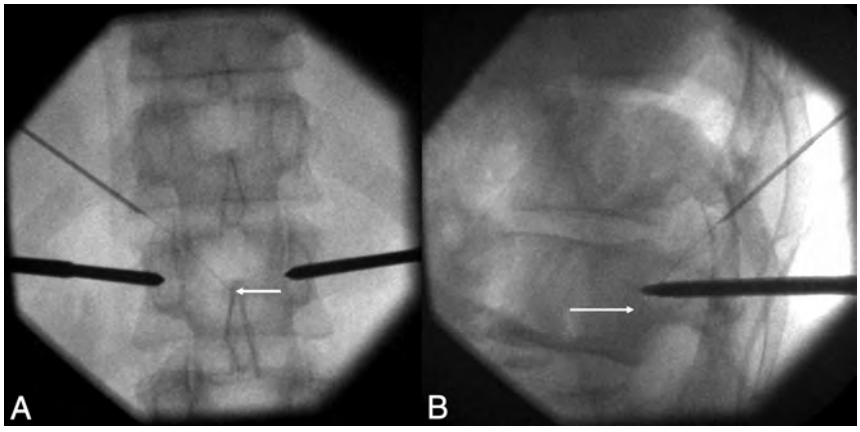

FIG 1. Double-oblique transforaminal approach on fluoroscopy (patient 12). Anterior-posterior (*A*) and lateral (*B*) fluoroscopic projections demonstrate the tip of the thermosensor (*white arrow*) just posterior to the vertebral body, at its mid portion (*B*), and in the midline (*A*), thanks to an oblique approach in both anterior-posterior and lateral views.

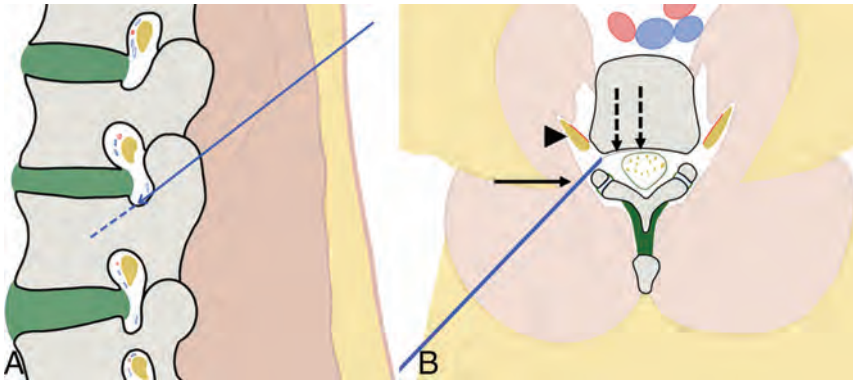

FIG 2. Representation and principle of the double-oblique approach. *A*, Drawing from a sagittal perspective. The craniocaudal approach in the sagittal plane enables going through the posterior and inferior parts of the foramen, away from the radicular nerve and vessels. *B*, Drawing from an oblique axial view (in the axis of the sagittal angulation). The lateromedial approach allows slipping along the facet joint with the 18-ga needle (*arrow*), away from the nerve and vessels (*arrowhead*). The 28-ga thermosensor (*dotted arrows*) can then be advanced into the anterior epidural space toward the posterior wall of the vertebral body.

therefore referred to as a thermosensor). The various steps of the double-oblique transforaminal approach are presented in Fig 3.

Additionally, hydrodissection using dextrose mixed with contrast (50:50 ratio for optimal visualization) can be combined with temperature monitoring. Here, before the insertion of the thermosensor, a Y-valve is connected to the hub of the 18-ga needle, and once the thermosensor has been introduced through the distal port of the valve, fluid may be injected through the lateral port (Fig 4).

RESULTS

Detailed results are listed in Table 2. The mean time to optimally position the thermosensor was 10.6 minutes (range, 5–38 minutes). There was a single case requiring >12 minutes for thermosensor insertion (a case requiring conebeam CT acquisition). Optimal positioning was achieved in 13 cases with a technical success rate of 93%. In the case considered unsuccessful, the thermometer was in the epidural space but 4 mm cranial and 5 mm lateral to the optimum, desired end point. Additional hydrodissection was performed through the same access in 11 cases and was effective in all cases except 2 (both cases with epidural extension). The mean maximal temperature displayed by the thermosensor was 42° (range, 39°–45°). None of the cases had premature stoppage of ablation. In a single case

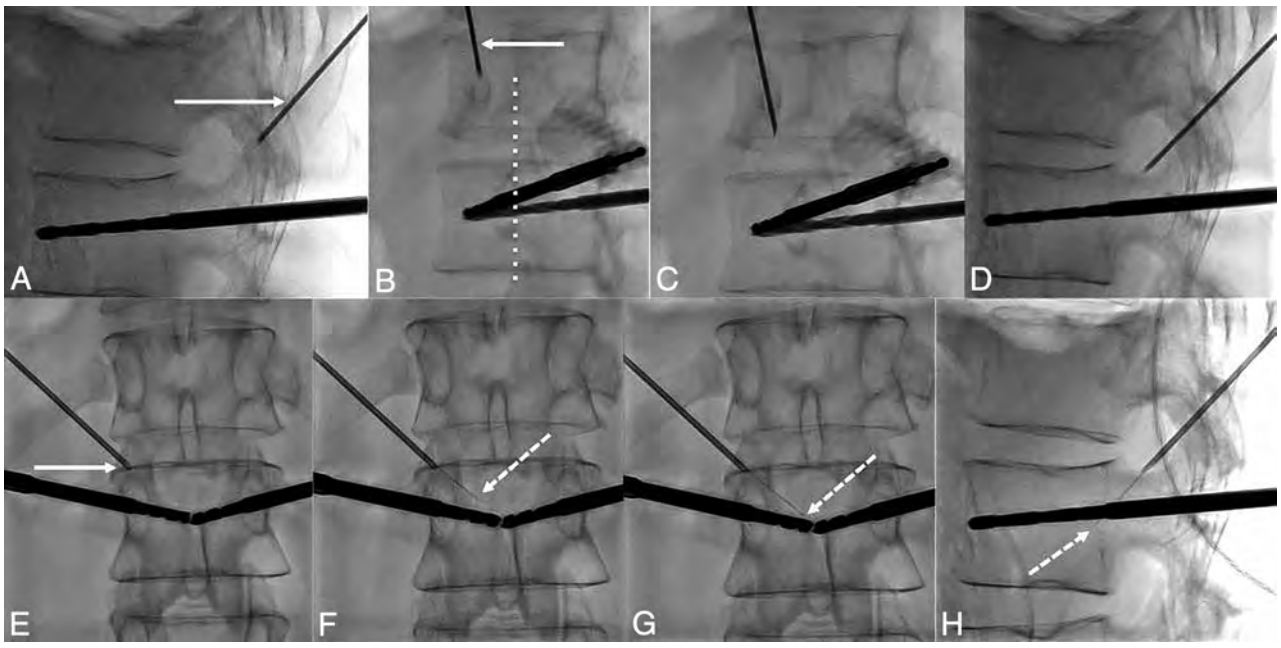

FIG 3. Fluoroscopic details of the technique of the transforaminal approach. *A*, The craniocaudal angulation in the sagittal plane is estimated on the lateral projection to point the 18-ga needle (*white arrow*) used as a landmark on the skin of the patient toward the posterior and inferior parts of the foramen. *B*, The 35° oblique view (from the anterior-posterior view) is then used to define the distance of the entry point laterally. The 18-ga spinal needle (*arrow*) should be pointed toward the lateral part of the facet joint (*dotted line*). *C*, The needle is advanced in the oblique view toward the foramen. *D*, Once in the vicinity of the foramen, the lateral view confirms that the needle enters it at its posterior and inferior parts. *E*, Satisfactory localization of the needle tip (*arrow*) inside the foramen is confirmed on anterior-posterior projection. *F*, The 28-ga thermosensor (*dotted arrow*) is gently advanced into the canal until it reaches the midline (*G*), where resistance is felt. *H*, At this point, the tip of the thermometer (*dotted arrow*) should be located at the middle portion of the vertebral body on the lateral view.

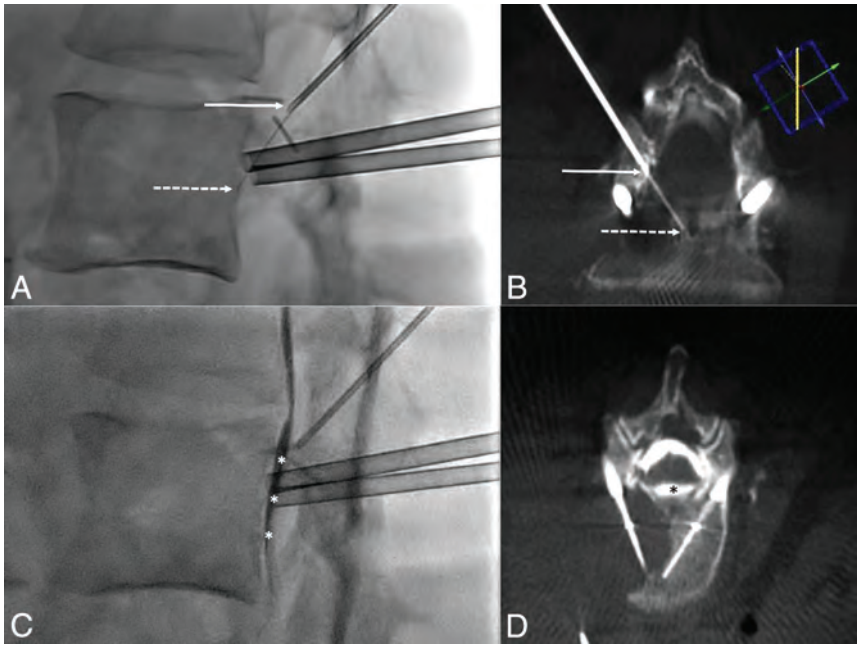

FIG 4. Thermal monitoring combined with hydrodissection. *A*, Lateral fluoroscopic view demonstrates the 18-ga needle in the foramen (*arrow*) and the thermosensor in contact with the posterior wall (*dotted arrow*). *B*, Conebeam CT acquisition with reconstruction in the axis of the needle and thermometer confirms the findings of fluoroscopy with the 18-ga needle (*arrow*) and the thermosensor (*dotted arrow*). *C*, Lateral view after injection of dextrose mixed with contrast shows satisfactory diffusion of the fluid into the anterior epidural space (*white asterisks*) separating the dural sac from the vertebral body. *D*, This is again outlined on the conebeam CT acquisition, which demonstrates the hydrodissection (*black asterisk*) between the posterior wall and the dural sac.

(performed with monopolar RFA), continuous irrigation of the anterior epidural space had to be performed to maintain the temperature at 45°. No postoperative neural deficits were encountered. MR imaging was performed in the early postoperative period in all patients within a mean of 13 days (range, 1–30 days) with no evidence of epidural hematoma, and fluid had completely reabsorbed in all patients who had benefited from additional hydrodissection.

DISCUSSION

As demonstrated in this case series, the transforaminal insertion of a small thermosensor into the anterior epidural space at the midlevel of a vertebral body is technically feasible, can be performed with stand-alone fluoroscopy, and adds little time to the procedure. Double-oblique access is mandatory to access the midlevel of the vertebral body wall because it allows lining up of the thermosensor with the ideal trajectory. Because the thermocouple is very thin, a more direct approach

Table 2: Results of transforaminal approach

Patient	Foramen	Guidance	Time (min)	Obliquity in the Sagittal Plane	Technical Success[a]	Hydrodissection	Maximal Temperature (°C)
1	T12–L1	Fluoro	11	40°	Yes	Yes, effective	39
2	L1–L2	Fluoro	11	40°	Yes	Yes, effective	41
3	T12–L1	CT & fluoro	9	36°	Yes	Yes, effective	45
4	L1–L2	Fluoro	12	35°	Yes	No	45
5	L2–L3	Fluoro	10	43°	Yes	Yes, effective	43
	L3–L4	Fluoro	6	38°	Yes	No	44
6	T12–L1	CT & fluoro	7	42°	Yes	Yes, effective	41
7	T12–L1	Fluoro	8	44°	Yes	Yes, ineffective	44
8	L1–L2	Fluoro & CBCT	38	33°	No (4 mm too cranial and 5 mm too lateral)	Yes, ineffective	39
9	T12–L1	Fluoro	5	36°	Yes	Yes, effective	43
10	L3–L4	Fluoro	8	47°	Yes	Yes, effective	38
11	L2–L3	CT & fluoro	9	37°	Yes	Yes, effective	39
12	T12–L1	CT & fluoro	7	47°	Yes	Yes, effective	45
13	L2–L3	CT & fluoro	7	44°	Yes	No	42

Note:—Fluoro indicates fluoroscopy; CBCT, conbeam CT.

[a] Technical success was defined by a position of the thermosensor in the midline on anteroposterior view and at the midportion of the posterior wall on lateral view.

(similar to a discal puncture) cannot achieve such positioning because the thermometer will not "take the curve" along the posterior part of the vertebral body. The craniocaudal approach should always be favored to avoid transgressing the danger zone located at the anterior and superior parts of the foramina, which contains the radicular nerve and adjacent vessels.[6] The double-oblique approach allows the safest passage (posterior and inferior) through the foramen.[7,8] In the aging spine, the anatomy of the foramen can, however, be modified by a bulging disc and/or osteophytes. Careful examination of the planning CT is therefore recommended before thermosensor insertion.

Although more challenging than a posterior epidural or a straight transforaminal approach, the technique is the only method to access the anterior epidural space at exactly the level of the RFA probes where fluctuations in local temperature are believed to be the most critical because of the shape and extent of the expected ablation zone. Moreover, it can easily be combined with hydrodissection, which allows separation of the dural sac from the ablation area if the tumor does not extend into the anterior epidural fat. The major challenge of the technique is to precisely navigate through the foramen under fluoroscopy with a double-oblique approach. Any deviation from the ideal trajectory might lead to either a suboptimal position or the impossibility of advancing the thermosensor because of bony interposition.

In this series, we had a single case in which active fluid injection was required to maintain the local temperature at a maximum threshold of 45°. This excellent safety profile of ablation might be explained by the preferential use of dedicated bone bipolar RFA devices that are known not to diffuse through an intact osseous cortex and form smaller, precise, and more predictable ablation zones than other ablation techniques (cryoablation, microwave, monopolar RFA).[2,9] Nevertheless, local thermal monitoring gives extra confidence and reassurance to the operating physician who can follow the real-time evolution of local temperatures, thereby increasing the safety profile of the procedure, even though the present study is not powered enough to statistically prove it. This technique is particularly useful if the procedure is being performed with the patient under general anesthesia without access to intraprocedural neurophysiologic testing to monitor neural conduction.[10] It can theoretically be used in combination with all heat- or cold-based ablation modalities (RFA, microwave, laser, cryoablation) to avoid breaching above 45° or below 0°, which are known to be the neurotoxic threshold temperatures.[11] Although favorable and with many potential uses, this technique is unfortunately not transferable to the dorsal spine because of the interposition of the ribs, which preclude a required steeper sagittal approach. The present study is limited by the small cohort of patients, which does not allow definitive conclusions regarding efficacy and safety. Moreover, all the procedures were performed by interventional radiologists trained in the spinal procedure, likely representing a bias in terms of reproducibility.

Disclosures: Julien Garnon—*UNRELATED*: *Consultancy*: BTG-Galil Medical; *Payment for Lectures Including Service on Speakers Bureaus*: Canon Medical, Medtronic. Afshin Gangi—*UNRELATED*: *Payment for Lectures Including Service on Speakers Bureaus:* Canon Medical; *Patents (Planned, Pending or Issued):* AprioMed.

REFERENCES

1. Khan MA, Deib G, Deldar B, et al. **Efficacy and safety of percutaneous microwave ablation and cementoplasty in the treatment of painful spinal metastases and myeloma.** *AJNR Am J Neuroradiol* 2018;39:1376–83 CrossRef Medline
2. Wallace AN, Hillen TJ, Friedman MV, et al. **Percutaneous spinal ablation in a sheep model: protective capacity of an intact cortex, correlation of ablation parameters with ablation zone size, and correlation of postablation MRI and pathologic findings.** *AJNR Am J Neuroradiol* 2017;38:1653–59 CrossRef Medline
3. Westbroek EM, Goodwin ML, Hui F, et al. **Thermal injury to the spinal cord, a rare complication of percutaneous microwave spine tumor ablation: case report.** *J Clin Neurosci* 2019;64:50–54 CrossRef Medline
4. Tsoumakidou G, Buy X, Garnon J, et al. **Percutaneous thermal ablation: how to protect the surrounding organs.** *Tech Vasc Interv Radiol* 2011;14:170–76 CrossRef Medline
5. Kastler A, Krainik A, Sakhri L, et al. **Feasibility of real-time intraprocedural temperature control during bone metastasis thermal**

microwave ablation: a bicentric retrospective study. *J Vasc Interv Radiol* 2017;28:366–71 CrossRef Medline
6. Hoshide R, Feldman E, Taylor W. **Cadaveric analysis of the Kambin's triangle.** *Cureus* 2016;8:e475 CrossRef Medline
7. Mandell JC, Czuczman GJ, Gaviola GC, et al. **The lumbar neural foramen and transforaminal epidural steroid injections: an anatomic review with key safety considerations in planning the percutaneous approach.** *AJR Am J Roentgenol* 2017;209:W26–35 CrossRef Medline
8. Kennedy DJ, Dreyfuss P, Aprill CN, et al. **Paraplegia following image-guided transforaminal lumbar spine epidural steroid injection: two case reports.** *Pain Med* 2009;10:1389–94 CrossRef Medline
9. Cazzato RL, Garnon J, Caudrelier J, et al. **Low-power bipolar radiofrequency ablation and vertebral augmentation for the palliative treatment of spinal malignancies.** *Int J Hyperthermia* 2018;34:1282–88 CrossRef Medline
10. Kurup AN, Schmit GD, Morris JM, et al. **Avoiding complications in bone and soft-tissue ablation.** *Cardiovasc Intervent Radiol* 2017;40:166–76 CrossRef Medline
11. Tsoumakidou G, Koch G, Caudrelier J, et al. **Image-guided spinal ablation: a review.** *Cardiovasc Intervent Radiol* 2016;39:1229–38 CrossRef Medline

Chimeric Antigen Receptor T-Cell Neurotoxicity Neuroimaging: More Than Meets the Eye

This letter is in response to the Practice Vignette "Chimeric Antigen Receptor T-Cell Therapy: What the Neuroradiologist Needs to Know" by Valand et al. The authors reviewed the neuroimaging findings in patients with chimeric antigen receptor T-cell (CAR T) and recommended that MR imaging of the brain be considered before treatment to better distinguish chronic from acute changes.

On the basis of our extensive experience with CAR T neurotoxicity, we would like to provide our perspective on the authors' conclusion that imaging findings in neurotoxicity are nonspecific. We and others have found several characteristic patterns in both children and adults with CD19-CAR T–related neurotoxicity.[1-4] The most common pattern includes reversible T2 hyperintensities and swelling in the bilateral thalami, pons, and medulla, often accompanied by symmetric white matter T2 hyperintensities that are subcortical or affect the external and extreme capsule (Fig 1*A*). Less specific, but still characteristic, are focal white matter T2 hyperintensities with or without contrast enhancement, which may occur at sites of prior CNS injury (Fig 1*B*). A rare variant is cortical diffusion restriction with subsequent cortical atrophy (Fig 1*C*). Finally, global cerebral edema is seen in the most severe cases, and the bithalamic swelling can often be appreciated in these patients (Fig 1*D*).

The role of CNS imaging before CAR T treatment is not well-defined at this point. In a pediatric cohort of 43 patients, we found a higher incidence of neurotoxicity in patients who had abnormal MR imaging findings before CAR T infusion, compared with those who had normal findings or no imaging.[3] However, this conclusion is tempered by the fact that pretreatment imaging was not available for all patients. We agree with the authors that comprehensive imaging before CAR T treatment would be very helpful in assessing whether any abnormalities during treatment are acute or chronic. This question should be answered via a clinical trial to rigorously evaluate the yield of routine head imaging in patients who undergo CAR T treatment. Imaging can be cumbersome and expensive, especially for pediatric patients who require sedation.

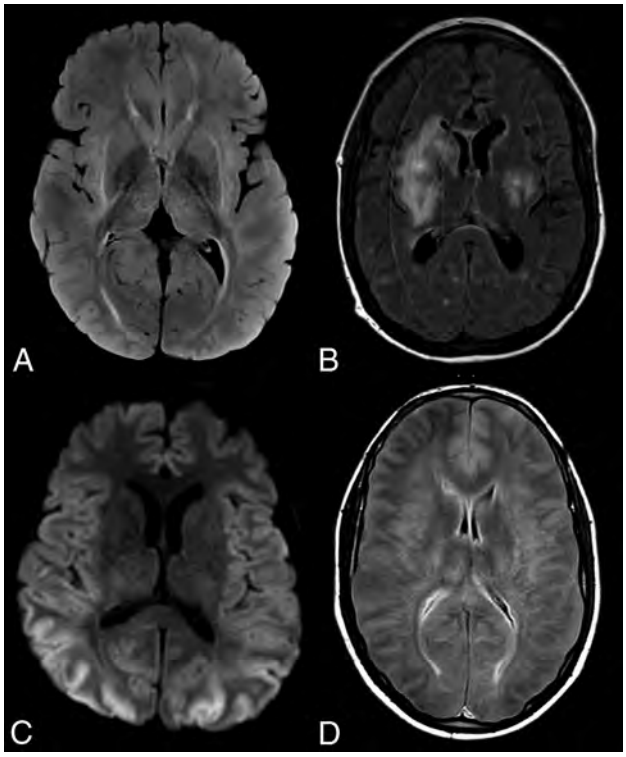

FIGURE. Characteristic imaging findings in CD19-CAR T–related neurotoxicity. *A*, FLAIR image showing bithalamic edema and symmetric white matter T2 hyperintensities. *B*, T1+gadolinium image of asymmetric enhancing white matter lesions. *C*, Diffusion-weighted image showing right > left occipital cortical diffusion restriction. *D*, FLAIR image of a patient with global cerebral edema.

Disclosures: Juliane Gust—*RELATED*: *Grant*: National Institute of Neurological Disorders and Stroke, *Comments*: Child Neurology Career Development Program K-12 award (1K12NS098482-02).* *Money paid to institution.

REFERENCES

1. Gust J, Hay KA, Hanafi LA, et al. **Endothelial activation and blood-brain barrier disruption in neurotoxicity after adoptive**

http://dx.doi.org/10.3174/ajnr.A6184

immunotherapy with CD19 CAR-T Cells. *Cancer Discov* 2017; 7:1404–19 CrossRef

2. Gust J, Taraseviciute A, Turtle CJ. **Neurotoxicity associated with CD19-targeted CAR-T cell therapies.** *CNS Drugs* 2018;32:1091–101 CrossRef Medline
3. Gust J, Finney OC, Li D, et al. **Glial injury in neurotoxicity after pediatric CD19-directed CAR-T cell therapy.** *Ann Neurol* 2019;86:42–54 CrossRef Medline
4. Santomasso BD, Park JH, Salloum D, et al. **Clinical and biological correlates of neurotoxicity associated with CAR T-cell therapy in patients with b-cell acute lymphoblastic leukemia.** *Cancer Discov* 2018;8:958–71 CrossRef Medline

J. Gust
Seattle Children's Division of Pediatric Neurology
Department of Neurology
University of Washington
Seattle, Washington

Center for Integrative Brain Research
Seattle Children's Research Institute
Seattle, Washington

G.E. Ishak
Seattle Children's Division of Radiology
Department of Radiology
University of Washington
Seattle, Washington

Chimeric Antigen Receptor T-Cell Therapy: Are Neuroradiologists Prepared?

I read with interest the Practice Vignette by Valand et al with regard to neurotoxicity of chimeric antigen receptor T-cell (CAR T) therapy for hematologic cancers.[1] The authors concluded that brain MR imaging is unremarkable in mild forms of neurotoxicity and only demonstrates nonspecific findings in the context of severe neurotoxicity, which can resemble chronic microvascular ischemia and migraine. While I agree that the imaging findings are not pathognomonic, 2 case series in patients with severe CD19-directed CAR T–induced neurotoxicity showed similar imaging findings of bilateral thalamic and brain stem involvement with extension to the basal gangRlia and extreme capsule, resembling central-variant posterior reversible encephalopathy syndrome or acute necrotizing encephalopathy in a subset of patients.[2,3] Another reported imaging finding was transient lesions of the splenium of the corpus callosum characterized by restricted diffusion and T2 prolongation with resolution on subsequent imaging.[2] In addition, a recent study indicated restricted diffusion in the bilateral occipital cortex, which demonstrated hypometabolism on subsequent FDG-PET imaging.[3] Considering that all the available studies only reported findings on conventional MR imaging, it should not be surprising that the authors detected abnormalities only in a subset of patients with severe neurotoxicity.

CAR T therapy neurotoxicity represents a continuum ranging from different degrees of neurotoxicity to severe brain edema in lethal cases, which is corroborated by postmortem studies.[2,3] Santomasso et al[2] analyzed excitatory agonists such as glutamate (Glut) and quinolinic acid (QA) in the CSF of 13 patients receiving CD19-directed CAR T treatment and demonstrated a significant increase in Glut and QA CSF levels during neurotoxicity compared with pretreatment. In addition, Gust et al[3] demonstrated increased CSF levels of S100 calcium binding protein B and glial fibrillary acidic protein in patients with neurotoxicity, indicating astrocyte injury, which would explain the presence of cerebral edema, given the key role of glial cells in osmotic regulation in the brain.

In conclusion, neuroradiologists should have a high level of suspicion for CAR T therapy neurotoxicity in patients with bilateral thalamic and brain stem involvement. Designing prospective studies with advanced MR imaging sequences focusing on the detection of early brain edema would be crucial to better understand this entity and discover early imaging findings of CAR T therapy neurotoxicity.

REFERENCES

1. Valand HA, Huda F, Tu RK. **Chimeric antigen receptor t-cell therapy: what the neuroradiologist needs to know**. *AJNR Am J Neuroradiol* 2019;40:766–68 CrossRef Medline
2. Santomasso BD, Park JH, Salloum D, et al. **Clinical and biological correlates of neurotoxicity associated with CAR t-cell therapy in patients with b-cell acute lymphoblastic leukemia.** *Cancer Discov* 2018;8:958–71 CrossRef Medline
3. Gust J, Finney OC, Li D, et al. **Glial injury in neurotoxicity after pediatric cd19-directed chimeric antigen receptor t cell therapy.** *Ann Neurol* 2019;86:42–54 CrossRef Medline

S.A. Nabavizadeh
Department of Radiology
Hospital of University of Pennsylvania
Perelman School of Medicine of the University of Pennsylvania
Philadelphia, Pennsylvania

http://dx.doi.org/10.3174/ajnr.A6186

REPLY:

Thank you for providing an opportunity to respond to the 2 letters, the first by Drs Gust and Ishak and the second by Dr Nabavizadeh. Our article focused on imaging findings of neurotoxicity of chimeric antigen receptor T-cell (CAR-T) therapy, an important new therapy for B-cell malignancies. As collective experience increases, so will reporting and understanding the imaging findings. Most published imaging findings of toxicity are in nonimaging journals. Adult neurotoxicity imaging findings were reported in *Cancer Discovery* in December 2017 by Gust et al;[1] *Cancer Discovery* in June 2018 by Santomasso et al;[2] and *CNS Drugs* in November 2018.[3] Subsequent to our May 2019 publication in the *American Journal of Neuroradiology*, *Annals of Neurology* published findings by Gust et al[4] in children and young adults in July 2019 and recently *Brain,* in May 2019, reported findings of acute stroke and hemorrhage.[5] As imaging findings of neurotoxicity are identified and published, neuroradiologists and the imaging community will benefit from continued interest and publication in this area.

http://dx.doi.org/10.3174/ajnr.A6231

REFERENCES

1. Gust J, Hay KA, Hanafi L-A, et al. **Endothelial activation and blood-brain barrier disruption in neurotoxicity after adoptive immunotherapy with CD19 CAR-T cells.** *Cancer Discov* 2017;7:1404–19 CrossRef Medline
2. Santomasso BD, Park JH, Salloum D, et al. **Clinical and biological correlates of neurotoxicity associated with CAR T-cell therapy in patients with B-cell acute lymphoblastic leukemia.** *Cancer Discov* 2018;8:958–71 CrossRef Medline
3. Gust J, Taraseviciute A, Turtle CJ. **Neurotoxicity sssociated with CD19-targeted CAR-T cell therapies.** *CNS Drugs* 2018;32:1091–101 CrossRef Medline
4. Gust J, Finney OC, Li D, et al. **Glial injury in neurotoxicity after pediatric CD19-directed CAR-T cell therapy.** *Ann Neurol* 2019;86:42–54 CrossRef Medline
5. Rubin DB, Danish HH, Ali AB, et al. **Neurological toxicities associated with chimeric antigen receptor T-cell therapy.** *Brain* 2019; 142:1334–48 CrossRef Medline

H.A. Valand
American University of Integrative Sciences
Brampton, Ontario, Canada
F. Huda
George Washington University Hospital
Washington, DC
R.K. Tu
Progressive Radiology
George Washington University, United Medical Center
Washington, DC

Hardly a Tweet Storm

We read with interest the Social Media Vignette, "The Continued Rise in Professional Use of Social Media at Scientific Meetings: An Analysis of Twitter Use During the ASNR 2018 Annual Meeting."[1] While we agree that there has been an increase in Twitter use during the 5-year period observed, we note that in Table 1, only 96 radiologists tweeted. This compares with an American Society of Neuroradiology membership of more than 4000, representing approximately 2.4% of the potential pool. Furthermore, as demonstrated in our recent publication,[2] only 12 of 75 American Neuroradiology Division Chiefs and 4 of 75 academic neuroradiology programs in the United States even had Twitter accounts. We lag behind our colleagues in neurology, neurosurgery, and the neurosciences in embracing social media. As far as Twitter goes, during 1 year (May 1, 2017 to April 30, 2018), only 1 of the neuroradiology programs (University of Southern California) had more than 5 tweets in the year, Mount Sinai had 5 tweets, and the 2 other divisions with Twitter accounts did not tweet at all.

Granted, tweeting at meetings by individuals is different from Neuroradiology Division tweet usage; however, the dissemination of Twitter in neuroradiology circles remains sparse.

http://dx.doi.org/10.3174/ajnr.A6187

We believe a more concerted effort to ramp up the neuroradiology community's use of social media would be helpful in getting our professional "message" out there.

Disclosures: David Yousem—*UNRELATED*: *Expert Testimony*: Medicolegal work; *Payment for Lectures Including Service on Speakers Bureaus:* American College of Radiology Education Center speaker; *Royalties*: Elsevier for 5 books, Analytical Informatics.

REFERENCES

1. D'Anna G, Chen MM, McCarty JL, et al. **The continued rise in professional use of social media at scientific meetings: an analysis of Twitter use during the ASNR 2018 annual meeting.** *AJNR Am J Neuroradiol* 2019;40:935–37 Medline
2. Charkhchi P, Sahraian S, Beheshtian E, et al. **Missed opportunity: neuroradiology training programs and social media**. *AJR Am J Roentgenol* 2019 Mar 5:1–6 [Epub ahead of print] CrossRef Medline

P. Charkhchi
S. Sahraian
E. Beheshtian
D.M. Yousem
Department of Radiology and Radiological Science
Division of Neuroradiology
The Johns Hopkins Medical Institutions
Baltimore, Maryland

REPLY:

We thank Dr Charkhchi and colleagues for their letter.[1] The purpose of our work[2] was to analyze the Twitter usage during the American Society of Neuroradiology (ASNR) annual meeting and, in particular, what topics and how many tweets occurred compared with previous meetings. We agree that a greater audience could help in disseminating ASNR's meeting messages and content and were encouraged by the increase in usage of this medium over prior years.

We are aware of the lag in the neuroradiologic social media community in contrast to other medical specialties: however, if we tried to put a perspective on this topic, only 20 radiologists/neuroradiologists used Twitter during the annual meeting 2014[3], so in just 4 years, we have made progress. Furthermore, our work showed that independent of the number of users, now a virtual and global community exists and that the community is growing in number and especially in its ability to engage in constructive dialogue regarding interesting cases, share neuroradiology-related knowledge, and disseminate key meeting-related information. While neuroimaging remains the most tweeted topic, during ASNR 2018, we noted additional great discussions often beyond the "classic" neuroradiologic topics, such as the Common Data Elements Project, or the importance of mentorship.

Talking about social media in radiology certainly will improve our presence, and it is important to continue using social media as tools for medical professionals to share accurate information. Furthermore, social media usage is very different between the United States and Europe, as evidenced by a similar analysis during the Annual Meeting of the European Neurological Society in 2018.[4]

We agree that it is also important for radiology/neuroradiology departments to be active on social media.[5,6] They are a powerful tool to engage students and young and senior colleagues in our specialty and our patients; our younger colleagues may be particularly reachable with social media, so a department or an academic institution should also use this channel to promote activities, courses, learning, and job opportunities.[7] However, we believe that comparing tweeting of neuroradiology divisions to all of the subgroups in our article is not a fair comparison. Divisions are a small subset of accounts tweeting at ASNR 2018. Use of institutional divisional social media accounts may be more restricted, and divisional Twitter accounts may have a different purpose than personal, society, or journal social media accounts. The purpose of a divisional account may be to promote activities, courses, training, and job opportunities from their insitutition.[7] Specialty societies and journal social media accounts may be more focused on disseminating accurate up-to-date information, engaging with people and members.

Our article points to growth in the use of social media and a trend in the right direction in the neuroradiologic community.

http://dx.doi.org/10.3174/ajnr.A6214

REFERENCES

1. Charkhchi P, Sahraian S, Beheshtian E, et al. **Missed opportunity: neuroradiology training programs and social media.** *AJR Am J Roentgenol* 2019 Mar 5:1–6. [Epub ahead of print] CrossRef Medline
2. D'Anna G, Chen MM, McCarty JL, et al. **The continued rise in professional use of social media at scientific meetings: an analysis of Twitter use during the ASNR 2018 annual meeting.** *AJNR Am J Neuroradiol* 2019;40:935–37 CrossRef Medline
3. Radmanesh A, Kotsenas AL. **Social media and scientific meetings: an analysis of Twitter use at the annual meeting of the American Society of Neuroradiology.** *AJNR Am J Neuroradiol* 2016;37:25–27 CrossRef Medline
4. D'Anna G, Pyatigorskaya N, Appelman A, et al. **Exploring new landmarks: analysis of Twitter usage during the 41st ESNR annual meeting.** *Neuroradiology* 2019;61:621–26 CrossRef Medline
5. Kohli MD, Daye D, Towbin AJ, et al. **Social media tools for department and practice communication and branding in the digital age.** *Radiographics* 2018;38:1773–85 CrossRef Medline
6. Kotsenas AL, Arce M, Aase L, et al. **The strategic imperative for the use of social media in health care.** *J Am Coll Radiology* 2018;15:155–61 CrossRef Medline
7. Kalia V, Ortiz DA, Patel AK, et al. **Leveraging Twitter to maximize the radiology meeting experience.** *J Am Coll Radiology* 2018;15:177–83 CrossRef Medline

G. D'Anna
Radiology Unit
Humanitas Mater Domini
Castellanza (Varese), Italy
M.M. Chen
Department of Radiology
University of Texas MD Anderson Cancer Center
Houston, Texas
J. McCarty
Department of Diagnostic and Interventional Imaging
University of Texas Health Sciences Center at Houston
Houston, Texas
A. Radmanesh
Department of Radiology
New York University School of Medicine
New York, New York
A.L. Kotsenas
Department of Radiology
Mayo Clinic
Rochester, Minnesota

Increasing Social Media Involvement around the American Society of Neuroradiology Annual Meeting

I read with great interest the social media vignette by D'Anna et al,[1] which describes the analysis of Twitter use during the American Society of Neuroradiology (ASNR) 2018 Annual Meeting. Although the analysis showed a substantial increase in Twitter use during the past 4 years, there is still room for improvement. More robust community engagement can be achieved by implementing some simple-but-practical strategies before the conference even begins.

Submission and acceptance of abstracts for original research articles, case reports, and educational posters are an integral part of every annual meeting and actively involve a large number of physicians. After the announcement of acceptances, development of a method to systematically share the abstract on social media would help increase the radiology community involvement in the conference and social media because physicians from multiple disciplines follow each other across social media platforms. Developing a central hashtag to share these abstracts will further help increase visibility and outreach (eg, #ASNR20Abstract).

http://dx.doi.org/10.3174/ajnr.A6185

Because a large number of fascinating keynotes, panels, and discussions take place during the conference, it is understandable that social media visibility for different events will vary because it depends on the social media involvement of the main speaker. However, to overcome this issue, the main Twitter account of the conference can conduct various Tweet chats beginning 2–3 months before the conference, and multiple speakers can give brief introductions of their topics. Conducting these Tweet chats will help increase the visibility of these events and generate enthusiasm for the actual event.

REFERENCE

1. D'Anna G, Chen MM, McCarty JL, et al. **The continued rise in professional use of social media at scientific meetings: an analysis of Twitter use during the ASNR 2018 annual meeting.** *AJNR Am J Neuroradiol* 2019;40:935–97 CrossRef Medline

T. Garg
Seth GS Medical College and KEM Hospital
Mumbai, Maharashtra, India

REPLY:

We thank T. Garg for his interest in our work,[1] and all his suggestions to improve ASNR social media engagement. We are so happy to show that the interest of a medical student so far from the United States is an example of the worldwide reach of the social media platform. The purpose of our work was to analyze the Twitter usage during the American Society of Neuroradiology (ASNR) annual meeting and, in particular, what topics and how many tweets occurred compared with previous meetings. We found that Twitter users are more comfortable sharing images of favorite lectures and commenting on lectures, compared with previous work.[2] At times, Twitter stimulated constructive dialogue on current topics such as patient-centered care, implementation of artificial intelligence, and so forth. Our observations are useful to improve the presence of neuroradiologists on-line and to implement new features in future meetings as you suggested. We appreciate T. Garg's suggestions and are encouraged to see others who are aware of the power of social media in spreading knowledge and scientific research. ASNR is proudly leading the neuroradiology Twitter community currently.

http://dx.doi.org/10.3174/ajnr.A6215

REFERENCES

1. D'Anna G, Chen MM, McCarty JL, et al. **The continued rise in professional use of social media at scientific meetings: an analysis of Twitter use during the ASNR 2018 Annual Meeting.** *AJNR Am J Neuroradiol* 2019;40:935–37 CrossRef Medline
2. Radmanesh A, Kotsenas AL. **Social media and scientific meetings: an analysis of Twitter use at the annual meeting of the American Society of Neuroradiology.** *AJNR Am J Neuroradiol* 2016;37:25–27 CrossRef Medline

G. D'Anna
Radiology Unit
Humanitas Mater Domini
Castellanza (Varese), Italy
M.M. Chen
Department of Radiology
University of Texas MD Anderson Cancer Center
Houston, Texas
J. McCarty
Department of Diagnostic and Interventional Imaging
University of Texas Health Sciences Center at Houston
Houston, Texas
A. Radmanesh
Department of Radiology
New York University School of Medicine
New York, New York
A.L. Kotsenas
Department of Radiology
Mayo Clinic
Rochester, Minnesota

An Important Pitfall in Diagnosing Intracanalicular Vestibular Schwannoma

Technical advances in MR imaging enable scanning of millimeter- and submillimeter-thick slices in a relatively short acquisition time, so sequences such as contrast-enhanced 3D T1 (eg, MPRAGE) are included in standard MR imaging protocols in many institutions. The MPRAGE sequence is especially important for the detection of small lesions such as a small intracanalicular vestibular schwannoma (Koos grade I).

The members of our interdisciplinary schwannoma board have encountered several patients with varying degrees of enhancement in the fundus of the internal auditory canal (IAC) who were referred to us with suspected schwannomas (Fig 1*A*–*D*). However, when we reviewed the patients' initial MR images and the follow-up images, that was a false-positive finding.

Enhancement in the fundus of the IAC is sometimes detected in subjects without pathologic conditions, and it can be unilateral or bilateral and present in varying degrees (Fig 1*A*, -*C*). This is most likely due to the enhancement of vascular structures such as the venous plexus surrounding the nerve sheath (eg, around the Scarpa ganglion) in the acoustic facial cistern[1] or due to the presence of capillaries in the meningeal layers covering the fundus.

In a recently published study performed using synchrotron phase-contrast imaging, Mei et al[2] demonstrated the presence of previously unknown pillars or villi that support the cranial nerves in the IAC and are occasionally associated with blood vessels, mostly capillaries. These vascular structures within the villi may play a key role in the enhancement in this region, and variation in the amount of blood vessels between different subjects may be one cause for the different degrees of enhancement observed on postcontrast MR images (Fig 1*A*, -*C*).

Therefore, on the basis of our experience, the presence of enhancement in this region should be always correlated with the CISS sequence to confirm or exclude the presence of a nodular lesion, which represents the schwannoma (Fig 1*F*).

Knowledge of this pitfall is important so that CISS can be added if such an incidental finding is present, to reduce the number of false-positive cases and thereby reduce the unnecessary follow-up scans and consequentially to lower health care costs. This precaution will also avoid instilling unnecessary fear in patients who incorrectly believe they have a tumor that may affect their hearing and lifestyle.

Disclosures: Arsany Hakim—*UNRELATED*: *Grants/Grants Pending*: Swiss Heart Association.* Franca Wagner—*UNRELATED*: *Grants/Grants Pending*: Swiss MS Society.* *Money paid to the institution.

REFERENCES

1. Lescanne E, Velut S, Lefrancq T, et al. **The internal acoustic meatus and its meningeal layers: a microanatomical study**. *J Neurosurg* 2002;97:1191–97 CrossRef Medline
2. Mei X, Schart-Morén N, Li H, et al. **Three-dimensional imaging of the human internal acoustic canal and arachnoid cistern: a synchrotron study with clinical implications**. *J Anat* 2019;234:316–26 CrossRef Medline

A. Hakim
F. Wagner
University Institute of Diagnostic and Interventional Neuroradiology
Bern University Hospital, Inselspital
University of Bern, Bern, Switzerland

http://dx.doi.org/10.3174/ajnr.A6192

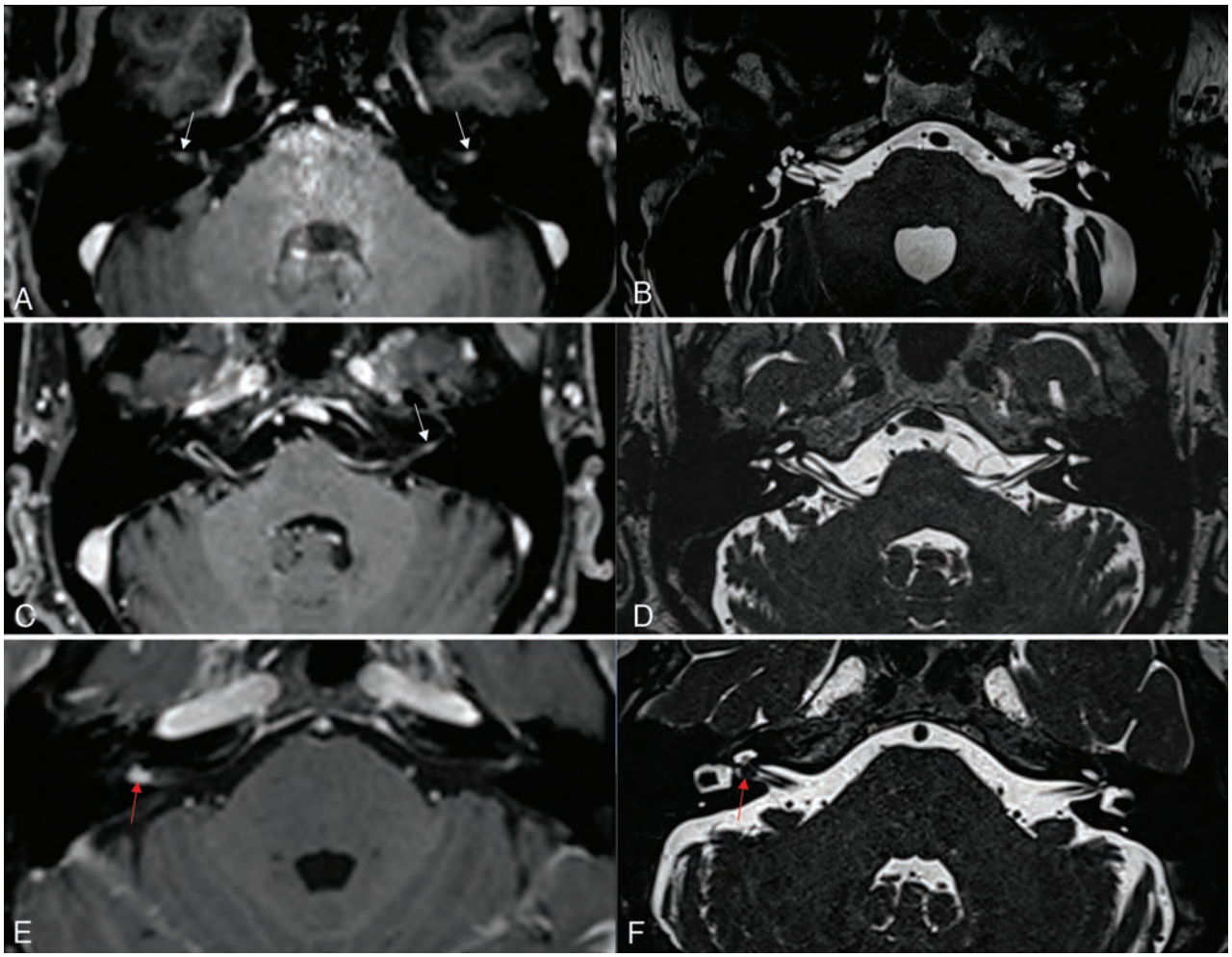

FIG 1. MPRAGE (*A*, *C*, and *E*) and CISS (*B*, *D*, and *F*) in 3 different patients (patient 1: *A* and *B*; patient 2: *C* and *D*; and patient 3: *E* and *F*). MPRAGE shows different degrees of enhancement in the fundus of the internal auditory canal bilaterally (left more than right) in patient 1 and on the left side in patient 2 (*white arrows* in *A* and *C*). However, in both patients, no analogous lesion was detected in the CISS sequence. Therefore, the enhancement was not due to the presence of a schwannoma but was most likely due to a vascular structure. In contrast, in patient 3, there was nodular enhancement in the fundus of the internal auditory canal on the right side (*red arrow* in *E*), which was accompanied by a corresponding lesion "filling defect" on the CISS sequence (*red arrow* in *F*) due to the presence of a small intracanalicular vestibular schwannoma (Koos I). Correlating findings in MPRAGE with the CISS sequence is crucial to avoiding misinterpretation of this enhancement.

Challenges in Differentiating Pediatric Autoimmune CNS Diseases with Similar Clinical and Imaging Phenotypes

We would like to commend Bulut et al[1] for their investigation of brain MR imaging findings that could potentially be useful in discriminating pediatric-onset neuromyelitis optica spectrum disorder (NMOSD) from acute disseminated encephalomyelitis (ADEM). These 2 entities exist within the broader category of immune-mediated CNS disease, which is so challenging to diagnose prospectively, given the complexity, heterogeneity, and clinical-radiologic overlap between these different immune-mediated conditions. Given the current limitations in our understanding of the underlying pathophysiology of these disorders, we would like to take this opportunity to provide a historical context for this article and highlight a few recent studies from *JAMA Neurology* with larger cohorts that adopt a more granular neuroimaging approach to disease characterization.

In their retrospective study of 10 pediatric patients with NMOSD and 10 pediatric patients with ADEM, Bulut et al identify MR imaging findings that could be potentially used to help differentiate NMOSD and ADEM in clinical practice. However, one must first acknowledge that, under the diagnostic criteria used in the study (2015 Consensus Diagnostic Criteria for NMOSD, https://www.ncbi.nlm.nih.gov/pubmed/26092914 and the 2007 Consensus Diagnostic Criteria for ADEM, https://www.ncbi.nlm.nih.gov/pubmed/17438241), it is possible for a single patient to meet both criteria. This highlights the tremendous clinical and radiologic overlap between these 2 general diagnostic categories and suggests that a NMOSD versus ADEM paradigm does not always allow adequate classification of the diseases. Even the term neuromyelitis optica (NMO) "spectrum disorder" implies that we currently lack an adequate understanding of the underlying pathophysiology to distinguish between specific entities within this 1 category, especially in the absence of antibodies against aquaporin-4 (AQP4), at least until another new causative autoantibody is identified. Similarly, ADEM is an umbrella term for entities often occurring after an infection or vaccination that share similar clinical phenotypes and imaging features, and it remains unclear how much of ADEM can be attributed to underlying autoantibodies such as those against myelin oligodendrocyte glycoprotein (MOG). Given these limitations, we should proceed with caution when drawing conclusions about MR imaging findings in these patients, especially when using small sample sizes and evolving disease classification systems.

In reality, patients in 2019 with new onset of immune-mediated CNS disease within the gray zone of NMOSD versus ADEM by imaging can end up with the clinical designation of ADEM if they meet the criteria for encephalopathy or present after a recent infection, but in some cases further discrimination can be rather arbitrary at initial presentation in the absence of positive anti-AQP4 or anti-MOG antibodies. This ongoing process of "greater discrimination through improved scientific understanding" is exemplified by the historical progression from "NMO is a variant of MS" to "NMO is a distinct antibody-mediated disease targeting AQP4" to "additional CNS antigens such as MOG can also be targeted by autoantibodies and result in a similar disease process."[2]

JAMA Neurology published a series of studies in 2018–2019 that provides additional insight into how best to characterize MR imaging findings in pediatric patients with new onset of immune-mediated CNS disease. For readers interested in exploring this topic in more detail, we specifically want to highlight the work of the following authors: Hacohen et al[3] wrote a prospective study of 102 pediatric patients with MOG antibody-associated disease (MOG Ab)–associated relapsing demyelinating syndromes initially given diagnoses of NMOSD, ADEM with subsequent optic neuritis, and multiphasic disseminated encephalomyelitis with relapsing optic neuritis who did not respond well to disease-modifying drugs but did respond to azathioprine, mycophenolate mofetil, rituximab and intravenous immunoglobulins. Dubey et al[4] wrote a retrospective study of 54 patients, including 16 children and 38 adults with MOG immunoglobulin G–positive (MOG-IgG +) myelitis with various clinical presentations, including isolated transverse myelitis, acute flaccid myelitis, and myelitis in combination with ADEM or optic neuritis who had imaging characteristics distinct from MS and AQP4-IgG myelitis. López-Chiriboga et al[5] wrote a retrospective study of 51 patients, including 31 children and 20 adults, with a clinical diagnosis of ADEM in which patients with persistent MOG Ab seropositivity had significantly higher rates of relapse.

It is always encouraging to see radiology contributing to the field of clinical research on NMOSD and ADEM that has largely been the domain of our neurology and pathology colleagues.

http://dx.doi.org/10.3174/ajnr.A6196

Neuroimaging will continue to have a tremendous impact in our understanding of these diseases, but further translational research and interdisciplinary collaboration with large cohorts of patients will likely be required before we can reliably distinguish immune-mediated CNS diseases that are currently incompletely characterized but have similar clinical and radiologic phenotypes.

REFERENCES

1. Bulut E, Karakaya J, Salama S, et al. **Brain MRI findings in pediatric-onset neuromyelitis optica spectrum disorder: challenges in differentiation from acute disseminated encephalomyelitis.** *AJNR Am J Neuroradiol* 2019;40:726–31 CrossRef Medline
2. Josep D. **Autoimmunity: The good, the bad, and the ugly.** *Neurol Neuroimmunol Neuroinflamm* 2015;2:e181 CrossRef Medline
3. Hacohen Y, Wong YY, Lechner C, et al. **Disease course and treatment responses in children with relapsing myelin oligodendrocyte glycoprotein antibody–associated disease.** *JAMA Neurol* 2018;75:478–87 CrossRef Medline
4. Dubey D, Pittock SJ, Krecke KN, et al. **Clinical, radiologic, and prognostic features of myelitis associated with myelin oligodendrocyte glycoprotein autoantibody.** *JAMA Neurol* 2019;76:301–09 CrossRef
5. López-Chiriboga AS, Majed M, Fryer J, et al. **Association of MOG-IgG serostatus with relapse after acute disseminated encephalomyelitis and proposed diagnostic criteria for MOG-IgG–associated disorders.** *JAMA Neurol* 2018;75:1355–63 CrossRef Medline

B.P. Kelley
P.A. Caruso
P.W. Schaefer
Department of Neuroradiology
Massachusetts General Hospital
Boston, Massachusetts

REPLY:

We appreciate your interest in our study and drawing the attention of neuroradiologists to our recent article, hence to the evolving field of neuroimmunology in the context of acute disseminated encephalomyelitis (ADEM), neuromyelitis optica spectrum disorder (NMOSD), and myelin oligodendrocyte glycoprotein (MOG) antibody–associated demyelinating diseases.

Our goal in the referenced article was to emphasize that children with NMOSD might present with clinical and MR imaging findings of ADEM and that neuroradiologists should be aware of this in the differential diagnosis. We think that as neuroradiologists it is our responsibility to suggest the possibility of NMOSD in our radiology reports so that the neurologists or pediatricians would consider antibody testing if they have not already done so. NMOSD is a relapsing autoimmune demyelinating disease, and the morbidity is high after every attack; therefore, antibody testing at the initial attack is tremendously important for timely diagnosis to avoid vision loss, paraplegia, and so forth. In the same context, neuroradiologists should be aware of the recent findings in the field of MOG antibody–associated demyelinating diseases, in which approximately 57% of children diagnosed with ADEM were tested positive for the MOG antibody in a recent large cohort study.[1] Therefore we believe that MOG antibody disease should also be in the differential diagnosis of ADEM in the neuroradiologists' reports when the imaging findings are suggestive.

We have known that ADEM is an umbrella term for immune-mediated acute demyelinating diseases of the CNS. As we have seen in NMOSD with historical progression from "NMO is a variant of MS" to "NMO is a distinct antibody-mediated disease targeting Aquaporin 4," we experience the same trend in MOG antibody–associated demyelinating disease in patients with seropositivity with unique and some overlapping imaging findings in patients diagnosed with ADEM. We believe that as more specific causative antibodies are discovered and as we observe different responses to treatments, there will be more emerging specific disease entities.

Thank you for your valuable contribution by highlighting a few recent important studies mainly focusing on impact of MOG antibody seropositivity in the course and treatment response of immune-mediated CNS diseases.[2-4] We also recommend our recently published articles on detailed imaging analysis of MOG-related encephalitis/encephalomyelitis, myelitis, and optic neuritis.[5,6] On the other hand, comparative studies particularly focusing on brain MR imaging findings of immune-mediated CNS diseases in children are limited, and future studies with larger cohorts in which MOG-antibody and aquaporin 4-antibody status is specified are needed.

http://dx.doi.org/10.3174/ajnr.A6216

REFERENCES

1. Hennes EM, Baumann M, Schanda K, et al. **Prognostic relevance of MOG antibodies in children with an acquired demyelinating syndrome.** *Neurology* 2017;89:900–08 CrossRef Medline
2. Hacohen Y, Wong YY, Lechner C, et al. **Disease course and treatment responses in children with relapsing myelin oligodendrocyte glycoprotein antibody-associated disease.** *JAMA Neurol* 2018;75:478–87 CrossRef Medline
3. Dubey D, Pittock SJ, Krecke KN, et al. **Clinical, radiologic, and prognostic features of myelitis associated with myelin oligodendrocyte glycoprotein autoantibody.** *JAMA Neurol* 2019;76:301–09 CrossRef Medline
4. Lopez-Chiriboga AS, Majed M, Fryer J, et al. **Association of MOG-IgG serostatus with relapse after acute disseminated encephalomyelitis and proposed diagnostic criteria for MOG-IgG-associated disorders.** *JAMA Neurol* 2018;75:1355–63 CrossRef Medline
5. Salama S, Khan M, Levy M, et al. **Radiological characteristics of myelin oligodendrocyte glycoprotein antibody disease.** *Mult Scler Relat Disord* 2019;29:15–22 CrossRef Medline
6. Salama S, Khan M, Pardo S, et al. **MOG antibody-associated encephalomyelitis/encephalitis.** *Mult Sclr* 2019:1352458519837705. [Epub ahead of print] CrossRef Medline

E. Bulut
Department of Radiology
J. Karakaya
Department of Statistics
Hacettepe University Faculty of Medicine
Ankara, Turkey
S. Salama
Department of Neurology and Psychiatry
University of Alexandria
Alexandria, Egypt
Department of Neurology
Johns Hopkins School of Medicine
Baltimore, Maryland
M. Levy
Department of Neurology
Johns Hopkins School of Medicine
Baltimore, Maryland
Department of Neurology
Massachusetts General Hospital and Harvard Medical School
Boston, Massachusetts
T.A.G.M. Huisman
Edward B. Singleton Chair of Radiology
Texas Children's Hospital
Houston, Texas
I. Izbudak
Section of Pediatric Neuroradiology, Division of Neuroradiology
The Russell H. Morgan Department of Radiology and Radiological Science
Johns Hopkins School of Medicine
Baltimore, Maryland

The authors regret that in the article "Surveillance of Unruptured Intracranial Saccular Aneurysms Using Noncontrast 3D-Black-Blood MRI: Comparison of 3D-TOF and Contrast-Enhanced MRA with 3D-DSA" (*AJNR Am J Neuroradiol* 2019;40:960–66), the legend for Fig 4 did not match the figure. A corrected legend with the original figure is reproduced below.

http://dx.doi.org/10.3174/ajnr.A6206

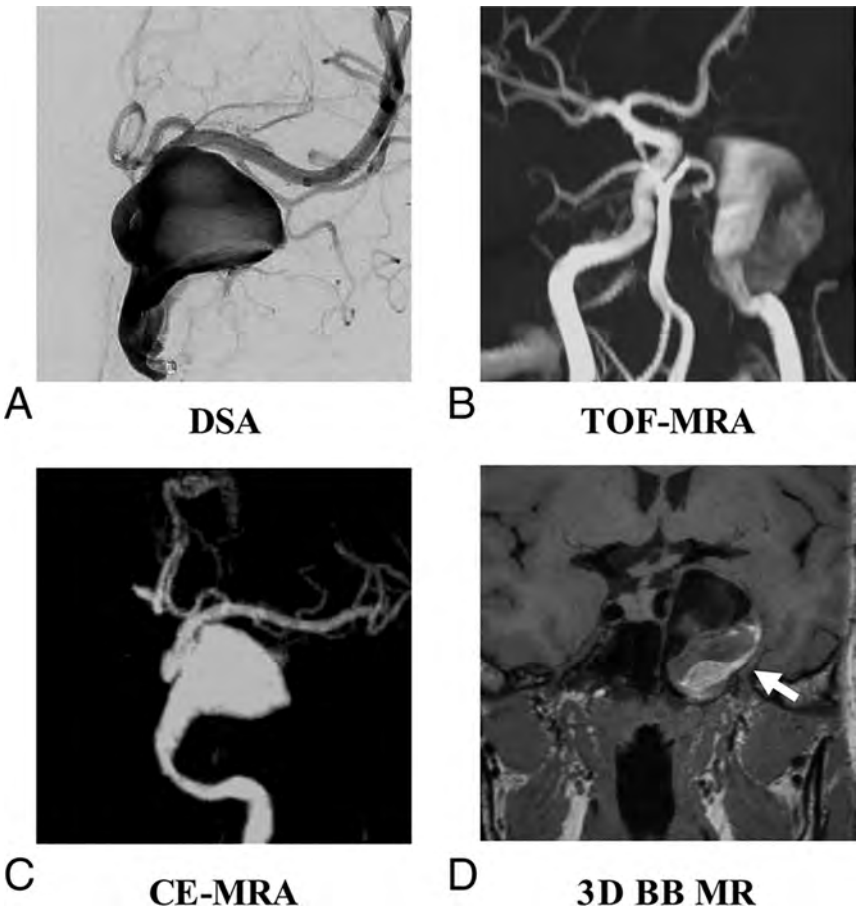

FIG 4. *A*, A 63-year-old woman with a right internal carotid artery aneurysm on DSA. 3D black-blood (BB) SPACE (*D*) can clearly visualize the sac and intraluminal thrombus of the aneurysm, which is superior to DSA (*A*), TOF-MRA (*B*), and contrast-enhanced (CE)-MRA (*C*).